Title

Exploiting Electron Magnetron Motion in a Penning-Malmberg Trap to Measure Patch Potentials, Misalignment, and Magnetic Fields

Author

Christensen, Andrew Jordan

Publication Date

2024

Peer reviewed|Thesis/dissertation

Exploiting Electron Magnetron Motion in a Penning-Malmberg Trap to Measure Patch Potentials, Misalignment, and Magnetic Fields

By

Andrew Christensen

A dissertation submitted in partial satisfaction of the

requirements for the degree of

Doctor of Philosophy

in

Physics

in the

Graduate Division

of the

University of California, Berkeley

Committee in charge:

Professor Joel Fajans, Chair
Professor Jonathan Wurtele
Professor David Attwood

Spring 2024

Abstract

Exploiting Electron Magnetron Motion in a Penning-Malmberg Trap to Measure Patch Potentials, Misalignment, and Magnetic Fields

by

Andrew Christensen

Doctor of Philosophy in Physics

University of California, Berkeley

Professor Joel Fajans, Chair

A sequence of electron clouds is extracted from an electron plasma reservoir. These clouds are highly reproducible and their $\mathbf{E}\times\mathbf{B}$ drift motion is nearly identical to that of a single particle, making them useful for measurements of electric and magnetic fields. First, by weakening the trapping potential confining the clouds we observe that they move off-axis, and we use this to measure the electric field due to patch potentials. Next, we measure the total charge of these clouds using small shifts in their magnetron frequencies. The misalignment between the trap electrodes and the external magnet is measured by imaging the clouds from different axial locations in the trap. By combining electron cyclotron resonance with the patch potential measurement procedure, we can measure the magnetic field strength up to a millimeter away from the trap axis. Finally, a new magnetometry technique called electron magnetron phase imaging (EMPI) is used to measure the rapidly changing magnetic field involved in observing the effect of gravity on antihydrogen. In EMPI, the magnetron frequency is measured precisely, and then we observe small changes to the magnetron frequency as the magnetic field decreases. In the process of analyzing the experimental data from each of these measurements, subtleties in the motion of electron clouds are revealed. Some of these measurement techniques help us to understand systematic errors in the ALPHA collaboration's test of the weak equivalence principle. Other techniques are used to inform experimental procedures and help explain the behavior of ALPHA's Penning-Malmberg traps. Most of these ideas could be applied to many Penning-Malmberg traps, provided that they have the ability to image charged particles. Unknown magnetic fields, patch potentials, and misalignment pose difficulties for many experiments, so implementing these cloud-based measurements could benefit other research groups.

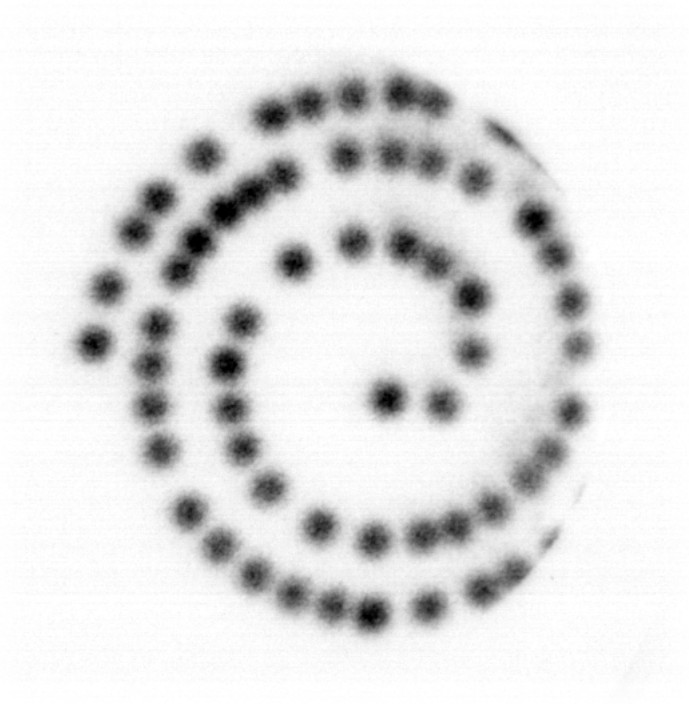

Contents

Acknowledgements

I thank Anke Stöltzel for three years of partnership in physics, alpinism, and life. I look forward to the coming years together in Berkeley. There were times when my work led to odd sleep schedules and stress, and in those times Anke was a source of support and joy.

I am deeply grateful for eight years of support from my advisor, Prof. Joel Fajans. Joel has mentored me since my third year of undergraduate—when I was, frankly, completely useless as a researcher. He afforded me an incredible learning experience by sending me to CERN for two summers as an undergraduate, and then for three years as a Ph.D. student. Being in different continents, Joel and I certainly didn't communicate every day, but when we did meet, Joel provided incredibly insightful solutions to challenges I was struggling with.

Prof. Jonathan Wurtele did an excellent job getting me through the final stages of my Ph.D. Jonathan has also mentored me since my undergrad, and I have benefited from his insights on my projects.

I thank the ALPHA collaboration for giving me the opportunity participate in the ALPHA-g measurement and for three years of fruitful teamwork. I am particularly grateful for the experimental time allocated to the ideas described in this thesis. I wish to acknowledge those who were involved in designing and constructing the ALPHA-g apparatus. This thesis presents measurement techniques that were not anticipated in the design of the experiment. These techniques were only possible because ALPHA-g is a precisely designed experiment with powerful controls and a plethora of diagnostic tools.

Prof. William Bertsche was consistently supportive of my ideas; he frequently advocated for them and provided useful input. Will's Ph.D. student Jaspal Singh has had success extending and improving on techniques described in this thesis, and I am excited to see how that work develops.

I thank Dr. Chris Ørum Rasmussen for enlightening discussions about the work in this thesis and about the ALPHA-g measurement. Chris' holistic understanding of the ALPHA experiment was critical for completing the ALPHA-g measurement. Chris also dedicated significant time explaining the underlying physics of ALPHA to me when I was an undergrad.

Dr. Eric Hunter has had significant influence on my path as a physicist. My first real research experience was analyzing the data Eric produced in his implementation of reservoir ECR—I benefited tremendously from that opportunity. Most of the work presented in this thesis is an extension of Eric's reservoir technique. Sec. 4 was inspired by advice Eric gave me.

This work was supported by the DOE Office of Fusion Energy Sciences and the NSF-DOE Program in Plasma Science.

1 Introduction

This thesis describes a collection of measurement techniques using "electron clouds" consisting of a few thousand electrons trapped in a Penning-Malmberg trap. These techniques were developed to support the ALPHA experiment at CERN. During my time at CERN, the ALPHA collaboration was working on measuring the effect of gravity on antihydrogen [1], the so-called ALPHA-g experiment. From one perspective, the value of this work is that it contributed to the ALPHA's tests of fundamental physics—tests of the weak equivalence principle and CPT symmetry. Another perspective is that I have introduced five measurement tools that could be used in other Penning-Malmberg traps, possibly requiring some modification depending on the particles and measurement devices available. I prefer to think that this thesis shows that electron clouds are versatile tools, not limited to the applications I envisioned.

This work is preceded by the discoveries of two of my advisor's previous graduate students. Dr. Celeste Torkzaban found a way to prepare highly reproducible electron plasmas [2, 3]. Dr. Eric Hunter then used these reproducible plasmas as a "reservoir," extracting a sequence of smaller electron clouds from that reservoir for magnetic field measurements and for studies of cyclotron cooling in an electromagnetic cavity [4, 5]. In my time at ALPHA, I realized that the $\mathbf{E} \times \mathbf{B}$ drift motion of these clouds, also called the "magnetron motion," is highly reproducible. As this motion depends on the electric and magnetic field, it can be used to measure these fields. The main results of this thesis are the following five new applications for electron clouds:

1. Sec. 3 describes measurements of patch potentials, variations in the electrostatic potential along nominally conducting surfaces. These patch potentials seem to heat plasmas trapped in ALPHA's Penning-Malmberg traps, as shown in Sec. 4. This heating disrupts antihydrogen production. To varying extents, patch potentials probably disrupt all applications of Penning-Malmberg traps. Thus, this measurement tool might be useful for understanding experimental difficulties and systematic errors in other researchers' traps.

2. In Sec. 5, I use the motion of the clouds to measure the total charge of the clouds. These measurements help verify models of systematic errors on the other techniques.

3. Sec. 6 presents measurements of the misalignment between the electrodes and the external magnet of the Penning-Malmberg trap. Similar ways of measuring this misalignment have been used before at ALPHA and in other experiments, but the use of electron clouds allows more rapid data collection. This facilitated more detailed alignment measurements and helped to reveal subtle sources of error. Like measurements of patch potentials, this technique could be applied in any Penning-Malmberg trap with the ability to image charged particles.

4. Dr. Eric Hunter measured magnetic fields along the symmetry axis of a Penning-Malmberg trap using electron cyclotron resonance (ECR). ECR involves exciting the cyclotron motion of electrons in a cloud with microwaves [5]. In Sec. 7, I explain how ECR can be combined with the patch potential measurement technique to measure magnetic fields a few millimeters away from the symmetry axis.

5. In Sec. 8, I describe another technique, electron magnetron phase imaging (EMPI), for measuring the magnetic field 30 times per second with an accuracy of roughly 1 part in 10^4. This magnetometer was particularly useful for measuring the rapidly changing magnetic field necessary for observing the effect of gravity on antihydrogen [1]. Although this precision and measurement frequency is not particularly impressive among magnetometers used in experimental physics, the cryogenic, ultra-high vacuum, and cylindrically symmetric environment of the ALPHA experiment made most other solutions unviable.

These new measurement techniques give rise to observations that may be useful for the ALPHA experiment moving forward. The following are the most important inferences we can make from the results of the cloud-based measurements:

1. In Sec. 2, I show that there are three known sources of variability in the initial positions of clouds extracted from a reservoir. One of those sources, the "intrinsic magnetron," has proven difficult to fix, and I can only provide an unproven hypothesis about the underlying cause. Any improvement in this issue by future researchers will lead to radical improvement of all the other measurement techniques.

2. In Sec. 3, I show that the 1S–2S laser for antihydrogen spectroscopy causes charging on the trap walls, despite the fact that the walls are nominally conducting. I also show that when ALPHA-g was first constructed, some other unknown procedural error led to charging that prevented antihydrogen trapping when we first attempted the ALPHA-g measurement.

3. In Sec. 4, I give tentative evidence that positron temperatures in ALPHA-g are limited by the heat they gain from expanding, and that this expansion is caused by either misalignment or patch potentials. Reducing these issues is likely to enhance antihydrogen trapping in ALPHA-g.

4. In Sec. 6, I show that the misalignment between the Penning trap electrodes and the external magnet cannot be characterized by a single "misalignment angle." Rather, both structures are not perfectly straight.

5. In Sec. 7, off-axis ECR is used to measure a small misalignment between the ALPHA-g electrodes and one of the magnets used to trap antihydrogen. In the first observation of the effect of gravity on antihydrogen, this leads to a negligible systematic error. However, similar off-axis magnetometry will be needed in future iterations of the ALPHA-g measurement.

6. In Sec. 8, EMPI and ECR are used to investigate the behaviors of "persistent currents": long-lasting eddy currents that form when we change the magnetic flux through superconducting wires. These persistent currents are small compared to the nominal magnetic fields in the ALPHA-g experiment, but they are typically larger than the effect of gravity. For the first ALPHA-g measurement, eddy currents were symmetric enough that they did not pose a major issue, but any errors in this symmetry will need to be carefully measured to improve the precision of the next ALPHA-g measurement.

1.1 Frequency versus angular frequency convention

Before I proceed, it is necessary for me to explain the atypical convention I use to describe frequencies. Nearly the entire thesis is concerned with circular motion, so this convention is applied often. The system used in this thesis is unambiguously better than the standard system taught to undergraduate students and asserted by the SI system. In SI, the unit of frequency is Hz and the unit of angular frequency is rad/s [6]. However, it is asserted that both of these units are equal to $1/s$ so that we can still write things like $\sin(\omega t)$ rather than $\sin[\omega t/(\text{rad})]$.

In my system, frequency and angular frequency are the same quantity, and I will call them simply "frequency." I will never define two different symbols, one being the frequency and one being the angular frequency. My "frequency" corresponds more closely to what most people call "angular frequency." As such, I will typically use the symbol ω with a subscript to prevent confusion for readers who have not read this note. For example, I might say "the cyclotron frequency is $\omega_c = q|\mathbf{B}|/m$."

In my system the units of frequency are $1/s$. However, frequency can also be reported in terms of Hz, which is equal to $2\pi/s$, or $1\,\text{cyc/s}$. It is uncommon that I will use the symbol rad—this will only happen in the axis labels of plots to remind the reader that an angle is being plotted. $1\,\text{rad}$ is simply equal to 1, or $1\,\text{cyc}/2\pi$. If I want to report the number one would type in a signal generator, what most people would call the ordinary frequency, I will report the frequency in Hz. For example, I might say "the cyclotron frequency for an electron at $|\mathbf{B}| = 1\,\text{T}$ is $28\,\text{GHz} = 1.8 \times 10^{11}/s$." In this system, we do not need two different symbols for Planck's constant. Although this thesis never refers to Planck's constant outside of the introduction, in this system one could write $\hbar = 1.055 \times 10^{-34}\,\text{Js} = 6.626 \times 10^{-34}\,\text{J/Hz}$.

1.2 The Penning-Malmberg trap

There are two commonly used types of traps for charged particles: the Penning trap and the Paul trap. The ALPHA experiment uses a variant of the Penning trap called a Penning-Malmberg trap, or "annular Penning trap." The original Penning trap consisted of an external magnetic field of magnitude B pointing in the $\hat{z}$ direction and electrodes specifically shaped to form an electrostatic potential given by:

$$V(z, r) = -k_2 \left(z^2 - \frac{r^2}{2} \right), \tag{1.1}$$

where k_2 is the "trap depth constant." I have chosen to write $-k_2$ instead of k_2 because most of this thesis involves trapped electrons, and electrons are attracted to maxima of the electrostatic potential. Unfortunately, it is not possible to achieve an electrostatic potential maximum in all three spatial directions in free space. Instead, the electrons are prevented from escaping in the $\hat{r}$ direction by the magnetic field—if an electron has some $\hat{r}$ velocity, the $\hat{z}$ magnetic field will curve the particle's trajectory back toward the center of the trap. Instead of shaping the electrodes to exactly achieve the potential given by Eq. 1.1, the Penning-Malmberg variant of the trap uses a "stack" of cylindrical electrodes (36 electrodes in ALPHA-g). In this geometry, charged particles can be transferred from one electrode to the next. This way, the ALPHA experiment can simultaneously have positrons confined

with a negative voltage on one electrode and electrons or antiprotons confined with a positive voltage on another electrode.

1.2.1 Single particle motion

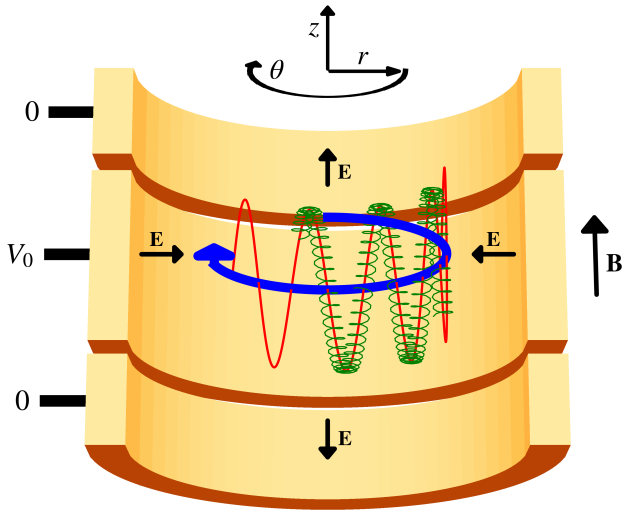

Figure 1.1: A cartoon of the motion of a single electron in a Penning-Malmberg trap. The gold electrodes are shown in the background. The blue circle indicates the magnetron motion. The red line shows the magnetron motion plus the axial bounce motion. The green line shows the full motion of the particle including cyclotron motion.

Penning-Malmberg traps can be used to trap individual charged particles or they can be used to trap larger plasmas consisting of up to hundreds of millions of particles. It is elucidating to derive how a single charged particle moves in this trap. Despite abandoning the original Penning trap designed specifically to create the electrostatic potential given by Eq. 1.1, when a charged particle is trapped in a Penning-Malmberg trap, it still is confined near an electrostatic potential maximum in z. Typically it is also close to the trap's symmetry axis ($r \ll R_w$, where R_w is the radius of the electrodes). Thus the trapping potential can still be approximated by Eq. 1.1. The equations of motion are then:

$$\ddot{z} = -2\frac{e}{m}k_2 z, \tag{1.2}$$

$$\ddot{x} = -\frac{e}{m}\left(-k_2 x + \dot{y}B\right), \tag{1.3}$$

$$\ddot{y} = -\frac{e}{m}\left(-k_2 y - \dot{x}B\right). \tag{1.4}$$

The equation of motion for z can be solved immediately, giving harmonic motion with a frequency $\omega_z = \sqrt{2ek_2/m}$ called the "bounce frequency." The other two equations can be solved by defining $v = x + iy$, giving:

$$\ddot{v} = \frac{e}{m}\left(k_2 v + i\dot{v}B\right). \tag{1.5}$$

Inserting $v = a\exp(i\omega t)$, we get:

$$\omega^2 - \omega_c\omega + \frac{1}{2}\omega_z^2 = 0, \tag{1.6}$$

where $\omega_c = qB/m$ is the cyclotron frequency. This gives rise to two frequencies of transverse motion (in the x, y plane), called the "modified cyclotron frequency" ω_+ and the "magnetron frequency/rotation frequency" ω_-.

$$\omega_\pm = \frac{\omega_c \pm \sqrt{\omega_c^2 - 2\omega_z^2}}{2}. \tag{1.7}$$

In all of the traps discussed in this thesis, the magnetic field is at least 1 T, so the cyclotron frequency for electrons is of order $1.8\times10^{11}/s = 28\,\text{GHz}$. The electrodes have a radius of 2 cm and they can be charged up to 150 V. Thus the order of magnitude for k_2 is $(150\,\text{V})/(2\,\text{cm})^2 \sim 4\times10^5\,\text{V/m}^2$, and the order of magnitude for the bounce frequency is $4\times10^8/\text{s}$. Thus it is valid to approximate $\omega_z \ll \omega_c$, giving

$$\omega_+ \approx \omega_c - \omega_-, \tag{1.8}$$

$$\omega_- \approx \frac{\omega_z^2}{2\omega_c} = \frac{k_2}{B}. \tag{1.9}$$

From here on, ω_- will be replaced with ω_r (r for "rotation").

Another perspective on the motion of a single particle in the Penning-Malmberg trap is that because $\omega_c \gg \omega_z \gg \omega_r$, the motion of our electrons is well-described by the guiding center approximation. In this approximation, the electrons perform ordinary inertial movement in the direction parallel to the magnetic field, and to zeroth order they execute a circular motion of frequency ω_c in the transverse plane. This circular motion "$\mathbf{E}\times\mathbf{B}$ drifts" with a velocity $\mathbf{E}\times\mathbf{B}/|\mathbf{B}|^2$. Inserting Eq. 1.1 for the electric field, we get the $\mathbf{E}\times\mathbf{B}$ drift velocity $\hat{\theta}rk_2/B$. This is circular motion with a frequency k_2/B; the guiding center approximation recovers the results of the exact solution to the equations of motion. The motion with frequency ω_r is reinterpreted as a circular $\mathbf{E}\times\mathbf{B}$ drift of the guiding center. The motion of a single particle is depicted in Fig. 1.1. However in Fig. 1.1 the length and time scales are completely wrong. Typically electrons in ALPHA's traps have $\omega_c \sim 500\omega_z \sim 500\omega_r$. The magnetron radius used in this thesis is up to about 2 mm versus the trap wall radius $R_w = 2\,\text{cm}$. The electrons typically have energies of order $(100\,\text{K})k_B$, which gives them a bounce motion length of order $100\,\mu\text{m}$ and a cyclotron radius of order 30 nm. Using these numbers would not produce a very compelling picture.

1.2.2 Plasma equilibrium

In this thesis I will also discuss trapped "nonneutral plasmas," usually composed of electrons, but occasionally composed of positrons or antiprotons. Like ordinary plasmas, when there is sufficient density, these nonneutral plasmas can "shield out" electric fields. However, because the plasma is charged, the electric field cannot be zero throughout the plasma. In the guiding center approximation, charges can move freely along the magnetic field, but their

motion transverse to the magnetic field is governed by $\mathbf{E} \times \mathbf{B}$ drift. Thus, when there are enough electrons to form a plasma, the electrons move such that they remove the electric field pointing along the magnetic field, but the transverse component remains. More precisely, when the Debye length ($\lambda_D = \sqrt{\epsilon_0 k_B T/ne}$, where n is the electron number density) exceeds the length scale of the distribution of electrons, electric fields parallel to the magnetic field are shielded out.

To find the equilibrium charge distribution of such a plasma, we begin with the fluid equation of motion, defining $\mathbf{u}(r, \theta, z)$ as the fluid velocity and $n(r, \theta, z)$ as the electron number density [7]:

$$mn\left(\dot{\mathbf{u}} + \mathbf{u} \cdot \nabla \mathbf{u}\right) = -en\left(-\nabla V + \mathbf{u} \times \mathbf{B}\right) - \nabla p. \tag{1.10}$$

In equilibrium $\dot{\mathbf{u}} = 0$. Further, we assume that the number density and the fluid velocity are only functions of r and z, reflecting the cylindrical symmetry of the trap. In equilibrium, the fluid velocity should resemble that of a rigid rotor: $\mathbf{u} = \omega_r r\hat{\theta}$. Our plasma will have a finite extent in r and z, so in equilibrium the fluid velocity in those directions must be zero. Then if different radial layers of plasma had different rotation rates, viscous effects would damp these differences [7]. A cartoon of this expected solution is shown in Fig. 1.2. Finally the pressure is taken to be that of an ideal gas $p = nk_BT$ With these assumptions, the z component of Eq. 1.10 is:

$$0 = en\nabla V - \frac{\partial n}{\partial_z} k_B T, \tag{1.11}$$

which is solved by:

$$n(r, z) = N(r) \exp\left[\frac{eV(r, z)}{k_B T}\right]. \tag{1.12}$$

The radial component of the fluid equation is :

$$mn\left(-\omega_r^2 r\right) = -en\left(-\frac{dV}{dr} + r\omega_r B\right) - k_B T \frac{dn}{dr}. \tag{1.13}$$

Inserting Eq. 1.12 into Eq. 1.13, we get:

$$m\omega_r^2 rN = m\omega_c\omega_r rN + k_B T \frac{dN}{dr}. \tag{1.14}$$

This is solved by:

$$N(r) = n_0 \exp\left[-\frac{(\omega_c\omega_r - \omega_r^2)m}{2k_B T} r^2\right], \tag{1.15}$$

or the full equation for n is:

$$n(r, z) = n_0 \exp\left[\frac{eV(r, z) - (\omega_c\omega_r - \omega_r^2)mr^2/2}{k_B T}\right]. \tag{1.16}$$

To trap electrons, we choose a V which becomes more negative as we move away from the axial trap center so n decreases with increasing $|z|$. This necessarily means the potential becomes more positive as we move away from $r = 0$, but as long as $(\omega_c\omega_r - r^2 m)r^2 > eV(r)$,

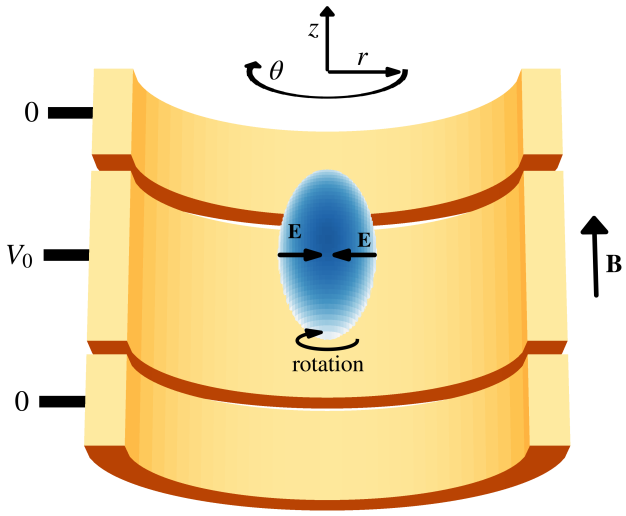

Figure 1.2: A cartoon of a cold electron plasma equilibrium in a Penning-Malmberg trap. An electric field points inward throughout the plasma, causing a uniform rotation. Only the radius of the plasma is exaggerated here. Our plasmas typically have a radius of around 1 mm versus a trap radius of 2.2 cm.

we will also have radial confinement.

Throughout this thesis, I investigate the charge distributions of plasmas using an "equilibrium solver." These equilibrium solvers find a self-consistent solution to Eq. 1.16—keep in mind that for a plasma $V(r, z)$ is affected by n through Poisson's equation. These equilibrium solvers discretize r and z into a grid, recording the plasma density $n(r_i, z_j)$ at each gridpoint (i, j). The solver begins by setting $V(r_i, z_j)$ to the potential set by the electrodes. It then applies Eq. 1.16 to find $n_0(r_i, z_j)$. Then we update our estimate of the potential, treating each gridpoint as a uniformly charged cylindrical shell of charge density $n(r_i, z_i)$ (See the appendix for the analytic potential of such a shell). This process iterates until convergence. In each step, we cannot just replace the old guess n_k with the new guess given by Eq. 1.16 n'_{k+1}. Rather, we must iterate n like $n_{k+1} = n_k(1 - \epsilon) + n'_{k+1}\epsilon$. The solver exhibits a bifurcation if ϵ is too large, oscillating between two or more incorrect charge distributions.

A confinement theorem [8] states that if the cylindrical symmetry of the trap is not broken, the mean-square charge radius of a plasma is conserved ($\propto \sum_i r_i^2$, where r_i is the radial coordinate of particle i). Additionally, when we image our plasmas, we observe the z-integrated charge distribution, giving a good measure of this conserved mean square radius. Thus it is more convenient if the equilibrium solver takes as parameters the total charge and the mean square charge radius of a plasma rather than the total charge and the rotation frequency ω_r. Therefore most of the equilibrium solvers used in this thesis iterate the above process, adjusting a guess for ω_r until the mean square charge radius matches the desired value. An example of a solved plasma equilibrium is shown in Fig. 1.3

Much like an ordinary plasma, when the temperature of an electron plasma goes to zero, the density becomes constant throughout the plasma. Of course, a purely electron plasma cannot flatten the electrostatic potential like a neutral plasma could. Instead, by noticing that Eq. 1.16 takes the form $\exp(eV_{\text{eff}})$, we realize that a cold electron plasma flattens the

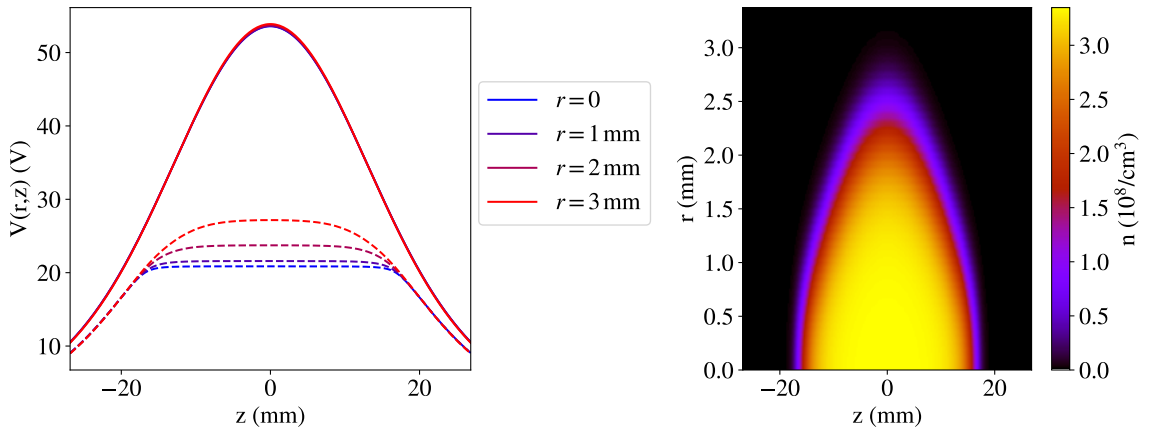

Figure 1.3: An example of the output of a plasma equilibrium solver. On the left, the potential versus z is plotted for four different radial positions. The solid lines are the potential created by the electrodes. The dashed lines are the potential including the influence of the plasma. On the right, the plasma density is plotted versus r and z. The plasma is confined by a 1 T axial magnetic field and a 2 cm long, 2 cm radius electrode at 100 V in an otherwise grounded infinitely long cylinder. The plasma has a root mean square radius of 1.5 mm, a total charge of 100 Me^-, and a temperature of 6000 K. The solved rotation frequency is 3.04×10^6/s.

"effective potential," given by:

$$V_{\text{eff}} = V(r,z) - \frac{m}{2e}(\omega_c\omega_r - \omega_r^2)r^2. \tag{1.17}$$

It is instructive then to discuss what happens when $T \to 0$ when the effective potential is fully flattened and the density is constant. The electrostatic potential is flattened in z, and because $\nabla^2 V = en_0/\epsilon_0$, the electrostatic potential in r must be $enr^2/4\epsilon_0$. Inserting this into the effective potential, we get:

$$\frac{en}{4\epsilon_0} = \frac{m}{2e}(\omega_c\omega_r - \omega_r^2). \tag{1.18}$$

This quadratic equation gives rise to a maximum possible charge density called the "Brillouin limit" [7]. However, at ALPHA we always operate in the limit where $\omega_r \ll \omega_c$, which gives $\omega_r = en/2\epsilon_0 B$. Like when we investigated single particle motion, we can arrive at the same answer by considering the $\mathbf{E} \times \mathbf{B}$ drift of an electron within the plasma.

The flattened on-axis electrostatic potential created by a cold charged plasma is called the "space charge potential," which is an important observable parameter of the plasma. For example, when we release a plasma from the trap, we lower the confining potential on one side of the plasma. Electrons begin to escape the plasma when the difference between the confining potential and the space charge potential is comparable to $k_B T$. Thus it is helpful to have a formula for the space charge potential. Such a formula can be derived in the special case of a plasma which is very long compared to the trap wall radius $l \gg R_w$. This plasma is confined axially by applying a positive voltage to two electrodes on either

side it, and the electrodes in between are grounded. If the plasma is very cold, it will simply be a long cylinder of radius r_p. Then the potential throughout space will be

$$V(r) = \begin{cases} \frac{nr_p^2 e}{2\epsilon_0}\left[\ln\left(\frac{r_p}{R_w}\right) + \frac{(r^2 - r_p^2)}{2r_p^2}\right] & r < r_p \\ \frac{nr_p^2 e}{2\epsilon_0}\ln\left(\frac{r}{R_w}\right) & r > r_p \end{cases} \tag{1.19}$$

Evaluating this equation at $r = 0$ gives a convenient formula for the space charge potential of long plasmas. We often inappropriately apply this formula to plasmas whose length is comparable to R_w for back of the envelope calculations.

1.3 The ALPHA experiment

The ALPHA collaboration forms trapped antihydrogen by mixing an antiproton plasma with a positron plasma [9]. We then measure the properties of these antihydrogen atoms as a test of fundamental symmetries of nature. Because of CPT symmetry, antihydrogen should have the same mass, total charge (0), lifetime (infinite), and spectrum as ordinary hydrogen. ALPHA's most precise test of CPT symmetry is the measurement of the 1S–2S two-photon transition [10, 11, 12]. Other spectroscopy results include the measurement of microwave transitions between the Zeeman sublevels of the 1S state [13], and the 1S–2P transition [14, 15], which was then used to laser cool the antiatoms [16]. The ALPHA collaboration has also tested the charge neutrality of antihydrogen [17].

The patch potential measurements described in Sec. 3 were initially motivated by the observation that the 1S–2S spectroscopy experiment would degrade over time. Most of the other measurements described in this thesis were in service of a new measurement undertaken by the ALPHA collaboration, the measurement of the effect of gravity on antihydrogen, which will be described in the next section.

A diagram of the ALPHA experiment is shown in Fig. 1.4. The two ingredients of antihydrogen are antiprotons and positrons. The only source of low energy antiprotons in the world is CERN's Antimatter Factory facility. A proton beam impacts a metal target, producing a variety of particles. Antiprotons are collected from this collision point and slowed to an energy of 5 MeV in the antiproton decelerator (AD) [18]. Since 2021, the antiprotons have been further slowed to 100 keV in the ELENA ring [19]. The ALPHA experiment traps these antiprotons by sending them through a $\sim 1\,\mu$m thick "degrader foil." Many of the $\sim 10^7$ antiprotons delivered to ALPHA annihilate against ordinary baryons in the degrader, but about 5×10^5 of them exit the other side with an energy under 5 keV. The degrader is inside the solenoid for ALPHA's first Penning-Malmberg trap, the "catching trap." Thus, the antiprotons that get through the degrader are confined radially by the magnetic field. Axially, the antiprotons fly through the catching trap until they reach an electrode energized to 5 kV. They bounce off the electrostatic potential created by this electrode, but before they reach the degrader again, another electrode is quickly energized to 5 kV, blocking their escape and trapping the antiprotons inside the catching trap.

There are four total Penning-Malmberg traps in the ALPHA experiment, which are listed below:

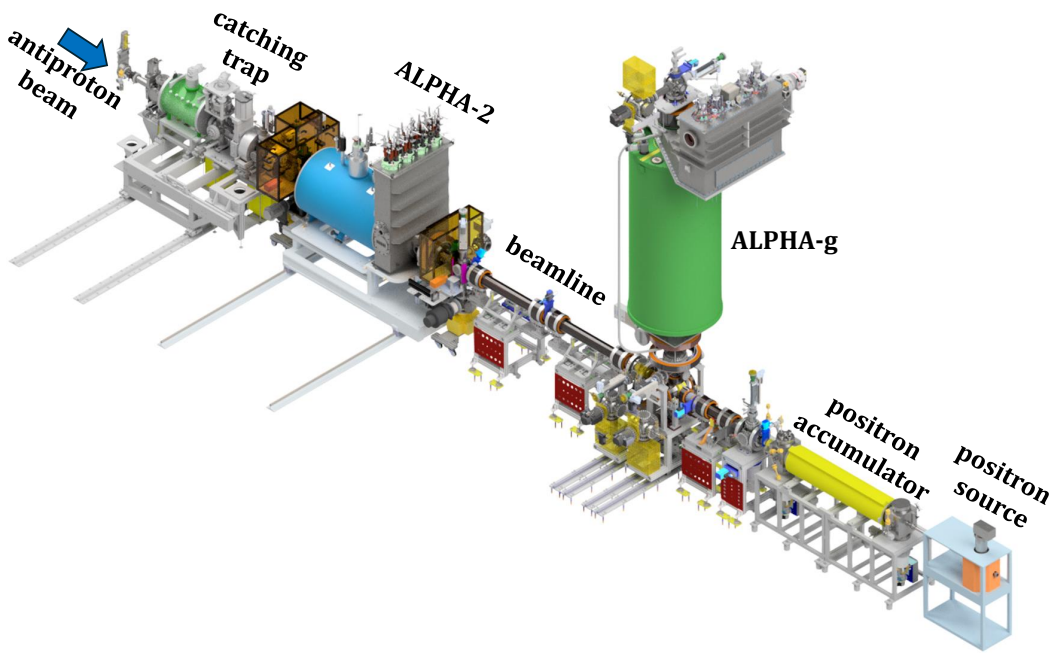

Figure 1.4: A rendering of the ALPHA experiment. This figure was created by Prof. S. A. Jones, another member of the ALPHA collaboration (used with permission).

1. The catching trap is used to catch the antiproton beam and to prepare a cold plasma of antiprotons to be sent to the two fundamental physics experiments, ALPHA-2 and ALPHA-g. The antiprotons are initially caught between two 5 kV electrodes. An electron plasma is also present between those electrodes. The antiprotons collide with the electrons and eventually cool into a mutual plasma consisting of electrons and antiprotons. This process is facilitated by the phenomenon of cyclotron cooling, whereby the acceleration associated with cyclotron motion causes Larmor radiation, allowing the electrons to radiate away the energy they recieve from the antiprotons over a timescale of a few seconds. Eventually, the electrons are removed, leaving a cold $\mathcal{O}$(100–1000 K) antiproton plasma which can be launched into the beamline toward ALPHA-2 or ALPHA-g.

2. The positron accumulator is a "Surko-style accumulator." [20, 21] A radioactive source is placed behind a solid Neon "moderator." The moderator behaves similarly to the degrader foil for antiprotons. It destroys some of the positrons, but others pass through and emerge on the other side with a lower energy. The accumulator is filled with a diffuse nitrogen gas. The positrons collide with the nitrogen, sometimes losing kinetic energy in the process, allowing them to be collected in the trapping potential created by a negatively biased Penning-Malmberg trap electrode. There is additional complexity in how the electrode radius, gas density, and voltages vary with distance from the moderator.

3. The ALPHA-2 experiment is the first of two fundamental physics experiments. The general structure of these experiments will be explained below. The ALPHA-2 ex-

periment has laser ports crossing diagonally through the Penning-Malmberg trap that can be used to excite transitions in antihydrogen. It also has a Fabry-Pérot cavity to enhance the circulating power of the 1S–2S laser.

4. ALPHA-g is the second fundamental physics experiment. It is oriented vertically—the magnetic field points up and the Penning-Malmberg electrode symmetry axis is vertical.

Positrons and antiprotons are delivered to the two antihydrogen experiments, ALPHA-g and ALHPA-2, through "magnetized beamlines" [22]. These beamlines consist of several normal conducting magnets whose current can be ramped to create a magnetic field line connecting the Penning-Malmberg traps that we want to send particles between. Antiprotons from the catching trap or positrons from the positron accumulator follow these field lines to either ALPHA-2 or ALPHA-g.

In addition to antiprotons and positrons, the catching trap, ALPHA-2, and ALPHA-g make extensive use of electron plasmas. These plasmas are prepared by energizing a hot cathode electron gun which points toward the Penning-Malmberg trap from 1–2 m away in the magnetized beamline. The electrons from the hot cathode stream into the trap, and a positive voltage is slowly applied to an electrode to gather the electrons into a trapping potential. The electron guns are located on movable "sticks." These sticks contain several pieces of equipment, and they extend to place one of these pieces of equipment in front of the entrance of a Penning-Malmberg trap. A cartoon of one of these sticks is shown in Fig. 1.5. For this thesis, another piece of critical equipment on the movable sticks is an microchannel plate (MCP)/phosphor screen/CCD camera detector. The MCP is an electron multiplier which produces a cascade of electrons whenever a charged particle enters one of its microscopic channels. This cascade of electrons collides with the phosphor screen, which glows. A CCD camera located outside of the vacuum chamber takes a picture of the phosphor screen. When a plasma is released from the Penning-Malmberg trap, the particles follow magnetic field lines toward the MCP. Thus their positions on the MCP reflect the transverse (x, y or r, θ) positions they had when they were inside the trap. In that sense, the MCP pictures are simply pictures of the plasma from the perspective of an observer looking through the trap from the outside, except that MCP imaging is destructive.

ALPHA-2 and ALPHA-g have the same basic structure. A diagram of the ALPHA-g experiment is shown in Fig. 1.5. Both experiments contain a Penning-Malmberg trap superimposed with a magnetic minimum trap for antihydrogen [23]. The "magnetic minimum trap" is an arrangement of magnets which makes a local minimum in the magnetic field magnitude located in the center of the trap [24]. If an antihydrogen atom is formed near the center of the trap in a Zeeman sub-level which increases in energy with the strength of the magnetic field, it will be attracted to the center of the trap. At ALPHA, these traps only have a depth of about $0.5\,\mathrm{K}k_B \approx 40\,\mu\mathrm{eV}$ for a magnetic field difference of about 0.7 T between the center of the trap and the edge of the trap. The radial confinement is provided by an octupole magnet—windings that produce a current density of the form $\hat{z}\cos(4\theta)$ and a magnetic field of the form $r^3(\hat{\theta}\cos 4\theta + \hat{r}\sin 4\theta)$. When this magnetic field is added to the nominal 1 T magnetic field in the $\hat{z}$ direction for the Penning-Malmberg trap, we find that the magnetic field magnitude increases with r. The axial confinement is provided by two short solenoids—also called "mirror coils," which simply boost the z component of the

magnetic field near their centers. In addition to the mirror coils and the octupole magnet, both ALPHA-2 and ALPHA-g have "booster solenoids" in the same liquid helium cryostat, which aid in plasma preparation by boosting the magnetic field from 1 T to 2 T (actually 3 T in ALPHA-2).

Antihydrogen is formed by first holding a positron plasma near the center of one electrode with a negative voltage and antiprotons near the center of the adjacent electrode with a positive voltage. These electrode voltages are then brought closer togeter over the course of 1 s, and at some point the antiprotons are injected into the positron plasma, where the two particles combine to form antihydrogen [25]. We have hypothesized that the antiprotons come into thermal equilibrium with the positrons more quickly than they form antihydrogen, and there are far more positrons than antiprotons. Thus the positron temperature sets the typical energies of produced antihydrogen, despite the fact that a formed antihydrogen atom's momentum is determined by the antiproton's initial momentum. This plasma temperature is roughly 20 K in ALPHA-2 and 40 K in ALPHA-g. As a consequence, in ALPHA-2 twenty antihydrogen are trapped per "mixing" of about 3 million positrons and 100 thousand antiprotons. In ALPHA-g, this is about two antihydrogen trapped per mixing.

The outermost layer of ALPHA-2 and ALHPA-g is the external superconducting magnet of the Penning-Malmberg trap, which provides the 1 T axial magnetic field. This magnet is in a separate cryostat from the magnets that form the magnetic minimum trap. Between the external magnet and the inner cryostat is a particle detector which detects the charged pions that are formed when an antiproton collides with the trap walls—in the end all of ALPHA's measurements of the properties of antihydrogen involve observing how many antiprotons collide with the trap walls when we subject the trapped antihydrogen to a measurement procedure. Inside of the detector, the superconducting magnets for the magnetic minimum trap are immersed in liquid helium. The electrodes for the Penning-Malmberg trap are inside those magnets. They are not immersed in liquid helium directly, but they are at 4 K because they are in thermal contact with the stainless steel cylinder which holds the helium. These cold trap walls are critical for producing cold positron plasmas, and they help achieve ultra-high vacuum conditions, which is necessary for having long lifetimes for the antimatter particles.

1.4 The ALPHA-g measurement

The ALPHA-g experiment provided the most direct evidence to-date that antihydrogen is gravitationally attracted to the Earth [1]. This measurement was performed by ramping down the mirror coils and observing which direction the antihydrogen escaped the trap with the particle detector. The mirror coil on the bottom of ALPHA-g is called "mirror A." The mirror coil on the top is called "mirror G." There are five other mirror coils between mirrors A and G that are intended for use in a future measurement. However, the experiment is not as simple as shutting off the magnets in an instant and observing all the antihydrogen hitting the bottom of the vacuum chamber. Despite its meager energy of $0.5\,\mathrm{K}k_B$, the antihydrogen velocity is of order 100 m/s, and it bounces between the top and bottom of the trap several hundred times per second. Thus, even if it was possible to shut off the mirror coils quickly compared to this bounce frequency, this would only result in the antihydrogen rapidly escaping through the top and bottom of the trap in equal numbers. Instead, we

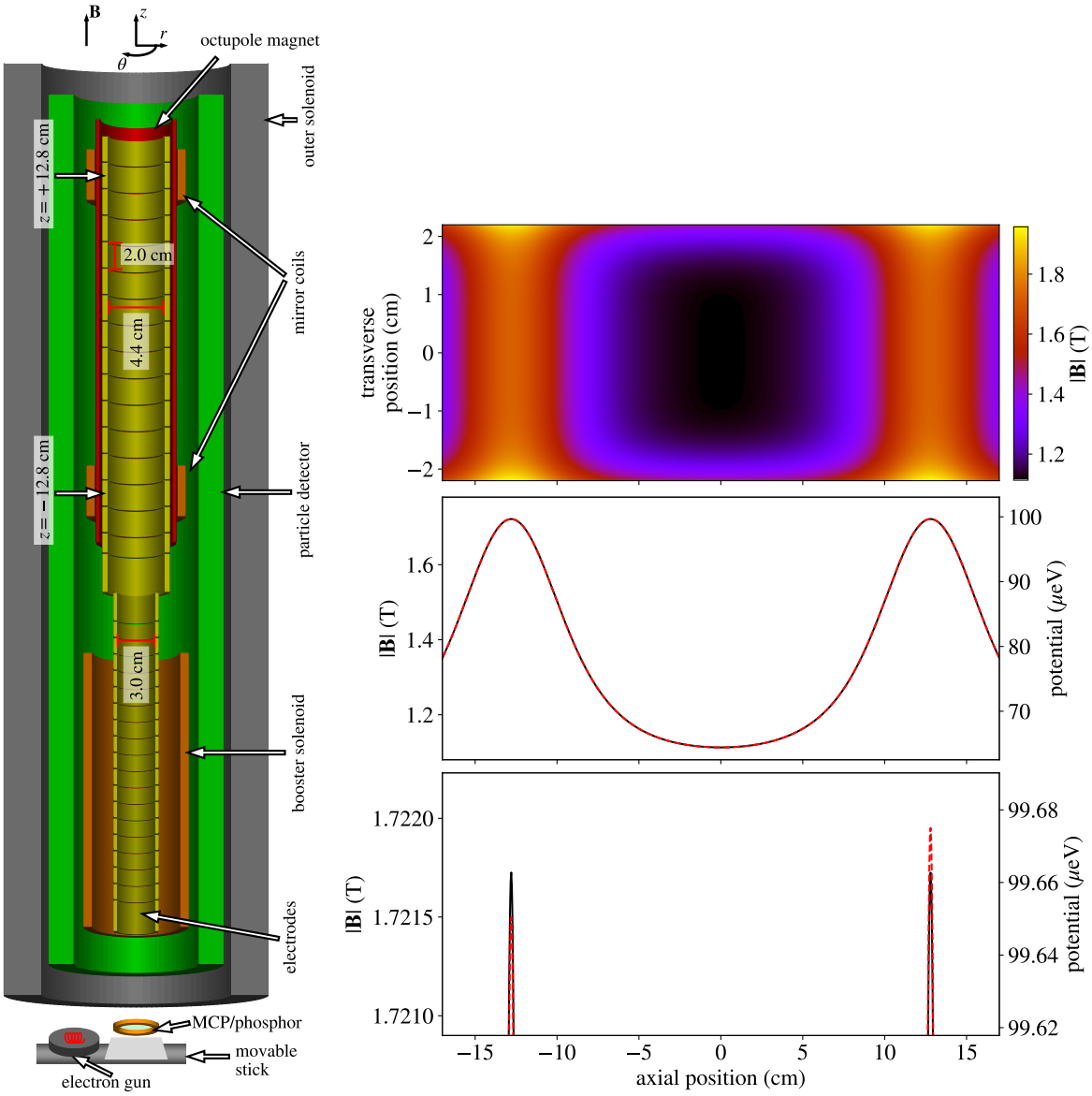

Figure 1.5: Left—a diagram of the ALPHA-g experiment with various components labelled. The diagram is not to scale, and some details are left out. For example the outer solenoid and the detector actually extend well beyond the top of the upper mirror coil, and the movable stick is much further away than depicted here. Upper right—the magnetic field magnitude is plotted versus transverse and axial position before the beginning of the mirror coil rampdown used to release antihydrogen. Middle right—the on-axis magnetic field is plotted versus axial position in black. The red dashed line is the on-axis potential perturbed by the effect of gravity. In this case, the bias is zero—the magnetic field is precisely equal on the top and the bottom of the ALPHA-g trap. Lower right—the same plot as the middle right, but zoomed in to perceive the effect of gravity.

decrease the current in the mirror coils over the course of 20 s. An antihydrogen atom escapes the trap whenever the potential barrier on either the top or the bottom is below

its energy. The effect of gravity on the potential is given by mgh, and the effect of the magnetic field on the potential is given by $\mu_B|\mathbf{B}|$, where μB is the Bohr magneton, a good approximation for the magnetic moment of the groundstate antihydrogen atom. Thus with $h = 25.6\,\mathrm{cm}$, the effect of gravity on antihydrogen is expected to be equivalent to a magnetic field difference of 0.45 mT. To do a detailed measurement, we vary the difference in on-axis magnetic field between the bottom and the top of the trap. This quantity is called the "bias." We can find a "balance point," where half the antiatoms escape up and half escape down, which occurs when the effect of gravity is compensated by the magnetic field in the center of mirror A being 0.45 mT higher than that of mirror G. We can also keep the magnetic field at the top and the bottom of the trap precisely equal, and we would expect to observe more antihydrogen atoms falling down than up. Fig. 1.5 depicts a model of the magnetic field used to perform the ALPHA-g measurement.

Consider the antihydrogen atoms to be classical particles bouncing between two "square" potential barriers which are lowered over time while maintaining a small bias. In this simple 1–D model, it would seem that this measurement technique is extremely powerful. If an antihydrogen atom traverses the length of the trap in the time that it takes for the potential barrier to decrease by an amount equal to the difference in potential between the two barriers, that antihydrogen atom is guaranteed to escape in the direction which has a lower barrier. Ramping down the mirror coils in 20 s, and taking the orbit frequency to be 200 Hz, we get that all antihydrogen are guaranteed to escape down as long as the potential barrier is larger than 0.088 mT.

Unfortunately, the universe is not one dimensional. An antihydrogen atom can be on an orbit where it is further off-axis when it approaches the bottom of the trap than when it approaches top of the trap, and since the magnetic field of the mirror coils and the octupole magnet increases further off axis, this atom is very likely to escape up not down regardless of the bias. Alternatively, an antihydrogen atom could have a larger r velocity component than z. It might have enough energy to escape the trap, but not enough energy directed in the $\hat{z}$ direction. Perhaps this antiatom suddenly hits some feature of the magnetic trap that deflects it either upward or downward, and it escapes in a random direction rather than the direction with the lower potential barrier [26]. Thus instead of observing all antihydrogen falling in the direction with a lower total potential barrier, we observe a fraction the antiatoms going in either direction which varies continuously with the bias. Fig. 1.6 shows the final result of the ALPHA-g experiment, the fraction of antiatoms that escaped the trap downward versus the bias.

The ALPHA-g experiment relied heavily on precise magnetometry. To release the antihydrogen, the magnetic field produced by the mirror coils near their centers decreased from 0.7 T to 0.01 T in 20 s. Thus, including the outer solenoid, the total magnetic field decreased from 1.7 T to 1.0 T. Throughout this time, a magnetic field difference on the order of 0.00045 T needed to be maintained with high precision. A slightly different current was applied to the two mirror coils, not only to produce a bias but also to compensate for construction errors. In order to choose these currents and to verify that they had the intended results, a variety of magnetometry measurements were performed.

The magnetic field measurements for ALPHA-g were performed with ECR and EMPI, two techniques that make use of electron clouds. Precise determinations of the bias were done with ECR measurements in static magnetic fields (unchanging magnet currents) [5].

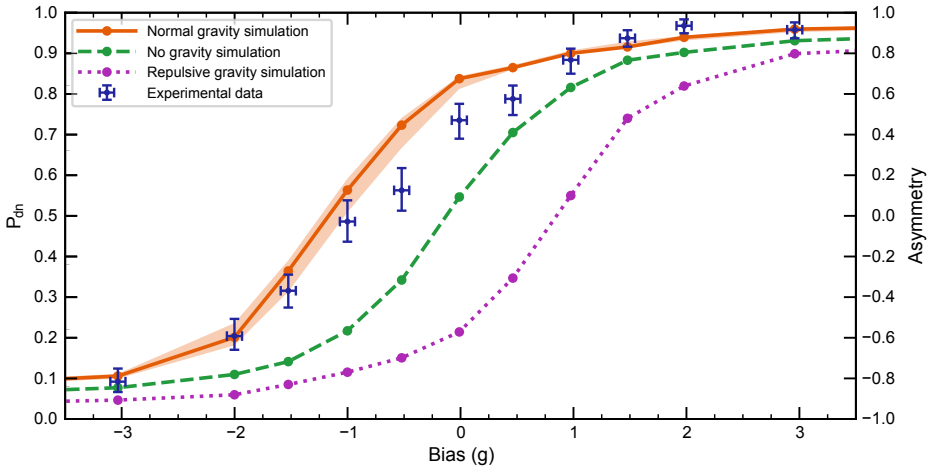

Figure 1.6: The fraction of antihydrogen atoms escaping the ALPHA-g trap downward is plotted versus the magnetic bias. The experimental data is shown with blue dots. The horizontal error bars convey systematic errors relating to the determination of the bias with magnetometry. The vertical error bars are statistical errors. The experimental data is compared to simulations assuming antihydrogen is affected by ordinary gravity, no gravity, and gravity repelling the antihydrogen from Earth. The error bar on the ordinary gravity simulation represents errors associated with modelling the magnetic field off-axis using only direct measurements of the on-axis magnetic field. This figure is taken from Ref. [1]. More detail is available in the original paper.

In this thesis, I will not describe these ECR bias measurements; this can be found in the original paper [1] and likely in Ph.D. student Adam Powell's upcoming thesis. I will describe off-axis ECR measurements, but ultimately off-axis ECR was not necessary for analyzing the ALPHA-g result because the systematic error it detected was negligibly small. EMPI was used to verify that the magnetic field behaved as expected during dynamic magnet ramps (see Sec. 8). EMPI was also useful for observing the qualitative behaviors of so-called "persistent currents" because EMPI could be performed more quickly than ECR.

1.5 Electron clouds

In Sec. 1.2, I showed how a single particle moves in a Penning-Malberg trap and I discussed the equilibrium state of a plasma consisting of many charged particles. These two situations can be seen as two limits of charge distributions. If there are very few charged particles, the electric field experienced by each particle will be dominated by the electric field created by the electrodes. If there are many charged particles, the electric field created by the charge distribution may dominate over the electrodes. The measurements described in this thesis are preformed with "electron clouds," typically containing $2\,\mathrm{k}e^-$—$10\,\mathrm{k}e^-$ (in Sec. 5 I will study larger clouds containing up to $150\,\mathrm{k}e^-$). These electron clouds typically have a root mean square charge radius of around $150\,\mu$m and a similar length, although the length strongly depends on the trapping potential. With these parameters, electron clouds are typically somewhere between the single particle regime and the plasma regime. Hence they

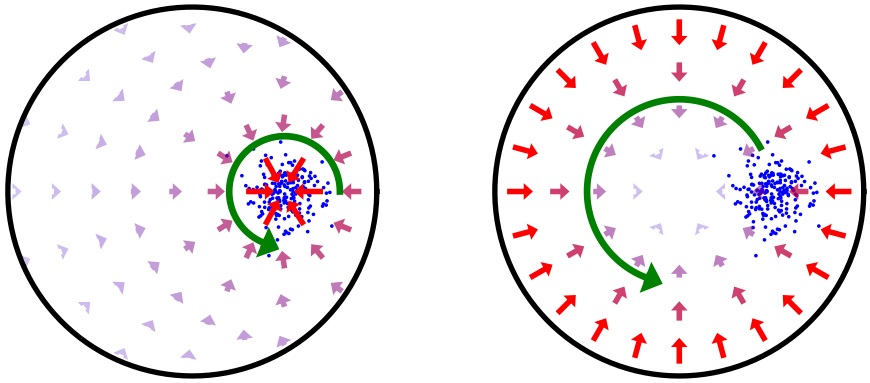

Figure 1.7: Left—a cartoon showing the electric field generated by an electron cloud, with the $\mathbf{E} \times \mathbf{B}$ drift generated by this electric field shown in green. Right—the electric field generated by the trap electrodes.

are not called "small electron plasmas," as their Debye length is typically comparable to their length and radius. Typically these clouds flatten the trapping potential significantly, but not completely. Sec. 5 will discuss the charge distributions of electron clouds in much more detail.

The reason electron clouds are so useful as measurement tools is that the clouds respond to the trapping field just like single electrons would. However it is easier to prepare and image a cloud of electrons than it is to prepare and image a single electron. Curiously, electron clouds exhibit this behavior even if their own electric field is not negligible. Fig. 1.7 shows a cartoon of the electric field produced by an electron cloud and the electric field produced by the trap. Most of the measurement techniques described in this thesis involve moving an electron cloud away from the symmetry axis of the trap. When an electron cloud is off-center, it produces an electric field that points toward the center of the cloud. This electric field generates an $\mathbf{E} \times \mathbf{B}$ drift that causes the electron cloud to rotate. The electric field generated by the cloud is added to that of the trap, which generally points toward the center of the trap. The $\mathbf{E} \times \mathbf{B}$ drift from the trapping field causes the cloud to rotate around the center of the trap. We call this the "magnetron motion" of the cloud because it is so similar to the magnetron motion of a single particle. Since the $\mathbf{E} \times \mathbf{B}$ drift velocity is linear in $\mathbf{E}$, the two motions are simply added together—the cloud is rotating around its own axis and it is orbiting the trap center, just like Earth rotates and while orbiting the sun. Typically the cloud's rotation frequency is about ten times its magnetron frequency.

Actually, the rotation of the cloud is necessary for it to remain cohesive. If the cloud did not rotate, and if the magnetron frequency depended slightly on the distance from the trap center, the outermost electrons would separate from the innermost ones [27]. If the cloud remains cohesive, then the cloud as a whole must $\mathbf{E} \times \mathbf{B}$ drift with a velocity given by the average $\mathbf{E} \times \mathbf{B}$ drift velocity of all the particles in the cloud. Although the electric field within the cloud is significantly perturbed the electrons, it is not possible for this to influence the $\mathbf{E} \times \mathbf{B}$ drift velocity of the cloud. This would imply that the electric field of the cloud averaged over the constituent electrons is not zero (assuming a constant magnetic

field). This in turn is impossible because it would imply that the cloud is exerting a force on itself, in violation of Newton's laws. There are two small caveats to this statement. First, when a cloud becomes big enough that its image charge is nonnegligible, the cloud's $\mathbf{E} \times \mathbf{B}$ drift velocity starts to depend on the total charge of the cloud. Second, a cloud with more charge will also be longer in z (the direction perpendicular to the plane shown in Fig. 1.7). The charge distribution length may change the average electric field experienced by particles in the cloud. These two effects give the appearance of the cloud affecting its own $\mathbf{E} \times \mathbf{B}$ drift.

Throughout this thesis, the $\mathbf{E} \times \mathbf{B}$ drift motion of electron clouds is used as a measurement tool of either the electric or the magnetic field. In most cases, the axial motion of the electrons is simply ignored. We assume the electron cloud sits at the top of an electrostatic potential maximum in z and otherwise nothing interesting happens in z. In most of these measurements, the electron cloud is moved off axis at some point. This is operation is preformed by weakening the trapping potential. This allows the motion of the cloud to be affected by patch potentials, unintended variations in the electrostatic potential along the walls of the trap.

It may be surprising at first that patch potentials can be exploited to move clouds off-axis in a predictable way. To explain this, we first approximate the trapping potential as:

$$V_T(z, r) = -k_2 \left(z^2 - \frac{1}{2} r^2 \right). \tag{1.20}$$

Because patch potentials lie along the walls of the trap (trap wall radius $R_w = 2.2\,\text{cm}$), but our electron cloud will remain localized to within a few millimeters of $z = r = 0$, the electrostatic potential created by patches can be approximated as a power series where each higher order term is suppressed by z/R_w or r/R_w. Of course, this potential must satisfy the Laplace equation, so the lowest order relevant term is:

$$V_P(z, r, \theta) = \varepsilon r \cos\theta. \tag{1.21}$$

Because $\mathbf{E} \times \mathbf{B}$ is perpendicular to $\mathbf{E}$, it traces out equipotential lines (assuming the z equilibrium position does not depend on the r, θ position of the cloud). In the presence of V_p and V_T given above, equipotential lines are circles displaced from the true trap center by a distance ε/k_2. To move a cloud off-axis, we can decrease k_2 and wait for the cloud to preform some fraction of an orbit around the displaced center of magnetron motion.

All of the measurement techniques described in this thesis using electron clouds are some sequence of the following operations:

1. The cloud can be moved along the trap axis. If this is done slowly, the magnetron radius is conserved, as discussed in Sec. 2.3.3. This is used to deliver a cloud to an axial position in the trap where we want to perform a measurement. This is depicted in Fig. 1.8.

2. The cloud can be imaged on the MCP by releasing it from the trapping potential with 10's of eV of kinetic energy. In this case, the electrons follow magnetic field lines. This is depicted in Fig. 1.9

3. The cloud can be moved off-axis slowly weakening the trapping potential slowly. The cloud follows the displaced center of magnetron motion as it moves away from the true trap center. This is described in Sec. 3.3.

4. The cloud can be moved off-axis more quickly by changing the center of magnetron motion much more quickly than the magnetron motion then waiting for the cloud to preform half an orbit around that displaced center. These two strategies for moving a cloud off-axis are shown in Fig. 1.10.

5. We can heat the cloud using microwaves near the cyclotron frequency [5].

6. Once a cloud has been moved off-axis, we can quickly increase k_2, moving the center of magnetron motion back to the center of the trap, and we can wait for the cloud to preform any number of magnetron orbits.

For example, the patch potential measurements described in Sec. 3 use the sequence $1 \rightarrow 3 \rightarrow 6 \rightarrow 2$. The off-axis ECR measurements described in Sec. 7 use the sequence $1 \rightarrow 3 \rightarrow 6 \rightarrow 5 \rightarrow 2$.

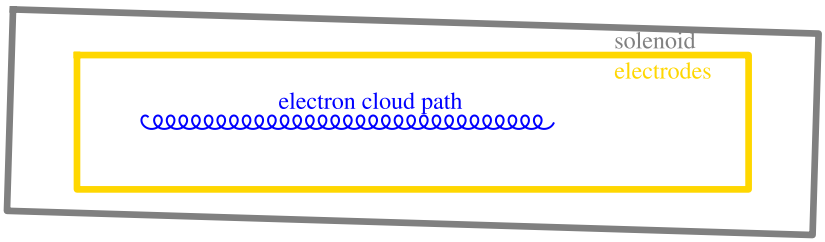

Figure 1.8: A cartoon of an electron cloud being moved along the trap axis. I exaggerate the misalignment between the electrodes and the external solenoid to emphasize that if this operation is done slowly compared to the magnetron frequency, the electron cloud follows the electrodes, not the field lines of the solenoid. The blue line represents the motion of the center of the electron cloud. Our electron clouds are always created slightly off-axis (see Sec. 2.3), so they preform a small magnetron orbit as we move them from the reservoir to a desired axial measurement location.

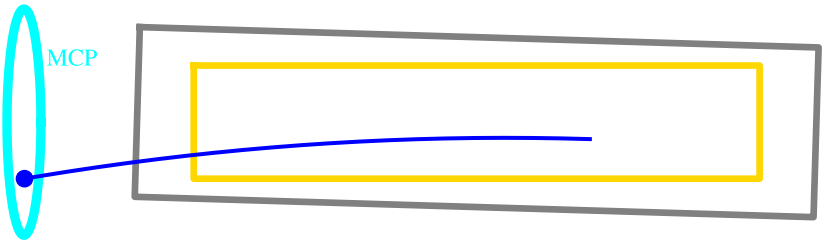

Figure 1.9: A cartoon of an electron cloud being imaged on the MCP. In this case, the electrons follow the magnetic field lines, not the electrodes.

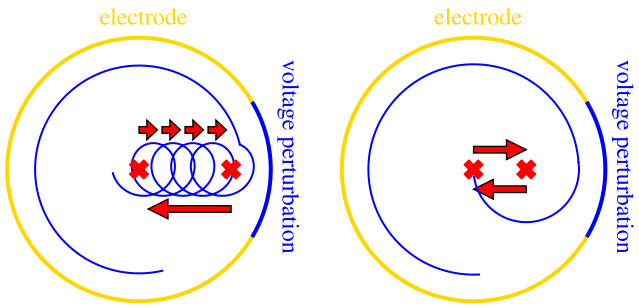

Figure 1.10: On the left, I show the adiabatic scheme for moving a cloud off-axis. The trapping potential is slowly weakened, and the cloud follows the center of magnetron motion as it slowly moves off-axis. Then we make the cloud orbit the center of the trap by quickly increasing the trapping potential. On the right, I show a quicker scheme for moving a cloud off-axis. The center of magnetron motion is changed quickly, then we wait for the cloud to preform half an orbit, then the center of magnetron motion is changed quickly again. The blue line represents the trajectory of the center of the electron cloud. The red X's are the centers of magnetron motion. The red arrows show the change in the center of magnetron motion; multiple arrows represent a slow change, and one arrow represents a fast change.

2 Electron plasma reservoir

An electron plasma "reservoir" is used to produce electron clouds, which are in turn used to perform the measurements described in this thesis. Future improvements to these measurement techniques are likely to begin with optimizing the extraction of electron clouds from the reservoir. In this section I describe the basic principles underlying the reservoir. I will also show some data which illustrates the challenges and optimizations required for implementing a reservoir. Most of this data was collected incidentally while optimizing a reservoir prior to using it for a specific purpose.

The electron plasma reservoir technique was first developed by Dr. Eric Hunter, one of the previous students of my advisor, Prof. Joel Fajans. It is described in Ref. [5] and in his thesis [4]. A similar idea was implemented by the BASE collaboration for extracting single antiprotons from an antiproton reservoir [28]. The technique is also related to one implemented at UCSD to extract positron beams from a positron plasma [29], but those positrons were released from the trap, and here the ejected particles remain confined.

Dr. Hunter used the reservoir to dramatically improve electron cyclotron resonance (ECR) magnetic field measurements at ALPHA. Before Dr. Hunter's time, ALHPA used a large electron plasma for ECR, and when injected microwaves were resonant with the cyclotron frequency of the electrons in the plasma, the plasma would heat [30]. The heating was then inferred by monitoring the frequency of an oscillation mode of the plasma, which was weakly temperature dependent [31]. The introduction of the reservoir improved the measurement in two critical ways. First, a new, nearly identical cloud of electrons was prepared for each new frequency. This avoided the issue where the plasma would remain hot from previous microwave injections, meaning that one could only clearly see the onset of the cyclotron resonance, not the width of the peak. Second, the electron clouds from a reservoir consisted of much fewer electrons confined in a much smaller physical space. This significantly reduced the influence of plasma effects [32, 33], which complicate the resonance by creating several resonant modes with plasma parameter dependent frequencies. Spatial variation of the magnetic field also implies that physically smaller charge distributions are subject to a more narrow distribution of magnetic field strengths. With electron clouds, the resonance structure could be explained with single particle dynamics rather than plasma physics. Additionally, the linewidth of the resonances was significantly reduced, and the resulting measurement had ppm-level systematic effects. Indeed, all of the measurement techniques introduced in this thesis also rely on the electron clouds being small.

2.1 SDREVC Reservoir Preparation

The first step in developing a reservoir is to make a highly reproducible electron plasma using SDREVC. The SDREVC technique was discovered by Dr. Celeste Torkzaban [2, 3] in the ALPHA collaboration, another one of my advisor's previous students. The "SDR" in SDREVC implies that the electron plasma is being compressed using a "rotating wall" [34], and that the amplitude of the rotating wall is high enough to be in the "strong drive regime" (SDR), where the plasma rotation frequency ω_r matches the applied rotation frequency of the electric field [35]. If the plasma is cold (Debye length$\ll$plasma dimensions), then the

rotation frequency is given by:

$$\omega_r = \frac{en}{2\epsilon_0 B}, \tag{2.1}$$

where n is the number density of the plasma, and B is the axial magnetic field magnitude in the Penning-Malmberg trap. Thus, by enforcing a certain value of ω_r, the SDR compression enforces a certain plasma density. SDREVC combines SDR compression with evaporative cooling (EVC), where the confining potential on one side of the plasma is slowly reduced, allowing the most energetic electrons to escape [36]. In the cold plasma limit, this simply means that the space charge voltage of the plasma remains just below the confining potential. When we have chosen a particular space charge voltage and a particular density for our plasma, most other parameters like radius and total charge are also fixed assuming rotational and thermal equilibrium at a sufficiently low temperature that Debye shielding occurs. SDREVC is then an ideal way to prepare a reservoir; I will show later that variability in the reservoir ultimately leads to variability in the total charge of extracted clouds.

There are several steps involved in implementing SDREVC, and to some extent these steps can be performed successfully in several different ways. However, in my time at ALPHA, I also witnessed many ways that one can think they established SDREVC, but they did not. For example, I recall one situation where SDR was established, but once EVC was added, the trapping potential changed so radically that SDR no longer worked. I have also seen situations where the trapping potential was lowered, but not far enough to actually evaporate any charge. The following steps are what I would consider a "careful" implementation of SDREVC which is very likely to produce a successful result.

The first step is to load an electron plasma with one of ALPHA's hot cathode "electron guns." I will not go into further detail on this step because I did not put significant effort into studying this process during my Ph.D. After giving that plasma tens of seconds to cool to a stable temperature, we find a trapping potential where charge would be lost if the the trapping potential was decreased by just a few volts on one side of the plasma. I will call this the "SDR potential." Such a potential is depicted in Fig. 2.1. Typically, I leave myself a few volts of extra space, because I am often going to compress the plasma, which will increase its space charge potential slightly, and the SDR rotating wall will almost certainly heat the plasma significantly. The length and overall shape of this trapping potential can often be stolen from previous implementations, but the depth will need to be tuned. This potential can be found by imaging the plasma after morphing to an SDR potential with a variable confining voltage on one side. Once the potential is no longer sufficient for confining the plasma, the resulting imaged plasma will be less dense and it will have a bigger radius. MCP images showing an implementation of this step are shown in Fig. 2.2.

Once the SDR potential has been established, we add the rotating wall and see if there is a range of frequencies which exhibit SDR compression. The first guess for the voltage of the rotating wall can be stolen from previous implementations (usually about 5 V at ALPHA). Experimentally, we vary the rotating wall frequency and we see if there is a linear relationship between frequency and plasma density, or frequency and 1/radius squared. The data from a successful SDR frequency scan is shown in Fig. 2.3

This analysis is simpler if the SDR potential is relatively "square," meaning it has a flat bottom and steep walls at the edges. This causes the plasma's length to be independent of the space charge voltage, and the density of the plasma can be inferred from the pixel

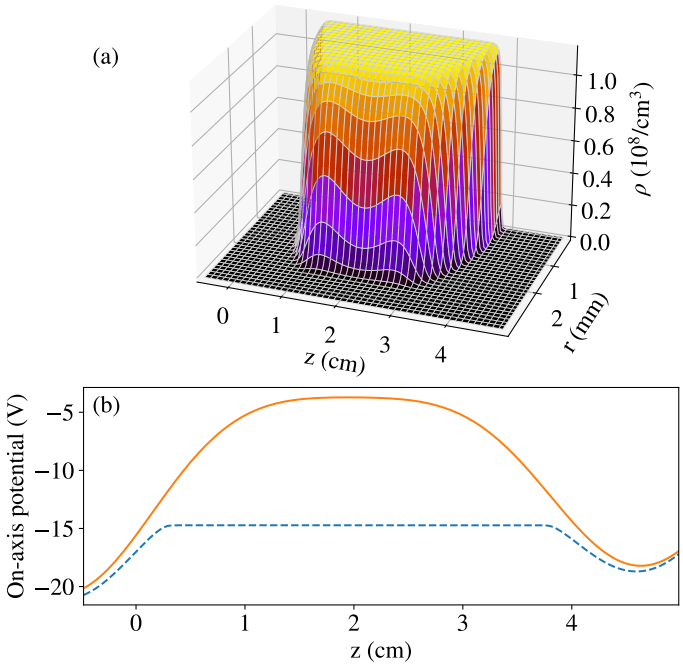

Figure 2.1: The plasma sitting in the SDR potential which serves as our starting point for establishing SDREVC. The upper plot shows the plasma density profile in thermal and rotational equilibrium with 47.5 Me^-, a root mean square radius of 1.5 mm, and a temperature of 500 K. The lower plot shows the on-axis potential produced by the electrodes in orange, and the blue dashed line shows the on-axis potential including the influence of the plasma. The potentials and plasma parameters are taken from a reservoir used in ALPHA-g.

brightness in the center of the MCP image of the plasma (which physically represents the 2–D z-integrated density of the plasma). However, previous authors have explained how such square potentials can cause plasma expansion [37, 38]. The mechanism behind this expansion seems to suggest that if we make the trapping potential less "square," the expansion rate should significantly decrease. Ref. [39] directly tested this and showed that confinement of a nonneutral plasma in a Penning-Malmberg trap is radically improved by simply making the confining potential harmonic instead of square. For us, these arguments simply mean that we should try a square SDR potential, but if there is an unacceptable expansion rate that cannot be overcome with the rotating wall, we should switch to a more harmonic SDR potential and accept that it will be harder to prove that the SDR compression is working.

If a no linear relationship between frequency and density is observed, or if we aren't satisfied with the density of the plasma we achieve (i.e. SDR compression doesn't extend to high enough frequencies), the rotating wall voltage should be increased. If that doesn't work, the trapping potential is changed, often to make the plasma shorter or longer. It's hard to say whether the length of the plasma should be increased or decreased, but it's easy to explain why this is a relevant parameter. First, elongating the plasma changes the effective strength of the rotating wall. Shortening the plasma causes a larger fraction of the charge

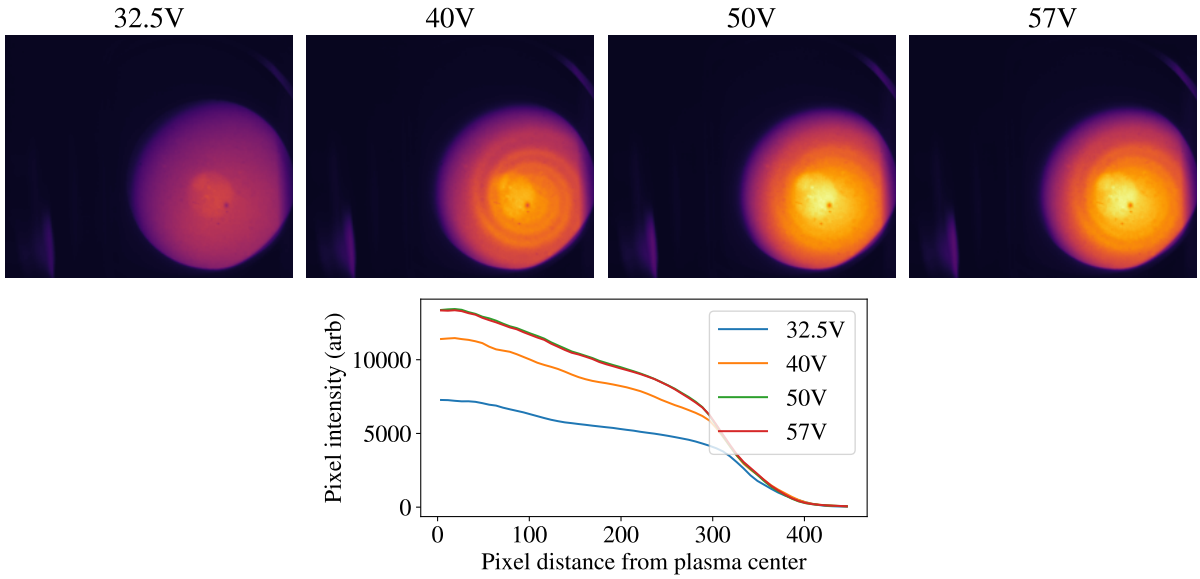

Figure 2.2: Above each of the four images, we list the trapping potential used as a possible SDR potential. The listed voltage is the difference between the lowest potential barrier confining the plasma and the electrostatic potential maximum where the plasma is trapped. We find that when the trapping potential is 50 V or 57 V volts, the resulting image is nearly identical. At 40 V, the brightness is slightly diminished. At 32.5 V, the brightness is significantly diminished. This can be seen more clearly when inspecting the actual pixel intensities, which are plotted below. In this case, the increasing radius of the plasma cannot be seen because the edges of the plasma in this MCP image are actually apertures the plasma encounters between the trap and the MCP. The "swirling" pattern visible in some of the plasmas likely represents the development of a diocotron instability while dumping the plasma to the MCP.

to be exposed to the rotating electric field. Also, as mentioned before, when the plasma is longer, it expands more quickly due to unintended asymmetries in the trap [40, 41, 42, 43, 44, 45]. This will, presumably, fight against the rotating wall compression. When ALPHA-g had egregiously bad patch potentials (discussed in Sec. 3.7), this issue prevented us from establishing SDR compression of positrons until the SDR potential length was significantly reduced. Conversely, there is a compelling pattern in the data from the original SDR paper [35] showing that elongating the plasma actually improves SDR compression. This probably says something about the underlying explanation for SDR which I am not well-versed in.

Next, with the rotating wall active, one adds evaporative cooling by lowering the confining potential on one of the two sides of the plasma. In my experience, the more the plasma is evaporatively cooled, the more reproducible the resulting plasma is. However, in some circumstances, a reasonably reproducible plasma with as many electrons as possible is preferred. One must simply verify that the confining potential is lowered far enough that charge actually escapes from the trap. One should observe that the central density doesn't change significantly, but the radius of the plasma decreases as the confining potential is lowered. Note that earlier when we evaporated electrons from the trapping potential, the radius increased because the mean square charge radius was conserved [8]. Now, with the

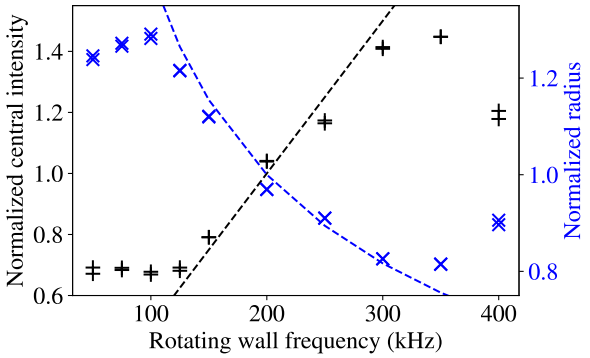

Figure 2.3: The plasma radius and central density (the pixel brightness of the MCP image in the center of the plasma) is plotted versus rotating wall frequency for one implementation of SDREVC on electrons in ALPHA-g. In this data, it isn't entirely clear whether the SDR extends from 125–200 kHz, or if it goes to 300 kHz, and some error in the procedure for finding the density and radius from an MCP image causes an offset. The SDR predictions (intensity$\propto$frequency and $1/r^2 \propto$ frequency), denoted by dashed lines, are chosen to make it look like the SDR frequency range is 125–300 kHz. For each frequency, two plasmas were prepared and imaged; the differences between trials were very small.

SDR rotating wall, the rotation frequency and density are conserved. It is uncommon for this step to pose any difficulty if the previous steps were followed carefully. Fig. 2.4 shows a successful implementation of this final step.

To prove that SDR is maintained despite changing the trapping potential, one should verify that density remains proportional to frequency after adding EVC, but often this step is skipped. This is more likely to be successful in a square potential, because the influence of the trapping potential on the rotation rate is changing less quickly in a more square trapping potential. Thus the changing trapping potential used to perform EVC is less likely to break SDR compression.

If plasma preparation time needs to be minimized, as a final step I will decrease the time for this process until the resulting plasma starts to change (indicating a failure of SDREVC). Otherwise performing this operation in 20 s often suffices.

2.1.1 Scooping

Once a reproducible reservoir has been established, after waiting ten or twenty seconds for the reservoir to cool via cyclotron cooling, we extract electron clouds from the reservoir. For each cloud, we perform these steps:

1. The reservoir rests in a trapping potential.

2. Elongate the reservoir so that it is two electrodes longer than it normally is.

3. Cut an electron cloud from the reservoir, using the electrode farther from the reservoir to trap the cloud (make its voltage more positive), and using electrode between the cloud and the reservoir to separate the two (making its voltage more negative).

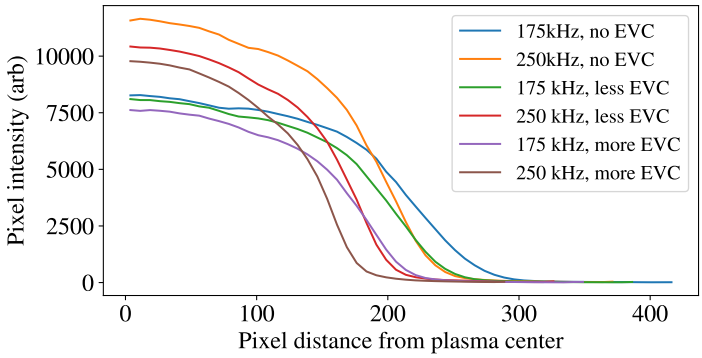

Figure 2.4: Radial MCP image brightness curves are shown for six imaged plasmas. The plasmas were prepared using three different final SDREVC potentials (three different degrees of evaporative cooling), and two different rotating wall frequencies. For the 175 kHz rotating wall, the radius of the plasma changes much more than the central intensity when we change the EVC final depth. Any difference in the central intensity is likely explained by the plasma's length decreasing with decreasing space charge voltage. For the 250 kHz rotating wall, the central intensity difference was more pronounced, possibly indicating that the 250 kHz rotating wall was not in the strong drive regime.

4-5. Move the cloud to a desired measurement location in the trap, and move the reservoir back to its "resting position."

An example of the electrode voltages used to perform these operations is shown in Table 1. These voltages are taken from the reservoir most commonly used in ALPHA-g. We call this

step	E2 potential (V)	E3	E4	E5	E6	E7	E8
1	0	60	60	0	0	0	0
2	0	60	60	$V_0 + S \times n$	$V_0 + S \times n$	0	0
3	0	60	60	-75	75	0	0
4	0	60	60	-75	75	75	0
5	0	60	60	0	0	75	0

Table 1: The sequences of voltages used to remove the n'th electron cloud from the reservoir. The step numbers correspond to the steps listed in the text. The electrode voltages are changed linearly between each step, with the 1–2 and the 2–3 transitions taking 1 ms and the later steps usually taking 5 ms. V_0 is typically about 45 V, and S is usually 2.5–20 mV.

operation "scooping," and in fact the electron clouds are colloquially referred to as "scoops" within the collaboration. In this thesis I retain the term "scooping," but I will refer to the things produced as electron clouds, not scoops. The potential applied to electrodes 5 and 6, $V_0 + s \times n$, is called the "scooping potential" of the n'th cloud extraction. So V_0 is the "initial scooping potential," and S is the "scooping step size." The potentials used in the other steps are almost arbitrary. The potentials used in step 1 simply need to be sufficiently positive for confining the reservoir. I have on one occasion chosen the potentials in step 3 so poorly that it was impossible to choose any V_0 such that there was any charge removed from the

reservoir. There may be some benefits to tuning these potentials; perhaps expanding and contracting the reservoir by a larger factor heats it more or drives expansion more. Frankly most of the time I just chose these voltages arbitrarily and the reservoir works acceptably.

In Fig. 2.5, I use a plasma equilibrium solver to show how the electron density evolves as the reservoir is cut between steps 2 and 3. It should be emphasized that the electron cloud is not separated from the reservoir immediately after the potential starts moving from step 2 to 3. Rather, two collections of electrons are separated at some point in between when a saddle-node bifurcation occurs in the on-axis electrostatic potential. After, the cloud and the reservoir sit in two local on-axis potential maxima separated by a local minimum. Further, between step 2 and 3, there is always a short time where the potential on electrode 5 is more negative than electrodes 4 and 6, but there is no corresponding local minimum in the on-axis potential. V_0 should be tuned such that in the moment that this local maximum is created, the potential of this local maximum is be very close to, or slightly above, the "space charge potential" of the reservoir.

The space charge potential is somewhat loosely defined as the on-axis potential in the center of the reservoir. It is not in any way a constant property of a reservoir. Rather, it changes with the reservoir's length and radius, which is clearly visible in Fig. 2.5. If the local maximum is slightly above the space charge potential, then the cloud will consist of only the most energetic electrons at the upper end of the Maxwell-Boltzmann distribution within the plasma. Often we want our clouds to consist of as few electrons as possible while still producing a clearly identifiable spot when they are imaged, so this is typically how scooping is done.

The charge in the first cloud is set by V_0 and the parameters of the reservoir (most importantly its space charge potential). With each successive cloud extraction, the cloud charge changes by a small fraction with the changing difference between $V_0 + S \times n$ and the space charge potential. After $\mathcal{O}(100)$ cloud extractions, the clouds converge to a constant charge which is dependent on S but not V_0. This is because in "equilibrium" the charge extracted from the reservoir should be just enough to reduce the reservoir's space charge voltage by S per cloud. If the reservoir's radius and length do not significantly change over the course of our extractions, the amount of charge needed to reduce the reservoir's space charge voltage by S will not change from one cloud to the next. This argument is turned into a calculation in Sec. 2.2.

If V_0 is not chosen well, it may take many extractions to reach this equilibrium. If V_0 is too positive, the local minimum meant to separate the cloud from the reservoir may be created below the space charge potential of the reservoir, and the reservoir's space charge voltage will be reduced by more than S. The situation is somewhat more dire when V_0 is far too negative; one will simply not extract any electrons until the scooping voltage increases sufficiently. Of course if V_0 is just a bit too negative, then the reservoir's space charge voltage will be initially reduced by less than S per cloud, and we will still see the cloud charges converge toward a constant value.

Once we have successfully implemented SDREVC, we tune V_0 and find a value for S which gives a constant and ideal cloud charge. The data collected in the process of tuning a reservoir's initial scooping voltage is shown in Fig. 2.6. A quick way of finding an ideal value for V_0 is to choose a V_0 which is unreasonably negative and an S that is unreasonably large (say 1 V). The extracted clouds are moved a short distance from the reservoir then

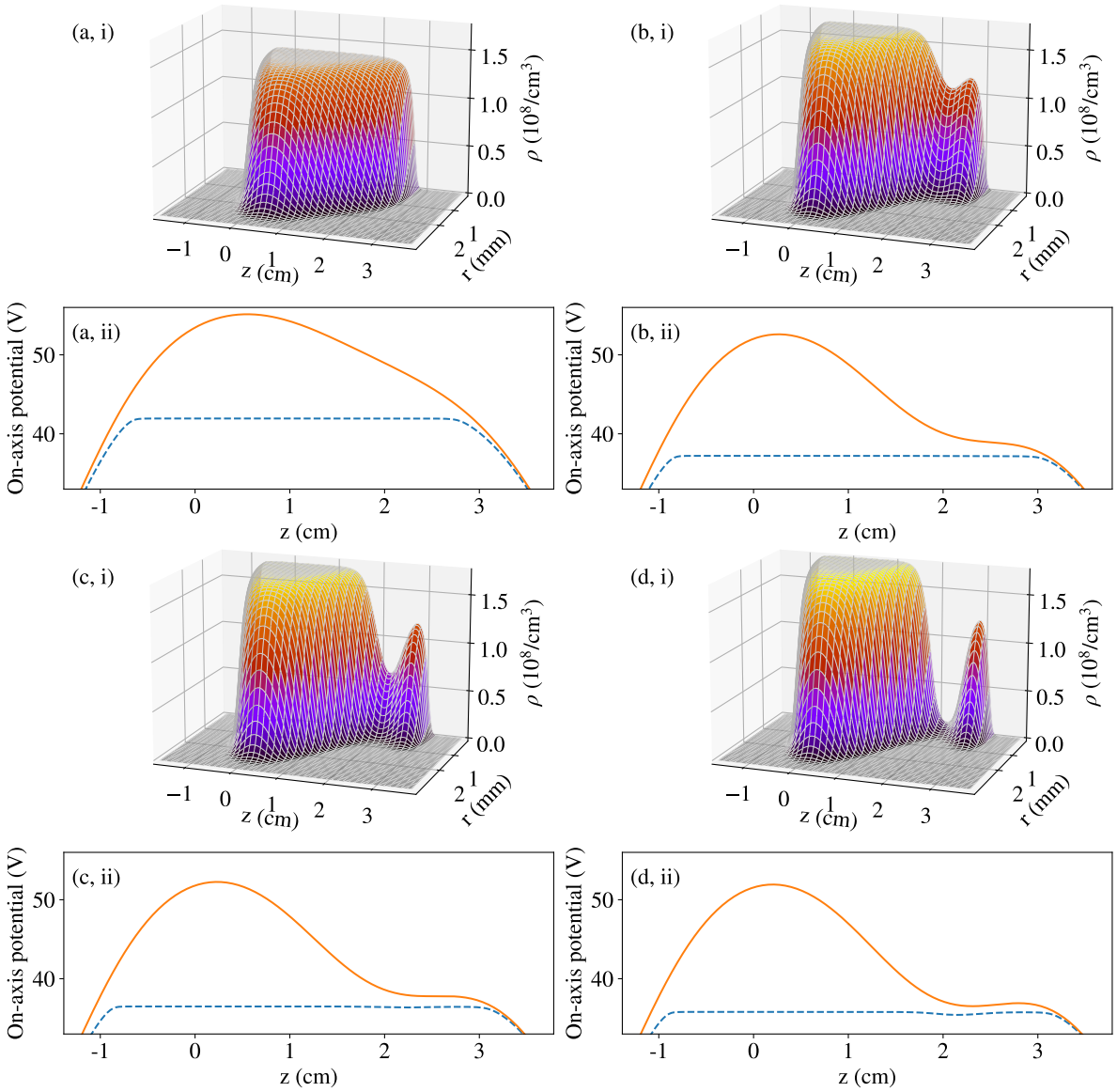

Figure 2.5: A plasma equilibrium solver is used to model the process of "scooping" an electron cloud from a reservoir. Plasma density distributions are shown for four successive times (a,b,c,d) during the voltage manipulation that cuts the reservoir. The potentials and electrode geometry are taken from a reservoir implemented in ALPHA-g. These calculations use a realistic mean square charge radius of 1.5 mm, a magnetic field of 1 T, and a total charge of 47.5 Me^-. The reservoir is given an unrealistically high temperature of 1500 K to achieve a manageable computation time (100 K is more likely to be the actual temperature). For each step, the upper plot (i) shows the plasma density distribution. The lower plot (ii) shows the on-axis potential due to the electrodes alone with an orange solid line; the full on-axis potential including the influence of the plasma is indicated by the blue dashed line.

imaged. At some point we will start to see charge in the clouds (with $S = 1\,\mathrm{V}$ these are proper plasmas, not just clouds). Then we "zoom in," setting V_0 just below where we started to see charge and reducing S significantly.

It should be noted that just because we saw the first charge appear at some scooping voltage $V_n = V_0 + S \times n$ does not mean that V_n is the ideal choice for V_0. Over time, the reservoir expands due to imperfections in the trap's construction (See Sec. 4). This reduces its space charge voltage with time. In a "well-behaving reservoir" in ALPHA's traps, this expansion rate is of order $1\,\mathrm{mV/s}$. Thus if n is large, V_n will be too high.

While still tuning V_0, setting V_0 conservatively below V_n is ideal because seeing no charge in the first few clouds gives more information than seeing too much charge. If we see no charge for the first $n-1$ extractions, we know that we should increase V_0 by approximately, but not exactly, by nS. If we see too much charge in the first cloud, we have no idea how far V_0 should be decreased, except if we do some complicated analysis summing the excess charge in the clouds. When we have "zoomed in" sufficiently far, and S is small enough that the cloud sizes are ideal, V_0 should be slowly increased until the first cloud is close to the cloud sizes that we converge to with large n. However this tuning process should not be done too carefully. Despite the use of SDREVC, the reservoirs will have some variation in their space charge voltage. In my experience this amounts to tens of millivolts from one reservoir to the next, and as much as a few hundred millivolts from one day to the next. Thus I usually prefer to set V_0 a bit too high and I just discard the first few clouds before the cloud charges have converged (if my cloud-based measurement is sensitive to cloud charge variations). Some evidence of reservoir space charge voltage variation is visible in Fig. 2.6.

SDREVC was originally used to prepare positron plasmas and electron/antiproton plasmas for antihydrogen formation. For this purpose, the reproducibility of the plasmas was essentially perfect. These plasmas are routinely imaged, and an image analysis software fits a function to their radial density profile. Often plasmas created using SDREVC are so reproducible that the fit parameters for two identically prepared plasmas are exactly the same. However, because scooping is sensitive to the plasma space charge voltage at the millivolt level, it reveals some lingering variability left after SDREVC. Anecdotally, if we increase the charge of the electron plasma before SDREVC, the result after SDREVC has slightly more charge. I hypothesize the following mechanism for this effect:

1. If there is more charge in the beginning, electrons evaporate from the plasma at a greater rate during EVC.

2. Thus the temperature of the plasma during SDREVC is lower.

3. The space charge potential of the plasma is typically going to be lower than the barrier voltage during EVC by a few multiples of the plasma temperature, so that only a small fraction of electrons are in the "loss cone" at a given moment in time.

4. Thus a colder plasma's space charge potential will be closer to the EVC barrier potential, indicating that it will have more total charge.

SDREVC is nonetheless nearly essential for a reservoir. SDREVC can turn an $\mathcal{O}(1)$ variability in the space charge potential and radius into a variability of order $k_B \Delta T / e\Phi$, where ΔT

is the variability in the temperature and Φ is the space charge potential. Even $k_B T/e\Phi \ll 1$ for the reservoirs used at ALPHA, so $k_B \Delta T/e\Phi$ is even smaller.

2.2 Reservoir Theory

Here I present a simple model where one can predict the charge of the clouds from the plasma parameters of the reservoir and the scooping voltage step size. The derivation is surprisingly insightful given how many approximations are necessary to set up a situation where the reservoir can be modelled without an equilibrium solver. Despite these approximations, we will be able to explain the order of magnitude of electron cloud charges, and we will be able to explain the qualitative observations that (1) electron cloud charge is proportional to voltage step size, and (2) electron cloud charge converges to a value which only depends on voltage step size regardless of small variations in the reservoir plasma parameters.

Suppose a reservoir is a cold electron plasma, consisting of N_r electrons with a length of $l_p \gg R_w \gg r_p$ and a radius r_p (R_w is the trap wall radius). The space-charge voltage of the reservoir is:

$$V_{ri} = \frac{eN_r}{2\pi\epsilon_0 l_p}\left[\frac{1}{2} + \ln\left(\frac{R_w}{r_p}\right)\right]. \tag{2.2}$$

When we extract N_c electrons from the reservoir, the space charge voltage of the reservoir will decrease for two reasons. Obviously, the total charge has decreased. However, one cannot neglect the fact that r_p will increase; the reservoir technique produces an electron cloud with a radius much smaller than r_p, and these electrons are extracted from near the center of the reservoir. The confinement theorem for Penning-Malmberg traps [8] then says that the mean square radius of particles before extraction must equal the mean square radius of particles after extraction. Thus we have the following relationship between the initial radius r_{pi} and the final radius after one extraction r_{pf}:

$$\int_0^{r_{pi}} \pi r^3 \frac{N_r}{\pi l_p r_{pi}^2} dr = \int_0^{r_{pf}} \pi r^3 \frac{N_r - N_c}{\pi l_p r_{pf}^2} dr. \tag{2.3}$$

Assuming l_p is not a function of r, integrating, and simplifying we get:

$$r_{pf} = r_{pi}\sqrt{\frac{N_r}{N_r - N_c}} \approx r_i\left(1 + \frac{N_c}{2N_r}\right). \tag{2.4}$$

And therefore the new reservoir voltage is:

$$V_{rf} = \frac{e(N_r - N_c)}{2\pi\epsilon_0 l_p}\left[\frac{1}{2} + \ln\left(\frac{R_w}{r_{pi}(1 + N_c/2N_r)}\right)\right] \approx V_{ri} - \frac{eN_c}{2\pi\epsilon_0 l_p}\left[1 + \ln\left(\frac{R_w}{r_p}\right)\right]. \tag{2.5}$$

Note that the final expression above comes from expanding to first order in N_c/N_r. As we successively remove clouds from the reservoir, we approach a limit where the change in reservoir space charge voltage $V_{rf} - V_{ri}$ equals the scooping voltage step size S. Thus the

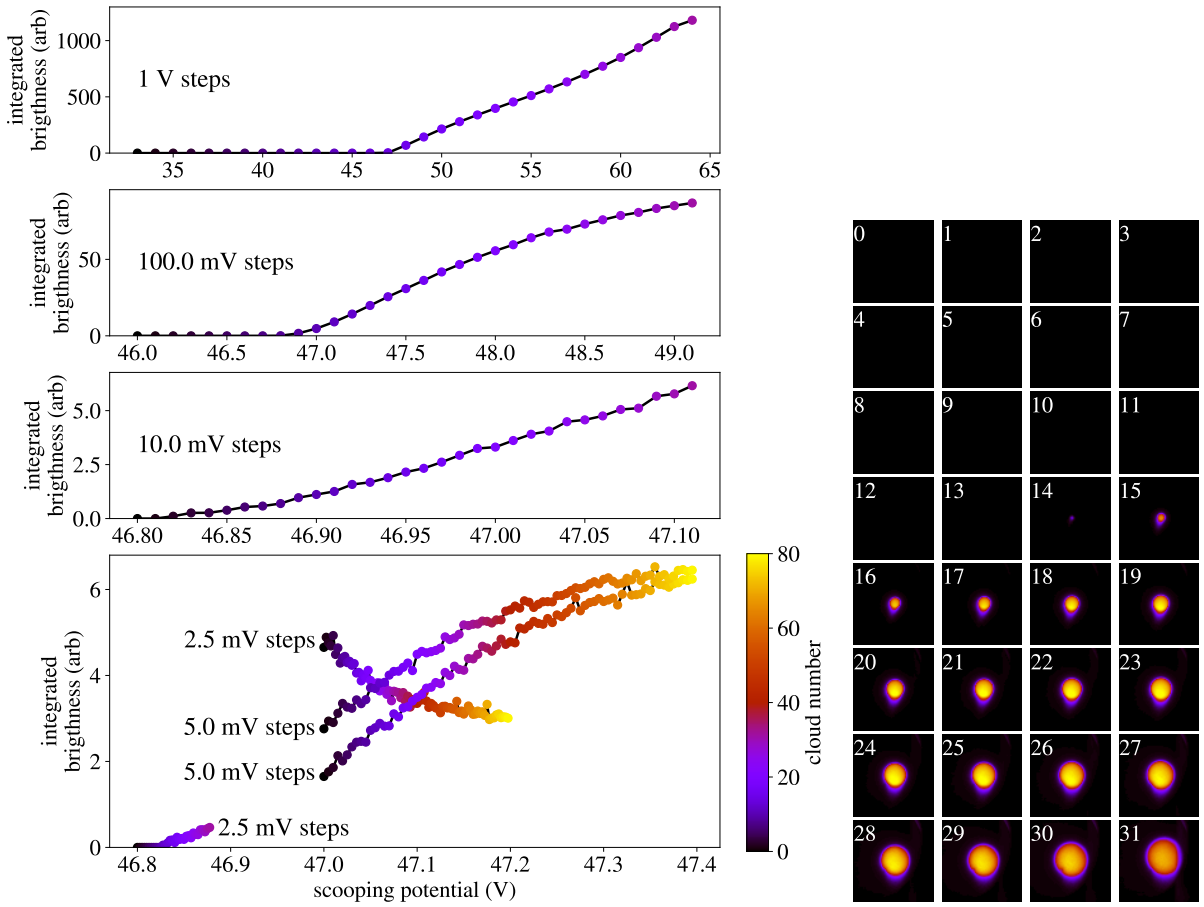

Figure 2.6: This is the data collected in the process of finding an initial scooping voltage V_0. Clouds are successively extracted from a reservoir then imaged with the MCP/phospohor screen/CCD camera detector. In the plots above, I record the total integrated brightness of the spot produced by the cloud, which is roughly proportional to the total charge of the cloud. This is plotted against the scooping potential $V_0 + nS$, and the order in which clouds are extracted, the "cloud number," is shown with color. First, I set V_0 to 33 V, which I believed to be unreasonably low, and I set S to 1 V. The results are shown in the top plot. The actual MCP images from this trial are shown on the right, with the numbers indicating the cloud numbers. They are cropped on the plasma, and the camera is grayscale, but I applied a color mapping. Next, I adjusted V_0 to roughly where charge first appeared, 46 V, and I reduced S by a factor of ten. In the third plot, S is again reduced by a factor of ten. I wanted to perform measurements with clouds extracted with $S = 2.5$ and 5 mV. So I set V_0 to 46.8 V and S to 2.5 mV (visible in the lower left of the bottom plot). In the 32 clouds imaged, the brightness was too variable, so I increased V_0 to 47 V to get more charge in the first cloud, and I imaged 80 clouds to see if cloud charges would converge. Finally, I imaged 80 clouds extracted with 5 mV steps with two separate reservoirs. The variation in the initial clouds between these two identical experiments indicates a variation in the space charge voltage of the reservoir. The 5 mV clouds converge to a charge that is slightly more than double the converged charge of the 2.5 mV clouds, because other sources of reservoir expansion lower the reservoir's space charge voltage with time.

total charge of the clouds in this limit is:

$$N_c = S\frac{2\pi\epsilon_0 l_p}{e}\frac{1}{1+\ln\left(\frac{R_w}{r_p}\right)} \tag{2.6}$$

If the initial reservoir charge is too high (low) given the initial scooping voltage, the first few clouds will have more (less) than this charge, and the reservoir space charge voltage will decrease more (less) quickly. Experimentally, this means that although there may be a small degree of variability in the total charge of the reservoir, after about 100 clouds, the reservoir will settle to producing roughly the same cloud charge from one cloud to the next. Similarly, when we don't have time to carefully tune the initial scooping voltage, we can just wait for the reservoir to converge to a consistent cloud size before using the clouds for measurements.

In Sec. 5, I discuss some evidence that cloud charges may be increasing over time, even after the initial settling period. I will discuss whether that is a real phenomenon or if it is an artefact of the imaging apparatus. In advance of this discussion, I should note that there is a theoretical reason that cloud charges should grow over time. When the total charge extracted from the reservoir is not small compared to the initial reservoir charge, the reservoir's length and radius can change, changing the predicted cloud charge. This effect can be explained in the model above by simply noting that Eq. 2.4 can be applied iteratively, forming a telescoping product, yielding the reservoir radius r_p after n cloud extractions:

$$r_{pf} = r_{pi}\sqrt{\frac{N_r}{N_r - \sum_{j=1}^{n} N_{cj}}}, \tag{2.7}$$

where N_{cj} is the charge of the j'th extracted cloud. Otherwise, Eq. 2.6 remains valid as long as one is aware that r_p is increasing with each extraction. I have neglected any other sources of reservoir expansion. Of course, one could trivially add a linear increase in reservoir radius with time, but the data shown in Sec. 5 is consistent with cloud removal being the leading cause of reservoir expansion. Counterintuitively, as the reservoir's charge is depleted and it expands radially, becoming less dense, more charge is delivered to the clouds. Conceptually, this occurs because when the radius of the reservoir increases, more charge must be removed to retain the same step size in the space charge voltage. Typically, our measurements are optimally performed with a very small cloud charge of $\mathcal{O}(10^4 e^-)$, so we get an incidental benefit having reproducible cloud charge because the total charge removed from the reservoir is insignificant.

Some commentary may be necessary to explore which approximations in this section were valid. First, typically clouds are extracted in a few milliseconds, which may be too quick for rotational equilibrium to be maintained between the forming cloud and the reservoir. However, this does not negate the validity of Eq. 2.4, because we only need to assume that rotational equilibrium is established within the reservoir in the time between scoops, and that the cloud's radius is much smaller than the reservoir's. Also, as depicted in Fig. 2.5, our electron clouds are typically not plasmas; the Debye length implied by their maximum density is longer than or comparable to the radius and length of the cloud, and that maximum density is much lower than the "flat top" density of the reservoir. This also means that the

electrons which end up in the cloud came from the upper edge of the thermal distribution of electrons in the reservoir. Although in some places we approximated the reservoir as a "cold plasma," the fact that electrons are removed because of their nonzero temperature does not hurt the validity of these approximations. It doesn't matter how electrons were removed, just that the reservoir's space charge voltage can be well approximated with the cold, infinite length formula. The approximation of the reservoir as "infinitely long" is rarely accurate for the reservoirs used at ALPHA. In reality, Eq. 2.2 does not accurately describe the space-charge potential of the reservoir, and the length may change just as much as the radius. This issue could be addressed by fully modelling the reservoir in a numerical equilibrium solver—a project which would take an inordinate amount of time and would not be very illuminating.

2.3 Initial cloud magnetron orbit

The main source of error for all the measurements presented in this thesis is the initial magnetron radius of the clouds. When a cloud is displaced from the center of the trap in the transverse direction (the direction perpendicular to the trap's symmetry axis), it orbits the trap center at the "magnetron frequency." Many of the measurement techniques described in this thesis involve intentionally exciting this magnetron motion and using it as a measurement tool. Most of the measurement techniques also involve imaging a cloud and inferring something about the electric or magnetic field in the trap from its position. The "initial cloud magnetron" refers to the cloud's displacement from the center of the trap before using that cloud for a measurement. Thus any variability in the magnitude or phase of this initial cloud magnetron constitutes an error on the initial position of the cloud, which translates into an error on the final position of the cloud. In this section I will describe the three causes for this phenomenon that I have found so far in my experiences making reservoirs in ALPHA-2 and in ALPHA-g. All three causes have been observed in both experiments.

2.3.1 Intrinsic cloud magnetron

The most mysterious cause of cloud magnetron, and the one that has been historically hardest to solve, I have taken to calling the "intrinsic cloud magnetron." This phenomenon occurs in both ALPHA-2 and ALPHA-g, but in ALPHA-g it has a smaller magnitude. The intrinsic cloud magnetron is characterized by scoops being created off-axis immediately after they are extracted from the reservoir. This displacement is the same magnitude and in the same direction for all clouds extracted from the same reservoir—it is in no way random. However, if we take hundreds of milliseconds to move the plasma through the trap to a desired measurement location, the phases of the clouds' magnetron orbits will spread out because small variations in the charges or temperatures of clouds will result in small variations of their magnetron frequencies. Given enough time, they will have seemingly random magnetron phases.

This behavior is displayed in Fig. 2.7. Clouds are extracted from a reservoir with 2.5 mV steps. They are moved along the trap over the course of about 500 ms, and then they are imaged. The variability in cloud charge, and perhaps temperature, causes variability in the magnetron frequency. Over the 500 ms between a cloud's creation and the moment it is

imaged, this small difference in the magnetron frequency integrates to an $\mathcal{O}(1)$ difference in the final magnetron phase. We find that clouds extracted from the reservoir first had more charge, and they subtended a smaller total magnetron angle. Because of variation in the reservoir's space charge voltage, the change in cloud charge is different when the experiment is performed twice. We see that the change in magnetron phase is smaller when the cloud charge variability is smaller. If the clouds began a fixed distance off-axis, but that displacement was in a random direction, the clouds would be randomly distributed around a circle at all later times. Instead, their position around the circle varies with their charge, and successively imaged clouds typically land in almost the same place.

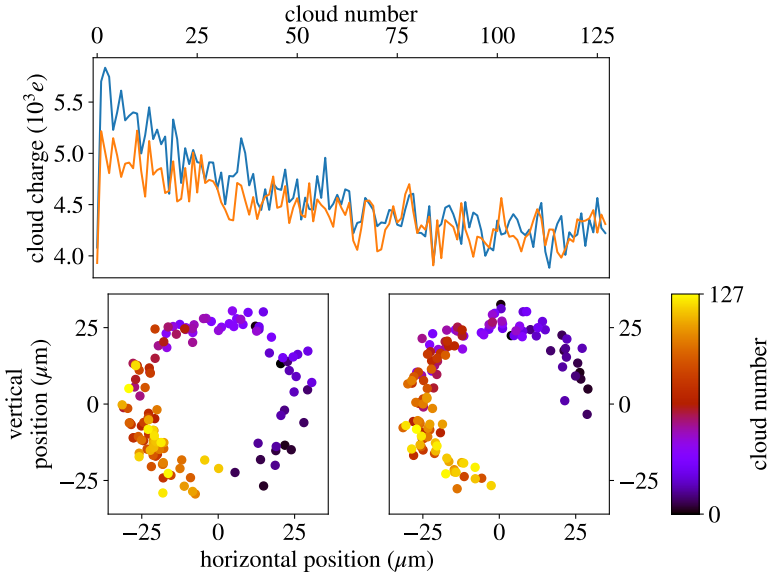

Figure 2.7: On top, the total charge of clouds successively extracted from a reservoir is plotted. The experiment was performed twice with identically prepared reservoirs (plotted in blue and orange). The total charge is inferred from the total brightness that the cloud produced in the MCP image, and this total brightness is calibrated using techniques described in Sec. 5. Below, the imaged positions of the clouds are plotted, with the colors indicating the order that they were extracted from the reservoir. The bottom left scatter plot corresponds to the blue curve above, and the bottom right corresponds to the orange curve. Note that one pixel in the original camera images of the clouds corresponds to about 5 μm of transverse distance within the trap—the units used in this plot. Therefore the $\sim 5\,\mu$m thickness of the circle could be a numerical limitation in our ability to identify cloud centers, not a genuine physical phenomenon.

In ALPHA-2, we see the same phenomenon, although it is much bigger (about 250 μm rather than 25 μm). Thus more time has been spent trying to reduce the intrinsic cloud magnetron in ALPHA-2. At this point, I am aware that Dr. Eric hunter [4], myself, and a team of three after me have tried to solve this issue with little progress. However, nobody has tried something as drastic as installing new equipment, for example, to recenter the clouds using a segmented electrode. In Fig. 2.8, I show evidence of the intrinsic cloud magnetron in ALPHA-2. Also in this figure, a new tool is introduced for diagnosing the source of a cloud's

magnetron motion. I began by introducing "random phase shifts" just before imaging the plasma to prove that the clouds were in a magnetron orbit, but that magnetron orbit was "phase locked," meaning that the clouds were all at the same phase in the moment they were dumped. This is implemented by estimating the magnetron frequency, then adding a random pause to the sequence between 0 and 5 times the magnetron orbit period (5 times in case there was any error in my estimation of the magnetron frequency). To determine the moment where the magnetron orbit is initiated, I pushed the random phase shift earlier and earlier in the sequence. Eventually, I determined that the magnetron phases were randomized even if the phase shift was added immediately after the clouds are extracted from the reservoir. Thus I say the clouds are "born with" the intrinsic magnetron.

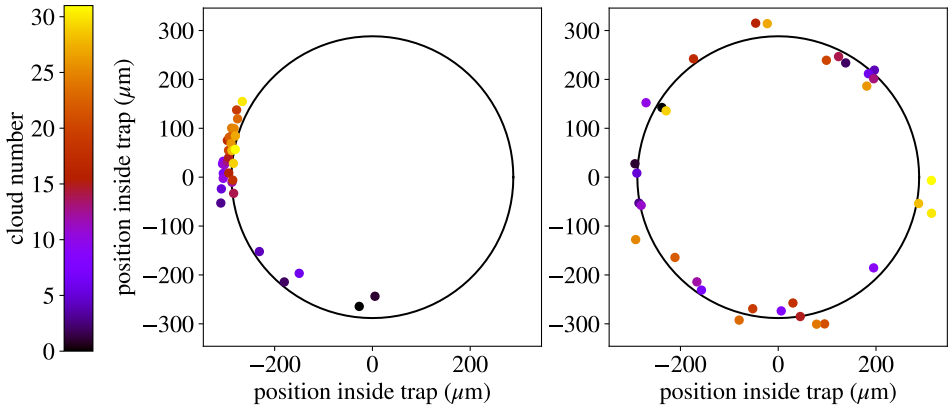

Figure 2.8: (left) Clouds are extracted from a plasma reservoir, then moved a short distance along the trap in about 50 ms then imaged. Because this is much quicker than in Fig. 2.8, the variation in magnetron phases due to the variation in scoop charge is much smaller. On the right, a randomized pause is added just after extracting the clouds from the reservoir. The final magnetron phase is randomized because of this.

I tried many things to reduce innate magnetron. Because it begins when the cloud is extracted from the reservoir, it seemed natural to vary the amount of time used to separate a cloud from the reservoir. This had no effect on the magnitude of the innate magnetron. The one thing that consistently affected the innate magnetron was moving the reservoir and performing the cloud cutting procedure with a different pair of electrodes. For example, in Fig. 2.9, I show a factor of two reduction in the innate magnetron after moving the reservoir one electrode to the left.

This operation had a major downside though—the reservoir was expanding vigorously, causing its space charge voltage to drop over time. With 10 mV steps, the cloud charge dropped to zero after about 30 extractions, meaning that the space charge voltage of the reservoir was dropping by more than 10 mV per extraction regardless of how much charge is extracted from the reservoir. With 100 mV we at least consistently extract clouds, but this step size is unusually large. I also found that the initial reservoir diocotron, and how it grew over time, depended on where the reservoir sat in the trap. This is discussed in more detail in the next section. In the end, this reservoir behavior was determined to be worse than a reservoir with larger innate magnetron but with more reproducible and smaller clouds. In

the end, we are unfortunately left with a procedure where we move the reservoir around and pick our favorite behavior based on a variety of upsides and downsides.

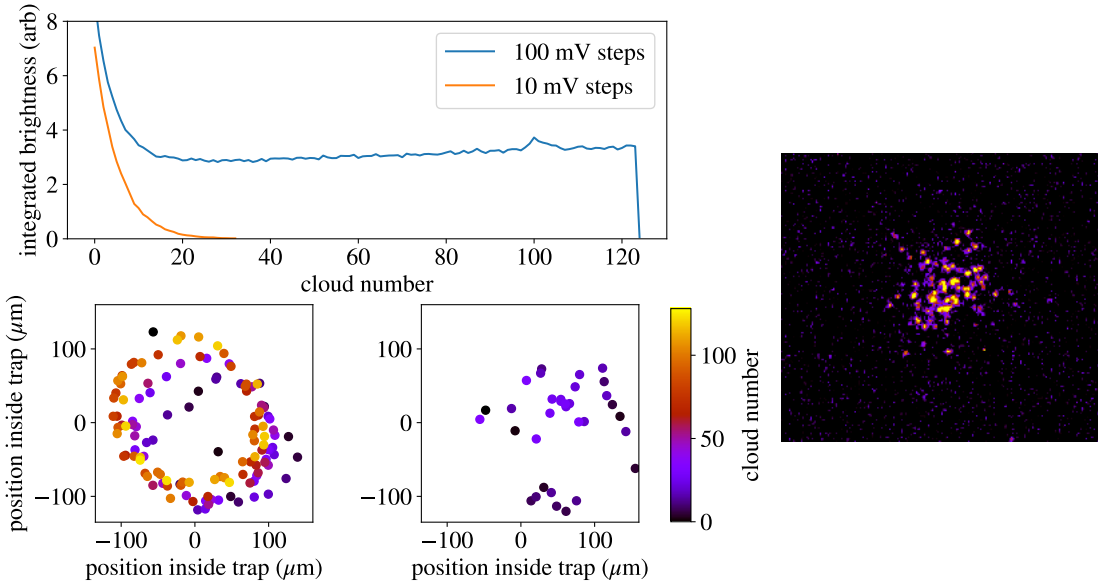

Figure 2.9: Two identically prepared reservoirs are used to sequentially extract clouds with 100 mV and 10 mV steps. Above, the integrated intensity is plotted for sequentially extracted clouds. In the bottom left, the imaged positions of the clouds extracted with 100 mV steps is plotted, with their color indicating the cloud number. The drift to the upper right with later extracted clouds is not a genuine phenomenon, but a systematic relating to the image artefacts discussed in Sec. 9.1. On the right, the 10 mV step clouds' positions are shown, but only about 30 clouds were extracted before their positions became impossible to determine. On the right, just for fun, one of the last few visible clouds with 10 mV steps is shown, showing what is likely individual electrons. When we apply the calibration factor between mcp total brightness and the number of electrons, we find that this imaged cloud should consist of roughly 100 electrons. We don't expect the electron detection efficiency to be 100%, but this image seems to suggest it also isn't far below 100%.

Given the qualitative behaviors described so far, it is very likely that the intrinsic cloud magnetron is caused by either patch potentials or misalignment between the trap electrodes and the external solenoid. When a cloud is extracted from the reservoir, it is moved quickly along the trap axis. In Sec. 2.3.3, I show that moving clouds quickly along the trap axis can excite a magnetron orbit. Also, when clouds are extracted from the reservoir, they are subjected to a "shallow trapping potential." In Sec. 3, it is clearly shown that in these shallow trapping potentials, clouds can be moved off-axis. However, here, the prediction of this effect would be significantly complicated by the reservoir's influence on the potential experienced by the cloud. Given that the innate magnetron seems to depend on where in the trap the extraction is performed, it is more likely that patch potentials are the dominant cause of the innate cloud magnetron. Thus efforts to reduce patch potentials like applying a colloidal graphite coating might be extremely beneficial in the vicinity of the reservoir.

2.3.2 Reservoir diocotron

Before I can discuss the diocotron motion of the reservoir, I should do some disambiguation. The story of the term begins with the "diocotron instability" [46], a well-studied phenomenon in nonneutral plasma and in beam physics where a hollow cylinder (a cylinder with an inner and an outer radius) of nonneutral plasma is unstable, and over time it chaotically folds itself into bundles (just search online for images of the "diocotron instability"). The $l = 1$ diocotron mode [47, 46] occurs when a cylinder of nonneutral plasma, hollow or not, is displaced from the center of a grounded conducting sphere. It then rotates around the center of the conducting sphere, $\mathbf{E} \times \mathbf{B}$ drifting from the electric field produced by its own image charge. Indeed, this is the $l = 1$ case of the unstable modes we refer to when we discuss the "diocotron instability." However, our plasmas do not have a hollowed out center, so they do not exhibit the "diocotron instability." They can have their diocotron modes excited; in fact these modes are even expected to grow over time [48, 49]. If the walls of the trap are at all resistive, the movement of the image charge converts mechanical energy into heat, and the diocotron modes are "negative energy waves"—when energy is lost the amplitude increases. However, this is not an instability in the same way that we mean when we talk about the "diocotron instability," which occurs regardless of the resistance of the trap walls. In my time at ALPHA, I observed plasmas performing an $l = 1$ diocotron motion very many times, and I often saw that this motion grew over time; I never observed evidence of any higher order modes. This $l = 1$ diocotron motion in nonneutral plasmas is discussed in Refs. [50, 51, 52].

The reader may note that the $l = 1$ diocotron motion of an electron plasma sounds a lot like what I call the "magnetron motion" of electron clouds. Indeed it is—these two forms of motion are two limits of the same phenomenon. We typically call the motion "diocotron motion" when the electric field causing the plasma to drift in circles is dominated by the plasma's image charge, and we call it magnetron motion when the electric field is due mostly to the trap fields. This distinction comes largely from the fact that the trapped ion community calls the $\mathbf{E} \times \mathbf{B}$ drift motion of single particles "magnetron motion." The name comes from the device used to produce microwaves—the motion of electrons resembles the motion of electrons in a magnetron. The motion of electron clouds is more similar to the motion of single particles.

With that aside, I'll begin to explain my evidence that in both ALPHA-g and ALPHA-2, a growing reservoir diocotron results in a growing cloud magnetron. I'll begin with ALPHA-2, where we have never successfully implemented a reservoir without a growing diocotron. To produce Fig. 2.10, we extract clouds from a reservoir then image them, with a random phase shift added so that the intrinsic magnetron is not phase-locked. Thus, the first few clouds' imaged positions form a clear circle. With time, the reservoir's diocotron grows. This seems to add another component to each clouds' initial magnetron motion in a random direction. One should keep in mind that the scooping operation is typically very slow compared to the reservoir diocotron frequency. A plausible model is that the cloud and the reservoir diocotron together until some moment where they are sufficiently decoupled. We would expect this to occur at a random diocotron phase unless there was a remarkable coincidence between the frequency with which we extract clouds from the reservoir and the reservoir's diocotron frequency. In this model, the cloud's displacement due to the intrinsic magnetron is a fixed

transverse displacement, a 2–D vector. We then add the cloud's displacement due to the reservoir diocotron, which points in a random direction with a slowly increasing magnitude. In Fig. 2.10, the direction of the resulting total vector is then randomized by the random phase shift, and the result is a circle whose thickness increases over time.

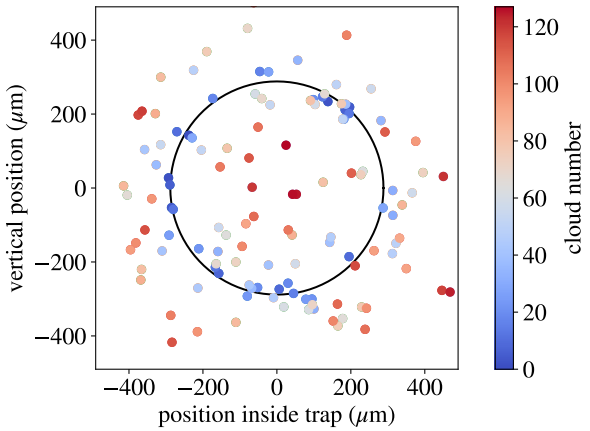

Figure 2.10: Each dot is the position of the center of a cloud imaged with the MCP. The clouds are successively extracted from a reservoir in ALPHA-2, and the reservoir's diocotron amplitude increases with time. The color of each dot indicates the order in which the clouds were extracted. We extract about one cloud per second for a total of two minutes.

The reservoir's diocotron can also be diagnosed by simply imaging the reservoir—for most plasmas, the diocotron frequency is much slower than the time it takes to release the plasma toward the MCP. In Fig. 2.11, I show the imaged positions of nine reservoirs. Each reservoir was used to extract and image 120 clouds. In fact, it is rather hard to find a set of reservoirs which clearly all have similar sizes but different centers. This is because the reservoir diocotron seems to facilitate reservoir expansion. Therefore, the most obvious observation is that when the imaged positions of clouds start to strongly deviate, the reservoir is also much larger. However, by finding a few reservoirs with very similar radii, we do observe some small displacement in their imaged positions. For this reason, I cannot rule out that the reservoir's expansion is changing the intrinsic magnetron, which may depend on the parameters of the reservoir (density, total charge, radius, etc.). This obviously complicates our interpretation of the data.

Now I move on to some data from ALPHA-g. Like in ALPHA-2, I begin with imaged cloud positions, shown in Fig. 2.12. This time, I have phase-locked the innate magnetron by imaging clouds only 30 ms after they are extracted from the reservoir (and I have not added a random phase shift). Here we see clearer evidence that the increasing reservoir diocotron acts like a vector of increasing magnitude and random direction—as opposed to a random but generally increasing magnitude. Consider for example the yellow points, which form a ring on the outside of Fig. 2.12.

On one particularly silly evening at ALPHA, I took the time to implement a positron reservoir. I'm not sure exactly why I was given the time to work on this. I may have snuck it into the schedule on a day that was allocated for measuring patch potentials or improving reservoir behavior. There are, however, legitimate justifications for a positron reservoir.

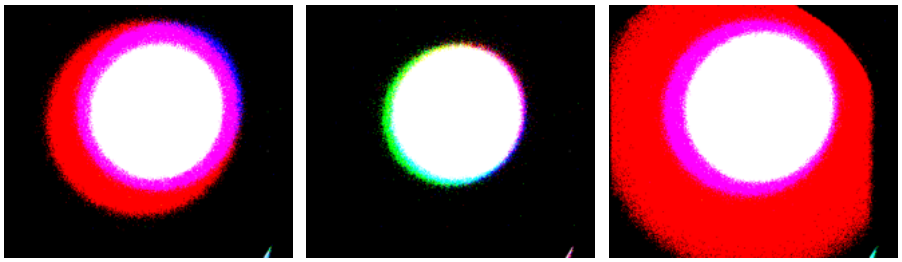

Figure 2.11: In each of the three pictures, three MCP images of reservoirs are shown (a total of nine imaged reservoirs are depicted). The reservoirs were prepared identically, then used for similar (but not identical) cloud-based measurements, then imaged. In each picture, one reservoir is assigned to red, one to blue, and one to green. Thus the white region is the region where all three reservoirs overlap, the red region only contains the red-assigned plasma, the purple region contains the red and the blue plasmas, etc. On the left, we see three reservoirs of different size; the blue reservoir is smaller than the red, but nonetheless there is a small blue sliver in the upper right, clearly indicating that the blue and the red reservoirs did not have the same center inside the trap. In the middle, we have three reservoirs of roughly equal size that do not overlap, indicating a small diocotron. On the right, there are three reservoirs with radically different size. They do seem to have different centers, but that is made unclear by their differences in size and the apertures of the imaging system.

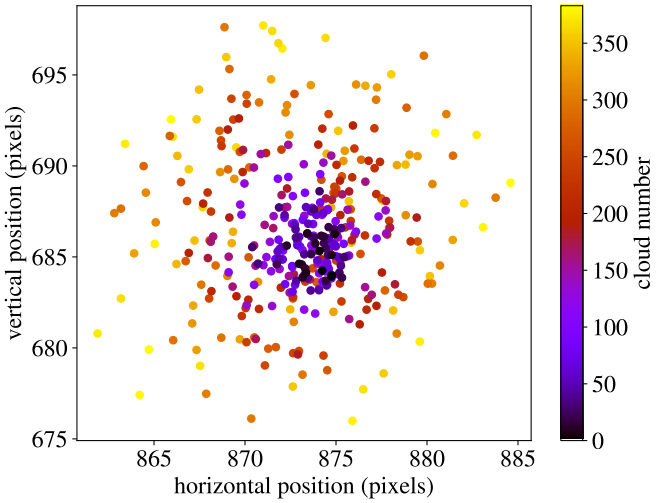

Figure 2.12: The positions that clouds land on the MCP when successively extracted from a reservoir in ALHPA-g which has an increasing diocotron amplitude. The color of each cloud position indicates the order in which the clouds were extracted. Clouds are imaged 30 ms after extraction from the reservoir to preserve phase coherence of the intrinsic magnetron. This isolates sources of magnetron motion which vary from one cloud to the next.

In this thesis I often suggest that certain effects are due to perturbations to the trapping potential from patch potentials. If we could use positron clouds, we would reverse the sign of the potential used to trap the clouds, and presumably we would flip the relative sign of the

shift due to patch potentials, confirming this hypothesis. This reservoir was never actually used for this purpose because the resulting clouds were much worse (bigger in radius and less reproducible), possibly stemming from the fact that the positron plasma contains far fewer particles than we can achieve with electrons.

However, the positron reservoir gives some additional experience on the phenomenon of reservoir diocotron. In one instance, I just prepared a positron reservoir and imaged 128 clouds on the MCP followed by the reservoir. The reservoir landed roughly where I expected if it were located in the trap center. The clouds landed somewhat randomly distributed within a small circle similar in size to the innate magnetron of electron clouds extracted using the same electrodes in ALPHA-2.

Next, I prepared a positron reservoir, then I turned on the solenoid which boosts the magnetic field in the region of the reservoir from 1 T to 3 T. The resulting reservoir had a rapidly increasing diocotron. This diocotron was so large that more than half of the clouds simply missed the MCP. When I tried to image the reservoir, it was barely visible peeking out of the right side of the MCP image. In a repeat trial, the reservoir was not visible at all on the MCP (but I'm sure it still existed because the last few clouds were still visible on the edge of the MCP). Unlike the prior electron examples, the positron diocotron grew faster than the plasma expanded. It's not clear whether the solenoid turning on initiated a diocotron which grew, or if it just facilitated the growth of a preexisting diocotron. The data from these trials is shown in Fig. 2.13.

Next I will comment on the phenomenon of "catastrophic reservoir diocotron failure," which occurs in both ALPHA-2 and ALPHA-g. In fact, all the reservoirs I have seen that exhibited some reservoir diocotron also exhibited this catastrophic failure eventually if one attempted to extract enough clouds. This phenomenon is characterized by a sudden rapid increase in cloud position variability (over the course of about ten extractions and ten seconds). The charge of the clouds decreases and their radius increases—a reflection of the reservoir expanding and its space charge voltage dropping. After this no more clouds are visible on the MCP, and if the reservoir is imaged it usually has expanded so much that it simply fills the entire MCP. Unfortunately, this phenomenon is not reproducible. It occurs after different amounts of time for identically prepared and utilized reservoirs, but this rarely differs by more than a factor of two. It typically happens after 100–200 extractions or 100–200 seconds.

Because this phenomenon happens nearly identically in ALPHA-g and in ALPHA-2, I will just present the data from ALPHA-g in Fig. 2.14, where I could find a slightly clearer dataset showing the phenomenon. The data from this figure was taken during misalignment measurements, so the clouds are not expected to all fall in the same place on the MCP ; I never took data exhibiting this phenomenon in isolation. Rather, we expect the clouds to fall along a line. A short line is visible in the first row, and a longer line is visible in the first 100 or so clouds in the third row. Fig. 2.14 shows the results of three reservoirs prepared in the course of a complete measurement of the misalignment of the trap with the external magnet. In the first row, we see a reservoir where the desired measurement was completed before the reservoir failed. In the second measurement, we see the onset of reservoir failure—the last few clouds have a significantly larger spread, and the cloud parameters are starting to change rapidly. In the third measurement, I tried to extract over 200 clouds from the reservoir, and it failed catastrophically after about 210 clouds. The last 50 or so clouds are spread wildly

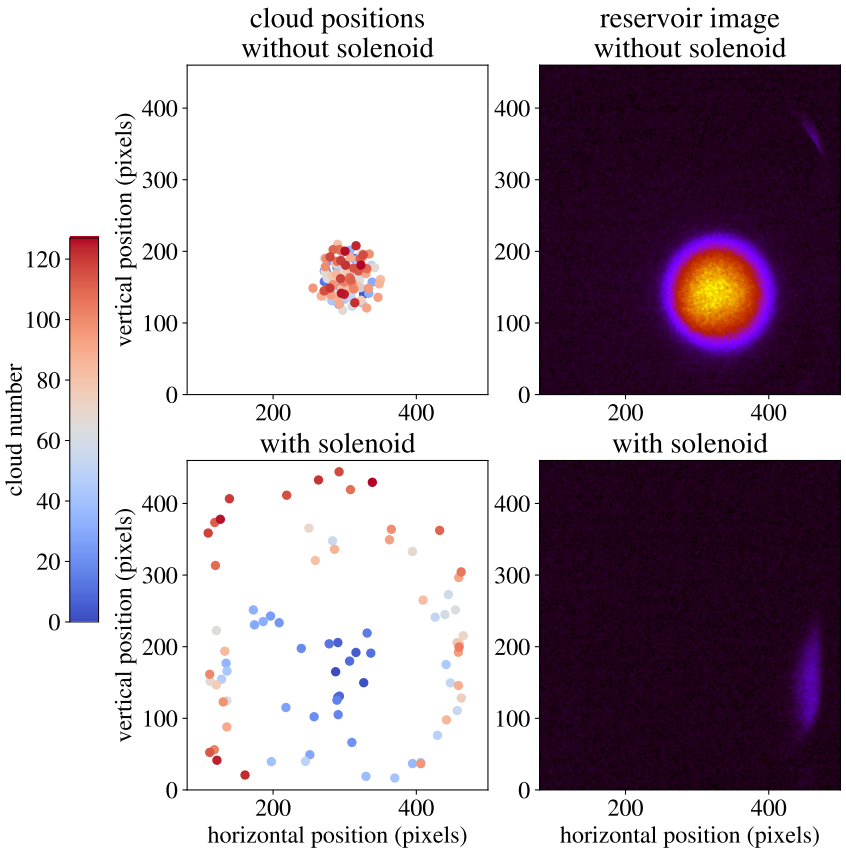

Figure 2.13: The top row shows the result of implementing a positron reservoir without an extra solenoid boosting the magnetic field from 1 T to 3 T. The left is the distribution of cloud positions on the MCP, with their color indicating the order in which they were extracted. On the right, the imaged positron reservoir at the end of 128 extractions. Below are the same results when the solenoid is turned on after preparing the reservoir. Less than half of the clouds were even visible on the MCP, and many of them are only visible because a small fraction of the cloud hit the outer edges of the imageable region. Thus the structure of the cloud positions apparent in the bottom left illustrates the MCP aperture shape.

around the MCP, rendering the measurement useless. The clouds' imaged brightness, and hence their charge, drops to zero, and their radius increases dramatically. Fig. 2.14 also shows the imaged reservoirs. The first shows zero diocotron, the second shows a small but clearly visible diocotron, and in the third, the reservoir has expanded so much that it fills the entire imageable region of the MCP.

In the year after I stopped physically working on the ALPHA experiment, Ph.D. student Jaspal Singh seems to have solved this problem. He discovered that when the "the scooping period"—the time between cloud extractions from the reservoir—was a multiple of $T_{\text{bad}} = 145\,\mu\text{s}$, the reservoir diocotron grew quickly. Jaspal varied the scooping period in small increments starting at 58 ms, observing several "resonances" where the reservoir diocotron grew rapidly. Depending on the parameters of the reservoir, T_{bad} is a plausible order of magnitude for either the diocotron period or the plasma rotation period. It would seem

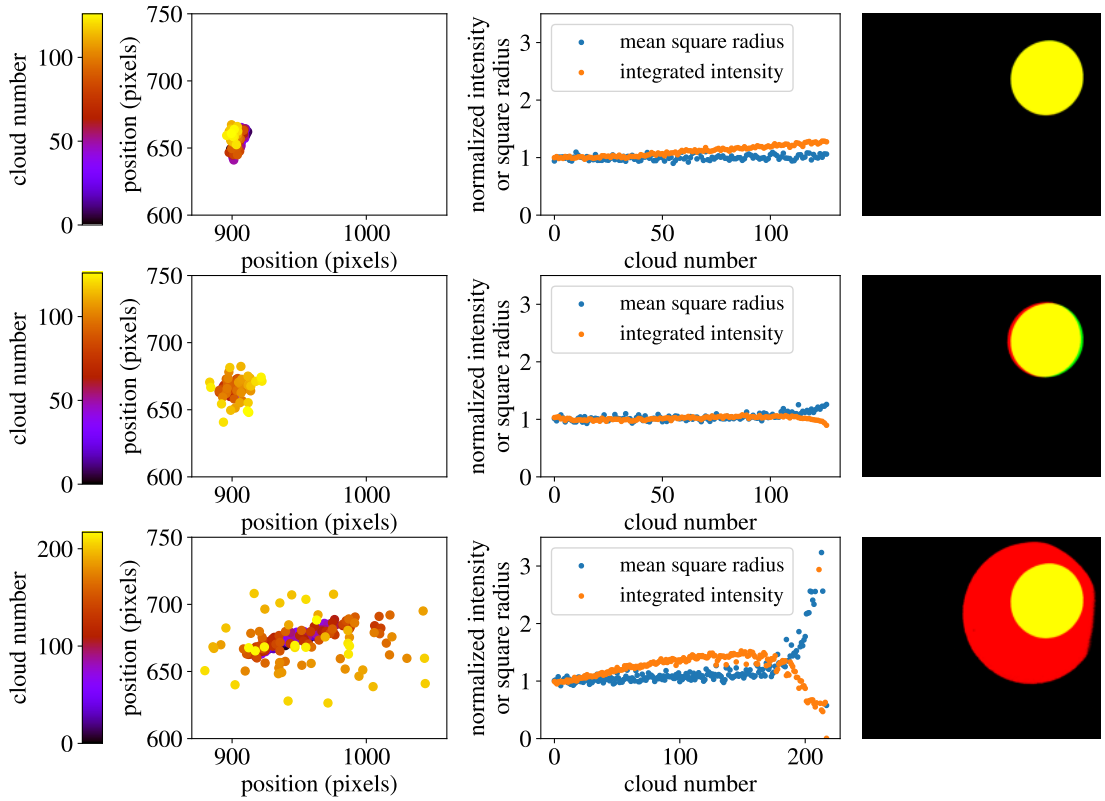

Figure 2.14: Three reservoirs used to measure the misalignment of the Penning-Malmberg trap electrodes with the external solenoid. Each row shows the results from one reservoir and one attempted cloud-based measurement. The first column shows the clouds' positions on the MCP, with their color indicating the order of extraction. The second column shows the clouds' mean square radius visible in their MCP images, and the integrated total brightness of the spot they produced in the image (roughly proportional to the total charge). Both are plotted with normalized units where the first few clouds have a normalized brightness and radius of 1. The last column shows the imaged reservoir at the end of the sequence. In this last column, I have assigned a high-contrast picture of a "reference reservoir" which was used for a successful measurement with no diocotron issues to the color green. I have assigned red to the reservoir used to collect this data. Thus the red region shows where this reservoir was on the MCP but not the reference reservoir, the yellow region is the overlap, and the green region is where only the reference reservoir was seen.

then that removing clouds from the reservoir perturbs the reservoir in an asymmetric way, and if the scooping period is a near-multiple of the diocotron period or the rotation period (whichever one T_{bad} ends up being), these small displacements add up over time. This reminds us of the intrinsic cloud magnetron—in fact we know that there is some transverse asymmetry in the scooping process. The two phenomena may be related.

In hindsight, Jaspal's observation is entirely consistent with my experiences. In most of my experiments, the scooping period was varying as I varied the parameters of whatever cloud-based measurement I was performing at the time. At some point, the scooping period

would be a multiple of T_{bad} for a few clouds in a row and I would get a catastrophic diocotron.

My only experience reducing reservoir diocotron was in ALPHA-g. The first reservoir I ever implemented had no evidence of any reservoir diocotron. The reservoir was developed in, and sat in, a 2 T magnetic field where the nominal 1 T from the outer solenoid was supplemented by an inner solenoid. I could extract a thousand clouds and they would only exhibit innate magnetron. That innate magnetron was also much smaller than what we find in ALPHA-2. This was cause for celebration—patch potential measurements and ECR magnetometry measurements were going to be much easier in ALPHA-g. However, the ALPHA-g gravity measurement required the extra solenoid to be off, because it introduced an unacceptable asymmetry in the magnetic field. Therefore, we developed a reservoir in the 1 T field without the extra solenoid so we could measure the magnetic field used for the ALPHA-g measurement. The data from this section is taken from that reservoir—as you have seen, it exhibited a catastrophic reservoir diocotron failure. In the final two weeks of operating ALPHA-g, when I was developing EMPI (see Sec. 8), I made a new reservoir in 1 T which didn't exhibit this behavior. I had noticed before that the 2 T reservoir had a lot more electrons—about 5×10^7 instead of 2×10^7, so I implemented a 1 T reservoir with the larger total charge. I also reduced the rotating wall used for SDREVC from 800 kHz to 300 kHz to match the frequency used in 2 T, thinking that some electronic peculiarity of the rotating wall might be initiating the diocotron. Increasing the charge would have increased the diocotron frequency, probably making it less likely that I would hit this resonance. It may also be that the width of this resonance depends on other parameters of the plasma. Hopefully Jaspal will be able to conduct further experiments on this phenomenon to better understand how to avoid it.

2.3.3 Moving clouds along the trap too quickly

This final source of cloud magnetron motion is much simpler than the previous two. It is also better understood and essentially trivial to solve. If the clouds are moved along the trap axis to a desired measurement location too quickly, they are thrown off-axis by trap construction errors, the misalignment of the electrodes with the magnetic field, and patch potentials. This sets a limit on how quickly we can move clouds along the trap axis. In EMPI, if we can move clouds more quickly along the trap axis we can perform more frequent measurements of a changing magnetic field, and in Sec. 8 I will show that more frequent measurements can also be more precise. Thus this effect is actually critically important for at least one cloud-based measurement, and it simply limits how quickly we can perform other measurements.

These three causes—construction errors, misalignment, and patch potentials—fall under a common explanation. A cloud which is located off-axis by a distance r orbits the trap center with a frequency ω_r. The frequency ω_r is set by the trapping potential, which can be approximated by

$$V(x,y,z) = -k_2 \left[(z-z_0)^2 - \frac{1}{2}(x-x_0)^2 - \frac{1}{2}(y-y_0)^2 \right], \tag{2.8}$$

giving $\omega_r = k_2/B$. The cloud is moved axially along the trap by changing z_0 with time. If any of these three issues are present, x_0 and y_0, the center of magnetron motion, also change

with time. If this "effective trap center" moves slowly compared to $r\omega_r$, then r is conserved adiabatically. This is discussed in much more detail in Sec. 3.3.

If the trap is misaligned with the external magnet by an angle θ, then θv_z needs to be much smaller than $r\omega_r$. In ALPHA-g, θ varies throughout the trap, but it generally is of order 1 mrad. Patch potentials cause the effective trap center to be displaced by $\vec{\varepsilon}/k_2$, where $-\vec{\varepsilon}$ is the transverse electric field (a 2–D vector) in the center of the trap produced by patch potentials. Thus they produce an effect equivalent to a misalignment of $\theta = d(\vec{\varepsilon}/k_2)/dz$. Throughout most of ALPHA-2 and ALPHA-g, $\vec{\varepsilon}$ is of order 5 mV/cm, and it varies over a length scale of roughly the trap wall radius, and we typically use k_2 of order 5×10^4 V/m^2 while moving clouds along the trap. Thus we find an effective misalignment of order 0.5 mrad—a similar order of magnitude as the true misalignment. It should be noted though that some trap regions have much stronger patch potentials, and there the patch effect will dominate. Finally, there is one particular region of the trap where one electrode is "non-concentric with," or displaced transversely from the next by about 60 μm. This does not mean that the effective trap center suddenly changes by this distance. Rather, the effective trap center will smoothly change from the center of one electrode to the center of the next as we move a cloud across the boundary. Thus an estimate of the effective misalignment due to this feature is $\theta = 60\,\mu\text{m}/2\,\text{cm} = 3\,\text{mrad}$ (the displacement divided by the length of an electrode). This is probably an underestimate of the maximum θ, because it assumes as conservatively as possible that the effective trap center changes linearly as we move the cloud linearly from one electrode to the next. Indeed for this small portion of the trap this displacement dominates the total effective misalignment. Finally, our typical initial displacement of the electron clouds is $r = 25\,\mu$m, so to conserve this we must must move very slowly compared to:

$$v_z \ll \frac{16\,\mu s}{\text{electrode}}\left(\frac{\text{electrode length}}{2\,\text{cm}}\right)\left(\frac{25\,\mu\text{m}}{r}\right)\left(\frac{0.5\times10^5/\text{s}}{\omega_r}\right)\left(\frac{\theta}{1\,\text{mrad}}\right). \tag{2.9}$$

Since we must move "very slowly," and because there are many electrodes (about 30 in ALPHA-g, about 15 in ALPHA-2) to move across and we don't want an error to accumulate, at least one factor of ten is probably going to be necessary.

Before I discuss the experimental tests of this effect, I should explain how clouds should be moved along the trap axis. In my time at ALPHA, I have seen three common strategies used when designing the electrode voltages that move clouds along the trap axis. These three strategies are shown in Table 2. In light of the model I'm describing for how clouds move off-axis, the optimal strategy is the one that maximizes ω_r. This trivially establishes that we should use the maximum voltage available to us. To see which strategy is best, we have to model the electrode geometry at ALPHA to see what values of k_2 are applied at different times throughout each of these sequences. To answer this question, we only need to compute k_2 values in three different situations—a voltage applied to only one electrode, the same voltage applied to two adjacent electrodes, and a voltage applied to one electrode and half that voltage applied to the two adjacent electrodes. If it's not clear when this third situation is encountered, consider the potentials that would be applied halfway between steps in the third strategy. The resulting k_2 values are presented in Table 3.

The first strategy is the worst. Halfway between step 1 and 2, we have half the maximum

step	E(N-1) potential (V)	E(N)	E(N+1)	E(N+2)	E(N+3)
1	0	75	0	0	0
2	0	0	75	0	0
3	0	0	0	75	0

step	E(N-1) potential (V)	E(N)	E(N+1)	E(N+2)	E(N+3)
1	0	75	0	0	0
2	0	75	75	0	0
3	0	0	75	0	0
4	0	0	75	75	0
5	0	0	0	75	0

step	E(N-1) potential (V)	E(N)	E(N+1)	E(N+2)	E(N+3)
1	75	75	0	0	0
2	0	75	75	0	0
2	0	0	75	75	0

Table 2: Voltage instructions used to move a cloud (or plasma) along the trap axis a distance of two electrode widths. In each of these three proposed strategies, the electrode potentials are changed linearly between each step. It should be noted that the first two strategies move the cloud from the center of electrode N to the center of electrode N+2. The third strategy starts midway between electrode N-1 and electrode N and it ends between N+1 and N+2. 75 V is the maximum voltage available on most of the electrodes in ALPHA-2 and ALPHA-g. A few electrodes have 150 V amplifiers, in which case we can trivially double ω_r by using the higher voltage.

voltage applied to two adjacent electrodes. Thus we find that strategy 1 is strictly worse than strategy 2.

- Strategy 1 varies k_2 between $c_1(75\,\mathrm{V})/R_w^2 = 1.04 \times 10^5\,\mathrm{V/m^2}$ (75 V applied to one electrode) and $c_2(37.5\,\mathrm{V})/R_w^2 = 2.88{\times}10^4\,\mathrm{V/m^2}$ (37.5 V applied to adjacent electrodes).
- Strategy 2 varies between $c_1(75\,\mathrm{V})/R_w^2 = 1.04 \times 10^5\,\mathrm{V/m^2}$ and $c_2(75\,\mathrm{V})/R_w^2 = 5.76 \times 10^4\,\mathrm{V/m^2}$.
- Strategy 3 is worse, but not so trivially. It goes between $c_2(75\,\mathrm{V})/R_w^2 = 5.76{\times}10^4\,\mathrm{V/m^2}$ and $c_3(75\,\mathrm{V})/R_w^2 = 6.24 \times 10^4\,\mathrm{V/m^2}$ (75 V applied to one electrode, and 37.5 V applied to the two adjacent electrodes).

I have used strategy 3 instead of strategy 1 on some occasions because it saves some memory in the FPGA used to control the electrode voltages—it needs half as many voltage states per electrode movement.

Of course, there are more sophisticated analyses and more sophisticated strategies we could use here. Technically, the conservation of r depends not only on k_2, but the ratio of k_2 to the speed at which the axial potential maximum holding the electrons moves. With this in mind, one could optimize a complicated sequence of linear voltage ramps that tries to move the clouds at a constant rate while maximizing k_2. Actually, in Sec. 3.3, I will show

Situation	E(N-1) potential (V)	E(N)	E(N+1)	k_2 (V/R_w^2)
strategy 1, step 1	0	1	0	c_1 =0.668
strategy 2, step 2	1	1	0	c_2 =0.372
strategy 3, between step 1 and 2	0.5	1	0.5	c_3 =0.403

Table 3: For each of three sequences of voltages applied to three adjacent electrodes, the k_2 value is computed. In the left column, one example from Table 2 where such a sequence of voltages arises is provided. The examples aren't unique; there are many instances in Table 2 where three adjacent electrodes have voltages proportional to the values in this table. Note that k_2 changes linearly when the voltages are scaled linearly, so we only need to do the computation with the maximum voltage set to 1 V. k_2 is presented in units of volts per wall radius squared, so the values computed here only depend on the length to radius ratio for our electrodes (about 0.9 in both ALPHA-2 and ALPHA-g).

step	E(N-1) potential (V)	E(N)	E(N+1)	E(N+2)	E(N+3)
1	−75	+75	−75	−75	−75
2	−75	+75	+75	−75	−75
3	−75	−75	+75	−75	−75
4	−75	−75	+75	+75	−75
5	−75	−75	−75	+75	−75

Table 4: The best way to move clouds along the trap axis. This assumes a maximum electrode voltage of ±75 V.

that changing the effective trap center in a more differentiable way suppresses the change in r more strongly. Thus if we wanted to put more effort into cloud movement, this would be the avenue to pursue. Currently, the cloud's axial position changes in a continuous, but not differentiable way. Making it "smoother" (i.e. once or more differentiable) would suppress changes in r with higher powers of $v_z/r\omega_r$. However, the "sequencer"—the piece of software where we can design a sequence of electrode voltages to be applied in the experiment—has limitations on how many states can be used. We provide a sequence of states, and it allows us to choose the time taken to linearly interpolate between each of those states. For now, it is not worth trying to improve our strategy for cloud movement, but this may change if the sequencer's memory is ever significantly upgraded.

Before I move on, I should note that ω_r can be doubled in all three strategies simply by changing all the zeros to the maximum negative voltage of −75 V. If we redefine zero potential to −75 V, we see that this is equivalent to simply doubling the voltage used to confine the electrons. This strategy was used in EMPI, where cloud movement speed was most critical. This upgraded strategy is shown in Table 4.

My best experimental test of this effect comes from studying the magnetron motion induced by crossing the aforementioned displacement. This construction error was first discovered in the misalignment measurements. These measurements and their errors are described in more detail in Sec. 6. Fig. 2.15 shows measurements of the positions of electrostatic potential minima created by the electrodes in a coordinate system where $x = y = 0$ corresponds to a single magnetic field line produced by the external magnet. In simpler

terms, a misalignment between the trap electrodes and the external magnet is indicated by deviations from $x = y = 0$. Although there are many notable features in this plot, I want to particularly highlight that when the axial position goes from electrode 19 to electrode 20, the horizontal position jumps by about 0.1 mm between two measurements. Because this displacement is mostly horizontal, it is more easily visible when we plot the horizontal displacement versus axial trap location; this is shown in Fig. 2.16. This axial trap location is also where the electrode radius changes from 1.5 cm to 2.2 cm. It is easy to imagine that this connection between different kinds of electrodes could result in an offset misalignment.

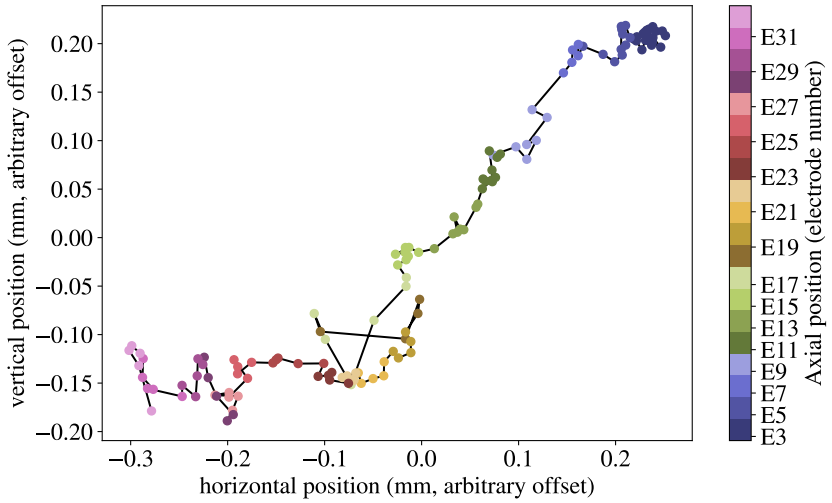

Figure 2.15: The transverse displacement between the electrodes and the external magnet. The color of each point shows where along the trap axis the measurement is performed, and adjacent axial positions are connected with a black line.

Seeking confirmation of the existence of this displacement, I moved electron clouds along this boundary at variable speeds. In this experiment, all other axial movement of clouds was performed very slowly. Upon reaching the electrode that I would image the clouds from, they were stored in eight different trapping potentials then imaged. This was done to phase-unlock the magnetron motion. For each different trapping potential, four repeats were performed. Thus phase-locked forms of magnetron motion like innate magnetron motion and the magneton induced by moving past this boundary would be visible between clouds treated to different trapping potentials. Within one trapping potential only incoherent sources of magnetron motion would be visible, like magnetron motion due to reservoir diocotron. The entire dataset was taken with one reservoir, and a reservoir diocotron is visible in the last three movement times measured, 0.7 ms, 0.1 ms, and 5 ms. Thus we see a bigger spread in these points.

The raw data from this experiment is shown in Fig. 2.17, and the resulting magnetron radius induced by the movement across the electrode misalignment is shown in Fig. 2.18. The data isn't sufficient for finding a real power law, but having vaguely plotted $1/T$ and $1/T^2$ power laws, it seems that $1/T$ is more consistent with the data. As we will see in Sec. 3.3, $1/T$ is the expected result for changes to the magnetron center which are continuous but not differentiable, which is exactly how movements between electrodes are performed. After

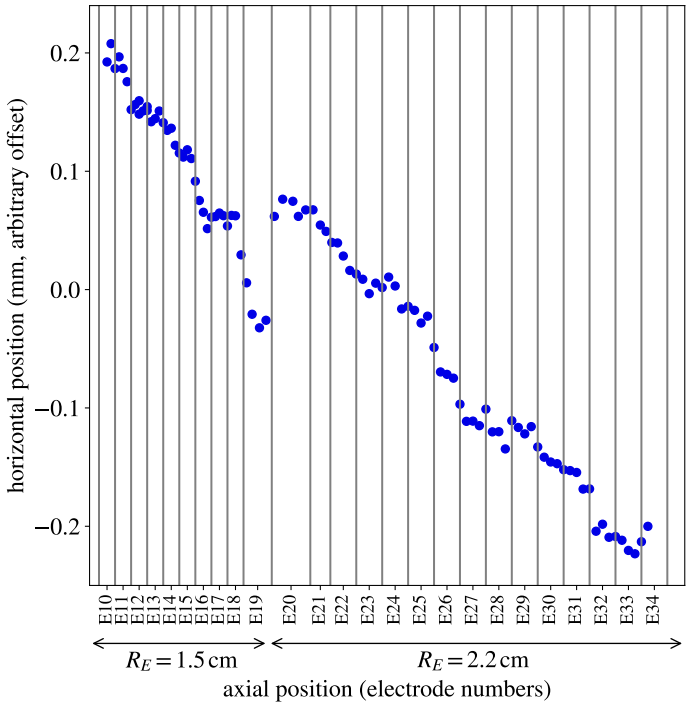

Figure 2.16: In this plot, only the horizontal position from Fig. 2.15 is plotted versus the axial position. The radius of each electrode is provided below the electrode numbers, in particular to highlight where the radius changes.

I collected this data, I typically moved clouds at a speed of 2.5–5 ms per electrode, and I never encountered this kind of initial cloud magnetron again.

The technique described here might actually act as a useful tool for measuring trap misalignment. Moving very quickly along the trap axis—as quickly as the electrodes can change voltage, or about 10 μs—could be used to measure the derivative of x_0 and y_0 with respect to z_0 in Eq. 2.8. This could be compared to, or used to supplement the measurements described in Sec. 6, which can be interpreted as absolute measurements of x_0 and y_0.

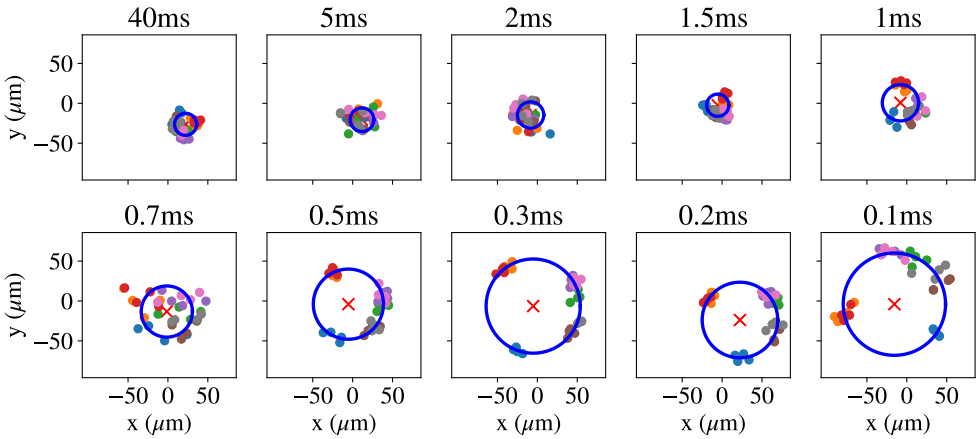

Figure 2.17: The data taken while measuring the magnetron motion induced by moving quickly across the electrode 19/electrode 20 boundary. Each subplot lists a different amount of time taken to move between the center of electrode 19 and the center of electrode 20. For each color, the clouds are trapped with a different trapping potential (a different k_2, and hence a different ω_r just before imaging). For each of these trapping potentials, the experiment is repeated four times, and the clouds centers are recorded above. The horizontal and vertical axes have been converted from pixels on an MCP image to microns of displacement inside the trap. A circle is fit to the data from each subplot, and the center of the circle is marked with a red X.

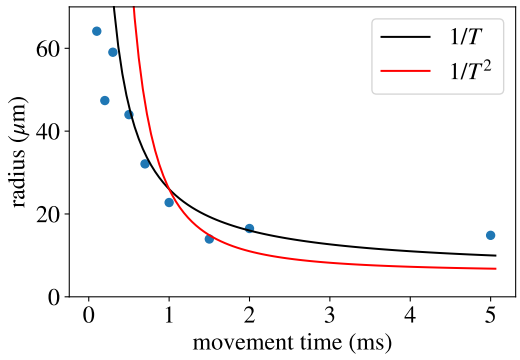

Figure 2.18: The circle radii from Fig. 2.17 are plotted versus the movement time across the construction error. An "eyeball fit" of a $1/T$ power law and a $1/T^2$ power law (plus an offset) is included to show that $1/T$ is more consistent with the data.

3 Patch potential measurements

"Patch potentials" are variations in the electrostatic potential along the surface of a nominally conductive material. They have been shown to perturb the motion of free falling test masses in satellites [53, 54, 55]. They also pose a challenge to measurements of the Casimir mechanism, where the force between two metal plates separated by a very small distance is measured [56, 57, 58, 59]. Patch potentials also make it nearly impossible to measure the effect of gravity on free charged particles [60, 61, 62]. They have been shown to move charged particles off-center in radio frequency traps, causing increased ion micromotion [63, 64]. I should note that when ions are laser cooled in microfabricated ion traps, they are often more sensitive to electric field noise, not DC offsets, emanating from conducting surfaces [65], which I consider to be a separate phenomenon. In Ref. [66], patch potentials in a Penning trap are blamed for degrading measurements of a trapped ion's cyclotron frequency. Finally, in Ref. [67], the authors observe a shift in the bounce frequency of charged particles in a a Penning trap that they attribute to patch potentials.

My original technique for measuring patch potentials has been published in Ref. [68]. These results are also discussed in this thesis, but with some improvements to the quality of the data. Additionally, I will discuss observations of patch potentials in ALPHA-g; for an unknown reason, much larger patch potentials patch potentials were observed in ALPHA-g.

3.1 Motivation for measuring patch potentials

The first novel thing I ever measured with clouds extracted from a reservoir was electric fields produced by patch potentials in the ALPHA-2 Penning-Malmberg trap. This measurement was performed during the summer after I graduated from undergrad (the summer before I started my PhD). The project I was assigned as an undergrad was to figure out why antiprotons created by photoionization of antihydrogen escape the ALPHA-2 trap. I made a simulation, and I included a number of errors in the magnetic field (misalignments, higher order moments, etc.), as well as a model for the electrical noise from the electrode amplifiers. No reasonable errors could cause the antiprotons to escape the trap—the axial solenoid and the weak trapping field [$\mathcal{O}(10\,\mathrm{mV})$] produced by the electrode voltages applied during spectroscopy experiments was easily strong enough to confine antiprotons indefinitely.

At the time, the collaboration was measuring the 1S–2S two-photon transition in antihydrogen [10, 11, 12]. Another mystery the collaboration was contending with was that after a few hours of laser exposure, the antihyrogen trapping rate would drop. Eventually the collaboration figured out that this was due to positron temperatures increasing. After this realization, the collaboration began routinely measuring "positron heating rates." A positron plasma is adiabatically expanded by transitioning from a deep trapping potential where the plasma has reached an equilibrium temperature to a shallow trapping potential where the plasma is much longer. Then the positron plasma temperature is measured 1, 2, 5, and 9 s after that transition. The results of this study are shown in Fig. 3.1. We see that when the 1S–2S laser is not actively being used, positron temperatures after 9 s remain roughly constant. Then in the days where 1S–2S spectroscopy is being performed, the temperatures steadily rise. The temperatures can also be restored to normal by warming the trap from cryogenic temperatures to room temperature; thus the temperature of the walls of the trap

is also plotted (and it is a somewhat humorous coincidence that the trap's temperature can be plotted with the same vertical scale as positron temperatures). When I asked around for what people thought was causing the temperature increase, some people suggested patch potentials were the culprit, and some suggested that the trap's vacuum was worsening.

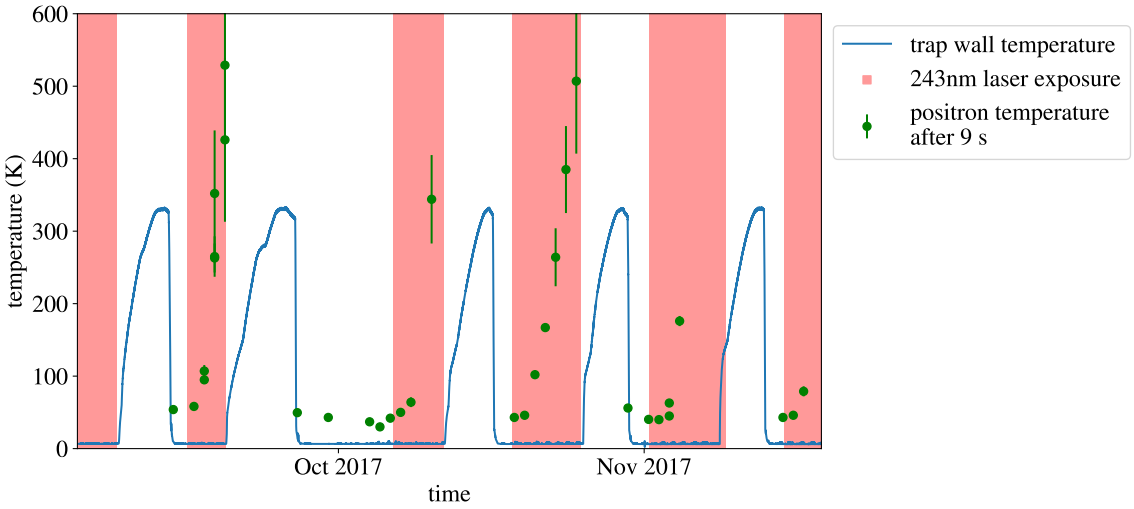

Figure 3.1: Positron temperatures after adiabatic expansion followed by 9 s of heating are reported from the 2017 1S–2S data taking campaign. Times when the 1S–2S was actively being used for spectroscopy are highlighted in red. Positron temperatures are plotted with green dots along with a statistical fitting errorbar. Trap temperatures are indicated with a blue line, only for the purpose of seeing when the trap is warmed to 300 K.

Around the same time, a postdoc was given a few hours of experimental time to perform an experiment that would shed some light on my undergraduate project. He simply prepared an antiproton plasma, then he put it in the same weak trapping field that is used during antihydrogen spectroscopy. The detector confirmed that these antiprotons hit the walls of the trap after about 20 ms. The phenomenon was also dependent on which electrode the antiprotons started in—in some locations it took several seconds to start seeing antiproton annihilation events. In hindsight, presumably in some locations either electrode offsets or patch fields themselves created traps for antiprotons.

I had the following idea: if very shallow trapping potentials cause antiprotons to hit the trap wall, but in strong trapping potentials plasmas are quiescent for long periods of time, then maybe intermediate strength trapping potentials will cause plasmas to move off-axis by an observable distance. Dr. Eric Hunter [4] was also at ALPHA at the time, and he had just implemented a reservoir for ECR. I decided to use Dr. Hunter's electron clouds for this experiment, mostly because it would allow me to image many clouds while varying the strength of the trapping potential. I don't think I understood at the time just how well my experiment was designed. Had I used any other plasma available to me (antiproton, electron, or positron plasmas nominally in use at ALPHA), the measurement wouldn't have worked; the space charge voltage would have been too high, and the plasma would simply evaporate and expand when placed in a shallow trapping potential. My choice of using 0.3–2 V trapping potentials to move the clouds off-axis was also absolutely perfect, and if I

remember correctly it was chosen absolutely arbitrarily.

Such a choice can be justified post-hoc by saying that 20 ms is the time needed for an antiproton to $\mathbf{E} \times \mathbf{B}$ drift to the trap wall due to an electric field from patch potentials. Thus $20\,\text{ms} = R_w/(|\mathbf{E}_p|/B)$; $\mathbf{E}_p \sim 10\,\text{mV/cm}$. 0.3–2 V trapping potentials are a good order of magnitude for producing displacements that are significant compared to the nominal variability of cloud positions, but this still leaves clouds within the imageable region of the MCP.

For small displacements, the displacement of a cloud from the center of the trap due to patch potentials can be explained with the following simple model. Near the center of the trap, the potential due to the electrodes, the "trap potential," can be approximated by (in cylindrical coordinates):

$$\Phi_T(z, r, \theta) \approx -k_2 \left(z^2 - \frac{1}{2} r^2 \right), \tag{3.1}$$

where k_2 is the "trap constant." As described in Sec. 1.2, in such a trapping field, an electron cloud will $\mathbf{E} \times \mathbf{B}$ in circles, a with a frequency $\omega_r = k_2/B$, where B is the magnitude of the $\hat{z}$ directed magnetic field. This is called the "magnetron motion." Unlike the potential due to the electrodes, a perturbing potential due to patch potentials on the surface of the electrodes can generate terms which are not azimuthally symmetric (terms which are functions of the azimuthal angle θ). However, we believe that these patch potentials physically lie on the electrode surface, so just like higher order terms in the trap potential, higher order terms generated by the patch potential are suppressed by $r, z/R_w$, where R_w is the trap wall radius. The lowest order term generated by patch potentials is simply a constant electric field of magnitude ε:

$$\Phi_P(z, r, \theta) \approx \varepsilon r \cos\theta. \tag{3.2}$$

I have neglected another term of nominally the same order which might be written $\varepsilon_z z$, which has no physical consequence unless higher order terms are included in the trapping or patch potentials. Because $\mathbf{E} \times \mathbf{B}$ drift is perpendicular to $\mathbf{E}$, $\mathbf{E} \times \mathbf{B}$ drift orbits follow electrostatic equipotentials. Given the leading order models for Φ_P and Φ_T, equipotentials are circles which are displaced from the true trap center $r = 0$ by a distance $\delta = \varepsilon/k_2$. Under this model, we can move clouds off axis by decreasing k_2, then we can image how far off-axis the clouds moved with the MCP. Because we cannot image plasmas that are displaced from the trap center by more than a few millimeters, and the trap wall radius is $R_w = 2.2\,\text{cm}$, this leading order model is likely to be sufficient for explaining the results of such a measurement.

Fig. 3.2 illustrates the procedure performed on a single cloud to measure patch potentials. The following sections contain more detail about how ε can be extracted from many imaged clouds which have been subjected to the same procedure.

3.2 Antiproton loss due to patch potentials

Our order of magnitude estimate for the electric field due to patch potentials was $\varepsilon \sim 10\,\text{mV/cm}$, and the trapping field present during antihydrogen spectroscopy was of order $k_2 \sim 1\,\text{mV/cm}^2$. The linear estimate described above suggests $\delta \sim 10\,\text{cm}$ (well beyond the trap wall). Of course this simply means that this leading order estimate is invalid, and antiprotons are likely to move chaotically until they eventually collide with the trap wall.

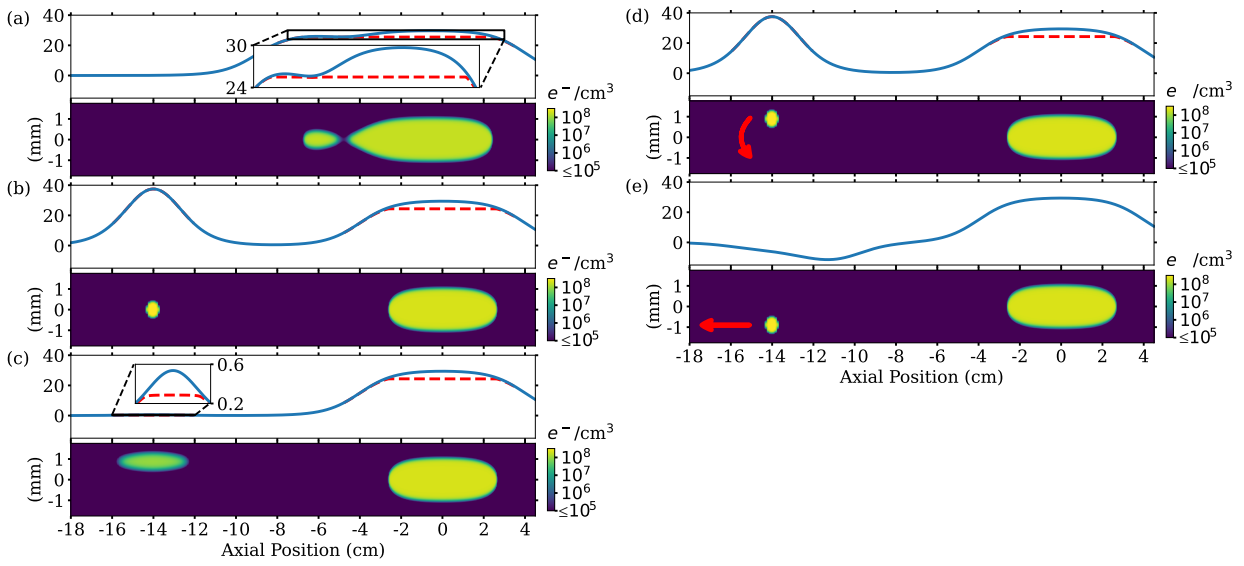

Figure 3.2: Five steps in the procedure for measuring patch potentials are shown. For each step, the upper plot shows the on-axis potential created by the electrodes in blue and the potential perturbed by the presence of the electrons in red. The lower plot shows the electron charge density. The size of electron clouds is exaggerated.
(a) An electron cloud is extracted from an electron plasma reservoir.
(b) The cloud is moved axially to a desired measurement location.
(c) The cloud is moved off-axis by subjecting it to a weak trapping potential where $k_2 = k_{2m}$.
(d) The trapping potential is quickly returned to a "deep" trapping potential, and the cloud orbits the trap center several thousand times.
(e) The cloud is released toward the MCP and imaged.

To investigate possible trajectories for antiprotons, I prepared a Boris algorithm [69, 70] simulation of antiproton motion in the presence of patch potentials and a single confining electrode of length 2 cm and radius 2.2 cm. Actually, to improve computation time, I increased the mass of the antiproton to decrease its cyclotron frequency so larger simulation timesteps could be used. This is unlikely to have any significant effect on the results; it remained true in the simulation that $\omega_c \gg \omega_z \gg \omega_r$ (the cyclotron frequency was much greater than the bounce frequency which was much greater than the magnetron frequency). My model for patch potentials was a 5×8 grid of square voltage perturbations. The squares are $l = 2\pi R_w/8$ in length so that they entirely cover the cylinder from $z = -5l/2$ to $z = +5l/2 = 4.3\,\text{cm}$, long enough that including more patches would have a negligible effect on the electric field near the center of the trap. Their voltages were sampled from a Gaussian, then for each of the two shown simulations, the randomly generated voltages were scaled up so that the transverse electric field near the center of the trap (ε) was the same between simulations. The antiprotons were initialized near the center of the trap with $e(1\,\text{mV})$ of kinetic energy in a random direction, the recoil energy they receive when a 2S antihydrogen atom is ionized upon absorbing a third photon from the 1S–2S laser. The trapping potential is adiabatically

decreased (as described in the next section) so that, at least according to the linear theory, the magnetron radius should be conserved and δ should slowly increase.

Two examples of randomly generated potentials are shown in Fig. 3.3, and the results of simulating antiprotons in these fields are shown in Fig. 3.4. A breadth of phenomena occur in these simulations, only some of which are captured in these examples. The most obvious fate for an antiproton is that of simulation (1). As the trap field weakens, the circular orbits become elliptical. This occurs when the quadratic coefficients of the trapping potential in the two transverse directions are not equal [$\Phi = k_x(x-x_c)^2 + k_y(y-y_c)^2$, where x_c and y_c are the equilibrium point that the antiproton orbits in its magnetron motion]. Eventually, one of these coefficients becomes negative, so the antiproton is now on a hyperbolic orbit which is destined to hit the trap wall. In simulation (1), the antiproton's displacement from the trap center quickly deviates from the linear theory $\delta = \varepsilon/k_2$, because the electric field near the trap center was much weaker than the electric field everywhere else. In simulation (2), the electric field near the trap center guides the antiproton into a region where the patch-created electric field was weaker, and the antiproton's displacement fell under the linear theory. Eventually, after surviving about 30 times longer than simulation (1), the antiproton finds the trap wall. Some other, more rare phenomena also occur in other simulations. The antiproton can be trapped forever in the potential created by the patch potentials alone. The antiproton can be released from its confining potential in z into a much wider, but still confining potential in z, suddenly changing its $\mathbf{E} \times \mathbf{B}$ drift orbit shape as it now averages over an entirely different set of z values.

3.3 Adiabatic change to shallow well

In my first attempt to measure patch potentials at ALPHA, clouds were initially trapped by applying 70 V to two adjacent electrodes. In this deep trapping potential the well constant is given by $k_2 = 70\kappa$, where $\kappa = 87\,\mathrm{mV/cm^2}$ is the trap constant resulting from 1 V applied to two adjacent electrodes in ALPHA-2. I then linearly decreased the trapping potential over the course of 100 ms to a variable final "shallow" potential of 0.3–2 V. The resulting minimum k_2 value I will denote as k_{2m}. Next, I "snapped" the potential back to 70 V as quickly as the amplifiers can change potential. After waiting an additional 100 ms, the clouds were imaged by launching them toward the MCP/phosphor screen/CCD camera detector. The results of this experiment are shown in Fig. 3.5. My logic at the time was crude. I simply wanted to "jostle" the clouds off-axis. I hadn't worked out the numbers on the timescale of magnetron motion. So I was hoping that at least by doing one movement "slowly," one movement "quickly," and waiting in-between, I maximized my chances of having some impact on cloud locations that wouldn't be cancelled out between the two operations. In this goal I was successful. In hindsight, the linear ramp from 70 V to the low voltage would have been too fast for the cloud to retain its initial magnetron orbit. It would have been thrown out to a higher radius magnetron orbit at a time which would be essentially random. Thus the final imaging position of the cloud would be randomly distributed, although it would still be true that the weakest k_{2m} would, on average, result in clouds landing farther from the center of the MCP.

When I called my advisor, Prof. Joel Fajans, he commended me, saying I had a great idea to do the first movement slowly, because it might move the clouds to a well-defined initial

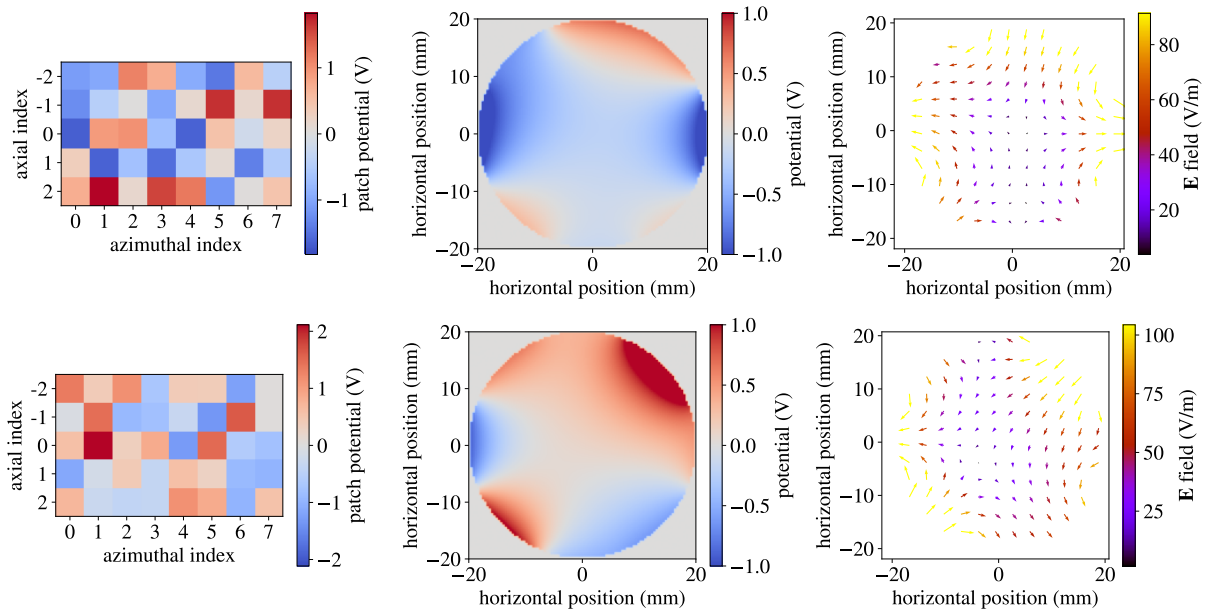

Figure 3.3: The randomly generated patch potentials that antiprotons are subject to in the simulation results shown in Fig. 3.4. The first row represents simulation (1), and the second row is simulation (2). The first column shows the randomly generated potentials of the square patches. The horizontal axis moves along the azimuthal angle (squares of length $2\pi R_w/8$), and the vertical axis moves axially. The second column shows the circular cross section of the potential due to these patches at $z = 0$. The third column shows the resulting electric field.

location, then after the fast movement the cloud might orbit the trap from a well-defined starting location. I had not thought my measurement through that well, and Prof. Fajans' idea, which he thought was my idea, would serve as the basis of many of the measurement techniques presented in this thesis. However, the "slow" movement was not nearly sufficiently slow; 100 ms was plenty of time, but a linear voltage change moved far too quickly through the last few volts, as I will explain in the following paragraphs.

When a Hamiltonian system has a periodic motion, and that Hamiltonian has a time dependence which is slow compared to the periodic motion, a quantity called the adiabatic invariant is conserved. This invariant is given by the action per cycle of the periodic motion: $S = \int pdq$. It isn't immediately obvious that our clouds' magnetron motion is a Hamiltonian system, because $\mathbf{E} \times \mathbf{B}$ drift is a velocity which is a function of time and space, unlike the most typical Hamiltonian system which has a force which is a function of time and space (then m times velocity is the canonical momentum of position). However, assume that $\mathbf{B} = B\hat{z}$, then $v_x = \mathbf{E}_y/B$, and $v_y = -\mathbf{E}_x/B$ (where $\mathbf{E}$ is averaged over the even faster bounce motion in z). Surprisingly, we have a Hamiltonian system where $H = \Phi(x, y)/B$; x and y are canonical conjugate pairs. Therefore, in the cloud magnetron orbit system, the adiabatic invariant is simply the area of the orbit. Thus if we have a cloud which has some small initial magnetron orbit of radius r, we can move the cloud away from the geometric trap center without changing r by adiabatically decreasing the trapping voltage.

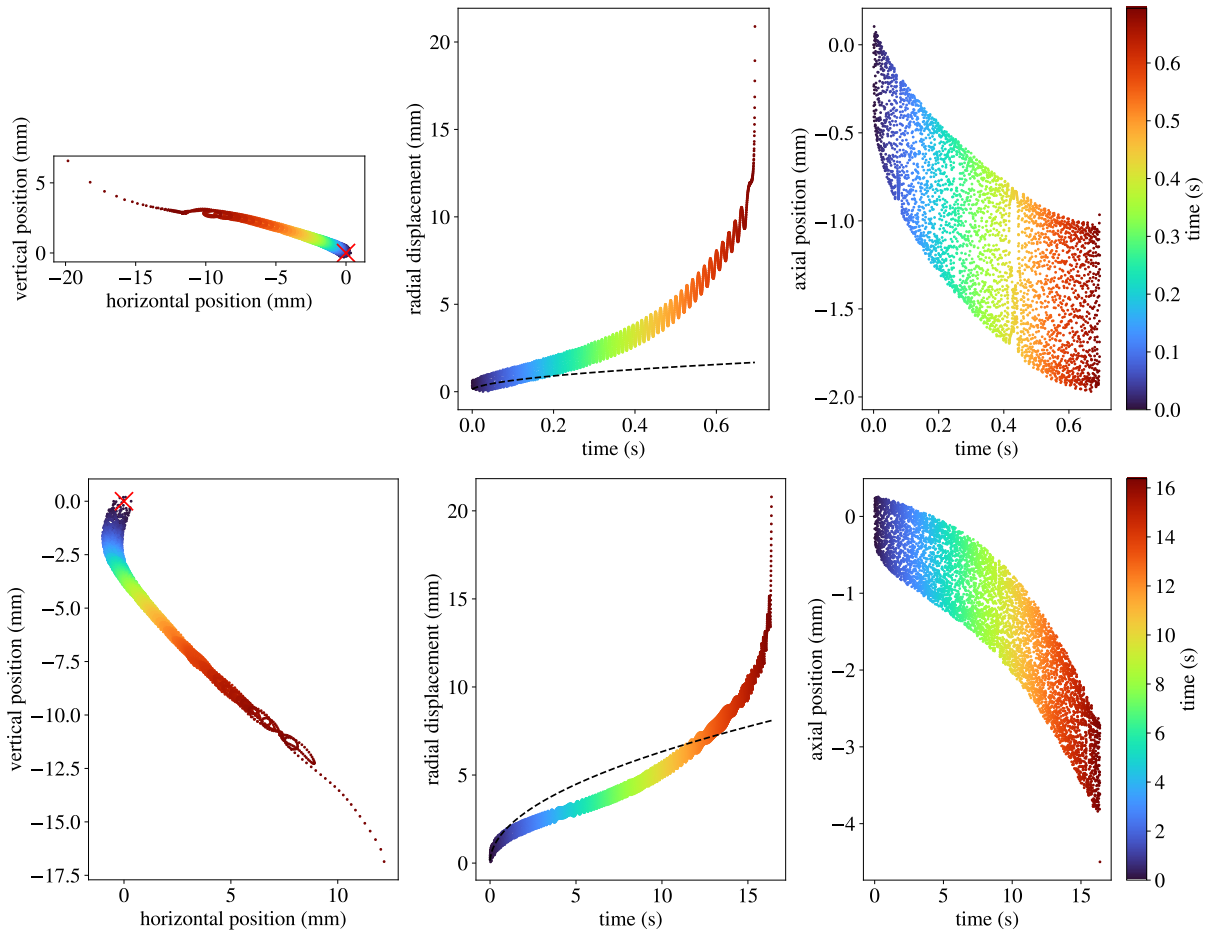

Figure 3.4: The results of simulations of antiprotons moving in the patch potentials shown in Fig. 3.3 and a slowly weakening electrode voltage. The first row represents simulation (1), and the second row is simulation (2). The first column shows the motion of the antiprotons in the transverse plane (the r, θ plane, or the x, y plane). A red X denotes the trap center. The second column shows the resulting total radial displacement r of the antiprotons as a function of time. A dashed line represents the linear theory $\varepsilon/k_2(t)$. The final column shows the axial position of the antiprotons as a function of time. The colorbar on the right applies to all three columns.

It is well known that the change in the adiabatically conserved quantity is suppressed by changing the controlled parameter in a more differentiable way. This has been shown in other nonneutral plasma systems[71, 72, 73], but there is also a significant body of literature [74] discussing this phenomenon for the quantum adiabatic theorem, because adiabatic quantum computers use adiabatic changes of a Hamiltonian to perform computations [75]. One commonly used strategy is to set the derivative of one's control variable to a polynomial which has an n–degree zero at the start and finish of the "adiabatic ramp:"

$$P_n(x) = 2^{2n}x^n(1-x)^n, \tag{3.3}$$

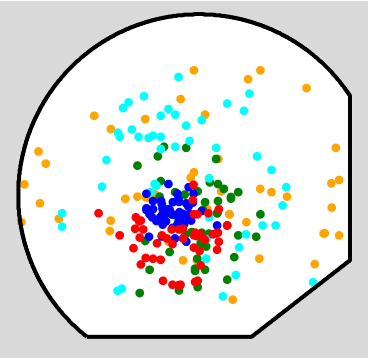

Figure 3.5: The results of the initial patch potential measurement. Each dot represents the center of a cloud seen on the MCP. The colors indicate the value of k_{2m} used for each cloud: 2.0κ (blue), 1.2κ (red), 1.0κ (green), 0.7κ (cyan), 0.5κ (orange), and 0.3κ (fuchsia); $\kappa = 87\,\mathrm{mV/cm^2}$. All of the clouds subjected to 0.3κ missed the MCP or were otherwise lost. The black outline is edge of the imageable region of the MCP—a combination of the bottom of the camera, a metal bar occluding the MCP, and a circular aperture that clouds have to pass through before hitting the MCP. This data is also presented in Ref. [68].

where $x = t/T$ ranges from 0 to 1, and T is the total time taken to change the Hamiltonian from an initial value to a final value. This strategy typically yields a change of the conserved quantity which is suppressed like $(1/T\omega)^{n+1}$, where ω is the frequency of the periodic motion.

This is not quite as trivial for us as it is for most systems. Our control variable is the trap constant k_2, which is proportional to voltage through the linearity of the Laplace equation. The displacement of the effective trap center is a function of k_2: $\delta = \varepsilon/k_2$, but so is the magnetron frequency: $\omega_r = k_2/B$. To suppress adiabatic error, we can change k_2 according to:

$$\frac{d\delta}{dt} = \omega_r r_m P_n\left(\frac{t}{T}\right), \tag{3.4}$$

where r_m is our adiabatic "small parameter." If we have some initial magnetron radius r, and r_m is much smaller than r, then the initial magnetron radius will be conserved (with the error begin proportional to some power of r_m). Later with a simulation I will also discuss the consequences of having a cloud initially at $r = 0$. After inserting the above equations for δ and ω_r, we get the separable differential equation:

$$-\frac{dk_2}{dt}\frac{\varepsilon}{k_2^3} = \frac{1}{B} r_m P\left(\frac{t}{T}\right), \tag{3.5}$$

which is solved by:

$$\left(\frac{1}{k_2(t)^2} - \frac{1}{k_2(0)^2}\right)\frac{\varepsilon B}{2r_m} = \int_0^t P\left(\frac{t'}{T}\right) dt', \tag{3.6}$$

$$k_2(t) = \left[\frac{2r_m}{\varepsilon B}\int_0^t P\left(\frac{t'}{T}\right) dt' + \frac{1}{k_2(0)^2}\right]^{-1/2}. \tag{3.7}$$

Usually I have an initial $k_2(0)$ given by the the potential used to trap a cloud and a I have

a desired final $k_2(T)$ which is about two orders of magnitude smaller. The above equations then tell us how long the adiabatic ramp needs to take:

$$T = \frac{\varepsilon B}{2r_m} \frac{\Gamma(2n+2)}{2^{2n}\Gamma(n+1)^2} \left[\frac{1}{k_2(T)^2} - \frac{1}{k_2(0)^2} \right]. \tag{3.8}$$

To test this theory, I set up a simulation of idealized $\mathbf{E}\times\mathbf{B}$ drift motion of electron clouds in the transverse plane in the presence of a patch potential $V = \epsilon\cos\theta$ with $\epsilon = 10\,\mathrm{mV/cm}$ and a purely quadratic trapping potential where k_2 is lowered from 10 to $0.05\,\mathrm{V/cm^2}$ as described above. Clouds are initialized at a distance $10\,\mu$m from the trap center (all realistic values), and r_m is varied from $0.1\,\mu$m (small compared to the initial radius) to 1 mm (half the entire distance that δ changes). Instead of directly implementing $\Delta x = E_y/B$, $\Delta y = -E_x/B$, the $\mathbf{E}\times\mathbf{B}$ drift is implemented as a rotation about the current trap center, given by $\epsilon/k_2(t)$. I believe this technically forms a "symplectic integrator," as it will never change a cloud's action (the area of the magnetron orbit) because of numerical errors. Additionally, to improve computation time in the presence of drastically changing timescales, each timestep evolves the angle by 0.005, rather than a fixed Δt. The results of the simulation are shown in Fig. 3.6.

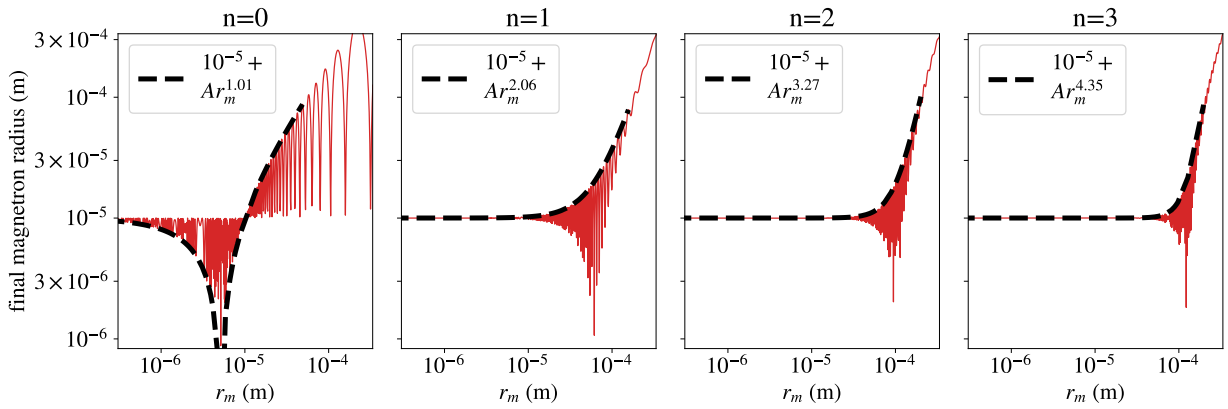

Figure 3.6: The results of the simulation of adiabatic changes to the the trapping potential in the presence of a patch potential. Four different n values are simulated (see Eq. 3.3). The red curve shows the final magnetron radius as a function of r_m (see Eq. 3.7), with the cloud's initial magnetron radius set to 10^{-5} m. The black dashed line shows a power law fit to the local maxima. In order to get a good fit to the $n = 0$ data, several local maxima had to be ignored. This is because the adiabatic error is clearly acting in the opposite direction to the initial magnetron radius, so the fit function would only fit the maxima to the right of a crossing point and the local minima to the left. Similar issues in the other datasets probably explain why the fit power law is not exactly r_m^{n+1}.

For me, there were several surprises in these simulation results. First, for higher n values, r_m can clearly be much bigger than the initial magnetron radius before the final magnetron radius significantly differs from the initial. Next, the scaling of the final radius with r_m does not just apply when the change in magnetron radius is small; most analyses of adiabatic theorem only consider a small change in the adiabatic invariant. All of this seems to indicate

that, speaking very informally, the adiabatic error behaves like a vector whose length scales like $[\varepsilon/k_2(T)]^{-n} r_m^{n+1}$ (r_m^{n+1} made dimensionally correct by multiply by powers of the total change in magnetron displacement $\delta = \varepsilon/k_2$, not the initial magnetron radius). At first this statement seems preposterous, because it implies that if $n > 0$, the adiabatic error decreases with increasing total change of δ. However recall that T is also proportional to $\varepsilon/k_2^2(T)$, so the result is not so astonishing. Then the initial magnetron radius is another vector, and the two are added together. It seems that for the $n = 0$ simulation, the adiabatic error is always subtracted from the initial radius—the fit parameter A is negative. This is probably just a coincidence of the chosen initial conditions.

The implementation of this adiabatic change in the voltage confining a cloud was the initial justification for designing software that could programatically write voltage sequences to be applied to the electrodes. The software which we use to set the voltage sequence applied to the electrodes allows for linear changes of voltages versus time. The linear changes are also implemented as a certain number of discrete voltage steps. Thus, the programmatic sequence editor was made to approximate Eq. 3.7 as ten linear changes of the trap voltage. I could have made one or two such sequences by hand, but I wanted to use 6 different $k_{2m} = k_2(T)$ values in many different axial trap locations.

I never really experimentally verified these power laws, nor did I experimentally vary the number of linear ramps used as an approximation or the number of discrete steps in each linear ramp. Usually I used $n = 1$ and I set r_m to a value that that was smaller than any reasonable initial magnetron radius. My choices were simply much better than necessary, and I rarely saw any effect from adiabatic error. On the one or two instances where I saw some adiabatic error, I simply made all three parameters better by a significant factor and the issue went away (r_m, number of linear ramps, and number of steps per linear ramp). When I implemented EMPI (see Sec. 8), even if I optimized adiabatic ramps to be as fast as possible with minimal error, they would take too long and they required too much FPGA memory, so I simply had to use an entirely different strategy to move clouds off-axis.

Upon implementing the proper adiabatic k_2 change, the data looks like Fig. 3.7, with the spiral shape depending on where in the trap the measurement is performed. After adiabatically decreasing k_2 to a final minimum value k_{2m}, the trapping potential was quickly changed back to the maximum value of 70 V. After the clouds spent 100 ms in this deep trapping potential executing a magnetron orbit, the potential was morphed to a "pre-dump" potential over the course of 20 ms, where the electrons were still trapped, but with the surrounding electrodes set to a negative voltage (e.g. using voltages of −65, −65, 70,70, −20,−20 on adjacent electrodes). At the end of the morph, the electrons were released toward the MCP with about 20 eV of kinetic energy by changing the potential quickly to −50 V on the electrodes that were previously confining the electrons with 70 V. At the time, I was expecting that clouds would be at a well-defined radius (plus or minus the clouds' initial variability in position), but with a random phase—a circle with some thickness. Until that point, ALPHA had no evidence that electrode amplifier voltages and timings were sufficiently reproducible to image clouds at a well-defined magnetron phase. In hindsight, although electrode voltages often differ from intended voltages by tens of millivolts, they are remarkably reproducible (at least at the 10^{-5} level). Although the timings of voltages are affected by amplifier slew rates and bandwidths and low pass filters between the amplifiers and the electrodes, the timings are reproducible at the nanosecond level. The results shown

in Fig. 3.7 are evidence that the clouds are subjected to the same exact sequence of potentials after snapping back to a deep potential, but that the magnetron frequency depends weakly on the displacement from the trap center.

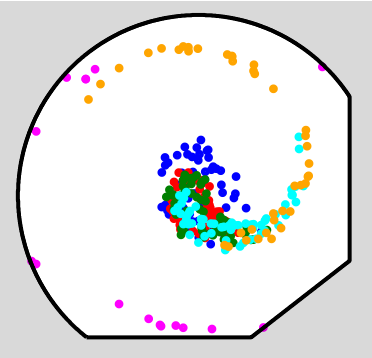

Figure 3.7: The results of the improved patch potential measurement with an adiabatic change of k_2 to k_{2m}. Each dot represents the center of a cloud seen on the MCP. The colors indicate the value of k_{2m} used for each cloud: 2.0κ (blue), 1.2κ (red), 1.0κ (green), 0.7κ (cyan), 0.5κ (orange), and 0.3κ (fuchsia); $\kappa = 87\,\mathrm{mV/cm^2}$. This data is also presented in Ref. [68].

3.4 Patch potential measurement analysis

A single patch potential measurement, shown for example in Fig. 3.7, involves imaging 360 clouds. Six different k_{2m} values are used, and for each k_{2m} value, 60 clouds are imaged after being subjected to identical electrode potentials. In the images, the center of each cloud is identified, and we aim to measure the strength of the patch potential from the distribution of cloud centers. The caption of Fig. 3.8 shows the process of identifying the center of a plasma from MCP images.

In principle, we could identify the trap center using a collection of clouds imaged without being moved off axis, then find just one k_{2m} value where the clouds are displaced from the trap center by much more than their initial position variability. The average displacement of the unmoved clouds from the moved clouds would be a measure of $\delta = \varepsilon/k_{2m}$. However, I designed a more elaborate analysis scheme, which certainly makes more efficient use of the data, especially when none of the k_{2m} values exhibit the perfect degree of displacement for the simpler analysis. It also allows for identification of the spiral shape evident in Fig. 3.7 simultaneously with measuring ε. In the following paragraphs, in the process of describing how electron clouds move during a patch potential measurement, I will construct a probability distribution that will later be fit to their positions on the MCP to measure the electric field created by patch potentials ε.

Even before being put in a shallow trapping potential, the clouds have some initial magnetron radius. In the original patch potential measurement technique, this initial magnetron motion had a random phase and radius. The reasons for this initial distribution were not known at the time of the first patch potential measurements, but they are now (see Sec. 2.3).

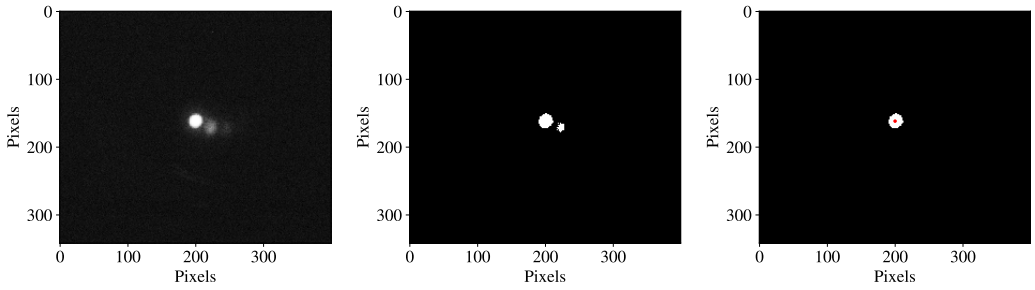

Figure 3.8: The image on the left is an example of a picture produced by imaging an electron cloud on the MCP (zoomed in by about a factor of two). The cause of the fainter bright spots to the right is ultimately unknown—further discussion of these spots is in Sec. 9.1. However we have reason to believe that only the bright central spot reflects the position of the charges inside the trap. Therefore to select the central spot alone I find the largest region of pixels with a brightness above some threshold. The binary image of pixels above the threshold is the second image. In some cases I simply find the center of mass of this selected region. In other cases I fit a "power Gaussian" $I(x, y) = \exp\{-[(x - x_0)^2 + (y - y_0)]^{n/2}/\sigma^n\}$ to the pixels in and near the selected region. In this case, the center of mass is used, which is shown with a red dot in the third image along with only the larger of the two regions in the second image. This data is also presented in the supplementary material of Ref. [68].

In the analysis of this data, I assume that the initial distribution is Gaussian:

$$P_1(x, y; x_0, y_0, \sigma) = \frac{1}{2\pi\sigma^2} \exp\left[-\frac{(x - x_0)^2 + (y - y_0)^2}{2\sigma^2}\right]. \tag{3.9}$$

The above equation describes the differential probability of a cloud being located at location x, y. The rest of the parameters of P_1 are fit parameters. x_0 and y_0 need to be fit parameters because we do not know a priori what position on the MCP corresponds to the center of the trap.

Next, when the trapping potential is adiabatically weakened, this distribution is shifted by a distance ϵ/k_{2m}. Because the current measurement is not sensitive to the direction of this patch field, we can define this to be the $\hat{x}$ direction:

$$P_2(x, y; k_{2m}; x_0, y_0, \sigma, \varepsilon) = \frac{1}{2\pi\sigma^2} \exp\left[-\frac{\left(x - x_0 - \frac{\varepsilon}{k_{2m}}\right)^2 + (y - y_0)^2}{2\sigma^2}\right]. \tag{3.10}$$

Note that I have introduced another semicolon in the parameters of P_2, this time for k_{2m}, which is an experimental knob—I will fit the same probability distribution to the landing positions of several imaged clouds subjected to several different k_{2m} values. During the 120 ms that the clouds sit in a deep trapping potential, they orbit the trap center roughly 7000 times, but the orbit frequency depends weakly on the distance from the trap center $r = \sqrt{x^2 + y^2}$ because of higher order terms in the trapping potential. The small change in the magnetron phase with r after 120 ms is evident as a spiral in Fig. 3.7. Consider a leading

order model of the deep trapping potential:

$$\Phi_{\mathrm{T}} = -k_2\left(z^2 - \frac{1}{2}r^2\right) + k_3\left(z^3 - \frac{3}{2}zr^2\right) + k_4\left(z^4 - 3z^2r^2 + \frac{3}{8}r^4\right) + \cdots . \tag{3.11}$$

For several years I was not aware that the k_3 term would have an effect on the spiral shape. It does because it gives rise to an r dependent z equilibrium $\langle z\rangle = -3k_3r^2/(4k_2)$. To leading order the angular frequency is given by:

$$\omega_r(r) = \frac{k_2}{B} - 6\frac{k_4\langle z^2\rangle}{B} + \left(\frac{9}{4}\frac{k_3^2}{k_2B} + \frac{3}{2}\frac{k_4}{B}\right)r^2 + \cdots , \tag{3.12}$$

Therefore we add an r-dependent rotation (rotation angle $\theta_0 + k_\theta r^2$) to the probability distribution:

$$P_3(x, y; k_{2m}; x_0, y_0, \sigma, \varepsilon, \theta_0, k_\theta) = P_2\left(\begin{bmatrix}\cos(\theta_0 + k_\theta r^2) & -\sin(\theta_0 + k_\theta r^2)\\ \sin(\theta_0 + k_\theta r^2) & \cos(\theta_0 + k_\theta r^2)\end{bmatrix}\begin{bmatrix}x\\ y\end{bmatrix}\right). \tag{3.13}$$

This function often performs poorly because the spiral arms become very thin; for large r the spiral thickness is σ/rk_θ. When this becomes small compared to errors in our ability to identify cloud centers, clouds that are obviously along a spiral arm are assigned an astronomically small probability density. Thus a simple smoothing procedure is implemented in the final probability distribution that will be fit to the data:

$$P = \begin{cases} \frac{1}{(5\text{ pixels})2k_\theta r}\int_{-(5\text{ pixels})k_\theta r}^{(5\text{ pixels})k_\theta r} P_3\left(\begin{bmatrix}\cos\theta & -\sin\theta\\ \sin\theta & \cos\theta\end{bmatrix}\begin{bmatrix}x\\ y\end{bmatrix}\right)d\theta & (5\text{ pixels})2k_\theta r < 2\pi \\ \frac{1}{2\pi}\int_0^{2\pi} P_3\left(\begin{bmatrix}\cos\theta & -\sin\theta\\ \sin\theta & \cos\theta\end{bmatrix}\begin{bmatrix}x\\ y\end{bmatrix}\right)d\theta & (5\text{ pixels})2k_\theta r \geq 2\pi \end{cases} \tag{3.14}$$

The first case sets a minimum spiral arm width of roughly 5 pixels. The second case covers the situation where the spiral can no longer be resolved and so we simply average over the entire circle. Curiously, the second integral can be completed analytically with the Jacobi-Anger expansion.

This probability distribution is then fit to a dataset, usually consisting of 360 cloud center positions spread across 6 k_{2m} values. This fit is done by maximizing the log likelihood function: the sum of the log of $P(x, y; k_{2m}; x_0, y_0, \sigma, \varepsilon, \theta_0, k_\theta)$ for each datapoint. The maximization was performed using a kind of modified Levenberg-Marquardt algorithm. Frankly the algorithm became more complicated over time and I implemented a wide variety of strategies to find the optimal fit parameters. The entire algorithm is not worth discussing here. The result of this fitting procedure is shown in Fig. 3.9 for four patch potential measurements performed in different axial locations in the ALPHA-2 trap.

In most patch potential measurements, some clouds are too far from the center of the trap and they do not reach the MCP. These clouds are assigned a proper probability (as opposed to a probability density), defined as one minus the integral of P over the region of the MCP that clouds could be imaged on—i.e. the probability of clouds missing the MCP altogether. There are several reasons that a cloud might not be visible in an MCP image. In

both ALPHA-2 and ALPHA-g, the clouds have to pass through a circular aperture between the MCP and the trap. In Sec. 3.5, I will explain that clouds follow magnetic field lines between the trap and the MCP. Therefore, if the cloud is released from the trap and it is on a magnetic field line that does not pass through this aperture, the cloud will be blocked from reaching the MCP. In ALPHA-g, this is the only reason that clouds are not seen in MCP images. In ALPHA-2, there are three other relevant obstructions: (1) there is a metal bar partially occluding the MCP; (2) the camera is not perfectly positioned, and some clouds simply land "out of frame;" (3) some clouds pass through the aperture, but miss the MCP, which is also circular. Because of imperfect alignments, when a cloud is sent from the center of the trap to the MCP, it does not pass through the center of the aperture, and it does not land in the center of the MCP. In both ALPHA-2 and ALPHA-g, when a cloud inside the trap is further off-axis than about 1–2 mm, it might not be successfully imaged.

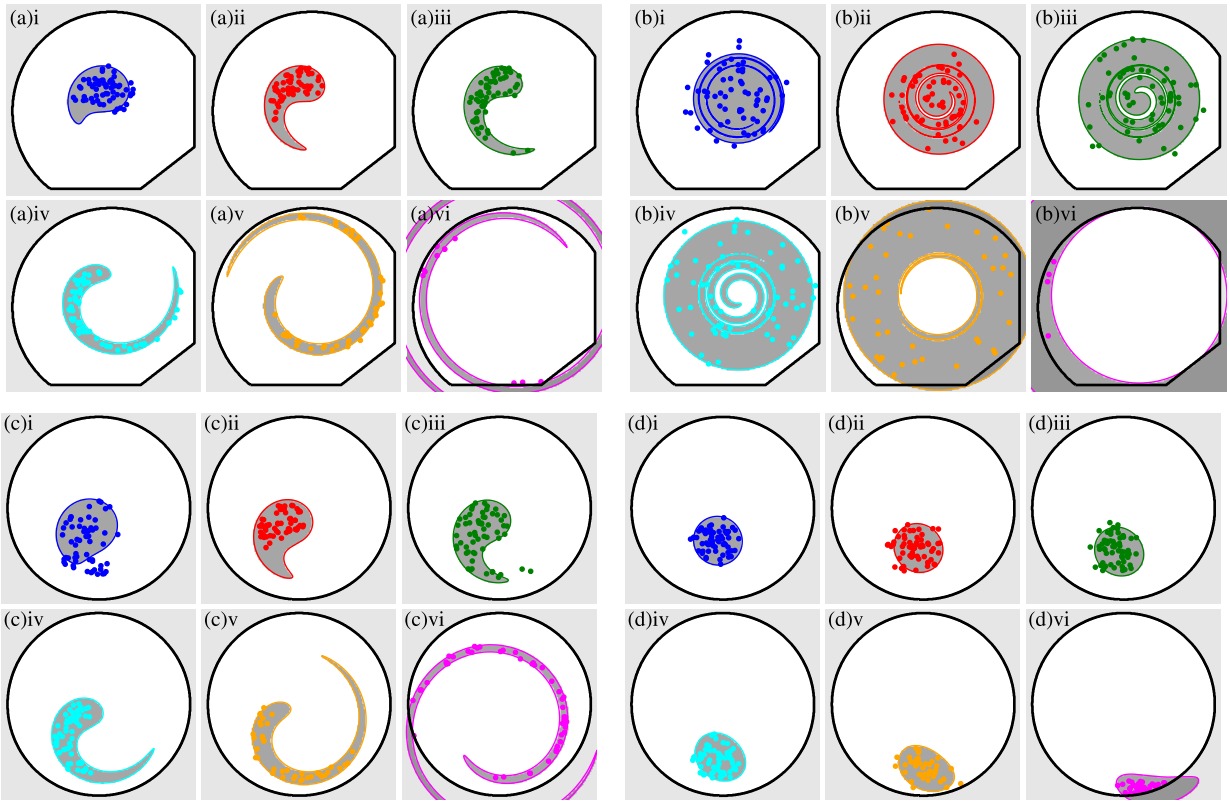

Figure 3.9: Four datasets used to measure patch potentials at four trap locations in ALPHA-2. Unlike in Fig. 3.7, each subplot of each dataset shows clouds' imaged positions after being subjected to a single k_{2m} value. The k_{2m} values and the colors are the same as in Fig. 3.7. The grey blobs with colored outlines are the 90% confidence interval of the probability distribution fit to the data from all six k_{2m} values. This data is also presented in the supplementary material of Ref. [68].

3.5 MCP imaging and distance calibration

In the previous section, three physically relevant quantities are extracted from distributions of imaged electron cloud positions: k_θ, ε, and σ. However, they are fit to the positions of the clouds in camera images, and at the moment, their units are rad/pixel^2, pixel V/m^2, and pixel respectively. Thus to measure the physical strength of patch potentials, we must estimate the relationship between pixels on the camera images and transverse distance inside the trap. A first obvious step is to find a feature in the images whose size is known. For us this is a circular face of the back of the phosphor screen, shown in Fig. 3.10. This can convert between pixels and mm outside of the trap. However, when electrons are imaged on the MCP, they

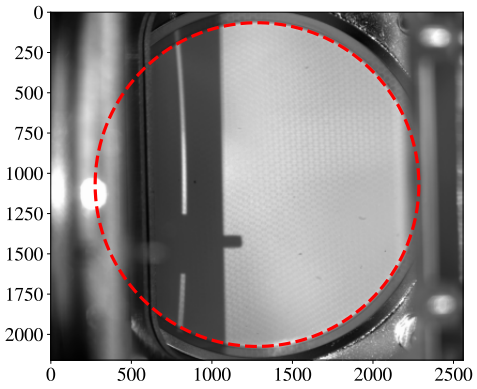

Figure 3.10: The MCP for ALPHA-g. The highlighted circular face is 44.45 mm in diameter. The horizontal and vertical axes are pixels.

follow magnetic field lines. Because the MCP is outside of the main $B_{\text{trap}} = 1\,\text{T}$ magnet for the Penning-Malmberg trap, the magnetic field at the MCP $B_{\text{MCP}} \sim 0.01\,\text{T}$ is much lower, and magnetic field lines expand by a factor of $\sqrt{B_{\text{trap}}/B_{\text{MCP}}} \sim 10$. This argument assumes that the guiding center approximation is good for describing the motion of the electrons. This relies on the magnetic field changing slowly compared to the cyclotron frequency:

$$\frac{1}{B}\frac{dB}{dt} \ll \omega_c \rightarrow a = \frac{dB}{dx}\frac{\sqrt{2mE}}{qB^2} \ll 1, \tag{3.15}$$

where E is the dump energy of the electron, and dB/dx is the change of the magnetic field along the electron's path, and a will be referred to as the "adiabatic parameter." At a typical dump energy of 20 eV, the electrons cover the 2 m distance to the MCP in about 700 ns, and the maximum value of a is about 0.01. This explains why antiprotons separate from electrons when a mutual plasma of electrons and antiprotons is imaged, as well as why the electron plasmas image as perfect circles but the antiprotons become ovals or even more complex shapes. For antiprotons, a approaches 0.5 near the MCP because of the scaling with m. An example of electrons and antiprotons imaged together on the MCP is shown in Fig. 3.11.

Even if the guiding center approximation is valid, there are "guiding center drifts" that might effect electrons' trajectories. First I'll consider curvature drift. Because the magnetic field doesn't have any significant turns, the curvature comes from field lines expanding and contracting with the changing magnetic field magnitude. For an electron which was initially

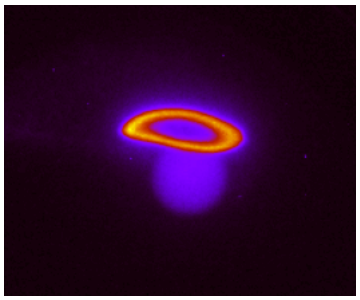

Figure 3.11: An MCP image from the ALPHA catching trap of a mutual plasma of electrons and antiprotons. The brighter ring are antiprotons, and the dimmer circle is the electron plasma. Inside the trap, both species form a circular plasma, and antiprotons have centrifugally separated from the electrons [76, 77, 78]. On the MCP, the two have separated, and because the guiding center approximation is much better for electrons, their shape on the MCP remains representative of their shape inside the trap.

displaced from the trap center by 2 mm, the minimum radius of curvature for our magnetic field lines is about 7 m. When I integrate the curvature drift using a model of the magnetic field in ALPHA-2, I get a total curvature drift of 26 μm.

$\mathbf{E} \times \mathbf{B}$ drift is harder to estimate exactly, but probably much more significant. An electric field of 1.3 V/cm along 20 cm near the end of the electron's trajectory where the magnetic field is about 0.01 T deflects the electron by 1 mm. It is entirely plausible for such an electric field to come from some charged-up piece of equipment, and the electric fields from the MCP itself are likely this big (it is charged to 100 V in the front and the phosphor screen in the back is at 5000 V). In both cases—$\mathbf{E} \times \mathbf{B}$ drift and curvature drift—the real concern would be gradients in the drifts imposing a different drift velocity on electrons which will land in different places on the MCP. We know these gradients are small not only from imaged cloud distributions but also from the nice circular shape of large electron plasmas imaged with the MCP.

To test these assertions about electron dumps to the MCP, I prepared a Boris algorithm simulation [69] of electrons being sent from the trap to the MCP. ALPHA had a preexisting magnetic field model of the entire beamline that electrons are dumped along, but that model could only be evaluated on-axis. Therefore, I approximated the on-axis potential with a series of well-placed solenoids. To improve the agreement, I performed gradient descent, allowing the lengths, radii, and positions of the solenoids to change in order to reduce the difference between my model's on-axis magnetic field and ALPHA's standard model. The final agreement between my multi-solenoid model and the on-axis magnetic field model was excellent. Then I sent electrons with 20 eV of axial energy and 2 eV of energy perpendicular to the magnetic field from the interior of the trap to the MCP. The MCP was approximated with a point charge located 5 mm behind the nominal location of the MCP. The magnitude of the point charge was scaled so that electrons are accelerated by 100 eV by the time they reach the MCP (this is the voltage actually applied to the front of the MCP). This model for the MCP is crude, but it should give the correct order of magnitude for the gradients in the MCP's electric field. The results of this simulation are shown in Fig. 3.12. To see how

distances inside the trap translate to distances outside the trap, I simulated two electrons displaced from the trap center by 1 mm in opposite directions, and I tracked how their distance evolved over the length of the beamline. The same simulation was performed on antiprotons dumped at a typical energy of 50 V to show how their trajectories follow field lines less precisely, and their magnetic moment isn't as precisely conserved. The results of the simulation are shown in Fig. 3.13.

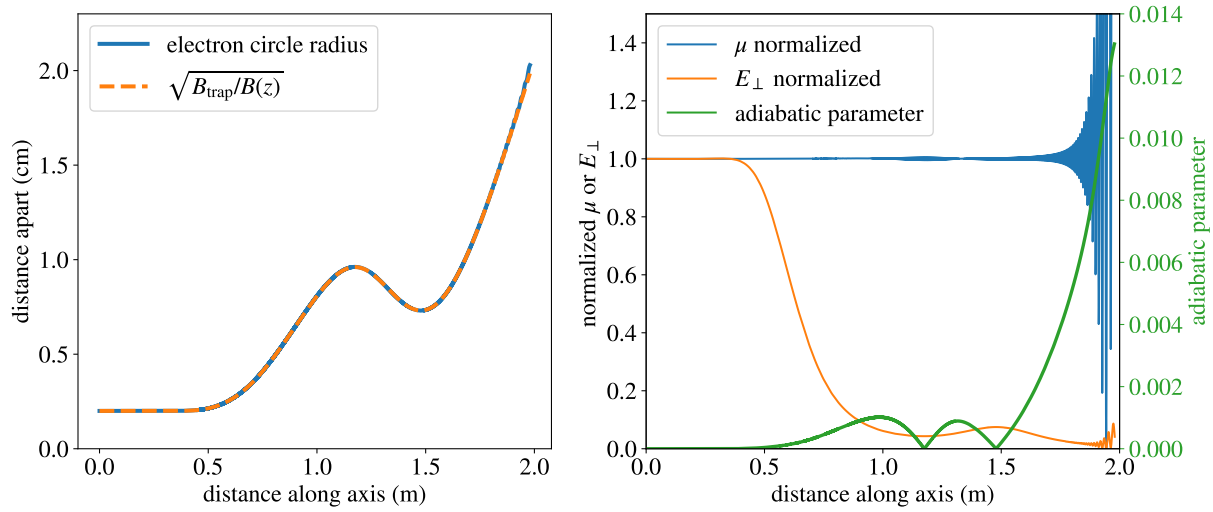

Figure 3.12: On the left, the distance between two electrons released from the trap simultaneously is plotted in blue. The electrons are initialized 2 mm apart. The theoretical prediction that this distance scales like $\sqrt{1/B(z)}$ is plotted with an orange dashed line. On the right, the blue line shows the magnetic moment μ of one of the electrons, which should be conserved as long as changes in the electric and magnetic field in one cyclotron orbit are small. The kinetic energy directed perpendicular to the magnetic field is also plotted in orange. The green line is the adiabatic parameter given in Eq. 3.15; the right vertical axis corresponds to the adiabatic parameter only. The clearly visible fluctuations in μ are the result of a component of the electric field perpendicular to the magnetic field, so the electron gains and loses energy as it moves up and down in that electric field. This does not strictly represent non-conservation of μ, which should be averaged over a cyclotron orbit. In fact, this gain and loss of perpendicular energy is exactly the mechanism underlying $\mathbf{E} \times \mathbf{B}$ drift, which the text suggested was the most likely cause of any deviations from field lines. Thus this is likely why a tiny deviation from the orange dashed line is visible at the very end on the left.

The aforementioned magnetic field model is not generally considered to be reliable. It relies on modelling the magnetic field produced by several magnets very far from their centers, and those magnets may be slightly misaligned. It has never been experimentally verified in any way—which would require moving an accurate magnetic probe along the enclosed vacuum region which hasn't been opened or disassembled for many years. We believe that the magnetic field is plenty strong that electron positions inside the trap are scaled up by exactly $\sqrt{B_{\text{trap}}/B_{\text{MCP}}}$, and B_{trap} is measured precisely with ECR, but we don't believe that magnetic field models give a precise prediction for B_{MCP}. Luckily the patch

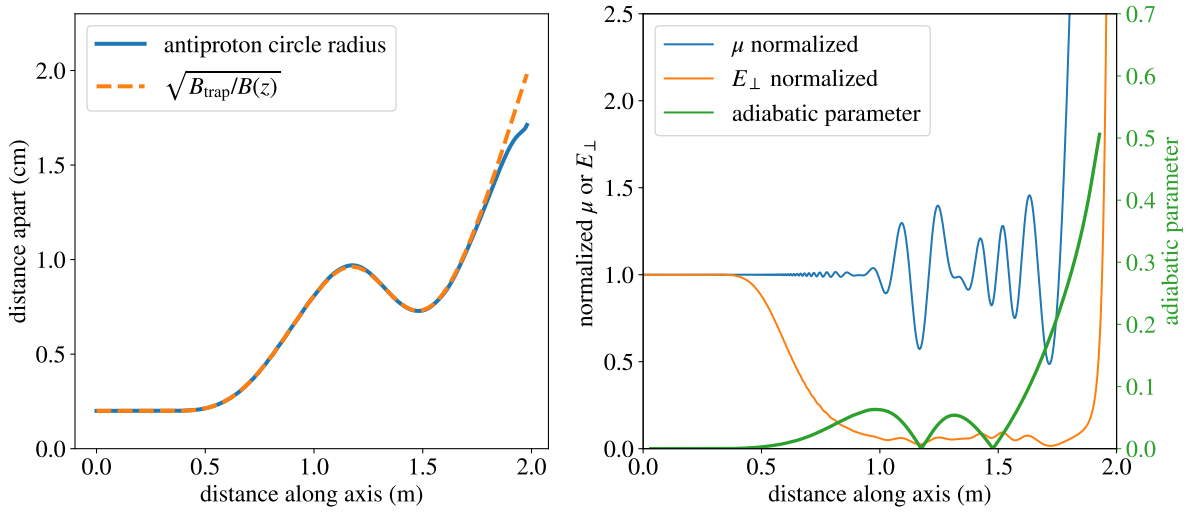

Figure 3.13: The same plots as Fig. 3.12, but this time antiprotons with 50 eV are simulated instead of electrons with 20 eV. As a result of the scaling with m, the adiabatic parameter is much higher, and the magnetic moment μ is less precisely conserved. At the end of the simulation, μ climbs to 1000 times its original value (showing this would make everything else too small to see).

potential measurements themselves provide a way of calibrating this.

The spirals shown in Fig. 3.9 were already explained as resulting from a small variation in ω_r with r in the form $\Delta\omega_r \propto r^2$. The fit parameter k_θ from the previous section can be related to the electrostatic field used to trap the electron clouds through Eq. 3.12. Given that we measure the final magnetron phase of the clouds, not their frequency, we find that k_θ is given by:

$$k_\theta = \int_{T_0}^{T_D} dt \left(\frac{9}{4} \frac{k_3(t)^2}{k_2(t) B} + \frac{3}{2} \frac{k_4(t)}{B} \right) \tag{3.16}$$

where T_0 is the moment when the trapping potential snaps from k_{2m} to a deep trapping potential, and T_D is the moment when the cloud is imaged on the MCP. Therefore, by constructing an electrostatic model of the on-axis potential due to the electrodes, we can come up with a predicted value for k_θ, this time in units of rad/mm$^2_{\text{trap}}$ (radians per millimeter of transverse distance inside the trap squared). The spiral constant k_θ extracted from distributions of cloud positions on the MCP comes in units of rad/mm$^2_{\text{MCP}}$ (radians per millimeter of transverse distance on the MCP squared). Thus we can divide the prediction by the measurement to find the magnetic field ratio between the inside of the trap and the MCP: $k_{\theta\,\text{predicted}}/k_{\theta\,\text{measured}} = \text{mm}^2_{\text{MCP}}/\text{mm}^2_{\text{trap}} = B_{\text{trap}}/B_{\text{MCP}}$.

In ALPHA-2 this data was collected incidentally. I simply integrated k_3 and k_4 as a function of time for the procedure shown in Fig. 3.2. Some, but not all, of the data had "moderate spirals" which were large enough to be measured with small statistical errors but small enough that they could still be resolved. However, in ALPHA-g I found a much better way of doing this measurement. I will go into more detail on the ALPHA-g magnetic field calibration, because this is how anybody else should do it going forward. In ALPHA-g,

instead of finding a predicted spiral constant for an entire sequence of potentials, I varied the time that clouds spent in two fixed trapping potentials. Then instead of comparing a full predicted spiral constant to an observed spiral constant, I found the difference in spiral constant that was accumulated by clouds spending extra time in a static trapping potential. Trying to predict k_3 and k_4 for changing trapping potentials invites systematic errors.

The entire sequence of potentials that clouds were subjected to is shown in Fig. 5.16. For the present discussion, suffice to say that after transitioning from a shallow potential to a deep one, the trapping potential was morphed to one with a negative k_4 then to another trapping potential with positive k_4. Both potentials had zero k_3 due to symmetry. A variable amount of time was spent in those deep wells: a time t_{pos} was spent with positive k_4, and t_{neg} was spent with negative k_4. Unlike in ALPHA-2 these potentials were modelled before being used, so the amounts of time were chosen specifically to make moderate spirals that would be easy to measure. Because the "positive well" had $k_4 = 1.28 \times 10^8\,\text{V/m}^2$, but the "negative well" only had $k_4 = -1.99 \times 10^7\,\text{V/m}^2$, t_{neg} was changed in larger steps than t_{pos}—this is just a consequence of the geometry of the electrodes. The data collected in this experiment is shown in Fig. 3.14. It is visually obvious that the spread in cloud positions is much smaller than in the ALPHA-2 data. This is explained in Sec. 3.8. One beneficial outcome of this was that in ALPHA-g, I did not have to use the complicated probability distribution fit described in the the previous section. Rather, I could simply measure the magnetron phase of each cloud, plot it against their distance from the trap center, and fit $\theta = k_\theta r^2 + mr$ to the resulting data. This fit is also shown in Fig. 3.14. Until now, no justification has been given for the linear term mr. This phenomenon is somewhat complicated to explain, but a somewhat speculative explanation is provided in Sec. 5.4.3.

Next, Fig. 3.15 shows the magnetic field magnification measured using the data shown in Fig. 3.14. Additionally, some of the same measurements were performed with a different magnetic field at the MCP. In ALPHA-g, three controllable magnets are near the MCP which affect its total magnetic field. Two wider short solenoids, about 60 cm in diameter are located just above and below the MCP. One smaller short solenoid, about 30 cm in diameter, is located further below the MCP. Fig. 3.15 shows the measured magnetic field at the MCP with and without this smaller magnet. The datapoints in Fig. 3.15 come with vertical error bars given by the statistical fitting error from the fits shown in Fig. 3.14. These statistical fitting errors are then propagated into the measured rate of change of k_θ in each trapping potential. When measured spiral constants are plotted versus predicted spiral constants $(3/2)k_4 t$, the magnetic field ratio is simply the reciprocal of the slope of the data.

In this final step, an additional 1% error is included because this is roughly how reliable I think my numerical methods for predicting k_4 are. This comes from two effects—first, I compared a COMSOL model to an analytic model of the electrodes and found roughly an 0.5% difference. Second, the COMSOL model outputs a discrete grid of voltages along the trap axis. The fourth derivative of a discretized function is highly numerically unstable, and one needs to plot the fourth derivative as a function of how many points are used to estimate it to find a value that has converged, but hasn't yet become sensitive to small numerical errors in the individual points. I get an additional 0.5% error from this process—the difference I get from using different extrapolation methods. The COMSOL model has a more complete description of the electrode geometry, but the analytic model has no such numerical issues; this is why they are both useful. The field ratios extracted from the positive and negative k_4

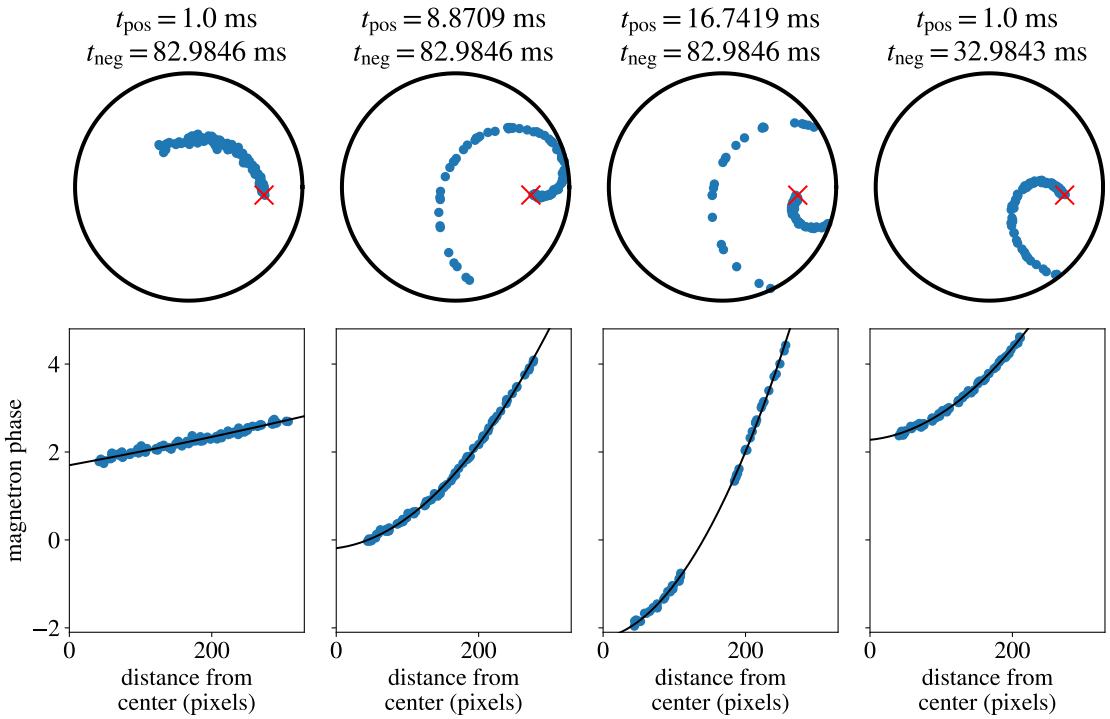

Figure 3.14: In the upper plots, the positions of electron clouds on the MCP is shown for the voltage sequence designed for calibrating the magnetic field at the MCP. Above each plot, the time spent in the trapping potentials with positive and negative quartic constant is shown. Below, the magnetron phase of each cloud is plotted versus their distance from the effective trap center on the MCP. A black line shows the result of fitting a function $\theta = k_\theta r^2 + mr$ to the data.

potentials are nearly in agreement, but there is clearly a systematic error. The difference is a reasonable order of magnitude for it to be due to patch potentials shifting k_4. This would shift k_4 by a fixed amount in both trapping potentials, and it is likely to be a much more significant effect in the negative quartic potential, where $|k_4|$ is smaller by about a factor of 6.

3.6 Patch potential measurement results in ALPHA-2

Finally I can describe the results of the patch potential measurements. We begin in the ALPHA-2 experiment. As described in the beginning of this section, observations of decreasing antihydrogen trapping rates and increasing positron heating rates generated the hypothesis that the laser used to stimulate the 1S–2S transition in antihydrogen was also generating patch potentials on the trap electrodes, and warming the trap from liquid helium temperature (4 K) to room temperature (300 K) could remove those patch potentials. A depiction of the ALPHA-2 electrodes is shown in Fig. 3.16.

Our first patch potential measurements confirmed this hypothesis, as shown in Fig. 3.17. Patch potentials were measured in a somewhat random handful of trap locations before any laser exposure, after some laser exposure, and after warming and re-cooling the trap. A few

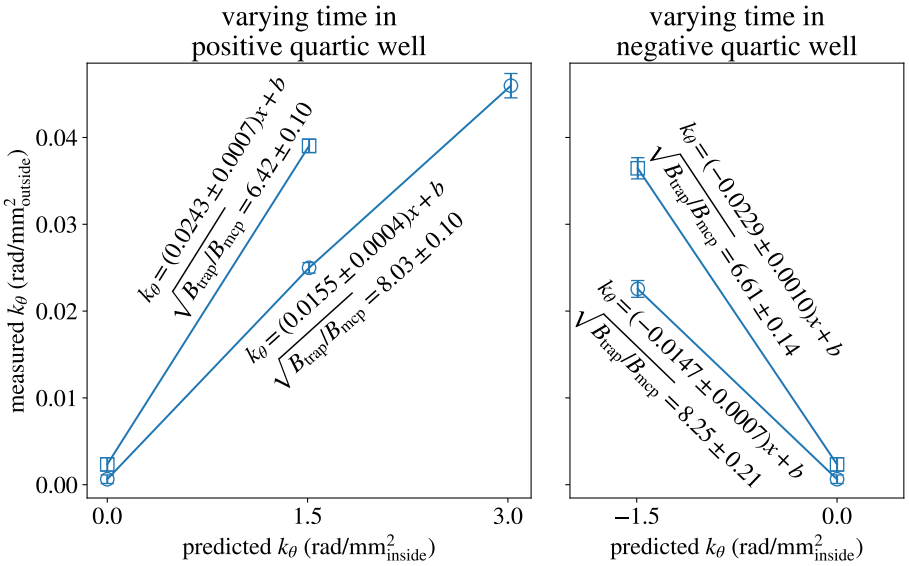

Figure 3.15: The magnetic field at the MCP is calibrated using the fit parameter k_θ from the data shown in Fig. 3.14. For each point, the abscissa is calculated by modelling the electrostatic potential, and the ordinate is calculated by fitting a quadratic function to clouds' angular positions on the MCP. The circular points show the measured k_θ values for the data shown in Fig. 3.14. The square points shown measured k_θ values using an additional magnet to boost the magnetic field at the MCP. The errorbars are statistical fitting error. Along each line, the rate of change of measured k_θ values with predicted k_θ values is shown, and the root magnetic field ratio (the MCP magnification factor) is extracted from that slope. On the left t_{pos} is varied, and on the right t_{neg} is varied. Rather than directly listing t_{pos} and t_{neg}, the horizontal axis is the predicted spiral constant given by $(3/2)k_4 t/B$. A model of the magnetic field suggests MCP magnetic field magnification factors of 6.4 and 7.6 with and without the additional magnet. This is in good enough agreement with the values measured here, although these measurements are probably more reliable.

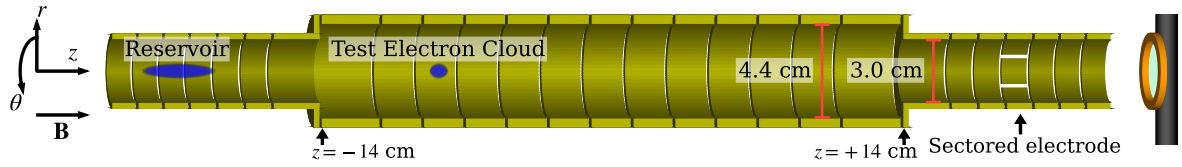

Figure 3.16: A depiction of the ALPHA-2 Penning-Malmberg trap electrodes. A cartoon of the electron plasma reservoir and an electron cloud used for patch potential measurements is included, but the reservoir's radial extent is exaggerated, and the length and radius of the electron cloud are exaggerated (else it would be little more than a pixel). A cartoon image of the MCP is shown on the right. In reality, the MCP is much further to the right (about 2 m away). The azimuthally segmented electrode, which will be used to create an artificial patch potential is labelled. This picture is also presented in Ref. [68].

additional observations beyond the laser induced patch potentials are evident here. First, warming the trap to 300 K and cooling back down to liquid helium temperatures does not remove patch potentials. It restores them to a nominal value. Second, although there is only one measurement shared between all three datasets in the smaller radius region of the trap, it seems that patch potentials are not significantly changed by the laser in this region. Finally, the nominal patch field is much stronger where the trap radius is smaller, which is perhaps to be expected (the electrodes are closer to the center of the trap). It should be noted that in ALPHA-2, there are two sets of "shorted electrodes," where some construction error has made it impossible to set these adjacent electrodes to a different voltage. This, along with the desire to measure patch potentials between electrodes, required designing shallow trapping potentials in several different electrode geometries—1 V on a single electrode provides a different k_{2m} value than 1 V applied to two adjacent electrodes. The fact that the measurements in the center of electrode 13 and between electrodes 12 and 13 are similar seems to confirm that this k_{2m} calibration was successful. Indeed the patch electric field should be a continuous function of axial position z, and it should vary significantly only when z has changed by a significant fraction of the trap wall radius.

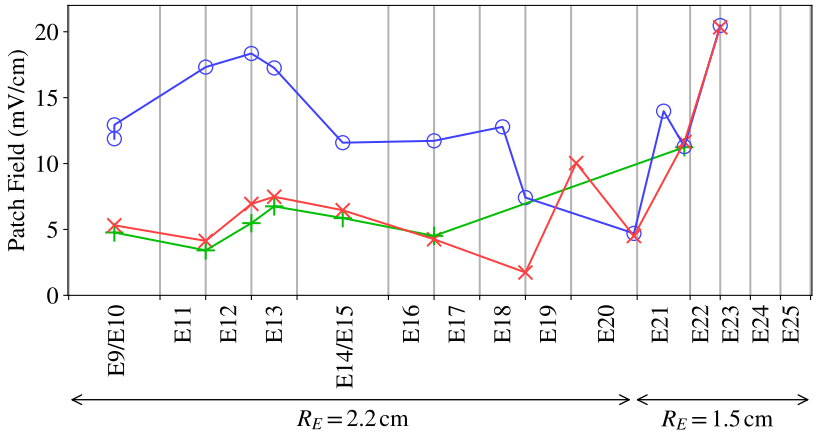

Figure 3.17: The results of the initial measurements of the patch potential induced electric field in the trap center (ε). The green + symbols are the measurements before any laser exposure. The blue circles are the measurements after some laser exposure, and the red X after warming the trap to 300 K then cooling back to liquid helium temperatures. It was difficult for me to find the power and total laser exposure time, as this data is very old. The horizontal axis shows the electrode numbers. This data is also presented in Ref. [68].

These measurements were dramatically improved in 2022. During a brief interlude in the ALPHA-g measurement campaign (due to some experimental issues with ALPHA-g), we operated the ALPHA-2 trap, and I was given the chance to measure patch potentials between periods of laser exposure. I should point out that the 1S–2S laser power is enhanced by a Fabry-Pérot cavity. The first few measurements took place while the 1S–2S team operated the laser, but without the cavity enhancement. Additionally, another ALPHA-2 team was working on laser cooling a plasma of Beryllium ions—one might wonder if their laser, or ion loss, influences patch potentials. As shown in Fig.3.18, none of these actions measurably increase patch potentials. A reasonable hypothesis is that patch potentials are

generated by laser light which is "scattered" (diffusely reflected) by the mirrors. A casual measurement by Prof. Steven Armstrong Jones at ALPHA suggests that the cavity mirrors scatter 0.1% of the incident light. Without locking the cavity, the incident beam has an intensity of tens of mW of power. With the cavity, this is hundreds of mW up to 1 W. The lasers operated by the Beryllium team are simply much lower power, and they are not an ultraviolet wavelength—although we have no data proving this is a necessary condition.

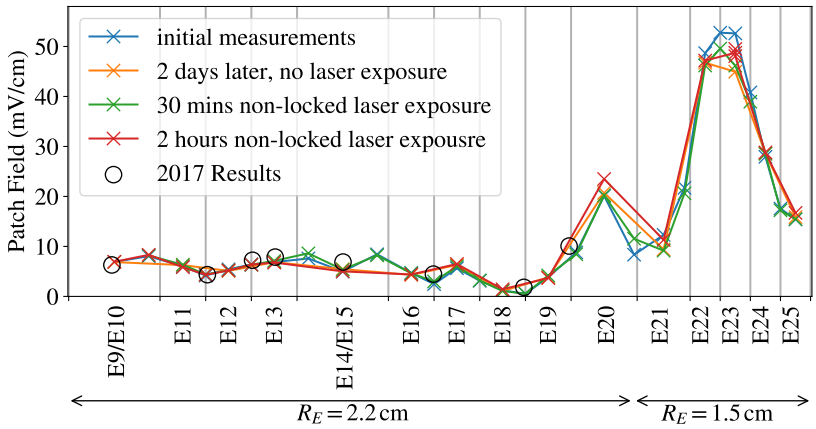

Figure 3.18: Patch potential measurements performed with the 1S–2S passing through the trap, but not locked to the cavity. Some of the measurements from Fig. 3.17 are also shown (refereed to as the "2017 results"), proving that the "nominal patch potentials" are stable for years.

Next, we introduce laser exposure at about 0.6 W of circulating power in the cavity. Measurements of patch potentials were performed after 36 minutes, and multiples of two hours beyond that. These results are shown in Fig. 3.19. We see patch potential strengths throughout the trap that seem to scale with exposure time. Additionally, a measurement was performed in 2023 after performing 1S–2S measurements with only 0.28 W of circulating power for about 6 hours. There is a small caveat in this data—there was a total of 18 hours of laser exposure before the most recent warmup to 300 K, but there was a trap warmup to 150 K after the first 12 hours. Altogether, this seems to suggest that a 150 K warmup is sufficient for removing patch potentials, and patch potentials are proportional to laser power (as opposed to laser power squared for example). The measurements after 36 minutes of exposure suggest that the patch field introduced by lasers is in a random direction that can either add to or subtract from the nominal patch potentials. With enough laser exposure patch potentials just grow over time, suggesting that the lasers create patch potentials in a reproducible direction with a magnitude that grows over time.

A few other observations in Fig. 3.19 are notable. From left to right, we begin by noticing that the patch field created by lasers at electrode 20 is much greater than elsewhere. This makes sense because electrode 20 is the last electrode before the change in radius. There is a metal plate facing straight toward the laser beam just to the right of electrode 20—a lot of solid angle for the scattered laser light to hit. Next, the patch field in the center of electrode 21, the first electrode with a smaller radius, is reduced by the laser. This is not a measurement error, I have carefully inspected the data by eye. I have no explanation for

this. Finally, lasers only seem to increase patch fields in the center of the trap, not the edges where the trap radius is smaller. It may be that the laser light does not scatter at an extreme enough angle to hit these regions.

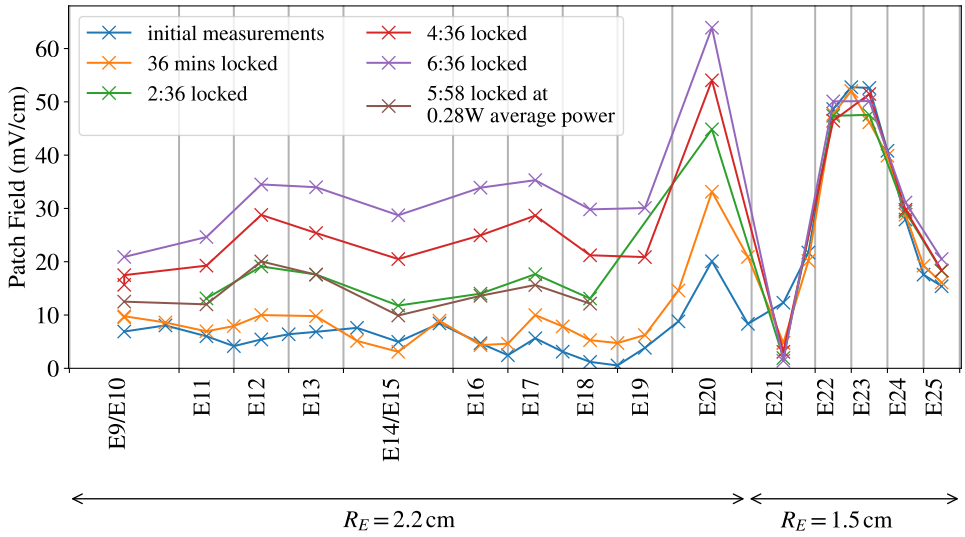

Figure 3.19: Patch potential measurements after varying amounts of laser exposure. The brown points are a separate measurement campaign a year later with lower laser power. The rest of the measurements are taken with varying amounts of time with about 0.6 W of laser power.

3.7 Patch potential measurement results in ALPHA-g

The ALPHA-g experiment, when I was working on it, did not involve lasers. Nonetheless when we were trying to perform the first ALPHA-g measurement, we encountered a novel issue with patch potentials.

The story begins with a general observation that working with positrons in ALPHA-g was hard in 2021. First, it was hard to recapture positrons sent from the positron accumulator to ALPHA-g. The potentials used do this in ALPHA-2 did not work. Eventually we found success giving the positrons much less time to cool down, pushing them quickly into a shorter, deeper trapping potential. Next, SDREVC compression on positrons was much harder—the same SDREVC potentials and frequencies that worked in ALPHA-2 did not compress positrons in ALPHA-g. Rather, these potentials rapidly expanded the positrons, and we did not manage to compress them until we confined the positrons in a much shorter, deeper trapping potential and we used a much higher rotating wall frequency. After that, positron temperatures were much higher in ALPHA-g than in ALPHA-2: 500 K versus 20 K. Finally, we were not able to produce any antihydrogen when combining positrons with antiprotons.

In hindsight, all of these observations are consistent with positrons rapidly expanding, and thereby heating as their electrostatic potential energy is turned into heat. A collective obsession throughout the collaboration with positron temperatures, rather than imaged positron plasmas, meant that there is poor data characterizing the expansion rate of these

plasmas, although this was the underlying cause of all the issues. This was compounded by collaboration-wide (including me of course) poor data-taking habits. Nobody was collecting datasets that told a clear story about what was happening. People were desperate to try as many new things as possible in the hopes that something would make the positron temperature diagnostic report 20 K so the plasma could be used to make antihydrogen. Everybody was convinced that, or otherwise acting under the assumption that there was actually nothing wrong with ALPHA-g that was preventing us from making cold positrons; we just hadn't yet found the one trick that would make it work. The best data I find that illustrates these issues is shown in Fig. 3.20. These images show not only that positrons expand significantly when left still for long periods of time, they show that when the positrons are confined in weaker trapping potentials, that expansion rate is faster. For reference, in ALPHA-2, positrons can be confined in any of these potentials for many seconds without any visibly obvious expansion.

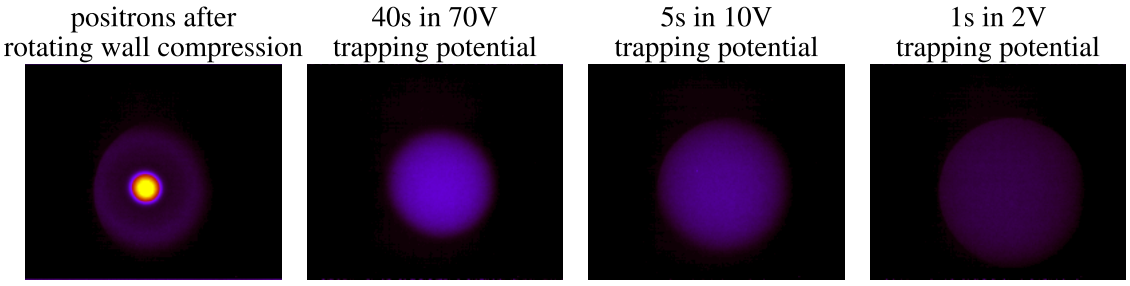

Figure 3.20: Positrons are imaged on the MCP after being subjected to a variety of trapping potentials. First, we show the positron plasma resulting from rotating wall compression. Next, these positrons spend 40 s in a "deep" trapping potential: −70 V applied to one electrode. Next positrons which spent only 5 s confined with roughly −10 V. Finally, 1 S trapped in a very shallow trapping potential. We also measured temperatures of identically prepared positron plasmas. The initial temperature was about 400 K. After waiting 40 s in the deep trapping potential, they cooled to about 80 K. Both of the final two plasmas had temperatures around 700 K.

Positron heating naturally led to the hypothesis that patch potentials were bad in ALPHA-g. However, the hypothesis at first seemed a bit outlandish because the positron heating issue was astronomically worse in ALPHA-g than it ever was in ALPHA-2. At CERN, the delivery of liquid helium Dewars ends a few weeks after the accelerator beams stop operating. This means that ALPHA can operate for a few weeks after the beam ends. I was given some of this time to measure patch potentials, and we immediately found that patch potentials were astronomically worse in ALPHA-g than they were in ALPHA-2. These initial patch potential measurements are shown in blue in Fig. 3.21. We haven't yet explained this issue or seen it again. I hypothesize that either the electron gun or an MCP was "commissioned" (i.e. tested with slowly increasing voltages) when the external magnet for the Penning-Malmberg trap was deactivated but the electrodes were cold. Both of these pieces of equipment emit charged particles, the MCP because it sparks while being first tested, and the electron gun for more obvious reasons. When the external magnet is on, because of the trajectories of magnetic field lines, it is nearly impossible for charged particles initialized outside of the

trap to find their way to the trap walls. With the magnet off, there is no such restriction, and the trap walls may have been painted with electrons.

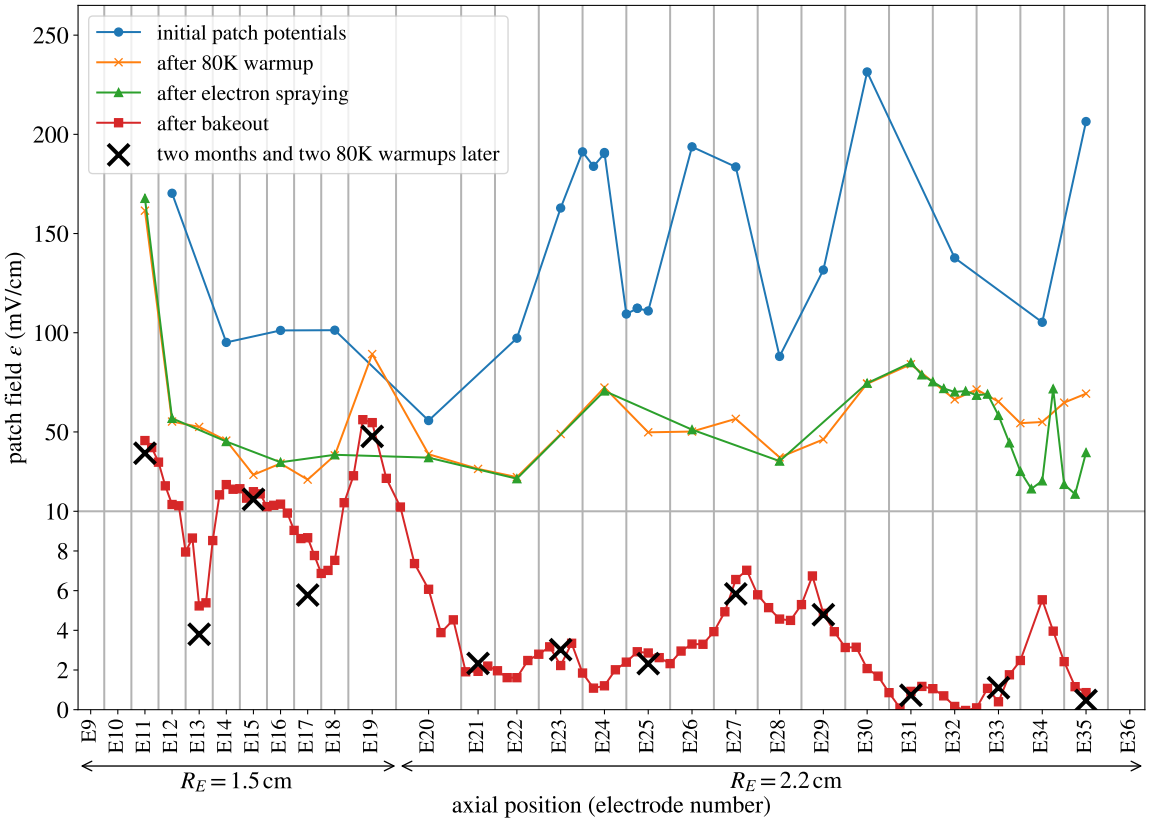

Figure 3.21: Initial patch potential measurements after the 2021 experimental run are shown with blue dots. Measurements taken after an 80 K warmup are shown with orange X's. Measurements after electron stimulated desorption near electrode 35 are shown with green triangles. The final patch potential strength is shown with red squares, and the results of a crude measurement two months later are shown with black X's. These crude measurements have larger errors (not shown), so we should pay no attention to small disagreements with the red squares. Note the nonlinear vertical axis, which was necessary to make all the measurements visible in the same plot.

While this patch potential issue was unfortunate, it was a boon for my status at ALPHA. It was my first year as a Ph.D. student, and I had diagnosed an issue that puzzled the collaboration for an entire beam season. The political capital from this success is the only reason I was allowed to perform any of the other measurements described in this thesis. Without this, other cloud based measurements would have been considered too fanciful to be worth experimental time.

Before the Christmas break at CERN, we tried two methods of reducing patch potentials. First, we heated the trap from liquid helium temperatures to 80 K (we didn't have time to go to 300 K as we typically do in ALPHA-2). The patch potential measurements after this operation are shown in orange in Fig. 3.21. Indeed, there was a significant improvement.

Next, we tried hitting the trap wall with the electron gun on purpose. The results of this experiment were somewhat odd, so they are discussed separately in Sec. 3.10.

Finally, after the Christmas break, we baked the entire ALPHA-g apparatus, warming the trap electrodes to 350 K. This reduced patch potentials to roughly the same order of magnitude that they are in ALPHA-2. On this fourth measurement, I realized that I could significantly reduce the number of clouds used to measure patch potentials in each axial location because of the excellent cloud position reproducibility in ALPHA-g. Thus many more axial trap locations were measured. Like in ALPHA-2, we find that this final patch potential strength never changes. Fig. 3.21 shows the results of this fourth patch potential measurement in red, and it shows a more crude measurement taken two months later in black. After this traumatic experience with patch potentials, we periodically measured patch potentials for a few months. For this purpose, I prepared a measurement that took only two minutes of experimental time (one reservoir), where patch potentials were measured crudely in 13 trap locations with 8 clouds each. However we eventually stopped this practice out of boredom as the patch potentials never changed after many months, several warm-ups to 80 K and to 300 K, and at least one additional bakeout. Unlike ALPHA-2, there are no lasers in ALPHA-g to induce patch potentials.

3.8 Improved measurements in ALPHA-g

The patch potential measurements in ALPHA-g were much more precise than in ALPHA-2 because (1) the innate magnetron was much smaller, only about 5 pixels, and (2) the reservoir showed no signs of any diocotron. This was not the result of any particular effort on my part—it was just luck. This enabled a simpler form of analysis, where I would simply have a predicted position for each cloud on the MCP given the fit parameter ε and the parameters of the spiral, and I would minimize the distance from each point to its predicted position. This is not strictly valid because it treats radial distance as equivalent to angular distance. In the probability distribution from the ALPHA-2 fits, a cloud can freely move along the spiral without radically changing its assigned probability density, but moving a small distance off of the spiral does radically change its assigned probability density. Although the probability distribution fit is technically more accurate, when the data is so high quality, this simpler (and vastly less computationally costly) method suffices. Also, in ALPHA-g, clouds that miss the MCP can simply be ignored. We have plenty of data for finding ε using only the positions of clouds that do hit the MCP.

Also, several corrections were clearly visible in this data that we would never be able to resolve with the initial cloud magnetron in ALHPA-2. First, when we go from a shallow well where $k_2 = k_{2m}$ to a deep trapping potential with $k_2 = k_{2i}$, the displacement is not exactly ε/k_{2m}. Rather, it should be $\delta = \varepsilon(1/k_{2m} - 1/k_{2f})$. This effect is visible in an offset of the data to the right in the linear plot, and that offset is easily fixed by including this correction. Next, in some datasets, a nonlinear correction to the displacement is visible. There are many ways to include a nonlinear term in the fitting procedure, but because of my experience from the artificial patch in ALPHA-2 (see Sec. 3.12), I decided that the best approach would be

to allow for a pole in δ by using the fit parameter ε_2 in:

$$\delta = \varepsilon \left[\frac{1}{\frac{1}{k_{2m}} - \frac{1}{k_{2f}}} + \varepsilon_2 \right]^{-1} \tag{3.17}$$

This parameter can physically be interpreted as a k_2 value imposed by patch potentials which depending on its sign can either confine clouds without any applied trapping potential or can eject clouds from the trap when $k_{2m} = -\varepsilon_2$. Finally, in a few datasets some higher order deviation from the spiral shape $\theta = k_\theta r^2$ is visible. This is handled by simply including a higher order term $\theta = k_\theta r^2 + k_{\theta 4} r^4$. I will leave it as a somewhat obnoxious exercise for the reader to derive how $k_{\theta 4}$ depends on parameters of the trapping potential. The most obvious term, but not the only term, comes from a perturbation to the trapping potential in the form:

$$\Phi_T = \cdots + k_6 \left(z^6 - \frac{15}{2} z^4 r^2 + \frac{45}{8} z^2 r^4 - \frac{5}{16} r^6 \right) + \cdots . \tag{3.18}$$

The effect was visible, but not so clearly visible that the measurements of $k_{\theta 4}$ were reliable enough to compare to a theoretical prediction. In Fig. 3.22, I show six examples of resulting fits from some of the measurements shown in Fig. 3.21 along the orange line. Consider also the fit shown in Fig. 3.23 from the first day of patch measurements, shown in blue in Fig. 3.21. This example illustrates several things. First, I was trying to measure patch potentials in more axial locations—four per electrode. Thus this location is named "E23/E24 right," as in the location between the center of E24 and the point between E23 and E24. Of course, within my code, all of these locations simply have an index value. Second, the spread of points is clearly larger than in Fig. 3.21. At the time, I wasn't specifically studying the phenomenon of scoop magnetron motion (see Sec. 2.3), so I didn't look into potential causes of this. I have two hypotheses for this difference:

1. My leading hypothesis for intrinsic scoop magnetron is that it is caused by patch potentials near the reservoir. Since patch potentials were dramatically weakened between these two measurements, this may be the cause of the larger spread in Fig. 3.23.

2. I may have used clouds with larger charge variability on the first day of measurements. It is possible then that the clouds had the same intrinsic magnetron on both days, but that it was phase locked in the later measurements.

The final difference between Fig. 3.22 and Fig. 3.23 is in the spacing of the cloud positions on the left in Fig. 3.23. On this day I was trying a scheme where the clouds would be roughly equally spaced along the spiral. To derive the sequence of k_{2m} values needed to accomplish this, consider that the difference between two clouds positions on the MCP is given by $\sqrt{[\Delta r]^2 + [\Delta(\theta r)]^2}$. Now assume that when the spiral becomes strong, the second term dominates. Since $\theta = k_\theta r^2$, we have $\Delta(\theta r) = \Delta(k_\theta r^3) \propto r^2 \Delta r$. Since $r \propto 1/k_{2m}$, we want $1/k_{2m}^2 \Delta(1/k_{2m}) = \text{const}$, or $1/k_{2m}^4 \Delta k_{2m} = \text{const}$. If we interpret Δ as d/dn, where n is the index of the k_{2m} values (as in $k_{2m\,n}$ is the k_{2m} value applied to the n'th cloud), we see that $k_{2m\,n} = \text{const}/n^3$. While this produced a fairly beautiful result, it wasn't ultimately very useful. This is because with 128 clouds, we can only span a factor of about 5 in k_{2m} values. If we apply this, to get a decent measurement of ε, we need to know what values

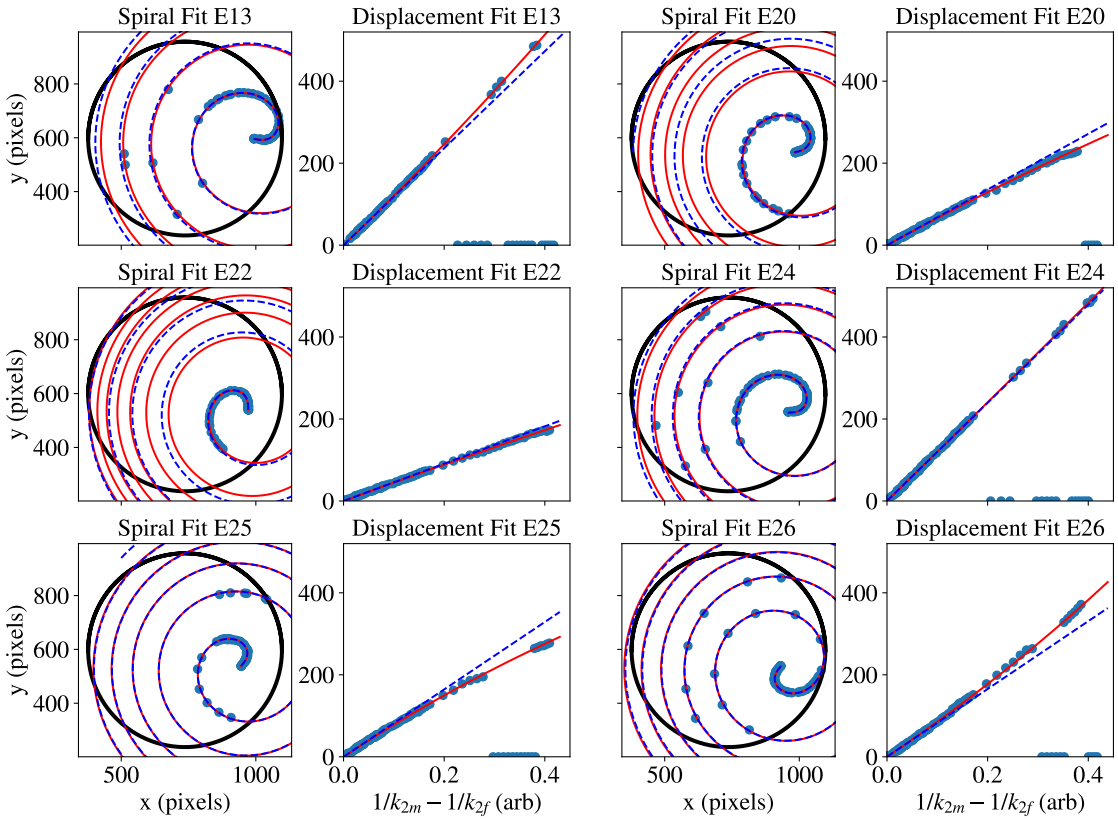

Figure 3.22: Six patch potential measurements are shown. For each of the six measurements, the electrode number (the axial position of the measurement) is shown above. On the left, the positions of the cloud centers in the MCP images are plotted with blue dots. The black circle is the aperture outside of which no clouds can be imaged. The red line is the result of fitting a spiral $\theta = k_\theta r^2 + k_{\theta 4} r^4$, and the blue dashed line is that spiral without the quartic term. On the right, the displacement of each cloud from the origin of the spiral is plotted versus $1/k_{2m} - 1/k_{2f}$, which should be proportional to displacement in the leading order model. Blue dots at displacement 0 on the right plot represent clouds which missed the MCP. In this right plot, the red line is the nonlinear fit presented in the text, and the blue dashed line is the result of setting ε_2 to zero.

we expect. This required a preliminary measurement followed by an improved measurement where the range of k_{2m} values was adjusted based on the initial measurement. Practically, it is more beneficial to space our k_{2m} values exponentially to cover the widest range of ε values possible, but I maintain that this equal spacing scheme could be useful if we ever find ourselves prioritizing measuring the spiral parameters.

The "cover picture" of this thesis (or rather, the picture at the beginning of the table of contents because of UC Berkeley's atrocious required title page) comes from one of these "equal spaced patch potential measurements." In this picture, the images of many different clouds are added together. I frequently used such summed images to quickly diagnose whether or not a measurement was working, because a lot of the analysis presented here was either computationally intensive or it wasn't prepared in advance of the data-taking. A

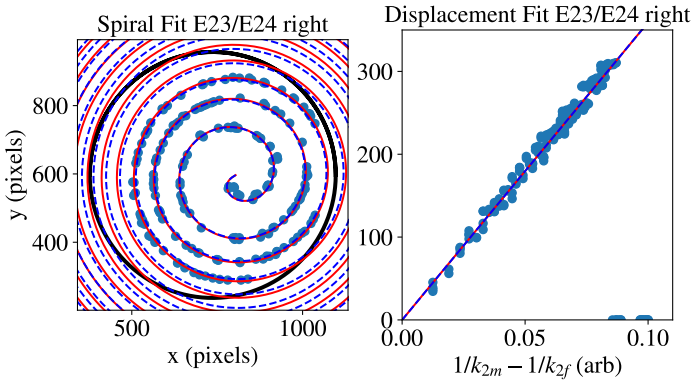

Figure 3.23: A measurement of patch potentials using the "equal spacing" scheme described in the text. The plot elements are described in the caption of Fig. 3.22.

background image, collected by averaging several MCP images without clouds, is subtracted to reduce the effect of some imaging artefacts like banding and hot pixels. 640 MCP images were taken for this particular measurement—several repeats of the same patch potential measurement. They are shuffled into a random order, and then added one at a time unless the cloud center was within 50 pixels of another cloud center already included in the summed image. The first few clouds of each reservoir, with higher total brightness, were also rejected. The picture is plotted in the proper greyscale, with black being the highest pixel intensity. Usually I apply a colormapping, but for the front cover I thought this was too dishonest. Of course, most of these edits are aesthetic decisions and not legitimate data analysis techniques.

3.9 Patch field scaling laws

To see how the electric field magnitude in the center of the trap scales with the physical size and magnitude of voltage variations along the trap wall, I propose a toy model where I attempt to calculate the electric field due to patch potentials at $z = r = 0$. When we inspect the general solution to the Laplace equation in cylindrical coordinates (see appendix), we find that the effect at $z = 0$ of a voltage perturbation originating at some axial position z is exponentially suppressed like $\exp(-|z|\alpha_1^0/R_w)$, where $\alpha_1^0 \approx 2.4$ is the first zero of the zeroth Bessel function. Thus I will sum the electric field produced by patches between $z = -R_w/2$ and $z = R_w/2$, asserting that all these patches generate an electric field at $r = z = 0$ of the same order of magnitude ($\sqrt{z^2 + R_w^2} \sim R_w$). If the patches have a length scale l, then we are summing over $R_w \times 2\pi R_w/l^2 = 2\pi R^2/l^2$ patches. One needs to be a bit careful when calculating how the electric field of a patch of voltage V_0 and length scale l scales with R_w. Consider the patches to be surface-charged squares of surface charge density σ sitting a distance d above an ideal conductor. Then σ scales like V_0/d (it does not vary with l), the total charge of the patch scales like $V_0 l^2/d$. Now to calculate the electric field near $r = 0$, we need to notice that as $d \to 0$, a patch and its image charge will form a dipole with dipole moment $D \sim V_0 l^2$. A dipole's electric field scales like D/R_w^3, so the electric field near the trap center should be $V_0 l^2/R_w^3$.

In case the above argument was too handwavy, we can consult the exact expression for a square patch of voltage perturbation on a grounded conducting cylinder. The following equations, taken from the appendix, give the potential in cylindrical coordinates of a patch of angular extent $\theta_0 = l/R_w$ centered at $\theta = z = 0$.

$$V_p(r,z) = \begin{cases} V_0 \sum_{m=0}^{\infty} d_m \cos(m\theta) \sum_{n=1}^{\infty} \frac{\exp\left(\alpha_n^m \frac{l/2+z}{R_w}\right) - \exp\left(-\alpha_n^m \frac{l/2-z}{R_w}\right)}{\alpha_n^m J_{m+1}(\alpha_n^m)} J_m\left(\alpha_n^m \frac{r}{R_w}\right) & z < -l/2 \\ V_0 \sum_{m=0}^{\infty} d_m \cos(m\theta) \sum_{n=1}^{\infty} \frac{-\exp\left(-\alpha_n^m \frac{l/2+z}{R_w}\right) + \exp\left(\alpha_n^m \frac{l/2-z}{R_w}\right)}{\alpha_n^m J_{m+1}(\alpha_n^m)} J_m\left(\alpha_n^m \frac{r}{R_w}\right) & z > l/2 \\ V_0 \sum_{m=0}^{\infty} d_m \cos(m\theta) \left[\left(\frac{r}{R_w}\right)^m + \sum_{n=1}^{\infty} \frac{-\exp\left(-\alpha_n^m \frac{l/2+z}{R_w}\right) - \exp\left(-\alpha_n^m \frac{l/2-z}{R_w}\right)}{\alpha_n^m J_{m+1}(\alpha_n^m)} J_m\left(\alpha_n^m \frac{r}{R_w}\right)\right] & -l/2 > z > l/2 \end{cases} \tag{3.19}$$

$$d_0 = \frac{\theta_0}{2\pi}; \qquad d_{n\neq 0} = \frac{2}{m\pi}\sin(m\theta_0/2). \tag{3.20}$$

In the above equations J_m is the m'th Bessel function of the first kind, and α_n^m is the n'th zero of the m'th Bessel function—excuse some notation abuse $[J_m(\alpha_n^m) = 0]$. The $m = 1$ term gives the only contribution to the transverse electric field at $r = 0$. To evaluate the electric field due to a small patch near $z = r = 0$, you might expect me to use the central case, but once we take the $l \to 0$ limit the region of validity of the expression also goes to zero. We have to be a little careful with the order of limits and sums here, because if we casually swap some of them, we arrive at an expression that no longer converges. To evaluate the electric field, we set $\theta = 0$ and we take the derivative with respect to r of the $z > l/2$ case. After finding the electric field we make the patch small, and only then do we take the limit as z goes to zero:

$$E_x = \lim_{z\to 0^+} l^2 \lim_{l'\to 0} \left.\frac{d}{dr}\right|_{r=0} V_0 \sum_{m=0}^{\infty} d_m \sum_{n=1}^{\infty} \frac{-\exp\left(-\alpha_n^m \frac{l'/2+z}{R_w}\right) + \exp\left(\alpha_n^m \frac{l'/2-z}{R_w}\right)}{l'\alpha_n^m J_{m+1}(\alpha_n^m)} J_m\left(\alpha_n^m \frac{r}{R_w}\right) \tag{3.21}$$

$$= \lim_{z\to 0^+} \frac{V_0 l^2}{2\pi R_w^2} \lim_{l'\to 0} \sum_{n=1}^{\infty} \frac{-\exp\left(-\alpha_n^1 \frac{l'/2+z}{R_w}\right) + \exp\left(\alpha_n^1 \frac{l'/2-z}{R_w}\right)}{l' J_2(\alpha_n^1)} \tag{3.22}$$

$$= \lim_{z\to 0^+} \frac{V_0 l^2}{2\pi R_w^3} \sum_{n=1}^{\infty} \frac{\alpha_n^1 \exp\left(-\alpha_n^1 \frac{z}{R_w}\right)}{J_2(\alpha_n^1)}. \tag{3.23}$$

This final limit cannot be brought into the sum, because the sum no longer converges when we take $z \to 0$, but it can be evaluated numerically giving $(0.28262)V_0 l^2/R_w^3$. It's somewhat surprising that it converges at all, as $\alpha_n^1/J_2(\alpha_n^1)$ for large n behaves like $(-1)^n n^{3/2}$. However, the exponential provides "exponential regularization." Actually, in mathematicians' preferred notation, any summand in the form $(-1)^n n^s e^{-\epsilon n}$ converges as $\epsilon \to 0$. When summed from $n = 0$ to ∞, it has the value $-(1 - 2^{1-s})\zeta(s)$, where ζ is the famous Riemann zeta function [79].

Having confirmed the electric field of small square patches, we can sum over the number of patches, letting the electric field scale with the square root of the number of patches. We

find an electric field strength of order:

$$|\varepsilon| = \mathcal{O}\left[\frac{V_0 l^2}{R_w^3}\left(\frac{2\pi R_w^2}{l_p^2}\right)^{1/2}\right] = \mathcal{O}\left[\frac{V_0 l}{R_w^2}.\right] \tag{3.24}$$

To verify this power law, as in Sec. 3.2, I prepared a grid of square patches with voltages sampled from a Gaussian distribution with standard deviation 1 V. I used patch sizes where between 10 and 50 patches would fit around the circumference of the cylindrical electrode. The patches were all square, and enough patches were added so that they extended from $z = -2.5R_w$ to $z = +2.5R_w$, far enough that patches farther out in z would have a minimal effect. For each patch size, I generated 4×10^4 random distributions and evaluated the transverse electric field at $z = r = 0$. The results of this computation are shown in Fig. 3.24, and we find agreement with the hypothesis that ε scales with l.

Curiously, in both ALHPA-g and ALPHA-2, when we compare typical patch fields in the "thin trap" with $R_w = 2.2\,\text{cm}$ to typical patch fields in the "normal trap" with $R_w = 1.5\,\text{cm}$, I don't see verification of this power law. It appears that patch fields in the smaller radius region are more than $(2.2/1.5)^2 \sim 2$ times patch fields in the larger radius region. We can upgrade our power law by one factor of l/R_w by removing the summation of random patches—i.e. assuming that patch potentials are comparable in size to R_w or that they are relatively rare, so a particular place in the trap can only see the effect of a few patches. Another way to upgrade the power law by a factor of l/R_W is to assume that instead of voltage perturbations, we have patches of some material with an electric polarization oriented parallel to the electrode surface, or patches with positive and negative sign located close to one another. Once we include the image charge of these patches, their effect on the center of the trap is that of a quadrupole, which will produce an electric field of order $V_0 l^3/R_w^4$.

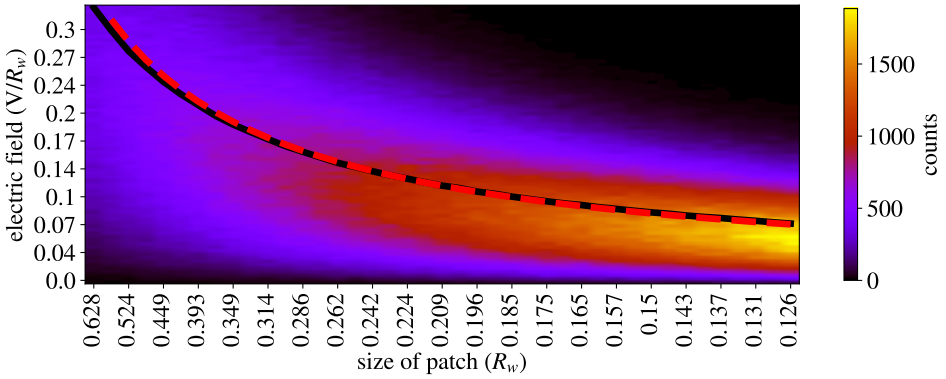

Figure 3.24: For each patch size, 4×10^4 random grids of square shaped voltage perturbations are simulated. A histogram of transverse electric fields at $r = z = 0$ is plotted, with the color of each bin being the number of counts in that bin. The average transverse electric field magnitude for each patch size is shown with the black line, and a power law scaling with the patch size is shown with a red dashed line.

Another interesting outcome of this computation is that the electric field in the axial

direction (z) is weaker than the electric field in the azimuthal directions (x, y, or r, θ). For a patch size of $2\pi R_w/50$, a histogram of electric field strengths for the 4×10^4 generated samples is shown in Fig. 3.25. This is intuitive because the patches along a ring closest to the center of the trap cannot generate a z-directed electric field; they can only contribute to the x and y components. We have to move a significant distance from the axial trap center (a distance in z) before patches start contributing to E_z.

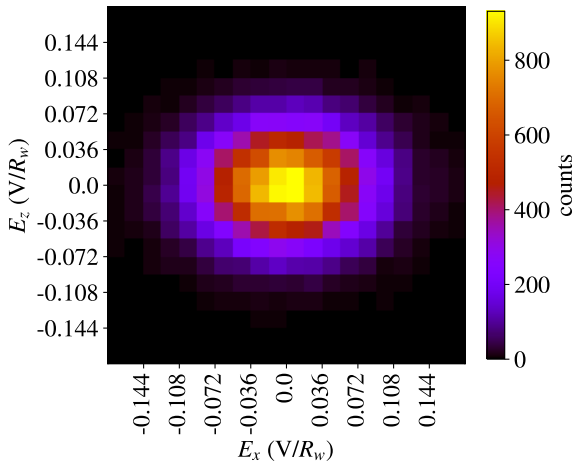

Figure 3.25: A 2–D histogram of the x and z components of the electric field. For each of 4×10^4 iterations, a random distribution of voltages has its electric field in the center of the trap evaluated.

Since I have prepared this computational tool, we can use it to verify an assertion used throughout these patch potential measurements—that the characteristic length scale for higher order terms in the electrostatic potential is R_w, regardless of the size of patch potentials. On one hand this might seem obvious. On another hand, it is certainly possible to make any on-axis potential (provided that it still solves the Laplace equation) using sufficiently small patches with sufficiently chosen voltages. In other words, the coefficient in front of higher order terms can be arbitrarily large.

This assertion leads to the conclusion that $\delta = \varepsilon/k_{2m}$ is approximately valid as long as $\delta \ll R_w$. It is this conclusion that I directly tested with a simulation. As before, I generated random voltage distributions, and this time I added the potential generated by an electrode. I calculated the magnetron center displacement δ as a function of k_2 applied by the electrode. The magnetron center is the potential minimum in z and the potential maximum in r, θ. Next, I found the value of δ where δ exceeded the linear estimate by 10%. I defined the "nonlinearity scale" as ten times that δ value. The results of this calculation for patch sizes between $2\pi R_w/4$ to $2\pi R_w/32$ is shown in Fig. 3.26. This calculation confirms that the nonlinearity scale does not depend on the size of patches.

3.10 Electron stimulated desorption attempt

In case warming the trap would not remove patch potentials, we tried ablating away whatever contained the patch potentials using the electron gun, which is nominally used to create an

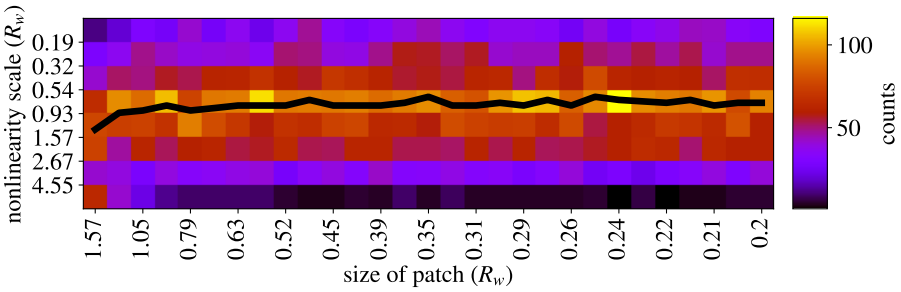

Figure 3.26: For each patch size between $2\pi R_w/4$ (left edge) and $2\pi R_w/32$ (right edge), the "nonlinearity scale" of 400 randomly generated grids of square voltage perturbations is recorded in a histogram. The color of each cell is the number of simulations that fell within that bin. The black line indicates the average nonlinearity scale for a each patch size. This data is also presented in the supplementary material of Ref. [68].

electron plasma in ALPHA-g. To do this, one of the ALPHA-g magnetic minimum trap magnets was reversed so that it would counteract the external solenoid. This meant that when the magnetic field produced by this magnet in its center was equal and opposite to the field produced by the external solenoid, the field lines would diverge and presumably intersect with the trap wall. The magnet was centered on the center of electrode 35, but it is likely that magnetic field lines would hit the wall somewhat "in front" of the magnet (electrons come from the left, or from beyond electrode 1, in Fig. 3.21).

This idea was inspired by "electron stimulated desorption," (ESD) a process commonly studied in accelerators or to benefit accelerators [80, 81, 82]. My hypothesis for the cause of these patch potentials is explained in more detail in a later section, but suffice to say for now that I believed that charges were resting on layers of cryopumped gas. The people in CERN's vacuum group told me that such gasses can be removed by bombarding them with electrons. The results of this third measurement of patch potentials is shown in Fig. 3.21 in green. At first glance, it looked like the electron bombardment was a success. However, upon closer inspection of the fits, it became apparent that the cloud displacement had become strongly nonlinear.

Experimentally, this operation was performed by turning on the electron gun with the magnet off, and a spike in the vacuum pressure above ALPHA-g was observed as gasses were produced where the beam struck. Next, the magnet current was increased and at some point the vacuum pressure above ALPHA-g returned to normal, indicating that the beam was now striking the ALPHA-g electrode surface and that the beam was no longer passing through the entire experiment. An electron beam energy of about 50 eV was used, which is generally somewhat low for ESD, and a current of about 100 μA was applied for several seconds. These are typical parameters used for loading an electron plasma into the Penning-Malmberg traps, and it was probably a mistake to not confer with the literature on ESD before trying it.

In Fig. 3.27, I zoom in on the data shown in Fig. 3.21. We see that except in one trap location, the transverse electric field due to patch potentials was reduced by a factor of 2–3. However, when we look at the actual datasets used to measure ε in these trap locations, we find that the cloud displacement is no longer well-approximated by the linear approximation

$\delta = \varepsilon/k_2$.

The data used to infer the starred points in Fig. 3.27 is shown in Fig. 3.28. Starting from the left, the first three measurements have an odd wiggle in cloud displacement versus $1/k_{2m}$, which I had never been seen before. Then the measurement between E34 and E35 and the measurement in the center of E35 are consistent with an unusually strong nonlinearity, or an unusually large ϵ_2. The measurement between those two (called "E34/E35 right") is particularly odd. As k_{2m} is decreased, the cloud displacement reaches a maximum then turns back over. In case there was any doubt that this was real, it is also evident in the spiral, where the last few clouds with the lowest k_{2m} start to traverse the spiral backwards. Of course, this made the fit function do all kinds of weird things to try to accommodate this absolutely forbidden behavior, so I adjusted this one fit by hand in Fig. 3.28 to best reflect my understanding of the situation.

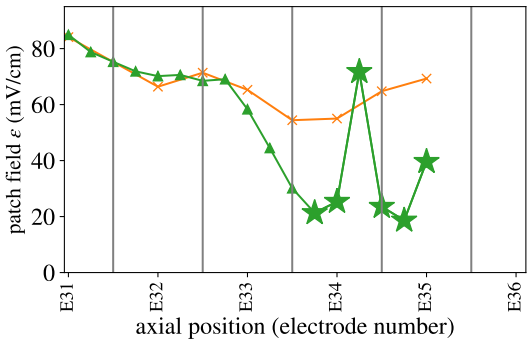

Figure 3.27: I zoom in on the difference between patch potentials before and after ESD, also shown in Fig. 3.21. The starred points are the measurements which are shown in Fig. 3.28. The green triangles are measurements after ESD, and the orange X's are before.

It does seem though that ε values were legitimately decreased by ESD—between the centers of electrodes 33 and 34, the fits are not so odd and they provide good measurements of a significantly decreased ε. My favorite hypothesis is that the electron spraying decreased ε but increased the on-axis potential due to patch potentials. This idea is depicted in Fig. 3.29. We cannot explain the behavior shown in Fig. 3.28 by simply including higher order terms in the small r, z expansion for the potential perturbation due to patch potentials. By including terms up to third order, I could explain things like a higher order term in δ or a small deviation from the spiral shape (if the electrostatic minima do not lie along a line as we vary k_{2m}), but I could not get anything close to the behaviour seen in the E34/E35 right dataset. Actually the lack of any deviation from the spiral indicates that terms like $r^2 \cos 2\theta$ are not present. This makes some sense—if this process suppressed the transverse electric field, created by a term in the potential of the form $\varepsilon r \cos\theta$, it probably also suppressed higher order azimuthally asymmetric terms. Then the fact that an ordinary spiral still develops probably suggests that in a deep trapping potential the potential created by patches is still small compared to the trapping potential.

Thus these observations can only be explained by an on-axis potential which cannot be approximated as a polynomial where higher order terms are suppressed by powers of $r, z/R_w$. Recall in the study of antiproton loss due to patch potentials, Sec. 3.2, that a

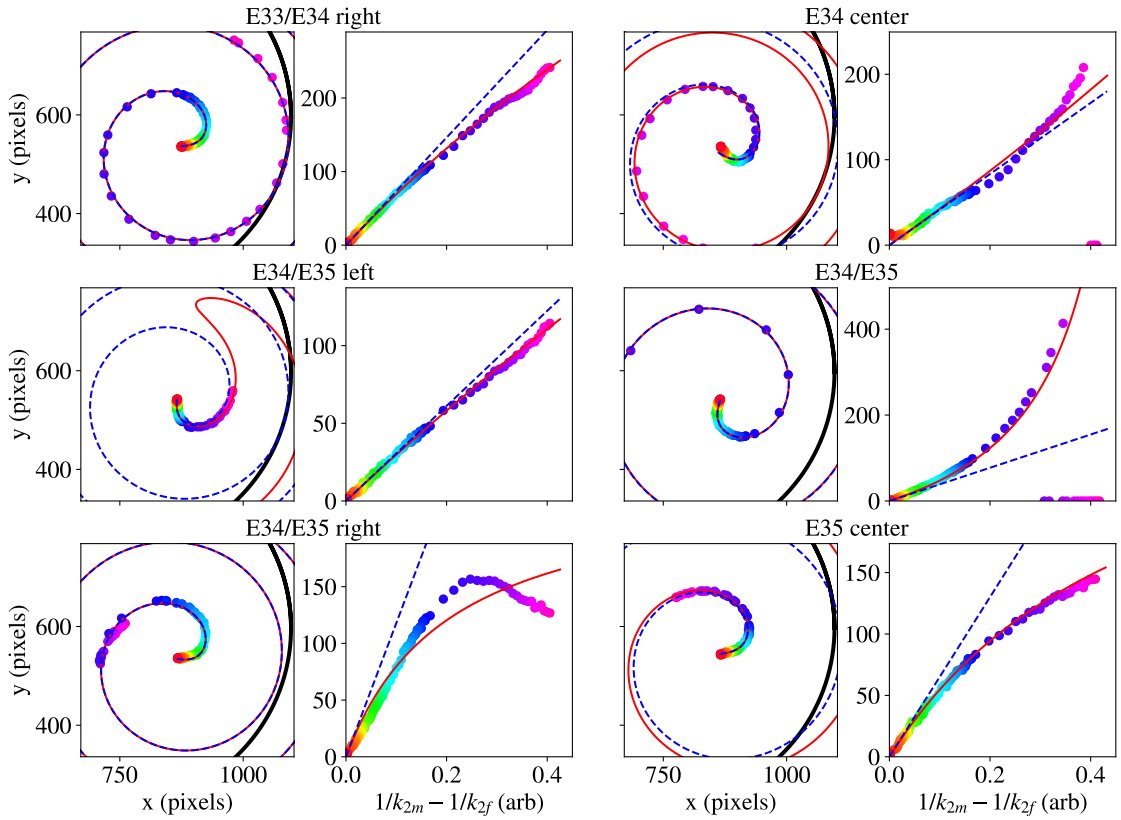

Figure 3.28: For six axial trap locations, the data collected during patch potential measurements after ESD is shown. The elements of this figure are described in the caption of Fig. 3.22. I have added colors to the points to indicate which point on the left subplot corresponds to a point on the right subplot.

plethora of strange behaviors can happen when we lower k_2 and the displacement is no longer small compared to R_w. We are seeing this behavior here, but very close to the trap axis (about 0.5 mm, compared to $R_w = 2.2$ cm). It may be that in the E34/E35 right dataset we see the electron clouds leave the trapping potential created by the electrodes and enter a nearby electrostatic trap created solely by patch potentials. My only regret is not taking the trapping potential to zero or even negative electron-repelling voltages to conclusively prove this hypothesis. Of course, this experiment was designed before I knew this was a possibility.

It's not entirely clear how the electrons from the electron gun would distribute themselves around the electrode. In Sec. 3.4, I explained that when we send an electron cloud from the trap to the MCP, if the cloud is further off-axis than about 1–2 mm, it will be blocked by a circular aperture. The electron gun is on the same movable stick as the MCP, so when we use the electron gun, it is in the same location that we place the MCP when imaging electron clouds. Therefore, the same argument about electrons following magnetic field lines applies, and the same aperture can obstruct those field lines. When electrons are sent from the electron gun they end up no more than 1–2 mm from the center of the trap. The only caveat is that the electron gun likely produces a plasma of electrons with complex dynamics; the electron beam cannot be accurately modelled as individual electrons following field lines.

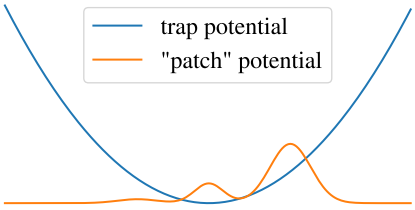

Figure 3.29: A cartoon of my hypothesis for what electron spraying did to the on-axis electrostatic potential in the trap. The blue line shows the ordinary trapping potential, and the orange line proposes that there is an on-axis perturbation to the electrostatic potential which which can do things like trap electrons, or eject them from the trap despite the presence of the trap potential (depending on axial position).

Nobody at ALPHA has put significant effort into modelling this beam, so it isn't clear if this is a uniform density beam of radius 1–2 mm, or if it is a narrower beam located a maximum distance 1–2 mm off-axis. In either case, the center of the beam will not be the center of the trap; in fact the trap is not perfectly aligned with the magnet (see Sec. 6). Even if the beam was centered in one axial trap location, it would not be centered further along the trap. Thus when the beam reached the magnetic zero created by the opposing magnet, we might have expected the beam to deviate in one particular direction and only hit one side of the electrode. This would be unlikely to significantly reduce ε. Thus the results seem to suggest that somehow the electrons reached the entire surface of the electrode. From there it's not clear what they did... did they ionize atoms in the outer layer of the cryopumped gas?... did they stick to the surface and create negative ions? Given the experimental results, it seems unlikely that the electrons simply performed their intended task of desorbing cryopumped gas from the electrode surface.

3.11 What are the patch potentials at ALPHA

Until this point I have done little speculation on what causes patch potentials at ALPHA, what causes them to change, and what could be implemented to reduce patch potentials. Patch potentials, or variations in the electrostatic potential just outside the surface of nominally conducting materials, have been studied extensively using "Kelvin probe force microscopy" [83, 84, 85, 86, 87, 88]. This effect is usually explained by noting that metals form "grain boundaries," where the metal is only a cohesive crystal within a grain boundary. Depending on the relative orientation of the crystal structure and the surface of the metal, a small perturbation to the potential of the metal just above the surface is generated. The electrostatic potential just above the surface of the conductor sets the boundary conditions for the trapping potential, not the potential within the conductor. Ref. [85] measures variations of tens of millivolts varying over length scales of a few microns for polished copper, Ref. [88] shows that the length scale is much smaller for a gold-plated surface, and Ref. [89] shows potential variations of $\mathcal{O}(100\,\mathrm{mV})$ with length scales of 100 nm for their "incrementally sputtered electroplated gold electrodes." The electrodes used at ALPHA are gold-plated aluminum. I am measuring the electric field produced by patch potentials 2 cm from the elec-

trode surface, so we would expect the effect of such tiny patches to "average out." This is derived properly in Sec. 3.9, where we find that the electric field should scale like $V_0 l/R_w^2$, where l is the length scale of the patch potentials and V_0 is size of the electrostatic potential variations. Thus it is not likely that this grain boundary effect explains the magnitude of patch fields observed at ALPHA. Of course, we would never be able to explain laser induced patch potentials with grain boundaries.

Ref. [90] discusses a probe which can measure potentials along larger length scales, and the authors find centimeter-scale, 20 mV scale potential variations which are affected by baking to 700 K and exposure to air. This is despite the fact that their surface, like ours, is gold-plated, and therefore nominally does not oxidize. Ref. [62] confirms these observations and shows that the effect varies over time, something we do not observe at ALPHA, perhaps because our vacuum is too good, or perhaps because we measure our patch fields long after this effect has settled. Ref. [91] also finds potential variations with centimeter length scales and 250 mV voltage scale on stainless steel cleaned with acid followed by alcohol. They find that glow discharge cleaning and colloidal graphite coating weaken these potential variations to 15 mV. Our electrodes are cleaned in an acetone ultrasonic bath followed by an ethanol ultrasonic bath. This reminds us that there may be "grime" on the surface of our electrodes which has a much more significant effect over large distance scales than crystal grain boundaries. It seems that most of the Kelvin force microscopy studies are insensitive to, or even disinterested in, such large-scale potential variations.

As for the effect of lasers in a cryogenic environment, Ref. [66] reports that measurements of the cyclotron frequency of an ion are degraded by laser exposure in a cryogenic Penning trap, and the author attributes this to patch potentials. Ref. [92] describes spikes in vacuum pressure which the authors attribute to an electrical breakdown that occurs when too much charge has been deposited on layers of cryopumped gas. The breakdown phenomenon isn't so useful to me. However the simple idea that the cryopumped gas is not conductive, and therefore charged particles can sit on it, is perfectly consistent with what we observe in ALPHA-g and ALPHA-2. It may be that I just haven't found the right search terms yet, but I cant find other published mentions of this. It seems to me that a wide variety of experiments would have electrodes in cryogenic environments, and that they might be able to observe that significant voltage perturbations can build up on their cryopumped gas.

Consider a square grid of ions with 20 Å between charges [a surface charge with $\sigma = e/(20\,\text{Å})^2$] resting on top of 5 Å of cryopumped gas on the surface of an electrode. In that 5 Å, there is an electric field given by σ/ϵ_0, and the potential on the surface of the charged layer differs from the voltage applied to the electrode by $(5\,\text{Å})\sigma/\epsilon_0 = 2.3\,\text{V}$. This perturbed potential is the boundary condition for the potential within the Penning-Malmberg trap, not the voltage applied to the conductor. Note that electrons start to tunnel out of atoms if the electric field exceeds roughly 1 V/Å. The electric field in the example above remains below this limit, so there will not be an electrical breakdown in the cryopumped gas. This is why the electric field in 2021 in ALHPA-g was possible—an electric field of 200 mV/cm implies that opposite sides of the electrode had a different potential by roughly 1 V. In fact, whatever caused the patch potentials in ALPHA-g may have been prevented from creating even worse patch potentials by electrical breakdowns. Further, ALPHA-2's 1S–2S laser provides more than enough photons to ionize enough atoms to change the surface potentials as much as it seems to (assuming that one photon is capable of removing one electron from at least some of

the molecules present). Also, given our vacuum pressures it is plausible, but not guaranteed, that one or more "monolayers" (layers one atom thick) of cryopumped gas are present on our electrode surfaces. Finally, most cryopumped gasses would be removed by warming to 300 K, or even 100 K, and we observe that warmups to these temperatures restores patch potentials to their nominal strength. This nominal strength is probably due to "grime"—large patches of contaminants left from cleaning or producing the electrodes which cannot be removed by heating.

Refs. [93, 91] report dramatic improvements in surface potential variations by coating the surface in colloidal graphite. This has become common in Penning-Malmberg trap construction. To my knowledge, many traps at UCSD, my advisor's trap at UC Berkeley, and the ASACUSA trap have this surface coating. This was done to reduce patch potentials, but I don't find papers from these groups reporting specific improvements—it seems to be more of a preventative measure. In the past, ALPHA was resistant to colloidal graphite because of fears that it would degrade the vacuum necessary for storing antimatter. In reality, the CERN vacuum scientists assure me that colloidal graphite significantly improves cryopumped vacuum systems, because it creates more surface area for gas to adhere.

Today, ALPHA is considering treating a small fraction of the electrodes in an upcoming trap as a trial. I would recommend that ALPHA adopt colloidal graphite in both ALPHA-g and ALPHA-2 to reduce the persistent patch potentials, but it isn't clear that colloidal graphite will have a beneficial effect on laser-induced patch potentials.

3.12 Artificial patch potential measurements

In ALPHA-2 we took the time to attempt to measure an "artificial patch potential." This topic is well covered in the published paper on patch potential measurements [68]. All of the Penning-Malmberg traps at ALPHA have at least one "rotating wall electrode" [34]. This electrode is actually six electrodes—six azimuthal segments which can which can be independently controlled. Its location in the trap is shown in Fig. 3.16. Typically it is used to apply a torque to a plasma by applying a sinusoidal signal to each segment, with each segment being out of phase from the next one by $\pi/3$. This creates a rotating electrostatic dipole, an electric field near the center of the trap that rotates at the frequency of the sinusoidal signals. Here we simply applied a nominal voltage V_E to five of the six segments and a perturbed voltage $V_S + V_E$ to one of the segments to act as an "artificial patch potential." Then we perform a patch potential measurement to see if we can verify the predicted patch potential strength.

The artificial patch is in a trap location which is far from any radial steps, and the gaps between electrodes at ALPHA are very small $\mathcal{O}(100\,\mu\text{m})$. It can be very well approximated by the electrostatic models presented in the appendix, where we assume that electrodes are surrounded on either side by an infinitely long grounded conducting cylinder. The potential due to the electrode is given by:

$$\Phi_E(r,z) = V_E - V_E \sum_{m=1}^{\infty} \frac{1}{\alpha_m^0 J_1(\alpha_m^0)} \left[\exp\left(-\alpha_m^0 \frac{l/2+z}{R_w}\right) + \exp\left(-\alpha_m^0 \frac{l/2-z}{R_w}\right) \right] J_0\left(\frac{\alpha_m^0 r}{R_w}\right). \tag{3.25}$$

We can evaluate k_2 by expanding to second order in z, then substituting the length of our electrode: $l = 1.322\,\mathrm{cm}$

$$\Phi_E(r,z) \approx V_E - V_E \sum_{m=1}^{\infty} \frac{1}{\alpha_m^0 J_1(\alpha_m^0)} \exp\left(-\alpha_m^0 \frac{l/2}{R_w}\right) \left[2 + \left(\frac{\alpha_m^0 z}{R_w}\right)^2\right] J_0\left(\frac{\alpha_m^0 r}{R_w}\right). \tag{3.26}$$

$$k_2 = \frac{V_E}{R_w^2} \sum_{m=1}^{\infty} \frac{\alpha_m^0}{J_1(\alpha_m^0)} \exp\left(-\alpha_m^0 \frac{l/2}{R_w}\right) \approx 0.6794 \frac{V_E}{R_w^2}. \tag{3.27}$$

And the potential due to the patch is given by:

$$\Phi_S(r,\theta,z) = V_S \sum_{n=0}^{\infty} d_n \cos(n\theta) \left[\left(\frac{r}{R_w}\right)^n - \sum_{m=1}^{\infty} \frac{\exp\left(-\alpha_m^n \frac{l/2+z}{R_w}\right) + \exp\left(-\alpha_m^n \frac{l/2-z}{R_w}\right)}{\alpha_m^n J_{n+1}(\alpha_m^n)} J_n\left(\alpha_m^n \frac{r}{R_w}\right)\right], \tag{3.28}$$

where $d_0 = \theta_0/2\pi$ and $d_{n\neq 0} = (2/n\pi)\sin(n\theta_0/2)$, and $\theta_0 = \pi/3$ is the angular extent of the patch. The transverse electric field at $r = z = 0$ is only due to the $n = 1$ term—it is everything attached to $r\cos\theta$ once we expand $J_1(x) \approx x/2$:

$$\varepsilon = \frac{V_S}{R_w}\frac{1}{\pi}\left[1 - \sum_{m=1}^{\infty} \frac{1}{J_2(\alpha_m^1)} \exp\left(-\alpha_m^1 \frac{l}{2R_w}\right)\right] \approx 0.2112 \frac{V_S}{R_w}. \tag{3.29}$$

Our expected displacement is $\varepsilon/k_2 = CR_wV_S/V_E$, where $C = 0.3109$.

The patch potential measurement in the presence of this artificial patch clearly exhibited greater cloud displacements when V_S was negative than when it was positive. This indicates the presence of nonlinear effects—that $\delta = \varepsilon/k_2$ was no longer accurate enough.

Rather than showing more spiral fits, this effect is shown in Fig. 3.30, where the average displacement of 40 clouds is reported while varying V_S and V_E. In this experiment, we also tried applying V_S to a diametrically opposed segment to observe the effect of natural patch potentials. Assuming the "patch field" ε from the artificial patch is generally much stronger than the natural patch field, only the component of the natural patch field pointing toward or away from the two segments used would matter. The natural patch field would boost ε in one direction and reduce it in the other.

In Fig. 3.30, we clearly see that nonlinear effects and a natural patch field together do not satisfactorily explain the discrepancy between expected and measured displacements. When we average the results of the measurements with diametrically opposed segments, we find that the nonlinear prediction is about 23% above the measurements. The data is very consistent with V_S being less than what we believe was applied by 23% or the magnetic field expansion ratio being lower by 23%. The latter hypothesis was somewhat exhaustively studied, and it is probably incorrect. The reduced V_S hypothesis is also very unlikely—I did not personally conduct these measurements, but V_S was predicted carefully by analyzing the circuit used then it was precisely confirmed with measurements performed outside of the trap.

The measurements could also be consistent with an offset of k_2 (equivalently, a constant shift of V_E). This idea led to my current favorite hypothesis—that the natural patch potentials in this trap location are strongly nonlinear. This is reminiscent of the patch field

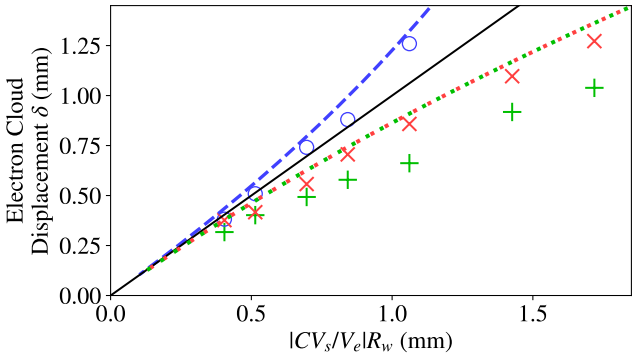

Figure 3.30: Average cloud displacements for 40 clouds subjected to the patch potential measurement procedure in the presence of an artificial patch potential. The horizontal axis is the linear prediction for the displacement of the clouds. The black line also represents the linear prediction ($y = x$, but the horizontal scale is stretched). For the blue circles, $V_S = -476\,\mathrm{mV}$ was applied to one segment of a segmented electrode. For the green +, $V_S = +476\,\mathrm{mV}$ was applied to the same segment. For the red X's, $V_S = +476\,\mathrm{mV}$ was applied to the diametrically opposed segment, in theory flipping the sign of the effect of natural patch potentials. The blue dashed line is the nonlinear theoretical prediction $\delta = f(V_S/V_E)$ for $V_S/V_E < 0$. The dotted green and red line is the nonlinear prediction for $V_S/V_E > 0$, which should have fallen between the green + and the red X. For all values of V_S, V_E was varied in 12 somewhat arbitrary steps between 0.2 V and 2 V, but points are only plotted if the average displacement is much greater than the spread in cloud positions and none of the clouds miss the MCP. This figure is published in Ref. [68].

measurements after electron stimulated desorption in ALPHA-g. We found that when we purposefully directed charged particles to the trap wall, ε was reduced, but patch fields produced a strong on-axis potential that could shift k_2. Charged particles are likely often lost near this rotating wall electrode. Sometimes when trying to compress a plasma, the wrong rotation direction is chosen and the plasma expands significantly. Probably in these events some charge even collides with the electrode. Also, when we compress a plasma, we often observe "halos" of charged particles that were "left behind" by the compression. We have seen some evidence in the catching trap that halos can be very large—too far from the trap center to ever be imaged on an MCP. Perhaps we regularly allow some electrons or positrons to hit the trap wall when we compress the bulk of the plasma. When we look at the patch potential measurement for $V_s = 0$, we do indeed see that ε is unusually small and that the displacements may not be following the linear estimate. However, I don't show this data here because it is quite poor quality—the k_2 values used were not well-chosen and most of the clouds have not been significantly displaced from the trap center.

In the supplementary material of Ref. [68], a number of other sources of error are analyzed, but these errors together did not explain the discrepancy. The most interesting sources of error are discussed elsewhere in this thesis. For example the largest error, finite length effects, are clearly observed and studied in more detail in Sec. 5.4.5. However, this error had the wrong sign for explaining the discrepancy.

3.13 Nonlinear cloud displacement

In the previous section, the function $f(V_S/V_E)$ was calculated numerically. However it's worth noting that the displacement can be nonlinear in the presence of natural patch fields. This is observed in Sec. 3.8. Here I will calculate the next to leading order term in δ coming from higher order Laplace-equation-solving terms in the potential. We expect this analysis to result in an equation in the form:

$$\delta = \frac{\varepsilon}{k_2}\left(1 + C\frac{\varepsilon}{k_2 R_w}\right), \tag{3.30}$$

Where C is a constant dependent on coefficients from the trapping potential. This form is useful because it clearly shows that displacements are linear unless δ is comparable to R_w. The next to leading order effect comes from considering terms of higher order in both the trapping field and the patch field:

$$\Phi_E = -k_2\left(z^2 - \frac{1}{2}r^2\right) + k_3\left(z^3 - \frac{3}{2}zr^2\right). \tag{3.31}$$

$$\Phi_P = \varepsilon\left[r\cos\theta + c_z z + \frac{\kappa_2}{R_w}\left(z^2 - \frac{1}{2}r^2\right) + \frac{\kappa_\theta}{R_w}r^2\cos[2(\theta-\theta_0)]\right]. \tag{3.32}$$

I admit that my choice of parameterization is somewhat odd here. At this point I have discussed k_2 and ε so much that they should stay and they should remain unitful. It should be noted though that k_2 is of order V_E/R_w^2, where V_E is the voltage applied to the electrode to confine the plasma. ε is of order V_P/R_w, where V_P is the order of magnitude of potential variations across the surface of the electrode. Because we only image plasmas when the displacement δ is much smaller than R_w, the measurements are always performed with $V_P/V_E \ll 1$. In order to arrive at the expected result shown in Eq. 3.30, I need unitless constants for the rest of the terms in the Laplace expansion for the patch field. Thus all the terms in Φ_P obtain their voltage units from ε, and if they need additional length units, I use R_w, the natural length scale for variations in the potential caused by patches located on the trap wall. Also note that I have chosen coordinates where $\theta = 0$ is the direction the patch field at $r = z = 0$ is pointed, and $z = 0$ is the position of the "center of the trap" imposed by the electrodes.

We begin by noting that the new equilibrium position in z is $\varepsilon c_z/2k_2$ (to sufficient order in ε/k_2R_w). The only effect of the k_3 term then is to shift k_2 by $-3k_3(\varepsilon c_z/2k_2)$, which is of order V_P/R_w^2. Usually when I move clouds off axis, I use symmetric trapping potentials where k_3 is zero. A notable exception is the patch direction measurements, explained in Sec. 6, where k_3 is exceptionally large. From here it is most convenient to find the zero in the electric field in Cartesian coordinates:

$$\begin{bmatrix}\mathbf{E}_x\\ \mathbf{E}_y\end{bmatrix} = \begin{bmatrix}-\varepsilon\\ 0\end{bmatrix} + \begin{bmatrix}k_2 + \frac{\varepsilon\kappa_2}{R_w} - \frac{2\varepsilon\kappa_\theta}{R_w}\cos(2\theta_0) - \frac{3k_3\varepsilon c_z}{2k_2} & -\frac{2\varepsilon\kappa_\theta}{R_w}\sin(2\theta_0)\\ -\frac{2\varepsilon\kappa_\theta}{R_w}\sin(2\theta_0) & k_2 + \frac{\varepsilon\kappa_2}{R_w} + \frac{2\varepsilon\kappa_\theta}{R_w}\cos(2\theta_0) - \frac{3k_3\varepsilon c_z}{2k_2}\end{bmatrix} \tag{3.33}$$

Of course to find the zero in the transverse electric field we multiply the vector by the inverse

of the matrix, giving:

$$\begin{bmatrix} x \\ y \end{bmatrix} = \frac{\varepsilon}{\left(k_2 + \frac{\varepsilon\kappa_2}{R_w} - \frac{3k_3\varepsilon c_z}{2k_2}\right)^2 - \left(\frac{2\varepsilon\kappa_\theta}{R_w}\right)^2} \begin{bmatrix} k_2 + \frac{\varepsilon\kappa_2}{R_w} + \frac{2\varepsilon\kappa_\theta}{R_w}\cos(2\theta_0) - \frac{3k_3\varepsilon c_z}{2k_2} \\ \frac{2\varepsilon\kappa_\theta}{R_w}\sin(2\theta_0) \end{bmatrix} \tag{3.34}$$

The first nonlinear effect we see is an angle which depends on a cloud's distance from the trap center. To leading order that angle is:

$$\theta \approx 2\kappa_\theta \frac{\varepsilon}{k_2 R_w}. \tag{3.35}$$

This angle increases linearly with δ to linear order. However, it cannot be used to explain the linear term in the magnetron angle in Sec. 5.4.3, because that linear term increased linearly with time, indicating that it is a frequency shift, not an initial offset. In principle, this should have been visible in the ALPHA-g patch potential measurements. However, in those fits, the starting position of the spiral is a free parameter. It is likely that in those fits the starting position was coerced to remove the linear term in the spiral shape.

Next, we calculate the distance from the trap center:

$$\delta = \frac{\varepsilon\sqrt{\left(k_2 + \frac{\varepsilon\kappa_2}{R_w} + \frac{2\varepsilon\kappa_\theta}{R_w}\cos(2\theta_0) - \frac{3k_3\varepsilon c_z}{2k_2}\right)^2 + \left(\frac{2\varepsilon\kappa_\theta}{R_w}\sin(2\theta_0)\right)^2}}{\left(k_2 + \frac{\varepsilon\kappa_2}{R_w} - \frac{3k_3\varepsilon c_z}{2k_2}\right)^2 - \left(\frac{2\varepsilon\kappa_\theta}{R_w}\right)^2} \tag{3.36}$$

For the artificial patch measurements, $\theta_0 = 0$, $\kappa_2 = 0.536$, $k_3 = 0$ and $\kappa_\theta = 0.976$. Setting θ_0 to zero gives a dramatic simplification:

$$\delta = \frac{\varepsilon}{k_2 + \frac{\varepsilon\kappa_2}{R_w} - \frac{2\varepsilon\kappa_\theta}{R_w}}. \tag{3.37}$$

Of course, this formula is only valid to first order, but I leave it in this form for now to illustrate an important point—higher order terms in the trapping and patch field can introduce a pole in $\delta(k_2)$ at nonzero k_2. Therefore leading order estimates of δ do not have a radius of convergence of R_w. Rather they typically have a radius of convergence smaller than R_w, limiting the accuracy of leading order expressions. For the artificial patch, the pole in $f(V_S/V_E)$ occurs at $V_S/V_E = -0.54$, where the leading order estimate only predicts that clouds should be displaced from the trap center by about $0.16R_w$, just beyond the imageable region. This is why the linear prediction fails so spectacularly for the artificial patch. When we look at randomly generated arrays of patches in Sec. 3.9, however, we see that this is a particularly nonlinear patch field. Finally, to leading order δ is:

$$\delta = \frac{\varepsilon}{k_2}\left[1 + \left(-\kappa_2 + \frac{3c_z}{2}\frac{k_3 R_w}{k_2} + 2\kappa_\theta\cos(2\theta_0)\right)\frac{\varepsilon}{k_2 R_w}\right] \tag{3.38}$$

.

Another nonlinear effect that one should be aware of is that cloud orbits become elliptical, rather than circular. To see why, consider a coordinate system where $x = y = 0$ is the

magnetron orbit center, and potential has been redefined so $V = 0$ occurs at $x = y = 0$. The potential near that point can be approximated by:

$$V(x, y) = \frac{1}{2}k_{xx}x^2 + k_{xy}xy + \frac{1}{2}k_{yy}y^2. \tag{3.39}$$

Further, we can eliminate the xy term by rotating the coordinate system. The κ_θ term from the expansion around the trap center causes k_{xx} to differ from k_{yy} in this expansion around the "effective trap center." Since magnetron orbits are along equipotentials, they are ellipses which are longer in x than in y by a factor $\sqrt{k_{yy}/k_{xx}}$. For patch field measurements in ALPHA-2, the most significant effect that this has is to increase the spread in clouds' distances from the trap center. Thus, we care most if this ellipse is stretched in the direction of the displacement from the true trap center. It should be noted, however, that when we move clouds off-axis we are adiabatically conserving the area of the magnetron orbits. This means the length of the orbit in the x direction is elongated by a factor $(k_{yy}/k_{xx})^{1/4}$ and the length in the y direction is elongated by $(k_{yy}/k_{xx})^{-1/4}$. Although this effect is in some sense "the same order of magnitude" as nonlinear displacement, it has no effect on the average cloud displacement shown in Fig. 3.30. The 1/4 power also helps make this effect too small to clearly observe in the data.

4 Positron expansion heating

In early 2022, we had just successfully fixed the catastrophic patch potential issue which ruined the 2021 experimental run, and we were hoping this would allow us to trap antihydrogen atoms. We prepared a positron plasma with SDREVC containing about 6 million electrons, but the plasma's temperature was about 50 K, about 2.5 times positron temperatures in ALPHA-2. Concerned that this would either prevent antihydrogen trapping or significantly reduce the trapping rate, I went to Dr. Eric Hunter, my advisor's previous student, for advice. He said he was aware of three mechanisms for plasma heating (most of these ideas are discussed in Ref. [94]):

1. The plasma can be heated by radiation from the surrounding environment. Although the trap walls are nominally 4 K, it has openings on both ends toward parts of the experiment at $\sim$ 70–300 K. Note that the plasma only interacts strongly with radiation near the cyclotron frequency, a frequency where our trap walls are highly reflective. Thus it is not entirely obvious what temperature a plasma would reach in equilibrium in the absence of other heating sources. However, this was not likely our issue. Our trap has much smaller openings than the trap discussed in Ref. [94], and the openings are similar in size and much farther from the plasma than in ALPHA-2.

2. The plasma expands. The plasma has several eV per positron of electrostatic potential energy. If it were to expand radially by just one percent, order one percent of that potential energy would turn into heat. This would increase the plasma temperature by a few hundred Kelvin. O'Neil's confinement theorem forbids plasma expansion if the trap is perfectly cylindrically symmetric, so plasma expansion relies on some trap error which breaks the cylindrical symmetry. In some cases, the equilibrium plasma temperature is more relevant than the heating rate. Cyclotron cooling causes the plasma to lose energy at a rate proportional to temperature. The equilibrium temperature occurs when sources of plasma heating are balanced by sources of plasma cooling. Thus, if we consider the only cooling source to be cyclotron cooling, the equilibrium temperature is proportional to the heating power per particle.

3. Electrode noise can heat the plasma by heating the axial motion of particles. Lower frequencies of noise which interact strongly with diocotron modes or Trivelpiece-Gould modes [95] can also cause expansion, which again heats the plasma. This mechanism seemed unlikely because we tried to reduce electrode noise by using amplifiers with lower bandwidths and RC filters, and this had no measurable effect on plasma temperatures.

The most likely explanation seemed to be that our positron plasmas were expanding, and the expansion was caused by either patch potentials or the misalignment between the trap electrodes and the external magnet. The train of thought here is a bit complicated, so I will review the basic steps in the argument:

1. Patch potentials or misalignment break the azimuthal symmetry of the trap, allowing the positron plasma to expand.

2. Expansion turns electrostatic potential energy into heat, increasing the temperature of the positron plasma.

3. When an antihydrogen atom is formed, the resulting atom's momentum mainly comes from the antiproton's momentum, but the antiprotons are likely thermalizing with the positrons, which are more numerous by about a factor of 20, before they form an antihydrogen atom.

4. The trap depth for antihydrogen atoms in both ALPHA-2 and ALPHA-g is about $0.5\,\mathrm{K}k_B$. Positron temperatures are 20–50 K. Thus only a small fraction of antiprotons are converted into trappable antihydrogen, and that fraction becomes smaller if the positron temperatures are higher.

As you will see in the following paragraph, nonneutral plasma expansion has been extensively studied for about 50 years. However, as far as I can tell, none of this work is directly usable to explain the patch potential induced expansion of positron plasmas at ALPHA.

It was originally thought that the expansion of a nonneutral plasma would be due to collisions with background gas. However, Malmberg and Driscoll observed that their electron plasmas were expanding much faster than they should have due to background gas [96]. These authors later posited that this expansion was due to "small azimuthal asymmetries in the applied magnetic or electric fields," and they found that the expansion rate scaled like $(L/B)^2$, where L is the length of the plasma and B is the magnetic field magnitude [40]. This phenomenon persisted in a newly built apparatus, but was reduced by a factor of 20 [91], again suggesting that construction errors were the cause. Subsequent experiments intentionally applied asymmetry and confirmed that this could cause a plasma column to expand [43, 44]. This phenomenon was explained theoretically in Refs. [41], [37]; both papers confirm that asymmetries can cause plasma expansion. The UCSD group's theory [37] depends on particles confined to a smaller region within the plasma by the asymmetry. This theory was confirmed in Ref. [38], which also provides a usable equation for the expansion rate. In our positron plasmas, this mechanism is essentially impossible. Our positrons are typically held in a harmonic potential, and the plasma length is short compared to the trap wall radius—the characteristic length scale of any voltage or magnetic field perturbations. Thus it is essentially unimaginable that patch potentials or magnetic field errors would create regions within the plasma where particles could be trapped. Ref. [39] has actually compared the expansion rate of plasmas confined with a harmonic trapping potential to the expansion rate when plasmas are confined with the "square" trapping potentials typically used in the UCSD experiments. They observed that indeed the expansion rate was drastically lower with the harmonic trapping potential, but not zero. This may or may not be related to UCSD's observation that as the plasma length goes to zero, the expansion rate enters a new regime where the expansion rate no longer depends on length, but still scales with an applied asymmetry [45]. Thus it seems like the mechanism causing our positrons to expand is not currently well understood. Note that all of these experiments intend to study the expansion rate or confinement time of a plasma. Here our primary interest is the heating induced by expansion.

As I clearly established throughout Sec. 3, a harmonic trapping potential with the addition of a constant electric field due to patch potentials is equivalent to a normal trapping

potential displaced by a distance ε/k_2. Thus a transverse electric field alone does not violate the premises of the confinement theorem and cannot facilitate plasma expansion. If the transverse electric field varies with distance along the trap, this is then equivalent to the trap being rotated by an angle $(d\vec{\varepsilon}/dz)/k_2$ relative to the external magnetic field, which does allow plasma expansion. It's worth noting here that the trap can also be genuinely rotated relative to the external magnetic field, as measured in Sec. 6. Of course, higher order terms, such as $r^2\cos(2\theta)$, in the potential due to patches can also contribute to expansion. Given that our plasma's length is much greater than its radius, it seems likely that misalignment and effective misalignment are the leading causes of expansion.

In ALPHA-g, we measured the misalignment of the trap with the external magnet to be about 1 mrad. In ALPHA-2, measurements are less reliable, but the misalignment has an upper bound of about 0.5 mrad. In both traps, without laser exposure, patch potential strengths are of order 5 mV/cm, and the patch field direction and magnitude vary over a characteristic length scale set by the trap wall radius. In the "pre-mix well" (explained in the next section, where we typically measure positron expansion and heating rates) the trap constant k_2 is $2 \times 10^4\,\mathrm{V/m^2}$. Thus the effective misalignment due to patch potentials is of order 1.25 mrad. Since patch fields are random, it is entirely possible for either patch potentials or the true misalignment to dominate in this well. However, positrons also cool in deeper trapping potentials with $k_2 \sim 5 \times 10^5\,\mathrm{V/m^2}$, where it is more likely that the misalignment is dominated by the actual misalignment, which is not suppressed by k_2.

4.1 Evidence of expansion heating

In this section I will discuss evidence that positron expansion heating is the primary limitation to positron temperatures, and by extension antihydrogen trapping rates at ALPHA. To do this, I will use MCP imaging to find the positron expansion rate. With an equilibrium solver, I will find the theoretical heating rate due to that expansion. I will show that in the positron plasmas most often used for forming antihydrogen, the heating rate of positron plasmas is consistent with the theoretical heating rate due to only expansion. In a plasma containing about 2.5 times as many positrons, the heating rate is observed to be greater than the theoretical rate for an unknown reason.

Before I begin showing the experimental results, I need to walk through the electrode voltage sequence used to form antihydrogen and for positron diagnostics. The relevant potentials in this sequence are shown in Fig. 4.1 and they are explained in the list below:

(a) After a positron plasma is formed using SDREVC [3], it is moved to the top of the ALPHA-g trap, where it cools for 40 s in the deepest potential we can create—one electrode with the maximum negative voltage of −150 V surrounded by two electrodes with the maximum positive voltage. This step was originally developed in 2021 when patch potentials were very bad and the positron plasma was expanding rapidly. We found that this was the only way to confine positrons for tens of seconds without them expanding so much that the plasma is simply lost. Today, the idea is that this still might minimize expansion rate, presumably leading to the lowest possible equilibrium temperature. This step also takes place at upper end of the magnetic minimum trap for antihydrogen, where the magnetic field is boosted to 2 T, which should also boost

cyclotron cooling by a factor of 4. Finally, cooling to equilibrium with the shortest possible plasma means the plasma will be colder when we expand it before mixing with antiprotons.

(b) Once the antiprotons are ready for mixing with positrons, the positrons are moved to this "pre-mix potential." The antiprotons are stored to the right of the positrons in Fig. 4.1(b). This potential is tuned so that if the antiprotons and positrons were brought any closer together, they would start to form antihydrogen. In this trapping potential, the positrons are significantly longer than in (a). Thus they benefit from adiabatic expansion cooling. The transition from (a) to (b) is done in tens of milliseconds, very long compared to the perp/parallel mixing time. Thus this adiabatic expansion is three dimensional, and the temperature scales as $l^{-2/3}$.

(c) To mix positrons and antiprotons together, we move the positron trapping potential up and the antiproton potential down. We linearly change from potential (b) to (c) over the course of a second. The minima and maxima of the on-axis potential are arranged so that positrons are ejected out of the experiment to the left while antiprotons (the more scarce species) are retained and can bounce through the positron plasma multiple times. Typically this process is stopped before all the positrons are lost and their temperature is measured as a diagnostic. We have observed correlations where more trapped antihydrogen is formed when positron temperatures are lower for identically prepared positron and antiproton plasmas.

(d/e) These potentials are used to perform the axial temperature measurement described in Ref. [97]. By linearly changing the potential from (d) to (e) over the course of 20 ms, the positron plasma is released. When charge first starts escaping the trap, an exponential increase in the signal versus time is observed, which is reflective of the Maxwell-Boltzmann distribution of positron velocities within the plasma.

(f) This is the "pre-dump" potential. To measure the positron expansion rate in a particular trapping potential, for example the pre-mix potential (b), we will hold the plasma in that potential for a variable time. Then we will morph in a few milliseconds to this pre-dump potential, then send the plasma flying toward the MCP imaging detector by increasing the negative potential to form a ramp pointing in the direction of the MCP. This dump is done as quickly as the electrode amplifiers can change (a few microseconds).

In this section, I will measure the positron expansion rate and the heating rate in the static pre-mix potential (b). The positrons heat in this potential because they have just been cooled by adiabatic expansion to below their equilibrium temperature. At this point I should explain that if the positrons expand axially (along magnetic field lines), they cool, but if they expand radially (transverse to magnetic field lines), they heat. Positrons can move freely along magnetic field lines, and they only exhibit Debye shielding in this direction. Thus if they expand axially they cool just like a monatomic ideal gas. Radially, there is an electric field of magnitude $ren_0/2\epsilon_0$ pointing outward that the positrons usual cannot move along (r is the radial coordinate, e is the positron charge, and n_0 is the density of the plasma). If

some asymmetry allows them to move outward in r, the electric field will do work on them, increasing their kinetic energy.

It should be emphasized that the heating rate in the pre-mix potential does not directly determine the temperature of the positrons when they are forming antihydrogen. Rather, the mixing process [the (b) to (c) transition] involves several processes that heat or cool the plasma, including cooling from positron evaporation from the trap, heating from incoming hotter antiprotons, cyclotron cooling, and expansion heating. Our goal in this study is to understand just the heating sources, and we assume that a higher heating rate in the pre-mix potential will cause the plasma to be hotter during mixing.

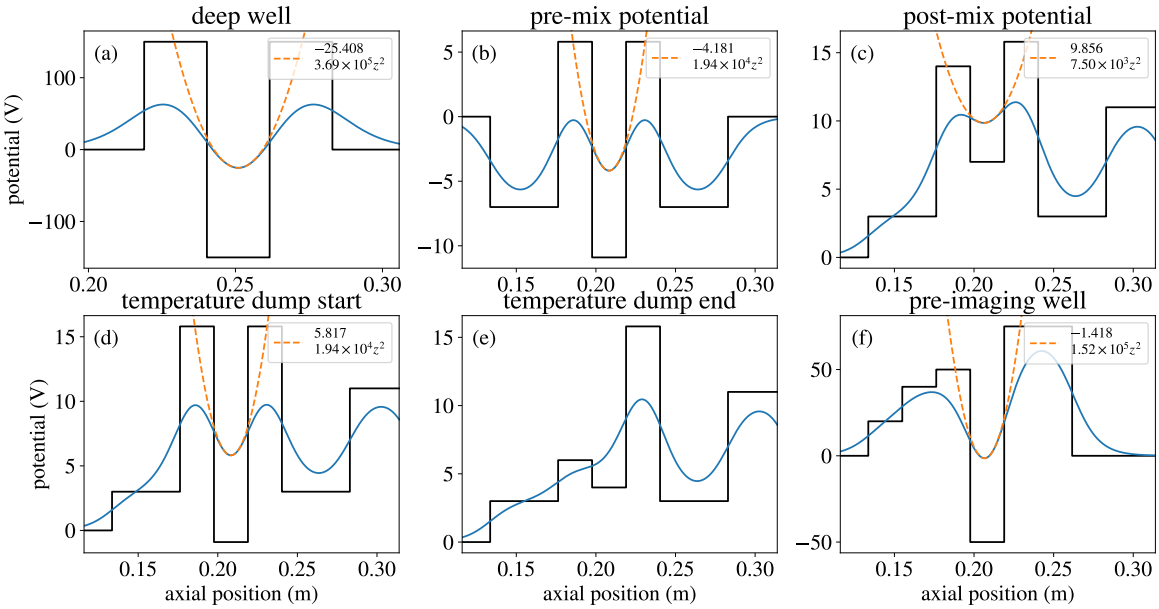

Figure 4.1: The six trapping potentials used to study positron expansion heating are shown. The purpose of each of these six confining potentials for positrons is described in the text. In each subplot, the black line shows the electrode voltages. The blue line shows the on-axis trapping potential created by the electrodes. With the exception of (e) where positrons have been ejected from the trap, an orange dashed line shows the axial potential well that positrons are confined in, and a quadratic fit to that trapping potential is provided in the legend.

So finally I can explain the experimental results. Because the plasma expansion is very slow, and expansion by a very small fraction will lead to a significant temperature increase, we image the plasma after 0, 10, 20, and 40 s in the pre-mix potential, even though temperatures will be measured after much smaller amounts of time. After spending this variable time in the pre-mix potential (b), we go to the pre-dump potential (f) then image the plasma. The resulting image intensity versus distance from the center of the plasma is shown in Fig. 4.2, and a small expansion is clearly observed over the course of the 40 s. I use these profile curves to calculate the root mean square charge radius, which increases from 0.462 mm to 0.516 mm after 40 s of expansion.

Next, we measure positron temperatures after 0 to 3 seconds, but before I discuss the

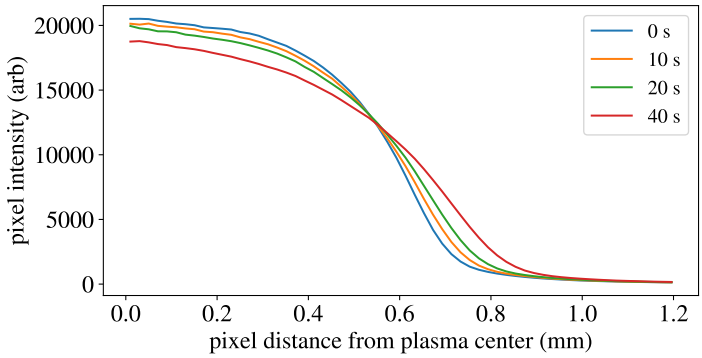

Figure 4.2: Average pixel brightness is recorded versus distance from the center of the plasma in MCP images. The positions of pixels is converted to a transverse distance scale inside the trap using the distance calibration described in an earlier section.

results of this study, I need to explain how I will infer absolute positron temperatures in the pre-mix well from the rate at which positrons escape the plasma when being released using a linear ramp from potential (d) to (e). Usually at ALPHA we denote the "escape energy" as the difference between the voltage at the bottom (V_b) of the trapping potential versus the voltage barrier that positrons would need to cross to escape toward the MCP (V_t). Then, as explained in Sec. 5.3 in more detail, the number of positrons with an axial energy above some threshold $E_0 = e(V_t - V_b)$ is given by their Maxwell-Boltzmann distribution:

$$N_{e^+} \propto \text{erfc}\left(\sqrt{\frac{E_0}{k_B T}}\right) \tag{4.1}$$

If we are observing only a handful of escaping positrons out of a plasma consisting of millions, then we are considering situations where the argument of the complementary error function is large. For large arguments, the complementary error function limits to $\text{erfc}(\sqrt{x}) \sim e^{-x}/\sqrt{x}$. We plot the log of the signal versus time, and assuming the $\sqrt{x}$ part changes very little over the course of our measurement, the log of the signal should linearly increase, and the slope of that linear increase can be identified as $(dE_0/dt)/k_B T$. dE_0/dt is found using electrostatic modelling. This signal is obtained by sending the positrons toward the MCP, and a silicon photomultiplier records the light produced on the phosphor screen versus time [98]. An example of a temperature measurement is shown in Fig. 4.3.

ALPHA has always been aware of a major flaw in this measurement technique as it applies to our positron plasmas. The use of the bottom of the trapping potential is completely arbitrary. In reality, the plasma flattens the on-axis potential, and V_b should be identified as the on-axis potential produced by the plasma, the "space charge potential." The space charge potential will change with time, and there is absolutely no reason to think it will change with time the same way the bottom of the unperturbed trapping potential will. Originally this temperature diagnostic tool was intended for use on plasmas which were very long, and their space charge potential would change very little over the course of a measurement. Thus V_b could be ignored altogether and an accurate temperature could be measured using only dV_t/dt. This does not suffice for our application. To regain accurate

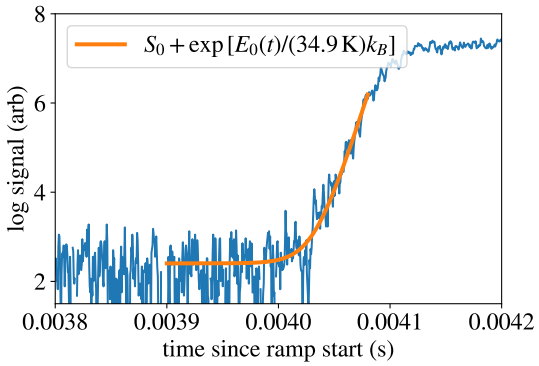

Figure 4.3: An example of the signal and fit function used to measure the temperature of a positron plasma in ALPHA-g. The horizontal axis is the time since the beginning of the linear potential change from (d) to (e). The vertical axis is the log of the signal from the SiPM. The orange line shows the fit function used to determine the temperature, which was measured to be 34.9 K in this dataset. The extent of the orange line shows the region of the data used for the fit.

temperature measurements, I used a plasma equilibrium solver to find how the space charge potential changes over the course of a temperature measurement.

As a first step, I used a plasma solver to find the charge of our positron plasmas using the moment where charge first started to escape the trap. I found the electrode voltages in the moment that charge first arrived at the MCP (roughly 0.00402 ms in Fig. 4.3). Those electrode voltages were used as an input to a plasma equilibrium solver, and I varied the total charge of the positron plasma until the solver said that 10 positrons had enough axial energy to escape the trap in that moment. The temperature was casually assumed to be 50 K, and because the the Debye length was short compared to the plasma length and radius, the charge measurement was fairly insensitive to the arbitrary choices of "10 positrons" and 50 K. In Sec. 5.3, this same method will be used to measure cloud charges. There, the charge estimate is very sensitive to these arbitrary choices, and so in that section the details of the calculation will be explained in more detail. Here, the charge estimate is mostly determined by the electrostatics of how many positrons can fit in a given trapping potential. The result was that our positron plasma consisted of 5.8 Me^+.

Next, for each of three plasma temperatures, 100, 70, and 50 K, I varied the trapping potential in small steps around that moment where charge was just barely escaping. For each small variation in the trapping potential, I found how many positrons should have enough energy to escape. The trapping potentials used for the 70 K plasmas are shown in Fig. 4.4 as an example. I find that the absolute number of escaping positrons is extremely sensitive to the computational parameters, including the number of gridpoints, the region of the plasma that I sum over when I count the number of escaping positrons, and the left bound of the computation region. However, leaving these computational parameters fixed and varying the trapping potential, I nonetheless observe the expected exponential increase in the number of positrons with escape energy versus time. This slope of the log of this exponential increase is also consistent with the expected rate given by the theory presented above. This is illustrated in Fig. 4.4. This study took a lot of my own time and a lot more computation time. Therefore

it is not practical to redo this study for every plasma. Rather, I find that the actual positron temperatures are lower than the measured positron temperatures by a factor of about 1.6. Interestingly, this factor depends a bit on the temperature of the plasma. This is not because the rate of change of the space charge potential depends on the temperature. Rather the rate of change of the barrier holding in the plasma depends on the temperature, because higher temperatures have a longer region over which the plasma density falls to zero. They "reach out farther" toward the barrier, influencing its height. This mechanism is probably real, but it may not be accurately predicted here because the equilibrium solver assumes that the positron plasma is perfectly in thermal equilibrium, even where the density becomes very low at the edge of the plasma.

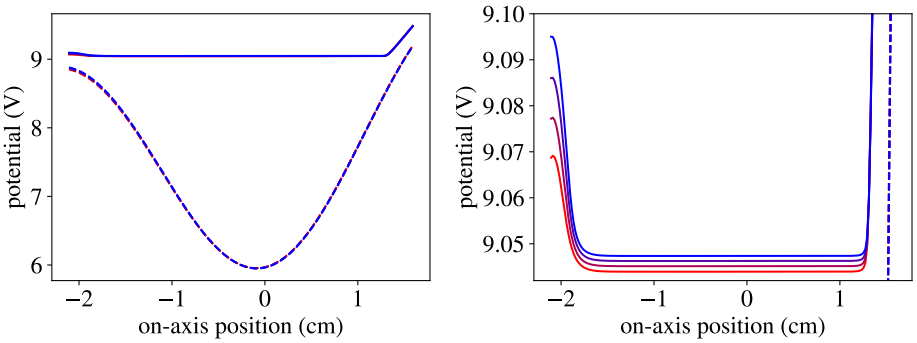

Figure 4.4: The on-axis potential due to the elecrodes is shown with a dashed line, and the on-axis potential including a 5.8 Me^+, 70 K positron plasma is shown with solid lines. The positrons are released by progressing from the red potential to the blue potential. On the right, I zoom in on the barrier holding the positrons (V_t) and the flattened space charge potential (V_b).

Before I can infer changes in the temperature of the positron plasma in the premix potential, I must include the effect of the adiabatic expansion between the premix potential and the moment where the temperature is measured. In the pre-mix potential, the RMS length $\sqrt{\langle (z-z_0)^2 \rangle}$ is 5.78 mm. In the moment before positrons are released, the RMS length is 6.26 mm. In a 3–D monatomic gas, $TV^{2/3}$ is constant, so the temperature scales like length to the $-2/3$ power. This predicts only a 5% correction. Part of the reason this factor is so small is that the pre-mix potential is actually tuned to barely contain the plasma—the whole point is to have mixing begin just after leaving the pre-mix potential.

Fig. 4.6 shows measured expansion rates and positron temperatures including both correction factors. I found that both the expansion rate and the heating rate varied as I varied the current in the octuple magnet. The octupole magnet, necessary for radial confinement of antihydrogen atoms, produces a magnetic field near the trap center of the form $r^3(\hat{r}\cos 4\theta + \hat{\theta}\sin 4\theta)$. Obviously, this is a source of asymmetry that can allow positrons to expand [23, 99], especially if it is slightly offset or imperfectly constructed so it produces a larger transverse field at $r = 0$. Of course I should note here that all this discussion of misalignment or patch potentials causing expansion heating only matters if the effect is significant compared to the expansion induced by the octupole. Thus Fig. 4.6 shows the expansion and heating of positron plasmas at four different octupole current values.

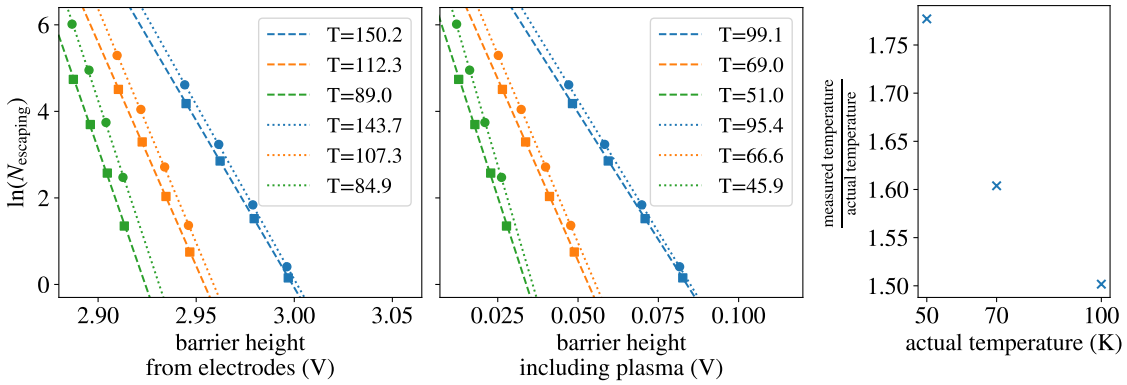

Figure 4.5: The number of positrons with sufficient energy to escape the plasma is plotted against the barrier height. On the left, the barrier height is calculated from the on-axis potential produced by the electrodes. In the middle, it is calculated from the difference between the plasma's space charge potential and the barrier potential to the left. In the legend, the inferred temperatures are listed using dE_0/dt calculated using these two different estimates of E_0. The green lines and dots come from an actual temperature of 100 K. The orange lines come from a temperature of 70 K, and the blue from 50 K. On the right, the correction factor to the nominal temperature diagnostic is listed. That is—the horizontal axis is the actual temperature of the plasma, and the vertical axis is the factor by which ALPHA's nominal temperature analysis would overestimate the temperature. The square dots versus circular dots are the result of varying the computational parameters described in the text. The absolute number of escaping positrons changes by nearly a factor of 2, but the slope of the log does not, and thus the measured temperatures do not significantly depend on the computational parameters.

Finally we have measured the expansion rate and the heating rate of positron plasmas in the pre-mix potential. The final step is to find a predicted heating rate from loss of eletrostatic potential energy. Our positron plasmas are well approximated by spheroids. The electric field throughout most of the plasma is $en_0r/2\epsilon_0$. If the entire plasma expands by a fraction f, a positron originally at a position r will move by a distance fr, and the electric field will do work $fen_0r^2/2\epsilon_0$. Thus the average positron will gain energy $fe^2n_0\langle r^2\rangle/2\epsilon_0$. Since the internal energy of a monoatomic ideal gas is $3k_BT/2$, the change in temperature will be $fe^2n_0\langle r^2\rangle/3k_B\epsilon_0$. Alternatively, we can consider an expansion rate given by $(d\sqrt{\langle r^2\rangle}/dt)/\sqrt{\langle r^2\rangle}$, then we expect a heating rate due to expansion given by:

$$\frac{dT}{dt} = \frac{d\sqrt{\langle r^2\rangle}}{dt}\frac{e^2n_0\sqrt{\langle r^2\rangle}}{3k_B\epsilon_0}. \tag{4.2}$$

I was tempted at first to account for the fact that the plasma expansion might not be perfect uniform expansion by a constant factor. At the very least, the plasma is not strictly 0 K, and therefore it does not have a perfectly constant density and its electric field is not exactly $en_0r/2\epsilon_0$. Thus I used a plasma solver which took as an input the imaged radial charge distribution provided by the MCP images rather than assuming rotational

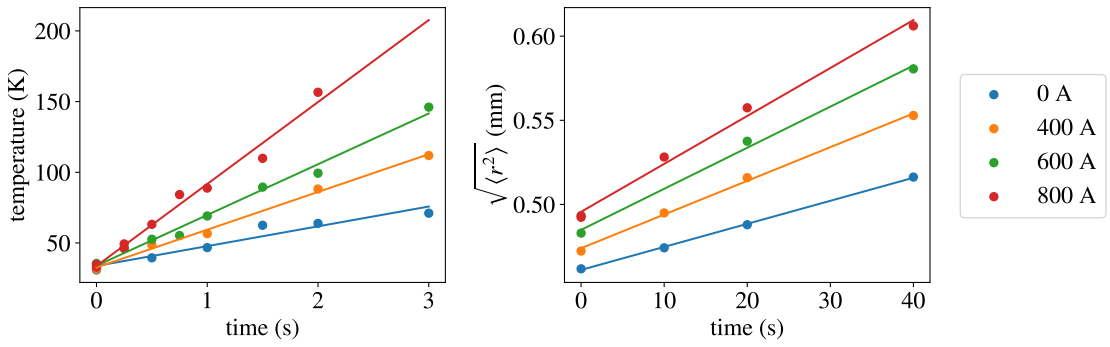

Figure 4.6: On the left, positron plasma temperatures are plotted versus time for a positron plasma consisting of about 5.8 Me^+ initially at about 30 K. On the right, the positron RMS charge radius versus time measured using MCP images is plotted. In both pictures, a linear rate is fit to the data, shown with solid lines. The different colors represent different currents in the octupole magnet. The initial radii are presumably different because the plasmas expand a different amount after cooling for 40 s in the deep potential (a). The similar initial temperatures suggest that the plasma nonetheless comes to the same equilibrium temperature in potential (a) regardless of its expansion.

equilibrium. An interesting caveat on this technique is that the plasma's potential energy is neither $\sum_i eV(x_i)$ nor $\sum_i eV(x_i)/2$. We have to consider the electrostatic potential created by the electrodes V_e separately from the electrostatic potential created by the plasma V_p. A system of point charges has potential energy $\sum_i eV(x_i)/2$, but point charges subjected to an external fixed electrostatic potential have potential energy $\sum_i eV(x_i)$ [100]. Thus the total potential energy that should be used to find the change in thermal kinetic energy is $\sum_i e[V_p(x_i)/2+V_e]$, although the V_p term ends up causing most of the change in temperature. Unfortunately, this took a lot of time but the results were not very good. As shown in Fig. 4.7, the plasma equilibrium solver with a fixed radial charge distribution suggested that the plasma was less dense in the center than it was farther out. This is a clear sign of MCP nonlinearity. The center of the plasma probably had the same density as the outer layers, but more charge per area hit the MCP in the center, and it produces a "saturated" response, not a total brightness that was linear with the charge per area in the plasma. This technique suggested that the positrons should heat by 10% more than expected from the assumptions outlined in the previous paragraph, but this is almost certainly largely due to the MCP nonlinearity issue, and this result should be thrown out. One interesting outcome of this study is that the plasma seems to have a longer radial "tail" than it would in full thermal/rotational equilibrium. This is probably a real observation, and it is reasonable that equilibrium conditions break down at low densities.

In Fig. 4.8, I plot the heating rate versus the expansion rate for this plasma. For the data taken with the octupole magnet off, the measured heating rate is about 50% higher than the theoretical rate from loss of electrostatic potential energy. As the octuple magnet current is increased, the heating rate grows faster than it should, rising to almost triple the theoretical rate. Although there are several sources of error on the level of 10%, this discrepancy is too large. With the octupole at full current, the plasma heating is probably not entirely due to

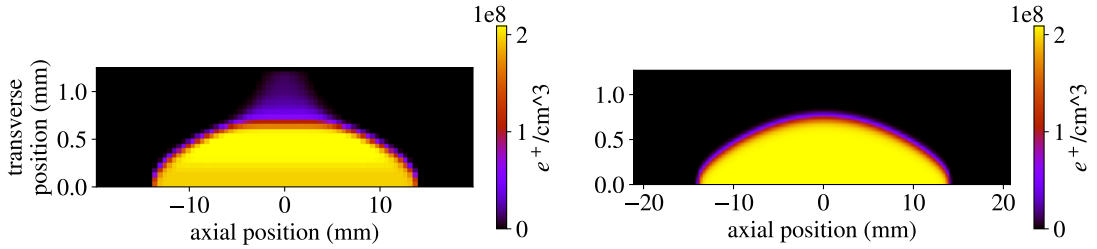

Figure 4.7: The plasma density versus transverse and axial position in the pre-mix potential. On the left, a plasma solver is used which takes its radial charge distribution from an MCP image, as shown in Fig. 4.2. On the right, a plasma solver is used which assumes the plasma is in perfect thermal and rotational equilibrium. The solver finds a rotation frequency which is consistent with a given mean square charge radius.

expansion.

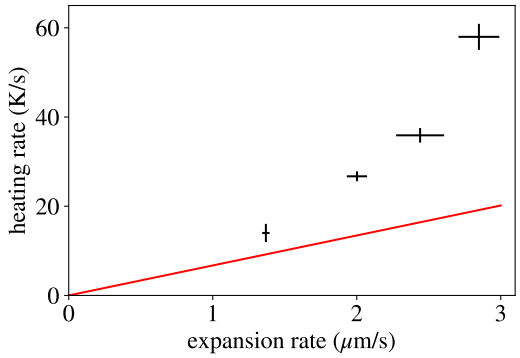

Figure 4.8: The heating rate is plotted versus the expansion rate for the plasma in ALPHA-g consisting of 5.8 million positrons. The two variables are varied by varying the current in the octupole magnet. Each datapoint has horizontal and vertical error bars from the statistical fitting error shown in Fig. 4.6. The red line shows the theoretical heating rate due to expansion for this plasma.

After this study was first conducted, I realized that the ALPHA-g plasma contained about twice as many positrons as the plasmas used in ALPHA-2. Initially, I thought that fixing this issue might lead to positron temperatures identical to those in ALPHA-2. This hope did not come to fruition, but in characterizing this new plasma, we obtain further results in the study of heating rate and expansion. Thus I prepared a positron plasma for mixing in ALPHA-g, trying to match the parameters of ALPHA-2's mixing positrons as closely as possible. All of the above analysis was repeated for this new plasma. The plasma now contains 2.3 million electrons. The temperature diagnostic calibration factor due to space charge potential is 1.5. The adiabatic expansion cooling is again 5%.

The temperatures and radii versus time are shown in Fig. 4.9. The heating rate is plotted against the expansion rate in Fig. 4.10. The results for this ALPHA-2-like plasma are quite different than the results with 5.8 million positrons. First, in ALPHA-g the expansion and heating rates did not change when the octupole was turned on. In ALPHA-2, both the

heating rate and the expansion rate are much lower than in ALPHA-g, and the octupole does affect the expansion rate. This probably explains why positron temperatures are about 2.5 times higher in ALPHA-g, and why the antihydrogen trapping rate was much lower (at least 5 times lower, but hard to estimate exactly). Something is causing the positrons to expand and heat more quickly in ALPHA-g, and the effect is big enough to outweigh the influence of the octupole. Amazingly, with this new plasma, in Fig. 4.10, we see clear evidence that the positron heating is entirely due to expansion. Of course, there have been several sources of error on the order of 10%, so the agreement is not perfect. I conclude that it is likely that improving asymmetry, either due to patch potentials or due to misalignment, is very likely to improve the antihydrogen trapping rate in ALPHA-g.

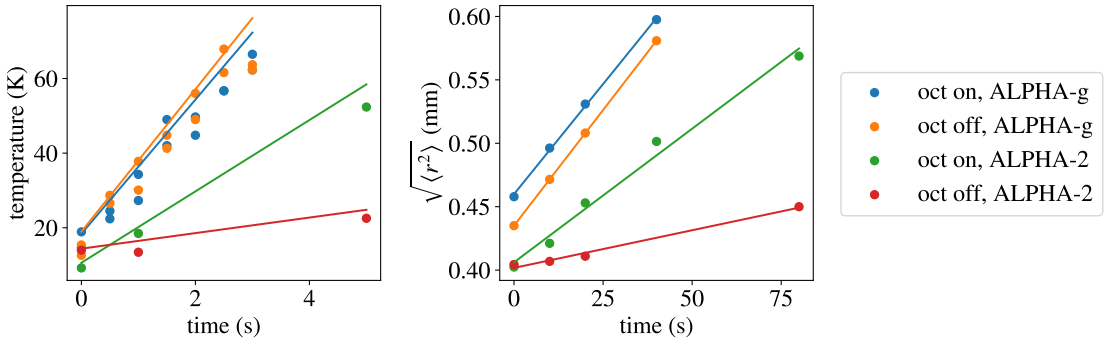

Figure 4.9: This plot is identical to Fig. 4.6, this time with a positron plasma consisting of 2.3 million particles. Rather than varying the octupole current in four steps, the expansion and heating rates are shown with the octupole fully off and fully on in ALPHA-g and in ALPHA-2.

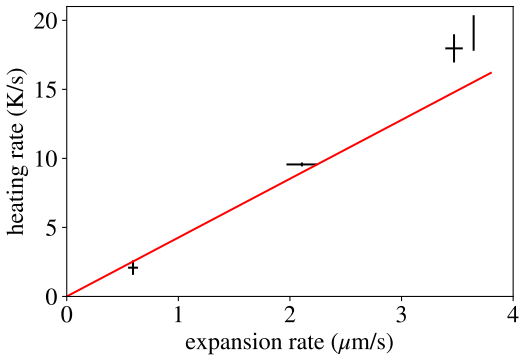

Figure 4.10: This figure is identical to Fig. 4.8 but with the 2.3 million particle plasma in ALPHA-g and ALPHA-2. Again, the red curve shows the theoretical heating rate due to plasma expansion. The two datapoints in the upper right are from ALPHA-g, and the result in the middle is from ALPHA-2 with the octupole on.

4.2 Positron heating in ALPHA-2 from laser-induced patch potentials

In this section I will abandon the study of positron expansion rates and I will focus on positron heating rates alone. I have already shown that the 1S–2S laser in ALPHA-2 increases the electric field due to patch potentials. Now I will show that it also increases positron heating rates. Fig. 4.11 shows positron heating rates in the pre-mix well after the trap was exposed to the 1S–2S laser with 0.6 W of circulating power for a variable amount of time. Heating rates are shown with and without the octupole at full current. The correction factors discussed in the previous section are not applied here—we really only care about relative temperatures in this discussion. There are several interesting observations here. First, equilibrium temperatures after long times (16 s) do not seem to depend on whether or not the octupole is energized. However, positron temperatures at early times strongly depend on the state of the octupole. These early time (0–4 s) heating rates without the octupole do not seem to increase significantly with laser exposure. They do increase with laser exposure when the octupole is energized. This seems to suggest that early-time positron expansion heating results from a kind of "cross-term" between patch potentials and the octupole. It may be that patch potentials are moving the positron plasma off-axis in the somewhat-shallow pre-mix potential, and when the positron plasma is moved off-axis it is exposed to a larger magnetic field perturbation from the octupole.

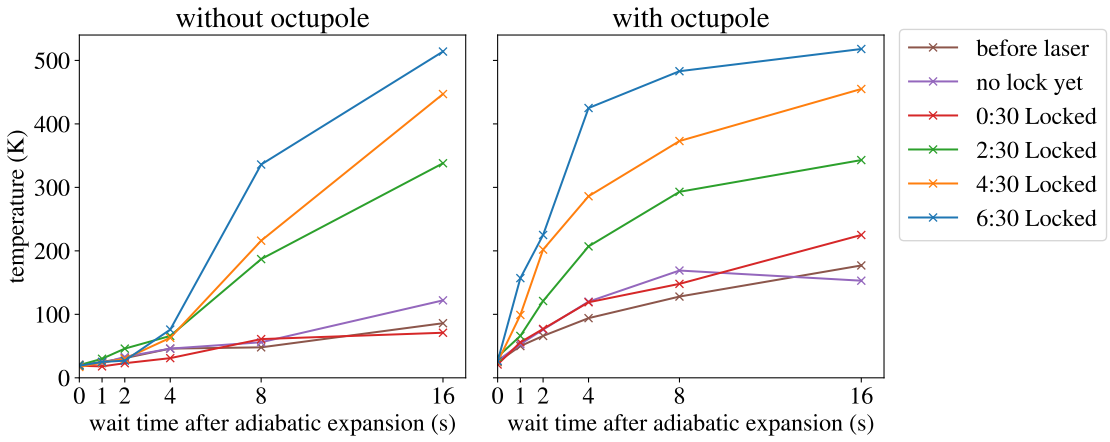

Figure 4.11: Positron temperatures are shown after a variable time in the pre-mix well. On the left, the positron heating rate is shown without the octupole. On the right, the octupole is energized.

Next, Fig. 4.12 shows positron heating rates in different trap locations before laser exposure, but with the octupole energized. To measure this, I attempted to reproduce the pre-mix potential in several different trap locations. We find that before laser exposure, positron temperatures are fairly independent of the plasma's location in the trap. Earlier I remarked that the misalignment due to patch potentials in the pre-mix well was expected to be the same order of magnitude as the true misalignment. However I noted that the random nature of patch potentials meant that either effect could be dominant, or they could be similar orders of magnitude. This seems to suggest that before laser exposure, positron

heating is dominated by a mechanism other than patch potentials. The strength of patch potentials should vary significantly with trap position. Thus heating may be dominated by either expansion due to the octupole alone or a cross term between the octupole and the actual misalignment of the electrodes with the external magnet. One notable exception is that the positron equilibrium temperature is higher in electrode 12. This may suggest either that the initial patch fields in that region are stronger or that I was not able to successfully reproduce the pre-mix potential near electrode 12 (this was done by hand).

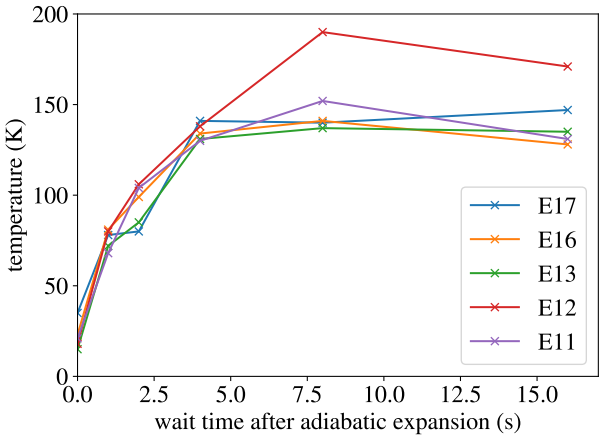

Figure 4.12: Positron temperatures are shown after a variable time in a pre-mix-like well centered on five different trap locations. The names of the five electrodes are listed in the legend.

On the other hand, we expect that patch potentials do eventually have a significant influence on positron heating, because we know that after long periods of laser exposure the antihydrogen trapping rate decreases. Fig. 4.13 shows positron temperatures 16 s after adiabatic expansion to the pre-mix well after 0 hours, about 3 hours, and about 6 hours of laser exposure. Indeed we find that after laser exposure positron temperatures become highly position dependent, reflective of the random nature of patch potentials.

In conclusion, it seems that when patch potentials are enhanced by laser exposure in ALPHA-2, patch potentials are the primary cause of positron heating. Before laser exposure, this may not be the case. In both ALPHA-2 and ALPHA-g, a positron plasma consisting of 2.3 million particles is used to form antihydrogen, and there is evidence that the temperature of this plasma is determined primarily by expansion-induced heating. With a plasma consisting of 5.7 million particles, another heating mechanism seems to be dominant. Altogether, it is likely that improving alignment and reducing patch potentials would reduce positron plasma temperatures. By extension, such efforts would increase the antihydrogen trapping rate. With the evidence presented in this chapter, these conclusions are tentative. I have attempted to outline a collection of techniques that could be used to study positron temperatures in more detail. Perhaps future researchers can generate more data and arrive at more concrete conclusions about how to enhance the antihydrogen trapping rate.

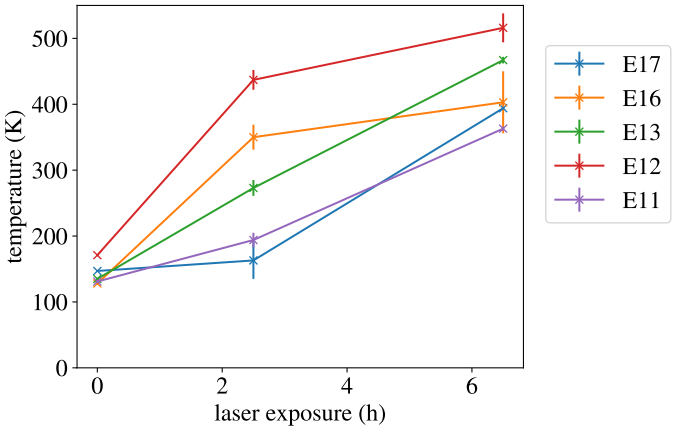

Figure 4.13: Positron temperatures 16 s after adiabatic expansion (roughly the equilibrium temperature of positrons in the pre-mix well) in various trap locations are plotted versus the accumulated laser exposure in the trap. In cases where an error bar is shown, the width of the error bar is the result of performing the same measurement twice.

5 Cloud charge determination

In this section I present three different methods for determining the total charge of clouds extracted from a reservoir. Together these three measurement techniques provide a convincing measurement of total cloud charge at the 20% level. However, each measurement technique by itself has major limitations, necessitating verification from multiple techniques.

The most important effect that cloud total charge has on the cloud-based measurements is a relatively small correction to the magnetron frequency. Even then, another effect at the same order of magnitude, the "finite-length effect," cannot be precisely predicted even with a good measurement of cloud charge. Even in the most precise magnetron frequency based measurement technique, EMPI, it is more useful to remove these two effects with calibration than to predict it and subtract it from measured magnetron frequencies. However, I believe that knowledge of the total charge of these clouds is important for understanding what they are and why they can be used for measurements. I am also open to the possibility that someday someone else will come up with a cloud-based measurement technique that does demand good knowledge of total cloud charge. For example, increasing the precision of ECR measurements of the magnetic field beyond the PPM level will probably demand a proper understanding of how the cloud's charge affects its rotation rate. So for these reasons I include this in my thesis, despite the fact that none of the measurements I preformed with these clouds really requires the results from this section.

5.1 Averaged Faraday cup signals

ALPHA has long used Faraday cups to measure the total charge of electron plasmas. Typically, the total charge of a reproducibly prepared plasma (often created using SDREVC) is measured several times. Then the plasma is imaged several times on the MCP. By assuming that the MCP brightness is linear with total charge, the MCP has then been calibrated and the total charge of other plasmas is inferred. In some of ALPHA's Penning-Malmberg traps, there is a dedicated piece of equipment on the stick for this purpose. In ALPHA-g, we disconnect the MCP from its power supply and we connect the front of the MCP to an NI card which measures voltage versus time.

However, usually these measurements are only possible when the plasma has over a million particles, at least 100 times the charge in most of the clouds. For any MCP voltage where our clouds are visible, a plasma with a million particles will "saturate" the MCP; we reach a maximum total brightness, not a total brightness which is linear with total charge. This means that calibrating the MCP with a large plasma will not work. So our first step is to use the the Faraday cup technique, but we average many signals to reduce electrical noise. Fig. 5.1 shows how the signal is improved with averaging. In addition to averaging, I did a fast Fourier transform (FFT) of the averaged signal, and I removed two obvious noise peaks before plotting the inverse FFT. Frankly, I was a bit surprised at how well this worked. Signal averaging removes uncorrelated electrical noise—were there any correlated noise sources, like noise generated by the reproducible voltages applied to the electrodes, averaging would not help. If I had known how well this would work, I would have averaged more signals, and I would have tried to measure smaller clouds. But I never got the chance to repeat this measurement after seeing the results.

Fig. 5.2 shows the result of this measurement. For each of three scooping voltage step sizes used to extract clouds from a reservoir, 380 signals are averaged. The first 30 signals are ignored; we assume the cloud charges have converged to a constant value after the first 30 extractions. The average cloud charge is inferred by fitting a linear function to the signal before clouds arrive, and an exponential decay plus a linear function after the clouds arrive. About 5 μs of the signal is not used for either fit, as the signal is clearly increasing due to the arrival of charge over this time. The fit functions are then extrapolated to the center of this ignored region, and the difference between the two fit functions is used to infer the total charge. Changing the fit functions, the amount of ignored signal, and the way the signal is extrapolated in the ignored region changes the measured total charge by about 15 ke^-. Of course, the choices described here are simply what looks best to my eye. The capacitance of the front of the MCP is measured with a handheld multimeter, and I found that changing the frequency used for the capacitance measurement changed the result by about 10% (another source of error), indicating that the load is not purely capacitive.

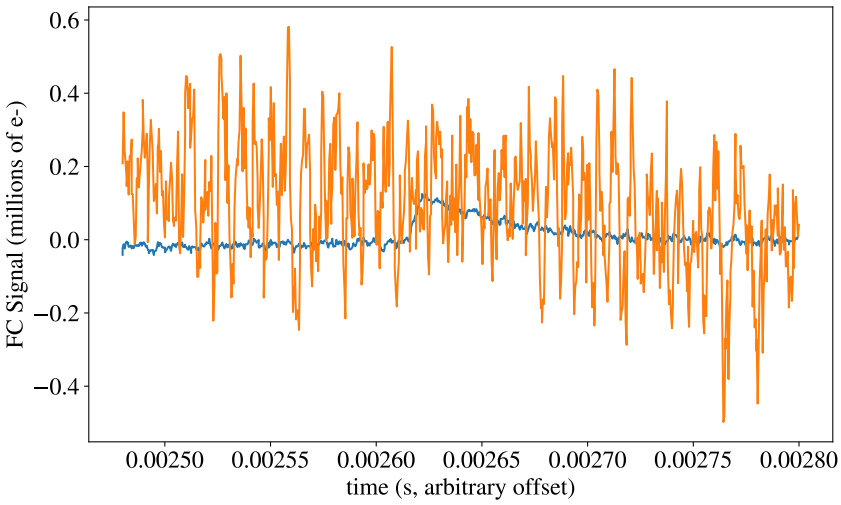

Figure 5.1: The Faraday cup signal is shown versus time. The orange signal is a single trace with a single cloud arriving on the MCP, showing the amount of noise in these signals. The blue curve shows the result of averaging 380 such signals, and the small bump due to charges arriving on the Faraday cup. In the vertical axis, the measured voltage is calibrated with the measured capacitance of the front of the MCP.

5.2 MCP image integrated brightness

Usually at ALPHA, the charge of a plasma is inferred from the total light collected by the camera imaging the phosphor screen. As mentioned before, this technique must be calibrated once using a Faraday cup measurement. Then future plasmas charge can be measured as long as the MCP/phosphor screen/CCD camera imaging detector produces a response which is linear in the total charge arriving at the MCP. In this subsection I attempt to use this

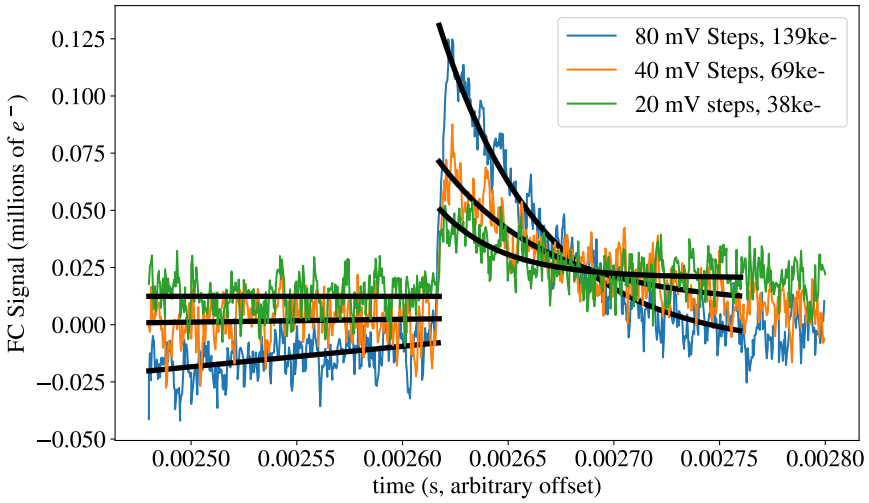

Figure 5.2: The total charge is determined using 380 Faraday cup signals averaged for three different scooping voltage step sizes used to extract clouds from a reservoir. Three different scooping voltage step sizes are used to extract clouds from the reservoir. The overlaid black curves show the fits used to infer the cloud charges.

idea to infer the total charge of some of the smallest clouds used in this thesis. I also present evidence that MCP nonlinearity poses a challenge to inferring the total charge of these small clouds.

Fig. 5.3 shows the integrated brightness of clouds imaged with the maximum voltage applied across the MCP: 1150 V. The total brightness is multiplied by a factor to enforce that the clouds made with 80 mV steps have an average charge of 139 ke^- to agree with the Faraday cup measurement (ignoring the first 30 as we did when averaging Faraday cup signals). Rather than simply adding up the pixel intensities in each image, I usually fit a function to the brightest spot in the image and integrate that fit function. This provides a more robust way of removing the background brightness of the image near where the plasma is located and other artefacts that might be in the image. This MCP voltage is the one I use most often when imaging clouds. Usually my clouds are very small (made with 2.5 or 5 mV steps), and the MCP gain is maximized, making them as bright as possible so that their centers can be reliably identified. One might contend that if this MCP gain is good for seeing clouds with 7000 electrons, it might produce a nonlinear response for clouds with 20 times the charge.

It is generally well known at ALPHA that lowering the MCP voltage restores linearity. This suggests that the actual MCP, not the phosphor screen or the camera, is what causes the nonlinearity. For example, it may be that the MCP has a limit to how many electrons it can produce in a single channel in a given period of time. Therefore, I imaged identically prepared clouds with an MCP potential of 1050 V. In Fig. 5.4, the total brightness of clouds extracted with 5–80 mV is compared between MCP potentials of 1150 V and 1050 V. To more directly compare nonlinearity, each cloud's total brightness is divided by the voltage step size. The reservoir's initial scooping voltage is different for the 1050 V dataset, causing a difference in the initial scoop charge; therefore we should only compare the brightness that

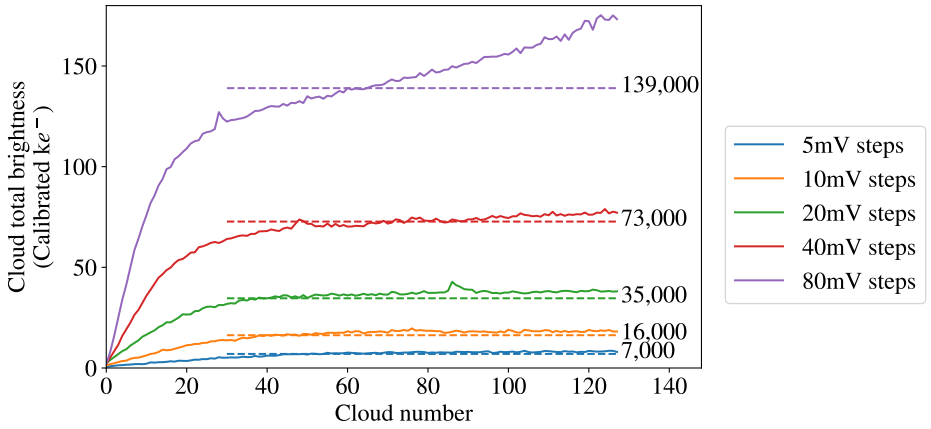

Figure 5.3: The total brightness of clouds successively extracted from a reservoir is recorded with an MCP potential of 1150 V. The total brightness is multiplied by a constant factor so that the total charge of clouds extracted with 80 mV steps agrees with the Faraday cup based measurement of cloud charge. Five different voltage step sizes are used with five identically prepared reservoirs, and we observe that cloud charge/total brightness is roughly proportional to voltage step size. The same initial scooping voltage is used for all reservoirs, so cloud charge rapidly increases in the first 20 clouds as we approach the regime where the reservoir space charge voltage has the same step size as the scooping voltage. The average total brightness of the clouds after the 30th is given on the right.

the clouds settle to after many extractions. Next, we note that for step sizes 10–80 mV, when the MCP potential is 1150 V, the predicted relation $N_c \propto S$ is observed. However, the 5 mV scoops fall short. When the MCP potential is 1050 V, each time we double the voltage step, the resulting brightness is more than doubled. Despite the theoretical prediction $N_c \propto S$, the 1050 V result is more reasonable. It is consistent with the reservoir losing 1 mV of space charge potential between cloud extractions for reasons other than the removal of charge for clouds. For example, the reservoir may be expanding radially with time. In the past, with worse behaving (faster expanding) reservoirs, I have observed that the reservoir does not deliver any charge to the clouds unless the step size is greater than 5 mV. So in reality, it is likely that doubling ΔV is more than doubling cloud charge, but when the MCP potential is 1150 S, MCP nonlinearity restores the proportionality between brightness and ΔV.

Another notable difference between 1050 V and 1150 V is that the difference between the 50th cloud and the 127th cloud with 80 mV steps is much bigger with the higher MCP voltage (the purple line has a bigger slope with 1150 V). For an unknown reason, with 80 mV steps, later clouds have a larger radius (although note that I have made no attempt to predict how cloud radius evolves with reservoir radius). This may imply that the same amount of charge spread out over a larger area will produce a greater total brightness when the MCP is "saturated." This is intuitively expected if the saturation mechanism is a limit on how many electrons a single MCP channel can produce. We can also compare both growth rates to the theory presented in Sec. 2.2 to determine which is more likely to be correct. To accomplish this, I simply used a reservoir of 50 Me^-, and I adjusted the "effective length" of the reservoir to get an average cloud charge of 139 ke^-. I then found the reservoir radial expansion rate

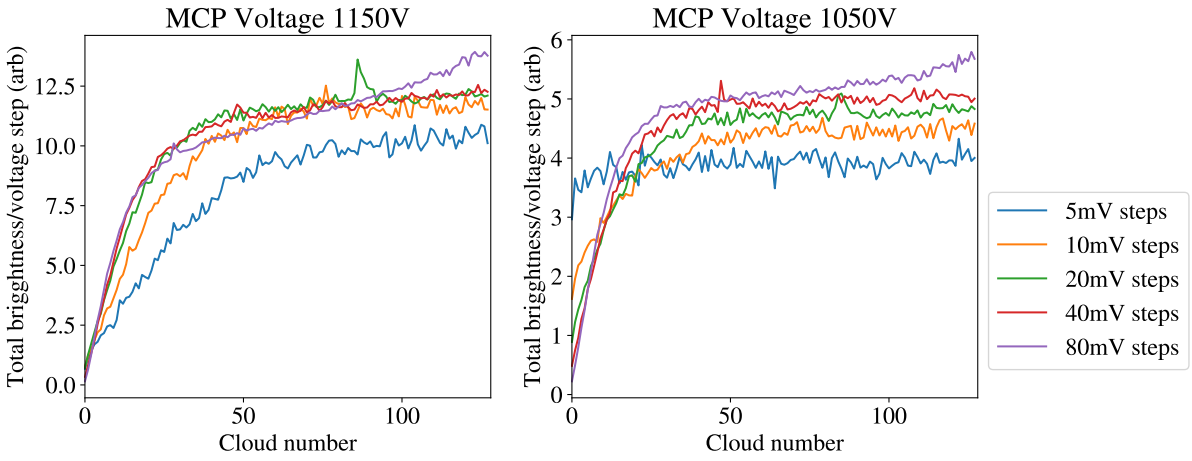

Figure 5.4: The total brightness of successively imaged clouds is recorded for two different MCP potentials. For each of the five different scooping voltage step sizes, we divide the total brightness by the voltage step to make the effect of nonlinearity more apparent.

due to charge removal and I plot how this causes cloud charge increase. With these numbers, 36% of the reservoir charge is extracted, but still a very small increase in cloud charge is predicted, because cloud charge only depends logarithmically on reservoir radius.

In Fig. 5.5, we see that the theory actually predicts a lower growth rate than we see with either MCP potential. This is probably due to lingering nonlinearity even with 1050 V. One might have thought it could also be the aforementioned 1 mV of reservoir space charge potential loss due to expansion. However, when the step size is 80 mV, the potential drop in the reservoir due to charge loss is $(80\,\text{mV})(0.5 + \ln(R_w/r_p))/(1 + \ln(R_w/r_p)) \approx 66\,\text{mV}$, and the potential drop due to the reservoir expanding because of losing charge near the center is the remaining 14 mV (reservoir radius 2 mm and wall radius of 14.8 mm). Thus 1 mV of additional expansion would be a very small correction to the reservoir expansion rate. Conversely, with 5 mV steps, if we ever saw the cloud charge growing, it would probably be mostly because of the reservoir's 1 mV expansion due to factors other than cloud extraction.

At this point, the reader probably doesn't need to be further convinced that we are seeing MCP nonlinearity. However, I will describe one final experiment, because I think it was a nice idea. I extracted two clouds from a reservoir, then combined them into one before imaging. I simply combined them by holding the two clouds in two positively biased electrodes separated by a negatively biased one. Then the separating center electrode's potential was slowly increased to match the other two, allowing the two clouds to meet in the middle. The result should be a cloud with roughly double the charge but a similar radius, and if the total brightness in the resulting image isn't doubled we will know it is because of nonlinearity. In Fig. 5.6, the total brightness (MCP potential 1150 V) of clouds extracted with variable voltage step is compared to half the total brightness of these "doubled clouds." We find that for 80 mV scoops, the doubled clouds have 33% lower total brightness than double the ordinary clouds. This difference becomes 29%, 17%, 13%, and roughly 0% for 40 mV, 20 mV, 10 mV, and 5 mV respectively. One might be tempted to actually use these numbers as a quantitative measurement of the effect of nonlinearity, and apply them as a

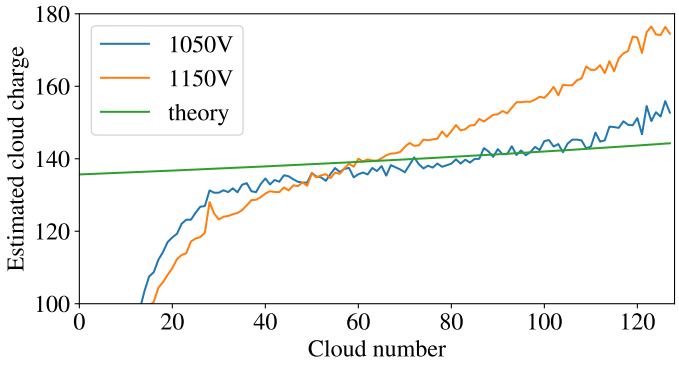

Figure 5.5: The total brightness of clouds successively extracted from identically prepared reservoirs is compared between MCP potentials of 1050 V and 1150 V. The total brightnesses are scaled to agree with the Faraday cup based measurement. The theoretical prediction for the growth rate of cloud charge is also plotted in green, with the reservoir's total charge set to 50 Me^- (found by matching the initial scooping potential with a plasma equilibrium solver) and its radius set to 2 mm (found by imaging the reservoir on the MCP).

multiplicative factor to remove nonlinearity. However, it should be noted that these clouds all have different radii, and we expect from data presented earlier that MCP nonlinearity actually depends on brightness per area, not total brightness. There is also no doubt that the degree of nonlinearity depends on how quickly charge arrives on the MCP. Therefore, any attempt to remove MCP nonlinearity will require a lot more sophistication. Consider also Fig. 5.7, where actual MCP images of normal clouds and "doubled clouds" are shown for an 80 mV step size. We find that the doubled cloud's maximum pixel intensity is not so different from the normal cloud, but that the doubled cloud is wider, a clear sign that the pixel intensity is saturated.

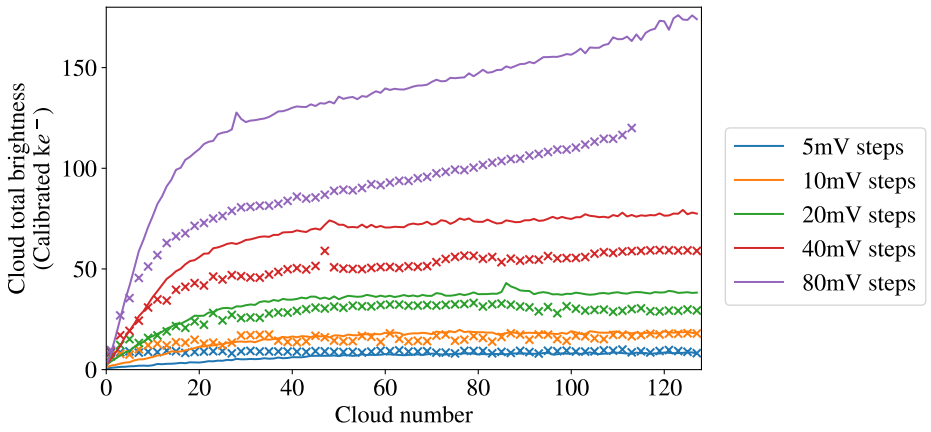

Figure 5.6: The imaged brightness of successively extracted and imaged clouds is plotted for the five different voltage step sizes. Half the imaged brightness of "doubled clouds" is shown with X's (with their abscissa being halfway between the two clouds that were added together). Nonlinearity is evident from the X's not falling along the solid lines.

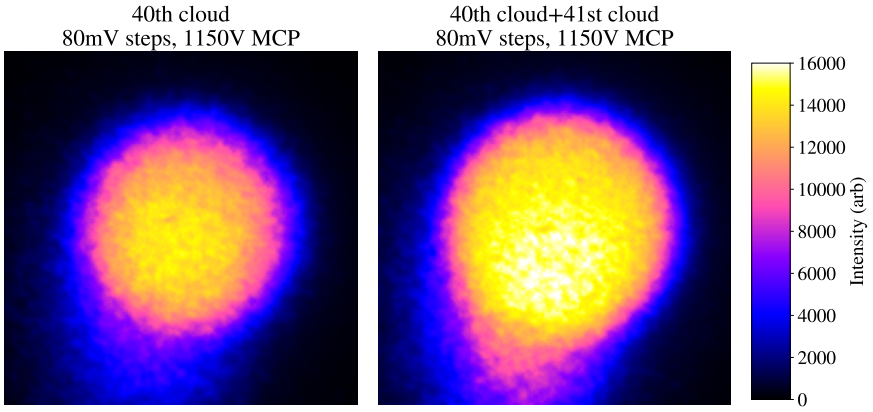

Figure 5.7: Left - the raw picture of the 40th extracted cloud with 80 mV steps. Right - the picure of the "doubled cloud," the result of combining the 40th and 41st extracted clouds. The colorbar on the right applies to both images. Of course, in both images I have zoomed in on a roughly 150 pixel by 150 pixel square centered on the cloud.

It should be noted that this is not a very "kosher" thing to do with plasmas. If one of the two confining electrodes had a slightly more negative potential, the electrons in that cloud would escape into the other with an elevated kinetic energy; thus this operation is expected to result in a drastically hotter cloud. Also, Ref. [101] points out that these kinds of potentials facilitate plasma radial expansion (although I haven't checked the numbers on whether or not this is a relevant effect here). It may be more relevant that the two clouds could be slightly displaced from the trap center. When combined their magnetron motions would be out of phase, and the resulting radius would be roughly the initial radii plus the magnetron motion radius times a random factor accounting for the phase difference. Thus in Fig. 5.8, I plot the RMS charge radius of ordinary clouds and of "doubled" clouds. It may also be interesting to see how scoop radius changes with extractions and with voltage step size, even if I've made no predictions to compare this data to.

5.3 Silicon Multiplier charge arrival timing

Our next method for determining the total charge is by inferring the space charge potential of the cloud by slowly releasing it toward an MCP with maximum gain, and we measure when charge starts to escape from the cloud. Fig. 5.9 shows the on-axis potential created by the electrodes used to perform this operation.

Between the camera and the MCP there is a Silicon photomultiplier (SiPM), a single-photon sensitive light detector. This piece of equipment was first installed at ALPHA to increase the precision of plasma temperature measurements, as described in Ref. [98]. Essentially it allows us to use the MCP as a timing-sensitive detector instead of a position sensitive detector. The procedure here is the same as what we would do to measure a plasma temperature, but instead I am primarily focused on a component of the temperature signal that is often ignored at ALPHA—when the signal first arrives. Some sample signals are shown in Fig. 5.10. In these signals, the output of the SiPM circuit is sent through a short cable to an SRS preamp, which applies a low pass filter [$\mathcal{O}(100\,\mathrm{Hz})$] and a high pass filter [$\mathcal{O}(1\,\mathrm{MHz})$].

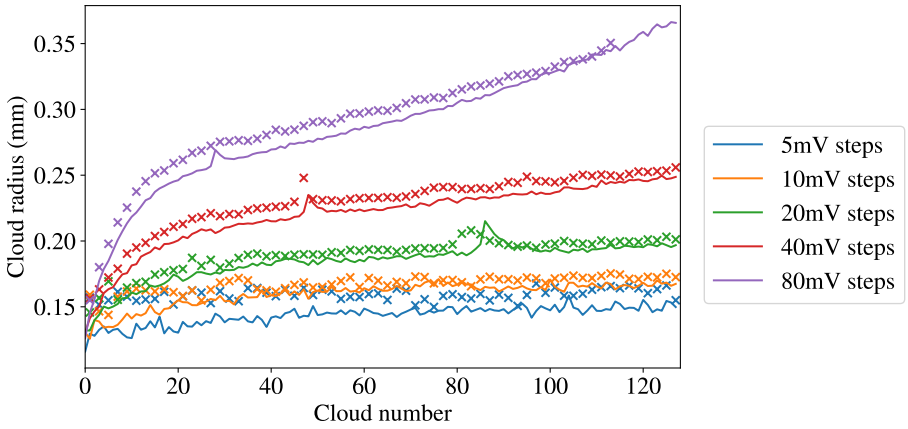

Figure 5.8: The mean square radius of successively extracted clouds is plotted for the five different voltage step sizes. The radius of "doubled clouds" is denoted with X's (with their abscissa being halfway between the two clouds that were added together). Like total brightness, the mean square radius is found by numerically integrating a function fit to the bright spot produced by imaging a cloud. We then multiply by the MCP B-field expansion ratio to infer the radius of the clouds when they were inside the trap (see Sec. 3.5).

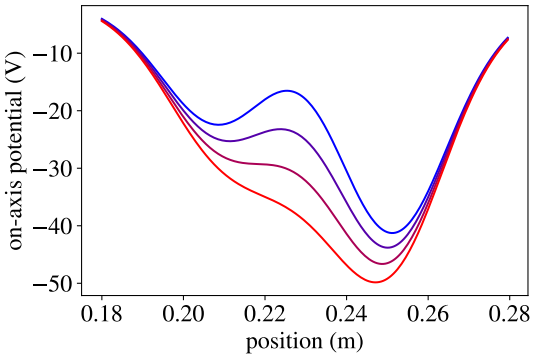

Figure 5.9: The electrode potential manipulation that releases the plasma toward the MCP to determine the temperature and space charge voltage of a cloud. Initially, the cloud is confined in the center of the blue potential, and in about 20 ms, electrode voltages are linearly changed to arrive at the red potential (where there is no longer a confining potential for electrons).

We later realized that the filters just make the signal harder to interpret without removing any noise that could just as well be removed with digital filters after the fact.

These signals clearly show an oscillation. The cause of this oscillation can be determined by noticing that the frequency is exactly equal to the frequency with which the electrode voltages are updated—the voltage instructions say that the electrode voltages should change between an initial value and a final value in 1000 steps in 20 ms. I have two hypotheses for how this ultimately causes a 50 kHz oscillation in the resulting SiPM signal. The first is that that the charge is released in spikes when the voltage step happens, and the low pass filter (or any other component of the circuit with a nonzero response timescale) turns that

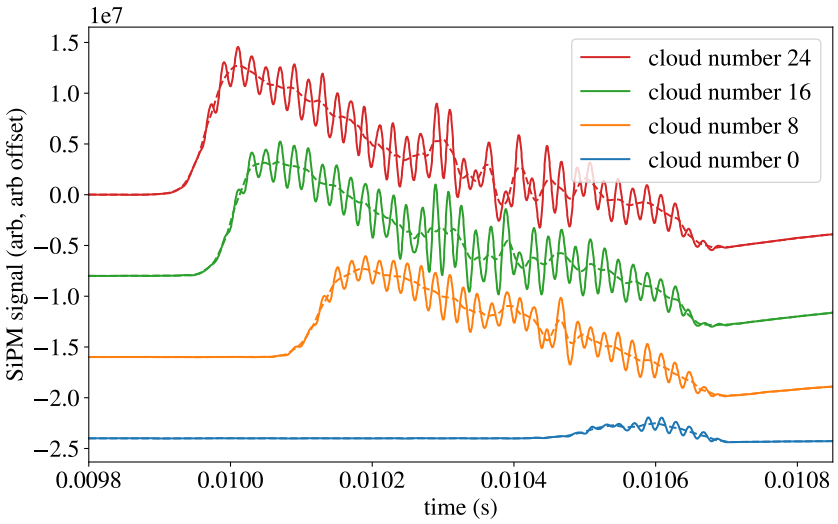

Figure 5.10: SiPM signals are shown for clouds extracted with 80 mV steps. The increase in cloud charge with extraction number can be inferred from the signal beginning earlier for later-extracted clouds. Solid lines show the raw signal; the dashed lines show the result of a rolling average periods of $20\,\mu$s $= 20\,$ms$/1000$.

into a sinusoidal oscillation. The second proposal is that the stepped voltage change is seen by the clouds as a 50 kHz drive. A system driven at 50 kHz will oscillate at 50 kHz even if this isn't necessarily a resonant mode. A simulation could resolve which proposal is correct, and making such a simulation wouldn't be worth anybody's time. In a later experiment, I confirmed that I could remove the oscillation by doing more voltage steps (10^4 instead of 10^3), but a less complete dataset was taken with this improvement, and the oscillation isn't very detrimental to this measurement. To more easily infer the cloud's temperature and space charge potential, I removed the oscillation by applying a rolling-average filter with the averaging time set to the period of the oscillation; the result of this is also shown in Fig. 5.10. Actually, the oscillation was rather helpful—it allowed me to see clearly when the signal ends (around 0.0107 s in Fig. 5.10). Of course, this can be predicted by modelling the on-axis potential produced by the electrodes, but the prediction differs from reality by about 0.1 ms, which is to be expected from small amplifier offsets and patch potentials.

Before estimating charge, I will use these signals to measure cloud temperatures. This technique is first introduced in Ref. [97]. In the beginning of each signal, an exponential increase is observed. This is related to the Boltzmann distribution of axial energies of electrons in the cloud, as discussed in more detail in Sec. 4.1. The "escape energy" for electrons is defined as the difference between the electrostatic potential maximum that the cloud sits in and the electrostatic potential minimum that electrons would need to pass in order to escape the confining potential and be released toward the MCP (times e of course). This potential difference is inferred using electrostatic modelling of the electrode voltages used to perform this operation. To infer temperatures, we naiively assume that the cloud's charge does not significantly perturb the trapping potential, and that the electrons can be modelled as hav-

ing a Maxwell-Boltzmann distribution, and that all electrons are located on the potential maximum. Under these bold assumptions, we find that this signal should be proportional to $\exp(-\text{escape energy}/k_BT)$, but only for the early-time/high exponential suppression part of the signal. The escape energy is decreasing linearly during this exponential increase in the signal, so the parallel energy needed to escape is $E_{\text{escape}} = e(V_0 - Ct)$. Then the temperature of the plasma is found by fitting an exponential (signal $= \exp(t/\tau)$) to the early part of the signal; then $T = \tau eC/k_B$. The temperatures of the clouds discussed throughout this section are shown in Fig. 5.11. The result is not very illuminating. Smaller clouds give less reliable temperature measurements (because the exponential increase lasts for a shorter time). And within the large, seemingly random measurement error, all clouds have roughly the same temperature of 60–85 K regardless of when they are extracted from the reservoir and what voltage step size is used, which is probably just the temperature of the reservoir.

The inaccuracies of the assumptions in the previous paragraph are related to the issue described in Sec. 4.1 with measuring temperatures of positron plasmas, but in that case the positrons formed a plasma, and that plasma had a well-defined "space charge voltage" which could replace the aforementioned electrode-produced electrostatic potential maximum. Most of these clouds are not plasmas, so a similar, but not identical analysis would be needed to infer absolute temperatures, and we would expect a reduction in measured cloud temperatures of order 30–50% as we observed in positrons. It required a lot of computational time and a lot of my own time to calculate this correction accurately for a single positron plasma, and it would need to be done independently for each different cloud size to account for this effect accurately here, so I have chosen not to repeat this analysis for electron clouds, and my temperatures will be wrong by 30–50%.

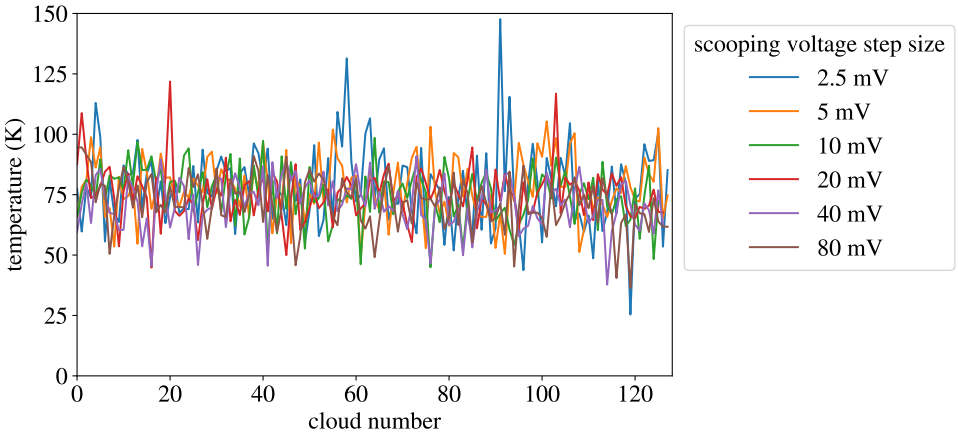

Figure 5.11: The temperatures of clouds extracted from SiPM signals. As usual, six voltage step sizes are used to extract the clouds from the reservoir, and 128 clouds are sequentially extracted from the reservoir then sent to the MCP.

Next, as a first step to inferring the charge of the resulting cloud, the "escape time" is identified as the first moment where the signal clearly exceeds the background. To do this, I found the standard deviation of the early-time signal well before any charges have hit the MCP, and I set a threshold as a somewhat arbitrary multiple of that standard deviation. Then I found the electrode voltages that were present in that moment, and I used those

voltages as the input of a plasma equilibrium solver. The result of this analysis is shown in Fig. 5.12. In that figure, the escape time is converted into a space charge potential—defined as the voltage difference between the barrier charges are escaping over and the voltage maximum where electrons are confined. To rule out systematics relating to the the speed with which the plasma is ejected, this analysis was performed with two different dump speeds. Although the charges first arrived at radically different times and the duration of the signals were radically different, both datasets show roughly equal space charge voltages for identically prepared clouds. It is notable that for the biggest scooping voltage step size, the space charge voltage of the clouds actually drifts down with later extractions. Later, we will see that this is largely, and perhaps entirely because clouds have a bigger radius, so with the same total charge there is a lower space charge potential.

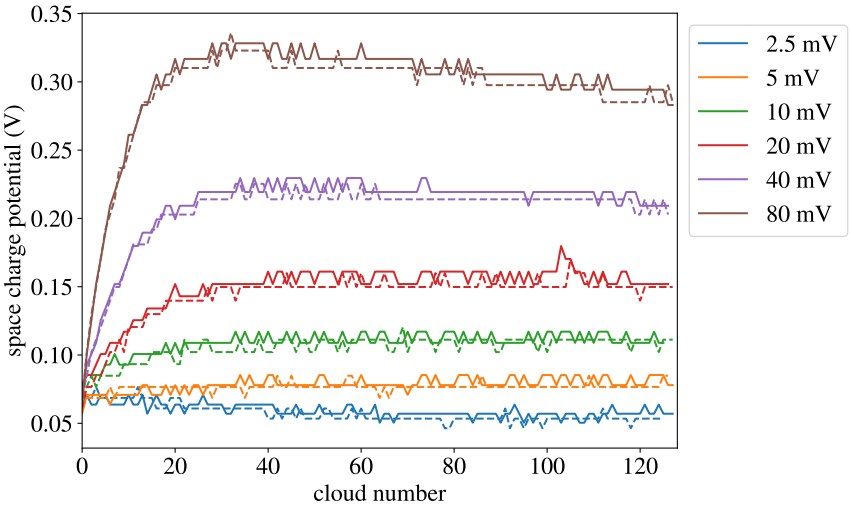

Figure 5.12: The space charge potential is shown for successively extracted electron clouds for the typical six different scooping voltage step sizes. The solid lines show the result of dumping the plasma to the MCP with the potential shown in Fig. 5.9. The dashed lines show the result of dumping the plasma at roughly twice the speed by starting in a confining potential which is roughly twice as deep.

The equilibrium solver used here was purpose-made for the task of estimating these clouds charge. Typically my equilibrium solvers have assumed "rotational equilibrium"—that the cloud's fluid velocity resembles a rigid rotor. However, when a low-density cloud is being released from the trap relatively quickly, the cloud might not remain in rotational equilibrium. It should be noted that the relevant timescale isn't 20 ms, the full timescale of the voltage change. Rather, for most of that 20 ms, the cloud is still in a roughly harmonic trapping potential (with a changing harmonic constant). Thus if it remains a cold plasma, it remains as a spheroid; if it is a hot cloud the whole time, it remains a Gaussian distribution (see Sec. 5.4.1). No movement of electrons across magnetic field lines is needed to maintain rotational equilibrium—the charge distribution simply elongates, barring a very minimal change due to the Debye length to cloud size ratio changing. It is only moments before charge is lost and while charge is being lost that the cloud significantly deviates from being a rigid rotor—a few tenths of a millisecond. So instead of assuming rotational equilibrium, I assumed that

the cloud's radial charge distribution remains fixed, and I extracted that charge distribution from pictures taken in separate experiments where the clouds are imaged normally on the MCP. I never really checked this guess—that a tenth of a millisecond was much faster than the rotational equilibration time. But the plasma solver was faster computationally, it was worth developing for other projects, and it gave predictions that differed by only about 10% for the total charge. So allow me this one unsubstantiated guess.

For each cloud, a plasma solver is given an image-extracted r distribution of charge, the time that charge first arrived at the MCP, and a temperature (a uniform guess of 70 K is used for all clouds). Then we vary the total charge, trying to find a value which suggests that 10 electrons have enough energy to escape the cloud at the identified moment where SiPM signals are above background. This number, 10, is obviously somewhat arbitrary. We know that the MCP/phosphor screen/SiPM can detect single electrons, but the efficiency is probably not 100%. So 10 is chosen, as it is the smallest number which is much bigger than 1. The following algorithm is used to solve for the total charge:

1. A heuristic guess is used as a starting point—150 ke^- for the biggest clouds, scaled linearly with space charge voltage for the smaller clouds.

2. If the initial guess is too big (small), I repeatedly divide (multiply) that guess by two until the resulting charge is too small (big).

3. From here, we have a number which we know is too small, and a number which we know is too big, and 10 steps of binary search are used to find a total charge where exactly 10 electrons would be escaping the confining potential.

The most difficult part of the above algorithm is computing the number of electrons with enough energy to escape for a given equilibrium solution. For each radial position, an escape voltage $V_{\text{esc}}(r)$ is computed—the most negative potential along that row. Then for each axial gridpoint in that radial grid location, the axial escape velocity is determined to be $|v_{\text{esc}}| = \sqrt{2e[V(r,z) - V_{\text{esc}}(r)]/m}$. The fraction of electrons with this escape energy is:

$$f_{\text{esc}} = \frac{\int_{v_{\text{esc}}}^{\infty} dv \exp\left(-\frac{mv^2}{2k_BT}\right)}{\int_0^{\infty} dv \exp\left(-\frac{mv^2}{2k_BT}\right)} = \text{erfc}\left(\sqrt{\frac{m}{2k_BT}} v_{\text{esc}}\right) = \text{erfc}\left(\sqrt{\frac{e[V(r,z) - V_{\text{esc}}(r)]}{k_BT}}\right) \quad (5.1)$$

Electrons that are already on or beyond the escape voltage already are not counted; they are considered to be unphysical computational artefacts. Three examples of equilibrium solver results are shown in Fig. 5.13. They show guesses for the total charge which have too many escaping electrons, just enough, and too few electrons.

The charges of each cloud predicted by this equilibrium modelling is shown in Fig. 5.14. The quality of the results of this study is disappointing. The charge of the clouds predicted by this analysis is dramatically sensitive to the arbitrarily chosen threshold of "ten escaping electrons." For example, changing this number to 100 shifts the 80 mV voltage step clouds total charge by 14 ke^-. Likewise, the prediction is dramatically sensitive to temperature, and I have already discussed the issues with these temperature measurements. For the smallest clouds, these issues are much worse, and essentially this method of charge estimation is

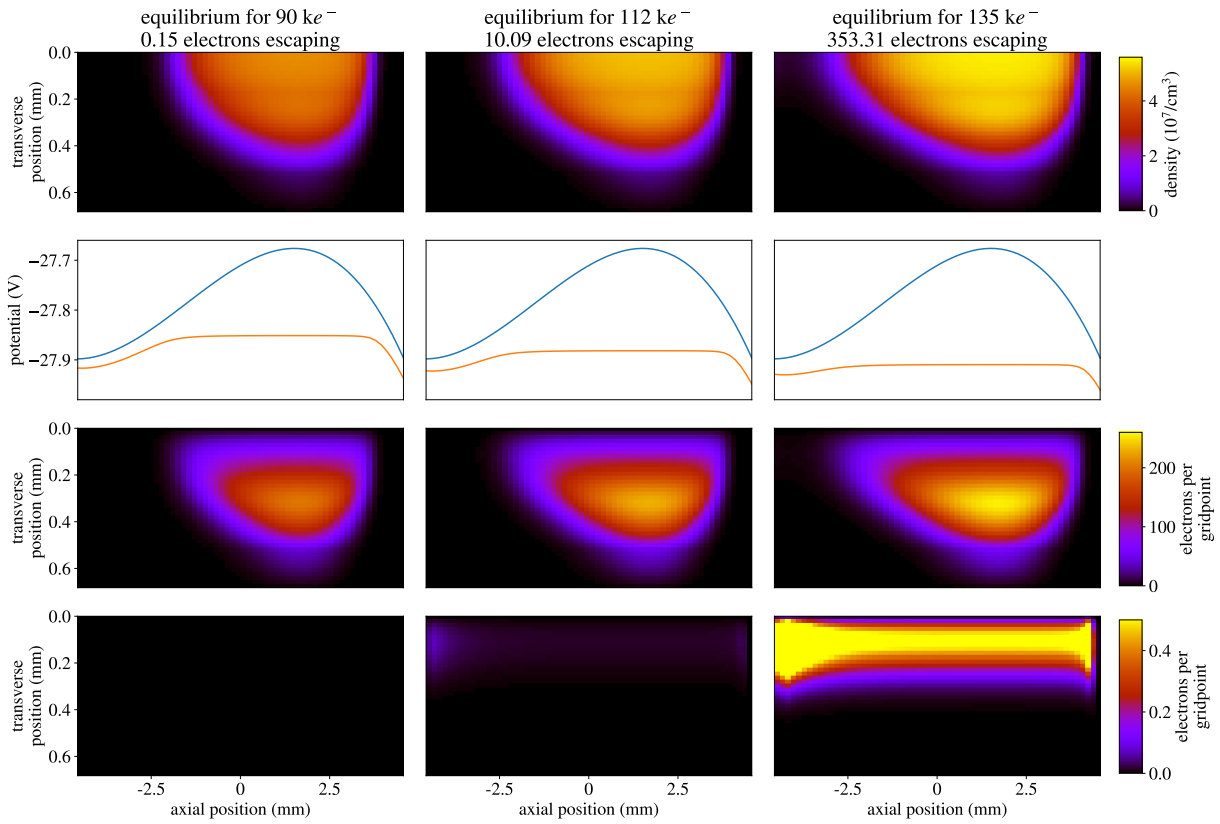

Figure 5.13: Three guesses for the total charge of the 128th cloud extracted from the reservoir with 80 mV steps. In the middle column, the actual solved charge 122 ke^- is shown. On the left and right, the plasma equilibrium with 20% less and more charge respectively. On the top row, the plasma density throughout space is shown. In the second row, the on-axis potential created by the electrodes is shown in blue, and the on-axis potential corrected by presence of the electrons is shown in orange. In the third row, the number of electrons per computational gridpoint is computed—that is, the data in the first row times the volume of each computational gridpoint. The final row shows the number of electrons in each gridpoint which have enough energy to escape the trap. The total number of electrons with escape energy is given on top of each column.

completely useless. However, as discussed earlier, there is good reason to expect that our temperature measurement of 70 K was overestimated by a factor of 1.5 to 1.8. Thus, I redid this calculation with a temperature of 40 K. These results are shown in Fig. 5.15, and the estimated cloud charges are much closer to what we find using other methods. This seems to be tentative confirmation that the same kind of temperature correction factor discussed in the context of positron plasmas in Sec. 4.1 also applies to non-plasma electron clouds.

Unlike the MCP total brightness estimations of cloud charges, the total charge of clouds extracted with 80 mV drops with later extractions regardless of temperature. This isn't as dramatic as the drop in space charge voltage shown in Fig. 5.12 because the radii of these clouds also increased. Probably this technique didn't go far enough and we will see in the next section that the charge of these scoops is more constant. Despite these issues, it is

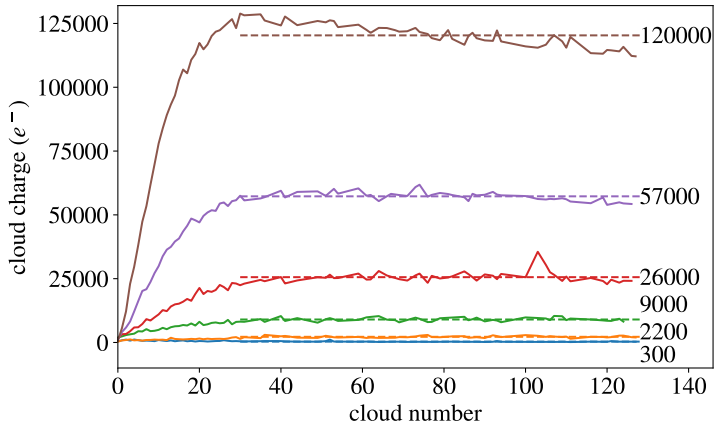

Figure 5.14: The cloud charge estimated using signal arrival timing combined with equilibrium modelling is shown for the six scooping voltage step sizes. The dashed lines and the numbers on the right show the result of averaging all the clouds after the 30th, as was done for other charge determination methods.

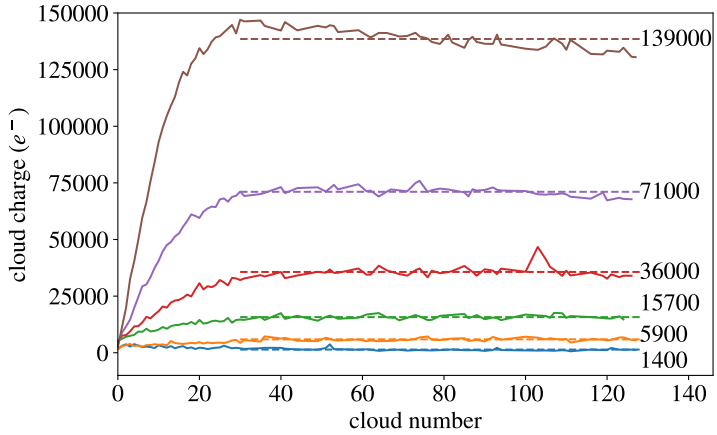

Figure 5.15: This plot is the same as Fig. 5.14, but with a plasma temperature of 40 K instead of 70 K.

also good to have an approximate independent verification of the results of the Faraday cup measurement—which was until this point the only absolute measurement of cloud charges.

5.4 Magnetron phase shift due to cloud charge

This final method of charge determination utilizes the same techniques developed throughout this thesis to measure magnetic fields and patch potentials. Clouds will be displaced from the trap center using patch potentials, and then they will orbit the trap several thousand times. I will take care to preserve phase coherence by eliminating the variability in magnetron frequency with radial distance from the trap center. We will observe a small phase difference between clouds with different charges. By theoretically predicting the relationship between charge and phase, we will extract a measurement of the total charge. There will also be an

interlude where it is shown how the total charge affects how far a cloud is displaced from the trap center by patch potentials (a systematic in the patch field measurements). In a sense, the systematic effect that charge has other cloud-based measurements is isolated and used to determine the charge of the cloud. Indeed, anything that affects your measurement device can be reinterpreted more positively as something your measurement device is sensitive to. There are many ways to interpret the importance of this chapter. The preceeding sections could be seen as a double check that this new measurement tool is accurate (or vice versa). Alternatively, this section could serve as proof that the systematic effects of cloud temperature and charge on other cloud-based measurements are well-understood.

In Fig. 5.16, the potentials used to perform this measurement are shown. Essentially I wanted to use the technique presented in the patch potential section to move the clouds off-axis. Then I wanted them to stay in the trap in a magnetron orbit for a long enough time that a significant perturbation due to the image charge could accumulate. However, in a nominal trapping potential this would mean that the variability of magnetron frequency with radius would completely randomize the cloud's final magnetron phase. Therefore, the trapping potentials are chosen to to have zero total variability with radius (at least in theory). Then when they are imaged, there will still be enough phase coherence that we can observe a small phase shift due to the effect of each cloud's total charge. Fig. 5.17 shows the resulting data for five different amounts of total time that the clouds spent in a magnetron orbit. Before discussing the analysis of this data I will derive the charge-dependent correction to the magnetron frequency.

(a) After being moved axially from the reservoir to the measurement location (roughly in the middle of the ALPHA-g trap), the trapping potential is weakened adiabatically, and patch potentials move the cloud off-axis (see Sec. 3.3).

(b) Once the cloud has been moved off-axis a desired distance, the trapping potential is instantaneously (well, as fast as the amplifiers can change voltage) changed to a deep trapping potential, and the cloud orbits the trap center. The cloud rests in this potential for about a millisecond. The logic of this step is that the analysis of how far the cloud moves off axis is simpler when the instantaneous change is just a single electrode changing voltage from low to high. Then the on-axis potentials just differ by a constant factor.

(c) The trapping potential is changed linearly from the previous one to a trapping potential with a negative quartic term. Then we rest here for a variable amount of time up to about a second. In this trapping potential, longer plasmas orbit the trap center faster, and plasmas that are displaced radially farther from the trap center orbit slower, making the phases develop a spiral in the shape of $\theta \propto r^2$.

(d) The trapping potential is changed linearly to a trapping potential with a positive quartic term. We rest here for a variable amount of time up to about a fifth of a second. Generally, the time spent in this positive quartic potential is chosen to cancel out the effect of the negative quartic potential so that there is very little spiral in the final data, making small phase shifts easier to observe.

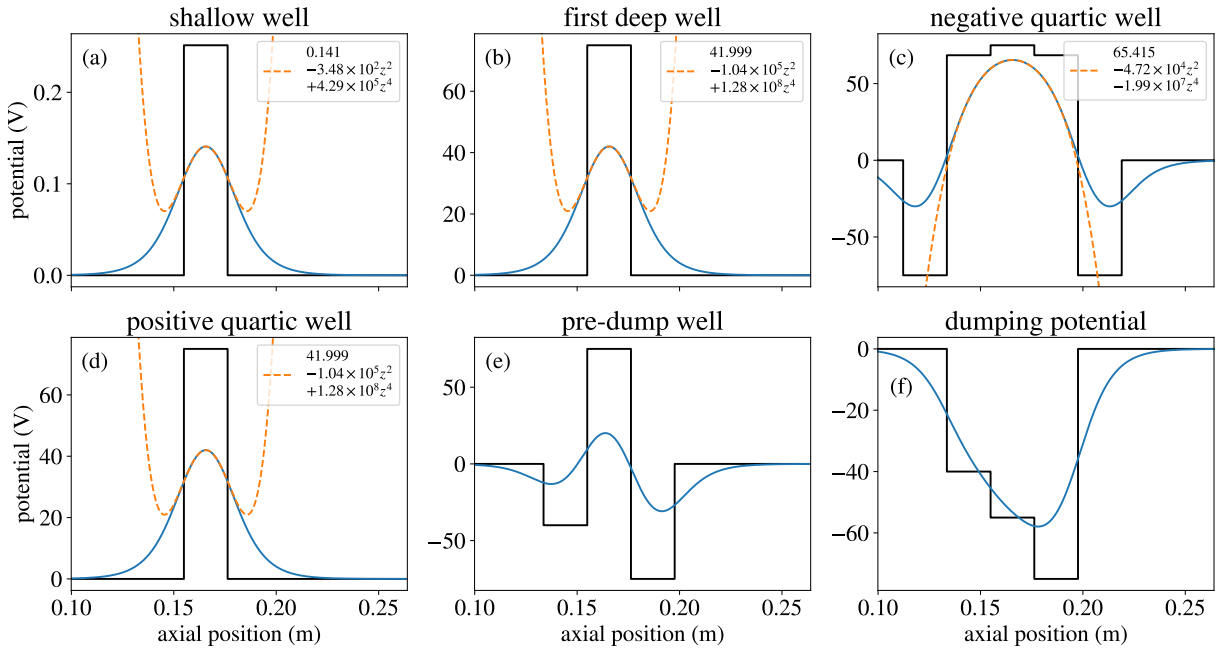

Figure 5.16: The sequence of electrode potentials used to measure the effect of cloud charges on their magnetron frequency. In each subplot, the blue line is the on-axis potential created by the electrodes as found by an electrostatic model. The orange dashed line is the result of a quartic fit to that potential. The black line shows the electrode voltages that create this on-axis potential. The purpose of each step is listed in the text.

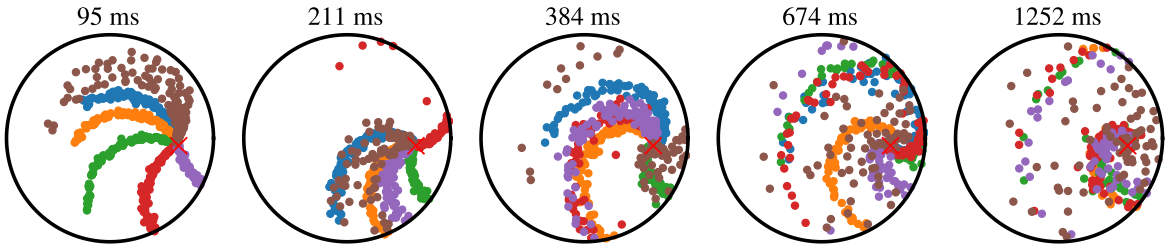

Figure 5.17: The entire dataset used in this section is shown. Above each circle, the time that the electron clouds spent in a magnetron orbit around the trap center is listed. The black circles represent the aperture, which is not the edge of the MCP, but nonetheless clouds that fall outside of this aperture are not imaged. Each dot is the center of a plasma which was imaged with the MCP. As usual, blue, orange, green, red, purple, and brown points correspond to clouds prepared with scooping step sizes of 2.5, 5, 10, 20, 40, and 80 mV respectively.

(e) In another millisecond, the trapping potential is linearly changed to this "pre-dump" potential, where we can release the electrons at a negative potential so they will fly toward the MCP.

(f) The cloud is sent toward the MCP to be imaged. This voltage change is instantaneous

like the (a)-(b) transition.

This describes the procedure performed on a single cloud, but of course the final measurement requires many clouds. For each reservoir, we first image 28 clouds with a small displacement and varied magnetron phases. This helps identify the effective trap center as seen on the MCP. The remaining 100 clouds are sent different distances off-axis using an adiabatic change to a varied shallow trapping potential (see Sec. 3.3). The shallow potentials are chosen so that, at least in theory, the clouds are evenly spaced radially. Therefore $1/k_{2m}$ for the shallow potentials is spaced linearly. However the order of these distances off axis is randomly shuffled so that we can still measure the variability of charge with extraction number without incurring a systematic effect from the variability of the magnetron frequency with radial position.

Next, the same procedure is performed for six identically prepared reservoirs with different scooping voltage step sizes. Finally, the entire sequence of six reservoirs is repeated for different amounts of time spent in potentials (c) and (d). The increasing time in those two potentials is chosen so that the total spiral accumulated remains zero. Using the numbers listed in Fig. 5.16, the time spent in potential (c) is 4.9 times the time spent in potential (d). The entire measurement took about four hours—about half a shift.

Once the clouds are in a "deep" trapping potential performing a magnetron orbit around the trap center, their radius is up to $r_c = 0.3\,\mathrm{mm}$ for the biggest clouds considered, and their length is up to about $l = 1\,\mathrm{mm}$. The clouds are also displaced a relatively small distance from the center of the trap: up to about $r = 2\,\mathrm{mm}$, because beyond that point the clouds miss the MCP and cannot be imaged. Because all of these length scales are very small compared to the trap wall radius, we can expand the trapping potential in powers of (r or l)$/R_w$, where R_w is the trap wall radius. Also, for the effect of the cloud's image charge on its magnetron frequency, the cloud can be approximated as a point charge in an infinite grounded cylinder. Thus we write the trapping potential near the trap center as:

$$\Phi_{\mathrm{T}} = -k_2\left(z^2 - \frac{1}{2}r^2\right) + k_3\left(z^3 - \frac{3}{2}zr^2\right) + k_4\left(z^4 - 3z^2r^2 + \frac{3}{8}r^4\right) + \cdots . \tag{5.2}$$

The third order term gives rise to an r dependent z equilibrium $\langle z\rangle = -3k_3r^2/(4k_2)$. Taking a negative derivative with respect to r to find E_r, then dividing by Br to find the frequency of $\mathbf{E}\times\mathbf{B}$ drift we get:

$$\omega_r(r) = \frac{k_2}{B} - 3\frac{k_3\langle z\rangle}{B} - 6\frac{k_4\langle z^2\rangle}{B} + \frac{3}{2}\frac{k_4}{B}r^2 = \frac{k_2}{B} - 6\frac{k_4\langle z^2\rangle}{B} + \left(\frac{9}{4}\frac{k_3^2}{k_2B} + \frac{3}{2}\frac{k_4}{B}\right)r^2 + \cdots , \tag{5.3}$$

Note that after the first equality, any lingering z's are turned into expectation values over the cloud's charge distribution. This is justified by realizing that an electron bounces in z much faster than it orbits the trap due to magnetron motion. The $\mathbf{E}\times\mathbf{B}$ drift of an electron, and indeed of the cloud as a whole, should be averaged over this fast z motion. This is summarized by the commonly stated order of scales in Penning traps: $\omega_c \gg \omega_z \gg \omega_r$ (the cyclotron frequency is much greater than the z bounce frequency which is much greater than the magnetron frequency).

In this measurement k_3 is zero except in potential (e), and $\int k_4 dt$ is made to be zero by

adjusting the time spent in potentials with negative versus positive k_4. Thus, except due to error in the models, there should be no r dependence in $\theta = \int \omega_r(r,t)dt$, meaning that small phase shifts will be more easily observable. Also, to eliminate systemics relating to modelling the trapping potential changing over time, I will only measure "differences in phase differences." That is—the first word "differences" is differences due to spending different amounts of time sitting in the static potentials (c) and (d). The second "differences" refers to differences in phase between clouds with different total charge.

Unfortunately, this experiment was designed before I fully understood some corrections to the magnetron frequency. I thought this would be a perfect measurement of the image charge effect alone, which is linear with a cloud's total charge and thus an unambiguous measurement of its charge. However, I didn't realize that the finite length effect $6k_4\langle z^2\rangle/B$ was the same order of magnitude (and actually twice as big). Had I realized this, I would have simply used one trapping potential with zero quartic coefficient to eliminate the finite-length effect. As it stands, the mean quartic coefficient is zero, but the mean $k_4\langle z^2\rangle$ is not zero, because the negative quartic potential has a lower k_2, so the plasma is longer there. Nonetheless, by properly studying how cloud lengths depend on k_2, with a bit more complexity, we can still extract a fairly reliable measurement of cloud charges. Note I also hadn't realized that k_3 contributes to the r^2 term in ω_r at this point, but here this doesn't really matter—a very short time is spent in asymmetric wells anyway.

5.4.1 Cloud lengths

There are two limits where the shape of the cloud can be calculated exactly—the cold spheroid plasma limit and the hot Gaussian cloud limit. If the Debye length is short compared to the length and the radius of the cloud, then the cloud will approximately have a spheroid shape. Its mean square radius is conserved by the confinement theorem [8], so only its length will vary so that the total electrostatic potential is constant with z inside of the plasma. If the Debye length is long compared to either the length or the radius of the cloud, then the cloud's charge will not significantly affect the trapping potential, and its charge distribution will be Gaussian. The radial extent of the Gaussian will be determined by the conserved mean square radius, and the axial extent will be given by $n_0(r)\exp(-ek_2z^2/k_BT)$. In both cases, the shape of the cloud will be calculated assuming the trapping potential is given by $V_T \approx -k_2z^2$. Then from the resulting shape I will calculate $\langle z^2\rangle$ and substitute the result into $6k_4\langle z^2\rangle/B$ to find the perturbation to ω_r. This is valid because the k_4 term gives rise to a very small perturbation to the shape of the plasma, and therefore a small perturbation to $\langle z^2\rangle$, and then a small×small contribution to ω_r.

In the Gaussian limit, the mean square length is a very simple calculation: $\langle z^2\rangle = k_BT/2ek_2$. For a cold plasma, the calculation is somewhat more complex. The first step is to simply be aware of a mathematical fun fact: the electrostatic potential generated by a spheroidal uniform charge distribution is exactly quadratic in z and r. That is, as a function of distance from the center, the potential is exactly given by $V_P = -en_0/\epsilon_0(A_zz^2 + A_rr^2)$, where n_0 is the plasma density, and A_z and A_r are coefficients. The oldest citation I can find for this is a 1929 book [102]. So we're in luck, this is exactly what we need from our plasma equilibrium solution. When the plasma is cold (Debye length is small compared to the plasma), it forms a uniform charge distribution, and it should shield out z-

directed electric field, so it should generate a potential in z which exactly cancels the trapping potential. These spheroidal plasmas were studied by the UCSD group experimentally [103] and theoretically [104] in the 90's.

Now I will outline the calculation of the coefficients A_z and A_r. Let the full length of the plasma in z be $2a$, and its radial width I will call $\sqrt{C}a$ for some constant C. Then the equation describing the plasma interior is:

$$z^2 + \frac{r^2}{C} < a^2. \tag{5.4}$$

Using only elementary electrostatics, we can find the on-axis potential by integrating disks of uniform surface charge density to arrive at:

$$V_P(z, r=0) = \int_{-a}^{a} \frac{en_0 dz'}{2\varepsilon_0} \left(\sqrt{(z'-z)^2 + C(a^2 - z'^2)} - |z'-z| \right) dz'. \tag{5.5}$$

This equation can be solved with shifts of variables and trig substitutions to arrive at the following result:

$$V_P(z, r=0) = -\frac{en_0}{\varepsilon_0} \left(A_z z^2 + Ba^2 \right). \tag{5.6}$$

$$A_z = \begin{cases} \frac{1}{2}\left[\arccos\left(\frac{-C+2}{C}\right)\frac{C}{2(C-1)^{3/2}} - \frac{C}{C-1}\right] & C > 1 \\ -\frac{1}{6} & C = 1 \\ \frac{1}{2}\left[-\operatorname{arccosh}\left(\frac{-C+2}{C}\right)\frac{C}{2(1-C)^{3/2}} - \frac{C}{C-1}\right] & C < 1 \end{cases} \tag{5.7}$$

$$B = \begin{cases} \frac{1}{2}\left[\arccos\left(\frac{-C+2}{C}\right)\frac{C}{2(C-1)^{1/2}}\right] & C > 1 \\ \frac{1}{2} & C = 1 \\ \frac{1}{2}\left[\operatorname{arccosh}\left(\frac{-C+2}{C}\right)\frac{C}{2(1-C)^{1/2}}\right] & C < 1 \end{cases} \tag{5.8}$$

Note that A_z and B are indeed continuous and infinitely differentiable at the boundary $C = 1$; the two cases are simply analytic continuations of one another. Then the Poisson equation determines how the potential varies in r:

$$V_P = -\frac{en_0}{\epsilon_0} \left(A_r r^2 + A_z z^2 \right). \tag{5.9}$$

$$\nabla^2 V_P = -\frac{en_0}{\epsilon_0} \left(4A_r + 2A_z \right) = \frac{qn_0}{\epsilon_0}. \tag{5.10}$$

$$A_r = -\frac{1}{4} - \frac{A_z}{2}. \tag{5.11}$$

Finally we will want to relate this to our conserved quantities—the total number of electrons N and the mean square radius $\langle r^2 \rangle$. So using:

$$N = \frac{4}{3}\pi C a^3 n_0. \tag{5.12}$$

$$\langle r^2 \rangle = \frac{2}{5} C a^2. \tag{5.13}$$

The latter can be inferred from the moment of inertia of a solid sphere. We have the condition that the trap constant k_2 be cancelled by the potential made by the plasma giving:

$$k_2 = \frac{-en_0}{\varepsilon_0} A_z(C). \tag{5.14}$$

Note that I have highlighted that A_z is a function of C. In terms of the conserved and measurable properties of the cloud, we have:

$$\frac{-4k_2\varepsilon_0\pi}{3eN}\left(\frac{5\langle r^2\rangle}{2}\right)^{3/2} = A_z(C)C^{1/2}. \tag{5.15}$$

$$a = \sqrt{\frac{5\langle r^2\rangle}{2C}}. \tag{5.16}$$

$$\langle z^2 \rangle = \frac{a^2}{5}. \tag{5.17}$$

The last equation, again, simply comes from the moment of inertia of a sphere (after noting that $\langle x^2\rangle = \langle r^2\rangle/2$). So finally we have a procedure for finding $\langle z^2\rangle$ for spheroidal plamas: we numerically solve Eq. 5.15 for the radial scale factor C, then we put the result into Eq. 5.16 and in turn insert that into Eq. 5.17.

I compared these two limits to the results of a plasma equilibrium solver. This was done not only to check my algebra, but also because I wanted to see if I could guess an equation for $\langle z^2\rangle$ that would be approximately valid in both limits to help extract the total charge from plasmas with Debye lengths comparable to their dimensions. Some examples of solved plasmas are shown in Fig. 5.18. A special plasma equilibrium solver was prepared for this calculation. This solver found whether the plasma was in the Gaussian limit or the spheroid limit, and in either case it would use the applicable theory to calculate the expected length and rotation frequency, and an appropriate initial guess for the shape of the plasma was used. This meant the rotation frequency was solved faster and the equilibrium charge distribution was found faster. Also, I didn't need to set the length or radial extent of the grid by hand. In the Gaussian limit, the solver was actually also aware of the leading order correction to the trapping potential from the charge being not-entirely negligible, but this theory is not very illuminating and quite a lengthy calculation, so I will not describe it in this thesis.

The $\langle z^2\rangle$ values found by the equilibrium solver are compared to the Gaussian hot cloud theory and the cold spheroid plasma theory in Fig. 5.19. Of course, the theories agree with the solver in either limit. Also, a heuristic guess is plotted in Fig. 5.19, which shows the result of guessing that $\langle z^2\rangle$ for any cloud is simply the sum of the theories in the two limits. This guess comes from acknowledging that if the cloud is mostly Gaussian but slightly perturbs the trapping potential, the repulsion between electrons will slightly elongate the cloud. Likewise, if the cloud is mostly spheroidal, its temperature will slightly elongate the cloud, making some charge extend into regions of higher potential energy than the flattened center. Therefore the full length is always greater than the length implied by either limit. Of course just guessing an equation (that is not justified by any formal approximation) is

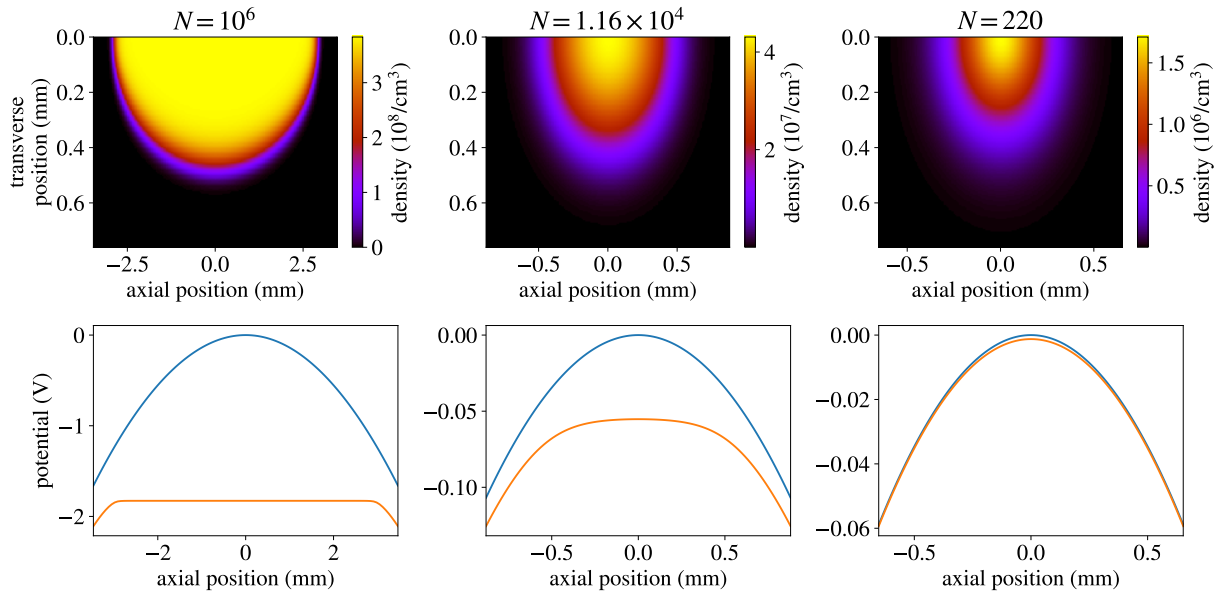

Figure 5.18: Three plasma equilibrium solutions found while calculating the blue curve in Fig. 5.19. Each column shows a different number of electrons (listed on top of the column) with the same temperature in the same purely quadratic trapping potential. The realistic trapping potential $k_2 = 10^6\,\mathrm{V/m^2}$ was used, the root mean square radius was set to 0.3 mm, and the temperature was set to 100 K. The upper plots show a cross section of the charge distribution. The lower plots show the trapping potential in blue (which was chosen to be purely quadratic, not an approximately quadratic trapping potential from realistic electrodes), and the potential perturbed by the charge is shown in orange.

not generally appropriate in physics, but I was satisfied that the simplest possible guess for a general equation was remarkably accurate, and in the rest of this section I will use this equation for analysis.

5.4.2 Image charge effects

As stated earlier, my primary intention for this experiment was to measure only the effect of a cloud's image charge on its magnetron frequency. To calculate this, we can approximate the clouds as point charges, because they are much smaller in radius and length than the size of the trap. Then the question is just what force does a grounded conducting cylinder exert on a point charge which is displaced from the trap center. I first obtained the formula for this effect from Ref. [105], and in turn they cite Ref. [106]. It was previously experimentally observed to have an effect on precision measurements of highly charged ions in Ref. [107]. Ref. [105] defines the "image potential" as:

$$\Phi_0^{\mathrm{image}}(r) = -\frac{q^2}{4\pi\epsilon_0 R_w} \sum_{l=-\infty}^{\infty} \frac{2}{\pi} \int_0^{\infty} dx I_l^2\left(x\frac{r}{R_w}\right) \frac{K_l(x)}{I_l(x)}, \tag{5.18}$$

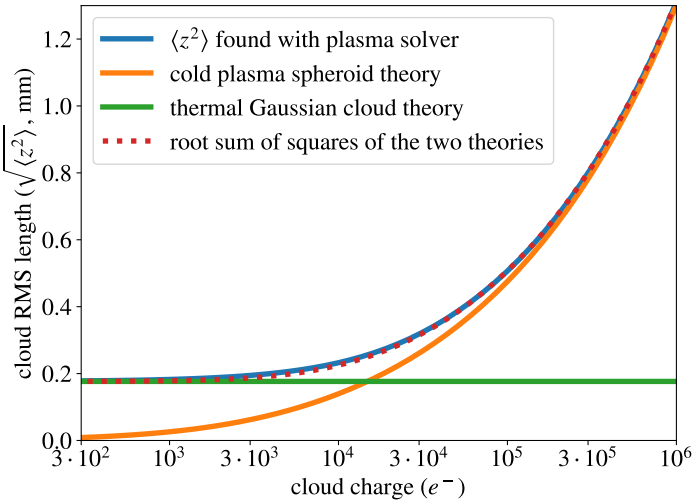

Figure 5.19: An electron cloud's root mean squared length is plotted as a function of the total charge for the parameters (trapping potential, temperature, and RMS radius) described in the caption of Fig. 5.18. The blue line is the result of numerically finding plasma equilibria for 60 different cloud charges between $3 \times 10^2\, e^-$ and $10^6\, e^-$. The green line is the theoretical result for hot gaussian clouds. The orange line is the theoretical result assuming the cloud temperature is zero (the cold spheroidal plasma limit). The orange dashed line is the square root of the sum of squares of the two theories.

where I and K are the modified Bessel function of the first and second kind respectively. The integrand is exponentially suppressed for large x whenever $r/R_w < 1$ (which it always is). It's hard to complete the integral with complex analysis when it isn't going from $-\infty$ to ∞, and it isn't symmetric with respect to $x \to -x$. However, we only want to calculate this for small r/R_w, so I expand the $I_l^2(xr/R_w)$ inside the integral for small r/R_w [108]:

$$I_l(z) = \left(\frac{1}{2}z\right)^l \sum_{k=0}^{\infty} \frac{\left(\frac{1}{2}z^2\right)^l}{l!\Gamma(l+k+1)}. \tag{5.19}$$

When we expand in powers of r/R_w, in Eq. 5.18, any contributions to some power n only come from $|l| < n/2$. Then I set up a numerical integrator for integrals of the form:

$$\int_0^{\infty} x^{2n} \frac{K_l(x)}{I_l(x)}, \tag{5.20}$$

and for the first few powers of r/R_w I summed up all the coefficients from the contributing l values and the expansion of I_l^2. The result is (up to the precision of my calculations):

$$\Phi_0^{\text{image}}(r) = -\frac{q^2}{4\pi\epsilon_0 R_w}\left[0.8707 + 1.00273\left(\frac{r}{R_w}\right)^2 + 1.00094\left(\frac{r}{R_w}\right)^4 + 1.00031\left(\frac{r}{R_w}\right)^6 + \cdots\right] \tag{5.21}$$

The electric field seen by the point charge is actually half the negative derivative of this image potential divided by q. It seems the image potential is defined more like the potential energy

between a point charge and its image charge (not that there's an "image charge solution" to this problem), and we know that the actual potential energy is half the potential defined in this way [100]. So then the contribution to the magnetron frequency is:

$$\omega_r^{\text{image}}(r) = -\frac{1}{2NeBr}\frac{d}{dr}\Phi_0^{\text{Image}} \approx \left(1.00273 + \mathcal{O}\left(\frac{r^2}{R_w^2}\right)\right)\frac{Ne}{4\pi\varepsilon_0 B R_w^3}. \tag{5.22}$$

As a bit of an aside, Prof. Dan Dubin from UCSD pointed me to Eq. 5.18 in one of his papers at a conference. I was trying to use elaborate and computationally intensive numerical methods to evaluate this contribution to the magnetron frequency, and to within the precision I could achieve, I hadn't found any difference between the force on a charged particle from a grounded cylinder of radius r versus a grounded sphere of radius r. At the time I was convinced that there was some mathematical trick I hadn't figured out yet which proved they were exactly the same, and I had this hypothesis written in a small box on my poster at the conference. Prof. Dubin came along and said he wasn't sure if this was true, but he doubted it, and he said he had a paper which had an exact equation which would be easier to evaluate than my scheme. In the end, the force is very close, but not the same. The image potential for the grounded sphere can be solved by placing an image charge of magnitude qR_w/r a distance R_w^2/r away from the center of the sphere [100]; then the potential is:

$$\Phi_0^{\text{image}} = -\frac{q^2}{4\pi\epsilon_0 R_w}\frac{1}{1-\left(\frac{r}{R_w}\right)^2} \tag{5.23}$$

Then using the commonly known sum for $1/(1-x)$, we get

$$\Phi_0^{\text{image}} = -\frac{q^2}{4\pi\epsilon_0 R_w}\sum_{n=0}^{\infty}\left(\frac{r}{R_w}\right)^{2n} \tag{5.24}$$

Indeed, when we compare the coefficients here to the coefficients in Eq. 5.21, we find that the force between a point charge and a grounded cylinder is very similar to the force between a point charge and a grounded sphere.

5.4.3 Linear phase correction

Now that I've explained the two effects that will contribute to the measured phase differences in this experiment, I can explain the analysis. However, in the very first step of this analysis we encounter a mystery. That first step is to plot the phase of each imaged plasma versus radial distance. Nominally, the phase is $\arctan_2(y-y_c, x-x_c)$, where x and y are the position of the center of the cloud on the MCP, x_c and y_c are the trap center, and $\arctan_2$ is the inverse tangent function with two inputs. However, this doesn't capture phase differences greater than 2π, which are obviously present in Fig. 5.17. Thus, a simple algorithm was used to find the total phase including full rotations—some 2π errors were fixed by hand, and most were identified by extrapolating from the results from shorter trap times. The results are shown in Fig. 5.20. The mystery comes from noticing that the phases aren't quadratic with distance from the trap center—they are linear. To make this more clear, consider Fig. 5.21, where I

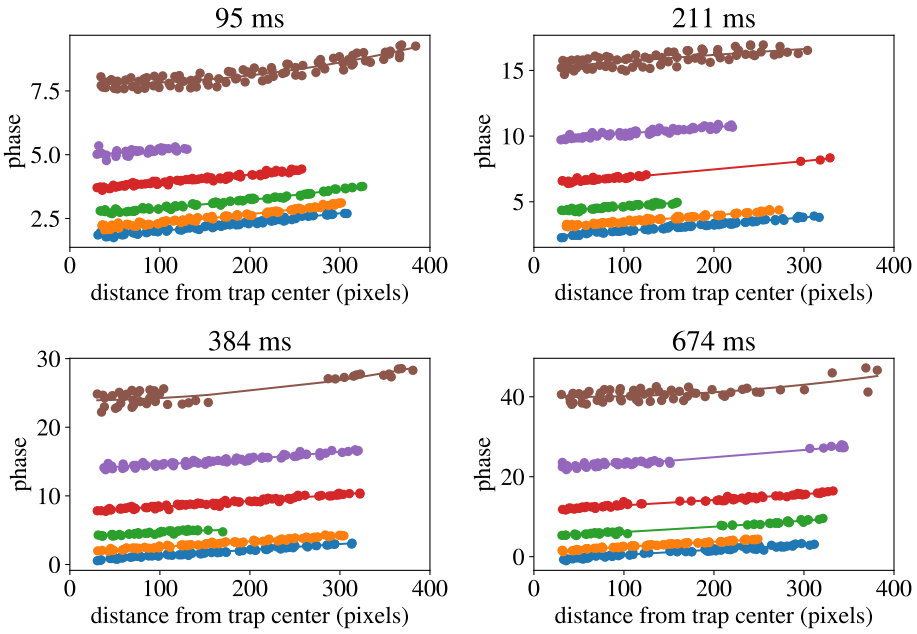

Figure 5.20: The final magnetron phases of the imaged clouds versus radial position from the trap center. The colors represent different sizes of clouds: the usual choices of scooping voltage step sizes (2.5, 5, 10, 20, 40, and 80 mV). Each subplot shows a different amount of time spent in a magnetron orbit, with the total time listed on top of each subplot. The plots look very similar to one another simply because the vertical axis is scaled and offset to fit the data, and at least in theory everything should be proportional to time. Gaps and missing r values can be explained by looking at Fig. 5.17: many clouds miss the MCP. The lines are fit quadratic functions. The 1252 ms data shown in Fig. 5.17 is not included in further analysis because something went wrong with the reservoir with 2.5 mV steps (notice the lack of blue points).

zoom in on some of the lower charge data. It is clear that a line is a good fit to the data, but a quadratic function (without a slope at $r = 0$) is not a good fit. Also, the coefficient on the linear term clearly increases with increasing time spent in the deep wells. This rules out a number of simple hypotheses, like errors relating to error in (x_c, y_c), or the transition from potential (a) to (b) not being sufficiently quick, or the effect of nonlinear patch fields discussed in Sec. 3.13. Such effects would only ever introduce phase offset proportional to r which is independent of the time spent in the magnetron orbit.

At first, this was extremely perplexing. The theoretical variation with r scales like r^2 (up to the order I calculated). But the reader may note that I only included azimuthally symmetric terms in my expression for the potential. In other words, I neglected perturbations to the potential due to patch potentials and electrode construction errors. Such terms initially seem hopeful, because this linear term is indeed small—only observable when the quadratic term is tuned to be small. However, regardless of the form of the perturbation, the magnetron frequency should respect the symmetry $r \to -r$. To test this argument, I set up a Boris algorithm integrator to see how different perturbations affected the magnetron frequency. I have gone up to third order in r and z [terms like $r\cos\theta(z^2 - 1/4r^2)$], and every

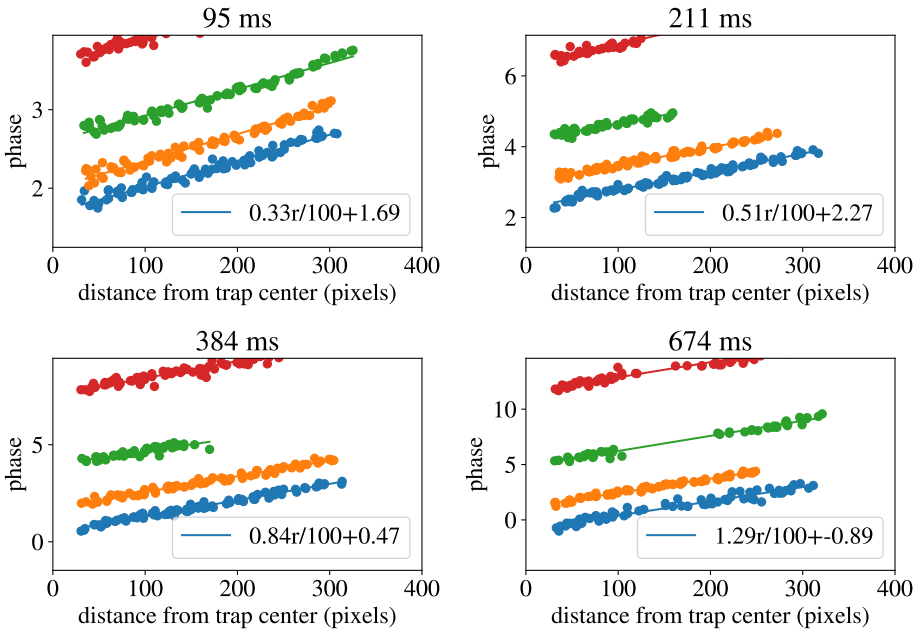

Figure 5.21: The same data and explanation as Fig. 5.20. Now the span of the vertical axis is zoomed in on the lower charge clouds. Also, the the fit parameters of a linear fit to the smallest clouds is shown.

term I have tried only contributes a constant shift and/or a correction which is proportional to r^2.

Before proposing a hypothesis that is consistent with all the observations, I will discuss and refute some other proposals that probably come to mind for the reader. First, there may be some kind of electrode amplifier hysteresis due to the shallow trapping potentials being different for clouds moved a different distance off-axis. In other words, having a different potential (a) might mean that potentials (b) and (c) are slightly different. However, this seems unlikely given that only in potentials (c) and (d) do these clouds spend a variable amount of time. It seems odd that any kind of hysteresis would persist after two voltage changes. My advisor, Prof. Joel Fajans, points out that he is aware of a theoretical reason for hysteresis: there is a resistor forming a feedback loop for an op-amp in the amplifiers that drive the electrodes. The resistor will have a resistance that depends on temperature, and the temperature of the resistor will depend on the history of voltages across it. This seems unreasonable though, because the only potential that varies here is the shallow trapping potential—roughly 0.1–1 V. If this significantly heats the resistor and causes hysteresis, then such effects should be plainly obvious in situations where 150 V is going to the electrode. The efficacy of EMPI (see Sec. 8) rules this out.

Next, consider a toy model which reproduces the $\propto r$ behavior and serves as the inspiration for my favorite hypothesis. The clouds may be heated by the instantaneous voltage change (a) to (b). Consider a Gaussian cloud in potential (a). Its length is $l \propto 1/\sqrt{k_{2i}}$ where k_{2i} is the trap constant of potential (a). Then naively assume that the electrode voltage changes much faster than electrons can move. Electrons a distance l from axial the trap center will gain an energy from the changing potential of $k_{2f}l^2 \propto k_{2f}/k_{2i} \propto k_{2f}r$. Then the finite

length phase change is proportional to temperature, and hence energy gained. Of course, this exact calculation is completely wrong: the electrodes do not move fast compared to the axial motion of the electrons (a few microseconds vs a few nanoseconds per cycle). Also, the effect described here clearly should depend on the cloud's charge, which significantly affects its length in the shallow and deep trapping potentials—the slopes in Fig. 5.21 do not really appear to vary with cloud charge.

Because this linear term doesn't seem to vary significantly with cloud charge, we can learn about its behavior using only the smallest clouds, varying the time spent in both wells (c) and (d). This is shown in Fig. 5.22. In that figure, I include data that was specifically taken to measure the charge of clouds, but also data mentioned in Sec. 3.5 to calibrate the MCP magnetic field, where I vary the time spent in wells (c) and (d) one at a time. We see weak evidence that the linear term decreases when the clouds are in potential (d), and that it increases when they are in potential (c). We also see clearly here that when the total time increases in both potentials, the linear coefficient increases roughly linearly with time. This is all consistent with the guess that clouds that are displaced further from the trap axis are longer, perhaps because their temperature has been increased.

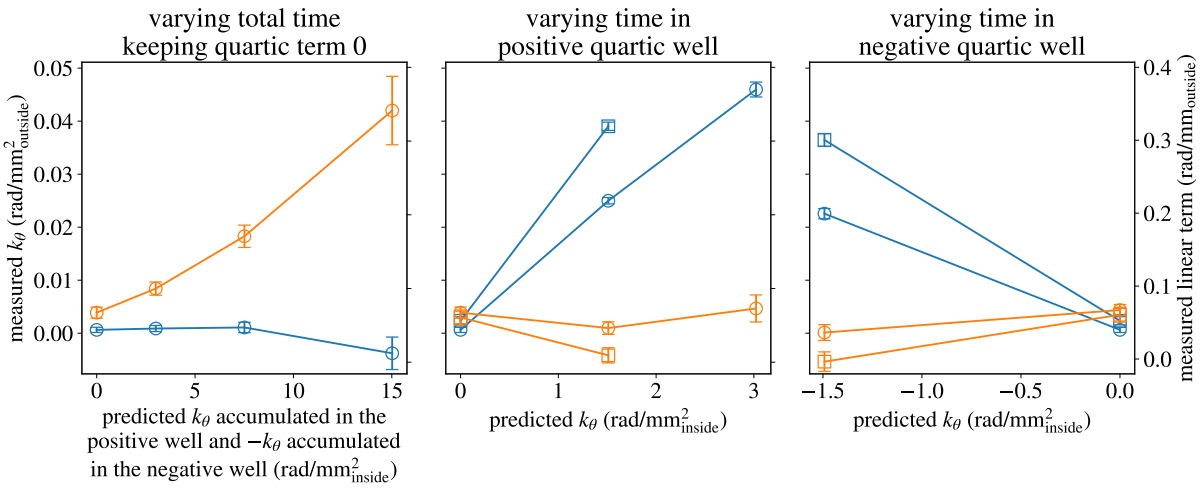

Figure 5.22: A quadratic function $\theta = \theta_0 + mr + k_\theta r^2$ is fit to measured magnetron phases versus distance from the MCP. These plots show how the linear coefficient m (orange points, right vertical axis) and the quadratic coefficient k_θ (blue points, left vertical axis) change as we vary the time spent in potentials (c) and (d). These potentials are referred to as the negative quartic well and the positive quartic well respectively. In the left plot, the time spent in both wells is increased so that the total k_θ should remain constant in theory. When k_θ is small, we can perform more reliable measurements of m, and we see that it increases linearly with time. All of this data was collected with 2.5 mV clouds.

So finally I will describe a plausible model. The adiabatic transition from a deep trapping potential to the shallow one where the clouds are off-axis can take up to 400 ms. As the cloud lengthens, it should lose heat due to adiabatic expansion. In the Gaussian cloud limit, this is because of single particle classical mechanics in a weakening harmonic potential: conservation of the adiabatic invariant says that the length of a particle's orbit times its maximum velocity

is conserved. In the spheroid plasma limit, this can be seen as the adiabatic increase of the volume of an ideal gas.

In both cases, if there is sufficient mixing of the motional degrees of freedom perpendicular and parallel to the magnetic field [109, 110, 111], the temperature should scale like $l^{-2/3}$, and if there is not sufficient mixing the "axial temperature" (the temperature associated with particles' motions along the magnetic field) should scale like l^{-2}. This timescale is calculated in Ref. [109] and experimentally verified in Ref. [111]. I will describe a simple argument that arrives at roughly the same timescale as the values given in these papers.

When two electrons encounter one another with a nonneutral plasma, if their impact parameter is much bigger than their Larmor radius, the "collision" is mainly described by the two particles $\mathbf{E} \times \mathbf{B}$ drifiting around one another [112, 113]. There is little perpendicular/parallel energy exchange in such a collision [114]. The typical Larmor radius of our electrons is $\sqrt{2k_BT/m}/\omega_c = 260\,\mathrm{nm}$. For 10^4 electrons in a cloud of radius 0.2 mm, the total area of all the electrons' cyclotron orbits accounts for about 2% of the cross sectional area of the cloud. Thus an electron needs to traverse the full length of the cloud 50 times before it comes within a Larmor radius of another electron. In the shallowest trapping potentials, our clouds may have lengths up to about $l_p = 0.5\,\mathrm{cm}$, thus they will have close encounters with other electrons roughly once every $50l/\sqrt{k_BT/m} = 7.5\,\mu\mathrm{s}$. Additionally, we must consider whether the distance of closest approach for these collisions is small enough that the two electrons scatter by a large angle—whether they come within the Landau length $2e^2/4\pi\epsilon_0 k_BT = 470\,\mathrm{nm}$ [115]. Because the Landau length and the Larmor radius are coincidentally similar, most collisions within a Larmor radius are also large angle deflections which will significantly mix perpendicular and parallel velocities.

The timescale for perp/parallel mixing is very slow compared to the time taken to move the clouds off-axis, but it is comparable to the time taken to quickly deepen the potential afterward (about $10\,\mu\mathrm{s}$, but the details of fast electrode voltage changes are discussed in Sec. 6.4). When a cloud is adiabatically expanded with perp/parallel mixing, but then contracted without mixing, and then over the following few microseconds the two degrees of freedom come back into equilibrium, the final temperature of the cloud is increased. This heating mechanism was used in Refs. [116, 117] to measure the perp/parallel mixing rate in electron plasmas. This net temperature increase occurs because the first and second operations do not increase the entropy of the cloud, but the third one—where two systems of different temperatures come into equilibrium—does increase the entropy of the cloud. This effect is expected to increase with how far the cloud is moved off axis, because clouds moved farther off axis are expanded to a greater length. The argument so far ignores the fact that the cloud lengths are changing quickly during this deepening, and apparently the clouds are heating, so the equilibration timescale also decreases over this time. Suffice to say that when we are snapping to a deep trapping potential, there is some time where the cloud is experiencing 1-D adiabatic compression, then some time when the perpendicular and parallel degrees of freedom recombine, and the total heating is somewhere between zero and what I will calculate below.

To simplify the discussion allow me to assume that the entire movement back to a deep well is fast compared to the perp/parallel mixing time. To calculate the expected magnitude of this effect, I first assumed that measured cloud temperatures of $T_1 = 70\,\mathrm{K}$ is actually

the cloud temperature in the shallowest trapping potential used. Both this measured temperature and this model are imprecise, so we only expect to confirm the observed order of magnitude. Note that in the moment when we measure measure cloud temperatures, they are about as long as possible (so long that they are escaping the trapping potential).

Next, I calculate the cloud's temperature in each shallow trapping potential used to move a cloud off-axis. All the operations preceding the shallow well, and all the operations before measuring a cloud's temperature are very slow compared to the perp/parallel mixing time. Therefore, the temperature of the cloud should be $T_2 = T_1(l_{\text{ref}}/l_{\text{shallow}})^{2/3}$. That is, it should be the original temperature times the length of the cloud in the shallowest trapping potential used, i.e. the "reference well," divided by its length in the shallow well it was subjected to, consistent with adiabatic compression from that reference well with three degrees of freedom. This requires finding a self-consistent temperature, because the length of the cloud depends on its temperature. This is less of a significant effect in the spheroid plasma limit, where the length is mostly set by electrostatics.

Next I apply the one dimensional adiabatic compression from the shallow well to the deep well. Again this requires finding a self-consistent parallel temperature, but this time the temperature is $T_3 = T_2(l_{\text{shallow}}/l_{\text{deep}})^2$. Only the parallel temperature is T_3, the other two degrees of freedom retain their temperature of T_2, so after a few microseconds, the temperatures should mix, making the final cloud temperature $T_4 = (2T_2 + T_3)/3$. From there I calculated the frequency shift due to the cloud's temperature, given by:

$$\omega_T = 6\frac{k_4\langle z^2\rangle_{\text{thermal}}}{B} = 6\frac{k_4 k_B T_4}{2ek_2 B}. \tag{5.25}$$

Recall that it is approximately valid to just add the thermal and charge contributions to $\langle z^2\rangle$, so here only the thermal contribution is necessary. ω_T must also be averaged over the time spent in the two trapping potentials (c) and (d), which each have their own values of k_4 and k_2. I also accounted for the fact that the clouds are adiabatically expanded (with full mixing) in potential (d), and their temperature is expected to be lower by about a factor of 0.81. The final result is shown in Fig. 5.21. We find that the measured frequency shift is about 5 rad/s between clouds with the highest displacement (300 pixels) and clouds with the lowest displacement (30 pixels). The k_{2m} values plotted in Fig. 5.23 are the same as the ones used to displace the clouds between 300 pixels and 30 pixels.

The idea that clouds are heated in the process of moving them off-axis is tentatively confirmed by measurements of off-axis cloud temperatures presented in Sec. 7.2. In that section, temperatures of off-axis clouds are measured for the purpose of observing heating due to microwaves, but we can also see that clouds which were off-axis but not yet heated by microwaves had temperatures of about 400 K. The analysis here suggests the clouds heated most by adiabatic contraction have temperatures of about 800 K. Once we account for the fact that clouds are necessarily re-expanded when we measure their temperature (slowly compared to perp/parallel mixing), we would expect this temperature to reduce to about 250 K—good enough agreement given the imprecision of this discussion. Of course, as mentioned in Sec. 5.3, cloud temperatures, both the 70 K used in this section and the 400 K of the off-axis clouds, are subject to an unknown correction factor, expected to be between 1/1.8 and 1/1.5. Nonetheless, these correction factors apply equally to both temperature

measurements, so cloud temperatures were indeed increased by a factor of roughly 6 by moving them off-axis in this manner. An increasing temperature with clouds farther off axis is not observed, but this could easily be because of insufficient precision in the temperature measurement or a systematic effect relating to the temperature measurement not being designed for off-axis clouds.

I conclude that this mechanism is very likely to be either correct or at least on the right track for explaining the linear frequency shift with radial distance. However, it is clear in Fig. 5.23 that the expected shape is not exactly linear. One can easily imagine though how, with limited data, a linear fit might look appropriate. Also, there is a significant difference between the effect on clouds with different charge. This is because the smallest clouds are somewhat in-between the spheroid and Gaussian limits, but the biggest clouds are fully in the spheroid plasma limit. This means that the way their lengths will will change with k_2 will not be identical. However, this effect should be overestimated here for the following reasons:

1. Because the clouds with more charge also have faster equilibration times, their heating will be overestimated more than for the smaller clouds.

2. Because of a cloud's charge and length effect on its displacement (see the next section), clouds with more charge are displaced farther, and we compare clouds at equal radius, not clouds subjected to equal k_2. This has the effect of stretching out the curves in Fig. 5.23 horizontally.

Nonetheless, if this explanation is correct, at least a few radians per second of phase difference between the smallest and the biggest clouds is due to the bigger clouds being adiabatically compressed by a bigger factor. This will nonetheless be ignored going forward, because the model described so far is not in any way accurate.

If I had known about this effect before finishing my experimental work, I would have invested significant effort into investigating this phenomenon. For example, if I had extended the measurement times by about a factor of four, I should have been able to observe an exponential decay in cloud temperatures due to cyclotron cooling—the timescale is about 4 s in this 1 T magnetic field. Of course, I would have collected more data and tried to show more thoroughly how this effect depends on k_2 and k_4. This phenomenon also presents opportunities for measurements of properties of the clouds, including their perp/parallel mixing timescales and their absolute temperatures in deep trapping potentials. We have no other way of accessing this temperature—we only measure cloud temperatures after they have significantly adiabatically expanded.

5.4.4 Charge determination

Regardless of the issue posed in the earlier section, my intention in this measurement was to observe phase differences between clouds with different amounts of charge, and there's no reason not to continue with this analysis. Despite a poorly understood variability with r, this phase difference is clearly visible.

First, I find the phase difference between a cloud at radius r and and the phase predicted by a linear fit to the 2.5 mV clouds. Next, as to not ignore the charge-caused phase shift of

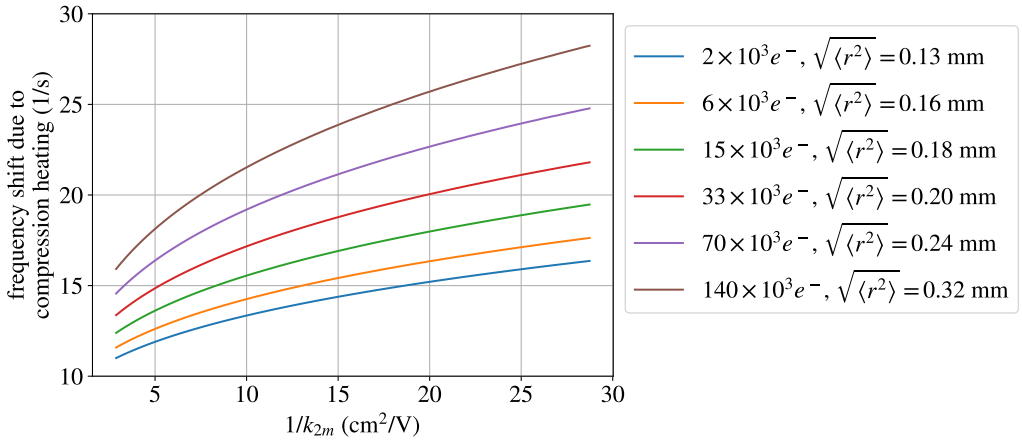

Figure 5.23: The predicted frequency shift of clouds is shown as a function of the reciprocal of the trap constant used to move the clouds off axis. The values of $1/k_{2m}$ used here are the same values used to move the clouds off axis by distances of 30–300 pixels. The calculation is performed with the six cloud sizes considered throughout the rest of this section. The approximate root mean square radii and average charge of the six cloud sizes is given on the right.

the 2.5 mV clouds themselves, I plot the average phase shift of the 2.5, 5, and 10 mV clouds versus their average brightness on the MCP (which is close enough to linear with charge for these small clouds). I extrapolate this average phase shift to 0 mV with a quadratic fit and apply this offset to all the clouds. Obviously, this procedure introduces error in the form of a constant offset. That error is most significant for the smallest clouds, and probably ultimately small compared to even the charge of the 2.5 scoops, but we should keep in mind that the charge measurement for the 2.5 and 5 mV scoops might be inaccurate now.

Next, for the n'th extracted cloud with a particular step size, I find the slope of how that phase difference increases with time. Of course, this is only possible when that cloud was successfully imaged on the MCP in at least two of the four datasets. The results of this are plotted in Fig. 5.24 on the left. Next, this frequency difference is related to the total charge of the cloud through the equation:

$$\Delta\omega_r = 1.00273\frac{Nq}{4\pi\epsilon_0 B R_w^3} - 6\frac{k_4\langle z^2\rangle}{B} \tag{5.26}$$

The value $k_4\langle z^2\rangle$ is averaged over the two trapping potentials (c) and (d) where a variable time is spent. In each of these potentials k_4 is found with electrostatic modelling, and $\langle z^2\rangle$ is found for a given charge using the theory in Sec. 5.4.1. As described in that section, the contributions from temperature and spheroid theory are simply added, and since a constant temperature is assumed (and weakly measured), it actually does not contribute any phase shift between clouds. The spheroid theory requires the mean square radius as an input, so the clouds' imaged mean square radius is used. The spheroid theory gives rise to a nonlinear relationship between phase and charge, so Eq. 5.26 is inverted numerically. Ultimately the two terms in Eq. 5.26 act in the same direction (because the length was greater for the well

with negative k_4), and the length effect is about twice as big. Finally, the extracted charge is listed in Fig. 5.24 on the right.

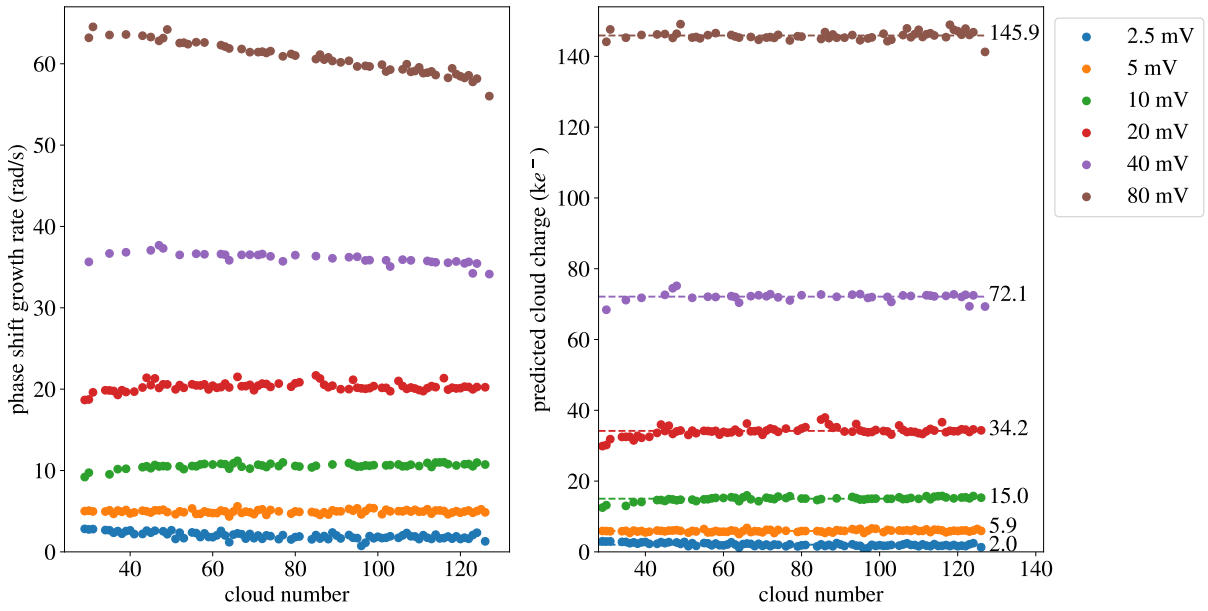

Figure 5.24: On the left, the phase growth rate is plotted for clouds sequentially extracted from a reservoir. On the right, the total charge of these clouds is inferred from the phase shift growth rate. As with other methods of charge determination, the average is denoted with a dashed line and the value of that average is written on the right in thousands of electrons. As stated in the text, the first 28 clouds are used to determine the position of the trap center so their charge was not measured.

The results in Fig. 5.24 are in remarkable agreement with the Faraday cup measurement shown in Fig. 5.2. Also, the clouds extracted with 80 mV steps exhibit a mostly constant total charge, indicating that their falling phase shift growth rate was entirely due to their radius increasing and their length thus decreasing. This is in good agreement with the the very slow charge growth rate predicted in Sec. 2.2. The charge ratios are also reasonably consistent with the lower, more linear MCP gain of 1050 V, but this measurement suggests that some MCP nonlinearity persists with this lower gain. In conclusion, I believe this to be the most reliable charge measurement—except for the smallest clouds where one should still assume MCP linearity to extrapolate from larger clouds. However, because of its complexity and novelty of this measurement technique I certainly needed the other measurement techniques as verification. Each of those techniques had their own issues, so I'm glad to have several forms of independent verification.

5.4.5 Charge and length effects on cloud displacement

Finite length and image charge effects can also be seen in the displacements of the clouds from the trap center in Fig. 5.17. As somewhat of a review of an earlier section, when a cloud is adiabatically lowered to a shallow trapping potential, it orbits a position displaced from

the true trap center by a distance $\delta = \epsilon/k_{2i}$, where k_{2i} is the shallow trap's well constant and ϵ is the magnitude of the transverse electric field due to patch potentials. We then quickly return to a deep trapping potential with well constant k_{2f}, and the cloud begins to execute a magnetron orbit of magnitude $r = \epsilon(1/k_{2i} - /k_{2f})$. Thus in Fig. 5.25 I plot the displacements of the clouds from the trap center to observe a roughly relationship with $(1/k_{2i} - 1/k_{2f})$. To avoid having any gaps, all of the data shown in Fig. 5.17 is combined into one plot in Fig. 5.25. Then in Fig. 5.27, after fitting a quadratic function to the 2.5 mV data, the linear part of that

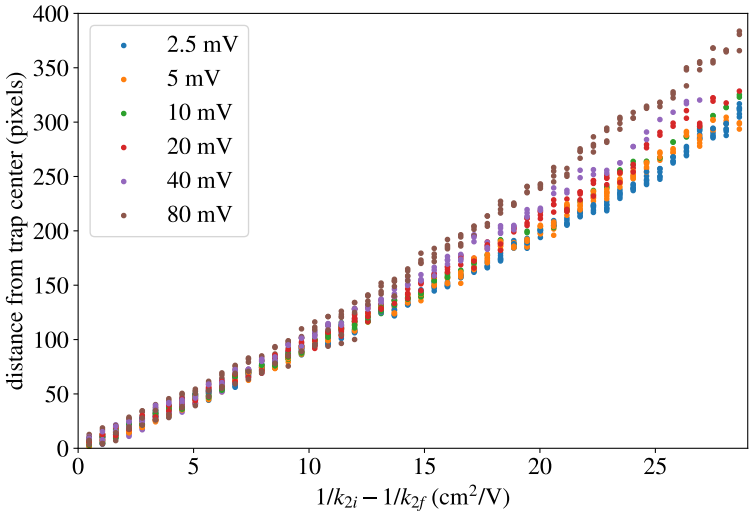

Figure 5.25: The distance between the trap center on the MCP and the position on the MCP that a cloud's center lands is plotted against $1/k_{2i} - 1/k_{2f}$, and we expect to find a roughly linear relationship. The $1/k_{2i}$ values used in this experiment were linearly spaced, and all clouds are subjected to the same k_{2f}.

quadratic function is subtracted. The first thing I'd like to highlight is the obvious presence of a quadratic term in the displacement. In Sec. 3.13 I discussed nonlinear corrections—that with higher order terms in the patch potential one could find $\delta = \epsilon/k_{2i}(1 + \kappa\epsilon/k_{2i}R_w)$ for some $\mathcal{O}(1)$ constant κ. Unfortunately, because κ is a linear combination of two different terms in the Laplace equation, it isn't so interesting to measure. Next I will explain the clear increase in the displacement with charge. In a shallow trapping potential, the cloud is in equilibrium (at the center of the magnetron orbit) when the $z-$averaged electric field due to the trap electrodes is equal and opposite to the $z-$averaged electric field due to patch potentials. Luckily, because of directional patch potential measurements (see Sec. 6), we can actually analyze both cases. However, the directional patch potential measurements in the vicinity of this measurement are actual remarkably linear with axial position, and so any z-averaged electric fields should be roughly equal to unaveraged electric fields. This is demonstrated in Fig. 5.26, and this is compared to the effect of averaging the trapping potential over z, which has a very significant effect for some of the longest clouds considered. For this reason, z-averaged patch fields are neglected in the rest of this analysis.

The effect of cloud length is readily seen in Eq. 5.2; the z-averaged transverse electric field is $(-k_2 r + 6k_4\langle z^2\rangle)r\hat{r}$. Thus a cloud's length shifts the effective k_2 value by $k_{2L} = -6k_4\langle z^2\rangle$. Similarly, a cloud's image charge shifts its effective k_2 value by $k_{2Q} = 1.00273Nq/4\pi\epsilon_0 BR_w^3$.

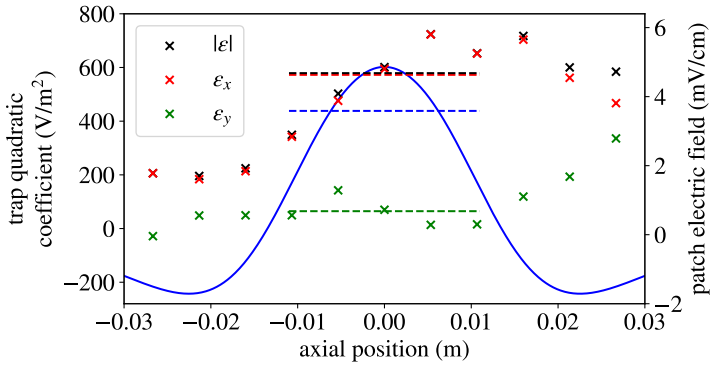

Figure 5.26: In blue (with the left vertical axis), half the second derivative of the on-axis trapping potential is plotted. That is—the trap constant k_2 as a function of z. This trap constant is then averaged over a length of 2 cm, about the length of the longest clouds considered here. The $z-$averaged trap constant is plotted with a dashed blue line, and it differs from the maximum of the blue curve by about 27%. Next, the red X symbols denote the x component of the transverse electric field due to patch potentials and the green X are the y component. The total magnitude of the transverse electric field is plotted with black X's. The z-averaged ε_x and ε_y values are also plotted with dashed lines, and they barely differ from the central values.

In other words, the effect of charge and length on displacement is essentially the same as its effect on ω_r. When determining a theoretical value for this perturbed displacement, there is some freedom with how one deals with the "cross terms" between nonlinearity and the perturbed k_2 value. Such terms are higher order than the validity of any of these arguments, but they are not insignificant, because nonlinearity, charge, and length together seem to increase the displacement for some clouds by up to 40%. My choice was to say that the unperturbed displacement was given by:

$$\delta_0 = \frac{\epsilon}{k_{2i}}\left(1 + \frac{\kappa\epsilon}{k_{2i}R_w}\right). \tag{5.27}$$

I also ignored k_{2f} in this analysis, which is a very small contribution relative to the other sources of nonlinearity. Then the theoretical value for the charge and length perturbed displacement is:

$$\delta = \frac{\epsilon}{k_{2i} + k_{2L} + k_{2Q}}\left(1 + \frac{\kappa\epsilon}{k_{2i}R_w}\right). \tag{5.28}$$

In more detail, I fit κ and ϵ to the 2.5 mV dataset, then I plot $\delta - \epsilon/k_{2i} - (\delta[2.5\,\text{mV}] - \delta_0)$ in Fig. 5.27. That is, the difference between the charge-corrected prediction and the linear prediction minus that difference for the 2.5 mV. Despite it's complexity, this is the right theoretical prediction to plot with this data. As a reminder, the data has the linear part of a quadratic fit to the 2.5 mV data subtracted from it to make small differences due to charge more visible. Then the fact that we fit κ to the 2.5 mV dataset meant that the length corrections present in the 2.5 mV data are already included in δ even with $k_{2L} + k_{2Q}$ set to zero. However this code can also report in the end how much nonlinearity would be expected

in the 2.5 mV data if κ were zero. The result is that about 40% of the nonlinearity in the 2.5 mV is due to finite length effects, and the rest is presumably due to nonlinear terms in the patch potential (nonzero κ). This length effect for the 2.5 mV data is largely due to its temperature, so smaller clouds would not eliminate this nonlinearity. Also, the experimental confirmation of this effect is nonexistent, and temperature cannot be determined from this data. The clouds all experience the same effect from temperature, so changing what we believe temperature to be would just change our estimate of the coefficient κ. As in the section describing the frequency perturbation due to length and charge, the length of the plasmas is calculated with their measured temperature of roughly 70 K and the spheroid cloud theory, and their charge is taken from the average values in Sec. 5.4.4. The theoretical values are compared to the experimental measurements in Fig. 5.27, and the agreement is very good given the crudeness of this analysis—the neglect of patch field averaging and an arbitrary choice of how higher order nonlinear terms are treated. Given these uncertainties and the spread in the data, this will never be a method of accurately measuring the charge of clouds. However, it is good to have data that verifies this theory for how image charges and cloud length affects displacement due to patch potentials.

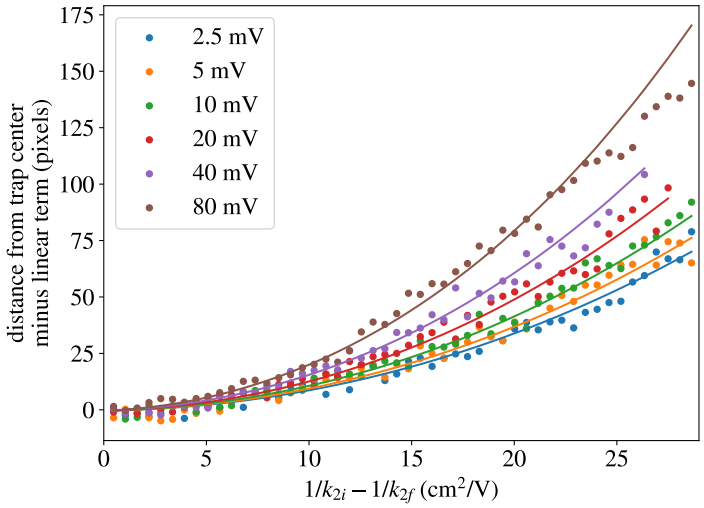

Figure 5.27: Each point is the average displacement from the trap center of 2–4 clouds moved off-axis with identical weak traps (k_{2i}). The linear component of this displacement ϵ/k_{2i} is subtracted so that the nonlinear part and the effect of charge is easier to see. The lines are the theoretical prediction for the effect of image charges and finite cloud length presented in this section.

6 Misalignment and patch potential direction measurements

The misalignment of a Penning trap's external magnet with its electrodes is known to cause plasma expansion [38, 118, 119]. As such it is common practice in the field to put some effort into aligning the two at the milliradian or sub-milliradian level. However, this critical step is often only mentioned as a throwaway sentence in a paper that is otherwise focused on something else. I am aware of four different methods for aligning the external magnet with the trap:

1. Dr. Eric Hunter in his Ph.D. studies at Berkeley quickly moved plasmas along the trap axis and he measured if this operation excited a diocotron. If the external magnet is misaligned with the electrodes, the fast axial motion will move the plasma along a magnetic field line which will cause it to no longer be centered with respect to the electrodes. In some sense I used the same technique in Sec. 2.3.3 to measure the presence of an offset between two electrodes.

2. Some groups will rotate the external magnet until the plasma expansion rate is minimized. In Ref. [120], the expansion rate of an electron plasma is measured versus tilt angle (with a special trapping potential applied which facilitates expansion). The quality of the data indicates that the technique could be used to align the magnet at the 0.1 mrad level. The authors of Ref. [118] also mention adjusting their misalignment angle to minimize expansion-induced heating. On one hand, this assumes that nothing else like patch potentials is causing an effective misalignment. On the other hand, if one's ultimate goal is to minimize expansion, this is probably the best approach. Also, Ref. [120] discusses a plasma which is 0.5 m long. As I will show in this section, in ALPHA-g, either the magnetic field or the electrodes is not straight at the 0.1 mrad level, so it wouldn't really be possible to achieve this level of alignment.

3. In Ref. [121], the author excites a diocotron in a 0.6 m long electron plasma. When the trap is misaligned, the distance between the plasma and the trap wall changes along the diocotron orbit, yielding an oscillating voltage on an electrode. The magnet can be tilted to minimize this signal, and the authors claim to achieve a misalignment angle of order 0.01 mrad. A 0.01 mrad tilt across 0.6 m yields a displacement of 6 μm. This is near the limit of machining precision for a single part, and the Penning-Malmberg trap is an assembly of multiple parts, which probably yields even larger construction errors. This author may be actually minimizing an average misalignment along the plasma or the misalignment near the detection electrode.

4. The ALPHA experiment has historically imaged plasmas from different axial locations in the trap. The misalignment is judged by seeing the plasmas land in different places on the MCP depending on where they were located in the trap axially. I will use this technique throughout this section.

5. The authors of Ref. [122] excite a diocotron orbit and image a plasma at different phases along that orbit in different axial trap locations. The misalignment is judged

by finding a different orbit center as a function of axial distance. I first heard about this from talking to someone from the APEX collaboration who used this to align their multi-cell positron trap [123]. It occurs to me though that there is not much advantage to doing this over just imaging a single plasma without a diocotron.

In this section, I will begin by discussing how I used technique (3) to align the ALPHA-g external magnet with the electrodes in the hopes that it would minimize positron temperatures. Because of experimental timing, no data could be collected on positron temperatures or expansion rates while varying the alignment. Of course, unlike in the usual ALPHA procedure, I will be using electron clouds from a reservoir. This means I can image many plasmas from many axial locations in a much shorter period of time. This enhanced data collection rate will allow me to investigate systematic errors due to patch potentials, and it will allow me to reveal that the misalignment between the electrodes and the external magnet cannot simply be characterized by a single angle.

6.1 Aligning the ALPHA-g magnet

If an electron cloud is moved slowly along the electrodes, its magnetron radius will be conserved adiabatically (see Sec. 2.3.3). The cloud will be confined in an electrostatic maximum in the axial direction (z), but the magnetron motion will be around an electrostatic minimum in the transverse direction (x, y or r, θ). Thus if the cloud is moved slowly, it will follow the electrostatic minima created by the electrodes. When the cloud is imaged, it moves toward the MCP along a magnetic field line quickly enought that $\mathbf{E} \times \mathbf{B}$ drift can be neglected (see Sec. 3.5). Assume for now that the magnetic field strength within the trap is a constant magnitude B and that it is misaligned with the electrodes by an angle $\theta \ll 1$. The center of magnetron motion created by the electrodes at axial position $z = 0$ and the center of magnetron motion created by the electrodes at $z = h$ will fall along different magnetic field lines. Within the trap, those field lines will be separated by a distance $h\theta$. If we follow these magnetic field lines to the MCP, they will be separated by a distance $h\theta\sqrt{B/B_{\mathrm{MCP}}}$, where B_{MCP} is the magnetic field strength at the MCP (see Sec. 3.5). This concept is depicted in Fig. 6.1.

In ALPHA-g, clouds were drawn from a reservoir then moved a variable distance along the trap axis. When a cloud reached its desired measurement position, we waited a random time so that clouds imaged from the same axial location would not have identical magnetron phases in case of any phase-locked sources of magnetron motion like the intrinsic magnetron (see Sec. 2.3). Then the cloud is sent toward the MCP to be imaged. The potentials each cloud is confined in before imaging are shown in Fig. 6.2. Fig. 6.3 shows imaged cloud center positions as a function of their distance along the trap axis.

Once the alignment was measured, the external magnet could be tilted to try to decrease the spread in cloud positions on the MCP. The external magnet, usually called the "Babcock magnet" weighs several tons and is 2.7 meters tall. It can be tilted by turning large screws holding it from below. Since the desired tilts were on the order of a few millimeters, four dial indicators were used to judge how far the top and bottom of the magnet moved when we turned the screws (two possible directions of displacement on the top and bottom, for a total of $2 \times 2 = 4$).

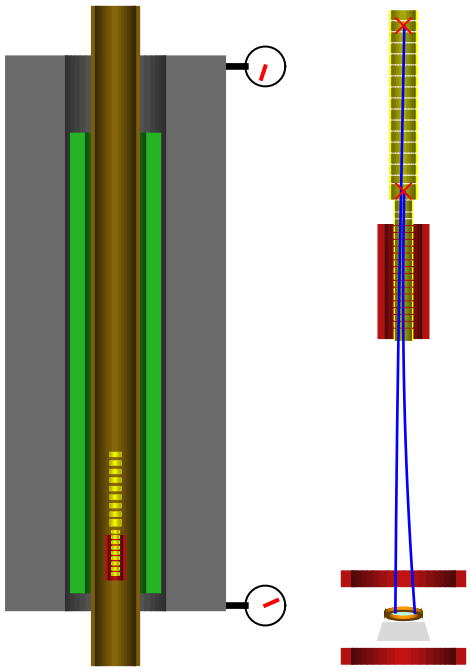

Figure 6.1: A cartoon explaining the basic idea behind aligning the ALPHA-g magnet. On the left is a depiction of the external magnet's cryocooler-cooled cyrostat (gray), the ALPHA-g detector (green), the internal liquid helium cryostat (brown), the ALPHA-g electrodes (yellow), and the bottom solenoid (red). On the top and bottom dial indicators are shown, which allow us to gauge how far the magnet has moved. The magnet cryostat is about 2.7 m tall, and the electrodes are about 0.6 m tall. On the right, I have zoomed in on the electrodes. Additionally, trajectories of electron clouds are shown after being dumped toward the MCP from two different axial locations in the trap. An initial distance of a few millimeters is magnified to several centimeters by the expanding magnetic field lines. The MCP/phosphor screen imaging detector is shown, along with the mirror that allows us to image the back of the phosphor screen. Three additional coils (only two are shown in red, the third is farther below the MCP) boost the magnetic field at the MCP to about 0.027 T. Neither image is to scale, but they are reasonably close. The most inaccurate part is that the MCP is about twice as far away from the bottom of the electrodes.

Fig. 6.4 shows the measurements of the alignment taken in the process of moving the Babcock magnet. The entire story of each measurement is as follows:

(a) This is the first measurement, performed in November of 2021 to see if the alignment was the cause of the positron expansion issue (discussed in Sec. 3.7). The misalignment angle was indeed about 6 times what it is in ALPHA-2, but ultimately patch potentials were the underlying cause of the issue. This first measurement revealed something surprising: the magnet and the electrodes weren't simply misaligned by an angle; the angle changed around electrode 21. However, this first measurement was performed with the "bottom solenoid" energized, the magnet which boosts the magnetic field from

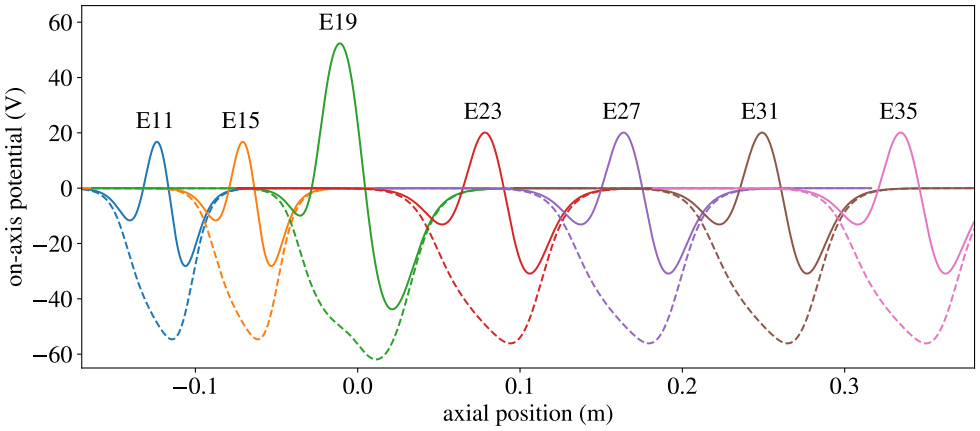

Figure 6.2: An electrostatic model of the trap is used to find the on-axis electrostatic potential confining clouds just before imaging them from seven example locations throughout the trap. Solid lines show the potential before imaging the cloud, and dashed lines show the potential we transform into to release the cloud toward the MCP.

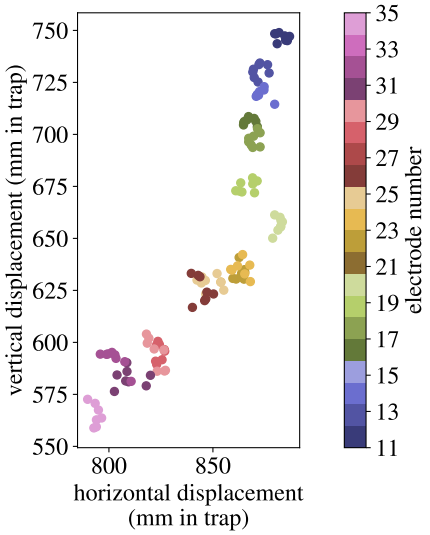

Figure 6.3: The imaged cloud positions on the MCP are shown for 13 axial locations throughout the trap. The horizontal and vertical positions on the MCP are converted to transverse distance in the trap using the MCP magnetic field expansion ratio.

1 T to 2 T for the lower electrodes (roughly electrodes 1 to 19). Thus it seemed logical that the Babcock and the lower solenoid might have different misalignment directions, and so the misalignment with the magnetic field lines would change angle where the lower solenoid started having a significant effect. It should be noted that the bottom solenoid is in the same cryostat as the electrodes and the relative positions of the two are fixed—the electrodes are inserted into a stainless steel cylinder with extremely tight tolerances. The bobbin that the bottom solenoid is wound around is attached to the same cylinder. Therefore, it was thought that the bottom solenoid would be

better aligned than the Babcock, which can freely move by several millimeters relative to the electrodes. It seems from the deviation imposed by the solenoid, though, that the bottom solenoid is misaligned by about 0.5 mrad. The only difference between measurements (e) and (f) is the activation of the bottom solenoid.

(b) This is a repeat measurement taken just before moving the magnet to see if the alignment had drifted. It should be noted that these first two measurements were taken with a worse performing reservoir than the rest. My best hypothesis is that the reservoir had higher initial scoop magnetron because patch potentials were very strong—these measurements were performed when ALPHA-g had the "egregious patch potentials" that prevented successful antihydrogen formation in 2021. This in turn leads to a bigger spread in measured imaged cloud positions, even after averaging 8 clouds per axial location.

(c) Before this measurement, the Babcock magnet was moved to try to reduce the misalignment angle. According to the dial indicators, the Babcock was rotated by 1.33 mrad horizontally and 1.56 mrad vertically (obviously the physical vertical direction, as in "away from the Earth," is actually the axial direction, and all rotations are perpendicular to this, I mean horizontally/vertically with respect to the MCP images, and the positions of imaged clouds shown in Fig. 6.4). Unfortunately, I was incorrect about which horizontal direction the trap should be rotated, so while the vertical misalignment was improved, the horizontal misalignment was nearly doubled. There are many minus signs involved in figuring out which way to rotate the magnet. We have a camera pointing at a mirror which shows the back of the phosphor screen, and our plasmas hit the front of this phosphor screen. The resulting image reflects the positions of the electrode within the magnet, but it is the magnet that we can freely rotate.

(d) I wanted to fix my mistake, but there were not sufficient personnel around to do a proper magnet move. I think I was desperate because no further time had been allocated toward aligning the magnet in the near future. There are screws holding the Babcock magnet in place, which are not ordinarily for moving the magnet. I pushed one of these screws further into the magnet and backed off the screw on the other side. At the time the indicators had been removed from the bottom of the magnet, so I don't have a definite measurement of the expected tilt. Judging only from the indicators on the top, where most of the motion should have happened with this particular movement, this resulted in a predicted tilt of 0.11 mrad vertically and 1.48 mrad horizontally. Again this is roughly consistent with the change measured.

(e) Later in that shift, a more senior member of the collaboration said they thought the previous action might put a strain on the outer wall of the Babcock magnet, so I was told to undo it. Moving the screws back into position didn't fully move the indicators back to their initial positions. This action resulted in a predicted tilt of 0.07 mrad vertically and 0.48 mrad horizontally in the opposite direction as step (d).

(f) This measurement was performed with the bottom solenoid energized. The magnet was not moved from (e) to (f). I include this measurement to show the influence of

the bottom solenoid on the alignment of the lower electrodes. The bottom solenoid extends from electrode 1 to 16. I also include this measurement because measurement (g) also occurs with the bottom solenoid energized.

(g) One final alignment movement was performed before the successful ALPHA-g experimental run in 2022. We achieved a predicted movement of 0.12 mrad vertically and 1.89 mrad horizontally. We were not able to tilt horizontally any further because the Babcock magnet collided with the frame it was held in. The variance of the measurements and the difference between predicted and measured tilts suggests an error of roughly 0.2 mrad on all the measurements. The rest of this section will describe more precise measurements of the alignment in this state.

6.2 Improved misalignment and patch potential direction measurements

In 2022, after we had successfully trapped antihydrogen in ALPHA-g, there was a brief window where we were considering improvements to the experiment before trying to actually measure gravity. At the time, I was arguing that the reservoir diocotron, the initial cloud magnetron, and the the higher positron temperatures in ALPHA-g versus ALPHA-2 might be improved by further movements of the Babcock magnet. I no longer believe that the misalignment is a significant factor in the reservoir's diocotron and the cloud magnetron. I blame these on complicated plasma physics and patch potentials respectively. But I still think that ALPHA-g's lower trapping rate is primarily caused by its alignment being worse than in ALPHA-2 (see Sec. 4). To better investigate this hypothesis, I requested and was granted one shift to do a more thorough measurement of the alignment. My stated purpose was to measure the alignment all the way down to electrode 2, where the reservoir normally sits. I was also proposing a new technique that could eliminate the influence of patch potentials on the misalignment measurements. The collaboration didn't know that I had come up with a way to measure the direction, not just the magnitude of patch potentials. I had wanted to perform this measurement for a long time, but I couldn't justify spending experimental time on the idea, because the results wouldn't change experimental procedures or modelling of experimental results. When I realized this patch potential direction measurement could also be an alignment measurement, and that I had good reason to believe alignment was causing significant problems for the ALPHA-g measurement, the whole thing suddenly became politically viable.

The idea for these measurements is this—in the patch potential measurements explained in Sec. 3, we create a shallow trapping potential to move clouds off axis by applying a small voltage (0.1–1 V) to a single electrode or a pair of adjacent electrodes. Then to image the cloud, we need to morph to a "pre-dump" potential where the cloud is confined at a negative absolute voltage, so that when we release the cloud it has some kinetic energy that allows it to reach the MCP. Now I will make the shallow well also a pre-dump well. These potentials are shown for one axial trap location in Fig. 6.5. These trapping potentials require a lot more algorithmic sophistication to produce. First, I find a sequence of voltages on six adjacent electrodes that will allow me to vary the trap depth constant and the axial

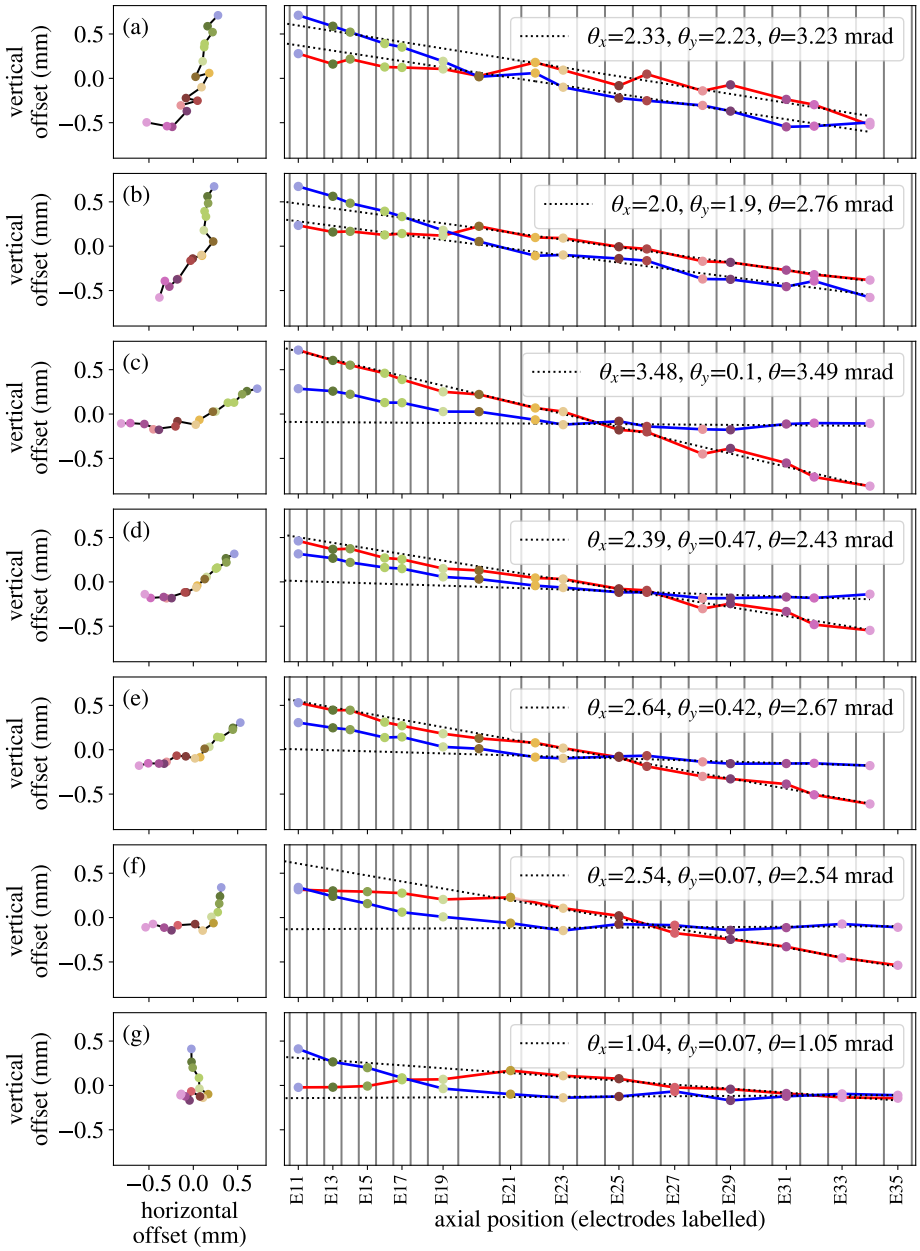

Figure 6.4: The collection of alignment measurements performed after various changes to the position of the external magnet. On the left, the averaged positions of cloud centers is shown. On the right, the horizontal positions are plotted in red, and the vertical positions are plotted in blue versus axial position, with the electrode numbers labelled (the entire axial distance shown is 48.3 cm). A line is fit to the horizontal and vertical positions between electrodes 21 and 35. The inferred horizontal and vertical misalignment angles, and the total misalignment angle are shown in the legend.

position of the electrostatic potential maximum in the vicinity of two electrodes. For the on-axis potentials shown in Fig. 6.5, the voltages [-18, -18, V_3, V_4, -20, -20] are applied to six adjacent electrodes, and varying V_3 and V_4 allows me to change the axial position and depth

of the well. I have come up with two equally usable methods for finding values of V_3 and V_4. The first method is gradient descent—I set a desired k_{2m} value and a desired axial location (z) of the electrostatic potential maximum. I give a gradient descent solver the ability to adjust V_3 and V_4, and it finds voltages on those two electrodes which provides the desired k_2 and z. In a second method, I simply scan a 2–D grid of V_3 and V_4, and for each pair of voltages I compute k_2 and z. Then for each desired pair of k_2 and z values, I identify the four pairs of V_3 and V_4 values that come closest to these k_2 and z values and I use linear interpolation to get the desired values.

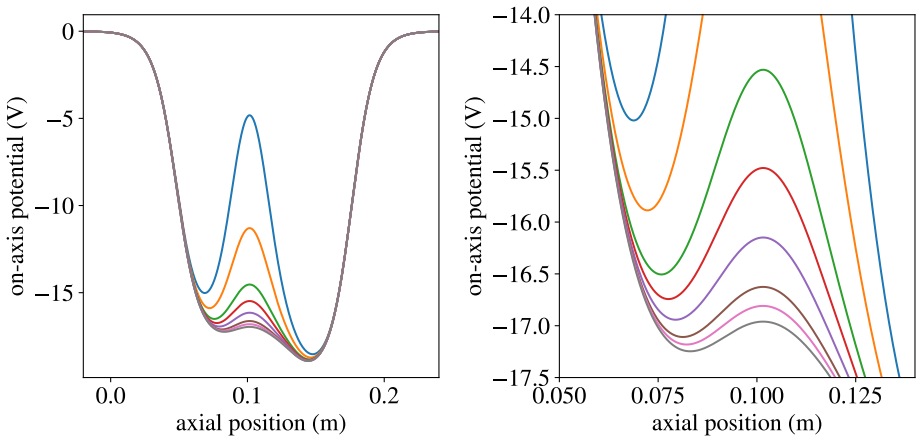

Figure 6.5: The 8 shallow pre-dump wells used to measure the alignment and patch field direction in one axial trap location. The plot on the right is simply a zoomed-in version of the plot on the left.

Experimentally, clouds are drawn from a reservoir then moved to a desired axial measurement location. Then the trapping potential is adiabatically changed to the shallow pre-dump well (see Sec. 3.3 for a description of the adiabatic movement). To image the clouds, V_3 and V_4 are changed quickly to $-19\,\mathrm{V}$ and $-19.5\,\mathrm{V}$, and the two electrodes to the left are changed to $-15\,\mathrm{V}$, releasing the clouds toward the MCP with about 15–18 eV of kinetic energy. In my first attempt to conduct this experiment, the clouds were only released with 3 eV of kinetic energy, and they did not reach the MCP (MCP images simply did not show a cloud). This is not entirely surprising—the ALPHA collaboration has always known that plasmas dumped with insufficient kinetic energy do not reach the MCP. This is likely because of stray voltages between the trap and the MCP that reflect the particles. This occurs for both positrons and electrons, indicating that there are positive and negative stray voltages between the trap and the MCP. Preparing this measurement takes several hours of my own time and several more hours of computation time, so it was not feasible to scan between 3 eV and 18 eV. I simply observed that 3 eV didn't work, and I increased the energy to a value that I had seen work in the past.

Before discussing results, because I am now measuring the direction of patch potentials, I should introduce some new notation. The electrostatic potential produced by patch potentials is now:

$$\Phi_p(z, r, \theta) = \varepsilon_x r \cos\theta + \varepsilon_y r \sin\theta, \tag{6.1}$$

where θ is now defined relative to the $+x$ axis in MCP images. The cloud is displaced from the trap center by $\vec{\delta} = \vec{\varepsilon}/k_2$, where $\vec{\varepsilon} = [\varepsilon_x, \varepsilon_y]$. It should be noted that the transverse electric field is actually $\mathbf{E}_\perp = -\vec{\varepsilon}$.

The data—positions of cloud centers on the MCP converted to transverse distance inside the trap—for six patch potential direction and alignment measurements is shown in Fig. 6.6. Fig. 6.6 shows the measurement results in six axial trap locations spanning the length of one and a half electrodes. The gradual change of the patch field is visible in the change of the spread of the points, and the gradual change in the trap center is visible in the change of the positions of the red X. For each axial trap location, clouds were imaged after being subjected to 8 different shallow pre-dump potentials (the ones shown in Fig. 6.5 come from one axial trap location). For each shallow pre-dump potential, four clouds were imaged. At the time, it came as somewhat of a surprise that the clouds did not simply fall along a line. Rather, the data is consistent with clouds falling in a random location along a circle, with the center of the circle being displaced from the trap center by a distance $\vec{\varepsilon}/k_2$. This indicates that the clouds have a phase-locked magnetron motion (probably the intrinsic magnetron, see Sec. 2.3.1). As clouds are adiabatically moved off axis in different shallow wells, they end up in different final magnetron phases. But clouds that were subjected to the same shallow wells have the same phase. The difference between imaged cloud positions subjected to identical trapping potentials is on the order of one pixel in the camera images—which is probably just image analysis error. Had I been aware of this issue in advance, I would have randomized the magnetron phases and I would have used more clouds per axial location. Of course, other models are also possible. For example, the clouds could have been thrown off axis by adiabatic invariant breaking (see Sec. 3.3). More data would be necessary to differentiate between these hypotheses.

For the analysis, I used five fit parameters for each dataset. First, the x and y position of the true trap center (a red X in Fig. 6.6). Next, the radius of the initial magnetron motion of the clouds (the radius of the black circles in Fig. 6.6). Finally, the two components of the patch field ε_x and ε_y. The fitting procedure begins by averaging the four imaged cloud positions for each trap depth k_{2m} (the blue X's in Fig. 6.6). Then for each k_{2m}, a trap center is computed as $\vec{\varepsilon}/k_2$, and the error is the squared distance between the averaged cloud position and the circle. I used gradient descent to minimize the total error across the 8 k_{2m} values.

In addition to accounting for patch potentials in the alignment measurements and performing far more axial measurements, I wanted to extend the measurements to lower electrode numbers. The following discussion will be irrelevant and uninteresting to readers from outside of ALPHA, and readers from ALPHA will be amazed I went through all this trouble. At this point I need to explain that electrodes 1–9 are controlled with a separate electrode voltage controller than electrodes 10–36. The controller for electrodes 1–9 is called the "recatching sequencer," and electrodes 1–9 are referred to as the "recatching trap" because they are responsible for "catching" the antiprotons and positrons from the catching trap and the positron accumulator. The controller for electrodes 10–36 is called the "atom sequencer," and those electrodes are called the "atom trap" because in these electrodes the antiproton and positron plasmas are combined to form antihydrogen. This setup is extremely convenient for cloud-based measurements. Cloud extraction can be done in the recatching trap, and cloud-based measurements are performed in the atom trap. When the cloud-based mea-

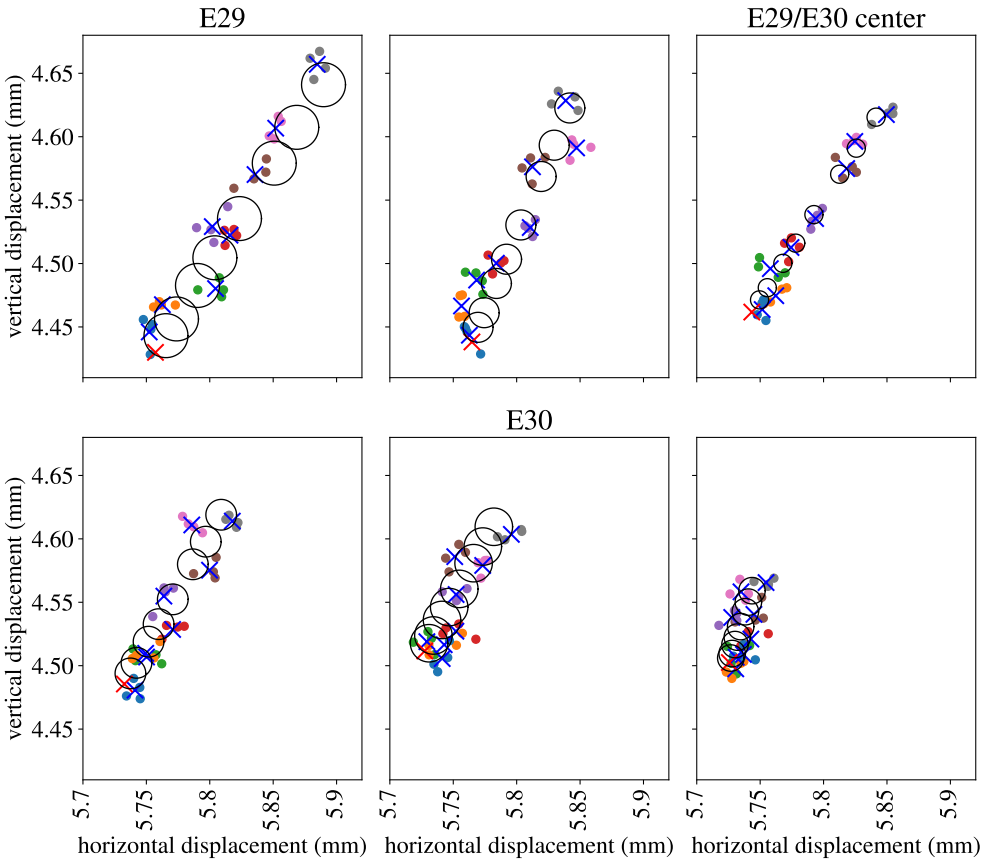

Figure 6.6: Imaged cloud center positions are shown with dots; they are converted to transverse distance inside the trap. The colors of the dots correspond to the shallow pre-dump potentials shown in Fig. 6.5. The blue and orange points were subjected to the deepest pre-dump potentials; the gray and pink points correspond to the shallowest pre-dump potentials. The blue X's are the averaged positions of the four cloud positions for a single shallow pre-dump potential. The black circles represent the magnetron orbit of the clouds, which the blue X's should fall along. The red X is the inferred trap center extrapolating the centers of the circles to infinite k_{2m}. These six measurements occurred in six axial trap locations separated by a quarter of an electrode length, or about 5 mm. The measurements in the centers of electrode 29 and 30, and the measurement between electrode 29 and 30 are labelled.

surement wants a new cloud, it triggers the recatching sequence to perform a new extraction. When that new cloud has reached electrode 9, the recatching sequence triggers the the atom sequencer to take that cloud. Thus the reservoir and cloud extraction can be changed without rewriting the entire measurement procedure, and one reservoir can be plugged into a different cloud-based measurement.

With this in mind, I implemented two improvements so that misalignment measurements could be performed in more axial locations. First, I made a sequence where the reservoir was transferred to the atom trap and clouds were extracted in the downward direction and sent to the recatching trap for a measurement. This reservoir appeared to have a much larger

diocotron, so the clouds extracted from it traced out a circle (see Sec. 2.3). This data is shown in Fig. 6.7. Because of the poorer quality data, only the deepest two shallow pre-dump potentials were used, with more clouds imaged per potential. The difference in the effective trap centers was not statistically significant, so the results from the two shallow pre-dump potentials are simply averaged for a somewhat rougher estimate of the true trap center than in the atom trap. In Fig. 6.9, I plot the alignment results from both the recatching trap and the atom trap.

Next, in order to perform measurements in the vicinity of electrodes 8-12, I made sequences where the recatching trap supplied the leftmost voltages confining the electrons (the voltages [-18, -18] on the left two of six electrodes confining the clouds), and sequences where the atom trap supplied the rightmost voltages (the [-20, -20]). There was only a one electrode wide gap between electrodes 9 and 10 where measurements were impossible, because V_3 and V_4 would fall on electrodes 9 and 10 respectively, massively increasing the complication of the sequences—it's not so hard for the sequencer handling the reservoir to supply a fixed voltage to hold in the electron clouds, it's very hard to make the sequencer handling the reservoir to vary that voltage.

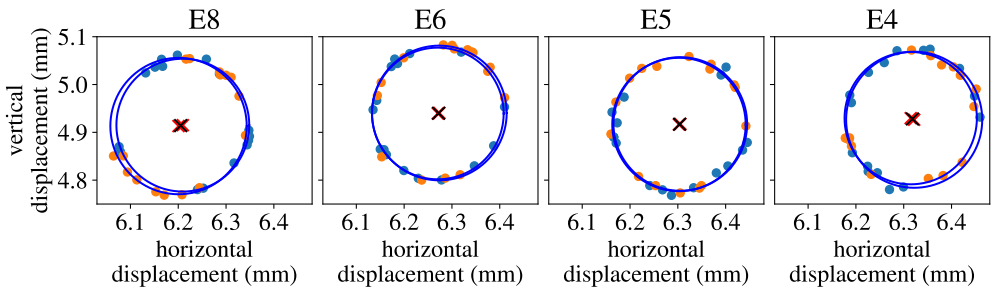

Figure 6.7: Imaged cloud center positions for measurements of the misalignment in four axial locations within the recatching trap. Two shallow pre-dump potentials are used, and the resulting cloud positions are shown in blue and orange. The blue circles are fit to the data from each of the shallow pre-dump potentials, and the centers are indicated with red X's. The two red X's are averaged to infer the trap center, the black X.

The directional patch field measurements are shown in Fig. 6.8. The results are essentially consistent with the directionless patch potential measurements in Sec. 3.7. These measurements are now about six months later than the ones described in Sec. 3.7, further confirmation that patch potentials are static over long timescales. Small differences are probably due to the neglect of nonlinear effects here. As expected, patch field directions are random and vary over roughly the length scale of the trap wall radius (essentially the same as the length of electrodes).

The alignment measurement results are shown in Fig. 6.9. Several features of this graph are highlighted and numbered, and they are discussed below. The list below is organized pedagogically. The paragraph numbers refer to the numbers in Fig. 6.9 where the salient features of the results are indicated.

2. The large patch potential, also visible in Fig. 6.8, clearly has some effect on the alignment measurements, which is exactly what I was trying to avoid with this new mea-

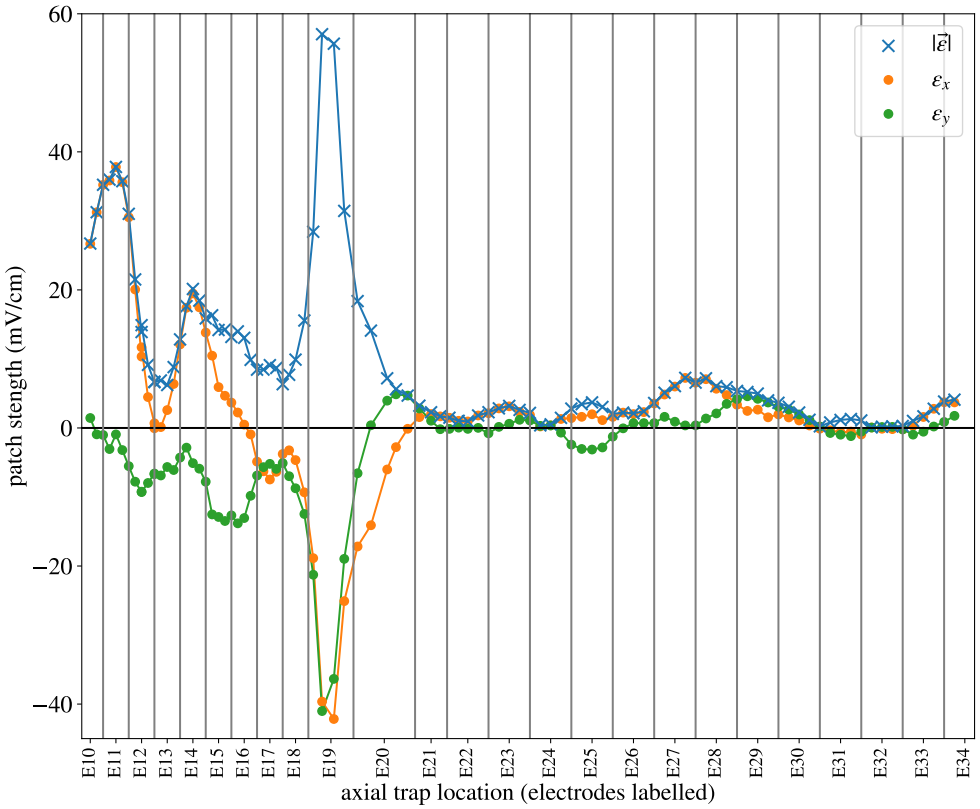

Figure 6.8: Directional patch field measurements from the ALPHA-g atom trap.

surement technique. One can easily imagine that if the points are more spread out in Fig. 6.6, there would be a bigger error in the extrapolated trap center. This is especially true if the displacements deviate at all from the linear model $\vec{\delta} = \vec{\varepsilon}/k_{2m}$. In Sec. 6.4, another theoretical cause for this effect is discussed, and the effect is more clearly visible in a second round of measurements described in Sec. 6.3.

3. A jump between electrode 19 and 20 is clearly visible. The existence of this jump was entirely believable because it occurs where the electrode radius changes (see Fig. 6.1). This jump was independently verified by showing that we can excite a cloud magnetron by quickly moving clouds across this junction. This measurement is explained in Sec. 2.3.3.

5. These "wiggles" are probably real construction errors in the electrodes. The patch field is so much smaller here that error due to patch potentials is too small to account for this $\sim 50\,\mu$m deviation.

6. Likewise, this gap, and some others like it, are probably real. Similar to item (3), they occur on electrode boundaries, but the deviation is closer to $10\,\mu$m, and the junction is simpler because it is the meeting point of two electrodes constructed in the same way.

4. This is the most mysterious feature. The alignment between the electrodes and the magnet seems to deviate around electrode 22. The people involved in the electrode

construction assure me that this absolutely cannot be because of a kink in the electrodes. They say if there was a deviation this big, the electrodes simply would not fit in the cylinder they get inserted into. My first hypothesis for this was that the electrodes might not be centered in the magnet. If B_0 is the homogeneous magnetic field in the center of the trap (roughly E23 to E35), then magnetic field lines expand by a factor $\sqrt{B_0/[B_0 - \delta B(z)]}$. If the trap is off-center by a distance d, we would see deviations in this plot given by $d(\delta B(z)/2B_0)$ assuming $\delta B(z)/B_0$ is small (it reaches a maximum value of 0.2 at electrode 1). Unfortunately, for this to explain what we see here, the magnet would need to be off-center by a centimeter—an entirely unreasonable distance, and it would need to be elevated (shifted vertically) from its designed position by about 5 cm, because the magnetic field actually doesn't start appreciably decreasing in magnitude until around electrode 19. Measurements of the Babcock's magnetic field using ECR [5] have verified that it is elevated by only about 2 cm. We are left with the conclusion that the Babcock magnet's field lines are the thing that deviates around electrode 22. This seems believable to me. Originally, the Babcock's cryostat's bore was aligned very carefully with the trap (at the sub-millimeter, sub milliradian level), but the field was misaligned by over 3 mrad. It was not physically possible to rotate the Babcock's cryostat enough that it would be aligned perfectly with the trap (see the previous section); eventually it collided with other parts of the experiment. This may indicate that the designers focused more on the homogeneity of the field magnitude than the direction. It may also be possible that the field lines are not perfectly straight. However, such direction changes would naturally occur over length scales comparable to the radius of the Babcock magnet (30 cm). This kink occurs over a much shorter length scale: one or two electrodes, or about 2–4 cm. Thus we are left with no convincing explanation for why this feature exists.

1. The magnetic field seems to "straighten out" and align very well with the electrodes around electrode 5. This is probably a similar effect to item (4). For this reason, I did not recommend further movements of the Babcock magnet. At the time, I was wondering if we could improve positron temperatures (for which the alignment in the vicinity of E23 to E35 would be most important) and reservoir behavior (for which the alignment in the vicinity of E2 to E5 would be most important) at the same time by adjusting the Babcock. This result suggested that any improvement to the positron temperatures might damage reservoir behavior. These operations take a few days, and they are somewhat risky (moving a multi-ton object can damage things). Further, the movements are difficult to do precisely, so returning to the previous position might not be possible.

6.3 Second alignment measurement

Because there were so many interesting features and some unknowns in the misalignment measurements described in Sec. 6.2, I was granted a second day to try to improve my measurement technique. We will find that this "improved measurement technique" was not strictly an improvement. Measurements of patch small fields will be significantly improved,

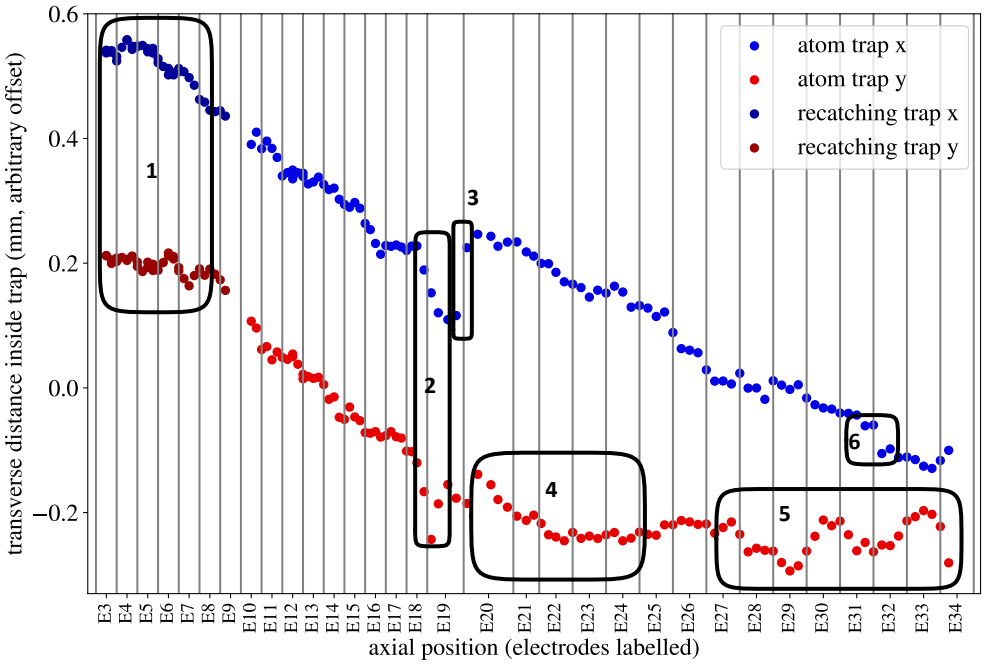

Figure 6.9: The horizontal (x) and vertical (y) deviations of the electrodes from a single magnetic field line are shown versus axial position in the trap. The blue points are the horizontal deviations and the red points are the vertical deviations. Slightly darker points indicate the measurements taken in the recatching trap. Several features are highlighted and discussed in the text.

and the misalignment measurement will be significantly worse. However, this result will reveal the most important systematic error in misalignment measurements.

The most significant change in this second round of measurements was a different choice of shallow pre-dump potentials. My idea was to use six shallower pre-dump potentials to obtain more cloud displacement to better measure the patch field when the patch field was weak. Then two of the eight potentials would be much deeper—nearly the maximum possible trap depth constant k_{2m}. These potentials are shown for one example axial trap location in Fig. 6.10. The shallowest trapping potential here confined the clouds by only 0.1 V, whereas in the previous section the shallowest trapping potential was 0.25 V. As a result, in a few axial trap locations, these weakest trapping potentials were actually not sufficient for confining the electron clouds. The effect this had on imaged clouds is shown in Fig. 6.11. The clouds subjected to the shallowest pre-dump potentials were less bright in MCP images and more spread out. The latter effect occurs because electrons are released from the center of the cloud, and the cloud has to expand to regain equilibrium while conserving its RMS charge radius [8]. This phenomenon only occurred in the vicinity of electrode 19, where we have the strongest measured patch field. Thus it isn't that 0.1 V is insufficient for confining the electron cloud, but that the on-axis potential perturbation due to patch potentials is also of order 0.1 V in that one location, and in this case this perturbation reduced the trapping potential to something that could not confine the electron clouds. This phenomenon is somewhat worrying for patch field measurements in this area—if electrons are

escaping, they are also experiencing a trapping potential that cannot be well-approximated by $\Phi(z) = -k_2 z^2$. Thus their positions are expected to deviate from the linear estimate $\delta = \varepsilon / k_{2m}$.

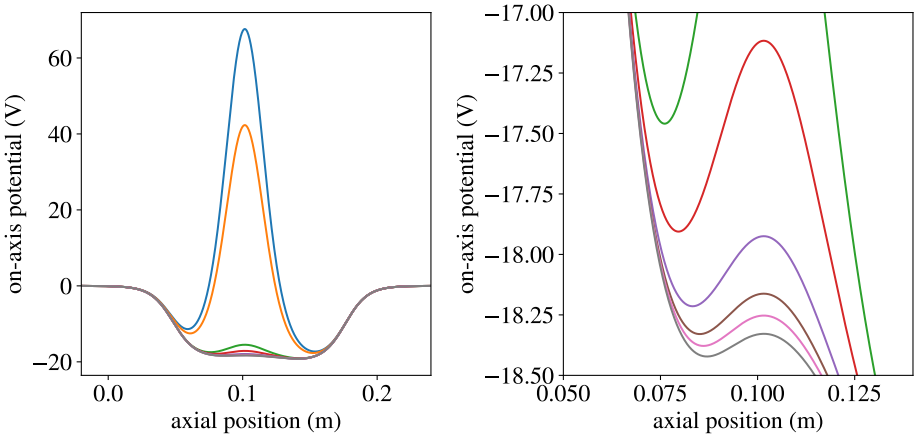

Figure 6.10: This figure is equivalent to Fig. 6.5, but the potentials shown here are those used in the second round of measurements described in this section.

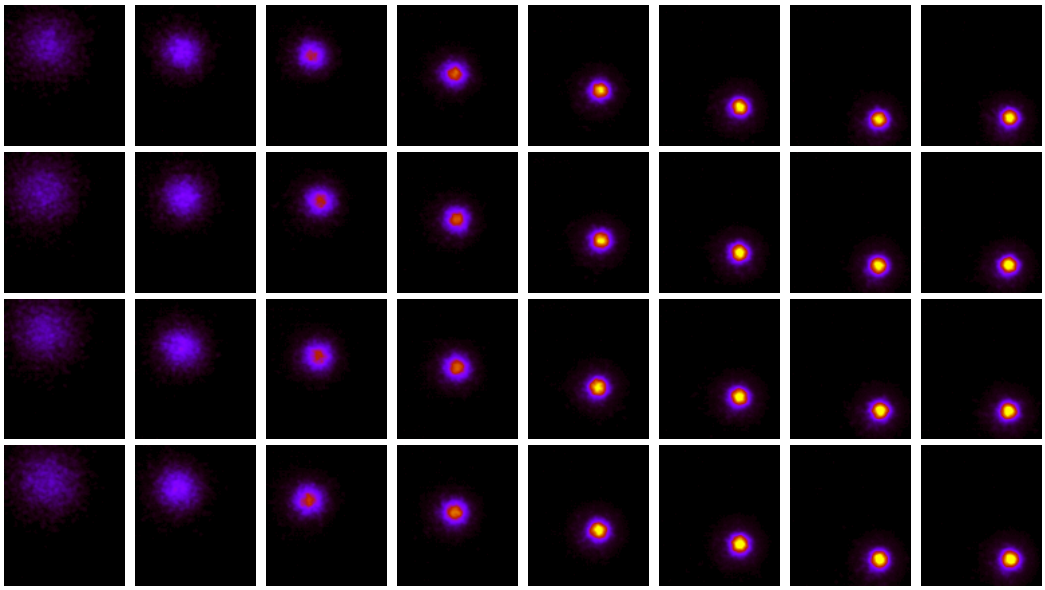

Figure 6.11: The entire set of 32 MCP images used to measure the trap center and patch field in one axial trap location. From left to right, clouds are subjected to stronger trapping potentials, or larger k_{2m} values. The four images in each column are four repeats—differences between repeats are not really perceptible with this image size. The effect of electrons evaporating out of the weak confining potential is evident from the clouds being less bright and bigger on the left. One can also observe the patch field pulling electron clouds to the upper left with lower k_{2m} values.

Another change was that I randomized the magnetron phases by inserting a random wait

just before releasing the clouds toward the MCP. This eliminates a lot of the complication in the fitting procedure described in the previous section—averaged cloud centers no longer fall along the edge of a circle, and instead they should simply fall along a line. So now the fit has one less parameter, and the error for a choice of fit parameters, which is again minimized by gradient descent, is simply the sum of squared distances between each cloud center and its predicted position on the MCP. The data for this measurement and the resulting fits are shown in Fig. 6.12

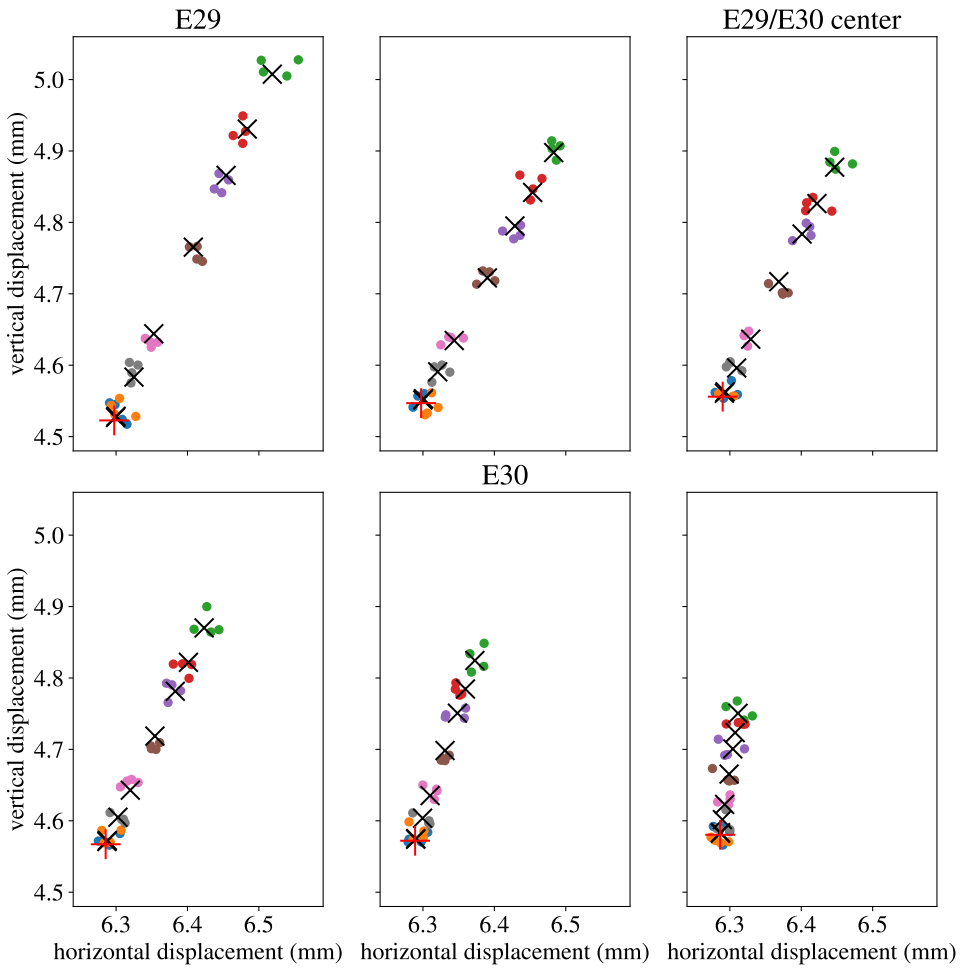

Figure 6.12: Imaged cloud positions are shown for the same six axial locations in the panels of Fig. 6.6. As in Fig. 6.6, the colors correspond to the shallow pre-dump potentials shown in Fig. 6.10. The black X's are the centers of magnetron motion predicted by the fit parameters for each shallow pre-dump potential. The red + is the extrapolated trap center. Unlike in Fig. 6.6, the extrapolated trap center should be very close to the blue and orange points. The absolute positions are different from Fig. 6.6 because another magnet at ALPHA was energized, tilting the magnetic field lines between the ALPHA-g trap and the MCP. Only the relative positions are physically meaningful here.

This new measurement procedure was extremely successful for measuring weak trapping potentials. These results are shown in Fig. 6.13. In fact the measurements are so good that

we could start to infer derivatives of the patch field: $d\vec{\varepsilon}/dz$, which are discussed in Sec. 4 as a potential cause of positron expansion and heating. Unfortunately, the positron heating rate is only measured in a variety of trap locations in ALPHA-2, and these measurements are from ALPHA-g. On the other hand, despite using deeper trapping potentials where clouds should have been closer to the trap axis, the misalignment measurements are much worse, shown in Fig. 6.14. In this new misalignment measurement, a large bump is clearly visible in the vicinity of electrode 19, which is clearly caused by the large patch potential in that area. Looking at the fits which produced this data, there is absolutely no way this error is due to statistical error in the fitting procedure. In the next section, this issue is giving a convincing explanation.

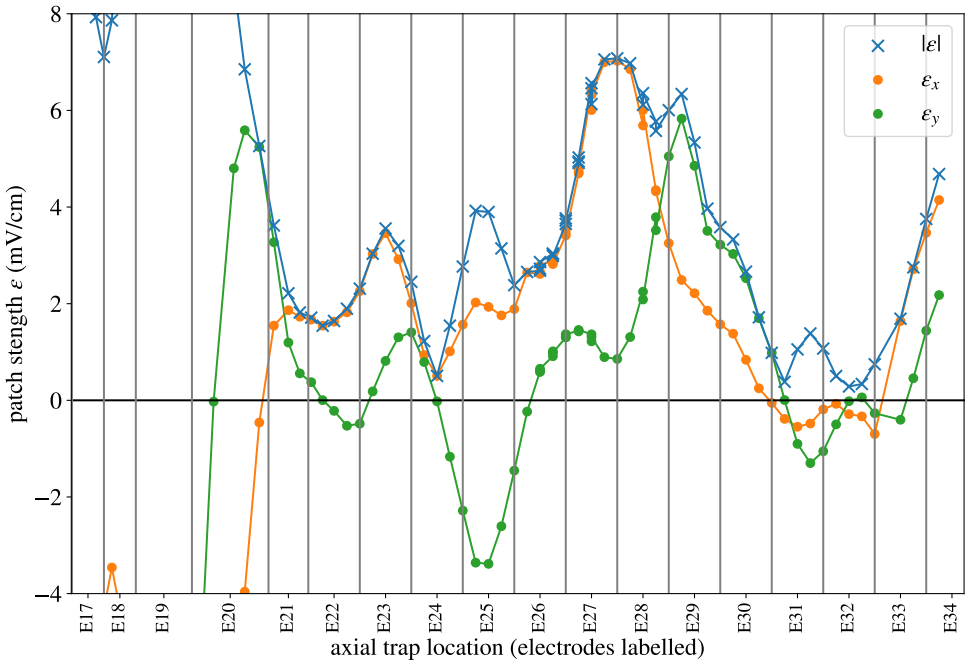

Figure 6.13: The patch field measurements extrapolated from the fits in Fig. 6.12. Unlike in Fig. 6.8, I have zoomed in on the weaker patch fields in the trap region with larger-radius electrodes, because the biggest improvement in the measurement quality is evident there.

6.4 Cloud release dynamics

Despite attempting to extrapolate to infinite trapping potential, patch potentials clearly influence the alignment measurements, especially in Fig. 6.14. This can be explained by investigating the process of imaging clouds in more detail.

When the amplifiers driving the electrodes are asked to change potential as quickly as possible, they are limited by their "slew rate." That is, looking at the amplifier output with an oscilloscope, we observe a roughly linear $40\,\mathrm{V}/\mu\mathrm{s}$ change in the voltage. The response is not precisely linear because the amplifier also has a finite output bandwidth, but this approximation will suffice for this discussion.

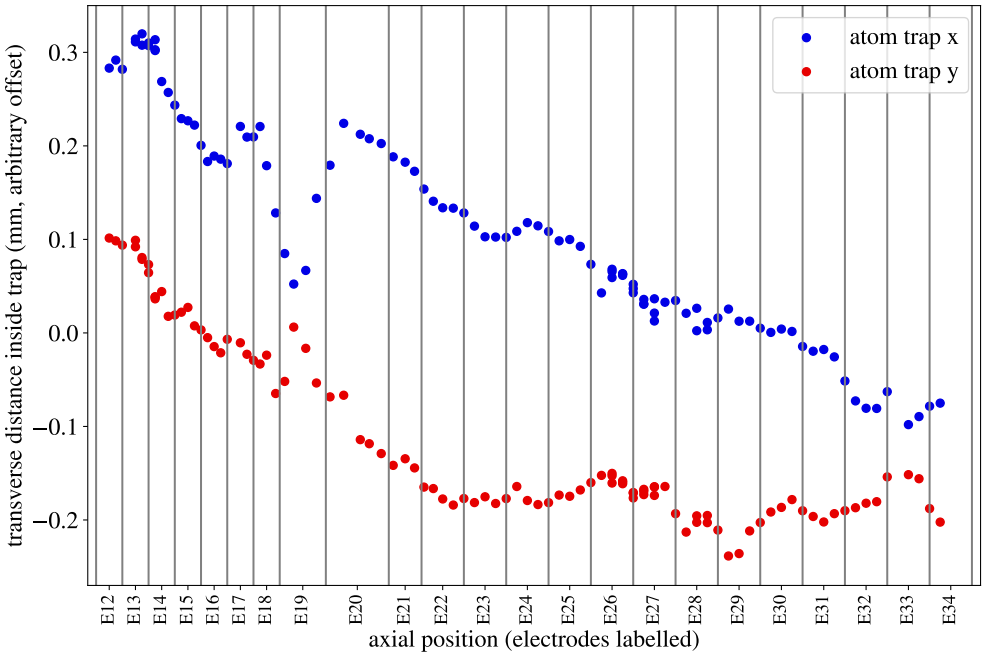

Figure 6.14: The horizontal (x) and vertical (y) deviations of the electrodes from a single magnetic field line are shown versus axial position in the trap. The blue points are the horizontal deviations and the red points are the vertical deviations.

This amplifier output is fed into a passive filter shown in Fig. 6.15. This circuit can be understood conceptually by first removing the 30 pF capacitor, whose impedance is much higher than the other circuit elements at a characteristic timescale of 1 μs. Then we have three low pass filters with increasing resistances, 50 Ω, 1 kΩ, and 3 kΩ. Thus they are somewhat well approximated as three low pass filters multiplied together.

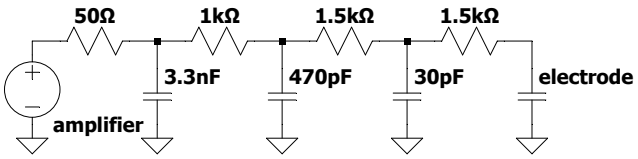

Figure 6.15: A circuit diagram showing the filters between the electrode amplifiers and the electrode.

Different electrodes have different capacitances to ground, and in fact their capacitance may be dominated by the cables between the filters and the actual electrodes. All of the electrode capacitances fall in the range of 650–1000 pF. The larger radius electrodes are around 800 pF, the smaller electrodes are around 650 pF, and electrode 20, having a somewhat unique geometry, is about 1000 pF. Thus the third filter (the one formed by the electrode) has a cutoff frequency around 80–50 kHz, and the other two have cutoff frequencies of 1 MHz and 350 kHz. The electrodes also have mutual capacitances with their neighbors of order 300 pF, which I will ignore in the rest of this discussion because it would significantly complicate the analysis. This will be the biggest inaccuracy in my discussion—it is of order 50%.

Moving forward, I will inspect the voltages use to perform the measurement in the trap location with the biggest patch potential—the center of E19, and I will discuss the deepest shallow pre-dump potential, where it takes the longest time to release the plasma toward the MCP. In the first set of misalignment measurements (Sec. 6.2), clouds are confined by applying the following voltages electrodes 17 to 22: [-18, -18, 17.089, 18.692, -20, -20]. They are released by switching to [-15, -15, −18.5, −19, -20, -20]. In the second set of alignment measurements (Sec. 6.3), we switch from [-19, -19, 128.307, 133.438, -20, -20] to [-19, -19, -19.75, -19.5, -20, -20]. Notice that the voltages -19.75 and -19.5 are in the wrong order for creating a left-facing ramp—an experimental mistake. The clouds are nonetheless released because the on-axis potential does not exhibit this local maximum, but the clouds are only barely released. In Fig. 6.16, the amplifier and the filtering is simulated to find how long it took to release the clouds for each of these two measurements. In the first round of measurements, it took 5.7 μs, and in the second round it took 16.1 μs.

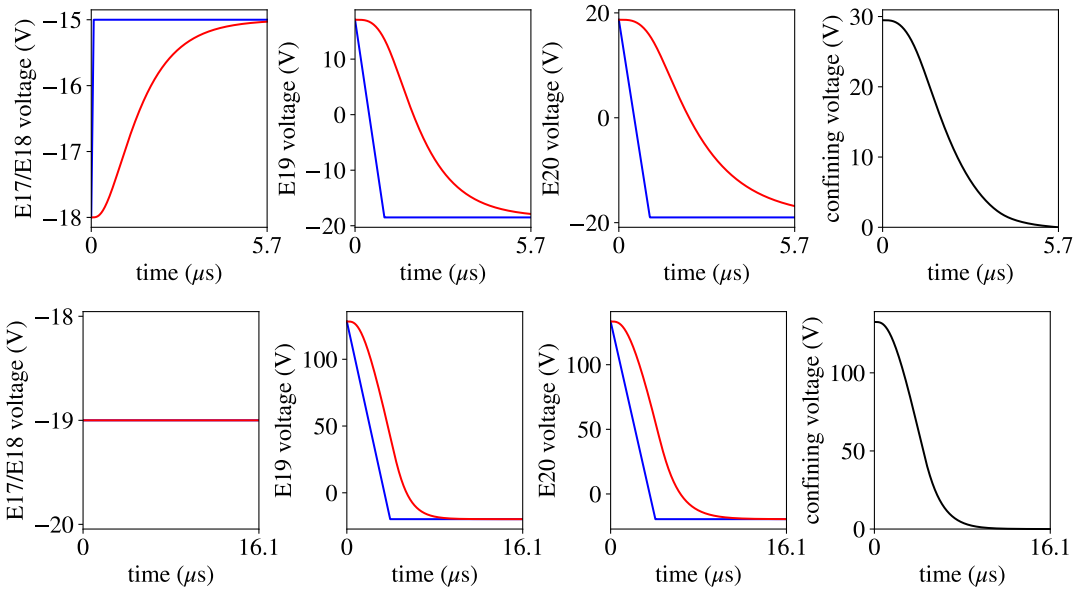

Figure 6.16: The voltages applied to electrodes 17 through 20 in the process of releasing an electron cloud toward the MCP. The first row illustrates the voltages applied during the first round of misalignment measurements (Sec. 6.2). The second row illustrates the voltages from the second round of measurements (Sec. 6.3). The first three columns show the amplifier voltage in blue and the voltage on the electrode in red. The fourth column shows the confining potential for the electron clouds, and the simulation ends when this reaches zero. Note that the horizontal axis differs between the two rows.

In both cases, the time to image the plasma is dominated by an exponential decay of the RC low pass filter formed by a 3 kΩ resistor and the electrode, not by the amplifier slew rate or the other filters. Because of this, this time is relatively independent of the shallow pre-dump potential, so it is nearly the same for all clouds within a measurement at one axial trap location. In the second round of measurements, this took much longer because the electrodes had to come much closer to the amplifier voltage before the cloud was released. In 16.1 μs, a cloud performs a small fraction of a magnetron orbit [$\mathcal{O}$(0.5 rad)], and the center

of magnetron orbit has moved far away from the cloud's initial position. Another way of looking at this situation is that the cloud is $\mathbf{E} \times \mathbf{B}$ drifting in the electric field solely from the patch potential, which we have otherwise measured to be about 60 mV/cm. Thus the strongest patch potential should have produced a deviation of 34 μm in the first round of measurements and 97 μm in the second round of measurements. This is very close to what is observed; by eye, the deviation looks like 150 μm in the second round of measurements. As mentioned before, the largest source of error in this approximation is the ignorance of cross-capacitance between electrodes, which is an error of about 30–50%. Note that this effect causes clouds to drift in the direction perpendicular to the displacement due to patch fields visible in Fig. 6.6. In this strongest patch field, $\vec{\varepsilon}$ points in the $-\hat{x}$, $-\hat{y}$ direction, so we expect to see a bump in the $-\hat{x}$, $+\hat{y}$ direction, which is what we observe (although the $-\hat{x}$ part is more clearly visible).

With this agreement between theory and experiment, it is tempting to try to apply this known correction to the misalignment measurements. However, the effect is quite small for the measurements in Sec. 6.2—at most 34 μm in the center of electrode 19, and much less everywhere else. Adding this correction produces a barely perceptible offset throughout most of the trap. The small bump near electrode 19 in that plot is actually probably mostly due to the strong patch potential simply making it harder to extrapolate to infinite k_{2m}, and not the $\mathbf{E} \times \mathbf{B}$ drift during dump. On the other hand, the effect is clearly visible in Sec. 6.3. At this point, we can just say we understand why the measurements are better in Sec. 6.2, and we can declare Fig. 6.9 to be the final result.

6.5 ALPHA-2 misalignment and patch direction measurements

As I have discussed in Sec. 3.8, patch potential measurements in ALPHA-2 are always significantly worse because of the larger initial cloud magnetron. However, I did get a chance to attempt to measure patch field directions and alignment in ALPHA-2. The results are passable.

Fig. 6.17 shows the cloud positions when I perform this measurement. The measurement procedure is most similar to the second procedure presented in Sec. 6.3—the magnetron phase is randomized. However, the data is clearly marred not only by a large intrinsic magnetron (see Sec. 2.3.1), but also by an increasing cloud magnetron due to a reservoir diocotron that grows over time. For analysis, I went with a kind of hybrid scheme between the analyses discussed in Secs. 6.2 and 6.3. Because circles were so clearly visible in some of the data taken with deep trapping potentials (the blue points in Fig. 6.17), I made a fit function which predicted that clouds should land along a circle which is displaced by $\vec{\varepsilon}/k_2$. The error for each cloud was its distance from the circle squared, and this was minimized by gradient descent.

These measurements were performed after about 2 Wh of integrated circulating power in the 1S–2S laser, so laser-induced patch fields were present. The directional patch field measurements are shown in Fig. 6.18. It is very interesting to see that the patch fields produced by the 1S–2S laser are not random in direction. They all seem to be in the $+\hat{y}$, $-\hat{x}$ direction. This would seem to imply that one side of the trap is exposed to more scattered laser light, and that an electric field is produced which points away from or toward that side of the trap. Recall from Sec. 3.6 that laser-induced patch fields only are produced between

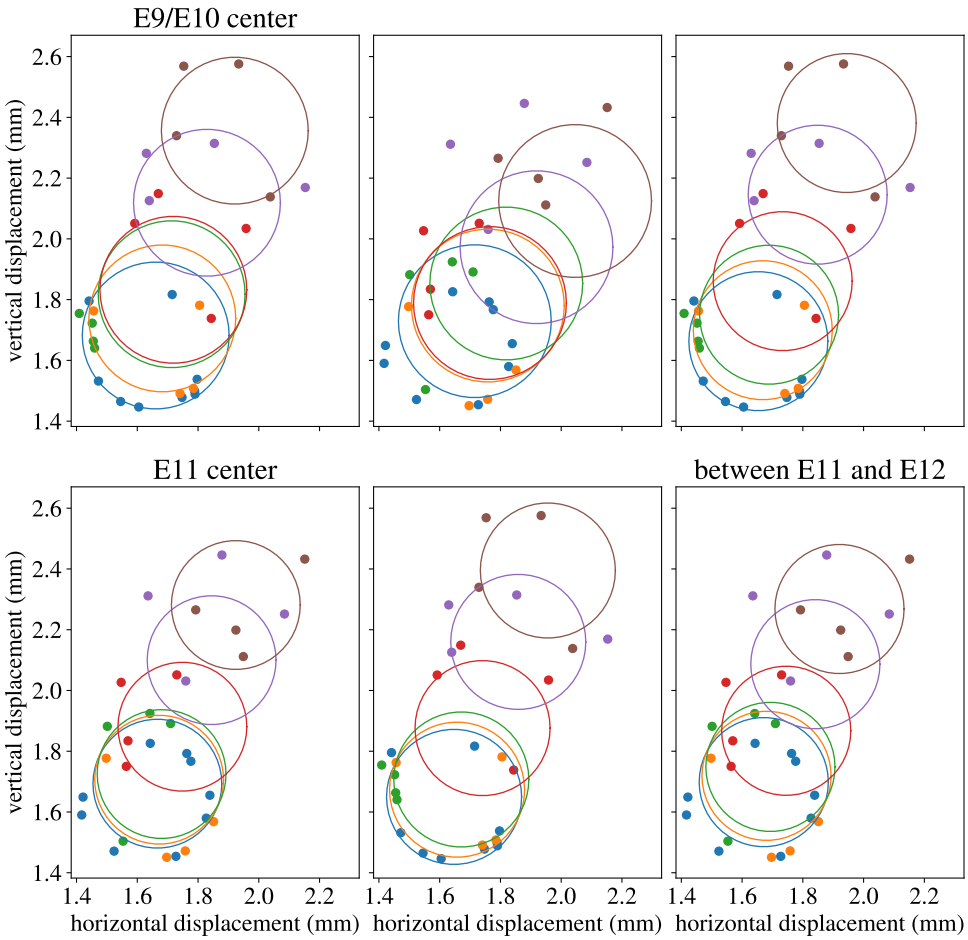

Figure 6.17: Imaged cloud center positions during measurements of the patch field direction and trap alignment in ALPHA-2. The positions on the MCP have been converted to transverse distance inside the trap. These measurements are from six adjacent axial locations, with some of the locations labelled above the plots. The different colors correspond to different shallow pre-dump potentials (different k_{2m} values). The circles are the positions of the cloud centers as predicted by the fitting procedure.

electrodes 9 and 19 in ALPHA-2.

The results of the misalignment measurements are shown in Fig. 6.19. The quality of these measurements is predictably much worse than in ALPHA-g. Essentially, no features can be discerned above the noise. We can kind of casually upper bound the misalignment of the electrodes to about 1 mrad. Note that the measurements in the vicinity of electrodes 14 and 15 are not reliable. The reservoirs used for those measurements developed a catastrophic diocotron (see Sec. 2.3.2) early in the measurement process and very few successful cloud images were used to produce these measurements. The patch field extraction from those cloud positions were more acceptable. As discussed in Sec. 2.3.2, Ph.D. student Jaspal Singh has recently discovered an explanation for the catastrophic diocotron, and this explanation yields an easy way to eliminate the issue. Thus this alignment measurement could be redone more quickly and more precisely with a diocotron-free reservoir.

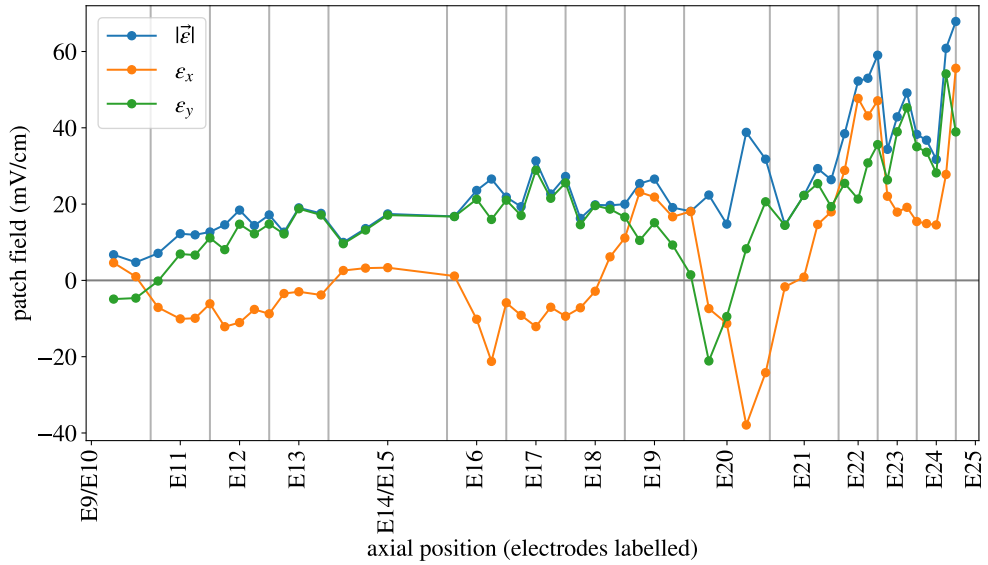

Figure 6.18: Patch field directions and magnitudes are shown versus axial position in ALPHA-2 after about 2 Watt hours of integrated laser exposure. In the horizontal axis, axial position is labelled with the electrode numbers, and some electrodes are combined because they are shorted together.

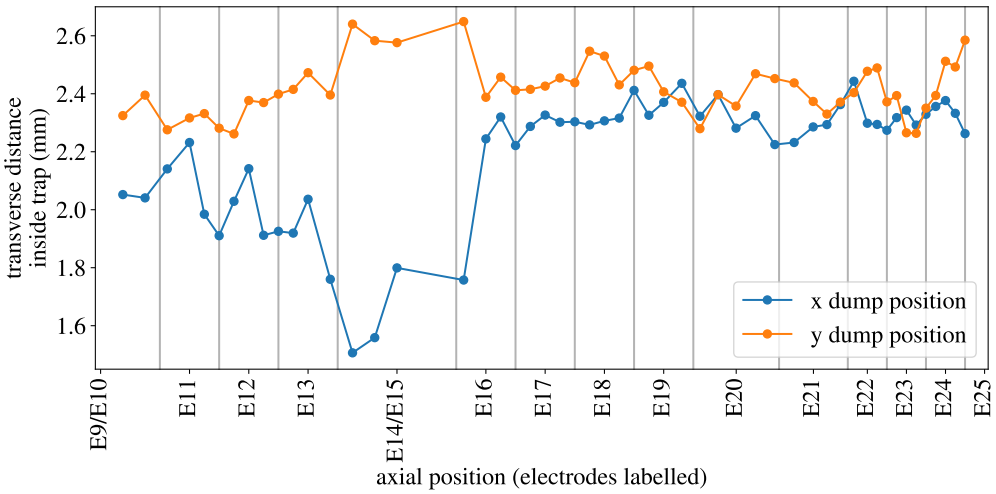

Figure 6.19: The horizontal (x) and vertical (y) deviations of the ALPHA-2 electrodes from a single magnetic field line are shown versus axial position in the trap.

7 Off-axis electron cyclotron resonance (ECR)

In this section, I will discuss a technique where I combine the technique described in Sec. 3 to move clouds off-axis with electron cyclotron resonance to measure magnetic fields beyond the trap symmetry axis. The basic steps involved in this measurement are shown in Fig. 7.1 and described as follows:

(a) A cloud is extracted from a reservoir.

(b) It is moved to a desired axial measurement location.

(c) It is moved off-axis adiabatically as described in Sec. 3.3 by decreasing the trap constant k_2.

(d) The trapping potential is quickly increased again, and the cloud orbits the trap center for about $100\,\mu$s.

(e) After $100\,\mu$s, we wait an additional few microseconds for the cloud to reach a desired magnetron phase, and then the cloud is exposed to microwaves for $3\,\mu$s (about 1/5 of a magnetron period). If the microwaves are resonant with the cyclotron frequency $\omega_c = q|\mathbf{B}|/m$, the electrons are heated. Because the cyclotron frequency is proportional to the magnetic field through fundamental constants, a precision measurement of the cyclotron frequency translates directly to a precision measurement of the magnetic field. The on-axis version of this technique has been used at ALPHA for several years [5].

(f) We measure the cloud's temperature by slowly (over the course of 20 ms) releasing it toward the MCP and observing the exponential increase in the signal reflective of the Maxwell-Boltzmann distribution in the cloud, as described in Sec. 4.

In the ALPHA-g experiment, an octupole magnet is used to radially confine antihydrogen. Two "short solenoids," also referred to as "mirror coils" are used to confine antihydrogen axially; the axial direction is also the vertical direction. A diagram of this setup is shown in Fig. 7.2. These mirror coils are slowly turned off while maintaining a well-measured difference in their on-axis magnetic field to release the antihydrogen. Any uncertainty in the magnetic field difference between these two coils translates directly into a systematic error on the measurement of antihydrogen's acceleration due to gravity. Off-axis ECR was used to measure how much mirror A—the mirror coil on the bottom of the ALPHA-g magnetic minimum trap—was displaced from the center of the electrodes, where the magnetic field is typically measured. A displaced of about $150\,\mu$m is observed. I should emphasize that this is not the same thing as "misalignment" by an angle, as discussed in Sec. 6. Here I am measuring the transverse displacement between the symmetry axes of mirror A and the electrodes. Although the ALPHA-g experiment was very sensitive to magnetic fields, this effect ends up being well below the ~ 0.1 mT level of precision needed for the first measurement of the effect of gravity on antihydrogen [1]. Unfortunately, due to time constraints the measurement was not repeated in mirror G.

This chapter also serves a useful pedagogical role in this thesis. In the next section, I will use ECR to calibrate a new magnetometry technique called electron magnetron phase

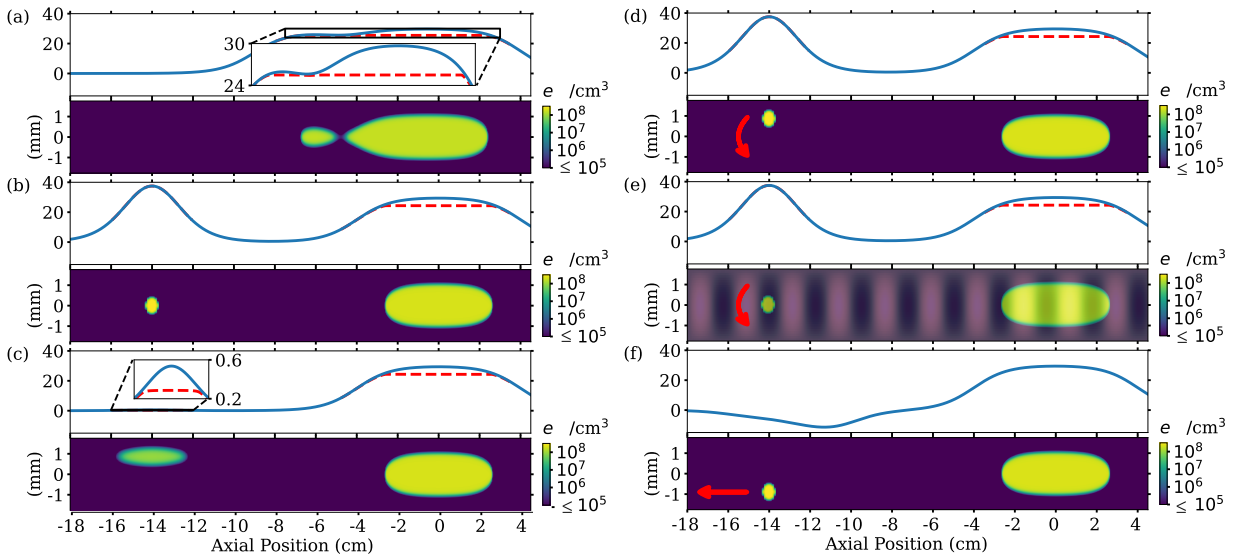

Figure 7.1: The measurement procedure for off-axis ECR is shown in six steps. For each step, the upper plot shows the on-axis potential produced by the electrodes in blue and the on-axis potential perturbed by the charge of the reservoir with a red dashed line. The lower plot shows the charge density of electrons. The red arrows indicate the motion of the electron cloud. The size (radius, length, and total charge) of the electron clouds is exaggerated to make them visible.

imaging (EMPI), so it is useful to explain ECR ahead of time here. In this chapter, I will also introduce a simple new tool in our manipulations of the positions of electron clouds—we change the amount of time they spend in a magnetron orbit by only a few microseconds and we observe a small phase difference in their magnetron motion. This is essentially the main tool in EMPI, where it is used to precisely measure the magnetron frequency.

Unfortunately, I was given about 24 hours of notice that I would have the chance to implement this technique. I spent one shift (about 8 hours) implementing off-axis ECR after not sleeping for 24 hours. Two subsequent shifts conducted by my colleagues were spent using this technique to perform a useful measurement. As such, much of the data is not "publication quality." If just a little more time was spent on this, it could be extremely useful for the ALPHA experiment. Alternatively, Ph.D. student Jaspal Singh, advised by Prof. William Bertsche, is currently working on proof-of-concept experiments to move electron clouds off-axis with intentionally applied potentials on an azimuthally segmented electrode rather than patch potentials. They hope to install azimuthally segmented electrodes in critical measurement locations in ALPHA-g. This is, frankly, a much better way of measuring magnetic fields off-axis. Therefore my version of off-axis ECR may be irrelevant in the future, but it does have the advantage of being available in the absence of segmented electrodes.

One particular flaw in this measurement was that we should have varied the depth of the "deep trapping potential" where electrons were performing a magnetron motion and where they were exposed to microwaves—steps (d) and (e) above. The deep trapping potential used throughout this section is shown in Fig. 7.3. The well constant k_2 is $3.963 \times 10^5\,\mathrm{V/m^2}$,

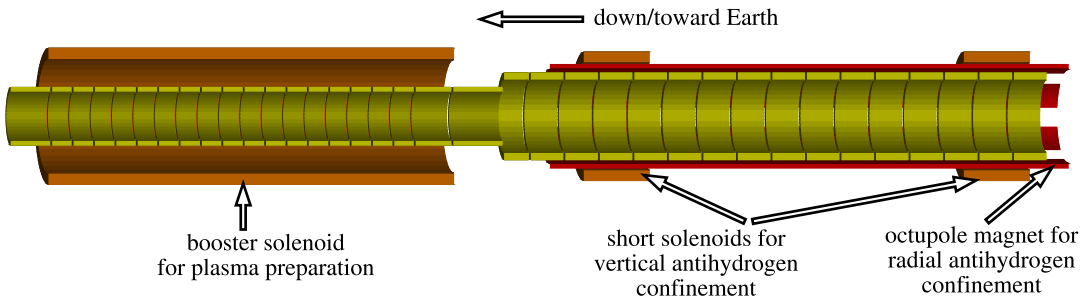

Figure 7.2: A diagram of the ALPHA-g Penning-Malmberg trap electrodes and four liquid helium cooled superconducting magnets that were most relevant for the first ALPHA-g measurement. The booster solenoid, shown on the left, is not very important for the discussion of off-axis ECR, but it was energized for some of the measurements shown in Sec. 6 and Sec. 8. The octupole magnet, shown in red, causes the magnetic field magnitude to increase with r. The two "short solenoids," also known as "mirror A" on the left and "mirror G" on the right, generate local maxima in the on-axis magnetic field near their centers. Together the octupole and the mirror coils form a magnetic minimum trap for antihydrogen. Note that this diagram is rotated 90 degrees. Mirror G is the top of the vertically oriented trap.

giving a magnetron period of $15.85\,\mu\text{s/cycle}\,(B/1\,\text{T})$. The cubic term is small, and the quartic term is $4.886 \times 10^5\,\text{V/m}^2$, which provides a variation in the magnetron period with radial displacement of $8.57\,\text{ms/cycle}\,(r^2/1\,\text{mm}^2)(B/1\,\text{T})$ (see Sec. 3.4 for the derivation of this effect). Typically for on-axis ECR, we use the deepest possible trapping potential. This provides three benefits as follows (all discussed in Ref. [5]):

1. The ECR resonance has sidebands separated by the axial bounce frequency of electrons in this trapping potential $\sqrt{2k_2q/m}$. By maximizing k_2, we move these sidebands farther from the central peak, making the central peak clearer.

2. Maximizing k_2 minimizes the axial length of the electron cloud. If there is any axial gradient in the magnetic field, this minimizes the variation in magnetic field strengths that different electrons are exposed to. We have never conclusively established the effect of a magnetic field gradient on the ECR resonance, but there is little doubt that a gradient would contribute to the ECR linewidth.

3. The ECR resonance also has sidebands separated by the rotation frequency of the cloud, as shown in Ref. [5] (much smaller than the bounce frequency). These sidebands were never observed in ALPHA-g, because we never evaporatively cooled the electron clouds as in Ref. [5], which results in an extremely diffuse cloud whose rotation frequency is k_2/B, unperturbed by the cloud's charge. Resolving these sidebands by maximizing the rotation rate enables an improved measurement technique that can be accurate at the parts per million level.

On the other hand, with a magnetron period of $16\,\mu\text{s}$, the microwave pulse needed to be microsecond-scale (we used $3\,\mu\text{s}$) in order for the pulse to occur when the cloud is at a well-defined magnetron phase. This imposes a spectral linewidth of order $0.3\,\text{MHz}$, which is 10^{-5}

times the frequency of the resonance, limiting the precision of the measurement. Thus, if we decreased the magnetron frequency by a factor of ten we could decrease the linewidth by a factor of ten. Alternatively, we could split the benefits and have the clouds subtend a smaller magnetron arc by a factor of three and decrease the linewidth by a factor of three. In the past, there was no reason to do anything other than maximize k_2.

On the other hand, the concern that decreasing k_2 would elongate clouds is valid. The measurements described here were performed near the center of mirror A, or at least within a millimeter axially of the center of mirror A. With this upper bound of one millimeter, the axial magnetic field gradient would have been at most 0.1 T/m. The length of the clouds is given by $\sqrt{\langle z^2 \rangle} = \sqrt{k_B T / 2 e k_2} \approx 70\,\mu$m (derived in Sec. 5.4.1), giving a variation in the magnetic field of at most 10^{-5}. These back of the envelope estimates show that the k_2 value used here wasn't ridiculous—the variation in the magnetic field is a similar order of magnitude to the spectral linewidth—but the appropriate thing would have been to vary k_2 and the microwave pulse length to find the configuration that minimizes the ECR linewidth. In addition, it would have been beneficial to more precisely find the position of the axial magnetic field maximum to minimize this gradient.

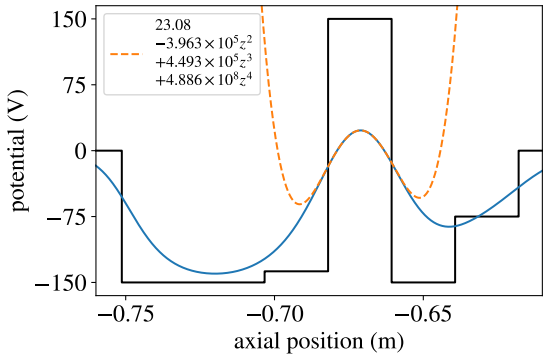

Figure 7.3: The electrode voltages applied while performing off-axis ECR are shown in black. This is the "deepest," i.e. highest well constant k_2 trapping potential that is possible which has the same axial position as the center of mirror A (also the center of electrode 23). The orange line is a quartic fit to the bottom of the trapping potential.

One final optimization that would improve these measurements is to vary the current in mirror A to find a configuration which is optimal for resolving how far off-axis mirror A is. Here the only current used is 10 A, which creates a 0.11 T perturbation to the nominal 1 T field in the center of mirror A. Two other values were attempted, 70 A and 40 A, but we were unable to observe any measurable heating of off-axis clouds with microsecond-scale microwave pulses at these higher magnetic fields. This is not really astonishing—we have very little understanding of how much microwave power propagates into the trap and the structure of microwave intensities throughout the trap. We have also never modelled the heating rate of the electron cloud subject to microwaves of a certain intensity. We have in the past observed that certain combinations of axial trap locations and microwave frequencies result in dramatically less heating, presumably indicating that there is a minimum in the oscillating electric field at that trap location. So far we have adopted an approach of "take

what you get" when it comes to whether or not a temperature peak can be resolved for a certain microwave power, pulse length, trap location, and cyclotron frequency.

7.1 Moving electron clouds to well-defined positions

The goal of off-axis ECR will be to measure how the magnetic field magnitude in a Penning-Malmberg trap varies with r and θ at a fixed axial position z. Thus, I need to begin by proving that I can deliver electron clouds to a well-defined transverse position.

First, clouds were moved off axis a variable distance adiabatically just as in Sec. 3.3. Then once they have reached the intended off-axis distance, the trapping potential is quickly changed to the one shown in Fig. 7.3. In this first experiment, I only intended to prove that clouds could be delivered to a well-determined magnetron phase, so after after orbiting the trap center for a variable time, they are released toward the MCP to be imaged. Later, of course, they will be exposed to microwaves for $3\,\mu$s, a short time compared to their magnetron period, before being released slowly to measure their temperature. In my first attempt, the clouds performed a magnetron orbit for tens of milliseconds (I cannot recover the exact amount of time because the sequences were deleted) plus a variable extra "phase shift time" between 0 and $12\,\mu$s; the resulting cloud positions on the MCP are shown in Fig. 7.4. In Fig. 7.4, clouds are delivered to two different radial positions, and seven different phase shift times were used. Each combination was repeated four times. Clouds that were intended to arrive at the same r and θ on the MCP did not. In hindsight, this can be easily predicted from the quartic coefficient. As discussed in the previous section, this trapping potential creates a radial variation in the magnetron frequency given by $\omega_r(r) = 2\pi/15.85\,\mu\text{s} + (2\pi/8.57\,\text{ms})(r^2/1\,\text{mm}^2)$. In this case, there was a small variation in the initial positions of the clouds, and because the time spent in the deep well was not short compared to 8 ms, the magnetron phases spread out for clouds subjected to identical electrode manipulations.

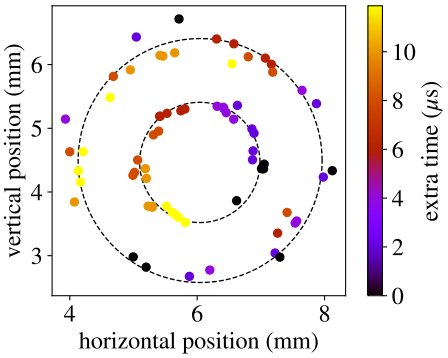

Figure 7.4: Clouds imaged on the MCP after spending several milliseconds in the deep well used for off-axis ECR. Two different magnetron radii are used (two different k_{2m} values, one being double the other, resulting in magnetron radii of about 1 mm and 2 mm). The clouds spend a time $T_0 + dt$ in a deep well, where T_0 is tens of milliseconds, and dt is indicated by each cloud's color.

This issue would be unacceptable for off-axis ECR, but luckily the resolution is very

simple—we need to spend less time in the deep well. Fig. 7.5 shows the result of clouds spending 100 μs and 200 μs in the deep well. In Fig. 7.5, clouds are delivered to two different radial positions; the clouds that are displaced by about 2 mm spend 100 μs in the deep well, and the clouds that are displaced by about 1 mm spend 200 μs in the deep well. Of course, this odd choice of varying two parameters at once was not intentional. I took a barely sufficient dataset for convincing myself at the time that off-axis ECR would work; I did not prioritize taking data to make plots for my thesis.

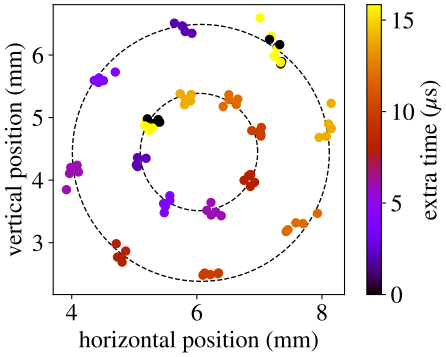

Figure 7.5: In this plot, clouds are subjected to the same procedure as in Fig. 7.4, but this time T_0 is 200 μs for the clouds with a magnetron radius of 1 mm and 100 μs for the clouds with a magnetron radius of 2 mm.

Before moving on to off-axis ECR, I doubled the time taken to adiabatically move the clouds off axis in the hopes that this would result in a smaller distribution of cloud positions. This was successful, as shown in Fig. 7.6. For the clouds shown in Figs. 7.4 and 7.5, I used an atypically fast adiabatic movement because I was hoping I could increase the repetition rate to perform off-axis ECR more quickly. It seems that adiabatic movement was too fast. Next, the issue where clouds moved to different radii are subjected to a different amount of time in the deep well has been fixed. Thus in Fig. 7.4 on the right, clouds moved to different radii have the same magnetron phase for the same amount of extra time in the deep well. Another modification in Figs. 7.6 is that mirror A is energized with 10 A on the left and 70 A on the right, corresponding to a magnetic field increase from about 1 T to 1.1 T and 1.7 T respectively.

This magnetic field increase has two impacts on the cloud positions. First, the magnetron frequency is decreased; to sufficient precision, with this short hold time, the magnetron frequency is k_2/B. This effect is clearly visible in the data and it is consistent with predictions. Second, the increasing magnetic field changes the radius of cloud positions on the MCP. It is extremely convenient that when we decrease the well constant to k_{2m}, the position of the magnetron center of motion inside the trap is not dependent on the magnetic field. It is located at the point in space which is an electrostatic potential maximum along the magnetic field and an electrostatic potential minimum in the two directions transverse to the magnetic field. This position can change slightly when the angle of the magnetic field relative to the symmetry axis of the electrodes changes, but near the center of the trap this angle is very small, and this effect is entirely negligible. Thus the radius of magnetron motion inside the trap is the same regardless of the current in mirror A. However, the ratio of magnetic

field strength between this axial measurement location and the MCP has changed—it has increased. Thus the radius of cloud center positions on the MCP changes. For this reason, the clouds that were given a magnetron radius of 2 mm inside the trap were all visible on the MCP in Fig. 7.5, but with mirror A energized to 70 A, many of these clouds fall outside the imageable region on the MCP. This is why clouds with the largest radius are only visible on the upper left and lower right in Fig. 7.6 on the right. Note that I have not taken the time to account for this effect in the calibration of the horizontal and vertical axis in Fig. 7.6, so the cloud positions are reported as actually having a larger radius inside the trap, although they actually do not.

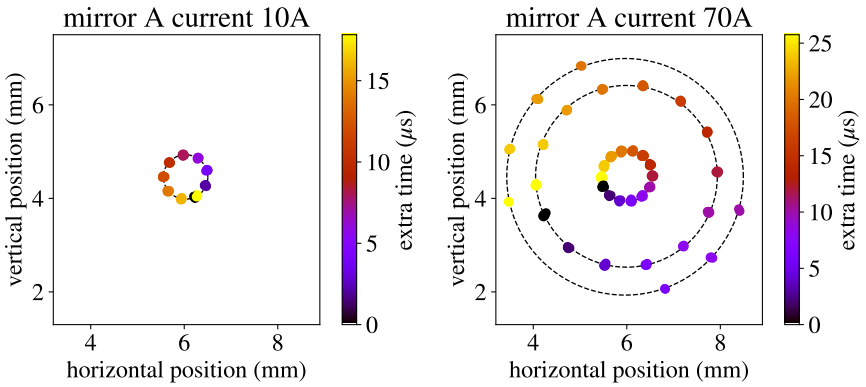

Figure 7.6: Positions of cloud centers are reported when clouds are displaced from the trap axis by about 0.41 mm with mirror A energized with 10 A and three different radii (0.41, 1.50, and 2.05 mm) with 70 A in mirror A. Note that positions reported in the horizontal and vertical axis are based on a calibration of positions inside the trap versus positions on the MCP that assumes, erroneously, that mirror A is not energized and that the magnetic field inside the trap is 1 T. This plotting choice illustrates that the radius on the MCP increases when the magnetic field inside the trap increases.

7.2 Observing a cyclotron resonance

Having used MCP imaging to confirm that clouds are reproducibly sent to a particular magnetron radius and phase, we inject microwaves into the trap near the cyclotron frequency for 3 μs when the clouds are at a particular magnetron phase. All of the experiments going forward were performed with a current of 10 A in mirror A, and the axial position is the designed axial center of mirror A, which is also the center of electrode 23.

To measure the magnetic field at a particular trap location, a sequence of clouds are delivered to the same trap location, and each cloud is exposed to a different microwave frequency. Then the clouds' temperatures are measured by releasing them towards the MCP over the course of 3 ms to observe an exponential increase in the signal versus time, reflective of the Maxwell-Boltzmann distribution within the cloud. This signal is taken from a silicon photomultiplier (SiPM) which can observe single photons from the phosphor screen behind the MCP [98]. Unlike the camera, this SiPM measures the light produced on the phosphor screen versus time, so it measures the rate at which electrons are striking the MCP. This

technique is described in Sec. 4.1, and there I also discuss that a correction factor is needed to infer actual temperatures. These measurements are nonetheless a valid way to measure changes in temperature, which is all we need to observe a resonance.

Measurements of cloud temperatures versus applied microwave frequency are shown in Fig. 7.7. Instead of plotting the SiPM signal versus time, I plot the SiPM signal versus the "escape energy." This is defined as the difference between the electrostatic potential maximum that the cloud sits in and the electrostatic potential minimum that electrons would need to pass in order to escape the confining potential and be released toward the MCP. This potential difference is inferred using electrostatic modelling of the electrode voltages used to perform this operation. As explained in Sec. 4.1, because of the electrons' Maxwell-Boltzmann distribution, we expect an exponential increase in the signal as the escape energy decreases linearly, and thus an exponential function is fit to the early-time/high escape energy part of the signal in Fig. 7.7. With this manner of plotting, the fit function is $S_0 + \exp(-E/k_B T)$, where T is the temperature, S_0 is the background signal, and E/k_B is the horizontal axis of the plots.

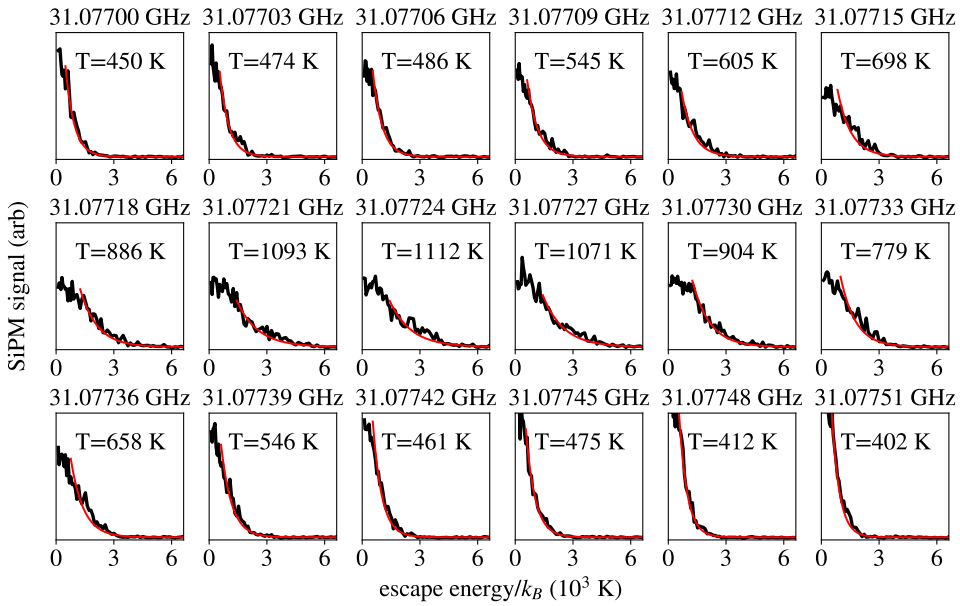

Figure 7.7: In black, the SiPM signal is shown versus the "escape energy" needed for electrons to escape their confining potential (plotted in temperature units). The red line is an exponential fit to the SiPM signal, with the fit region chosen using simple, somewhat arbitrary heuristics. In each plot, the microwave frequency applied to the electron cloud is listed above, and the deduced temperature is listed inside the plot region. A resonance is observed, with the maximum heating occurring somewhere between 31.07721 and 31.07727 GHz.

The cyclotron resonance can also be observed in the positions of electrons on the MCP. In Fig. 7.8, in addition to measuring the temperature of a cloud with the SiPM, I triggered the camera with a shutter speed that covered the entire 3 ms of the temperature dump. In fact, the reason I performed the temperature dump in 3 ms rather than the typical 20 ms was that I wanted to be able to image these clouds. Some of the observations were expected.

I expected that clouds would be "smeared" along their magnetron orbit—some electrons are still trapped and executing $\mathbf{E} \times \mathbf{B}$ drift while others have already escaped, causing the electron positions to form a streak rather than a dot. I expected that this streak would be longer when the cloud temperature increased due to resonant microwaves. I also expected that the magnetron phase of the clouds would change as the plasma temperature increased. As the clouds heat, they become longer, and this affects the magnetron frequency in the few milliseconds between the microwave pulse and releasing the cloud toward the MCP, as shown in Sec. 5.4.1. I did not expect that the clouds that were heated most would have a smaller magnetron radius—notice that cloud 29 in Fig. 7.8 is imaged near the center of the magnetron orbit indicated by the streaks of clouds 27 and 28. It's not clear to me whether this is due to complications in the process of dumping the clouds or if is the result of motion toward the trap center induced by the microwaves. This unexpected phenomenon can probably be avoided by using sufficiently weak microwaves.

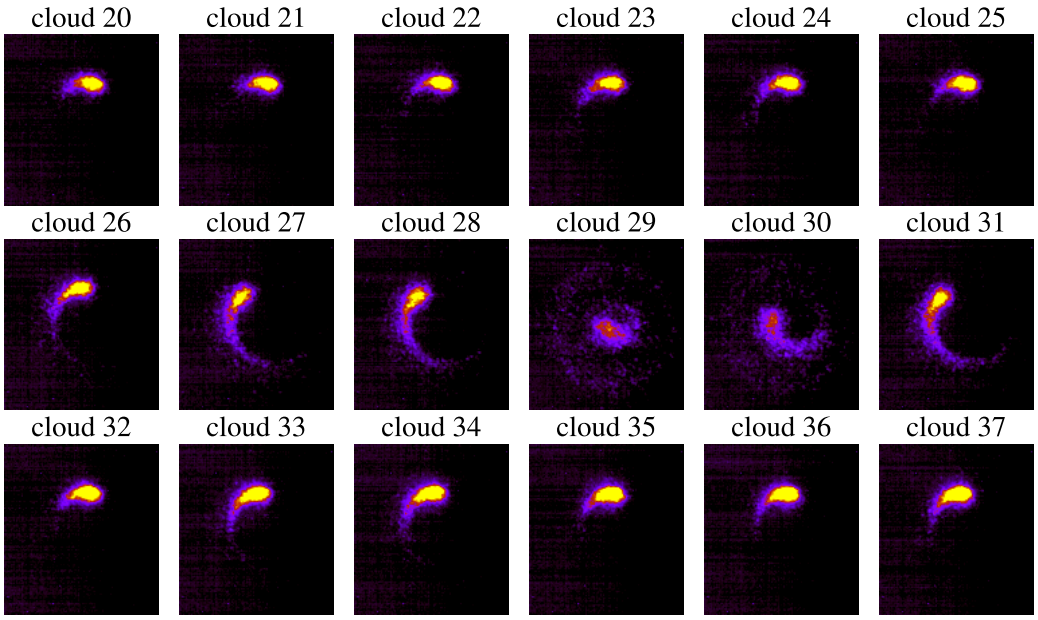

Figure 7.8: Clouds are successively imaged after being moved off-axis then exposed to microwaves of linearly increasing frequency. Unlike in Fig. 7.7, the cloud number is listed instead of the microwave frequency that the clouds were exposed to. This is also not the same dataset as was used in Fig. 7.7—in both cases the dataset shown was the one that most clearly illustrates the point I want to make.

7.3 Off-axis ECR results

Before showing the temperature versus frequency for various magnetron radii and phases, I should explain that with many preicsion ECR measurements, we need to account for the magnetic field drifting with time. We attribute this to the decay of persistent currents, which will be discussed in Sec. 8. During the course of these measurements, the magnetic field decreased at a rate of about 0.009 mT/h, and the measurement took about four hours.

This was observed by occasionally measuring the magnetic field on axis between off-axis measurements. Without correcting for this drift, the effect of mirror A's displacement would not be apparent.

Fig. 7.9 shows the cyclotron resonance at three different magnetron radii and four different magnetron phases. Each measurement was repeated 2–4 times, but only one temperature versus frequency curve is shown per radius and phase here. In Fig. 7.9, a correction of $((q/m)(0.009\,\mathrm{mT/h})$ is applied to the microwave frequencies. This is a peculiar way to account for the drift, but it allows me to illustrate the effect of mirror A's displacement in the resonance curves themselves. At all radii, the heating peak for the clouds at magnetron phase 2.85 radians is slightly shifted right relative to the heating peak for the clouds at magnetron phase 0. Also, as expected, the magnetic field is stronger at higher radii. In each of these curves, a Gaussian is fit to a few of the temperature values near the highest measured temperature. There are many reasonable choices for the fit function—Gaussian, Lorentzian, Gaussian with Lorentzian tail, the Fourier transform of the microwave pulse, etc. The most reasonable thing to do is to admit we don't have a full accounting of the collection of effects that leads to the ECR lineshape. Therefore I choose to fit a generic function only to the center of the visually apparent peak. It is notable that the width and height of the ECR peak depends on location in the trap. To some extent, this may be due to the cloud's magnetron motion changing the magnetic field experienced by the electrons throughout the microwave pulse. As the cloud moves, it may be brought in or out of resonance with the microwaves. The difference in heights is likely explained by variations in the microwave amplitude with position. This effect is unfortunate, as it probably also "pulls" the heating peaks—keep in mind that these clouds are executing 1/5 of a magnetron orbit in the $3\,\mu$s that microwaves are active. As stated in the introduction to this section, it is likely that this measurement can be improved by decreasing the magnetron frequency. Note however that the power of microwaves at various magnetron positions is not clearly visible in these plots, because the microwave power was adjusted in some cases to restore a clearly visible peak.

To explain why the magnetic field is expected to vary with magnetron phase, consider that near the center of the axial magnetic field maximum created by mirror A, the magnetic field can be approximated by:

$$B_z(z) = B_0 + B'z + cz^2. \tag{7.1}$$

The magnetic scalar potential as a function of r and z is then:

$$-\Phi_B(r,z) = B_0 + \frac{B'}{2}\left(z^2 - \frac{1}{2}r^2\right) + \frac{c}{3}\left(z^3 - \frac{3}{2}r^2 z\right). \tag{7.2}$$

So the off-axis magnetic field is:

$$B(r,z) = \left(B_0 + B'z + cz^2 - \frac{1}{2}cr^2\right)\hat{z} - \left(\frac{1}{2}B'r + crz\right)\hat{r}, \tag{7.3}$$

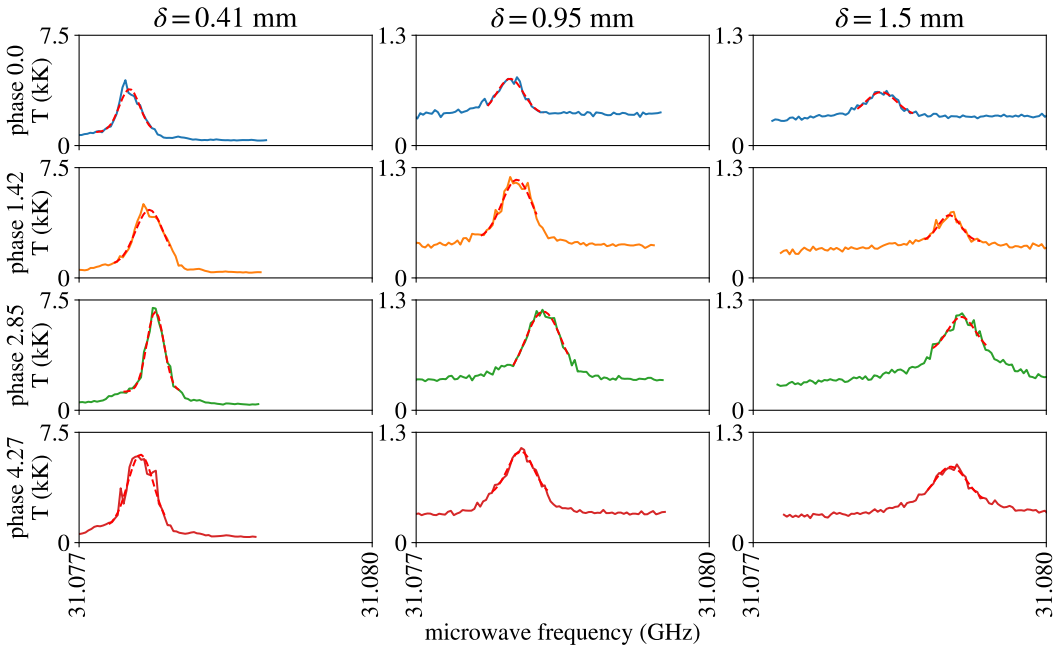

Figure 7.9: For each of four magnetron phases and three magnetron radii, cloud temperatures are measured after exposing 100 clouds to different microwave frequencies. A Gaussian is fit to each heating curve, with the resulting fit shown with a red dashed line.

and the magnitude is:

$$|B(r, z = 0)| = B_0 + \left(-\frac{1}{2}c + \frac{1}{4}\frac{B'^2}{B_0}\right) r^2 \tag{7.4}$$

If the center of magnetron motion—the center of the electrode confining the clouds—is displaced in the $\hat{x}$ direction by a distance Δ, then when the clouds' magnetron radius is δ and its phase is θ, the cloud's radial distance from the transverse magnetic field magnitude minimum is: $r = \sqrt{(\Delta + \delta\cos\theta)^2 + (\delta\sin\theta)^2}$. Using a model of the as-designed magnets of the ALPHA-g trap, I determined that $c = -57.73\,\mathrm{T/m^2}$ in Eq. 7.1, and that B' would have a negligible effect because the measurement was performed close to the axial magnetic field maximum. However, this model predicted that the increase in magnetic field due to the 10 A in mirror A would be about 10% less than what is observed, so there is clearly a roughly 10% error in my magnetic field model. This model was then fit to the observed heating peaks. This theory suggests there should be three free parameters: the angle of mirror A's displacement (we cannot assume that mirror A is displaced in the same direction as "magnetron phase zero" in Fig. 7.9), the displacement of mirror A Δ, and the magnetic field in the center of mirror A. However, a fourth parameter was necessary to achieve a reasonably good fit—a "fudge factor" on c. This is reasonable because as mentioned before, there seems to be a 10% error in the magnetic field model used to predict c. This fudge factor is also equivalent to scaling all the magnetron radii—so it can account for any error in our calibration of positions inside the trap versus positions on the MCP (discussed in Sec. 3.5).

The fit to all of the resonance measurements is shown in Fig. 7.10. The fit is not great, but in the course of describing this measurement I have given plenty of sources of error—frequency pulling from gradients in the microwave power, any nonlinearity in the drift of the magnetic field due to persistent current decay, the changing magnetic field throughout the magnetron motion of the clouds, etc. The fit suggests that the fudge factor is 0.76, and the displacement of mirror A's transverse magnetic field minimum from the electrostatic trap center is $196 \pm 15\,\mu$m (the error bar is statistical fitting error only). Of course, given the large fudge factor, the quality of the fit, and all the known sources of error, the displacement is probably farther from $196\,\mu$m than the statistical error bar suggests. However, the telltale sign of an existing displacement, a sinusoidal variation in the magnetic field with magnetron angle, is clearly visible in the data. It seems clear that this effect is real, even if it isn't precisely measured here. This displacement means that when we measure the on-axis magnetic field, the actual magnetic field minimum is lower by $1.5 \times 10^{-6}\,$T. This translates directly to an error of $0.003g$ on the measured acceleration of antihydrogen due to gravity. The first measurement of gravity on antihydrogen had a total error bar of roughly $0.25g$, so we are a factor of 100 away from this being a dominant error, and probably a factor of 10 away from having to include this effect in the list of known errors [1].

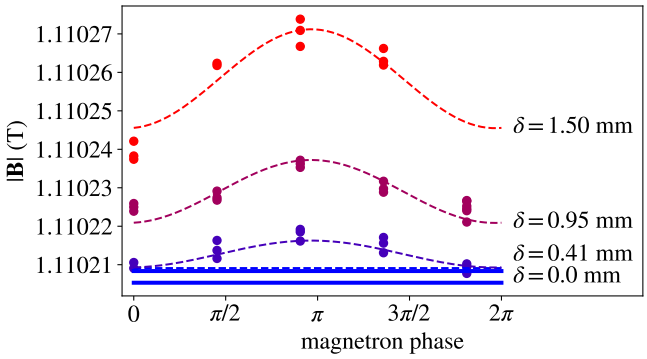

Figure 7.10: The dots show measurements of the magnetic field magnitude inferred from ECR heating peaks. The solid blue lines show the ±1 standard deviation bounds of the measurements of the on-axis magnetic field taken throughout this measurement campaign. Four dashed lines show the fit function to all the data at once—the expected magnetic field variation due to mirror A being displaced by $196\,\mu$m.

8 Electron magnetron phase imaging (EMPI)

This section describes a new technique for magnetic field measurements which takes advantage of the magnetron motion of electron clouds. The basic idea is that magnetron frequency is given by $\omega_r \approx k_2/B$, where B is the axial magnetic field and k_2 is the "trap constant," where the electrostatic trapping potential created by the electrodes is approximated by $\Phi_t = -k_2(z^2 - r^2/2)$ near the trap center. Thus if k_2 is sufficiently stable—if the electrodes create the same trapping potential from one cloud to the next—precision measurements of the magnetron frequency can serve as precision measurements of the magnetic field. We know from Sec. 5.4 that clouds can orbit the trap for an entire second, tens of thousands of magnetron orbits, and they will arrive at the same magnetron phase, forming a coherent line as we move clouds to different radii then image them after a second of magnetron motion. Therefore k_2 values seem to be static at the 10^{-6} level or better, at least over the few hours in which those measurements were performed. This also proves that our electron clouds are sufficiently reproducible, so that fluctuations in their charge, radius, or temperature don't cause fluctuations in the magnetron frequency above the 10^{-6} level.

I have also shown in Sec. 7 that we can image clouds at different magnetron phases by changing the total time in a magnetron orbit in small increments—which we can use to measure the magnetron frequency—hence this technique is called electron magnetron phase imaging (EMPI). This works despite the fact that it takes $\mathcal{O}(10\,\mu\text{s})$, or roughly one magnetron orbit, to release clouds toward the MCP and to initiate their magnetron orbits (the so-called "instantaneous" electrode voltage changes). During these voltage changes, k_2 is changing in ways that are hard to predict (described in Sec. 6.4). The important thing is that these operations occur the same way from one cloud to the next.

Of course, our predictions of k_2 are nowhere near the 10^{-6} level. Patch potentials should affect k_2 at the 10^{-4} level (10 mV/100 V). The electrode amplifiers have voltage offsets at the 10^{-5} level—but these offsets are not observed to change with time. The electrodes thermally contract by from 300 K to 4 K by about 0.4%, causing k_2 values to deviate from predictions by twice this fraction. It is also likely that the COMSOL model of the electrostatic potential in the trap also has numerical errors at this level. However, all of these effects are unchanging with time. In ALPHA-2, the changing patch fields with laser exposure would presumably cause an issue at the 10^{-4} level, but in ALPHA-g patch fields have been measured to be unchanging over many months. To account for these issues, we will need to calibrate EMPI using ECR.

My first application of this method was to verify which version of one of the superconducting magnets was actually built and installed in ALPHA-g. The "booster solenoid," which increases the magnetic field from 1 T to 2 T for plasma preparation, underwent several changes in its design. It also would quench before reaching the current it was designed to reach. As such, there was some question whether this magnet was actually a different number of coils than we thought it was. Without calibration of the k_2 values, I was able to verify that this magnet did produce the magnetic field we expected it to at the 1% level. This measurement had an advantage over ECR because EMPI can be performed at any magnetic field strength. ECR has a lower field limit from the cutoff frequency of the waveguide, and it has an upper limit from the output of the microwave generator. EMPI has been vastly improved since this first measurement, so it will not be presented here. This measurement

also wasn't really of any consequence—the person who actually designed the magnets, Dr. Chukman So, knew with certainty what was installed; other members of the collaboration were confused because they were looking at out-of-date design documents.

For a long time after that first measurement, EMPI was "a solution seeking a problem." It was clear to me that I could perform magnetometry measurements more quickly than ECR, which would be useful for making on-axis magnetic field maps throughout ALPHA-g. However this wasn't enough to convince the collaboration to give me time on the experiment to work on EMPI. The aforementioned first measurement was snuck into a day where I was nominally meant to be measuring patch potentials. What did eventually convince the collaboration was that I figured out a way to measure the magnetic field during the 20 s where the magnetic field is decreasing to release antihydrogen during the gravity measurements.

The idea for measuring a changing magnetic field was to successively image clouds performing a magnetron orbit for a fixed period of time. As the magnetic field changes from one cloud to the next, a difference in the final magnetron phase would be observed. We could sum up the phase shifts to find the total change in the magnetron angle, and by relating $\omega_r \propto 1/B$, we could find how the magnetic field magnitude varied with time. However a measurement idea isn't useful until one has checked that there will be sufficient precision. At the time I was able to image clouds once every ~ 100 ms. The ALPHA-g measurement involved decreasing the magnetic field strength from 1.7 T to 1.0 T over 20 s, so the magnetic field would change by 3.5×10^{-3} T per cloud. If the clouds did a magnetron orbit of 600 radians, their phase would change by less than π per cloud, meaning we could easily track the changes in magnetron phase. The highest magnetron frequency achievable is 4×10^5 radians per second, so this would take 1.5 ms, which is negligible compared to the 100 ms it took to transport clouds from the reservoir to the axial measurement location (see Sec. 2.3.3). Because of the intrinsic magnetron of clouds prepared in ALPHA-g, there would be a variability in the magnetron phase of 0.1 radians (see sec. 2.3.1), and when dividing by the total angle of 600 radians, we find that the precision of the magnetic field measurements is roughly 1.7×10^{-4} T. The effect of gravity on antihydrogen is equivalent to 4.5×10^{-4} T, so measurements would need to be comparable to this precision to be useful, and they are. Many of the numbers presented in this paragraph will change by factors of two or three; ultimately, the precision will improve by a small factor, and the measurement frequency will improve by about a factor of 2–3.

This back of the envelope argument convinced the collaboration to allocate experimental time for developing EMPI. This time took the form of two weeks after the end of the antiproton run during which the first ALPHA-g gravity measurement was performed. On one hand, this is roughly double the time allocated to all of the measurements described in the other chapters of this thesis. On the other hand, I had been advocating for a long time that I be given significantly less total experimental time spaced out more widely so that I could analyze the results and think about what to do next. Because these measurements were performed in a short period of time, there are mistakes that weren't noticed until long after ALPHA-g was disassembled, and these mistakes cannot be fixed with further analysis.

So-called "phase imaging" has been implemented before in Penning traps for precision measurements of the masses of short-lived isotopes [124, 125, 126]. In these measurements, the isotopes are moved off-axis using a segmented electrode; here I will use patch potentials, which allows me to measure the magnetron frequency at more than one axial trap location.

Also, these experiments can convert between cyclotron motion and magnetron motion, because the cyclotron frequency for ions is slow enough that it can be addressed with ordinary electronics (in our case, microwaves are necessary for interacting with the cyclotron motion). This means they can excite a large cyclotron orbit, then convert the cyclotron phase into a magnetron phase, then image the particle. In this way, both the cyclotron frequency and the magnetron frequency can be measured using phase imaging. These experiments typically measure the ratio of the masses of two different isotopes by measuring the ratio of their cyclotron frequencies. With a known particle mass, the measurements could be interpreted as precise measurements of the magnetic field.

8.1 Sequence improvements for EMPI

In principle the operations we perform on a single cloud during EMPI measurements could be identical to the operations performed during many of the other measurements presented in this thesis. Like in the patch potential measurements (Sec. 3), the clouds are moved off axis using patch potentials. Like in the off-axis ECR measurements (Sec. 7), after the cloud is moved off axis, it orbits the trap center in a deep trapping potential for a variable amount of time, then we image the cloud on the MCP to determine its magnetron phase. However a number of improvements were implemented that drastically improved the efficacy of these phase measurements for the purpose of measuring magnetic fields. Most of these improvements facilitate imaging clouds more quickly than in previous cloud-based measurement techniques. For most EMPI measurements, we image 20–40 clouds per second and a total of 1000–2000 clouds are extracted from a reservoir.

Fig. 8.1 shows the electrode potentials used to image one cloud during EMPI measurements. Similar figures were produced to explain other cloud-based measurements, for example Fig. 7.1 from Sec. 7 and Fig. 3.2 from Sec. 3.1. This figure is different in that it shows the entire sequence of voltages taken from an actual EMPI measurement—there are no simplifications and no skipped steps. I will describe each step shown in Fig. 8.1 at the end of this section. Before I can do that, I will describe each sequence improvement over previous cloud-based measurements. The following 8 sections are in increasing order of "physical significance." Readers who are interested in understanding the underlying physics of EMPI should read only Secs.8.1.9 and 8.1.10, and skip the next paragraph. Readers from other collaborations hoping to implement EMPI should probably skip only Secs.8.1.1 and 8.1.2. Only readers from the ALPHA collaboration who want to implement EMPI should read the entirety of this section.

Many of these sequence improvements rely on some understanding of the systems involved in applying voltages to the electrodes. "The sequencer," is the name given at ALPHA to the collection of LabVIEW software and National Instruments hardware that applies a sequence of voltages to the electrodes. In the software, we can design a sequence of voltages called "states" to be applied to the electrodes, and between each state we can linearly change the electrode voltages in a certain number of "ramp steps." Some states also do not change the electrode voltages, but instead trigger digital bits, for example to trigger the camera to take a picture. When we prepare to run a sequence on the actual experiment, part of the sequencer called the "analog sequencer" loads our voltage sequence onto an FPGA. The "digital sequencer" loads our sequence of digital bits onto another FPGA, and when we

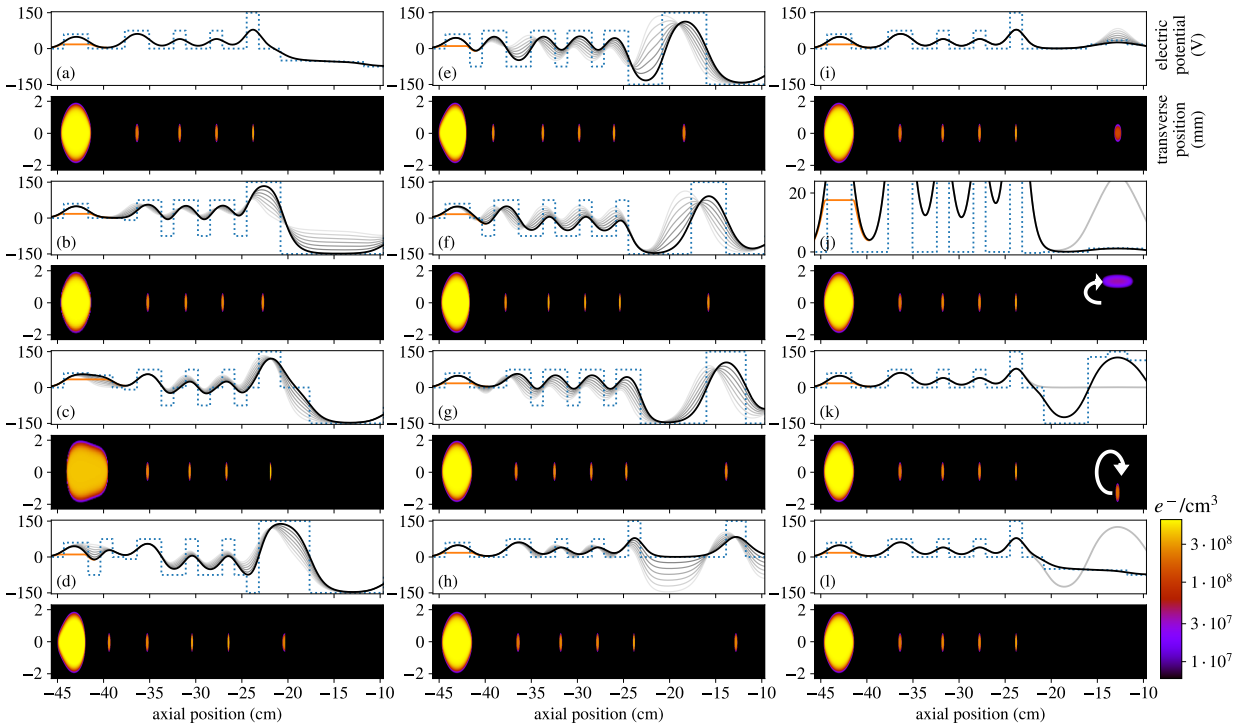

Figure 8.1: Sixteen steps are shown in the potential manipulations used to perform an EMPI measurement with one electron cloud. Each step is described in Sec. 8.1. For each step, the plot above shows the electrostatic potential, and the plot below shows the electron plasma reservoir and the electron clouds. Above, the dashed line shows the electrode potentials. The solid black line shows the on-axis potential created by the electrodes. The orange line shows the on-axis potential perturbed by the reservoir's space charge. If the potential manipulation between two steps is a linear change, grey lines show how the potential changes from the previous step to the current one. If the potential manipulation is "instantaneous" i.e. as fast as the electrode potentials can change ($\sim 10\,\mu$s), only one grey line shows the potential of the previous step. Note that the vertical scale changes in step (j) to show the much smaller shallow potential used to move a cloud off-axis. Below, the electron density is plotted along a cross section of the trap. The reservoir's plasma parameters are roughly accurate, but the electron cloud charge, temperature, and radius are exaggerated to make them larger than a single pixel. In steps (j) and (k), a white arrow indicates the electron cloud's magnetron orbit and the electron cloud is shown off axis.

"execute" the sequence, an 80 MHz clock (1/12.5 ns) on the digital sequencer maintains the timing of the sequence. In addition to outputting the digital triggers for various pieces of equipment, the digital sequencer sends a trigger to the analog sequencer when a new voltage is to be applied to the electrodes. The NI hardware has analog outputs between -10 and 10 V, which change to the next value in the sequence when triggered, and these voltages are amplified by amplifiers purpose-build for the ALPHA collaboration which come in either ± 75 V or ± 150 V variants. Both the analog and the digital sequencer have memory limits

on their respective FPGAs. A single sequence can have about 205,000 ramp steps and about 3400 states (including both endings of linear voltage ramps and digital output bits). The bottom 9 electrodes in ALPHA-g and the top 27 electrodes have separate sequencers, called the "recatching sequencer" and the "atom sequencer" respectively (this was already described in Sec. 6.2). During EMPI measurements, the recatching sequencer is in control of the reservoir, and the atom sequencer controls the clouds for measurements. Some digital bits need to be sent between the two sequencers to make sure that they stay synchronized (i.e. the recatching sequencer shouldn't attempt to transfer a cloud to the atom sequencer when the atom sequencer doesn't have a trapping potential ready to contain the cloud).

8.1.1 Sequence bridging

It takes about 15 states in the atom sequencer to perform the EMPI measurement procedure for a single electron cloud. This is dramatically less than the $\sim$ 50–100 states in previous cloud based measurements. Thus with the 3400 state limit, only about 200 clouds can be imaged before we need to load a new sequence. A limit of 200 magnetic field measurements is not really acceptable. Thus while maintaining the reservoir in place, new voltage instructions are loaded into the FPGA then executed. This process takes about a second. To retain well-defined timing, I always ensure that either the recatching or the atom sequence is running. If a new atom sequence needs needs to be loaded in, the recatching sequence first waits for a digital bit signalling the end of the previous atom sequence. When it receives that signal it waits for 1 second, during which time the new atom sequence should be loaded in, then the recatching sequence sends a digital bit to the new atom sequence to start. Thus the loading of a new atom sequence takes exactly 1 second, rather than some random amount of time less than a second. Luckily, when a sequence has ended the voltages applied to the electrodes at the end of that sequence remain in place until a new sequence is executed. Typically, a single recatching sequence handles 400 cloud extractions from the reservoir, and an atom sequence handles 200 clouds performing an EMPI measurement, so the atom sequence has to be reloaded twice as often. The recatching sequencer's responsibility in this process requires fewer states per cloud. The end result of this is that every 200 clouds there is a pause in EMPI measurements of one or two seconds.

Unfortunately, the one second wait was a mistake—the most consequential mistake I made in the EMPI measurements. Some of the sequences, particularly the EMPI measurements higher in the trap, took a bit longer than one second to load. The way I implemented sequence bridging, this meant that the new sequence would start after some undefined time greater than one second. If I had designed the sequences to fail if they took longer than a second to load, this issue would have been immediately noticed and fixed, but I did not. If I had designed any external measurement of the sequence timing, this issue could have been fixed with post-hoc analysis, but I did not. All of the EMPI measurements took place in the final two weeks of the 2022 ALPHA-g experimental run. Most of the analysis was done long after it became impossible to perform further measurements. Of course, performing a complicated novel measurement in such a short time on extremely limited sleep is bound to result in a few errors; I'm pleasantly surprised that there is any usable data from that time.

8.1.2 One-sided syncs

Throughout the ALPHA experiment, "syncs" are used to make one sequencer wait for another. A sync involves sequencer A waiting for a digital bit from sequencer B, then sequencer A sends a digital bit back to sequencer B. Meanwhile sequencer B leaves a digital bit on until it receives the response bit from sequencer A. Thus when either sequencer reaches the point in the sequence with the sync, it waits for the other one to reach the sync as well, and then they both proceed.

Typically when we perform a cloud-based measurement, the atom sequencer "syncs" with the recatching sequencer when it has just finished with one cloud to signal that it wants a new one, and when the recatching sequencer has the next cloud ready to transfer to the atom sequencer, the two sync again. Each sync uses 3 states, for a total of 6 states per cloud. This is an unacceptable waste. Thus I reduced this to 1 state per cloud by only having the recatching sequencer wait for a bit to come from the atom sequencer, and the atom sequencer receives nothing in response. This requires some care—now that the atom sequencer isn't told when a cloud is coming, the atom sequence needs to be aware of how much time passes from when it sends the trigger to when a cloud is delivered. This is not difficult, but previously we could change the amount of time it takes to extract a cloud from the reservoir without changing the atom sequence, and this no longer works. Also, if the recatching sequencer isn't ready to receive the trigger when it comes, the trigger is simply missed and the atom sequence will perform a cloud-based measurement without any cloud present. The telltale sign of this failure is that the recatching sequence doesn't complete when the atom sequence does, and it continues to wait for an additional trigger that will never come.

8.1.3 Negative voltages during cloud movement

This upgrade was previously discussed in Sec. 2.3.3 when I discussed optimal ways to move clouds along the trap. There, I explained that when a cloud is moved along the trap axis by transferring it from one electrode to the next, the cloud can be moved off-axis if it is moved too quickly. Here "too quickly" is specifically defined as the speed of the "effective trap center" being comparable to (as opposed to much smaller than) the speed of magnetron motion—this is called the "adiabatic condition." The effective trap center is the center of magnetron motion, which can differ from one electrode to the next because of patch potentials or misalignment between the electrodes and the external magnet.

The goal of these axial cloud movements is to go as quickly as possible without exciting the magnetron motion. The clouds used for EMPI were initialized with a small magnetron orbit of about $25\,\mu$m due to the so-called "intrinsic magnetron" (see Sec. 2.3.1). My goal was to not increase that initial magnetron orbit. By increasing the trapping voltage used to confine electrons as they are moved along the trap axis, the magnetron frequency increases, meaning we can move the clouds more quickly without violating the adiabatic condition. Of course, this meant the maximum positive voltages allowed on each electrode were always used. Additionally, when clouds were being moved along the trap axis, all the other electrodes not containing a cloud were set to the maximum negative voltages. This is equivalent to simply doubling the voltages used to confine the electrons.

8.1.4 Bad amplifiers

When I first attempted EMPI measurements, I found that under some electrodes the measurements would fail. An example of this failure is shown in Fig. 8.2. In the top row, electrons are moved to electrode 35, then they are moved off axis, then they orbit the trap for about 100 ms, then they are imaged. On the bottom row, electrons are moved to electrode 23 instead. In each of the four images, I am slightly changing the trapping potential that the clouds perform a magnetron orbit in, but this doesn't really matter (I did not take any data specifically to illustrate this issue). What matters is that in each subplot, if the electrodes are behaving properly, the cloud positions should form a coherent spiral. Not only does this not occur in electrode 35, the effect seems to be intermittent. In the second plot, most of the cloud positions fall along a spiral, but a few do not. In the fourth plot, almost no pattern is visible. Sometimes, in other repeats of this experiment, no issue is observed at all.

These observations are explained by the voltage on at least one electrode not being consistent from one cloud to the next. It seems that an amplifier will apply a desired voltage during one cloud's magnetron orbit, but the amplifier's performance can drift for a few seconds, or become noisy for a few seconds, then return a few seconds later. The magnetron frequency, and by extension the electrode voltage, only needs to drift by about 1 part in 10^4 to explain this effect. Each cloud arrives at the correct magnetron radius, but sometimes not at the correct magnetron phase, which is how we know the electrode is not grossly changing voltage—the shallow well used to move clouds off axis still seems to work. The amplifiers were not designed with precision stability in mind, although it seems most of the amplifiers achieve precision stability anyway. The problem was solved by simply swapping electrode amplifiers one at a time until the offending amplifier was identified. The bad amplifier is now assigned to control electrode 9 because there are no spare 150 V amplifiers; I cannot imagine wanting to perform a precision measurement with electrode 9, and the stability of a plasma confined there is unlikely to be affected by this kind of low frequency ($\mathcal{O}$(1–100 Hz)), low amplitude ($\mathcal{O}$(0.1–1 mV)) noise. Later I found that another electrode somewhere in the vicinity of 27–30 was also problematic, but this is much less important because the ALPHA-g measurement was only precisely sensitive to the magnetic field near mirror coils A and G, centered on electrodes 23 and 35 respectively.

It still isn't entirely clear to me why these measurements were affected by this issue but previous cloud-based measurements, specifically patch potential measurements, were not. During patch potential measurements, there were certainly times when clouds would perform a magnetron orbit for tens of milliseconds under the affected electrode and still image as a coherent spiral. It could be that the amplifier degraded over time. Alternatively, EMPI measurements demand more power from the amplifiers. The amplifiers switch between +150 and −150 V several hundred times per second in EMPI measurements, and about 2 per second for patch potential measurements. It could be that the resulting strain causes the electronics to behave differently.

8.1.5 Cloud pipelining

The clouds are moved at a speed of 2.5–5 ms per electrode along the trap depending on the trap location. With 30 electrodes to move across, if every new cloud was transported from the reservoir to the measurement location, it would take about 150 ms. To reduce

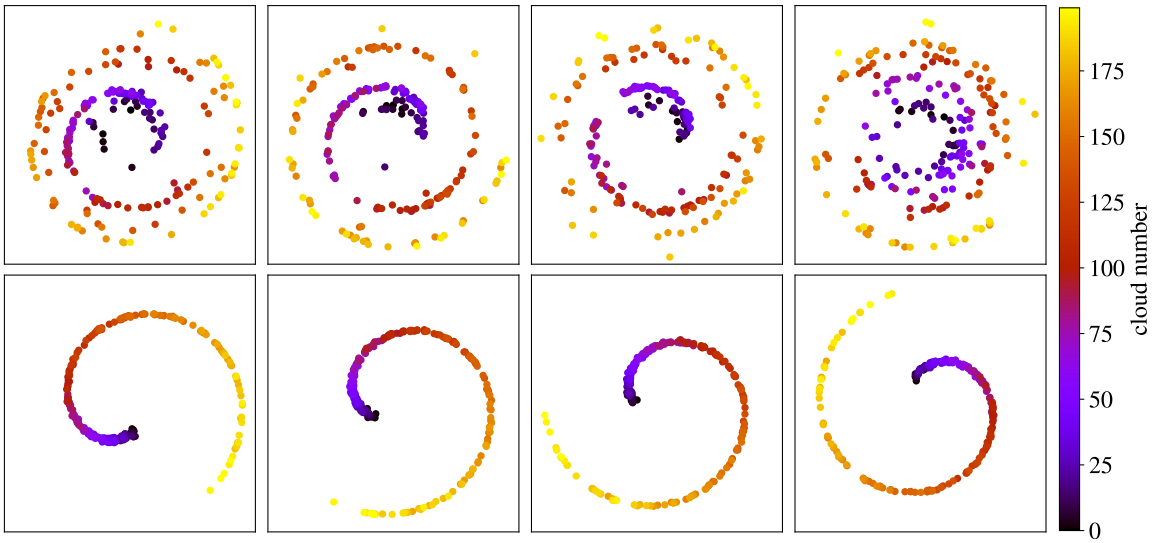

Figure 8.2: Imaged cloud positions on the MCP after after being moved off axis then performing a magnetron orbit for about 100 ms in electrode 35 (top) and electrode 23 (bottom). Each cloud is moved a different distance off axis, with the first clouds in each dataset being moved the shortest distance off axis. In each column, a different trapping potential is applied during the magnetron motion, explaining the different positions of the spirals in the bottom row, but this difference is not important for the current discussion.

this time and to reduce the number of voltage states needed to move the clouds, instead of extracting a cloud from the reservoir and moving it to the measurement location, several clouds are stored between the reservoir and the measurement location. When one cloud is imaged, every existing cloud is moved one step to the right, and a new cloud is placed in the beginning of the "line." This is shown in Fig. 8.1. Pipelining is a term from computer science, where a similar idea is used to make more efficient CPU's by having multiple CPU instructions execute during the same clock cycle.

Typically clouds are stored in one in three or one in four electrodes. Note that it is not possible to store clouds in every other electrode (consider what would happen when you tried to transfer each cloud to the next electrode). For some electrodes with large patch potentials or electrodes which are poorly aligned (electrodes 18–20, see Sec. 6), clouds are only allowed to be moved at a speed of one electrode per 5 ms with 150 V used to confine the electrons and the adjacent electrodes being set to -150 V. In other electrodes without such issues, clouds are allowed to be moved at a speed of one electrode per 2.5 ms, and some electrodes are only connected to ± 75 V amplifiers. Thus the algorithm for designing these cloud movements was very complicated (and frankly not very elegant).

I never fully tested if these precautions were necessary, or if clouds could be moved more quickly in some trap locations. I based these numbers on a somewhat conservative interpretation of the data from Sec. 2.3.3. It is observed that the clouds have only an intrinsic magnetron when they arrive at the measurement location, indicating that these speeds were sufficiently slow.

The final cloud in the "pipeline," or the next cloud to be used for a measurement,

needs to be a bit further from the cloud currently being used for a measurement. This is mostly because the shallow well used to move the current cloud off axis is very sensitive to the perturbation from the confining potential of the next cloud. Thus this cloud is stored typically 5–6 electrodes away from the measurement location, and this is really what sets a minimum time between EMPI measurements.

8.1.6 Shielding voltages

When a voltage V_0 is applied to an electrode centered at $z = z_0$ in an otherwise infinitely long grounded cylinder, the on-axis potential far from that electrode ($z - z_0 \gg R_w$) takes the approximate form $A\exp[-(z-z_0)\alpha_1^0/R_w]$, where α_1^0 is the first zero of the zeroth Bessel function of the first kind, R_w is the trap wall radius, and A is a constant which is proportional to the voltage applied. If we apply a voltage $-V_0\exp(-l\alpha_1^0/R_w)$ to the adjacent electrode a distance l to the right of the first electrode (assuming identical electrodes), the potential far from these two electrodes is now:

$$A\exp\left[-\frac{(z-z_0)\alpha_1^0}{R_w}\right] - A\exp\left(-\frac{l\alpha_1^0}{R_w}\right)\exp\left[-\frac{(z-z_0-l)\alpha_1^0}{R_w}\right] = 0. \tag{8.1}$$

Of course further terms with stronger exponential suppression like $A_1\exp[-(z-z_0)a_2^0/R_w]$ take over, but the point remains that the the on-axis potential far away is much smaller. Thus these "shielding voltages" are used to reduce the impact of cloud pipelining on parts of the EMPI sequence which sensitively depend on the trapping potential. This occurs in two circumstances—the first cloud in the pipeline has a shielding voltage on its left to prevent it from perturbing the potentials used to extract a new cloud from the reservoir, and the last cloud in the pipeline has a shielding voltage on its right to prevent it from perturbing the potentials used to move a cloud off-axis. These potentials are barely visible in Fig. 8.1 [in steps (b), (c), and (j) it is possible to perceive them], because $-V_0\exp(-l\alpha_1^0/R_w)$ is fairly small, but they do make it quite a bit easier to design EMPI measurements.

8.1.7 Deep pre-dump potentials

In Sec. 3, the clouds were moved off-axis using a "shallow" trapping potential, then they performed a magnetron orbit in a "deep" trapping potential, then they were transferred to a "pre-dump" potential. The pre-dump potenital held the electrons at a negative absolute potential so that they could be released toward the MCP with a few eV of kinetic energy. In Sec. 6, this procedure was upgraded by having the shallow potential and the pre-dump potential be identical. Similarly, here, the electon clouds only perform a magnetron orbit in one trapping potential—a deep pre-dump potential. The clouds go from a shallow potential to a deep potential with an "instantaneous" voltage change. The deep potential confines the electrons with a positive voltage surrounded by negative ones, for example $[-150, 150, -150]$ applied to three adjacent electrodes. Then to release the electrons toward the MCP, the barrier on the side of the MCP is lowered, and the potential in the center is raised, all in a single instantaneous voltage change, so we might go to $[-80, -100, -150]$ to image the clouds. This ensures that, with the exception of the $\mathcal{O}(10\,\mu\text{s})$ that it takes for the electrode voltages to change in these instantaneous voltage changes, the clouds perform a magnetron orbit in only one trapping potential. This makes the calibration of the magnetron frequency versus magnetic field simpler—there is only one magnetron frequency to keep track of.

8.1.8 Axially offset shallow potentials

As measured in Secs. 3 and 6, the patch potential created transverse electric field ε varies randomly throughout the trap. In some axial trap locations, it is nearly zero. Here we rely on significant patch fields to quickly move the electron clouds off-axis. In the past, the axial position of the shallow trapping potential used to move clouds off axis was the same as the axial position of the deep trapping potential. In fact, the deep trapping potential was the shallow one times a large constant. Here, in order to achieve comparable measurement frequencies in all trap locations, in many cases, the axial position of the shallow trapping potential is offset from the deep one by up to 3/4 of an electrode length (1.5 cm).

This shouldn't have any negative effect on the measurements. The (10 μs) that it takes for the electrode voltages to change between the shallow and the deep well is still adiabatic with respect to the axial bounce motion of electrons. Therefore the clouds simply move axially, following the moving minimum of the trapping potential without heating. The only exception to this is if the electrons are "dropped off a cliff," as illustrated in Fig. 8.3. If the confining potential for electrons is changed by too much in one of these operations, it is possible for there to be a moment between the shallow and the deep wells where there are two local maxima, and the electrons are eventually released from one local maximum into the other one, causing them to gain several eV of kinetic energy, which equates to tens of thousands of Kelvin of temperature after the system comes to equilibrium. This can be avoided by carefully modelling the electrode potentials versus time as described in Sec. 6.4. Alternatively, I chose to conservatively set a maximum axial distance of 1.5 cm, where it is impossible for this to occur regardless of how the electrode voltages change from their initial to their final values. This gives me enough freedom to avoid having to use exceptionally weak patch fields to move clouds off-axis.

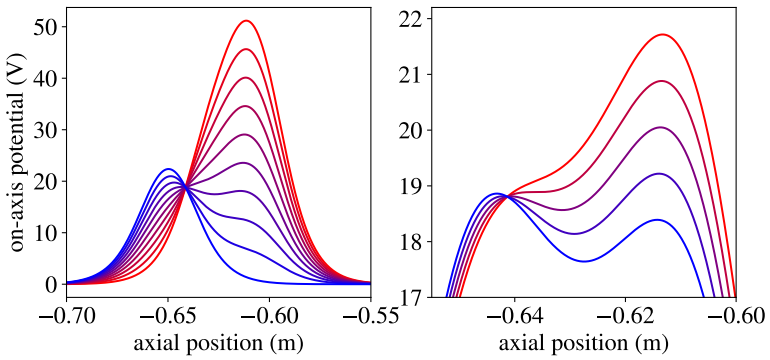

Figure 8.3: The trapping potential on three adjacent electrodes is changed from $[40, 0, 0]$ to $[0, 40, 75]$, moving the axial trap center by over 1.5 electrode lengths. On the left, the on-axis trapping potential is shown over time, with the beginning of the process being the blue curve and the end being the red curve. On the right, I zoom in on the point in time where the issue occurs. I assume that the trapping potential is changed linearly from the start to the end, which is not really accurate as described in Sec. 6.4, but this is just a toy model meant to illustrate a possible issue.

8.1.9 Purely quadratic trapping potentials

In my first attempt at performing EMPI measurements, when the clouds were performing a magnetron orbit, I used the highest magnetron frequency possible by applying confining voltages of $[-150, 150, -150]$ on three adjacent electrodes. With these potentials, we achieve a magnetron frequency of about $4 \times 10^5/s$ in $B = 1\,\mathrm{T}$. Most of the EMPI measurements required about 2000 radians of magnetron motion, which takes only 5 ms. However, in this trapping potential $k_4 \approx 5 \times 10^8\,\mathrm{V/m^2}$, and the resulting variation in magnetron frequency with radial position causes a significant variation in magnetron phase through the variations in the clouds' initial positions. I realized that in our specific application, it would be better to use a trapping potential which was optimized to have $k_4 \approx 0$. This would significantly reduce the magnetron frequency (by about a factor of 2), but because it already takes about 10 ms to move the clouds to the measurement location and about 5–10 ms to move the clouds off-axis, this would not actually significantly reduce the measurement frequency.

I made software which would find trapping potentials with $k_4 \approx 0$ at each axial location where I wanted to perform EMPI measurements. However, in this software there were two mistakes. First, at the time, I was not aware that a k_3 term in the trapping potential would also cause a variation in the magnetron frequency with r (although this effect is generally smaller than the spiraling from a k_4 term). Second, finding the fourth derivative of the trapping potential is quite numerically unstable, and I wasn't sufficiently careful about how I was evaluating the k_4 term. As a result, when I measured the spiraling in each axial trap position, I found that there was still a significant remaining k_4 in the trapping potentials. Despite these mistakes, the trapping potentials I designed had significantly less spiraling than if I had made no attempt to do this optimization.

In one particularly critical trap location, the center of mirror A, I ameliorated this mistake by tuning the trapping potential to exhibit less spiraling. In this trap location, the software described above found that there should be zero spiral coefficient when the following voltages were applied to electrodes 18–26: [150.0, −0.335, −150.0, −150.0, 142.809, 150.0, 128.801, −75.0, −75.0]. The positive voltage on electrode 18 holds the next cloud in the pipeline, and the small negative voltage on electrode 19 is a shielding voltage. The software found that this potential provided the maximum magnetron frequency while having the cloud centered in the center of electrode 23 with $k_4 = 0$. To adjust the spiral constant while changing the axial position of the well very little, I changed the voltages on electrodes 22–24 to $[142.809 + \Delta_V, 150.0, 128.801 + \Delta_V]$. For several different values of Δ_V, clouds were moved off axis a variable distance, then they orbited the trap center for about 100 ms, and then they were imaged.

In Fig. 8.4, I show the result of this experiment. The entire dataset was taken with 1200 clouds extracted from a single reservoir (the first 200 clouds are discarded as the reservoir settles), and each set of 200 clouds is handled with one sequence. Thus, between each set of 200 clouds, there is either a 1 or 2 second pause. The clouds only have precisely identical charge if they are extracted at a constant rate. Thus after the pause between sequences, the first 40 or so clouds have a different charge or temperature. This is why, in each dataset in Fig. 8.4, the clouds closest to $r = 0$, which are extracted first, deviate from the predicted spiral shape $\theta \propto r^2$. Thus I ignore the first 50 clouds when I fit a spiral constant to the

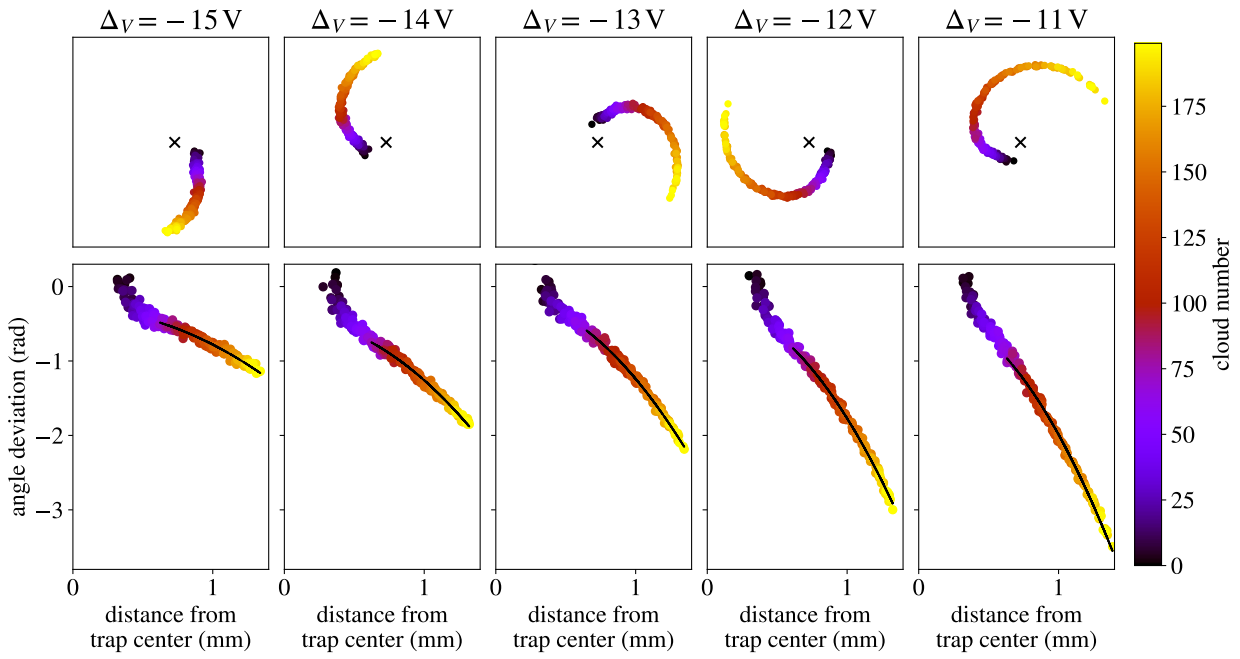

Figure 8.4: Top row: the positions of clouds on the MCP are shown for five different Δ_V values, with the center of the trap indicated by a black X. Bottom row: the cloud angular positions are plotted versus distance from the trap center, and a spiral $\theta \propto r^2$ is fit to this data.

clouds' angular positions versus distance from the trap center.

In Fig. 8.5, I show a proper way of predicting the spiral constant with an electrostatic model of the trap. Two different electrostatic models are used. The first is an analytic model which makes an inaccurate assumption about the shape of the radial step between electrodes 19 and 20, and which assumes that there is an infinitely long grounded cylinder beyond the ends of the first and last electrode. The second model is generated with COMSOL by Dr. Chukman So. For each model, I fit a quartic polynomial to a variable length of the on-axis potential. We expect to find that when the fitting length is too short, numerical instability will take over, and that we will be able to see the reliable fits approach a constant value as the length goes to zero. We find that when the fitting range reaches about 2 cm, the COMSOL model starts to deviate from the analytic model (which should be very accurate in this trap region), and at about 1 cm the COMSOL model clearly suffers from numerical instability. The analytic model gives a reliable value for k_4 even when the fitting length is a few millimeters. It appears that for estimating fourth derivatives, the analytic model is simply much better. It's hard to recover exactly what I used when originally designing these trapping potentials, but if I remember correctly the COMSOL model was used—so it's clear why the resulting trapping potentials still exhibited spiraling. Similar plots were produced to estimate k_2 and k_3, but these lower order constants are subject to less numerical instability.

With these carefully estimated trapping potential coefficients, the predicted versus observed spiral coefficients are in reasonable agreement, as shown in Fig. 8.6. In the end,

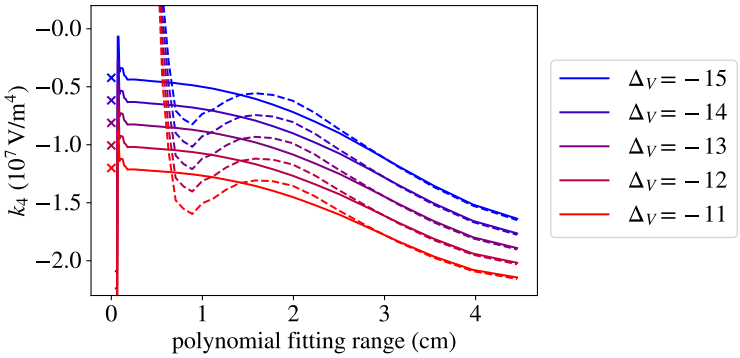

Figure 8.5: k_4 values are plotted versus the length of the trapping potential used to fit a quartic function. The dashed lines come from fitting to the on-axis potential predicted by COMSOL. The solid lines are the result of fitting a quartic function to the on-axis potential predicted by the analytic model. The X's are the result of extrapolating the reliable values from the analytic model to fitting range 0. This was what I considered to be the best estimate of k_4. The analysis is performed on five different trapping potentials with five different electrode voltage perturbations Δ_V.

$\Delta_V = -16$ was used for further experiments. Although this wasn't tested here, it is clear from a simple extrapolation that this will produce minimal spiraling. This dataset is also the first direct evidence that the term $(9/4)k_3^2/k_2$ contributes to the spiraling.

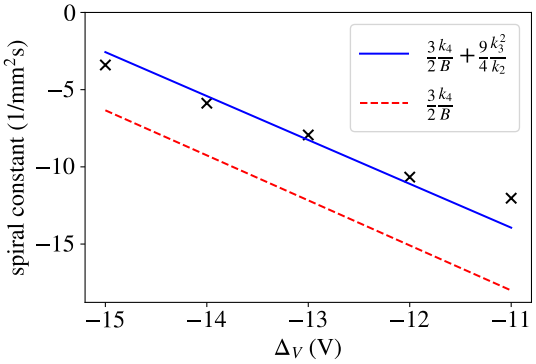

Figure 8.6: The spiral constant extracted from the data in Fig. 8.4 is plotted versus Δ_V. The red dashed line is an incomplete prediction of the spiral constant including only k_4, and the blue solid line is the full prediction.

8.1.10 Instantaneous shallow wells and initial magnetron phase randomization

In all the previous cloud-based measurements, when I wanted to move clouds off axis, I used the adiabatic procedure described in Sec. 3.3. In a typical patch field, it takes about 100 ms to move a cloud off-axis by about a millimeter in this way. This is not strictly unacceptable. I could move clouds off axis a bit less than a millimeter and accept a measurement repetition rate of about 10 Hz. However, I realized that we could move clouds off-axis a lot

more quickly if we "instantaneously" switched to a shallow trapping potential, having the clouds orbit an effective trap center displaced by $\vec{\varepsilon}/k_2$. The clouds will start at the true trap center, and after half an orbit they will be displaced by $\vec{\delta} = 2\vec{\varepsilon}/k_2$. The time taken for this process will be $\pi B/k_2$, or in terms of the distance off axis, $\pi B\delta/\varepsilon$. This is dramatically faster than the adiabatic procedure, which needs to go to half the k_2 value for the same displacement, and which requires many magnetron orbits instead of half a magnetron orbit.

Unfortunately, this manner of moving clouds off-axis relies on knowledge of the magnetic field, which is exactly what we hope to measure with EMPI. However, with a simple model of the magnets present in the experiment, we can achieve a prediction of the magnetic field which is accurate at the 1% level. With this 1% error, there will be an error in the initial positions of clouds of about $10\,\mu$m (assuming a typical $\delta \sim 1\,$mm). The error in the radial positions of the clouds will be significantly smaller because we finish this operation at the radial position maximum of the orbit. With the cloud's initial magnetron diameter of $50\,\mu$m, the variability in initial cloud positions is much bigger than this error. Our resulting measurements of the magnetic field will be much more precise than the 1% prediction needed to set up the measurement.

In future applications of EMPI, we should keep in mind that the adiabatic procedure has its own advantages. The adiabatic procedure is only sensitive to the magnetic field in that when the magnetic field increases, the magnetron frequency decreases. Therefore the adiabatic movement must be sufficiently slow that it remains adiabatic if the magnetic field increases by a factor of two. If this condition is satisfied, the adiabatic procedure essentially delivers clouds to the same position independent of the magnetic field—an electrostatic potential maximum along the magnetic field and a minimum in the direction transverse to the magnetic field. One further caveat is that the angle of the magnetic field relative to the electrodes can be changed by energizing magnets, and this can shift the position of the electrostatic trap center, but this really is an absolutely negligible effect for the current level of precision.

In a bit more detail, when I have finished moving an electron cloud to a desired axial measurement location, it sits in a trapping potential formed by applying 75 V or 150 V to one or two electrodes. I begin by adiabatically reducing that potential to 10–20 V to reduce the magnetron frequency. The well constant k_2 in this medium-depth well will be called k_{2a}. From there, the trapping potential is instantaneously lowered to the weak trapping potential used to move the clouds off-axis (typically of order 0.5 V), where the well constant will be called k_{2i}. The purpose of the well with $k_2 = k_{2a}$ is to reduce the $\mathbf{E} \times \mathbf{B}$ drift velocity of the electron cloud so that when we go to k_{2i} in a few microseconds, the electrode potential change can be better approximated as instantaneous. I never really checked if this precaution was necessary. When the cloud has reached its desired position, we snap to the trapping potential discussed in the previous section where the cloud will perform many magnetron orbits for an EMPI measurement. The trap constant in this final well will be labelled k_{2f}. In the first well with $k_2 = k_{2a}$, the cloud will be located a distance ε/k_{2a} from the true trap center. Then when we go to $k_2 = k_{2i}$, the cloud will be in a magnetron orbit of radius $\varepsilon(1/k_{2i} - 1/k_{2a})$. It will perform half an orbit, arriving at a distance $\varepsilon(2/k_{2i} - 1/k_{2a})$ from the trap center. In the end, the cloud will be in a magnetron orbit of radius $\varepsilon(2/k_{2i} - 1/k_{2a} - 1/k_{2f})$, of course plus or minus the initial magnetron radius due to the intrinsic magnetron of the cloud.

Another use of the intermediate trapping potential with $k_2 = k_{2a}$ is that I pause in this trapping potential for a variable time to phase-unlock the initial magnetron motion. For all EMPI measurements, the movement time along the trap axis and the reservoir have been tuned so that the clouds' initial magnetron motion is due to the intrinsic magnetron. As discussed in Sec. 2.3.1, the intrinsic magnetron can be phase locked if the clouds are sufficiently reproducible. To avoid this resulting in a systematic error on EMPI measurements, for the n'th cloud, I wait in this trapping potential for a time given by $(n \bmod 4)\pi B k_{2a}/2$ so that each successive cloud has a different initial magnetron phase by $\pi/2$. I neglected to realize that when the cloud currently being used for a measurement is sitting in this trapping potential, the next few clouds in the pipeline are also accumulating magnetron phase, and there is really no reason to think that the initial magnetron phase difference will really be $\pi/2$—it could be anything. When the magnetic field is changing rapidly during the most important EMPI measurements, the end result is that the initial magnetron phase is essentially random. In fact, it would have been much better to produce random phase shifts on purpose than to proceed in steps of $\pi/2$.

In Fig. 8.7, this procedure is performed, then clouds do a large magnetron orbit for a very short time before being imaged. However, instead of the cloud spending a time $\pi B/k_2$ in this trapping potential, I vary this time between $2\pi B/k_2$ and $\pi B/2k_2$ to illustrate the circular motion of the clouds. The cloud positions are as expected. Note that in Fig. 8.7, the influence of k_{2a} and k_{2f} is ignored. In Fig.8.8, instead of varying the time in the shallow well,

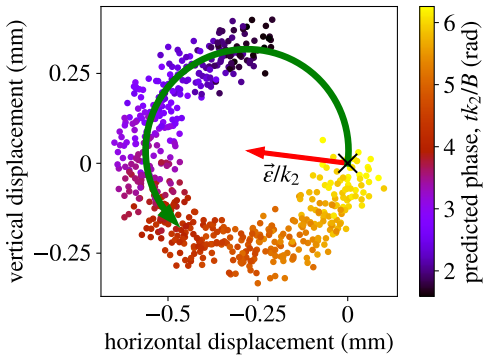

Figure 8.7: Imaged cloud center positions after spending a variable time in the shallow trapping potential with $k_2 = k_{2i}$. The green arrow indicates the direction of the magnetron orbit. The red arrow indicates the inferred direction of the displacement between the true trap center, marked with a black X, and the displaced trap center due to patch potentials.

I use the nominal time of $\pi B/k_{2i}$ and I vary k_{2i} to vary the clouds' displacement from the trap center. As expected, the clouds form a line. I also plot the clouds' radial displacements from the trap center versus k_{2i} and fit a line. A small offset in this line is the right order of magnitude to be due to patch potentials perturbing the trap constant in the shallow well. Note that k_{2f} is ignored in this analysis—the offset is about 8 times the effect of k_{2f}, so it wouldn't make sense to include this contribution if another source of error had a much more significant effect.

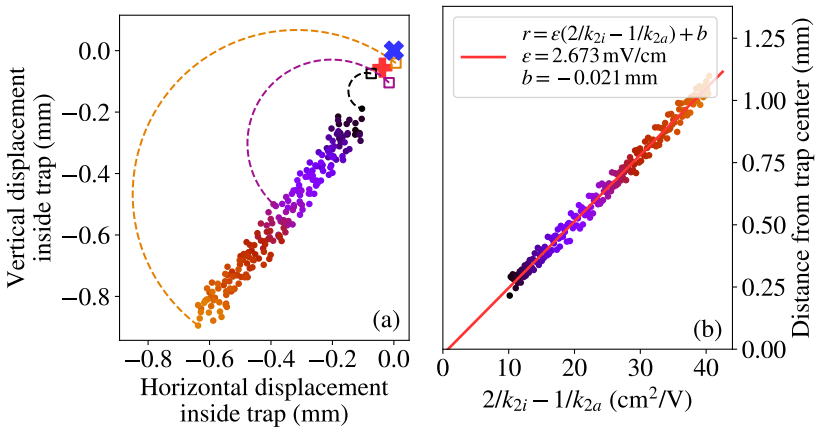

Figure 8.8: On the left, cloud positions are shown for a variable k_{2i} used to move clouds off-axis. Dashed lines show the presumed magnetron orbit of the clouds used to move them off-axis, with boxes indicating their initial magnetron position at the beginning of this operation. The red plus is the effective trap center when the clouds are in the trapping potential with $k_2 = k_{2a}$, and the blue X is the true trap center. On the right, the same clouds' radial displacement from the trap center is plotted versus $2/k_{2i} - 1/k_{2a}$, and the red line is a linear fit to the data.

8.1.11 Breakdown of the EMPI voltage sequence

At this point I have finished describing the underlying concepts for the design of EMPI sequences, and I can breakdown the sequence of voltages used to image a single cloud during EMPI. The steps below correspond to the steps shown in Fig. 8.1. The amount of time for each step is listed as well, but these numbers are specific to the measurement shown here, the one in the center of mirror A. In some axial measurement locations, a different number of steps is needed to move the clouds axially, and there is a different number of clouds in the pipeline. The amount of time needed to move the clouds off-axis also varies with the strength of nearby available patch fields and with the desired distance off-axis. The amount of time in the magnetron orbit also varies with what electrode voltages are available (75 or 150 V) in a given trap region, and of course it varies with the number of magnetron orbits used in a specific EMPI measurement:

(a) 0.1–6.3 ms—This is the state that the potentials are left in from the release of the previous cloud toward the MCP. We wait here for a moment to ensure that clouds are extracted from the reservoir at regular intervals (which is not strictly necessary, but it simplifies some parts of the analysis). This wait is used to account for variability in the timing of other steps.

(b) 2.4 ms—The negative voltages are applied to increase the magnetron frequency of the pipeline clouds, and some clouds are moved by half an electrode.

(c) 1.0 ms—The reservoir is elongated in preparation for extracting a cloud in the electrodes controlled by the recatching sequencer, and clouds are moved by about a quarter

of an electrode in the atom sequencer.

(d) 1.0 ms—A new cloud is cut from the reservoir by the recatching sequencer, and clouds are moved by about a quarter of an electrode in the atom sequencer.

(e) 2.4 ms—Clouds are moved along the trap.

(f) 2.4 ms—Clouds are moved along the trap.

(g) 2.4 ms—Clouds are moved along the trap.

(h) 2.4 ms—The negative voltages are removed, and some of the clouds are moved a final half an electrode to their final position.

(i) 2.9–3.5 ms—The "target cloud" which will be used for an EMPI measurement is adiabatically put in the shallower trapping potential with $k_2 = k_{2a}$. We also pause here for 0.1–0.6 ms to vary the initial magnetron phase.

(j) 6.6–11.4 ms—We quickly change the trapping potential to the shallow one used to move the cloud off-axis, and we wait for the cloud to execute half a magnetron orbit. The times listed here are for the best measurements of the magnetic field during the 20 s rampdown used to release antihydrogen in the ALPHA-g measurement. In those measurements, it took 11.4 ms to move the cloud off-axis in $|B| = 1.7\,\mathrm{T}$ and 6.6 ms in $|B| = 1.0\,\mathrm{T}$

(k) 22.5 ms—The cloud is put in the deep, purely quartic trapping potential used for EMPI. Again the time listed here is for one axial trap location and for the measurements during the 20 s magnet rampdown, which used a total magnetron phase of 2000 radians.

(l) The cloud is released toward the MCP to be imaged. This is the same step as (a).

8.2 Corrections to the magnetron frequency

8.2.1 Spiraling in the presence of an inhomogeneous magnetic field

In Sec. 3.4 it was shown that a trapping potential approximated by:

$$\Phi_{\mathrm{T}} = -k_2\left(z^2 - \frac{1}{2}r^2\right) + k_3\left(z^3 - \frac{3}{2}zr^2\right) + k_4\left(z^4 - 3z^2r^2 + \frac{3}{8}r^4\right) + \cdots \tag{8.2}$$

results in an r dependent z equilibrium position: $\langle z\rangle = -3r^2k_3/4k_2$ and a magnetron frequency given by:

$$\omega_r(r) = \frac{k_2}{B} - 6\frac{k_4\langle z^2\rangle}{B} + \left(\frac{9}{4}\frac{k_3^2}{k_2B} + \frac{3}{2}\frac{k_4}{B}\right)r^2 + \cdots . \tag{8.3}$$

Now, I want to additionally introduce a spatial variation in the magnetic field, taken from Sec. 7.3.

$$B(r,z) = \left(B_0 + B'z + cz^2 - \frac{1}{2}cr^2\right)\hat{z} - \left(\frac{1}{2}B'r + crz\right)\hat{r}. \tag{8.4}$$

The electric field is:

$$\mathbf{E} = \left(2k_2 z - 3k_3 z^2 + \frac{3}{2}k_3 r^2 - 4k_4 z^3 + 6k_4 z r^2\right)\hat{z} + \left(-k_2 r + 3k_3 z r + 6k_4 z^2 r - \frac{3}{2}k_4 r^3\right)\hat{r}. \quad (8.5)$$

The first step is to determine the z equilibrium position as a function of r, which can be found by solving for z in $\mathbf{E}\cdot\mathbf{B} = 0$. We only need to calculate this dot product to second order in r and first order in z, giving:

$$2k_2 z B_0 + \frac{3}{2}k_3 B_0 r^2 + \frac{1}{2}B' k_2 r^2 = 0, \quad (8.6)$$

$$z = -\left(\frac{3}{4}\frac{k_3}{k_2} + \frac{1}{4}\frac{B'}{B_0}\right) r^2. \quad (8.7)$$

The magnetron frequency is given by $(\mathbf{E}\times\mathbf{B})\cdot\hat{\theta}/r|\mathbf{B}|^2$, and I will start with finding $|\mathbf{B}|^2$:

$$|\mathbf{B}|^2 = \left(B_0^2 + 2B' z B_0 + 2cB_0 z^2 - cB_0 r^2\right) + (B'z)^2 + \frac{1}{4}B'^2 r^2. \quad (8.8)$$

$$= B_0^2\left(1 + \frac{2B'}{B_0}z + \left(\frac{2c}{B_0} + \frac{B'^2}{B_0^2}\right)z^2 + \left(\frac{1}{4}\frac{B'^2}{B_0^2} - \frac{c}{B_0}\right)r^2\right). \quad (8.9)$$

Later we will need $1/|\mathbf{B}|^2$ to second order in r and z, which is:

$$\frac{1}{|\mathbf{B}|^2} \approx \frac{1}{B_0^2}\left(1 - \frac{2B'}{B_0}z - \left(\frac{2c}{B_0} - 3\frac{B'^2}{B_0^2}\right)z^2 - \left(\frac{1}{4}\frac{B'^2}{B_0^2} - \frac{c}{B_0}\right)r^2\right). \quad (8.10)$$

And now we calculate $\mathbf{E}\times\mathbf{B}$, going to third order in r and z, because all of the terms will include a factor of r, which will be eliminated when we find the magnetron frequency:

$$\mathbf{E}\times\mathbf{B} = -\hat{\theta}\left[B_0\left(-k_2 r + 3k_3 z r + 6k_4 z^2 r - \frac{3}{2}k_4 r^3\right) + B' z(-k_2 r + 3k_3 z r) + \left(cz^2 - \frac{1}{2}cr^2\right)(-k_2 r)\right]$$
$$- \hat{\theta}\left[\frac{1}{2}B' r\left(2k_2 z - 3k_3 z^2 + \frac{3}{2}k_3 r^2\right) + crz(2k_2 z)\right]. \quad (8.11)$$

So if we ignored the off-center corrections to $|\mathbf{B}|^2$, then the magnetron frequency would be:

$$\frac{\mathbf{E}\times\mathbf{B}\cdot\hat{\theta}}{rB_0^2} = \frac{k_2}{B_0} + \left(-3\frac{k_3}{B_0}\right)z + \left(-6\frac{k_4}{B_0} - \frac{3}{2}\frac{k_3 B'}{B_0^2} - \frac{k_2 c}{B_0^2}\right)z^2 + \left(\frac{3}{2}\frac{k_4}{B_0} - \frac{1}{2}\frac{k_2 c}{B_0^2} - \frac{3}{4}\frac{k_3 B'}{B_0^2}\right)r^2. \quad (8.12)$$

The final magnetron frequency is:

$$\omega_r = \frac{k_2}{B_0} + \left(-3\frac{k_3}{B_0} - \frac{2B'k_2}{B_0^2}\right)z + \left(-6\frac{k_4}{B_0} + \frac{9}{2}\frac{k_3 B'}{B_0^2} - 3\frac{k_2 c}{B_0^2} + 3\frac{k_2 B'^2}{B_0^3}\right)z^2$$
$$+ \left(\frac{3}{2}\frac{k_4}{B_0} + \frac{1}{2}\frac{k_2 c}{B_0^2} - \frac{3}{4}\frac{k_3 B'}{B_0^2} - \frac{1}{4}\frac{B'^2 k_2}{B_0^3}\right)r^2. \quad (8.13)$$

And when we realize that z^n should be replaced with $\langle z^n \rangle$, we obtain:

$$\omega_r = \frac{k_2}{B_0} + \left(-6\frac{k_4}{B_0} + \frac{9}{2}\frac{k_3 B'}{B_0^2} - 3\frac{k_2 c}{B_0^2} + 3\frac{k_2 B'^2}{B_0^3} \right) \langle z^2 \rangle + \left(\frac{3}{2}\frac{k_4}{B_0} + \frac{9}{4}\frac{k_3^2}{k_2 B_0} + \frac{1}{2}\frac{k_2 c}{B_0^2} + \frac{3}{2}\frac{k_3 B'}{B_0^2} + \frac{1}{4}\frac{B'^2 k_2}{B_0^3} \right) r^2. \quad (8.14)$$

The coefficient attached to $\langle z^2 \rangle$ is the frequency shift depending on the length of the cloud, assuming that $\langle z \rangle^2 \ll \langle z^2 \rangle$, which is generally true for all the clouds we consider here (the cloud is displaced in z much less than its length). This correction will be generally ignored going forward. The important thing is the coefficient attached to r^2, the "spiral coefficient." The k_4 and k_3^2/k_2 terms were already calculated in Sec. 3.4, and the $k_2 c$ term is an obvious consequence of the magnetic field decreasing with r (assuming c is positive). The other terms are a combination of z varying with r, the magnetic field changing with r, and the electric field varying with r through k_3. Notice that every possible term with the correct units appears in the coefficient in front of r^2.

8.2.2 Higher order $\mathbf{E} \times \mathbf{B}$ drift of electron clouds

In the introduction, I showed that the motion of a single electron in a trapping potential $-k_2(z^2 - r^2/2)$ and a constant magnetic field $\mathbf{B} = B_0 \hat{z}$ is exactly solvable. It has an axial "bounce frequency" along the magnetic field of $\omega_Z = \sqrt{2ek_2/m}$, and the motion perpendicular to the magnetic field is a linear combination of two circular motions, one with a "modified cyclotron frequency" (ω_+), which differs slightly from the free space cyclotron frequency $\omega_C = qB_0/m$, and one with a "modified rotation frequency" (ω_-), both given by:

$$\omega_\pm = \frac{\omega_c}{2}\left[1 \pm \left(1 - \frac{2\omega_z^2}{\omega_c^2}\right)^{1/2}\right] \approx \frac{\omega_c}{2}\left[1 \pm \left(1 - \frac{\omega_z^2}{\omega_c^2} - \frac{\omega_z^4}{2\omega_c^4}\right)\right]. \quad (8.15)$$

It is notable that the modified rotation frequency has a correction which is not proportional to $1/|B|$, and which is not linear with the trapping field:

$$\omega_- \approx \frac{\omega_z^2}{2\omega_c} + \frac{\omega_z^4}{4\omega_c^3} = \frac{k_2}{B} + \frac{k_2^2 m}{eB^3} = \omega_{r0} + \frac{\omega_{r0}^2}{\omega_c}. \quad (8.16)$$

This correction is roughly 1/s, or a fractional correction of 2.5×10^{-6}, with $k_2 = 4 \times 10^5\,\mathrm{V/m^2}$, the highest achievable k_2 in ALPHA-g, and $B = 1\,\mathrm{T}$. Note, however, that lower values of k_2 around $1 \times 10^5\,\mathrm{V/m^2}$ were used for most of the EMPI measurements for ALPHA-g.

Because this correction is not linear with $\mathbf{E}$, one might be concerned that we can no longer use the assumption that the cloud's own electric field does not modify its magnetron frequency. Throughout this thesis, it was previously assumed that because $\mathbf{E} \times \mathbf{B}$ drift is linear with $\mathbf{E}$, the cloud's own electric field causes it to rotate around its own axis at a frequency of order 10^6/s, generally significantly higher than the magnetron frequency. But this does not otherwise modify the magnetron frequency. The cloud's self rotation is critical for keeping the cloud together—otherwise variation in the magnetron frequency with radial

position would cause electrons at higher radii to separate from electrons at lower radii [27]. Thus when we consider normal, linear $\mathbf{E} \times \mathbf{B}$ drift, the $\mathbf{E} \times \mathbf{B}$ drift of the cloud as a whole is caused by the electric field from the trap only averaged over the electrons in the cloud. With this description in mind, we find a stronger reason that the cloud cannot influence it's own magnetron frequency—a cloud's electric field averaged over all the electrons in the cloud must always be zero because an object cannot exert a force on itself. Note that two caveats on this statement are provided in Sec. 1.5. Because of image charges and finite length effects, varying the charge of an electron cloud does change the magnetron frequency, but not because of forces between electrons in the cloud.

To address how this higher order term in the magnetron frequency affects electron clouds, we consider another method of deriving it which does not rely on the equations of motion for a single particle being explicitly solvable in a special case. Ref. [127] gives a higher order version of $\mathbf{E} \times \mathbf{B}$ drift (slightly modified to apply to the case of a constant magnetic field and an electron with $q = -e$):

$$v = \frac{\mathbf{E} \times \mathbf{B}}{B_0^2} - \left[\frac{d}{dt}\left(\frac{\mathbf{E} \times \mathbf{B}}{B_0^2}\right)\right] \times \frac{m\mathbf{B}}{eB_0^2} \tag{8.17}$$

In this light, the higher order term in Eq. 8.16 takes the form of an $\mathbf{F} \times \mathbf{B}$ drift, where the force comes from the time derivative of ordinary $\mathbf{E} \times \mathbf{B}$ drift. We can re-derive Eq. 8.16 by noting that the nominal $\mathbf{E} \times \mathbf{B}$ drift is $r\omega_r\hat{\theta}$, so the time derivative is $-r\omega_r^2\hat{r}$. When we cross this with $\hat{b}$, we get $r\omega_r^2\hat{\theta}$, and we find a correction to the velocity $r\omega_r^2/\omega_c$, as expected.

A single electron is subject to the electric field of the rest of the electrons in the cloud, imposing a circular $\mathbf{E} \times \mathbf{B}$ drift around the center of the cloud. It is also subject to the electric field of the trap, imposing a circular $\mathbf{E} \times \mathbf{B}$ drift around the center of the trap. When we consider the time derivatives of these drifts, we find that the time derivative of the electron's motion around the center of the cloud (trap) looks like an acceleration pointing toward the center of the cloud (trap). Thus this higher order term imposes a slightly higher velocity in the rotation of the electron around the center of the cloud (trap). Just like the cloud's self-field averaged over all the electrons was zero, this higher order term averaged over all the electrons is zero. In conclusion, the correction ω_{r0}^2/ω_c which applied to a single electron also applies to the collective motion of an electron cloud, and despite the fact that this correction is nonlinear in the electric field, it does not allow the cloud's own electric field to influence its magnetron frequency. Because this effect is $\mathcal{O}(10^{-6})$, it can be ignored. But this may become important for future higher precision EMPI measurements.

8.2.3 Confirmation with simulation

To confirm the theory of the previous two sections, I simulated charged particles using the Boris algorithm in the presence of a realistic trapping potential and a realistic magnetic field gradient. The magnetic field comes from a model of the mirror coils providing axial antihydrogen confinement in ALPHA-g energized to 70 A, the highest current used in the first ALPHA-g measurement. The trapping potential came from three adjacent electrodes, 2 cm in length and 2.2 cm in radius, with potentials of 30, 75, and −30 V. These are reasonable voltages in ALPHA-g, but I have intentionally made the trapping potential asymmetric so

none of the terms derived in Sec. 8.2 are zero. Also, single antiprotons are simulated instead of electrons. This makes the system dramatically more computationally tractable, and it makes the correction from Sec. 8.2.2 larger and easier to resolve.

For each of seven radial positions between 0.5 mm and 2 mm, the z equilibrium position is calculated, and the antiproton is initialized there with about $(1\,\mathrm{K})k_B$ of kinetic energy. The simulation proceeds for about half a magnetron orbit, then the function $[x, y] = [r\cos\omega t, r\sin\omega t]$ is fit to the antiproton's position versus time to find the magnetron frequency. This is also done for seven different positions of the trapping potential (achieved by simply shifting the three electrodes by 1 mm). The trapping potentials and the magnetic field are shown in Fig. 8.9. The measured magnetron frequency is shown in

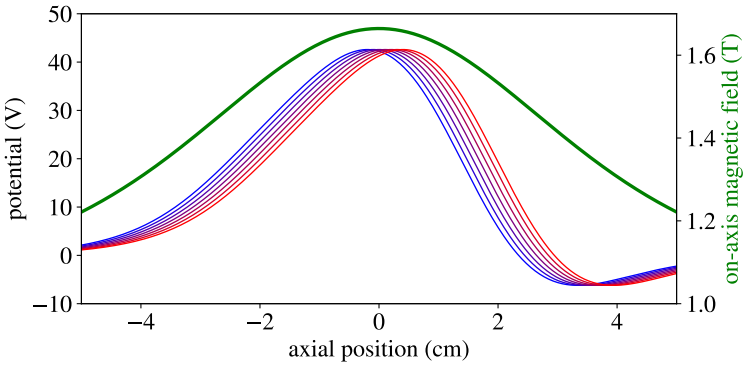

Figure 8.9: The on-axis trapping potential and the on-axis magnetic field magnitude are plotted versus axial position. The blue/purple/red curves are the seven trapping potentials used in the simulations, corresponding to the vertical axis on the left. The green curve is the on-axis magnetic field produced by the mirror coil, which was identical for all seven simulations, corresponding to the vertical axis on the right.

Fig. 8.10, and it is compared to the theoretical prediction including corrections derived in Sec. 8.2 and Sec. 8.2.2. At this level of analysis, the agreement is essentially perfect. However, with this trapping potential, k_4/B is by far the largest contribution to the variation in magnetron frequency with r, and this is identical for all axial positions of the trapping potential. In Fig. 8.11, I confirm the theory with higher precision by fitting a quadratic function to $\omega_r(r) \approx \omega_0 + k_\theta r^2$ for each axial position. On the left, the frequency at $r = 0$ is plotted versus axial position. This is compared to k_2/B and to $k_2/B + k_2^2 m/eB^3$, and the latter is found to agree much better with the measured values. On the right, the quadratic coefficient is plotted versus axial position. To illustrate the role of each term found in Sec. 8.2, I plotted three different "theoretical values," where in each curve I exclude a different set of terms. Of course, the best agreement comes from including all known terms, but there remains an offset. The offset can be reduced by including a fourth order term in the fit function $\omega_r(r) \approx \omega_0 + k_\theta r^2 + k_{\theta 4} r^4$. The fourth order term is then disregarded, because I don't have a theoretical prediction to compare it to, but adding this term to the fit function brings predicted and measured k_θ terms much closer together. Evidently, the quartic term in $\omega_r(r)$ was "pulling" the fit value of the quadratic term when the fit function neglected the quartic term. The remaining error is the right order of magnitude for numerical error

in my estimation of k_4. It should be noted that "precision simulation" is often difficult. The computational parameters need to be carefully checked one at a time to ensure that unacceptable errors are not introduced by imprecise calculations of the electric and magnetic field, an insufficiently small timestep ($1/60\omega_c$ was used here), an insufficient total simulation time, and error in the fitting procedure for finding ω_r. With the precision achieved here, we can verify all of the terms in the r^2 coefficient in Eq. 8.14 except $(1/4)B'^2k_2/B_0^3$. The $\langle z^2 \rangle$ coefficient was not investigated with this simulation, because this coefficient is not needed for analyzing EMPI measurements. We can also verify the correction described in Sec. 8.2.2.

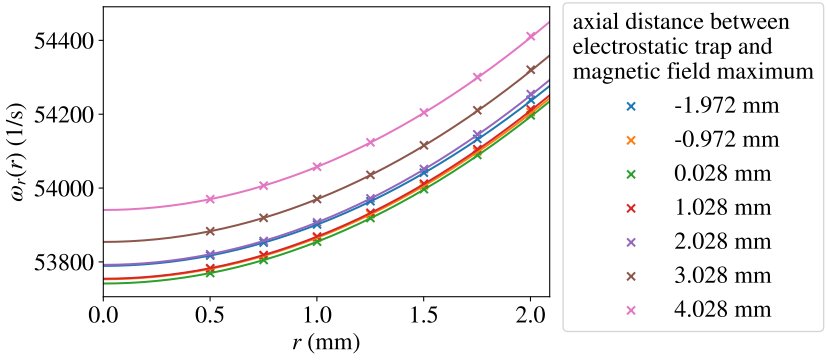

Figure 8.10: The magnetron frequency determined by simulation is shown with X's for seven radial positions and seven axial positions (indicated by color). For each axial position, the theoretical $\omega_r(r)$ prediction is plotted with the same color as the X's.

8.3 Calibration and static field map measurements

As you will soon see, our predictions of the magnetron frequency from electrostatic modelling of the trap are only good to a few parts in 10^3. As a result, if we only compare the magnetron frequency to an expected magnetron frequency at 1 T, we achieve a measurement of the magnetic field which is not sufficiently accurate to inform the ALPHA-g measurement. This motivated calibrating EMPI by measuring the magnetron frequency in the presence of a known magnetic field measured more accurately using ECR. Additionally, the precision of EMPI increases dramatically with the magnetron radius, but the magnetron frequency shifts with radial position according to Eq. 8.14. The initial magnetron motion of the clouds can be seen as a random variation in the initial position of the clouds at the start of the larger, intentionally excited magnetron orbit. Thus the variation in the initial magnetron phase of the clouds is that initial position variation divided by the distance the clouds are moved off-axis. Thus the most accurate and precise measurements are achieved when we move the clouds reasonably far off-axis, but we also find the relationship between off-axis magnetron frequencies and the magnetron frequency in the limit where the displacement goes to zero. That distance off-axis is, of course, limited by the restrictions imposed by the time it takes to move the clouds off-axis and the need to keep them within the imageable region of the MCP.

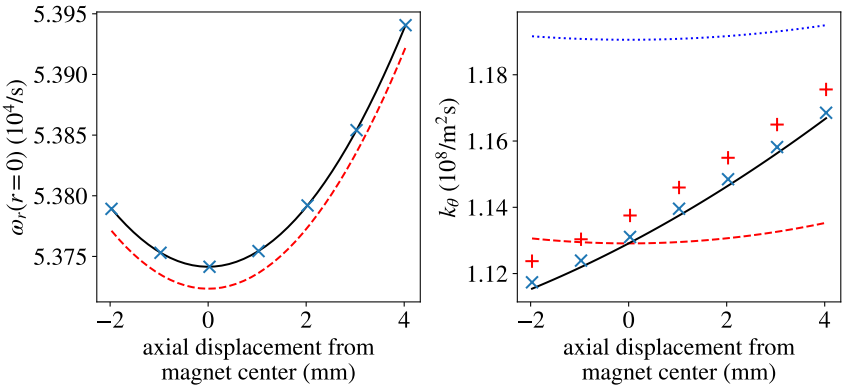

Figure 8.11: On the left, the magnetron frequency at $r = 0$ is plotted versus axial position. The blue X's are the simulation results. The red dashed line is k_2/B, and the black solid line is $k_2/B + k_2^2 m/eB^3$. On the right, the "spiral constant" is plotted versus axial position. The blue dotted line includes only the contributions from the trapping potential $[(3/2)k_4/B + (9/4)k_3^2/k_2 B_0]$, the red dashed line additionally includes the "purely magnetic terms" $[(1/2)k_2 c/B_0^2 + (1/4)B'^2 k_2/B_0^3]$, and the black solid line is the entire prediction from Eq. 8.14. The red + symbols are the result of fitting a quadratic function to $\omega_r(r)$ as found in the simulation. The blue X's are the result of fitting a quartic function to the simulation results, but plotting only the resulting quadratic coefficient here.

In this section, I will describe the EMPI measurements that were used to find the radial variation in the magnetron frequency and to calibrate EMPI. Similar measurements will also be used to measure static magnetic fields. Of course, static fields can also be measured using ECR at a somewhat higher precision, especially where the magnetic field gradient is small. There may actually be an avenue for EMPI to be more accurate in large gradients; my colleagues have observed that the ECR resonance structure becomes complicated and hard to interpret in a strong gradient, and in contrast I will show that the effect of a gradient on the magnetron frequency is observable and well-understood, but this benefit has not been conclusively established yet. The most comprehensive measurements of the magnetic field across several different magnet currents and axial positions were performed using EMPI. The EMPI measurements are significantly faster—this is largely due to the sequence improvements described in Sec. 8.1, which allowed us to image one cloud every 30–50 ms. In contrast, the ECR measurements took about 300 ms per cloud, but it is likely that if we apply similar improvements to ECR measurements the same repetition rate would be achievable.

A more fundamental reason that EMPI can be performed more quickly is that it requires less work from the person operating the experiment. When an operator is performing ECR measurements, they need to adjust the range of microwave frequencies to ensure that ECR resonance heating is observed at several different frequencies so a clear heating peak can be resolved—this range of frequencies is usually about 50 MHz wide versus an absolute frequency of about 30 GHz at 1 T, so the magnetic field needs to be known in advance to about 2 parts in 10^3. Usually modelling the magnetic field does not provide sufficient accuracy, and the operator needs to search for the right range of frequencies or interpolate earlier measurements

to infer the correct range for the next measurement. They also need to be careful not to mistake a bounce frequency sideband with the central cyclotron frequency resonance and they need to occasionally adjust the microwave power depending on the strength of the microwave electric field at a particular trap location. As I described in Sec. 8.1.11, moving the clouds off-axis the same distance requires knowing the magnetic field in advance at a few parts in 10^2, but even this requirement can be relaxed by either moving the clouds off-axis adiabatically or simply accounting for the changing magnetron radius with magnetic field (note I did not attempt either of these methods, so I cannot verify with certainty they would work). As a result, maps of the magnetic field versus axial position can be performed with little input from the experimenter.

Additionally, in this section I will introduce the effect of persistent currents on the ALPHA-g measurement, which are small current loops induced within superconducting wires produced when one attempts to change the magnetic flux through those wires. Although the persistent current effect was first observed in the dynamic EMPI measurements described in Sec. 8.4, these static measurements yield a clearer measurement of the effect.

8.3.1 ECR measurements

In order to calibrate EMPI, I first did ECR measurements of the magnetic field in every axial trap location where I wanted to perform EMPI, then I did precise measurements of the magnetron frequency, and then I repeated the ECR measurements to see if the magnetic field drifted. In Sec. 7, I sufficiently explained how ECR measurements are performed—the only difference being that here the clouds are not moved off axis. I am only measuring the on-axis magnetic field here. I performed EMPI calibration measurements twice; in the first calibration measurement, the reservoir was stored in a 2 T magnetic field boosted by the bottom solenoid. Later I managed to develop a reservoir in 1 T without the bottom solenoid that I could also extract thousands of clouds from without exciting a reservoir diocotron (see Sec. 2.3.2). This was preferable for EMPI measurements because the actual ALPHA-g measurement did not include the bottom solenoid; better to not have the bottom solenoid energized than to try to carefully measure and remove its effect on the magnetic field. The different reservoir was likely to produce clouds with a different charge, although the scooping voltage step size was the same for both reservoirs, and the cloud charge affects the magnetron frequency as described in Sec. 5.4.

The ECR measurements of the on-axis magnetic field from the first calibration measurement are shown in Fig. 8.12. The bump on the right side of the plot was at first unexpected. Today we have a better qualitative understanding of persistent currents. This bump exists because the most recent change in magnet currents was that mirrors A and G were ramped from 70 A to 0 A. This generates persistent currents that oppose this change in the magnetic field, leaving a small bump resembling the field that used to be produced by mirror G. A similar bump is not clearly visible near mirror A because the field produced by the bottom solenoid obscures it. Persistent currents also decay over time—although this certainly isn't as simple as an exponential decay. In some of the axial locations, the magnetic field was measured after measuring magnetron frequencies, and the inferred decay rate is shown in Fig. 8.13. Naively it would seem that the bump near mirror A is decaying more quickly than the bump near mirror G, but in reality this is because there was more time between the

initial and final measurements near mirror A. The decay was not precisely linear; it slowed over time (like an exponential decay would, but again, the decay is not well-modeled by an exponential), so the inferred decay rate near mirror G was lower. Also, between the two mirrors, the magnetic field increased over time. It seems the persistent currents produced by ramping down mirrors A and G actually makes a small negative perturbation far from the centers of the two magnets. To infer the magnetic field that was present during measurements of the magnetron frequency, I took the initial ECR measurements shown in Fig. 8.12, and I added the effect of the drift. To estimate the drift, I linearly interpolated the drift rate measurements and multiplied by the time between the initial ECR measurements and the magnetron frequency measurements. I estimate an error of roughly 1 part in 10^5 to account for the inaccuracy in these linear approximations.

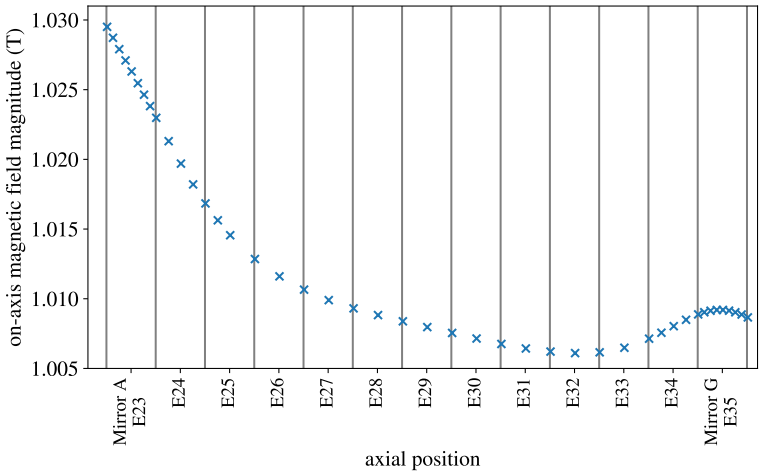

Figure 8.12: The ECR magnetic field magnitude measurements are shown versus axial position in the trap.

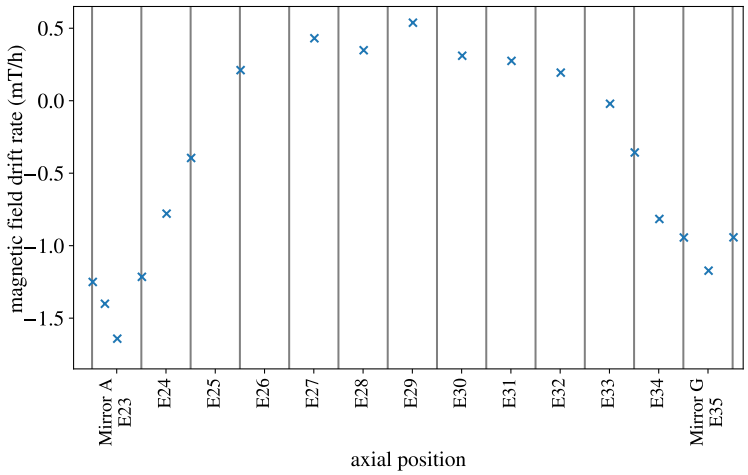

Figure 8.13: The magnetic field rate of change is plotted versus axial position in the trap.

The second set of ECR measurements for the second EMPI calibration are shown in

Fig. 8.14. There the bottom solenoid was off, yielding a more homogeneous magnetic field. Also, the most recent magnet rampdown was the octupole magnet. The octupole magnet produces very little magnetic field at the center of the trap [$\mathbf{B} \propto r^3(\hat{r}\cos 4\theta + \hat{\theta}\sin 4\theta)$], and persistent currents "resemble" the field produced by the original magnet—because persistent currents oppose a change in magnetic field (more precise statements about persistent currents can be found in Secs. 8.3.4 and 8.5). Therefore, the persistent currents induced by ramping down the octupole are expected to be much smaller on-axis, and the field should not be observed to decay over time. This is indeed what we find. With the exception of two axial trap locations, the initial and final ECR measurements agreed to within one part in 10^5, and these disagreements didn't show any clear trend when plotted versus axial position, indicating that they were simply measurement errors. The two ECR measurements that showed disagreement were found to be potentially erroneous because they weren't performed with a sufficiently narrow frequency range and the peak was very narrow and not clearly resolved.

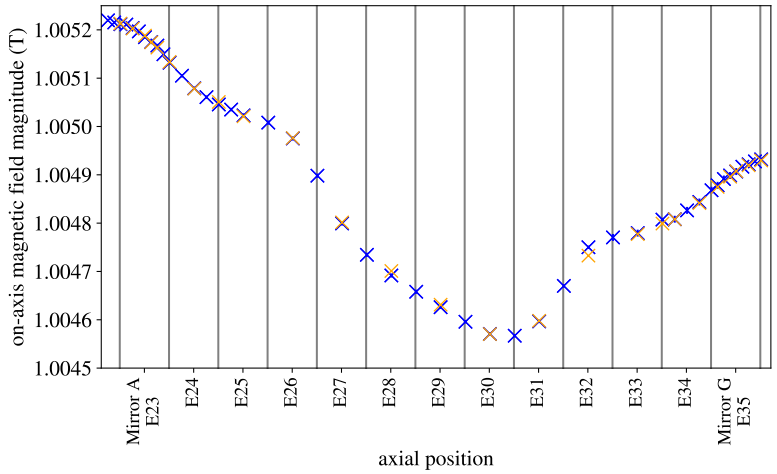

Figure 8.14: Two sets of ECR measurements of the on-axis magnetic field versus axial position are shown for the second EMPI calibration measurement. The measurements taken before measuring the magnetron frequency are shown in blue, and the measurements after are shown in orange.

The point of developing a reservoir that could be used for EMPI without the bottom solenoid was to have the same magnets energized for EMPI measurements that were present during the actual ALPHA-g measurement. However, one set of magnets, the so-called "bottom extraction magnets" had to be energized for EMPI which were not energized during ALPHA-g. Near the MCP (about a meter below the bottom electrode), there are three normal conducting magnets which boost the magnetic field near the MCP. This reduces the expansion of magnetic field lines and allows us to image clouds which are much further off-axis. ECR measurements on-axis can still be performed without these magnets energized, which is why they were not used during the ALPHA-g measurement. Thus in order to compare EMPI measurements to the ECR measurements that were most relevant for ALPHA-g, I needed to measure the effect of these magnets and subtract it from the final EMPI results. In Fig. 8.15, I show the result of ECR measurements from Fig. 8.14 in addition to

ECR measurements taken after turning off these three additional magnets. The difference between the two measurements is shown in Fig. 8.16. Because we are discussing magnets which are much further away than their radii, they are well approximated as dipoles. Thus I fit the parameters m and z_0 in the equation $m/(z - z_0)^3$ to this data. The differences between the measurements and the fit are less than one part in 10^5, typical errors for ECR measurements. This fit function was used to approximate the bottom extraction magnets in future measurements.

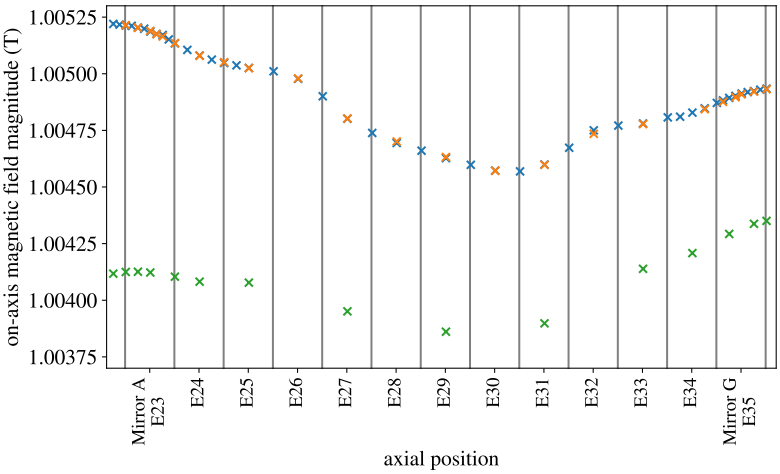

Figure 8.15: ECR measurements of the magnetic field are shown with and without the "bottom extraction magnets" which boost the magnetic field near the MCP to facilitate imaging off-axis electron clouds. The blue and orange X's are the same data as in Fig. 8.14. The green X's are the ECR measurements without the bottom extraction magnets.

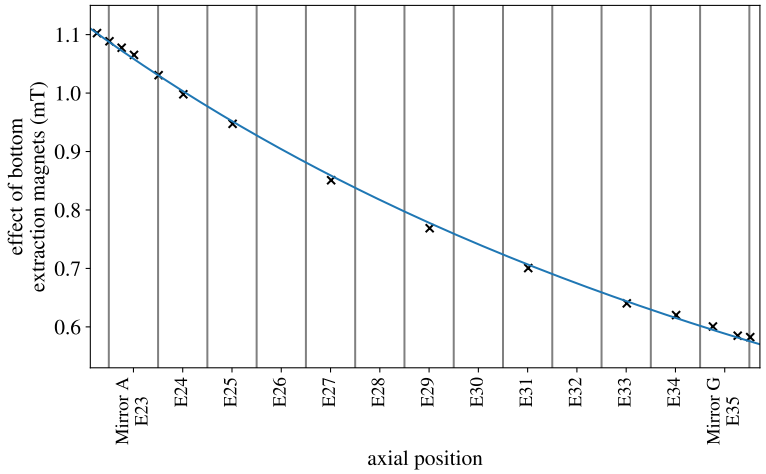

Figure 8.16: The difference between the blue X's in Fig. 8.15 and the green X's in Fig. 8.15 is plotted versus axial position in the trap. The blue line is a dipole fit to the data.

8.3.2 Exponential magnetron phase increase procedure

The first step in the calibration is to accurately measure the magnetron frequency at one magnetron radius. The most naive scheme is to image clouds subjected to a varying total time spent performing the magnetron motion, with the n'th cloud performing a magnetron motion for a time $T_n = T_0 + n\Delta t$. The nominal magnetron time T_0 is necessary because over the timescale of tens of microseconds, the voltages on the electrodes are still settling to their final values (see Sec. 6.4). Frankly, there's not any reason we should try to observe this effect; our goal is to measure the magnetron frequency in the unchanging potential created by the electrodes once the voltages have settled; a small correction to EMPI measurements due to this effect will be discussed later. If Δt is somewhat less than the magnetron period: $\Delta t = \epsilon 2\pi/\omega_r$ (ϵ of about 0.5 is reasonable), we can track the total phase difference between the N'th cloud and the 0'th cloud by adding the phase difference between each cloud and the previous one. With an initial magnetron radius of about 25 μm, if the clouds are displaced from the trap center by 1 mm, we would achieve a measurement precision limited by the random phase variations divided by the total phase: $(25\,\mu\text{m}/1\,\text{mm})/(N\epsilon 2\pi)$. Of course, if the initial magnetron phase was randomized, we would benefit from this error averaging out, reducing it by roughly $1/\sqrt{N}$. In all of these measurements the initial magnetron phase was intentionally varied in steps of $\pi/4$ for successively imaged clouds as described in Sec. 8.1, but the measurements were performed in a random order, so essentially the initial magnetron phase was randomized. That is, to avoid certain systematic errors, I did image clouds after several different total magnetron times, but the order of the measurements was shuffled.

Instead of using this naive method, the magnetron phase was increased exponentially. First I image two clouds which performed a magnetron orbit for times T_0 and $T_1 = T_0 + \Delta t$, and we observe a phase difference θ_1; Δt is chosen so that $\theta_1 < 2\pi$. We find that the magnetron frequency is $\theta_1/\Delta t$ with a maximum error of $2\Delta r/r$, where Δr is the variability in the initial magnetron position and r is the large magnetron orbit radius. Note that for all of the EMPI measurements, the initial magnetron position was due to the intrinsic cloud magnetron (see Sec. 2.3.1), so the positions were distributed around a circle, not according to a Gaussian distribution or any other distribution that might yield errors greater than 2π with a low probability. Now that we know the magnetron frequency is $\theta_1/\Delta t \pm 2\Delta r/r$, we can predict the phase of the next cloud with an error of $\pi/4$ if the next cloud performs a magnetron orbit for a time $T_2 = T_1 + r\pi/8\Delta r$. When we perform this measurement and observe the actual phase of the next cloud, we can refine our estimate of the magnetron frequency and again increase the timestep for the next cloud. We find that if we assume a variability in measurements of the magnetron phase given by $2\Delta r/r$, we can exponentially increase the time each cloud spends in a magnetron orbit. Therefore, after performing a few measurements with phase differences $< 2\pi$, I imaged a sequence of clouds, with the n'th cloud performing a magnetron orbit for a time $T_n = T_0 + (\Delta t)c^n$, where c was typically between 1.2 and 1.5. In reality, since the initial magnetron orbit causes the radial positions of the clouds to vary, and the magnetron frequency varies with r as $\omega_r = \omega_0 + k_\theta r^2$, eventually the constant error in the magnetron phase is overcome by variability that increases linearly with time. This could justify a slightly more complicated schemes like decreasing c with n or imaging multiple clouds to average down the error in the magnetron phase. For all the measurements I describe in this thesis it sufficed to just choose a conservative value for

c then abort the measurements when the variability in the magnetron phase exceeded $\pi/2$ radians.

Fig. 8.17 shows two examples of these measurements. For these static field/calibration measurements, I used $c = 1.2$, and I tried to choose parameters that would yield a measurement of the magnetron frequency with a statistical error of about one part in 10^5. In Fig. 8.17 on top I show the result of performing this exponential angle increase procedure in the axial trap location where I tuned the trapping potential to minimize the variation in ω_r with r. Below, I show an example from another trap location with significant "spiraling," or variation in ω_r with r, and the difference between predicted magnetron phase and observed magnetron phase clearly increases with the orbit time.

The magnetron frequency calibrations found throughout the trap are shown in Fig. 8.18. Magnetron frequencies vary from $3.5\times10^4/s$ to $2\times10^5/s$, depending on whether the measurement occurs in the center of an electrode or between two electrodes, whether the surrounding electrodes have 150 V amplifiers or 75 V amplifiers, and what trapping potential was found in my attempt to reduce spiraling (discussed in Sec. 8.1). The measurement failed in one trap location between electrodes 24 and 25, where the spiraling was too strong and the magnetron phase could not be tracked. It also failed for many measurements in the vicinity of electrodes 31 and 32; the failure looked exactly like the issue described in Sec. 8.1—it seems one of these two amplifiers was bad, but this is not a critically important measurement location, and the issue was only identified after the experiment was disassembled.

In Fig. 8.19, I show the ratio of measured magnetron frequencies to predicted magnetron frequencies using an electrostatic model of the trap. It wasn't originally my intention to try to find agreement between these two quantities; the whole point of calibrating EMPI was to remove any need to accurately predict the magnetron frequency, but there are actually some interesting observations here. At first, all of the measured magnetron frequencies exceeded the predictions by about 1%. This is explained by the fact that the electrostatic model was based on the dimensions of the trap at room temperature. The mostly-aluminum electrodes will contract by 0.41% when they are cooled to 4K, and if this contraction is uniform for the entire electrode stack, this will simply scale up all k_2 coefficients by a factor of 1.0041^2. Once we account for this effect, the agreement improves—I actually find it remarkable that we can resolve the effect of thermal expansion in this data. Now, in many axial trap locations the agreement is much better than 0.1%, and in about a third of the locations it is between 0.1% and 0.4%, and the measured frequency is usually greater than the predicted frequency. There could be several different explanations for these discrepancies:

1. Patch potentials create an electric field in the center of the trap of order 5 mV/cm. Thus they should be generated by potentials of order 20 mV, which may be a correction of order 2×10^{-4}, about a factor of ten smaller than the largest errors seen here. Really, if we wanted to observe the effect of patch potentials, we should vary the intentionally applied voltages and observe that the magnetron frequency does not scale with the applied voltages. One would have to be careful to avoid any unexpected voltage offsets in such an experiment. First, the voltage on the electrode should be measured using a precise multimeter, not just the voltage we intended to apply with an imperfectly calibrated amplifier. The only thing between the multimeter and the electrode should be a wire. One would also need to monitor the voltages on nearby electrodes or actually

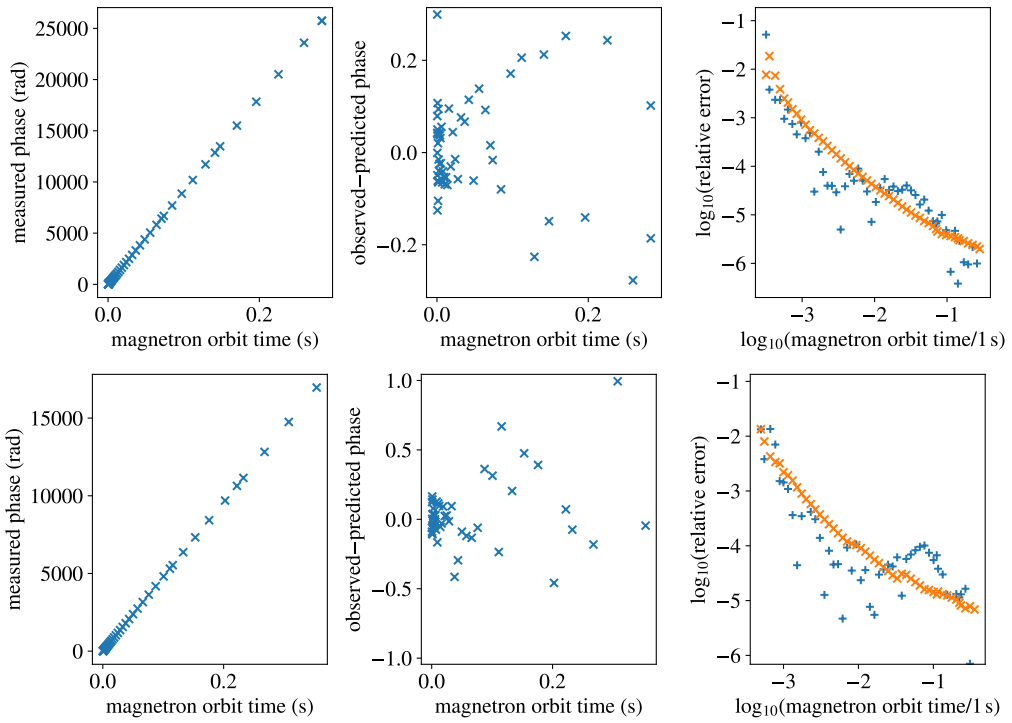

Figure 8.17: Top row: the data from the exponential magnetron phase increase procedure is shown for EMPI measurements in the center of mirror A. Bottom row: a less optimized trapping potential is used to do EMPI measurements a few millimeters below mirror A. In the first column, the measured magnetron phase is plotted versus the magnetron orbit time. Of course, at this level of precision, no deviation from a linear relationship can be observed. For each magnetron orbit time, before we observe the cloud's position on the MCP, we predict what final magnetron phase it will have using a linear fit to all the previous measurements. In the middle column, each cloud's deviation from its predicted magnetron phase is plotted; if this deviation approaches π, there is a chance we could miscount the total number of revolutions, or in other words we would "lose a 2π" in the total accumulated magnetron phase. In the right column, in orange, I plot the statistical fitting error of the measured slope of magnetron phase versus orbit time when we track the magnetron phase over an increasing total time. The blue +'s indicate the difference between the final extracted magnetron frequency and the magnetron frequency estimate having only included the data up to a certain total orbit time, which are expected to be just above or anywhere below the orange points.

ground them, not just set their applied voltage to zero on an amplifier. Curiously, if the materials of the wires between the electrodes and the amplifiers differed, or if the temperatures of the electrodes differed, the Seebeck effect would also produce static voltage differences between electrodes. If one were to successfully avoid voltage offsets, they could observe a frequency shift due to patch potentials which should be a continuous function of axial position. This could be used to measure the on-axis voltage perturbation due to patch potentials. In Ref. [128], the authors attribute an

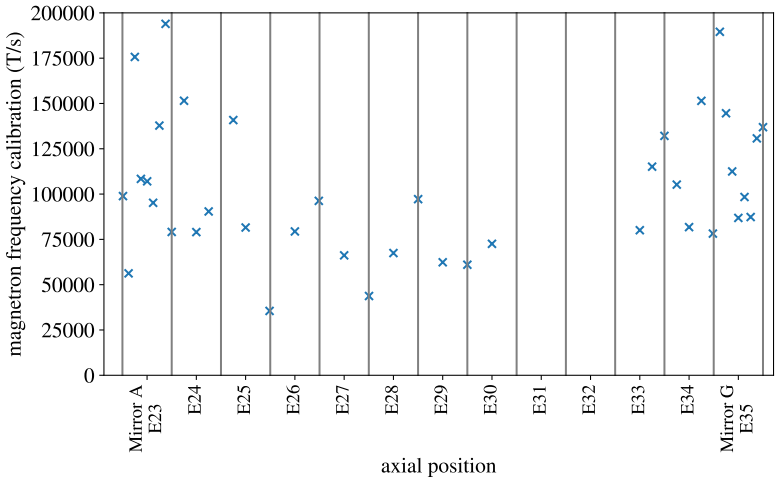

Figure 8.18: The magnetron frequency is plotted versus axial position in the trap.

offset in the bounce frequency of a charged particle to patch potentials in one axial trap location. The measurement is only described in an appendix, so there is little detail about the precautions taken to avoid other kinds of voltage offsets.

2. There are voltage offsets in the amplifiers; in ALPHA-2, these can be as large as 10 mV. In ALPHA-g, I never carefully measured the amplifier voltages, but I observed offsets of 1–2 mV with a handheld multimeter, a 10^{-5} effect.

3. The analytic electrostatic model used to predict k_2 is not entirely accurate, as I have already described to some extent. This model neglects the gaps between electrodes of order 100 μm. The predictions near electrode 23 are affected by an inaccurate model of the radial step three electrodes to the left. The predictions near electrode 35 are affected by inaccurately modelling the space beyond electrode 35 as an infinitely long grounded cylinder of radius 2.2 cm.

4. Probably the biggest source of error is numerical error in our estimation of k_2.

As stated in the previous section, the calibration procedure was performed twice, with the second calibration being done one day later and with a slightly different magnetic field (up to a 3% difference). The difference between the two calibration factors is plotted in Fig. 8.20. In more detail, this calibration procedure finds the coefficient C (units of Tesla per second) between magnetron frequency and magnetic field: $\omega_r = C/B$. Fig. 8.20 shows the difference between the two estimates of C divided by their average. Fig. 8.20 also has purely statistical error bars—statistical fitting errors from the linear fit to magnetron phase versus time plus the statistical fitting error of the extrapolated magnetron frequency at $r = 0$ described in the next section. It is also reasonable for magnetic field measurements to have errors of about 1 part in 10^5. When we consider both of these errors, in most trap locations the two calibration measurements are in good agreement. There are a few outliers, but in those axial trap locations there is a large statistical error bar, which actually is a sign that there was significant spiraling in that trapping potential, making the measurement harder

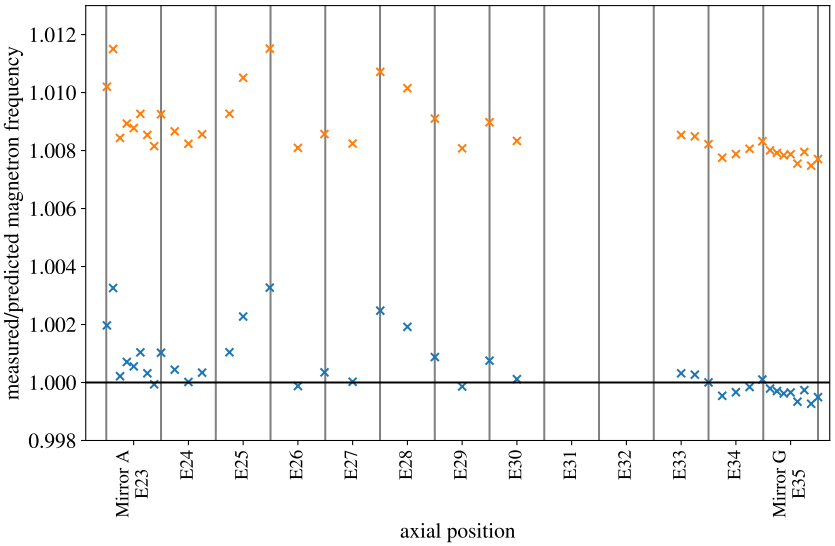

Figure 8.19: The ratio of the measured magnetron frequency to the predicted magnetron frequency is plotted versus axial position in the trap. The orange X's are the result of predicting k_2 with the analytic electrostatic model, and the blue X's are the result of adjusting this model to account for thermal contraction.

and likely leading to systematic errors. I had originally hoped we might see the effect of the clouds being different as they had different radii, temperatures, and total charge, but it seems we cannot resolve this effect.

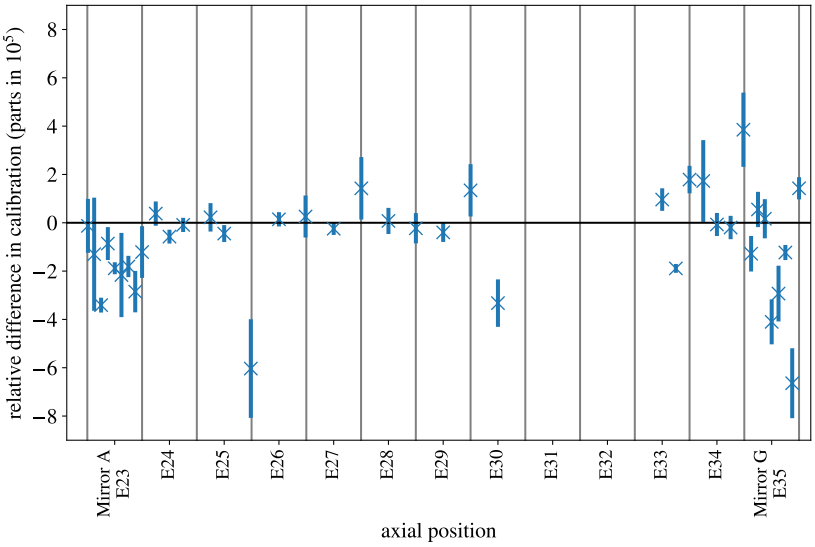

Figure 8.20: The fractional difference in the two calibration measurements is plotted versus axial position. The error bars are purely statistical errors on the magnetron frequency measurements.

8.3.3 Variation of ω_r with r

In order to achieve the desired precision for EMPI of a few parts in 10^5, we needed to not only calibrate with ECR, but also find the relationship between the magnetron frequency at $r = 0$ and the magnetron frequency at the radial position we will typically use. Further, my original pitch to the collaboration for EMPI was that it could measure magnetic fields off-axis. In this section, we will find that this is indeed true, but that the interpretation of these results is complicated. Also, at least in the data presented here, the measurement of off-axis magnetic fields is no better than what we can achieve with an off-axis expansion of the measured on-axis field. This is in contrast to off-axis ECR, discussed in Sec. 7, where an asymmetric contribution to the magnetic field is observed which cannot be predicted using off-axis expansion.

Interspersed in the measurements of the magnetron phase with varying total time, I measured the magnetron phase versus r for three different total times. The total times differed by factors of two—typically these spirals would be observed after about 50 ms, 100 ms, and 200 ms, but the exact numbers would vary based on the magnetron frequency in that axial trap location. In total, 200 clouds were imaged to calibrate EMPI and find the r variation for each axial location. With one reservoir, I extracted 1200 clouds, and I discarded the first 200 clouds (waiting for the reservoir to settle) and performed measurements in five axial locations with the remaining 1000.

The data from one axial trap location is shown in Fig. 8.21. Fig. 8.22 also shows two more extreme examples, one with very significant spiraling, and one with almost no spiraling. The first step in the analysis is to fit a circle to the data described in the previous section (not shown). Imaging clouds after a variable time performing magnetron motion results in a lot of cloud positions distributed somewhat randomly around a circle. This gives us a great measure of the effective trap center. Next, a line is fit to the radial displacement of clouds versus axial distance from the trap center; essentially this is a measure of patch fields. Finally, we need to find the magnetron phase versus radial position. Of course, I have performed similar analyses throughout this thesis, but here I designed a somewhat different algorithm which was more robust in this situation of having wildly varying spiral constants. First, we identify the magnetron phase and radial position we would expect from the linear fit of magnetron phase versus time described in the previous section. This is marked with a red X in Fig. 8.21 in all three subplots. Next, in the spiral with the shortest magnetron orbit, we find the angle difference between each cloud and this expected angle. For the clouds whose angle difference is less than $\pi/2$, we fit a quadratic function to angle deviations versus radial distance. At first, this discards a significant fraction of the data. However, we repeat this process, now using the angle deviations from the quadratic fit. This process is iterated until as much of the data as possible is used. In some cases, some data points never conform to the quadratic fit, and they are indeed discarded. Next, this process is repeated for the two stronger spirals formed by clouds subjected to twice and four times the total orbit time. In those cases, we start with a known spiral constant—double and quadruple the spiral constant found in the first fit.

Later, this data is used to subtract out the effect of measuring the magnetron frequency at a nonzero radial displacement. Because $r = 0$ falls outside of the measured data, we will need to carefully assess the statistical errorbars on the fit function. Standard curve fitting

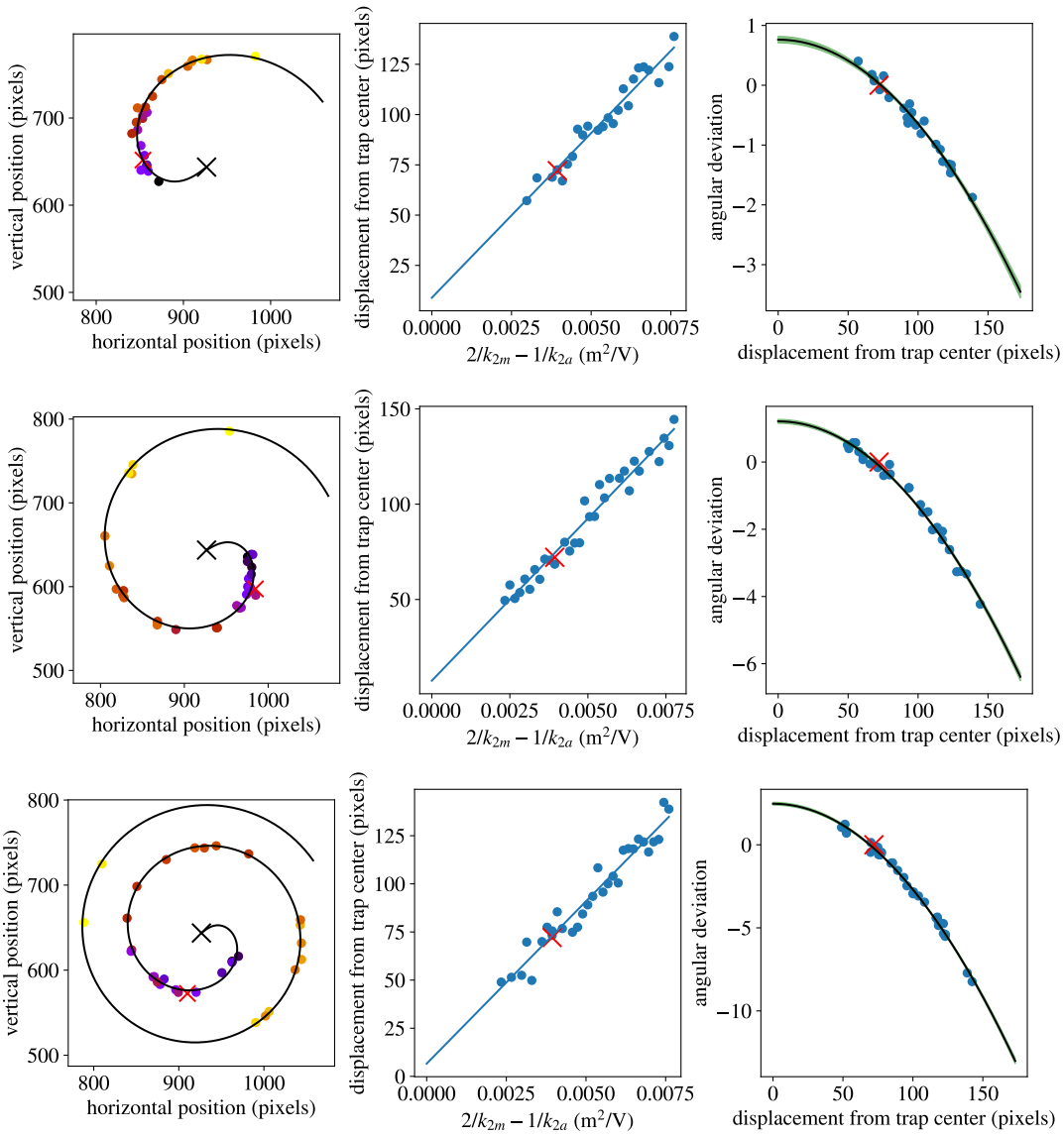

Figure 8.21: The data and fits used to find the variation in the magnetron frequency with r in one axial trap location. On the left, I show the positions of the cloud on the MCP in units of the pixels on the camera image. The black X is the center of the trap, and the black spiral line is the resulting fit of the angular deviation versus radial position. The red X indicates the radial position and phase predicted by the data from the exponential angle increase procedure. In the middle plot, I show the radial position versus $1/k_{2m} - 1/k_{2a}$, which theory predicts should be proportional to displacement. The blue line is a linear fit. On the right, I plot the angular deviation versus radial distance, only including the points which ultimately were within $\pi/4$ of the fit function (although in this dataset none of the data was excluded). The black line is the result of fitting $\theta = \theta_0 + k_\theta r^2$ to the data, and the green highlighted region is the statistical errorbar on the fit function.

software packages typically return a covariance matrix C_{mn} in addition to the found fit

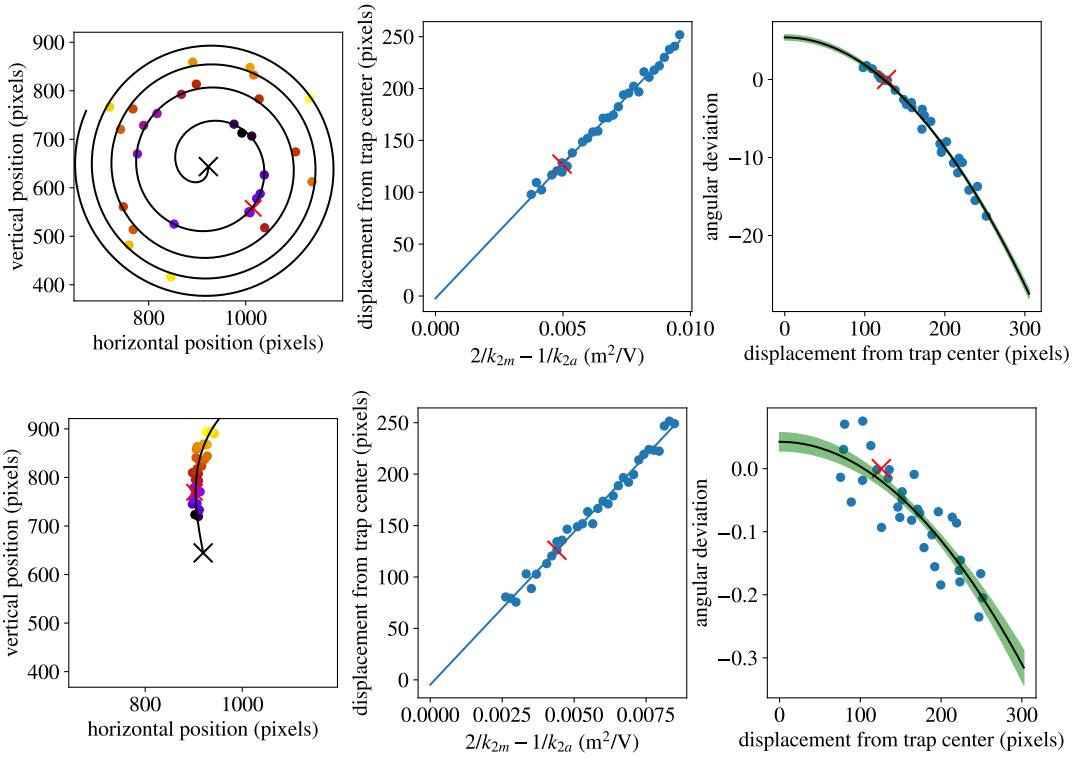

Figure 8.22: This figure shows the positions of clouds on the MCP at two different axial locations with the maximum time performing magnetron motion. The elements of this plot are described in the caption of Fig. 8.21.

parameters P_n. When known errorbars for the datapoints are not provided, this covariance matrix can be described as follows:

1. Assume that the data is drawn from the fit function $F(x, P_n)$ plus a Gaussian error.

2. Assume that the standard deviation σ of that Gaussian distribution is the deviation of the points from the fit function.

3. Define the "probability of a dataset" given a set of fit parameters as the product of the probability densities of each datapoint, i.e. $p_i \propto \exp(-[F(x_i, P_n) - y_i]^2/2\sigma^2)$.

4. The returned fit parameters maximize the probability of the dataset, and the covariance matrix tells us how the "loss function," defined as twice the log of the probability of the dataset, increases as we change the fit parameters.

It is well known that, given these assumptions, the statistical error in the n'th fit parameter is $\sqrt{C_{nn}}$. That is, if we resampled the data from this Gaussian distribution many times, that fit parameter would have a standard deviation given by $\sqrt{C_{nn}}$. However, it is absolutely not valid to assume that the statistical error in the fit function is given by $F(x, P_n + \sqrt{C_{nn}}) - F(x, P_n)$. This neglects the off-diagonal elements of the covariance matrix. For example, in my quadratic fits, the fit function is $\theta(r) = \theta_0 + k_\theta r^2$. My covariance matrix may suggest that

θ_0 could be lower by -0.1, but only if k_θ increases to compensate, bringing the fit function back in reasonable agreement with the data. Note also that if I replaced my fit function with $\theta(r) = -\theta_0 + k_\theta r^2$, I would get the same exact fit (but the fit value for θ_0 would change sign), but $F(x, P_n + \sqrt{C_{nn}}) - F(x, P_n)$ would be different, which is not acceptable.

The correct way to estimate the errors of the fit function is given in Refs. [129] and [130]. Both authors lament how few people are aware of this method. First we take the derivative of the fit function with respect to the fit parameters: $\nabla_{P_m} F(x, P_m)$. Then the variance of the fit function is (in Einstein notation) $\nabla_{P_n} F(x, P_n) C_{nm} \nabla_{P_m} F(x, P_m)$. The standard deviation is the square root of the variance. Critically, this error is not constant—it is a function of x through $\nabla_{P_n} F(x, P_n)$. Typically this gives rise to the intuitive behavior that the fit function has larger errors outside of the domain of the data. These proper standard errors are plotted in green in Figs. 8.21 and 8.22.

In Fig. 8.23, I show how the measured spiral constants compare to those predicted Eq. 8.14—although note that this calibration was performed with a very homogeneous magnetic field, and the B' and c terms will be absolutely negligible. With the exception of the two most extreme spirals, there is excellent agreement. The datapoint in the upper right was identified to be erroneous because of a numerical issue in estimating the predicted spiral constant. The datapoint in the lower left did not suffer from the same numerical issue, but it is generally true that stronger spirals are harder to measure. Similar measurements are used to calibrate the difference in magnetic field between the MCP and the trap (see Sec. 3.5), so in some sense this is confirmation that field ratio is well-estimated.

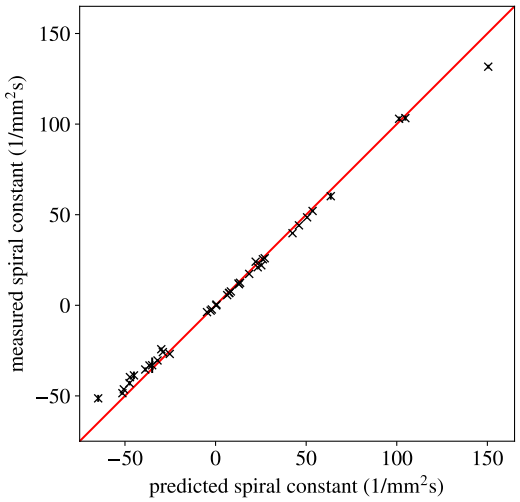

Figure 8.23: The measured spiral constants are plotted against the predicted spiral constants for the measurements used to calibrate EMPI without any current in the mirror coils. The red line is $y = x$.

As you will see in the next section, in addition to precisely measuring the magnetron frequency at one known magnetic field, I used the same experimental procedure to do precise measurements of the magnetic field while varying the current in mirrors A and G. This data also allows us to see how the spiral constant varies with magnetic field, allowing us to observe the effect of the magnetic terms in Eq. 8.14. In Fig. 8.24, I plot measured spiral

constants in 15 axial trap locations versus the current in mirrors A and G. Note that one needs to account for the changing magnetic field ratio between the MCP and the trap in order to find the spiral constant in units of $1/\text{mm}^2\text{s}$ rather than $1/\text{pixel}^2\text{s}$. Luckily, we are also measuring the changing magnetic field inside the trap here (in fact that was the main purpose of the measurements), and the magnetic field at the MCP does not change. Therefore, we can account for the changing relationship between transverse distance inside the trap and transverse distance on the MCP by multiplying the spiral constants on the MCP by $B(I,z)/B(0)$, where $B(I,z)$ is the magnetic field magnitude with mirror current I and axial position z. When $I = 0$, the magnetic field is constant enough with z that the variations can be neglected for this analysis.

In Fig. 8.24, there is conclusive evidence that the measured spiral constants are affected by the variation in the magnetic field with r. The measured spiral constants are compared to the full Eq. 8.14, with B_0, B', and c estimated by fitting a quadratic to the on-axis magnetic field measurements, and k_3 and k_4 estimated as described in Sec. 8.1.10. I also plot the result of only including the trapping potential terms, and the agreement is very poor. The data is also compared to Eq. 8.14 neglecting the "cross term" proportional to $k_3 B'$. This term generally has a very small effect, so there is less conclusive evidence that this term is needed for good agreement. The agreement is especially excellent in the center of mirror A where the spiral constant was tuned to be small. In some datasets, there is an offset between the data and the theory, suggesting either numerical error in estimating k_4 or higher order terms in the spiral "pulling" the fit value of the quadratic term, just as we observe in the simulation described in Sec. 8.2.3. Also, in some cases when the spiraling is strong, it is also hard to measure, and there are some random-looking deviations of the data from the theory curves. It is clear that if we intentionally varied k_3, and if the spiraling was more effectively minimized as it was in the center of mirror A, we expect we would be able to resolve the effect of the $k_3 B'$ term. This would provide a potentially useful measure of the magnetic field and its first and second derivatives. One application of such a measurement would be to identify error in our predicted axial trap locations. Until now, the axial location of each measurement is based on an electrostatic model; errors in that electrostatic model and the influence of patch potentials are assumed to be negligible. This could be confirmed by finding B' and c at one axial trap location, then finding how different B_0 is at the next axial trap location. Also, if a deviation from Eq. 8.14 is ever observed, it could indicate the presence of azimuthally asymmetric terms in either the magnetic field or the trapping potential. It is not clear in this dataset that the precision could be increased enough for these ideas to be useful.

8.3.4 EMPI field maps

In addition to measuring the magnetron frequency precisely at a known magnetic field through the procedure described in the previous two sections, I repeated the same EMPI procedure in "unknown" magnetic fields. After the first calibration measurement, I increased the current in mirrors A and G to 70 A in five steps. After reaching 70 A, the current was again decreased to 14 A—the first of five steps, then to 0 A. The magnetic field was inferred by extrapolating the magnetron frequency at $r = 0$ and scaling the calibrated on-axis magnetic field like $1/\omega_r$. The resulting maps of the magnetic field are shown in Fig. 8.25. To

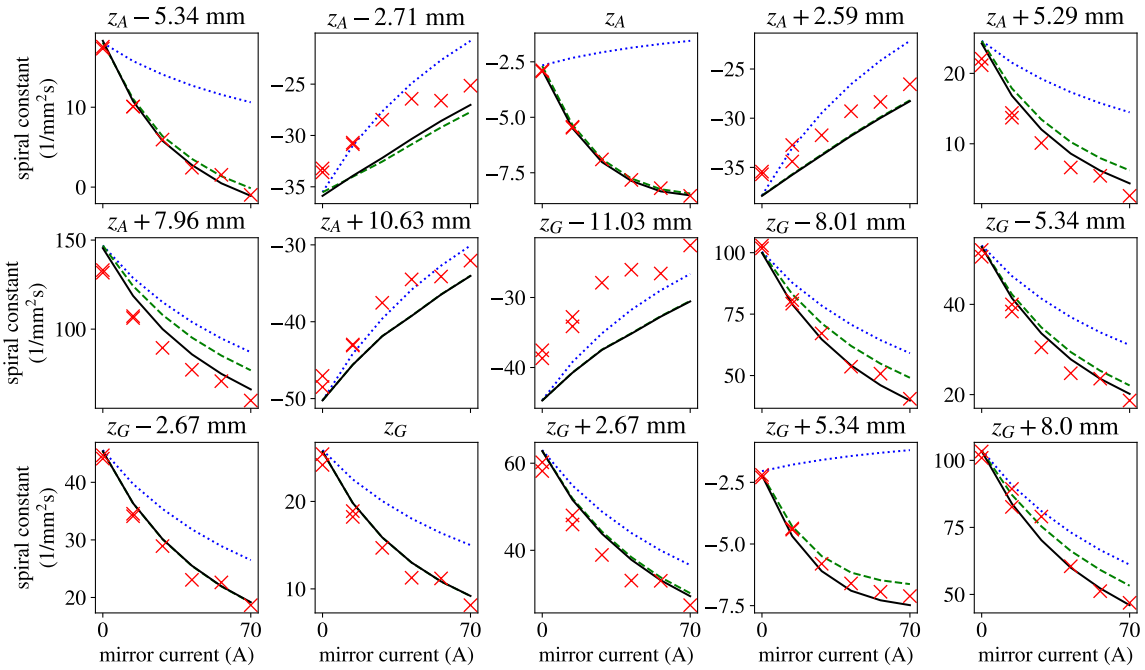

Figure 8.24: The measured spiral constant is plotted versus current in the mirror coils for 15 axial trap locations where I successfully performed the static field EMPI measurement for six different currents in the mirror coils. The red X's are the measurement results. The black solid line is the theoretical prediction from Eq. 8.14. The blue dotted line is the result of only including the trapping potential terms in Eq. 8.14. The green dashed line is the result of neglecting the "cross term" proportional to $k_3 B'$. The center of mirror A is denoted z_A, and the center of mirror G is denoted z_G. For the other axial trap locations, I give the vertical displacement from either mirror A or G.

save time, not all measurements were performed at all currents.

Because a fairly comprehensive field map was performed after ramping up to 14 A then down from 70 A to 14 A, we can get an excellent measurement of the effect of persistent currents induced by these field changes by subtracting the two measurements. When the current is increased from 0 to 14 A, negative persistent currents are generated that oppose the nominal effect of the mirrors. When it is decreased from 70 to 14 A, positive persistent currents are generated that oppose the reduction of the field produced by the mirrors. By subtracting the latter dataset from the former, we get a map of roughly double the on-axis persistent current effect we get from changing the mirror currents. This is shown in Fig. 8.26. As expected, there are bumps centered on mirrors A and G. It is a bit surprising, but in hindsight reasonable, that there is a negative effect between the two mirrors. Persistent currents do not flow all the way through the wire to the power supplies, so they cannot produce a field which is simply proportional to the original field. Rather, they typically flow in one direction on one side of a wire and in the opposite direction on the other side of the wire. We can generate a crude model of the field we expect persistent currents to produce with the current distribution shown in Fig. 8.26. The individual wire filaments in a mirror coil can roughly preserve the magnetic flux through the superconducting material by having

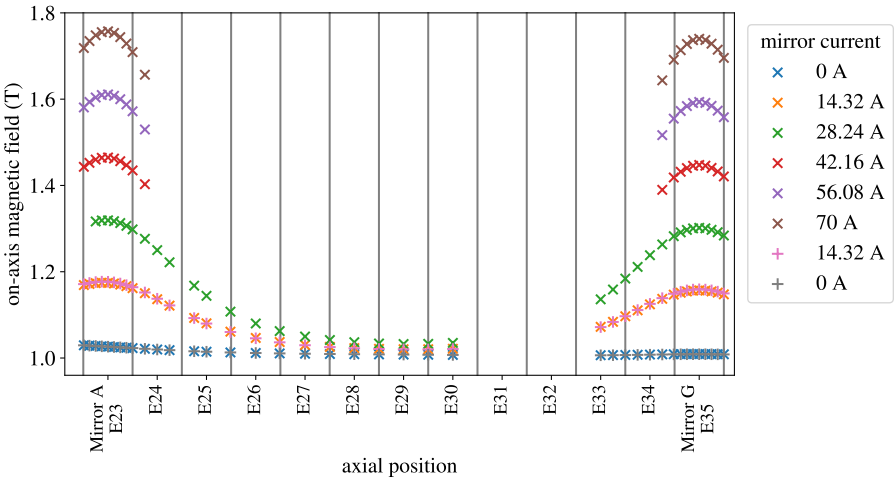

Figure 8.25: The magnetic field is measured for different axial positions using EMPI at varying current in the mirror coils. The order of the measurements is indicated in the legend—the current was ramped up then back down. Note also that a few of the measurements failed, which can be seen from missing datapoints.

a current running in one direction on the outer side of the wire (the side farther from the trap center) and in the opposite direction on the inner side of the wire. In turn, this can be approximated as a current running in one direction on the outermost layer of windings and a current running in the opposite direction on the innermost layer—the current density in the layers between will cancel out. Near the center, there would be a positive bump where the current on the inside has a larger effect. Farther from the center, there would be a negative perturbation because the outer current has a larger dipole moment. Alongside the measurements, I have plotted the result of this model for the distribution of persistent currents. The current in this model is chosen to agree with the data, which occurs when we assume about 45 A is running through the superconducting wires in this way. It is interesting that the current scale is similar to the absolute currents that were initially in the magnets. This is likely because the current value of 70 A was chosen to be near the limit that would cause the magnets to quench. The production of persistent currents is limited by the same mechanism, but with a more complicated distribution of current density within the wires. We find then that the effect of persistent currents is only small because when the coil is energized normally, there is current running through all 8 layers of windings in the same direction. When persistent currents run through the coils, there is a similar amount of current, but it runs in one direction only on the innermost coils and in the other direction only on the outermost coils (or rather, the persistent currents on the layers between largely cancel with the adjacent layers). It is also interesting that the agreement is so good between the data and this handwavy model. Obviously, there are many superconducting magnets nearby mirrors A and G, so it would take significant effort to properly model this. Luckily (or rather, by design) all of these magnets are roughly symmetric about the center of the trap, so there is no perceptible asymmetry, except a tiny difference that is likely due to having performed measurements near mirror G later, so the persistent currents had some extra time to decay.

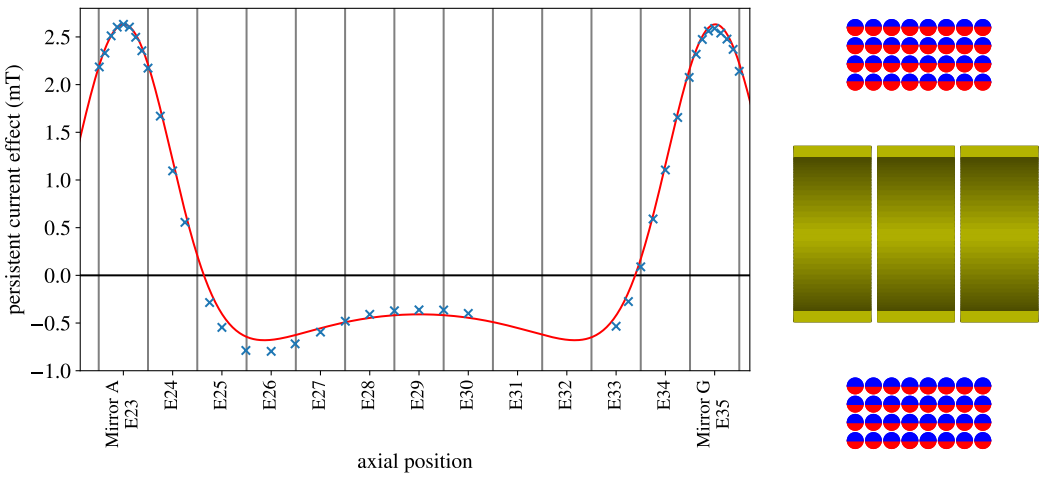

Figure 8.26: The effect of persistent currents versus axial position is shown with blue X's. The red line is a theoretical prediction based on the model shown on the right. The cartoon on the right shows a cross-section of a mirror coil, with red representing current running out of the page and blue representing current running into the page. Three electrodes are shown inside to clarify the orientation of the cross-section. The cartoon is not to scale, and there are 8 layers of 90 windings in the mirror coils, not 4 layers of 8 windings.

In Fig. 8.25, and even in Fig. 8.26, the measurement errors are too small to be perceptible. However, they are perceptible if we subtract the initial measurement at 0 A from the final measurement at 0 A. Both of these measurements were performed after ramping the mirror coils down from full current to 0 A, so even persistent currents should be identical. Fig. 8.27 shows the result of this subtraction, this time with statistical error bars. Note that the statistical errorbars come from a total of four fits—the spiral fit to the magnetron phase versus r and the linear fit to the magnetron phase versus magnetron orbit time for both of the two measurements ($2 \times 2 = 4$). Ordinarily, this kind of plot would additionally suffer from the statistical error from the calibration measurements, but in this case one of the two measurements is the calibration. There is an unexpected tiny perturbation near mirror G, but there is not one near mirror A. I suppose that in one of the two measurements, there was actually some nonzero current flowing through mirror G. This phenomenon has occurred many times at ALPHA; if we want the mirror coils to have no current, the power supplies need to be on and they need to be using a PID to apply 0 A of current. Otherwise external circuits like the quench detection system put a tiny current through the coils. It seems in one of these two measurements, I wasn't careful about having the power supplies in the right state. Otherwise, the difference between the measurements is consistent with zero.

In addition to studying persistent currents versus z, we can study how persistent currents grow as we increase the magnet current. To do this, in Fig. 8.28, I have plotted the deviation of the magnetic field from a linear fit to the field versus mirror current in six axial locations. The resulting data strongly resembles an exponential decrease plus a linear increase. This indicates that persistent currents are well-described by an "exponential saturation." There is some field strength $A(z)$ that the persistent currents are approaching according to the

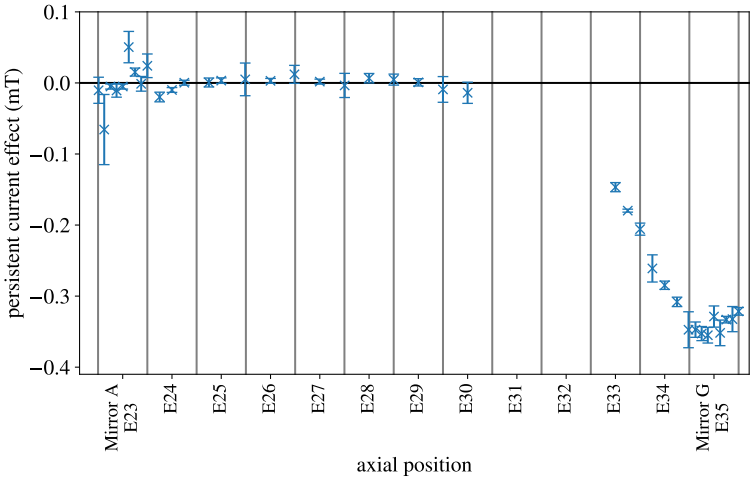

Figure 8.27: The initial and final measurements of the magnetic field versus axial position are subtracted from eachother. The error bars are the statistical errors from four fits involved in producing this plot.

equation $A[1 - \exp(-\Delta I/I_0)]$, where ΔI is how much the current has been changed (it is always positive), and I_0 is the "current change scale" of the exponential saturation. To quantify this, I have fit a linear function plus an exponential saturation function to the data from each axial location. We find I_0 values between 19 A and 23 A, so by the end of the magnet ramp persistent currents are changing very little. This "exponential saturation" model is not well-motivated. We do understand that persistent currents should approach a constant value, which occurs when the current through the superconductor is saturated (i.e. the maximum current density before the superconductor quenches). We do not have a model that suggests this process should be exponential. The remaining linear increase needed for the fit function is just the ordinary effect of putting a current through coils, which the original linear fit subtracted from the data was not allowed to capture because it needed to also account for the nonlinear changing persistent currents. In Fig. 8.29, the magnitude of persistent currents, found from the A parameter of the fit described above, is plotted for axial positions near mirrors A and G. At this point, fitting errors have a clearly visible affect on the data.

Unfortunately, while this is a much more complete dataset than we ever obtained with ECR, and while it was taken at least a factor of 10 more quickly than any of the ECR field maps, it was not useful for the analysis of the ALPHA-g measurement. The bottom solenoid was energized, but it was not in the ALPHA-g measurement, and it would be difficult to precisely remove the effect of this magnet. By the time I managed to make a reservoir without the bottom solenoid, there wasn't enough experimental time to repeat the procedure.

8.3.5 Cloud charge variability

A subtle correction to EMPI comes from the variability of the properties of the clouds—their total charge, temperature, and mean square radius. In particular, if the clouds used to perform the calibration measurements differed from the clouds used to perform an actual

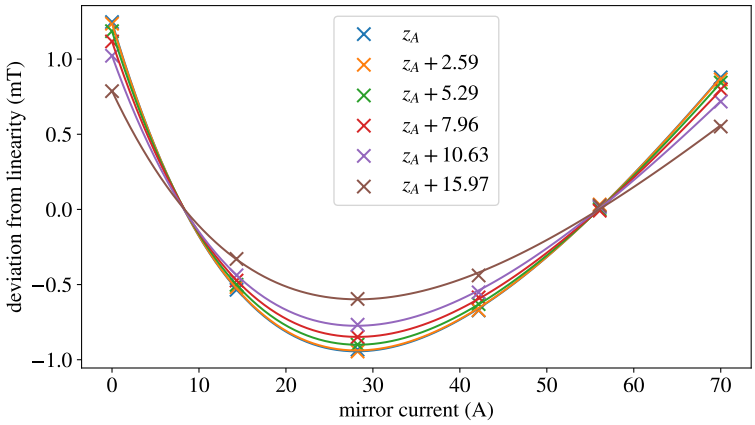

Figure 8.28: For six axial trap locations, the deviation of the magnetic field from a linear relationship with current is plotted versus current. The lines are the result of fitting an exponential decay plus a linear function to the data.

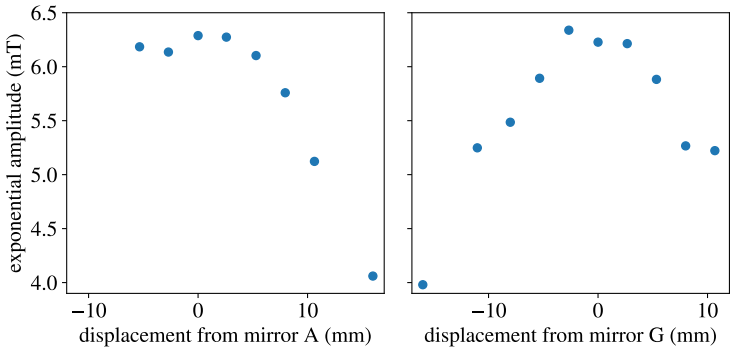

Figure 8.29: The amplitude of the exponentially saturating persistent currents is plotted versus axial position. There are only measurements of the magnetic field for all six mirror currents in a few axial locations near mirrors A and G.

measurement, and if the magnetron frequency depended on those cloud properties, there would be a systematic error in the EMPI measurements. My original motivation for studying this effect was the observation that when we pause scooping for 1–2 s for sequence bridging (see Sec. 8.1), the first 30 or so clouds after the pause have a different magnetron phase. This effect is visible in Fig. 8.4. Additionally, the first few hundred clouds extracted from the reservoir have a different magnetron phase, which will be more clearly visible in Sec. 8.4.

Often, we measure cloud charge variability by seeing how bright of an image it produces on the MCP. There are two issues with this technique. First, for very small clouds, this metric is very noisy (a variability of about 30% is typical for clouds that land in the same place on the MCP). Second, the MCP itself responds differently in different places. To map out the MCP's response I took all the data collected in EMPI measurements (about 100,000 pictures), and I found the average integrated cloud brightness as a function of position on the MCP. The results are shown in Fig. 8.30. The dark feature on the right side of Fig. 8.30 is a metal bar, which is out of focus, but partially obstructs the camera's view of the MCP.

The other features visible in Fig. 8.30 could be caused by the MCP, the phosphor screen, the mirror behind the phosphor screen, or the window between the mirror and the camera.

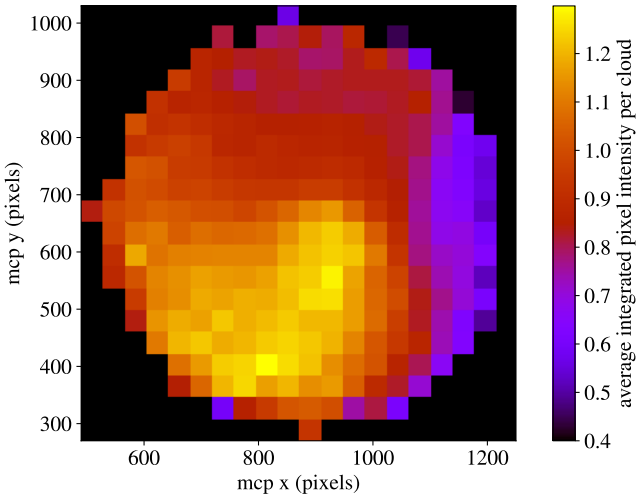

Figure 8.30: The normalized brightness of clouds is shown as a function of position on the MCP. For each pixel in this image, we collect all the clouds that were observed in that position on the MCP, and we average their brightness.

In Fig. 8.31, I show how the cloud charge evolves over the course of one reservoir. The data comes from averaging the cloud brightnesses across the entire dataset used for calibration measurements. We find a somewhat atypical reservoir behavior—the cloud charge drops in the first 300 extractions, then it increases and reaches a stable level after about 600 extractions. Most of the studies of reservoir behavior described in Sec. 2 extracted larger clouds from reservoirs, and only up to 200 clouds. I believe this behavior is due to the reservoir cooling after its initial preparation. I likely didn't wait sufficiently long to start extracting clouds after SDREVC (see Sec. 2.1). Extracting smaller clouds makes us more sensitive to small changes in the reservoir's temperature and space charge voltage.

Another source of cloud charge variability is that the cloud charge changes with the rate at which extract clouds from the reservoir. To some extent this mechanism was described in Sec. 2—the reservoir expands over time for reasons other than cloud extraction, decreasing its space charge voltage. This means that if we extract clouds from the reservoir more slowly, the clouds will have lower charge; we need to extract less charge from the reservoir to reduce its space charge voltage by the scooping voltage step size.

An accidental measurement of this effect occurred during the EMPI calibration measurements. Because different trap locations had different patch potential strengths and different magnetron frequencies, when calibration measurements were performed in different axial trap locations, the rate at which clouds were extracted from the reservoir changed. In Fig. 8.32, I show how cloud charges decreased when the time between extractions increased.

Ultimately, charge variability alone has a very small effect on EMPI measurements. With clouds consisting of 2000 electrons, the cloud's image charge will boost its magnetron fre-

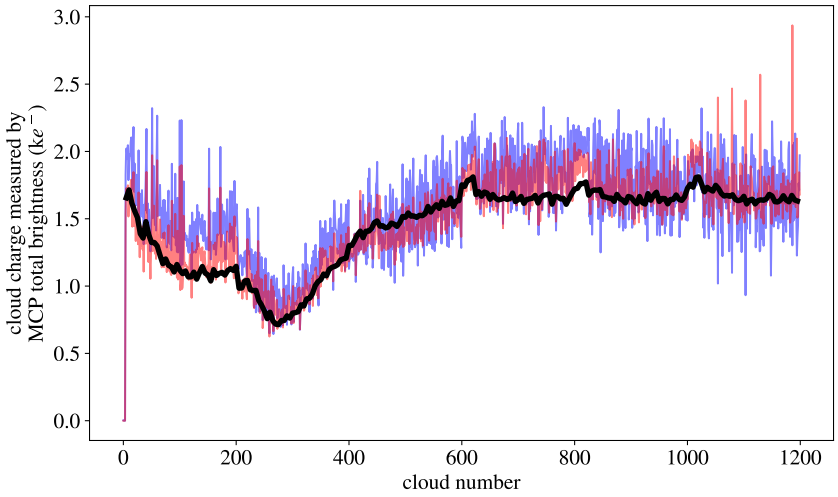

Figure 8.31: The charges of clouds successively removed from the reservoir for EMPI are reported. The blue line represents the integrated brightness of clouds extracted from one reservoir. For the red line, I divide by the average cloud brightness for that cloud's position on the MCP to remove the effect of variability in the MCP's response. The black line is the average brightness of 10 consecutive clouds additionally averaged over many reservoirs. The brightness of the clouds on the MCP is converted to a total charge by multiplying by a calibration factor described in Sec. 5.

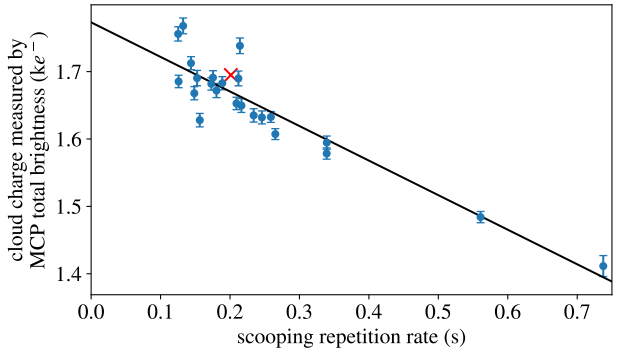

Figure 8.32: Average cloud charge is plotted versus the scooping repetition rate. The black line is a linear fit to the data. The red X shows the result from the calibration measurement at the center of mirror A, which is the most important location for EMPI measurements because it was the only location where EMPI measurements were enhanced by tuning the trapping potential to remove spiraling (see Sec. 8.1.10).

quency by 1.3/s (see Sec. 5.4.2). For a typical magnetron frequency of 10^5/s, this is a correction of only 1 part in 10^5. Additionally, this contribution scales as $1/B$ (just like the magnetron frequency induced by the trapping potential), so calibrating EMPI removes this effect entirely. It is only the variability in cloud charges that could produce a systematic error. In Sec. 8.4, I will attempt to validate the absolute accuracy of EMPI by looking at the agreement between ECR and EMPI at a magnetic field strength far from the field used

to calibrate. Those measurements were performed in the center of mirror A with a much shorter time between cloud extractions than was used for the calibration measurements. The linear fit shown in Fig. 8.32 suggests that this should increase cloud charges by 6%, yielding an absolutely negligible change to the magnetron frequency.

However, in Sec. 5.4, I showed that the magnetron frequency is also affected by a cloud's length if the quartic constant of the trapping potential is not zero. In turn, the cloud length is affected by its charge and its temperature. The length effect and the image charge effect on the magnetron frequency are typically comparable. Note that even in the center of mirror A, because I tuned the trapping potential to reduce the spiraling, k_4 will be smaller than in most trapping potentials. However, it will not be zero because spiraling is caused by k_4 and the cubic term k_3, so k_4 alone was not specifically tuned to be zero. In Sec. 5.4.3, I provided tenuous evidence that cloud temperatures were causing $\mathcal{O}(5/\mathrm{s})$ variations in magnetron frequencies. Therefore, I think it is most likely that the variations described in the beginning of this section are primarily due to variations in the cloud temperature, not the cloud charge. Unfortunately, I never measured the temperatures of the clouds used for EMPI, and when cloud temperatures were measured in the past, they were measured with larger clouds extracted at a maximum frequency of 1 cloud per second. Even if I tried to measure cloud temperatures, the temperature measurement technique is very imprecise and it may not have been enlightening. I propose that the first few hundred clouds extracted from the reservoir have a different magnetron phase because the reservoir is either cooling down after its initial preparation or it is being heated by cloud extraction. I also think the reservoir cools when we pause cloud extraction for sequence bridging, thereby changing the temperatures of extracted clouds, and less significantly, changing their total charge. The data shown in this section only proves that clouds' total charge is varying, but I take this data as a suggestion that the clouds' other properties might also be varying.

8.4 EMPI measurements in a rapidly changing magnetic field

The most important contribution to the ALPHA-g measurement from the EMPI studies were measurements of the magnetic field during the mirror coil rampdowns that were used to release antihydrogen. To be clear, these measurements were not performed during the actual ALPHA-g measurement, but rather during identical magnet ramps after the completion of the ALPHA-g measurement. It was only after the conclusion ALPHA-g that time was allocated for EMPI. However, there has been no evidence that the magnetic field varies from one magnet ramp to the next, so it is safe to infer that the measurements I describe in this section are a good description of what occurred during ALPHA-g.

In principle, dynamic EMPI measurements can be performed by first doing an exponential angle increase operation to find the total magnetron angle subtended by one cloud after some maximum time T. From there, we repeatedly image clouds after they perform a magnetron orbit for the same amount of time. At some point, we start ramping down the mirror coils, and as the magnetic field decreases, the magnetron frequency increases. In order to be able to track the changes in the magnetron frequency, T should be chosen such that the phase difference from one cloud to the next is less than π. Note that the time between measurements T_m is not equal to T, because a significant fraction of T_m is used to move the clouds along the trap axis and to move the clouds off-axis. Thus the condition for dynamic

EMPI is $T_m|d\omega_r/dt|T < \pi$, or in terms of the magnetic field $T_m|k_2(dB/dt)/B^2|T < \pi$. If this condition is not satisfied, it may be ambiguous whether the magnetic field has increased or decreased. In extreme cases, it might be ambiguous whether, for example, the magnetron phase has changed by $3\pi/2$ or $7\pi/2$. I refer to such errors as "losing a 2π." Obviously, this condition can be relaxed when the rate and direction of change of the magnetic field is roughly known, but keeping the magnetron phase change less than π also means that the analysis software is much easier to design. I considered more complicated designs, such as alternating between measurements with a higher T for higher precision and measurements with a lower T that are easier to track. Such designs may be useful in the future, but for this first set of measurements I decided to stick with the simpler scheme. It is also likely that future ALPHA-g measurements will be performed with slower changes in the magnetic field, which is probably the easiest way to quickly boost the precision of dynamic EMPI measurements.

The gaps in the measurements due to sequence bridging (see Sec. 8.1.1) slightly complicate these measurements—it is necessary to pause measurements for 1–2 s after every 200 phase measurements. I took some care to make sure that these gaps did not occur precisely at the beginning or end of the mirror ramp. After these gaps, I first imaged 20 clouds normally, then I performed a new exponential angle increase operation in case the total number of magnetron orbits was ambiguous. The total magnetron phase of each cloud in a standard dynamic EMPI measurement for a 130 s rampdown of the mirror coils is shown in Fig. 8.33.

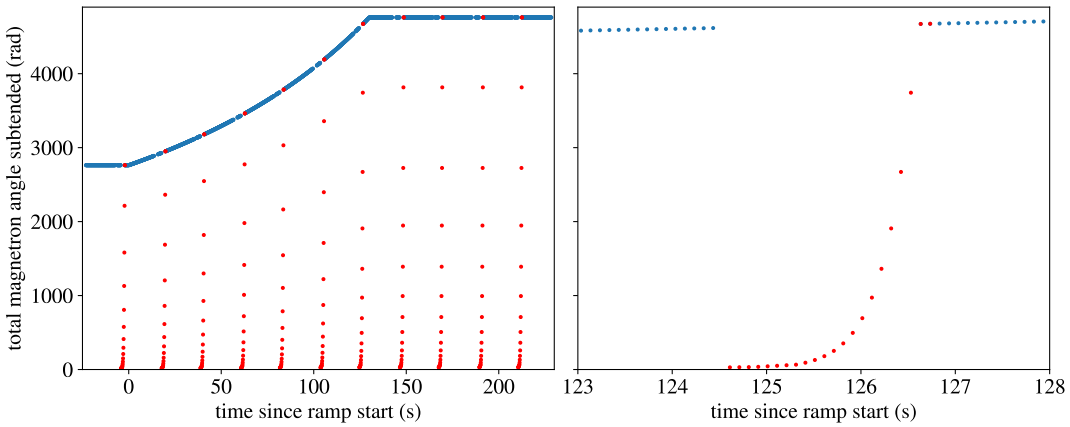

Figure 8.33: The total magnetron angle is shown for each EMPI measurement in the center of mirror A performed during a 130 s rampdown of the mirror coils. The blue dots indicate EMPI measurements taken with a constant magnetron time T. The red dots indicate EMPI measurements done with an exponentially increasing angle to find the total number of orbits. On the right, I zoom in on one such exponential angle increase operation. Despite the lack of noise, this is indeed experimental data. Noise is imperceptible at this scale.

Ultimately, these exponential increase operations were not strictly necessary. By fitting a line to a few EMPI measurements before the sequence bridge, we can predict the phase of the cloud after the sequence bridge with an error significantly less than π. However, these exponential increase operations were still useful for two reasons. First, when I was still tuning the analysis software, these absolute measurements of the total magnetron angle

helped me identify if I had lost a 2π or if there was any other issue in the analysis. Second, these measurements revealed a small correction to EMPI that I hadn't previously considered. When I analyze an exponential angle increase, I fit a line to the magnetron phase versus time to find the magnetron frequency. Of course, a line comes with a slope and an intercept. This intercept can be interpreted as the direction of the patch potential used to move the cloud off axis. It was at first unexpected that this "reference angle"—the base angle that we measure all other magnetron phases relative to—changes over the course of the measurement, as shown in Fig. 8.34. The reference angle always increases, and it always increases by about 0.1 radians. This observation could be explained by T being less than expected by about 1–2 μs. In Sec. 6.4, I showed that it takes about 10 μs for the electrode potentials to settle after quickly changing them. For example, it takes about this time to dump the electron clouds and to go from the shallow well used to move them off-axis to the deep well where the magnetron orbit is performed. Thus this 1–2 μs correction is due to the time taken for the dump being slightly shorter than the time taken to move to the deep well. This asymmetry is expected because these two operations involve different voltage changes. When the electrode voltages are still changing, the magnetron frequency is changing as well. In some sense, we are really measuring $\int k_2(t)/B(t)dt$. Note this means technically we are measuring the average magnetic field over a total time of 10 ms. Since the change in k_2 is localized to the first and last 10 μs of the EMPI measurement, we can account for this issue by simply adjusting T by 1–2 μs—whatever is consistent with the change in reference angle. Another outcome is that we are actually measuring the magnetic field about 10 μs later in time than we thought we were. This latter issue turns out to be insignificant, because the magnetic field changes by a few parts in 10^7 in 10 μs. In the analysis, the reference angle was coerced to linearly change between the reference angle at the beginning and the reference angle at the end of the ramp. This is equivalent to adjusting T. Otherwise, if we measure each magnetron phase relative to the most recently measured reference angle, statistical error in the reference angle leads to unphysical jumps in the measured magnetic field. This also allows us to benefit from averaging multiple measurements of the reference angle to reduce statistical uncertainty.

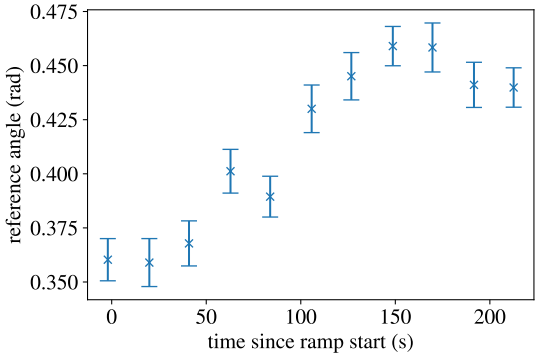

Figure 8.34: The measured reference angle is reported for 11 exponential angle increase operations during a 130 s rampdown of the mirror coils. The error bars are the statistical error from the linear fit that is used to infer the reference angle.

Nominally, the magnetron frequency is the magnetron angle of each cloud divided by T, and the magnetic field is the calibration factor found in Sec. 8.3 divided by the mag-

netron frequency. However, before we can report the magnetic field during the ALPHA-g measurement sequence, we need to include quite a few corrections. In Fig. 8.35, I show the measured magnetic field using EMPI in the center of mirror A for a 130 s rampdown of the mirror coils. I also show the deviation from the expected magnetic field if we assume the magnetic field changes linearly from the ECR measurements done before the ramp to the ECR measurements after the ramp. The following corrections are applied sequentially in Fig. 8.35:

1. The first plot simply shows the nominal measured magnetic field.

2. The second plot shows this measured magnetic field minus the linear expectation from ECR.

3. In the third plot, I have subtracted the effect of the bottom extraction magnets (see Sec. 8.3.1).

4. In the fourth plot, I have accounted for the fact that we are measuring the magnetron frequency off-axis. To do this correction, I first find k_4 from the spiraling found in the calibration measurements in a roughly constant magnetic field versus z. Next, a model of the magnetic field is used to find the predicted first and second derivatives of the magnetic field. The error in this model is roughly 1%. Eq. 8.14 is used to relate these off-axis magnetron frequency measurements to the near-axis magnetron frequency, and this corrected magnetron frequency is used to get a more accurate measurement of the on-axis magnetic field. This fourth plot is the final measured magnetic field.

5. In the fifth plot, I have fit an exponential saturation plus linear function to the measured magnetic field, and I have subtracted the exponential saturation part of that fit function. This allows us to see smaller unexpected deviations—given that at this point we understand and expect persistent currents.

I first want to discuss the remaining deviation between the magnetic field measured with EMPI and the magnetic field measured with ECR before the magnet ramp starts and after it ends. The deviation is about 0.05 mT after the ramp ends and about 0.08 mT before it starts. The known sources of error on the absolute accuracy of these EMPI measurements are as follows:

1. The error in our subtraction of the bottom extraction field is 0.008 mT, the typical deviation between the ECR measurements of the bottom extraction field and the fit function used to approximate it. These deviations are likely errors in the ECR measurement; the fit function is expected to be accurate.

2. The statistical error of the calibration factor is 1.47 parts in 10^6; in other axial trap locations with more spiraling this error is usually larger (up to a factor of 10 larger).

3. The error in the ECR measurement used for calibration is about 0.01 mT—this directly translates to the same error in these measurements. Actually at 1.7 T the error grows to 0.017 T. This estimate is somewhat crude—it comes from noticing that there is nonlinear persistent current decay between the first and last measurements in the first

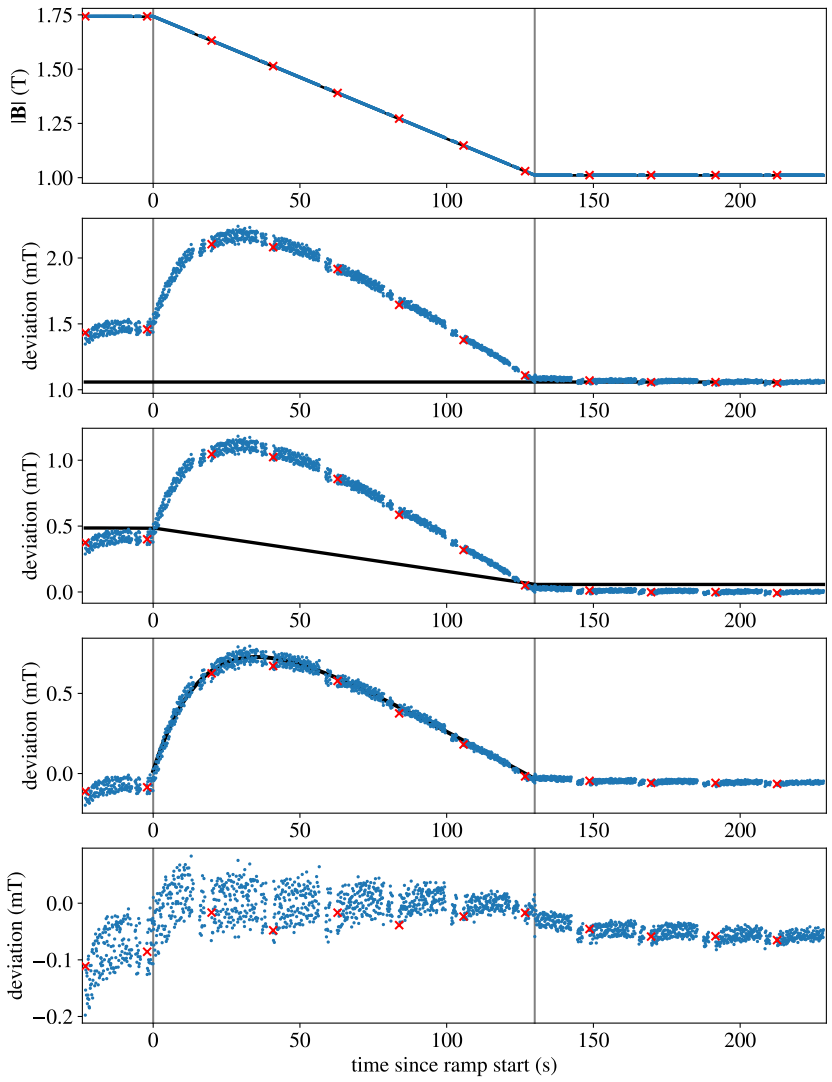

Figure 8.35: The measured magnetic field is plotted versus time since the mirror coils start ramping down. The sequence of plots is explained in the text. In each subplot, the blue dots are the magnetic field measured using EMPI. The red X's are the results of the exponential angle increase measurements. The black line is the correction which will be subtracted from the blue dots for the next subplot.

calibration measurement which I cannot account for by assuming the magnetic field changes linearly between these measurements. In the second calibration measurement, there was no persistent current decay, but in some axial trap locations there was still a disagreement between the initial and final ECR measurements of up to 0.01 mT. This simply reveals that this is the typical variation in the fit ECR peak center with the ECR frequency scan ranges I was using at the time. This estimate for ECR error is backed up by the fact that the two calibration measurements disagreed by 2 parts in 10^5

4. The statistical error in the spiral constant from the calibration measurement is 2.4%.

Further, the error in the magnetic field model used to infer the off-axis correction with the mirrors energized is about 1%. This correction is at most 0.5 mT, so we arrive at a total error of 0.017 mT. This error is larger with the mirror coils energized in this axial trap location, but not in all of them.

5. The trapping potentials used for ECR were not identical to those used for EMPI. This could mean that the magnetron frequency and the magnetic field were not measured in identical axial trap locations for the calibration measurements. This is a particularly significant issue in this axial trap location, where the trapping potential was tuned, slightly altering the position of the trap center. An electrostatic model of the trap finds that there was a displacement of 300 μm. This leads to a negligible error at the end of the ramp, where the magnetic field does not significantly vary with axial position, but there is an error of roughly 0.027 mT at the maximum field.

6. The statistical error on the reference angle is 0.01 radians, leading to an error in the measured magnetic field of 0.006 mT.

7. There PPM level errors discussed in other sections, like the higher order $\mathbf{E} \times \mathbf{B}$ drift correction discussed in Sec. 8.16, and the effect of relying on an imperfect magnetic field model to move the clouds off-axis discussed in Sec. 8.1.11

For the maximum magnetic field, when I add these errors in quadrature, I get a total error of 0.035 mT. When I add them linearly, I get a total of 0.070 mT. At the minimum magnetic field, the totals are 0.019 mT and 0.038 mT. In both cases, the observed deviations are slightly larger than even the results of summing the known errors linearly. My leading hypothesis for this is the issue discussed in Sec. 8.3.5—the temperatures and the charges of the clouds is varying over the course of the measurement, and there may also be a difference between these cloud parameters used for a dynamic measurement and these cloud parameters used for the calibration measurements. Further study will be needed on this effect to break the 0.1 mT accuracy barrier. Alternatively, if we just do an ECR measurement just before and just after these dynamic EMPI measurements, we can coerce the EMPI measurements to agree with the ECR measurements, essentially eliminating all of the systematic errors listed above. Here, I preferred to include the disagreement so I could point out potential flaws in my understanding of the magnetron frequency.

Before I move on to discuss other dynamic EMPI results, I want to highlight a few features visible in Fig. 8.35 which will also be visible in many other dynamic EMPI measurements.

1. The magnetic field drifts over the course of the first 200 measurements before magnet starts ramping. This is not a real drift in the magnetic field; it is the 9reservoir settling, as discussed in Sec. 8.3.5. It is unfortunate that I didn't wait longer for the reservoir to settle before starting the magnet ramp.

2. After each 1–2 s gap in measurements due to sequence bridging, there is a deviation in the measured magnetic field. Again, this is because of cloud properties changing after a 1–2 s pause in extractions from the reservoir.

3. The spread of the measurements is greater at the beginning of the ramp than at the end. This is because in this axial trap location, there is stronger spiraling at 1.7 T than at 1.0 T, causing the initial magnetron motion of the clouds to yield a larger magnetron phase variability (see Sec. 2.3).

4. There is a rapid increase in the deviation visible in the bottom subplot of Fig. 8.35 at the beginning of the magnet ramp. This is because the freeze-in of persistent currents is not perfectly modeled as an exponential saturation curve.

8.4.1 Dynamic EMPI results

In this section I will simply present a few measurement results from dynamic EMPI. First, in Fig. 8.36, I show the measured magnetic field in the 12 axial trap locations where the measurements were successful. The issue preventing successful measurements in other axial locations is described in the next section. At this level of precision, nothing remarkable is really perceptible. In Fig. 8.37, I show the same data, this time plotted versus axial position.

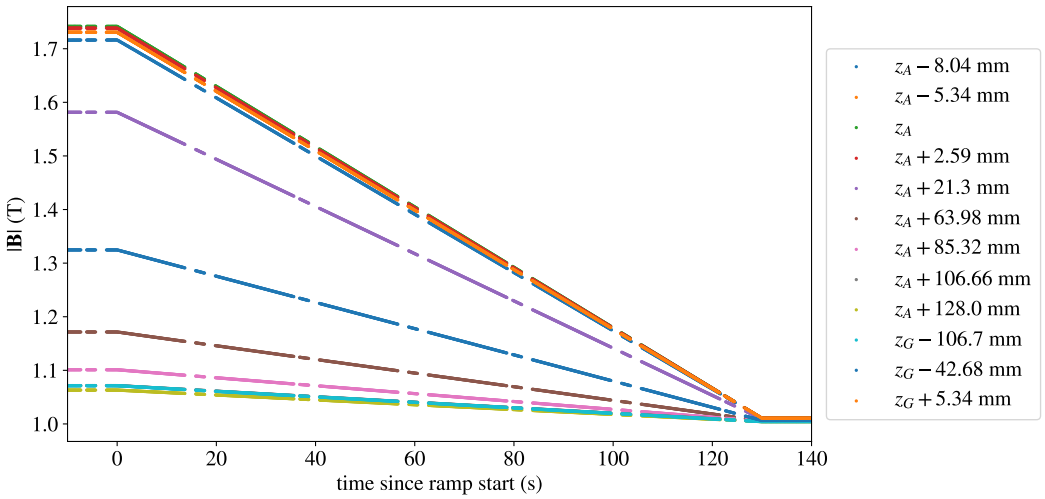

Figure 8.36: The magnetic field measured with dynamic EMPI for 130 s magnet ramps is plotted versus time since triggering the mirror coil ramps. The axial positions of each measurement are provided in the legend on the right, with z_A being the center of mirror A and z_G being the center of mirror G.

More interesting features are visible in the data when I plot only the nonlinear component. In Fig. 8.38, I plot the same data as the previous two figures. This time I have subtracted a linear approximation from each measurement. This linear approximation comes from averaging a few datapoints before the start of the ramp and a few datapoints after the end of the ramp. This is also the only possible linear approximation, since ECR does not provide us with expected start and finish magnetic fields in more than two axial trap locations. Like we observed in Sec. 8.3.4, near mirrors A and G the persistent currents are a positive contribution the magnetic field. Between the two magnets, persistent currents are a negative contribution to the magnetic field. We also clearly see that in different axial locations the spread of the measurements is different. This is because the different axial locations have

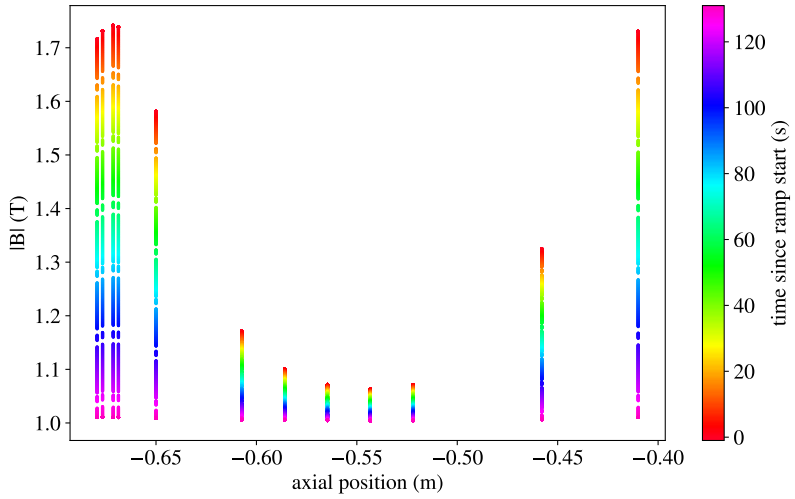

Figure 8.37: The same data as in Fig. 8.36 is plotted in the form of magnetic field versus axial position, with the color of each datapoint indicating the time since the start of the magnet ramp.

different degrees of spiraling. When the spiraling is more significant, the measurements are more spread out.

Most of the ALPHA-g data came from 20 s rampdowns of the mirror coils. Until now, I have presented data from 130 s rampdowns, first because the data is more beautiful, and second because I am quite sure that future implementations of ALPHA-g will involve longer magnet ramps or they will involve a smaller change in the magnetic field. Fig. 8.39 shows dynamic EMPI measurements from the center of mirror A during a 20 s rampdown.

Here we observe two effects that were much smaller in the 130 s rampdowns. First, notice in the last subplot of Fig. 8.39 that there are two erroneous measurements in the very beginning and end of the magnet ramp. This is a real effect; during the magnet rampdown, the currents are controlled by a PID, and that PID does not perfectly produce a linear change of the current. This effect is more significant when we attempt to change the magnetic field more quickly. Fig. 8.40 shows the measured currents during the magnet rampdown. EMPI magnetic field measurements are overlaid on these measured currents to show that these deviations at the start and end of the ramp are marginally perceptible in the EMPI data.

The second effect that is more clearly visible in the 20 s data is an offset between the field just before the end of the ramp and just after the end of the ramp. In theory this offset should also be present at the start of the ramp, but it is harder to observe because the non-exponential part of the persistent current freeze-in is also clearly visible there as a short linear increase. This offset comes from two effects. First, the aforementioned PID does not only have errors at the start and end of the ramp. Also, the PID generates more current than intended throughout the ramp by about 6 mA, essentially causing the entire ramp to be offset forward in time. Second, there are five other mirror coils between mirrors A and G (called mirrors B, C, D, E, and F). These mirror coils are intended for future measurements. The rampdown of mirrors A and G creates inductive currents in these mirrors, which are measured externally. About 8 mA is generated in mirrors B and F, about 3 mA in mirrors C

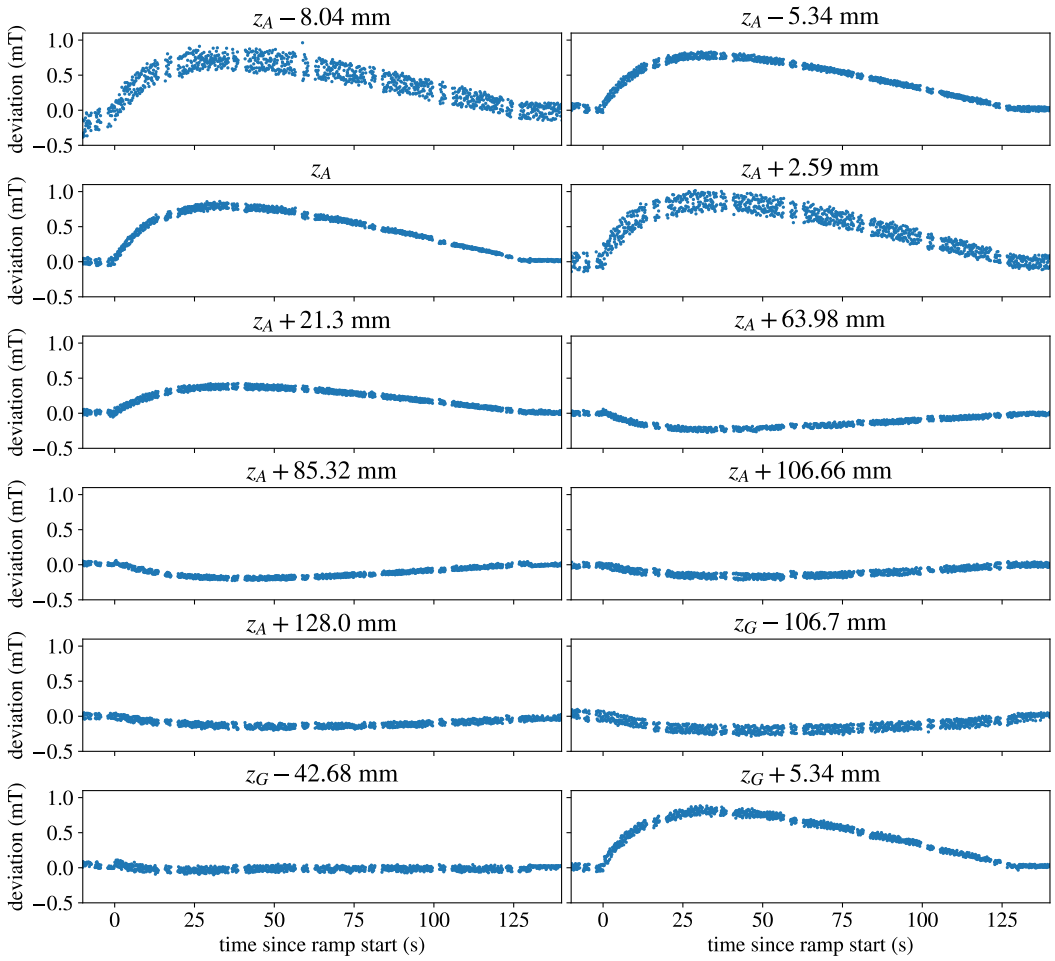

Figure 8.38: The deviation of EMPI-measured magnetic fields from linearity is plotted versus time since the magnet ramp starts. Each subplot is data from a different axial location in the trap.

and E, and about 2 mA in mirror D. Altogether these current errors are expected to create an offset of about 0.07 mT during the rampdown, which is roughly what we observe. Fig. 8.41 shows the expected effect on the trap's magnetic field from these current errors.

In the ALPHA-g measurement, we varied the magnetic field difference between mirrors A and G in steps of 0.45 mT to create a so-called "bias" [1]. A bias of "$-1g$" indicated that the expected effect of gravity was being compensated by boosting the magnetic field at mirror A by 0.45 mT. Thus I performed dynamic EMPI measurements at several different biases with 20 s rampdowns. Unfortunately, because most of the data from the center of mirror G had to be thrown out due to the issue described in the next section, I don't have a great variety of data to present here. In Fig. 8.42, I show measurements from the center of mirror A for four biases, $2g$, $1g$, $0g$, and $-2g$. The $-2g$ measurement was repeated accidentally; I intended to measure at $-1g$, which would have made the plot a lot more interesting, but I apparently entered the wrong setting. Further, the $2g$, $1g$, and $0g$ measurements are identical because these biases are created by changing the magnetic field in mirror G, not in mirror A. An

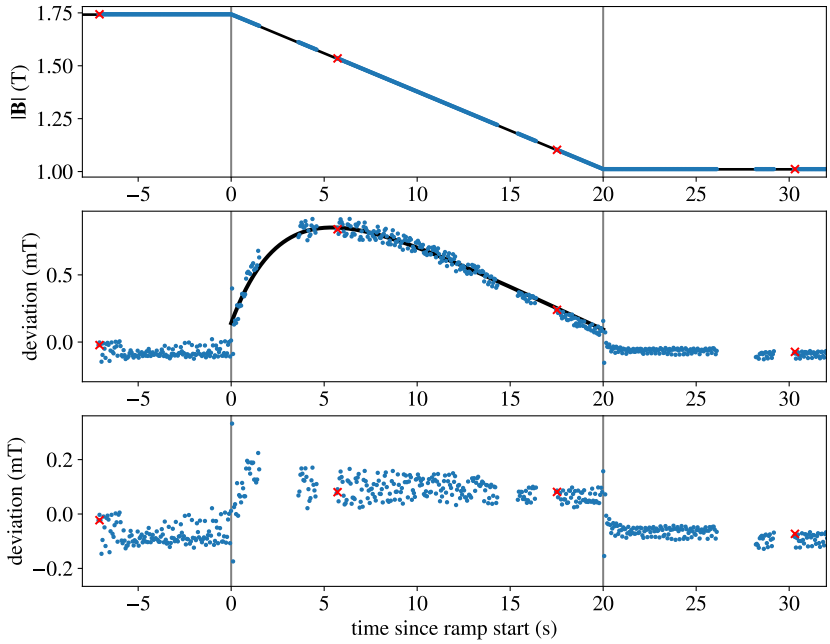

Figure 8.39: EMPI measurements from the center of mirror A during a 20 s rampdown. The fist subplot shows the raw magnetic field measurements. The second subplot shows the magnetic field after I have subtracted a linear approximation assuming the magnetic field changes linearly from the initial and final ECR-measured field strength. I have also subtracted the effect of of the bottom extraction magnets. The black line in this second subplot is the exponential saturation of persistent currents taken from the 130 s rampdown (because an exponential plus linear fit to this data would not be very effective because there is far less data). In the third subplot, this exponential persistent current saturation is subtracted out.

interesting observation in this data is that the magnetic field is 0.9 mT higher at the end of the ramp for the $-2g$ bias. This was expected given the currents used to achieve the bias. For a reason I don't recall, we chose to implement $-2g$ by removing some current in mirror G at the start of the ramp and adding some current in mirror A and the end of the ramp.

8.4.2 EMPI sequence timing error

The result that members of the ALPHA collaboration were most interested in from EMPI was a comparison of the magnetic field in the center of mirror A and the center of mirror G during the rampdown that released antihydrogen. Such a measurement could be used to bound errors in the ALPHA-g gravity measurement that could not be characterized by ECR performed in static magnetic fields. Unfortunately, there was a mistake in the EMPI sequences that was not noticed until after the experiment was disassembled, and this essentially ruined all of the dynamic EMPI measurements from the center of mirror G.

As discussed in Sec. 8.1, sequence bridging is only effective if the time taken to load a new sequence onto the FPGA controlling the electrode voltages is less than a second. Otherwise, the time between subsequences is unknown, and from that moment forward,

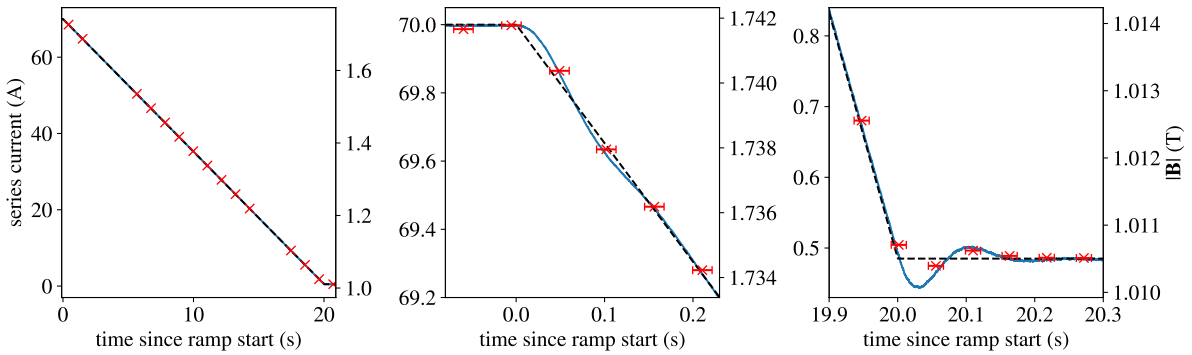

Figure 8.40: The intended linear current ramp is shown with a black dashed line. A blue line shows the measured current through the mirror coils during the rampdown. In the first subplot, red X's show the EMPI measurements (only one in 20 measurements are shown)—the magnetic field measurements are scaled to lie on top of the current measurements. In the second and third subplots, I zoom in on the start and end of the ramps. The horizontal bars are not error bars; they indicate the time over which EMPI measures a time-averaged magnetic field.

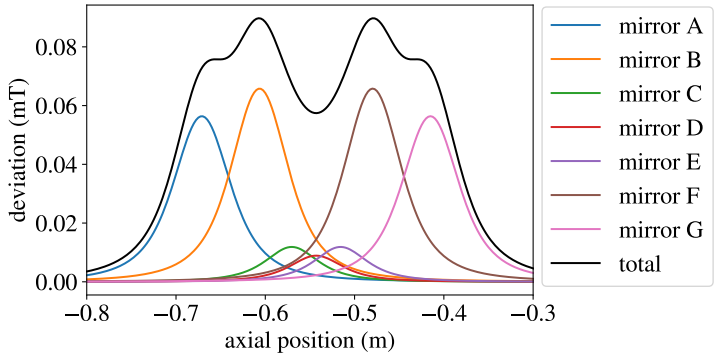

Figure 8.41: The magnetic field created by the current errors described in the text is plotted versus axial position in the trap. The colored curves show the magnetic field created by the current error in each individual magnet. The black curve shows the total.

while the magnetic field measurements will remain accurate, it will not be known what time those measurements correspond to. Of course, if this issue was anticipated, it could have been fixed in any number of ways. Fig. 8.43 shows a very clear example of this effect. The analysis software proceeds normally assuming that the sequence bridging functioned as planned. Instead of seeing a smooth variation of the magnetic field versus time, between subsequences the deviation of the magnetic field from linearity jumps downward. This is because the magnetic field is being measured up to 100 ms later than the analysis software believes it is. In this example, it seems that every subsequence took about 25–100 ms longer to load than the 1 s they were allotted by sequence bridging. The issue seems to be dependent on axial trap location—perhaps some sequences are more complicated and take slightly longer to load. Alternatively, we have noticed that the sequencer software slows down with continued use. It may be that data taken later in the day was more likely to exhibit this

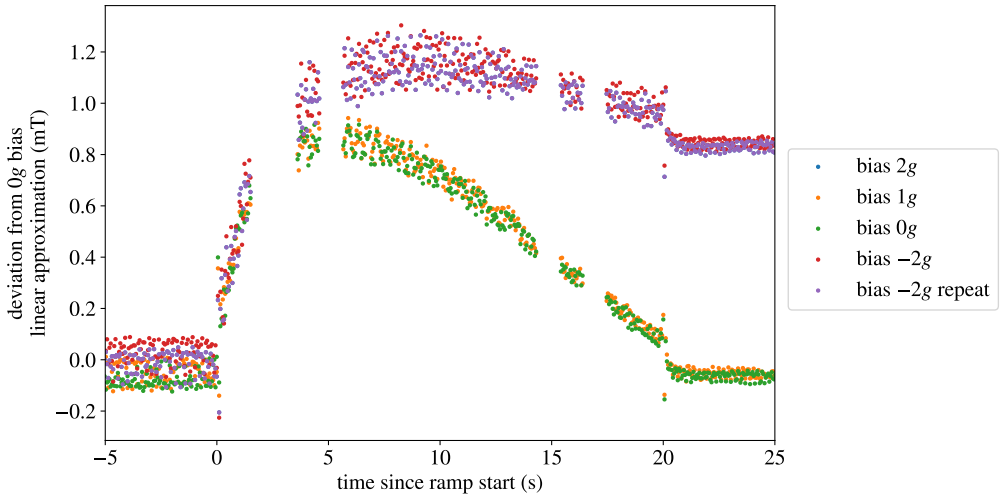

Figure 8.42: The deviation of EMPI measurements from a linear approximation is reported for five trials with different "biases." The measurements are from a 20 s rampdown in the center of mirror A. For all five datasets, the "linear approximation" subtracted from the data comes from ECR measurements before and after the ramp with $0g$ bias. This way the difference between $-2g$ bias and the other datasets is visible in the plot.

issue. Occasionally, this issue can be hard to differentiate from losses of 2π in the phase tracking algorithm, which also manifests as an unexpected jump in the magnetic field, and is more likely to occur during sequence bridging. However, the telltale sign of this particular failure is the four dots located near 130 s in Fig. 8.43. These dots show that the magnetic field is increasing when the linear approximation believes it should no longer be changing—a clear sign that we are mistaken about what time the data was taken.

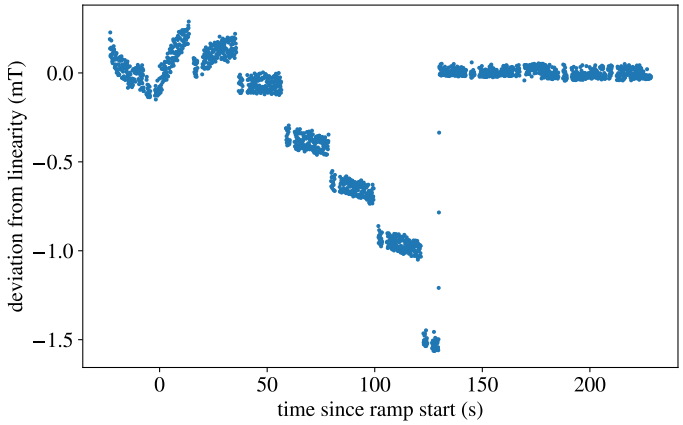

Figure 8.43: The deviation of the magnetic field from linearity measured by EMPI is reported versus time since the mirror rampdown began. This dataset exhibits the failure of sequence bridging. The linear approximation which is subtracted from the data is found by averaging the measurements before the ramp starts and after the ramp completes.

Fig. 8.44 shows the EMPI measurements of the 20 s rampdown of mirror G, clearly

exhibiting the same issue. However, I wanted to at least attempt to fix the data. In this data, there are two sets of 200 measurements separated by sequence bridges which are affected by the sequence bridging failure. There is one sequence which triggers the magnet rampdown, so the timing of that sequence cannot be wrong. Then there is a second sequence which performs most of the measurements during the rampdown, and then there is a third sequence which is used to observe the ending of the rampdown. First, in the analysis, I adjusted the measurement times for this third sequence so that the analysis agreed with the measurements in the center of mirror A about when the ramp ended. In more detail, in both the mirror A and the mirror G measurements, I fit lines to a few measurements before and after the ramp ends, and I found what time those lines intersected, which was 20.0025 s. The timing of the mirror G data was adjusted to agree on this "inferred ramp end timing." Next, the timing of the middle sequence was adjusted so that a linear fit to the last few measurements of that sequence agreed with a linear fit to the first few measurements of the next sequence. Of course, both of these methods introduce a tremendous amount of bias that the measurements at mirror G should agree with the measurements at mirror A, and that is exactly what I was attempting to measure. Therefore, one should not take these measurements too seriously. It is worth pointing out however that by fixing this error we can get good agreement between the dynamic EMPI measurements in mirrors A and G, as shown in Fig. 8.45. Barring a particularly coincidental magnetic field error—a bump in the magnetic field that spans exactly 4–15 s after the ramp starts, or the ramp ending at a different time in mirrors A and G—this measurement is useful for ruling out errors in the ALPHA-g measurement that cannot be measured in static fields. Note that the offset between the two measurements before the ramp starts is not physical; it is ruled out by ECR measurements in these static magnetic fields. This must be the result of a measurement error; some sources of error are discussed in the beginning of Sec. 8.4. In fact, because the spiraling was not tuned near the center of mirror G as it was near the center of mirror A, most of these systematic errors are much larger in the mirror G measurements. This is also why the spread of the measurements is much larger for mirror G.

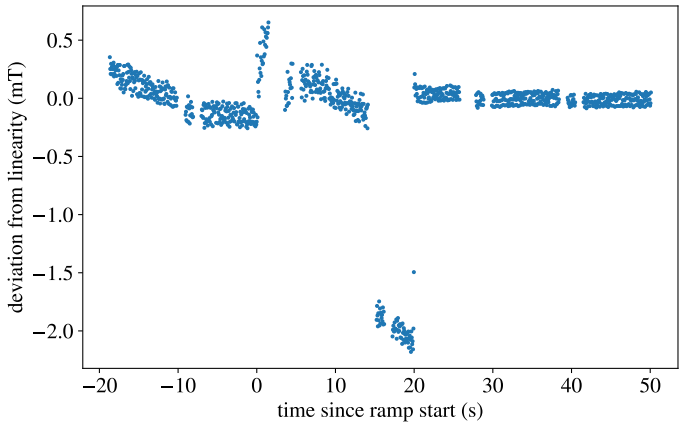

Figure 8.44: Measurements of the magnetic field using dynamic EMPI in the center of mirror G during a 20 s rampdown of the mirror coils.

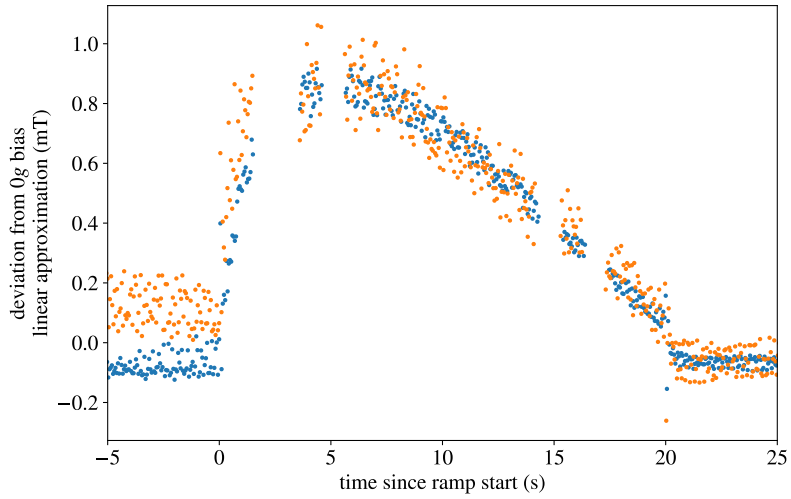

Figure 8.45: The EMPI magnetic field measurements are compared between the center of mirror G (orange) and the center of mirror A (blue). These measurements were performed during a 20 s rampdown of the mirror coils with $0g$ bias—the magnetic field in both axial locations was meant to be the same. I have subtracted the same linear approximation from both measurements—the ECR measured magnetic field in the center of mirror A during identical magnet ramps.

8.4.3 Octupole deviations

The ALPHA collaboration has long known that when plasmas are dumped from a combined Penning-Malmberg and magnetic minimum trap with the octupole for the magnetic minimum trap energized, the plasmas do not image as circles. An example of a positron plasma dumped toward the MCP in ALPHA-2 is shown in Fig. 8.46.

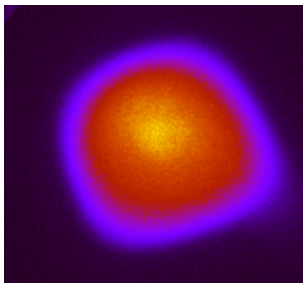

Figure 8.46: An MCP image of a positron plasma dumped in the presence of an octupole field.

The effect of the octupole is very weak in the center of the trap—far too weak to actually perturb the shape of the plasma to this extent. Rather, this effect occurs because the positrons follow magnetic field lines as they move toward the MCP; the octupole magnet distorts the magnetic field lines. We expect circular plasmas to appear on the MCP as more of a square shape due to this effect. The magnetic field of the octupole is proportional to $r^3[\hat{r}\cos 4\theta + \hat{\theta}\cos 4\theta]$. Therefore every 90 degrees there should be a magnetic field pointing

outward, deviating magnetic field lines outward, and between those angles there should be a magnetic field pointing inward. The effect we observe is clearly asymmetric though, which probably indicates some misalignment between the octupole, the electrodes, the external solenoid for the Penning-Malmberg trap, the magnets that boost the magnetic field at the MCP, or any combination of these elements. Of course some of these components are known to have imperfect alignment (see Sec. 6), but I have not checked if these known misalignments can explain the magnitude of the effect seen here.

I was initially concerned that this would be a significant disruption to EMPI measurements. Instead of the clouds landing along a circle, that circle would be distorted, leading to some error in the measured magnetron phase versus time. I was even resistant to trying EMPI measurements in the presence of the octupole magnet, but other members of the collaboration insisted that EMPI measurements would be much more interesting if they were performed in a magnetic field that was as similar as possible to the fields used for the actual ALPHA-g measurement. Ultimately, I tried dynamic EMPI with the octupole energized, and the issue was not bad at all—in fact all of the measurements presented in this section were performed with the octupole energized.

In Fig. 8.47, I show the position that clouds land on the MCP for a very large number of clouds observed at various magnetron phases during EMPI measurements. As expected, we find that the deviation from a circular shape is worse the further the clouds move through the octupole on the way to the MCP. Near the center of mirror A, the bottom of the antihydrogen trap, and very close to the bottom of the octupole, the deviation from a circle is nearly imperceptible. Near the center of mirror G, the effect is clearly visible. However, when we fit a circle to the mirror G data, the maximum deviation of the shape from the circle is less than the spread of the cloud positions due to their initial magnetron motion. This data does not illustrate the angular deviation of the cloud positions from the nominal angular position, but we can infer that these angular deviations will be roughly the same size as the radial deviations divided by the radius. Thus, for measurements closer to mirror A, this issue is essentially negligible. For measurements closer to mirror G, the maximum possible error is a bit less than half the nominal spread of measurements.

I wonder if this effect could be used in any way to measure the magnetic field of the octupole, or even to measure errors in the magnetic field of the octupole. It would be a very significant research project to figure out how to interpret these results.

8.5 Persistent Currents

Originally, the term "persistent current" referred to a current running through a closed loop of superconducting wire. Such a situation can be achieved by cooling a superconducting loop below the phase transition temperature in the presence of an external magnetic field, then turning off the externally applied magnetic field. Like in an ordinary conducting loop, a current will be generated which preserves the magnetic flux through the superconducting loop. Unlike in an ordinary conducting magnet, this current will not decay over time.

In this section I discuss persistent currents that are unintentionally generated by attempting to change the current in a superconducting magnet. The ALPHA-g magnets are not closed superconducting loops; they are driven by power supplies at 300 K. However, superconducting loops still exist within the wires. Current can run in one direction on the

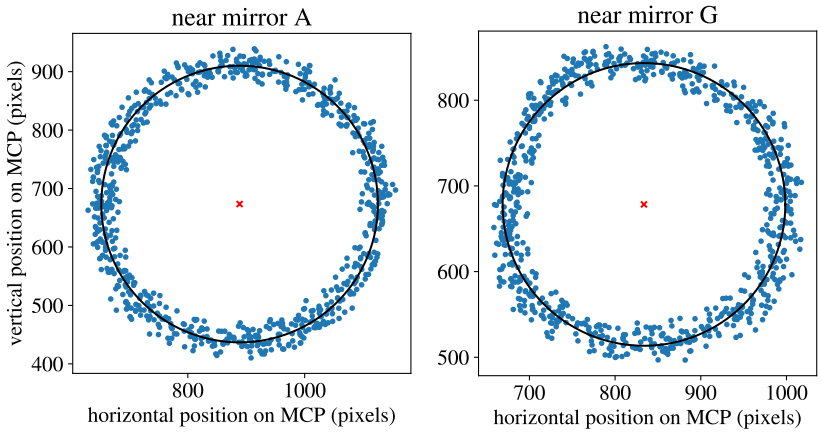

Figure 8.47: The position of the centers of clouds imaged on the MCP during EMPI measurements is shown with blue dots. The black circle is fit to the data, and the red X indicates the center of that fit circle.

top of a single superconducting filament and in the opposite direction on the bottom. The loop could be closed at the end of the superconducting wire. When we change the externally applied current in one of the magnets, we attempt to change the magnetic flux through such superconducting loops in nearby magnets (and especially in the magnet whose current we change). This effect is limited by the "saturation current"—at a certain magnetic field strength and temperature, there is a maximum current that a superconductor can support before it reverts to a normal-conducting phase.

This was first discovered as an experimental difficulty in the Tevatron, where it was observed that the behavior of the beam depended on the history of the magnets and that the magnetic field changed with time [131, 132]. Since then, the effect has been studied at DESY [133], RHIC [134, 135], the LHC [136, 137], and as part of a design study for the FCC [138]. These studies show effects that are qualitatively similar to what we observe at ALPHA, and they are a similar order of magnitude.

In ALPHA-g, we first observed slow decreases in the magnetic field ($\mathcal{O}(0.1\,\mathrm{mT})$ over several hours), which we measured with ECR. We attributed this to persistent currents, and we assumed the size of this decay reflected the size of the persistent currents. However, EMPI provided the first observation that changing the currents in any of our magnets would induce persistent currents which would perturb the magnetic field by $\mathcal{O}(1\,\mathrm{mT})$. These changing persistent currents also caused the magnetic field to change nonlinearly with the current change in a magnet. Only some small fraction of that effect was observed to decay. However, I did not immediately assume the effect was real—at the time I had not read any papers about the effect. The effect is large enough that it could have been easily measured with ECR, so I assumed that the nonlinearity I observed in EMPI measurements of the magnetic field during magnet ramps was instead a correction to the magnetron frequency that I hadn't considered. In hindsight, many earlier ECR measurements did show bumps in the magnetic field near the mirror coils that were undoubtedly due to persistent currents. At the time, we blamed these bumps on small currents that might have been running through the coils due to small errors in the power supplies.

EMPI was able to show this effect of persistent currents before ECR simply because it could measure the magnetic field at several hundred current values between 70 A and 0 A in 20 s, the time it takes to ramp down the current. Later we confirmed with ECR that if we change the current in the magnets in steps, we also observe a nonlinear change in the magnetic field from the creation of persistent currents. Because of the amount of input needed from the operator, these measurements took several hours. This is also why such a measurement was never done prior with ECR—the ALPHA collaboration is often operating with extremely limited time, and these measurements were not deemed to be important enough.

8.6 ECR measurements of persistent currents

In Sec. 8.3, I showed several qualitative features of persistent currents in ALPHA-g. I showed that persistent currents resist a change in the magnetic flux through superconducting material, and I showed the on-axis effect of persistent currents generated while ramping down a mirror coil. I also showed that the creation of persistent currents resembles an "exponential saturation." In this section, I will describe ECR measurements of persistent currents that will introduce a few more qualitative features.

First, we observe that after a magnet's current is changed, the persistent currents that were created by that change decay over time. Ph.D. student Adam Powell designed an ECR measurement procedure where one reservoir was used to measure the magnetic field 8 times in quick succession. He extracted 200 clouds from a reservoir; for the first 25 clouds, the microwave frequency was swept and a cyclotron resonance was observed. For the next 25 clouds, the microwave frequency sweep was reset so that a second resonance could be observed at a later time. This data, shown in Fig. 8.48, shows that after the mirror coils were ramped down for the ALPHA-g measurement, the magnetic field decayed by about 0.05 mT in 100 s. This effect is hard to observe with EMPI because it lacks sufficient precision; in some measurements, it is arguably observable, but not very clearly. Fig. 8.49 further shows how the magnetic field decays over the course of hundreds of seconds after the mirror coil rampdown.

The "exponential saturation" behavior of persistent currents was confirmed with ECR measurements after being observed with EMPI. As a reminder, in Sec. 8.3, I showed that when we changed the current in the mirror coils, the magnetic field change in a particular axial trap location z had a nonlinear component that is well-approximated by $A(z)[1 - \exp(-\Delta I/I_0)]$, where ΔI is the (strictly positive) change in the current, I_0 is an "exponential current scale," and $A(z)$ is the maximum effect that persistent currents will have for a very large change in the current. Further, with ECR, we found that persistent currents depend on which other magnets are energized in the moment that one magnet's current is changed. In Fig. 8.50, I show the exponentially saturating part of the change in the magnetic field in five different situations where the mirror coil currents are changed in 10 steps between 0 A and 70 A. First, we observe that when the mirror coils are ramped down with the octupole magnet energized, the persistent current effect is about half as big. Although the octupole provides very little magnetic field on-axis, it significantly increases the magnetic field where the superconducting material is located. Thus we expect that the octupole reduces the critical current and will reduce the effect of persistent currents—the critical current is lower

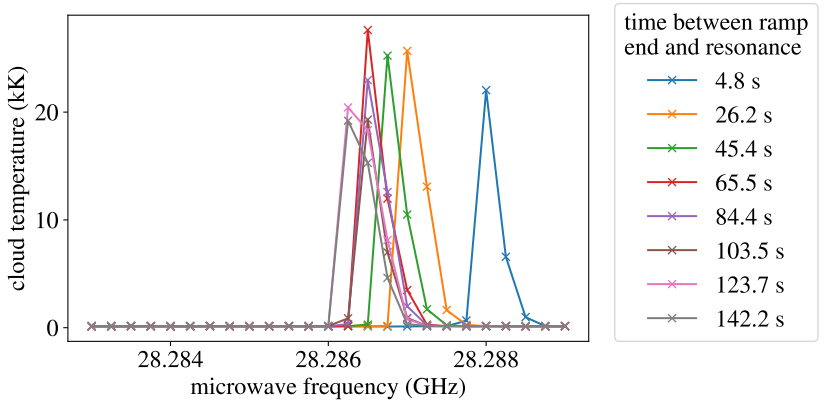

Figure 8.48: Cloud temperatures are plotted versus microwave frequency for the 8 microwave frequency sweeps used to measure the decay of the magnetic field shortly after ramping down the mirror coils. This data was collected by Dr. Chris Rasmussen, and the original measurement technique was designed by Ph.D. student Adam Powell.

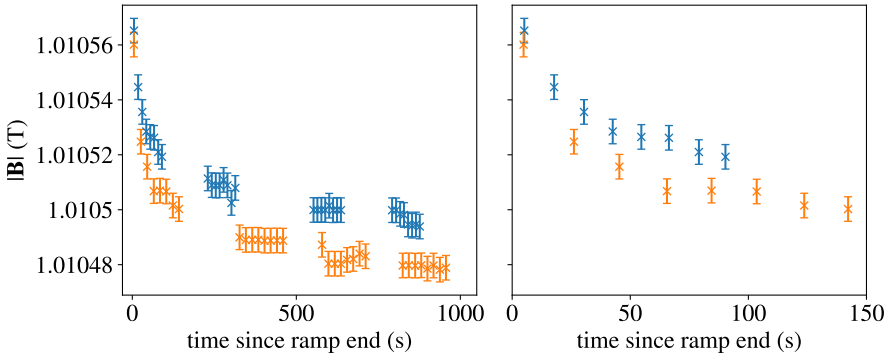

Figure 8.49: The magnetic field, measured with ECR, is reported versus time after ramping down the mirror coils. Four reservoirs are used, and with each reservoir, the magnetic field is measured 8 times in the manner shown in Fig. 8.48. On the right, I zoom in on the first 8 measurements. The orange data comes from the center of mirror G, and the blue data comes from the center of mirror A. This data was collected by Dr. Chris Rasmussen, and the original measurement technique was designed by Ph.D. student Adam Powell.

when the magnetic field in a superconductor is higher. Interestingly, with the octupole energized, we find that $A(z)$ is roughly halved, and I_0 is also halved, likely indicating a relationship between the two variables. Next, we observe that when the mirror coils are ramped down after just having been ramped up, we get twice the exponential saturation than if the most recent magnet operation were something else. In the experimental protocol for the ALPHA-g measurement, the last magnet operation before ramping down the mirror coils was to ramp down the "long octupole." This magnet was intended to boost the field of the "short octupole," enhancing antihydrogen trapping, but it was not symmetric about the center of the trap, so we needed to ramp it down before performing the ALPHA-g measurement. We believe that this operation "deleted" the persistent currents that were

induced by ramping the mirror coils up. Without this long octupole rampdown, when we ramp down the mirror coils, we are both creating persistent currents from ramping down and removing the persistent currents from previously ramping up.

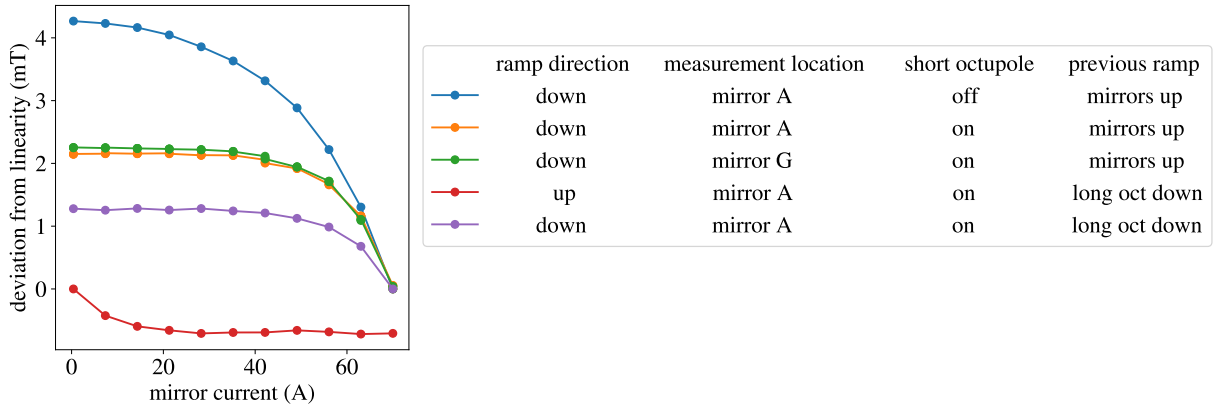

Figure 8.50: The exponential saturation of persistent currents is plotted as we change the current in the mirror coils. In the legend, the relevant context for each measurement is provided. The exponentially saturating part of the magnetic field is calculated by fitting a linear function plus an exponential saturation function to the magnetic field versus mirror current. Then the linear component of that fit is subtracted from the data.

In hindsight, we had evidence of a nonlinear change in the magnetic field long before I developed EMPI. At one point, we were concerned that the on-axis magnetic field produced by the octupole magnet would be a significant issue in the ALPHA-g measurement. To investigate this field, we first measured the magnetic field versus octupole current in two on-axis trap locations. This data is shown in Fig. 8.51. In one trap location, we find that the exponential saturation is nearly as big as the nominal effect of the octupole. At the time, we thought this might be explained by the octupole field pointing in a different direction than the nominal on-axis field, but this model is not a good fit to the data, and the octupole should not be creating such a large on-axis transverse magnetic field. In hindsight, this is clearly a change in persistent currents from changing the current in the octupole. This does not necessarily mean persistent currents have a significant effect on the on-axis magnetic field when the octupole has saturated persistent currents ($\Delta I \gg I_0$). It is possible (likely, even), that Fig. 8.51 is showing how the octupole ramp removes the persistent currents generated by whatever magnet was ramped prior.

After this measurement, we attempted to measure the on-axis effect of the octupole magnet by measuring the magnetic field versus z with and without the octupole energized. The results are shown in Fig. 8.52. Qualitatively, we observe the expected result—that the "end turns" of the octupole produce an easily measurable on-axis magnetic field. This end turn field was at most about 6 mT, a similar order of magnitude to the persistent currents generated by ramping the mirror coils. However, the shape of this effect was not in good agreement with a model of the octupole, and we also did not expect to find that the magnetic field in the center of the trap was significantly perturbed.

Earlier, in Sec. 8.3.1, I argued that the on-axis effect of persistent currents generated

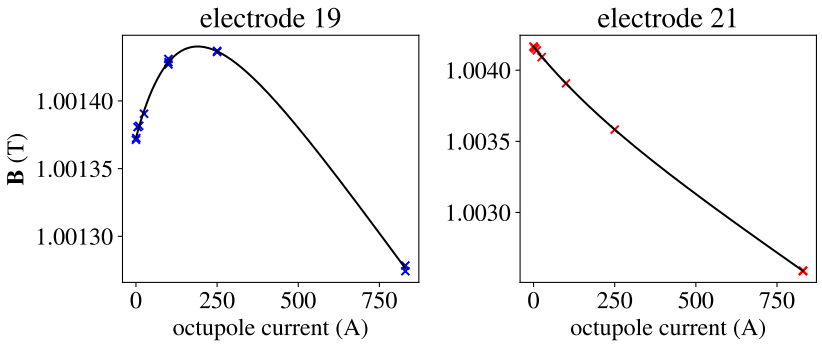

Figure 8.51: The on-axis magnetic field is measured in two axial trap locations versus current in the octupole. The black lines are exponential saturation plus linear fits.

by ramping the octupole should be very small (smaller than the ordinary on-axis effect of persistent currents). This is because most of the magnetic field produced by the octupole near the superconducting material is proportional to $\cos 4\theta$. Thus it seems natural that most of the magnetic field produced by persistent currents generated when ramping the octupole would have the same azimuthal variation. By extension, the on-axis effect would be very small; any magnetic field that varies azimuthally like $\cos 4\theta$ must also be proportional to r^3 for small r. This assertion was experimentally confirmed in Sec. 8.3.1 by the observation that the on-axis magnetic field does not measurably change over time after ramping the octupole down. However, this is a very imprecise way of measuring persistent currents because only a small fraction of the total effect decays over time. That observation probably cannot rule out persistent currents that are five or ten times weaker on-axis than those produced by ramping the mirror coils. Such a correction would still be perceptible in Fig. 8.52. Also, this $\cos 4\theta$ argument might break down when we consider the persistent currents generated in mirror coils by the octupole ramp, or when we consider the end turns of the octupole. In conclusion, the persistent currents produced by ramping the octupole are simply not well-measured, and field maps like Fig. 8.52 may be affected by these persistent currents. In the future, to resolve this debate, one should simply measure the magnetic field versus z for several different octupole currents to separate the linear effect from the exponentially saturating effect. Then we will know with greater certainty how much on-axis magnetic field is produced by octupole construction errors.

Because the on-axis effect of octupole ramp persistent currents is at least significantly smaller than those induced by mirror ramps, octupole ramps can be used to "reset" persistent currents and to create a highly reproducible on-axis magnetic field. This technique relies on the fact that octupole ramps were observed to "saturate" persistent currents—in Fig. 8.51, the fit value of I_0 was much smaller than the change in current $\Delta I = 800\,\mathrm{A}$. In Fig. 8.53, I begin by measuring the on-axis magnetic field after having just ramped down the octupole. Next, I ramp the mirror coils up and down, producing bumps of about 3 mT from persistent currents. Finally, I ramp the octupole back up and down, and the bumps have been removed. Actually, it is very beneficial for the ALPHA-g measurement that most of our magnet operations seem to saturate persistent currents. Otherwise, the magnetic field would not have been reproducible from one trial to the next.

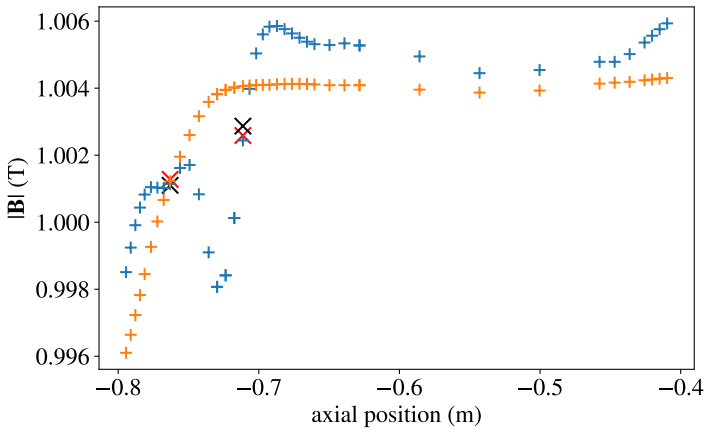

Figure 8.52: The magnetic field is plotted versus axial position with the octupole energized (blue +) and after ramping down the octupole (orange +). Also, the measurements of the magnetic field at full octupole current shown in Fig. 8.51 are shown with a red X, and the result of subtracting the exponentially saturating persistent currents is shown with a black X. This is meant only to illustrate the order of magnitude of the persistent currents. The measurements with the octupole energized were performed first, and the only magnet operation between the two datasets was a rampdown of the octupole.

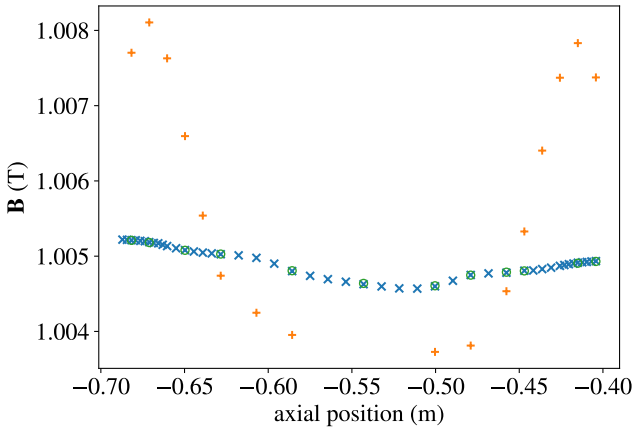

Figure 8.53: The initial magnetic field magnitude versus axial position is shown with blue X's. The magnetic field after ramping the mirror coils up and down is shown with orange +'s. The magnetic field after "resetting" persistent currents by ramping the octupole current up and down is shown with green O's.

9 Unsolved mysteries

9.1 Imaged cloud "reflections"

This last chapter describes a caveat that applies to the analyses of all the other chapters in this thesis. Occasionally, when we image an electron cloud on the MCP, we see multiple spots, as seen in Fig. 9.1. We initially assumed that this was just a reflection of light—for example light could be bouncing off the front of the camera lens then again off the vacuum window between the MCP and the camera, similar to a "lens flare." This phenomenon occurs in both ALPHA-2 and in ALPHA-g. In both cases, there are certain regions of the MCP where it is more prevalent. In ALPHA-g, it is the right side of the imageable region of the MCP. Another proposed explanation for this was that electron clouds were bouncing axially in the trapping potential, and when they are being dumped, a spurt of electrons is released a few times when this bounce motion approaches the escaping edge of the trapping potential. However, this explanation is not consistent with the fact that the "reflections" are always displaced in the same direction (to the lower left in ALPHA-g). This explanation would require the reflections to trace out the magnetron orbit of the cloud.

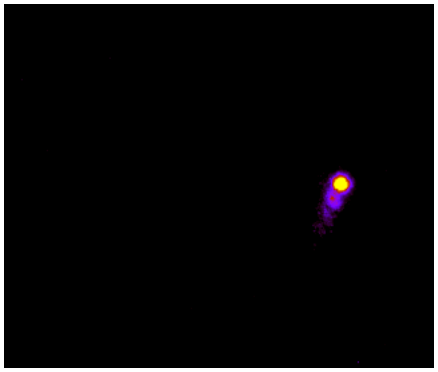

Figure 9.1: An example of an MCP image of an electron cloud where multiple spots appear.

One day while doing patch potential measurements, I saw conclusive evidence that these were not optical reflections. The magnet that boosts the magnetic field near the MCP shut off unexpectedly in the middle of my measurement, and I noticed that these "reflections" got further apart as the magnet ramped down. Thus I set up an experiment where I tested this effect intentionally. Clouds were repeatedly moved to a test location in the trap, moved off axis, then imaged when they were at a particular magnetron phase where this effect could be clearly observed. I imaged about one cloud per second, and I ramped down the magnets near the MCP over the course of 100 s. Some MCP images from this experiment are shown in Fig. 9.2. We clearly observe these reflections moving farther apart as the magnet ramps down.

In case there was any remaining doubt that these secondary spots are the effect of real electrons hitting the MCP, consider that when the magnetic field at the MCP is low enough, with the clouds becoming larger from the magnification and the secondary spots becoming further apart, we see individual electrons. Second, the "reflections" still are visible when the magnetic field at the MCP has gotten so low that the primary cloud misses the MCP

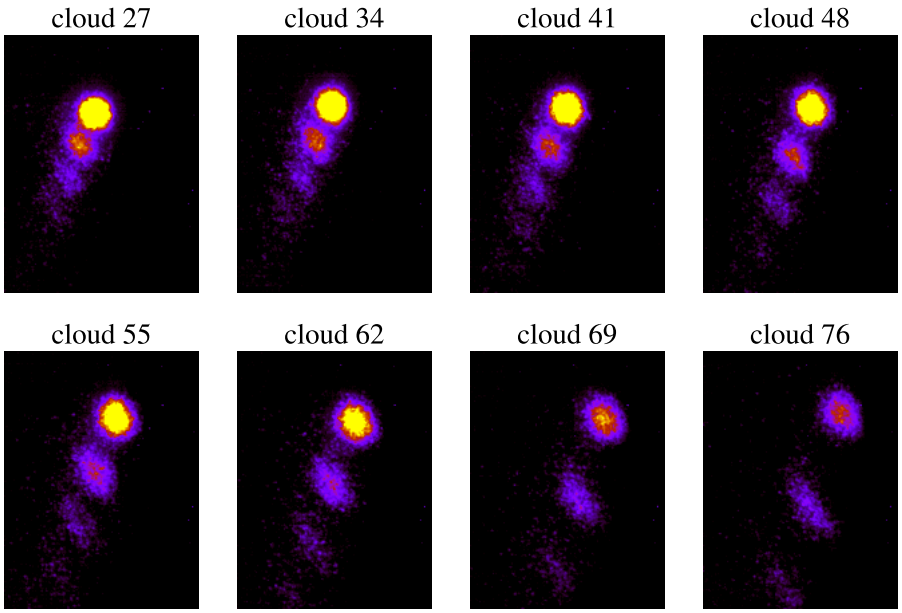

Figure 9.2: MCP images of clouds over the course of the experiment where the magnetic field at the MCP was ramped down. Unlike in Fig. 9.1, I have zoomed in on the interesting part of the picture.

altogether and is not successfully imaged at all. Examples of these phenomena are shown in Fig. 9.3.

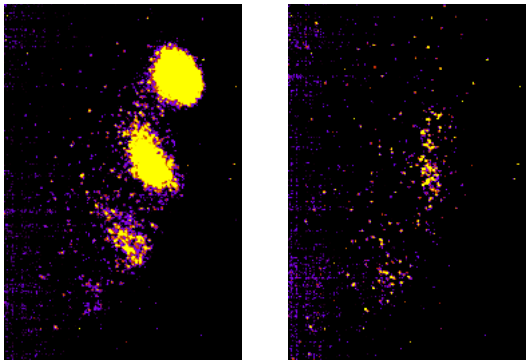

Figure 9.3: Two examples of MCP images of electron clouds with a very weak magnetic field at the MCP. The brightness is increased dramatically relative to the other MCP images shown in this section.

Dr. Chris Ørum Rasmussen, the technical coordinator of the ALPHA collaboration, suggested that these so-called reflections may be electrons that bounce off the front of the MCP, and by the time they return to the MCP they land in a slightly different place. Previous authors have studied the phenomenon of electrons bouncing off metal surfaces for the purpose of optimizing accelerator performance. These so-called "secondary electrons" can disrupt the beam in an accelerator. In Refs. [139] and [140], electrons are directed

toward a metal surface, and the energy distribution of electrons ejected from that surface is measured. Not only are electrons observed coming off the metal surface, some electrons "bounce," coming off the metal surface with nearly the same energy they had initially. This "elastic peak" decreases in magnitude as the electron energy increases, but it is still clearly visible at the energies of our electrons (about 150 eV). I highlight this elastic peak because the front of the MCP is charged to 100 V. If secondary electrons are generated with less than 100 eV, they will not stray far from the MCP surface. If they are elastically reflected, they may even follow magnetic field lines all the way back to the interior of the trap and bounce off the potential inside the trap that was initially used to eject them toward the MCP.

If the electrons are perfectly following magnetic field lines, they should simply return to the same location on the MCP that they came from. However, in Sec. 3.5, I showed that it was plausible that electrons dumped toward the MCP are slightly affected by $\mathbf{E} \times \mathbf{B}$ drift from the electric field of the MCP. This could explain why this phenomenon is more visible closer to the edge of the MCP; the electric field should have a larger component perpendicular to the magnetic field there. Thus I propose that secondary electrons are generated all across the MCP, but only in some locations do they land in a visibly different location on the MCP when they return.

To further study this phenomenon, I analyzed how the distance between the dots on the MCP varies with the magnetic field. For each picture in the experiment described above, I fit a "Gaussian peak series" to the dots visible on the MCP. In more detail, the fit function was a sum of Gaussians of standard deviation σ (in units of pixels) and maximum value A. Each successive Gaussian was displaced from the previous one by (Δ_x, Δ_y), and each successive Gaussian had a smaller maximum value by a factor of f. An example of one such fit function and the image it fits to is shown in Fig. 9.4

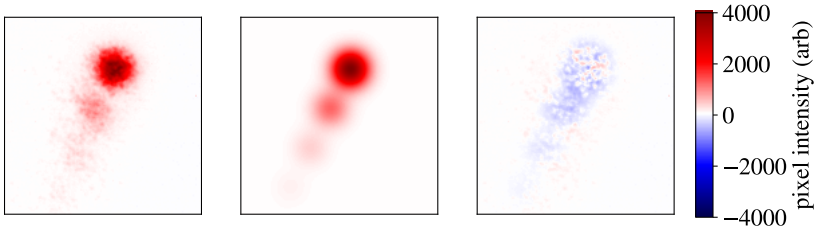

Figure 9.4: The left plot is an MCP image of a cloud. The middle plot is the resulting Gaussian peak series fit. The third plot is the difference between the two.

The resulting cloud radii and distances between spots is shown in Fig. 9.5. Using a model of the magnetic field, we can find the power law relationship between these distances and the magnetic field at the MCP. The cloud radii are expected to scale like $\sqrt{B_{\text{trap}}/B_{\text{MCP}}}$, and we find a power law of $1/B_{\text{MCP}}^{0.39}$. The cloud radii are much harder to precisely determine than the distance between clouds because the radius is much smaller. The power law for the distance between dots is found to be $1/B_{\text{MCP}}^{1.27}$. Given the error on the radius power law, we don't expect this power law to be extremely accurate. This measurement could be consistent with either $1/B_{\text{MCP}}$ or $1/B_{\text{MCP}}^{1.5}$. It is certainly not consistent with $1/B_{\text{MCP}}^{0.5}$, further proving that these dots are not simply electrons that were dumped from a different transverse position within the trap.

Whether the electrons return all the way to the trap or if they only reach a short distance above the MCP, the expected power law is $1/B_{\mathrm{MCP}}$. If we assume the $\mathbf{E}\times\mathbf{B}$ drift occurs near the surface of the MCP, the electrons $\mathbf{E}\times\mathbf{B}$ drift with a velocity proportional to $1/B_{\mathrm{MCP}}$ for a fixed amount of time (not a function of B_{MCP}). Some complication may occur because in this experiment, the clouds were drifting further toward the edge of the MCP as the magnetic field decreased. This may enhance the observed power law. We know that the phenomenon is more clearly visible further toward the right edge of the MCP, but I have not managed to study the dependence on MCP position in detail.

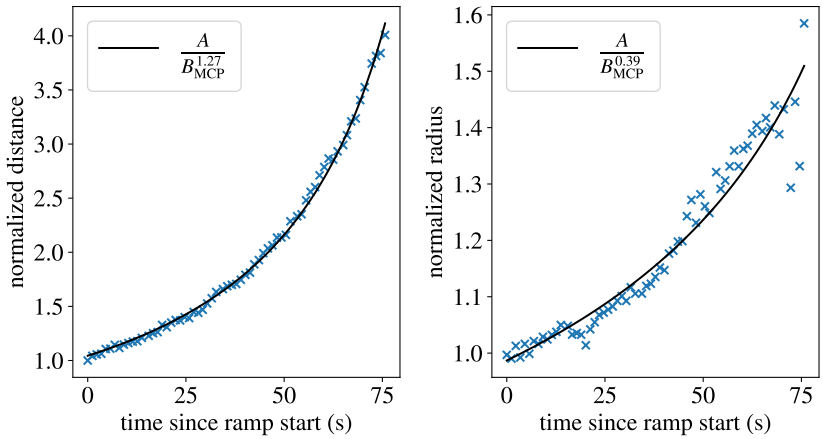

Figure 9.5: The normalized distance between dots in the MCP images (left) and the normalized radius of the dots (right) is plotted versus time since triggering the MCP magnet rampdown. Note that after about 75 s, the clouds are no longer visible on the MCP, although the magnets are continuing to ramp down. A power law fit function is shown with a black line.

This phenomenon is concerning for the analyses presented throughout this thesis for several reasons. First, when the secondary spots overlap with the primary spots, they drag the identified cloud center slightly toward the bottom left of the MCP. Second, the model I have described for these secondary spots implies that there is some non-negligible $\mathbf{E}\times\mathbf{B}$ drift experienced by the electrons on their way to the MCP, and that this drift is not uniform across the face of the MCP. This may mean that circles inside the trap are distorted by this drift. So far, this effect has not been clearly visible in any data, but if we ever want to rely on the position of a cloud center on the MCP for precision measurements, we may need to study this phenomenon in detail. In the most precise measurement in this thesis, EMPI, the precision of the measurement does not so much rely on the precision of one identified cloud center; it relies on the cloud performing many magnetron orbits. Thus I don't believe that this effect is a significant source of error for any of the cloud-based measurements in this thesis. However it is somewhat embarrassing that I don't have a conclusive explanation for one of the most obvious features of the data used throughout this thesis.

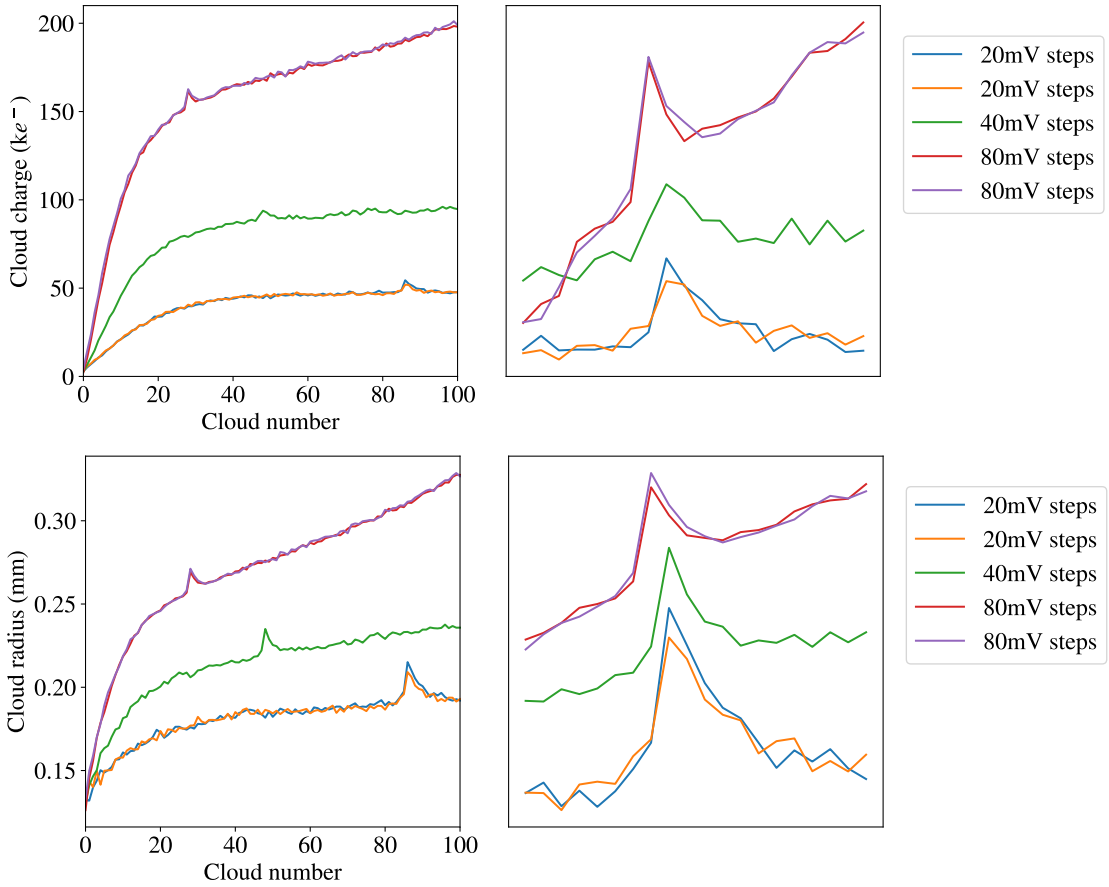

Figure 9.6: The cloud charge and radius is plotted for clouds successively drawn from a reservoir. The charge is found using the calibrated brightness of the cloud in its MPC image. The radius is calibrated using the technique described in Sec. 3.5. On the right, I have zoomed in on the peaks using arbitrary horizontal and vertical offsets.

9.2 Cloud charge spike

When fairly large scoops are removed from the reservoir, we occasionally see "spikes" where 2–5 clouds will suddenly have greater charge and radius than the others. These spikes are visible in Fig. 9.6. When we vary the charge in each cloud by varying the scooping voltage step size, we find that this spike occurs later in the scooping process if the clouds are smaller. This suggests that the phenomenon occurs either when a fixed amount of total charge is removed from the reservoir or when the electrode voltages used to extract clouds from the reservoir have reached a certain value. Thus understanding the spike probably would require delving into the plasma physics of the reservoir. It certainly cannot be explained within the simple electrostatic model of the reservoir described in Sec. 2.2.

Of course, I cannot be completely sure that this is "real physics," and not some quirk of the electronics controlling the experiment. One piece of evidence that it is a real phenomenon is that when I slightly reduced the cloud charge by roughly doubling the extraction frequency, the spike occurred slightly later. This phenomenon may depend on any number

of parameters, for example the exact potentials used to extract clouds from the reservoir; I have not performed any dedicated experiments to study it.

This spike may be an issue for EMPI measurements at high precision, or at least it should be avoided. The changing cloud properties affect the cloud's magnetron frequency, possibly leading to an erroneous measurement showing that the magnetic field has "spiked."

10 Conclusions

In this thesis, I have introduced a collection of measurement techniques using electron clouds. The techniques fall into two categories: precision magnetic field measurements and measurements of experimental issues that plague all Penning-Malmberg traps. With each measurement technique, systematic errors are investigated, revealing subtleties in the motion of electron clouds or the behavior of the trapping apparatus. The end result is a comprehensive description of electron cloud dynamics in a Penning-Malmberg trap. Electron clouds can be used as versatile measurement tools—they can be used to directly measure sources of error in precision measurements, and they can be used to deduce the underlying causes of unexpected experimental phenomena.

I hope that future researchers implement plasma reservoirs and find new applications for the clouds extracted from those reservoirs. To that end, in Sec. 2, I have written a complete guide on how to implement a reservoir and I have pointed out issues with reservoirs observed at ALPHA. In Sec. 5, I have described how to measure the properties of the electron clouds extracted from a reservoir.

The first two things I measured with electron clouds were patch potentials and misalignment. These two construction errors have long been blamed for plasma expansion and heating in Penning-Malmberg traps. With electron clouds, we now have a way of measuring patch potentials and misalignment independent of plasma expansion. Perhaps future authors will use these techniques to study the relationship between asymmetry and plasma heating. In Sec. 4, I provide a number of hypotheses about what effects limit our ability to cool positrons, and I give tentative evidence to support those hypotheses. If this work continues, it may lead to concrete suggestions for how the ALPHA experiment can achieve lower positron temperatures and increase antihydrogen trapping rates.

Electron clouds have been used for two kinds of magnetometry: ECR and EMPI. Sec. 7 described a novel extension of ECR where the clouds are moved off-axis. This thesis also provides a complete explanation of EMPI and the sources of error present in EMPI measurements. Although EMPI is much more complicated then ECR in implementation and analysis, it complements ECR by performing measurements more quickly and with less day to day tuning. EMPI can ultimately achieve a sufficient measurement precision for informing measurements of gravity on antihydrogen—1 part in 10^4 for dynamic measurements and 1 part in 10^5 for measurements of unchanging magnetic fields.

These new measurement techniques have revealed several observations that affect the way ALPHA is operated today.

1. We know from the misalignment measurements that there is a $\sim 70\,\mu$m offset between two electrodes in the ALPHA-g Penning-Malmberg trap, so now electron clouds are moved more slowly through that region to prevent this misalignment from exciting a magnetron orbit. We have also learned that the external magnet may not be perfectly straight, so further attempts to align may result in a trade-off involving plasma behavior improving in some trap locations and worsening in others.

2. Using the patch potential measurements, we were able to understand why the 1S–2S laser degrades antihydrogen trapping, and we were able to understand why warming the

trap restores nominal behavior. We also were able to identify the issue that prevented antihydrogen trapping entirely in the 2021 ALPHA-g experimental run.

3. Off-axis ECR revealed a misalignment of about 100 μm between one of the ALPHA-g magnets and the trap electrodes. This kind of misalignment produces a systematic error on the measurement of the effect of gravity on antihydrogen. The systematic error was not significant enough to be listed in the sources of error for the first ALPHA-g measurement, but the ALPHA collaboration hopes to improve their measurement in the future. They should keep in mind that this kind of magnetic error is possible, and these misalignments should be measured carefully.

4. EMPI revealed several qualitative features of persistent currents that were not seen in ECR measurements. EMPI was used to measure how persistent currents increase with time when we change the magnetic flux through superconducting wires, and it was used to map the effect of persistent currents versus axial position in the trap. The magnitude of these persistent currents is well above the required magnetometry precision needed for ALPHA-g measurements. Thus it should not be assumed that the magnetic field changes linearly with magnet current in ALPHA-g.

Throughout this thesis I have identified many sources of error that, to varying extents, apply to all cloud-based measurements. Below I list some systematic effects that one should be aware of if they intend to use electron clouds for precision measurements:

1. A critical conclusion of Sec. 5.4 is that a cloud's length and its image charge affect its magnetron frequency and how far it is moved off axis by patch potentials.

2. In Sec. 5.4.3, I show an unexpected linear variation in the magnetron frequency versus distance from the trap axis. I proposed that this is due to the clouds being significantly heated by the process used to move them off-axis.

3. Using an "artificial patch potential," I showed that there can be nonlinear corrections in the method used to move clouds off-axis (see Sec. 3.13).

4. In order to investigate systematic errors for EMPI, I derived higher order corrections to the magnetron frequency of electron clouds, and I derived how the magnetron frequency varies with radial displacement in the presence of imperfect trapping potentials and a non-constant magnetic field (Sec. 8.2). I later verified those equations with simulations and experimental data.

5. In Sec. 6.4, I showed that a cloud's position on the MCP can be significantly affected by the rate at which electrode voltages change.

6. In Sec. 9.1, I explained our observations of as-of-yet unexplained secondary spots in MCP images, which pose challenges for our analysis of cloud positions on the MCP.

There is the potential for radical improvement in every measurement technique described in this thesis. If the variability of the initial positions of clouds is reduced, all of the cloud based measurements will become more precise or they could be performed more quickly.

Two sources of cloud position variability—cloud movement speed and reservoir diocotron—are essentially well understood and can be avoided. However, the intrinsic magnetron is still only explained by a tentative hypothesis. This hypothesis suggests that if patch potentials or misalignment near the reservoir are reduced, the intrinsic magnetron will probably be reduced. Alternatively, if intrinsic magnetron cannot be fixed, the clouds could be forced back to the center of the trap. Other members of the ALPHA collaboration have considered using a segmented electrode to move clouds on-axis. They have proposed using a backwards autoresonant drive [141] or simply implementing a reversed version of the technique used to move clouds off-axis.

EMPI was implemented under significant time pressure, and as such many mistakes are visible in the final data. Just by fixing the following four mistakes the measurements will be much more precise and thorough:

1. There was an issue with the "sequence bridging" which ruined EMPI measurements in many axial trap locations. Alternatively, one could remove the need for sequence bridging by improving the hardware controlling the electrode voltages.

2. Trapping potentials with zero spiraling should be used. This was implemented in one axial trap location, and as a result the EMPI measurements from that location are vastly improved.

3. One badly behaving electrode amplifier was fixed, but another was not identified early enough, so EMPI measurements near that electrode failed.

4. The reservoirs were not given sufficient time to settle to stable behavior before performing EMPI measurements.

Moreover, there is a lingering disagreement between ECR measurements and EMPI measurements at the 10^{-4} level, as described in Sec. 8.4. This disagreement is only about a factor of 2–3 bigger than known errors, so perhaps general improvements to the measurement procedure will resolve the issue. Alternatively, in Sec. 8.3.5, I suggested that that this discrepancy could be due to variability in cloud temperatures, but this hypothesis is yet to be tested in any way. The EMPI/ECR disagreement may or may not be related to the mystery presented in Sec. 5.4.3—the observation of a magnetron frequency shift which was linear with magnetron radius, which was also explained with cloud temperatures. This linear frequency shift was ignored in the EMPI analysis because it wasn't visible in the EMPI calibration data. In general we can say that more research will be needed to understand how cloud temperatures are affected by different measurement procedures (and how the measurements are affected by cloud temperatures).

I did not have enough time to sufficiently explore the parameter space for off-axis ECR. It is likely that significant improvements in the precision of off-axis ECR could be achieved by tuning the microwave pulses and varying the magnetron frequency of the clouds. Similarly, the data from the misalignment measurements revealed a discrepancy that I hadn't anticipated. I provided a well-justified hypothesis that might explain the issue. If someone were to validate this hypothesis, they may be able to confidently claim $\sim 10\,\mu$m precision in their misalignment measurements.

I will not personally be implementing these improvements; I will start a postdoc doing precision measurements of the fine structure constant with atom interferometry [142]. However, I will happily support anyone else who wants to develop properly optimized versions of these cloud-based measurements.

Bibliography

[1] E. K. Anderson, C. J. Baker, W. Bertsche, N. M. Bhatt, G. Bonomi, A. Capra, I. Carli, C. L. Cesar, M. Charlton, A. Christensen, R. Collister, A. Cridland Mathad, D. Duque Quiceno, S. Eriksson, A. Evans, N. Evetts, S. Fabbri, J. Fajans, A. Ferwerda, T. Friesen, M. C. Fujiwara, D. R. Gill, L. M. Golino, M. B. Gomes Gonçalves, P. Grandemange, P. Granum, J. S. Hangst, M. E. Hayden, D. Hodgkinson, E. D. Hunter, C. A. Isaac, A. J. U. Jimenez, M. A. Johnson, J. M. Jones, S. A. Jones, S. Jonsell, A. Khramov, N. Madsen, L. Martin, N. Massacret, D. Maxwell, J. T. K. McKenna, S. Menary, T. Momose, M. Mostamand, P. S. Mullan, J. Nauta, K. Olchanski, A. N. Oliveira, J. Peszka, A. Powell, C. Ø Rasmussen, F. Robicheaux, R. L. Sacramento, M. Sameed, E. Sarid, J. Schoonwater, D. M. Silveira, J. Singh, G. Smith, C. So, S. Stracka, G. Stutter, T. D. Tharp, K. A. Thompson, R. I. Thompson, E. Thorpe-Woods, C. Torkzaban, M. Urioni, P. Woosaree, and J. S. Wurtele. Observation of the effect of gravity on the motion of antimatter. *Nature*, 621(7980): 716–722, Sep 2023. ISSN 1476-4687. doi: 10.1038/s41586-023-06527-1. URL `https://doi.org/10.1038/s41586-023-06527-1`.

[2] Celeste Carruth. *Methods for plasma stabilization and control to improve antihydrogen production*. PhD thesis, University of California: Berkeley, 2018.

[3] M. Ahmadi, B. X. R. Alves, C. J. Baker, W. Bertsche, A. Capra, C. Carruth, C. L. Cesar, M. Charlton, S. Cohen, R. Collister, S. Eriksson, A. Evans, N. Evetts, J. Fajans, T. Friesen, M. C. Fujiwara, D. R. Gill, J. S. Hangst, W. N. Hardy, M. E. Hayden, C. A. Isaac, M. A. Johnson, S. A. Jones, S. Jonsell, L. Kurchaninov, N. Madsen, M. Mathers, D. Maxwell, J. T. K. McKenna, S. Menary, T. Momose, J. J. Munich, K. Olchanski, A. Olin, P. Pusa, C. Ø. Rasmussen, F. Robicheaux, R. L. Sacramento, M. Sameed, E. Sarid, D. M. Silveira, C. So, G. Stutter, T. D. Tharp, J. E. Thompson, R. I. Thompson, D. P. van der Werf, and J. S. Wurtele. Enhanced control and reproducibility of non-neutral plasmas. *Phys. Rev. Lett.*, 120:025001, Jan 2018. doi: 10.1103/PhysRevLett.120.025001. URL `https://link.aps.org/doi/10.1103/PhysRevLett.120.025001`.

[4] Eric Hunter. *Cavity and Microwave Experiments on Electron Plasma*. PhD thesis, University of California: Berkeley, 2019.

[5] E. D. Hunter, A. Christensen, J. Fajans, T. Friesen, E. Kur, and J. S. Wurtele. Electron cyclotron resonance (ECR) magnetometry with a plasma reservoir. *Physics of Plasmas*, 27(3):032106, 03 2020. ISSN 1070-664X. doi: 10.1063/1.5141999. URL `https://doi.org/10.1063/1.5141999`.

[6] D. B. Newell and E. Tiesinga. The international system of units (si). *NIST Special Publication*, 330:1–138, 2019. URL `https://doi.org/10.6028/NIST.SP.330-2019`.

[7] M. Knoop, N. Madsen, and R. C. Thompson. *Trapped Charged Particles*. WORLD SCIENTIFIC (EUROPE), 2016. doi: 10.1142/q0004. URL `https://www.worldscientific.com/doi/abs/10.1142/q0004`.

[8] T. M. O'Neil. A confinement theorem for nonneutral plasmas. *The Physics of Fluids*, 23(11):2216–2218, 11 1980. ISSN 0031-9171. doi: 10.1063/1.862904. URL https://doi.org/10.1063/1.862904.

[9] G. B. Andresen, M. D. Ashkezari, M. Baquero-Ruiz, W. Bertsche, P. D. Bowe, E. Butler, C. L. Cesar, S. Chapman, M. Charlton, A. Deller, S. Eriksson, J. Fajans, T. Friesen, M. C. Fujiwara, D. R. Gill, A. Gutierrez, J. S. Hangst, W. N. Hardy, M. E. Hayden, A. J. Humphries, R. Hydomako, M. J. Jenkins, S. Jonsell, L. V. Jørgensen, L. Kurchaninov, N. Madsen, S. Menary, P. Nolan, K. Olchanski, A. Olin, A. Povilus, P. Pusa, F. Robicheaux, E. Sarid, S. Seif el Nasr, D. M. Silveira, C. So, J. W. Storey, R. I. Thompson, D. P. van der Werf, J. S. Wurtele, and Y. Yamazaki. Trapped antihydrogen. *Nature*, 468(7324):673–676, Dec 2010. ISSN 1476-4687. doi: 10.1038/nature09610. URL https://doi.org/10.1038/nature09610.

[10] M. Ahmadi, B. X. R. Alves, C. J. Baker, W. Bertsche, E. Butler, A. Capra, C. Carruth, C. L. Cesar, M. Charlton, S. Cohen, R. Collister, S. Eriksson, A. Evans, N. Evetts, J. Fajans, T. Friesen, M. C. Fujiwara, D. R. Gill, A. Gutierrez, J. S. Hangst, W. N. Hardy, M. E. Hayden, C. A. Isaac, A. Ishida, M. A. Johnson, S. A. Jones, S. Jonsell, L. Kurchaninov, N. Madsen, M. Mathers, D. Maxwell, J. T. K. McKenna, S. Menary, J. M. Michan, T. Momose, J. J. Munich, P. Nolan, K. Olchanski, A. Olin, P. Pusa, C. Ø Rasmussen, F. Robicheaux, R. L. Sacramento, M. Sameed, E. Sarid, D. M. Silveira, S. Stracka, G. Stutter, C. So, T. D. Tharp, J. E. Thompson, R. I. Thompson, D. P. van der Werf, and J. S. Wurtele. Observation of the 1s–2s transition in trapped antihydrogen. *Nature*, 541(7638):506–510, Jan 2017. ISSN 1476-4687. doi: 10.1038/nature21040. URL https://doi.org/10.1038/nature21040.

[11] M. Ahmadi, B. X. R. Alves, C. J. Baker, W. Bertsche, A. Capra, C. Carruth, C. L. Cesar, M. Charlton, S. Cohen, R. Collister, S. Eriksson, A. Evans, N. Evetts, J. Fajans, T. Friesen, M. C. Fujiwara, D. R. Gill, J. S. Hangst, W. N. Hardy, M. E. Hayden, C. A. Isaac, M. A. Johnson, J. M. Jones, S. A. Jones, S. Jonsell, A. Khramov, P. Knapp, L. Kurchaninov, N. Madsen, D. Maxwell, J. T. K. McKenna, S. Menary, T. Momose, J. J. Munich, K. Olchanski, A. Olin, P. Pusa, C. Ø Rasmussen, F. Robicheaux, R. L. Sacramento, M. Sameed, E. Sarid, D. M. Silveira, G. Stutter, C. So, T. D. Tharp, R. I. Thompson, D. P. van der Werf, and J. S. Wurtele. Characterization of the 1s–2s transition in antihydrogen. *Nature*, 557(7703):71–75, May 2018. ISSN 1476-4687. doi: 10.1038/s41586-018-0017-2. URL https://doi.org/10.1038/s41586-018-0017-2.

[12] C Ø Rasmussen, N Madsen, and F Robicheaux. Aspects of 1s-2s spectroscopy of trapped antihydrogen atoms. *Journal of Physics B: Atomic, Molecular and Optical Physics*, 50(18):184002, sep 2017. doi: 10.1088/1361-6455/aa854c. URL https://dx.doi.org/10.1088/1361-6455/aa854c.

[13] M. Ahmadi, B. X. R. Alves, C. J. Baker, W. Bertsche, E. Butler, A. Capra, C. Carruth, C. L. Cesar, M. Charlton, S. Cohen, R. Collister, S. Eriksson, A. Evans, N. Evetts, J. Fajans, T. Friesen, M. C. Fujiwara, D. R. Gill, A. Gutierrez, J. S. Hangst, W. N. Hardy, M. E. Hayden, C. A. Isaac, A. Ishida, M. A. Johnson, S. A. Jones, S. Jonsell,

L. Kurchaninov, N. Madsen, M. Mathers, D. Maxwell, J. T. K. McKenna, S. Menary, J. M. Michan, T. Momose, J. J. Munich, P. Nolan, K. Olchanski, A. Olin, P. Pusa, C. Ø Rasmussen, F. Robicheaux, R. L. Sacramento, M. Sameed, E. Sarid, D. M. Silveira, S. Stracka, G. Stutter, C. So, T. D. Tharp, J. E. Thompson, R. I. Thompson, D. P. van der Werf, and J. S. Wurtele. Observation of the hyperfine spectrum of antihydrogen. *Nature*, 548(7665):66–69, Aug 2017. ISSN 1476-4687. doi: 10.1038/nature23446. URL https://doi.org/10.1038/nature23446.

[14] M. Ahmadi, B. X. R. Alves, C. J. Baker, W. Bertsche, A. Capra, C. Carruth, C. L. Cesar, M. Charlton, S. Cohen, R. Collister, S. Eriksson, A. Evans, N. Evetts, J. Fajans, T. Friesen, M. C. Fujiwara, D. R. Gill, J. S. Hangst, W. N. Hardy, M. E. Hayden, E. D. Hunter, C. A. Isaac, M. A. Johnson, J. M. Jones, S. A. Jones, S. Jonsell, A. Khramov, P. Knapp, L. Kurchaninov, N. Madsen, D. Maxwell, J. T. K. McKenna, S. Menary, J. M. Michan, T. Momose, J. J. Munich, K. Olchanski, A. Olin, P. Pusa, C. Ø Rasmussen, F. Robicheaux, R. L. Sacramento, M. Sameed, E. Sarid, D. M. Silveira, D. M. Starko, G. Stutter, C. So, T. D. Tharp, R. I. Thompson, D. P. van der Werf, and J. S. Wurtele. Observation of the 1s–2p lyman-α transition in antihydrogen. *Nature*, 561 (7722):211–215, Sep 2018. ISSN 1476-4687. doi: 10.1038/s41586-018-0435-1. URL https://doi.org/10.1038/s41586-018-0435-1.

[15] M. Ahmadi, B. X. R. Alves, C. J. Baker, W. Bertsche, A. Capra, C. Carruth, C. L. Cesar, M. Charlton, S. Cohen, R. Collister, S. Eriksson, A. Evans, N. Evetts, J. Fajans, T. Friesen, M. C. Fujiwara, D. R. Gill, P. Granum, J. S. Hangst, W. N. Hardy, M. E. Hayden, E. D. Hunter, C. A. Isaac, M. A. Johnson, J. M. Jones, S. A. Jones, S. Jonsell, A. Khramov, P. Knapp, L. Kurchaninov, N. Madsen, D. Maxwell, J. T. K. McKenna, S. Menary, J. M. Michan, T. Momose, J. J. Munich, K. Olchanski, A. Olin, P. Pusa, C. Ø Rasmussen, F. Robicheaux, R. L. Sacramento, M. Sameed, E. Sarid, D. M. Silveira, C. So, D. M. Starko, G. Stutter, T. D. Tharp, R. I. Thompson, D. P. van der Werf, J. S. Wurtele, and The ALPHA Collaboration. Investigation of the fine structure of antihydrogen. *Nature*, 578(7795):375–380, Feb 2020. ISSN 1476-4687. doi: 10.1038/s41586-020-2006-5. URL https://doi.org/10.1038/s41586-020-2006-5.

[16] C. J. Baker, W. Bertsche, A. Capra, C. Carruth, C. L. Cesar, M. Charlton, A. Christensen, R. Collister, A. Cridland Mathad, S. Eriksson, A. Evans, N. Evetts, J. Fajans, T. Friesen, M. C. Fujiwara, D. R. Gill, P. Grandemange, P. Granum, J. S. Hangst, W. N. Hardy, M. E. Hayden, D. Hodgkinson, E. Hunter, C. A. Isaac, M. A. Johnson, J. M. Jones, S. A. Jones, S. Jonsell, A. Khramov, P. Knapp, L. Kurchaninov, N. Madsen, D. Maxwell, J. T. K. McKenna, S. Menary, J. M. Michan, T. Momose, P. S. Mullan, J. J. Munich, K. Olchanski, A. Olin, J. Peszka, A. Powell, P. Pusa, C. Ø Rasmussen, F. Robicheaux, R. L. Sacramento, M. Sameed, E. Sarid, D. M. Silveira, D. M. Starko, C. So, G. Stutter, T. D. Tharp, A. Thibeault, R. I. Thompson, D. P. van der Werf, and J. S. Wurtele. Laser cooling of antihydrogen atoms. *Nature*, 592 (7852):35–42, Apr 2021. ISSN 1476-4687. doi: 10.1038/s41586-021-03289-6. URL https://doi.org/10.1038/s41586-021-03289-6.

[17] C. Amole, M. D. Ashkezari, M. Baquero-Ruiz, W. Bertsche, E. Butler, A. Capra,

C. L. Cesar, M. Charlton, S. Eriksson, J. Fajans, T. Friesen, M. C. Fujiwara, D. R. Gill, A. Gutierrez, J. S. Hangst, W. N. Hardy, M. E. Hayden, C. A. Isaac, S. Jonsell, L. Kurchaninov, A. Little, N. Madsen, J. T. K. McKenna, S. Menary, S. C. Napoli, P. Nolan, K. Olchanski, A. Olin, A. Povilus, P. Pusa, C. Ø Rasmussen, F. Robicheaux, E. Sarid, D. M. Silveira, C. So, T. D. Tharp, R. I. Thompson, D. P. van der Werf, Z. Vendeiro, J. S. Wurtele, A. I. Zhmoginov, and A. E. Charman. An experimental limit on the charge of antihydrogen. *Nature Communications*, 5(1):3955, Jun 2014. ISSN 2041-1723. doi: 10.1038/ncomms4955. URL https://doi.org/10.1038/ncomms4955.

[18] S. Maury. The antiproton decelerator: Ad. *Hyperfine Interactions*, 109(1):43–52, Aug 1997. ISSN 1572-9540. doi: 10.1023/A:1012632812327. URL https://doi.org/10.1023/A:1012632812327.

[19] S. Maury, W. Oelert, W. Bartmann, P. Belochitskii, H. Breuker, F. Butin, C. Carli, T. Eriksson, S. Pasinelli, and G. Tranquille. Elena: the extra low energy anti-proton facility at cern. *Hyperfine Interactions*, 229(1):105–115, Oct 2014. ISSN 1572-9540. doi: 10.1007/s10751-014-1067-y. URL https://doi.org/10.1007/s10751-014-1067-y.

[20] C. M. Surko, R. G. Greaves, and M. Charlton. Stored positrons for antihydrogen production. *Hyperfine Interactions*, 109(1):181–188, Aug 1997. ISSN 1572-9540. doi: 10.1023/A:1012657517779. URL https://doi.org/10.1023/A:1012657517779.

[21] M. J. T. Collier, L. V. Jørgensen, O. I. Meshkov, D. P. van der Werf, and M. Charlton. Development and testing of a positron accumulator for antihydrogen production. *AIP Conference Proceedings*, 498(1):13–18, 12 1999. ISSN 0094-243X. doi: 10.1063/1.1302096. URL https://doi.org/10.1063/1.1302096.

[22] C. J. Baker, W. Bertsche, A. Capra, C. L. Cesar, M. Charlton, A. J. Christensen, R. Collister, A. Cridland Mathad, S. Eriksson, A. Evans, N. Evetts, S. Fabbri, J. Fajans, T. Friesen, M. C. Fujiwara, D. R. Gill, P. Grandemange, P. Granum, J. S. Hangst, M. E. Hayden, D. Hodgkinson, C. A. Isaac, M. A. Johnson, J. M. Jones, S. A. Jones, A. Khramov, L. Kurchaninov, N. Madsen, D. Maxwell, J. T. K. McKenna, S. Menary, T. Momose, P. S. Mullan, J. J. Munich, K. Olchanski, J. Peszka, A. Powell, C. Ø. Rasmussen, R. L. Sacramento, M. Sameed, E. Sarid, D. M. Silveira, C. So, D. M. Starko, G. Stutter, T. D. Tharp, R. I. Thompson, C. Torkzaban, D. P. van der Werf, and J. S. Wurtele. Design and performance of a novel low energy multispecies beamline for an antihydrogen experiment. *Phys. Rev. Accel. Beams*, 26:040101, Apr 2023. doi: 10.1103/PhysRevAccelBeams.26.040101. URL https://link.aps.org/doi/10.1103/PhysRevAccelBeams.26.040101.

[23] J. Fajans and A. Schmidt. Malmberg–penning and minimum-b trap compatibility: the advantages of higher-order multipole traps. *Nuclear Instruments and Methods in Physics Research Section A: Accelerators, Spectrometers, Detectors and Associated Equipment*, 521(2):318–325, 2004. ISSN 0168-9002. doi: https://doi.org/10.1016/j.nima.2003.11.194. URL https://www.sciencedirect.com/science/article/pii/S0168900203031127.

[24] David E. Pritchard. Cooling neutral atoms in a magnetic trap for precision spectroscopy. *Phys. Rev. Lett.*, 51:1336–1339, Oct 1983. doi: 10.1103/PhysRevLett.51.1336. URL https://link.aps.org/doi/10.1103/PhysRevLett.51.1336.

[25] G.B. Andresen, W. Bertsche, P.D. Bowe, C. Bray, E. Butler, C.L. Cesar, S. Chapman, M. Charlton, J. Fajans, M.C. Fujiwara, D.R. Gill, J.S. Hangst, W.N. Hardy, R.S. Hayano, M.E. Hayden, A.J. Humphries, R. Hydomako, L.V. Jørgensen, S.J. Kerrigan, L. Kurchaninov, R. Lambo, N. Madsen, P. Nolan, K. Olchanski, A. Olin, A. Povilus, P. Pusa, F. Robicheaux, E. Sarid, S. Seif El Nasr, D.M. Silveira, J.W. Storey, R.I. Thompson, D.P. van der Werf, J.S. Wurtele, and Y. Yamazaki. Antihydrogen formation dynamics in a multipolar neutral anti-atom trap. *Physics Letters B*, 685(2):141–145, 2010. ISSN 0370-2693. doi: https://doi.org/10.1016/j.physletb.2010.01.066. URL https://www.sciencedirect.com/science/article/pii/S0370269310001371.

[26] M. Zhong, J. Fajans, and A. F. Zukor. Axial to transverse energy mixing dynamics in octupole-based magnetostatic antihydrogen traps. *New Journal of Physics*, 20(5): 053003, may 2018. doi: 10.1088/1367-2630/aabb84. URL https://dx.doi.org/10.1088/1367-2630/aabb84.

[27] D. L. Eggleston. Electron vortex dynamics in an applied shear flow. *AIP Conference Proceedings*, 331(1):54–63, 1995. doi: 10.1063/1.47904. URL https://aip.scitation.org/doi/abs/10.1063/1.47904.

[28] C. Smorra, A. Mooser, K. Franke, H. Nagahama, G. Schneider, T. Higuchi, S.V. Gorp, K. Blaum, Y. Matsuda, W. Quint, J. Walz, Y. Yamazaki, and S. Ulmer. A reservoir trap for antiprotons. *International Journal of Mass Spectrometry*, 389:10–13, 2015. ISSN 1387-3806. doi: https://doi.org/10.1016/j.ijms.2015.08.007. URL https://www.sciencedirect.com/science/article/pii/S1387380615002560.

[29] J. R. Danielson, T. R. Weber, and C. M. Surko. Extraction of small-diameter beams from single-component plasmas. *Applied Physics Letters*, 90(8):081503, 02 2007. ISSN 0003-6951. doi: 10.1063/1.2709522. URL https://doi.org/10.1063/1.2709522.

[30] C. Amole, M. D. Ashkezari, M. Baquero-Ruiz, W. Bertsche, E. Butler, A. Capra, C. L. Cesar, M. Charlton, A. Deller, N. Evetts, S. Eriksson, J. Fajans, T. Friesen, M. C. Fujiwara, D. R. Gill, A. Gutierrez, J. S. Hangst, W. N. Hardy, M. E. Hayden, C. A. Isaac, S. Jonsell, L. Kurchaninov, A. Little, N. Madsen, J. T. K. McKenna, S. Menary, S. C. Napoli, K. Olchanski, A. Olin, P. Pusa, C. Ø. Rasmussen, F. Robicheaux, E. Sarid, D. M. Silveira, C. So, S. Stracka, T. Tharp, R. I. Thompson, D. P. van der Werf, and J. S. Wurtele. In situ electromagnetic field diagnostics with an electron plasma in a penning–malmberg trap. *New Journal of Physics*, 16(1):013037, jan 2014. doi: 10.1088/1367-2630/16/1/013037. URL https://dx.doi.org/10.1088/1367-2630/16/1/013037.

[31] M. D. Tinkle, R. G. Greaves, C. M. Surko, R. L. Spencer, and G. W. Mason. Low-order modes as diagnostics of spheroidal non-neutral plasmas. *Phys. Rev. Lett.*, 72:352–355, Jan 1994. doi: 10.1103/PhysRevLett.72.352. URL https://link.aps.org/doi/10.1103/PhysRevLett.72.352.

[32] R. W. Gould and M. A. LaPointe. Cyclotron resonance in a pure electron plasma column. *Phys. Rev. Lett.*, 67:3685–3688, Dec 1991. doi: 10.1103/PhysRevLett.67.3685. URL https://link.aps.org/doi/10.1103/PhysRevLett.67.3685.

[33] E. Sarid, F. Anderegg, and C. F. Driscoll. Cyclotron resonance phenomena in a non-neutral multispecies ion plasma. *Physics of Plasmas*, 2(8):2895–2907, 08 1995. ISSN 1070-664X. doi: 10.1063/1.871189. URL https://doi.org/10.1063/1.871189.

[34] R. G. Greaves and C. M. Surko. Inward transport and compression of a positron plasma by a rotating electric field. *Phys. Rev. Lett.*, 85:1883–1886, Aug 2000. doi: 10.1103/PhysRevLett.85.1883. URL https://link.aps.org/doi/10.1103/PhysRevLett.85.1883.

[35] J. R. Danielson and C. M. Surko. Torque-balanced high-density steady states of single-component plasmas. *Phys. Rev. Lett.*, 94:035001, Jan 2005. doi: 10.1103/PhysRevLett.94.035001. URL https://link.aps.org/doi/10.1103/PhysRevLett.94.035001.

[36] G. B. Andresen, M. D. Ashkezari, M. Baquero-Ruiz, W. Bertsche, P. D. Bowe, E. Butler, C. L. Cesar, S. Chapman, M. Charlton, J. Fajans, T. Friesen, M. C. Fujiwara, D. R. Gill, J. S. Hangst, W. N. Hardy, R. S. Hayano, M. E. Hayden, A. Humphries, R. Hydomako, S. Jonsell, L. Kurchaninov, R. Lambo, N. Madsen, S. Menary, P. Nolan, K. Olchanski, A. Olin, A. Povilus, P. Pusa, F. Robicheaux, E. Sarid, D. M. Silveira, C. So, J. W. Storey, R. I. Thompson, D. P. van der Werf, D. Wilding, J. S. Wurtele, and Y. Yamazaki. Evaporative cooling of antiprotons to cryogenic temperatures. *Phys. Rev. Lett.*, 105:013003, Jul 2010. doi: 10.1103/PhysRevLett.105.013003. URL https://link.aps.org/doi/10.1103/PhysRevLett.105.013003.

[37] D. L. Eggleston and T. M. O'Neil. Theory of asymmetry-induced transport in a non-neutral plasma. *Physics of Plasmas*, 6(7):2699–2704, 07 1999. ISSN 1070-664X. doi: 10.1063/1.873225. URL https://doi.org/10.1063/1.873225.

[38] A. A. Kabantsev, J. H. Yu, R. B. Lynch, and C. F. Driscoll. Trapped particles and asymmetry-induced transport. *Physics of Plasmas*, 10(5):1628–1635, 05 2003. ISSN 1070-664X. doi: 10.1063/1.1564089. URL https://doi.org/10.1063/1.1564089.

[39] T. Mohamed, A. Mohri, and Y. Yamazaki. Comparison of non-neutral electron plasma confinement in harmonic and rectangular potentials in a very dense regime. *Physics of Plasmas*, 20(1):012502, 01 2013. ISSN 1070-664X. doi: 10.1063/1.4773900. URL https://doi.org/10.1063/1.4773900.

[40] C. F. Driscoll and J. H. Malmberg. Length-dependent containment of a pure electron-plasma column. *Phys. Rev. Lett.*, 50:167–170, Jan 1983. doi: 10.1103/PhysRevLett.50.167. URL https://link.aps.org/doi/10.1103/PhysRevLett.50.167.

[41] R. Keinigs. Field-error induced transport in a pure electron plasma column. *The Physics of Fluids*, 27(6):1427–1433, 1984. doi: 10.1063/1.864763. URL https://aip.scitation.org/doi/abs/10.1063/1.864763.

[42] C. F. Driscoll, K. S. Fine, and J. H. Malmberg. Reduction of radial losses in a pure electron plasma. *The Physics of Fluids*, 29(6):2015–2017, 1986. doi: 10.1063/1.865580. URL https://aip.scitation.org/doi/abs/10.1063/1.865580.

[43] J. Notte and J. Fajans. The effect of asymmetries on non-neutral plasma confinement time. *Physics of Plasmas*, 1(5):1123–1127, 1994. doi: 10.1063/1.870762. URL https://doi.org/10.1063/1.870762.

[44] D. L. Eggleston. Confinement of test particles in a malmberg–penning trap with a biased axial wire. *Physics of Plasmas*, 4(5):1196–1200, 1997. doi: 10.1063/1.872299. URL https://doi.org/10.1063/1.872299.

[45] J. M. Kriesel and C. F. Driscoll. Two regimes of asymmetry-induced transport in non-neutral plasmas. *Phys. Rev. Lett.*, 85:2510–2513, Sep 2000. doi: 10.1103/PhysRevLett.85.2510. URL https://link.aps.org/doi/10.1103/PhysRevLett.85.2510.

[46] R.C. Davidson. *Theory of Nonneutral Plasmas*. Frontiers in physics. W. A. Benjamin, 1974. ISBN 9780805323467. URL https://books.google.com/books?id=lWosAAAAYAAJ.

[47] R. H. Levy. Two New Results in Cylindrical Diocotron Theory. *The Physics of Fluids*, 11(4):920–921, 04 1968. ISSN 0031-9171. doi: 10.1063/1.1692026. URL https://doi.org/10.1063/1.1692026.

[48] W. D. White, J. H. Malmberg, and C. F. Driscoll. Resistive-wall destabilization of diocotron waves. *Phys. Rev. Lett.*, 49:1822–1826, Dec 1982. doi: 10.1103/PhysRevLett.49.1822. URL https://link.aps.org/doi/10.1103/PhysRevLett.49.1822.

[49] G. Bettega, F. Cavaliere, B. Paroli, R. Pozzoli, M. Romé, and M. Cavenago. Excitation of the l=2 diocotron mode with a resistive load. *Physics of Plasmas*, 15(3):032102, 03 2008. ISSN 1070-664X. doi: 10.1063/1.2890773. URL https://doi.org/10.1063/1.2890773.

[50] K. S. Fine, C. F. Driscoll, and J. H. Malmberg. Measurements of a nonlinear diocotron mode in pure electron plasmas. *Phys. Rev. Lett.*, 63:2232–2235, Nov 1989. doi: 10.1103/PhysRevLett.63.2232. URL https://link.aps.org/doi/10.1103/PhysRevLett.63.2232.

[51] K. S. Fine and C. F. Driscoll. The finite length diocotron mode. *Physics of Plasmas*, 5(3):601–607, 03 1998. ISSN 1070-664X. doi: 10.1063/1.872752. URL https://doi.org/10.1063/1.872752.

[52] J. Fajans, E. Gilson, and L. Friedland. Autoresonant (nonstationary) excitation of the diocotron mode in non-neutral plasmas. *Phys. Rev. Lett.*, 82:4444–4447, May 1999. doi: 10.1103/PhysRevLett.82.4444. URL https://link.aps.org/doi/10.1103/PhysRevLett.82.4444.

[53] W.J. Weber, L. Carbone, A. Cavalleri, R. Dolesi, C.D. Hoyle, M. Hueller, and S. Vitale. Possibilities for measurement and compensation of stray dc electric fields acting on drag-free test masses. *Advances in Space Research*, 39(2):213–218, 2007. ISSN 0273-1177. doi: https://doi.org/10.1016/j.asr.2006.03.045. URL https://www.sciencedirect.com/science/article/pii/S0273117706004972.

[54] M. Armano, H. Audley, G. Auger, J. T. Baird, P. Binetruy, M. Born, D. Bortoluzzi, N. Brandt, A. Bursi, M. Caleno, A. Cavalleri, A. Cesarini, M. Cruise, K. Danzmann, M. de Deus Silva, I. Diepholz, R. Dolesi, N. Dunbar, L. Ferraioli, V. Ferroni, E. D. Fitzsimons, R. Flatscher, M. Freschi, J. Gallegos, C. García Marirrodriga, R. Gerndt, L. Gesa, F. Gibert, D. Giardini, R. Giusteri, C. Grimani, J. Grzymisch, I. Harrison, G. Heinzel, M. Hewitson, D. Hollington, M. Hueller, J. Huesler, H. Inchauspé, O. Jennrich, P. Jetzer, B. Johlander, N. Karnesis, B. Kaune, C. J. Killow, N. Korsakova, I. Lloro, L. Liu, J. P. López-Zaragoza, R. Maarschalkerweerd, S. Madden, D. Mance, V. Martín, L. Martin-Polo, J. Martino, F. Martin-Porqueras, I. Mateos, P. W. McNamara, J. Mendes, L. Mendes, A. Moroni, M. Nofrarias, S. Paczkowski, M. Perreur-Lloyd, A. Petiteau, P. Pivato, E. Plagnol, P. Prat, U. Ragnit, J. Ramos-Castro, J. Reiche, J. A. Romera Perez, D. I. Robertson, H. Rozemeijer, F. Rivas, G. Russano, P. Sarra, A. Schleicher, J. Slutsky, C. Sopuerta, T. J. Sumner, D. Texier, J. I. Thorpe, C. Trenkel, D. Vetrugno, S. Vitale, G. Wanner, H. Ward, P. J. Wass, D. Wealthy, W. J. Weber, A. Wittchen, C. Zanoni, T. Ziegler, and P. Zweifel. Charge-induced force noise on free-falling test masses: Results from lisa pathfinder. *Phys. Rev. Lett.*, 118:171101, Apr 2017. doi: 10.1103/PhysRevLett.118.171101. URL https://link.aps.org/doi/10.1103/PhysRevLett.118.171101.

[55] S. Buchman and J. P. Turneaure. The effects of patch-potentials on the gravity probe b gyroscopes. *Review of Scientific Instruments*, 82(7):074502, 2011. doi: 10.1063/1.3608615. URL https://doi.org/10.1063/1.3608615.

[56] J. L. Garrett, J. Kim, and J. N. Munday. Measuring the effect of electrostatic patch potentials in casimir force experiments. *Phys. Rev. Res.*, 2:023355, Jun 2020. doi: 10.1103/PhysRevResearch.2.023355. URL https://link.aps.org/doi/10.1103/PhysRevResearch.2.023355.

[57] R.O. Behunin, D.A.R. Dalvit, R.S. Decca, and C.C. Speake. Limits on the accuracy of force sensing at short separations due to patch potentials. *Physical Review D*, 89(5), Mar 2014. ISSN 1550-2368. doi: 10.1103/physrevd.89.051301. URL http://dx.doi.org/10.1103/PhysRevD.89.051301.

[58] J. L. Garrett, D. Somers, and J. N. Munday. The effect of patch potentials in casimir force measurements determined by heterodyne kelvin probe force microscopy. 2014. doi: 10.1088/0953-8984/27/21/214012. URL https://arxiv.org/abs/1409.5012.

[59] J. Xu, G. L. Klimchitskaya, V. M. Mostepanenko, and U. Mohideen. Reducing detrimental electrostatic effects in casimir-force measurements and casimir-force-based microdevices. *Phys. Rev. A*, 97:032501, Mar 2018. doi: 10.1103/PhysRevA.97.032501. URL https://link.aps.org/doi/10.1103/PhysRevA.97.032501.

[60] T. W. Darling, F. Rossi, G. I. Opat, and G. F. Moorhead. The fall of charged particles under gravity: A study of experimental problems. *Rev. Mod. Phys.*, 64:237–257, Jan 1992. doi: 10.1103/RevModPhys.64.237. URL https://link.aps.org/doi/10.1103/RevModPhys.64.237.

[61] G. Testera. The role of the patch effect electric fields in the penning trap method of measuring the gravitational force on antiprotons. *Hyperfine Interactions*, 109(1): 333–343, Aug 1997. ISSN 1572-9540. doi: 10.1023/A:1012682123230. URL https://doi.org/10.1023/A:1012682123230.

[62] F. Rossi and G. I. Opat. Observations of the effects of adsorbates on patch potentials. *Journal of Physics D: Applied Physics*, 25(9):1349–1353, sep 1992. doi: 10.1088/0022-3727/25/9/012. URL https://doi.org/10.1088%2F0022-3727%2F25%2F9%2F012.

[63] D. J. Berkeland, J. D. Miller, J. C. Bergquist, W. M. Itano, and D. J. Wineland. Minimization of ion micromotion in a paul trap. *Journal of Applied Physics*, 83(10): 5025–5033, 1998. doi: 10.1063/1.367318. URL https://doi.org/10.1063/1.367318.

[64] M. Harlander, M. Brownnutt, W. Hänsel, and R. Blatt. Trapped-ion probing of light-induced charging effects on dielectrics. *New Journal of Physics*, 12(9):093035, sep 2010. doi: 10.1088/1367-2630/12/9/093035. URL https://doi.org/10.1088/1367-2630/12/9/093035.

[65] C. Noel, M. Berlin-Udi, C. Matthiesen, J. Yu, Y. Zhou, V. Lordi, and H. Häffner. Electric-field noise from thermally activated fluctuators in a surface ion trap. *Phys. Rev. A*, 99:063427, Jun 2019. doi: 10.1103/PhysRevA.99.063427. URL https://link.aps.org/doi/10.1103/PhysRevA.99.063427.

[66] Matthew Bohman. *Sympathetic Cooling of a Proton with Resonant Image Current Coupling*. PhD thesis, Heidelberg University, November 2020. URL https://archiv.ub.uni-heidelberg.de/volltextserver/29319/.

[67] F. Heiße, S. Rau, F. Köhler-Langes, W. Quint, G. Werth, S. Sturm, and K. Blaum. High-precision mass spectrometer for light ions. *Phys. Rev. A*, 100:022518, Aug 2019. doi: 10.1103/PhysRevA.100.022518. URL https://link.aps.org/doi/10.1103/PhysRevA.100.022518.

[68] C. J. Baker, W. Bertsche, A. Capra, C. L. Cesar, M. Charlton, A. Christensen, R. Collister, A. Cridland Mathad, S. Eriksson, A. Evans, N. Evetts, J. Fajans, T. Friesen, M. C. Fujiwara, D. R. Gill, P. Grandemange, P. Granum, J. S. Hangst, M. E. Hayden, D. Hodgkinson, E. D. Hunter, C. A. Isaac, M. A. Johnson, J. Jones, S. A. Jones, S. Jonsell, A. Khramov, L. Kurchaninov, H. Landsberger, N. Madsen, D. Maxwell, J. T. K. McKenna, S. Menary, T. Momose, P. S. Mullan, J. J. Munich, K. Olchanski, A. Olin, J. Peszka, A. Powell, P. Pusa, C.Ø. Rasmussen, F. Robicheaux, R. L. Sacramento, M. Sameed, E. Sarid, D. M. Silveira, C. So, G. Stutter, T. D. Tharp, R. I. Thompson, C. Torkzaban, D. P. van der Werf, E. Ward, and J. S. Wurtele. Measurements

of penning-malmberg trap patch potentials and associated performance degradation. *Phys. Rev. Res.*, 6:L012008, Jan 2024. doi: 10.1103/PhysRevResearch.6.L012008. URL https://link.aps.org/doi/10.1103/PhysRevResearch.6.L012008.

[69] J.P. Boris, R.A. Shanny, United States. Office of Naval Research, and Naval Research Laboratory. *Proceedings: Fourth Conference on Numerical Simulation of Plasmas, November 2, 3, 1970*. Naval Research Laboratory, 1972. URL https://books.google.com/books?id=zqxSAQAACAAJ.

[70] Hong Qin, Shuangxi Zhang, Jianyuan Xiao, Jian Liu, Yajuan Sun, and William M. Tang. Why is Boris algorithm so good? *Physics of Plasmas*, 20(8):084503, 08 2013. ISSN 1070-664X. doi: 10.1063/1.4818428. URL https://doi.org/10.1063/1.4818428.

[71] J. Notte, J. Fajans, R. Chu, and J. S. Wurtele. Experimental breaking of an adiabatic invariant. *Phys. Rev. Lett.*, 70:3900–3903, Jun 1993. doi: 10.1103/PhysRevLett.70.3900. URL https://link.aps.org/doi/10.1103/PhysRevLett.70.3900.

[72] R. Chu, J. S. Wurtele, J. Notte, A. J. Peurrung, and J. Fajans. Pure electron plasmas in asymmetric traps*. *Physics of Fluids B: Plasma Physics*, 5(7):2378–2386, 1993. doi: 10.1063/1.860721. URL https://doi.org/10.1063/1.860721.

[73] N. C. Hurst, J. R. Danielson, D. H. E. Dubin, and C. M. Surko. Adiabatic behavior of an elliptical vortex in a time-dependent external strain flow. *Phys. Rev. Fluids*, 6:054703, May 2021. doi: 10.1103/PhysRevFluids.6.054703. URL https://link.aps.org/doi/10.1103/PhysRevFluids.6.054703.

[74] A. T. Rezakhani, A. K. Pimachev, and D. A. Lidar. Accuracy versus run time in an adiabatic quantum search. *Phys. Rev. A*, 82:052305, Nov 2010. doi: 10.1103/PhysRevA.82.052305. URL https://link.aps.org/doi/10.1103/PhysRevA.82.052305.

[75] Ari Mizel, Daniel A. Lidar, and Morgan Mitchell. Simple proof of equivalence between adiabatic quantum computation and the circuit model. *Phys. Rev. Lett.*, 99:070502, Aug 2007. doi: 10.1103/PhysRevLett.99.070502. URL https://link.aps.org/doi/10.1103/PhysRevLett.99.070502.

[76] T. M. O'Neil. Centrifugal separation of a multispecies pure ion plasma. *The Physics of Fluids*, 24(8):1447–1451, 08 1981. ISSN 0031-9171. doi: 10.1063/1.863565. URL https://doi.org/10.1063/1.863565.

[77] D. J. Larson, J. C. Bergquist, J. J. Bollinger, Wayne M. Itano, and D. J. Wineland. Sympathetic cooling of trapped ions: A laser-cooled two-species nonneutral ion plasma. *Phys. Rev. Lett.*, 57:70–73, Jul 1986. doi: 10.1103/PhysRevLett.57.70. URL https://link.aps.org/doi/10.1103/PhysRevLett.57.70.

[78] G. B. Andresen, M. D. Ashkezari, M. Baquero-Ruiz, W. Bertsche, P. D. Bowe, E. Butler, C. L. Cesar, S. Chapman, M. Charlton, A. Deller, S. Eriksson, J. Fajans, T. Friesen, M. C. Fujiwara, D. R. Gill, A. Gutierrez, J. S. Hangst, W. N. Hardy,

M. E. Hayden, A. J. Humphries, R. Hydomako, S. Jonsell, N. Madsen, S. Menary, P. Nolan, A. Olin, A. Povilus, P. Pusa, F. Robicheaux, E. Sarid, D. M. Silveira, C. So, J. W. Storey, R. I. Thompson, D. P. van der Werf, J. S. Wurtele, and Y. Yamazaki. Centrifugal separation and equilibration dynamics in an electron-antiproton plasma. *Phys. Rev. Lett.*, 106:145001, Apr 2011. doi: 10.1103/PhysRevLett.106.145001. URL https://link.aps.org/doi/10.1103/PhysRevLett.106.145001.

[79] Sangchul Lee. Why does this nominally divergent limit of an infinite sum of bessel functions converge. Mathematics Stack Exchange. URL https://math.stackexchange.com/q/4853532. (version: 2024-01-30).

[80] M. J. Drinkwine and D. Lichtman. Electron stimulated desorption: A critical review. *Progress in Surface Science*, 8(3):123–142, 1977. ISSN 0079-6816. doi: https://doi.org/10.1016/0079-6816(77)90002-8. URL https://www.sciencedirect.com/science/article/pii/0079681677900028.

[81] R.D. Ramsier and J.T. Yates. Electron-stimulated desorption: Principles and applications. *Surface Science Reports*, 12(6):246–378, 1991. ISSN 0167-5729. doi: https://doi.org/10.1016/0167-5729(91)90013-N. URL https://www.sciencedirect.com/science/article/pii/016757299190013N.

[82] M. Haubner, V. Baglin, and B. Henrist. Electron conditioning of technical surfaces at cryogenic and room temperature in the 0–1 kev energy range. *Vacuum*, 207:111656, 2023. ISSN 0042-207X. doi: https://doi.org/10.1016/j.vacuum.2022.111656. URL https://www.sciencedirect.com/science/article/pii/S0042207X22007783.

[83] J. B. Camp, T. W. Darling, and Ronald E. Brown. Macroscopic variations of surface potentials of conductors. *Journal of Applied Physics*, 69(10):7126–7129, 1991. doi: 10.1063/1.347601. URL https://doi.org/10.1063/1.347601.

[84] M. Nonnenmacher, M. P. O'Boyle, and H. K. Wickramasinghe. Kelvin probe force microscopy. *Applied Physics Letters*, 58(25):2921–2923, 1991. doi: 10.1063/1.105227. URL https://doi.org/10.1063/1.105227.

[85] N. Gaillard, M. Gros-Jean, D. Mariolle, F. Bertin, and A. Bsiesy. Method to assess the grain crystallographic orientation with a submicronic spatial resolution using kelvin probe force microscope. *Applied Physics Letters*, 89(15):154101, 2006. doi: 10.1063/1.2359297. URL https://doi.org/10.1063/1.2359297.

[86] C. D. Fosco, F. C. Lombardo, and F. D. Mazzitelli. Electrostatic interaction due to patch potentials on smooth conducting surfaces. *Phys. Rev. A*, 88:062501, Dec 2013. doi: 10.1103/PhysRevA.88.062501. URL https://link.aps.org/doi/10.1103/PhysRevA.88.062501.

[87] K. Li, H. Yin, C. Song, M. Hu, S. Wang, P. Luo, and Z. Zhou. Precision improvement of patch potential measurement in a scanning probe equipped torsion pendulum. *Review of Scientific Instruments*, 93(6):065110, 06 2022. ISSN 0034-6748. doi: 10.1063/5.0091226. URL https://doi.org/10.1063/5.0091226.

[88] J. L. Garrett, J. Kim, and J. N. Munday. Measuring the effect of electrostatic patch potentials in casimir force experiments. *Phys. Rev. Res.*, 2:023355, Jun 2020. doi: 10.1103/PhysRevResearch.2.023355. URL https://link.aps.org/doi/10.1103/PhysRevResearch.2.023355.

[89] D. A. Hite, K. S. McKay, and D. P. Pappas. Surface science motivated by heating of trapped ions from the quantum ground state. *New Journal of Physics*, 23(10): 103028, oct 2021. doi: 10.1088/1367-2630/ac2c2c. URL https://dx.doi.org/10.1088/1367-2630/ac2c2c.

[90] J. H. Parker Jr. and R. W. Warren. Kelvin Device to Scan Large Areas for Variations in Contact Potential. *Review of Scientific Instruments*, 33(9):948–950, 12 2004. ISSN 0034-6748. doi: 10.1063/1.1718036. URL https://doi.org/10.1063/1.1718036.

[91] S. Robertson, Z. Sternovsky, and B. Walch. Reduction of asymmetry transport in the annular penning trap. *Physics of Plasmas*, 11(5):1753–1756, 2004. doi: 10.1063/1.1688337. URL https://doi.org/10.1063/1.1688337.

[92] C. Benvenuti and N. Hilleret. Cold bore experiments at cern isr. *Nuclear Science, IEEE Transactions on*, 26:4086 – 4088, 07 1979. doi: 10.1109/TNS.1979.4330707. URL https://doi.org/10.1109/TNS.1979.4330707.

[93] J. B. Camp, T. W. Darling, and Ronald E. Brown. Effect of crystallites on surface potential variations of Au and graphite. *Journal of Applied Physics*, 71(2):783–785, 01 1992. ISSN 0021-8979. doi: 10.1063/1.351358. URL https://doi.org/10.1063/1.351358.

[94] E.D. Hunter, C. Amsler, H. Breuker, S. Chesnevskaya, G. Costantini, R. Ferragut, M. Giammarchi, A. Gligorova, G. Gosta, H. Higaki, Y. Kanai, C. Killian, V. Kletzl, V. Kraxberger, N. Kuroda, A. Lanz, M. Leali, V. Mäckel, G. Maero, C. Malbrunot, V. Mascagna, Y. Matsuda, S. Migliorati, D.J. Murtagh, Y. Nagata, A. Nanda, L. Nowak, E. Pasino, M. Romé, M.C. Simon, M. Tajima, V. Toso, S. Ulmer, U. Uggerhøj, L. Venturelli, A. Weiser, E. Widmann, T. Wolz, Y. Yamazaki, and J. Zmeskal. Minimizing plasma temperature for antimatter mixing experiments. *EPJ Web of Conferences*, 262:01007, 2022. ISSN 2100-014X. doi: 10.1051/epjconf/202226201007. URL http://dx.doi.org/10.1051/epjconf/202226201007.

[95] Johnny K. Jennings, Ross L. Spencer, and K. C. Hansen. Numerical calculation of axisymmetric electrostatic modes for cold finite-length non-neutral plasmas. *Physics of Plasmas*, 2(7):2630–2639, 07 1995. ISSN 1070-664X. doi: 10.1063/1.871228. URL https://doi.org/10.1063/1.871228.

[96] J. H. Malmberg and C. F. Driscoll. Long-time containment of a pure electron plasma. *Phys. Rev. Lett.*, 44:654–657, Mar 1980. doi: 10.1103/PhysRevLett.44.654. URL https://link.aps.org/doi/10.1103/PhysRevLett.44.654.

[97] D. L. Eggleston, C. F. Driscoll, B. R. Beck, A. W. Hyatt, and J. H. Malmberg. Parallel energy analyzer for pure electron plasma devices. *Physics of Fluids B: Plasma Physics*,

4(10):3432–3439, 10 1992. ISSN 0899-8221. doi: 10.1063/1.860399. URL https://doi.org/10.1063/1.860399.

[98] E. D. Hunter, J. Fajans, N. A. Lewis, A. P. Povilus, C. Sierra, C. So, and D. Zimmer. Plasma temperature measurement with a silicon photomultiplier (SiPM). *Review of Scientific Instruments*, 91(10):103502, 10 2020. ISSN 0034-6748. doi: 10.1063/5.0006672. URL https://doi.org/10.1063/5.0006672.

[99] J. Fajans, W. Bertsche, K. Burke, S. F. Chapman, and D. P. van der Werf. Effects of extreme magnetic quadrupole fields on penning traps and the consequences for antihydrogen trapping. *Phys. Rev. Lett.*, 95:155001, Oct 2005. doi: 10.1103/PhysRevLett.95.155001. URL https://link.aps.org/doi/10.1103/PhysRevLett.95.155001.

[100] D. J. Griffiths. *Introduction to electrodynamics*. Fourth edition. Boston : Pearson, [2013] ©2013, 2013. URL https://search.library.wisc.edu/catalog/9910134691602121.

[101] D. H. E. Dubin, A. A. Kabantsev, and C. F. Driscoll. Enhanced superbanana transport caused by chaotic scattering across an asymmetric separatrix a). *Physics of Plasmas*, 19(5):056102, 03 2012. ISSN 1070-664X. doi: 10.1063/1.3694053. URL https://doi.org/10.1063/1.3694053.

[102] O. D. Kellogg. *Foundations of potential theory*. Springer, 1929. URL http://eudml.org/doc/203661.

[103] D. J. Heinzen, J. J. Bollinger, F. L. Moore, Wayne M. Itano, and D. J. Wineland. Rotational equilibria and low-order modes of a non-neutral ion plasma. *Phys. Rev. Lett.*, 66:2080–2083, Apr 1991. doi: 10.1103/PhysRevLett.66.2080. URL https://link.aps.org/doi/10.1103/PhysRevLett.66.2080.

[104] D. H. E. Dubin. Theory of electrostatic fluid modes in a cold spheroidal non-neutral plasma. *Phys. Rev. Lett.*, 66:2076–2079, Apr 1991. doi: 10.1103/PhysRevLett.66.2076. URL https://link.aps.org/doi/10.1103/PhysRevLett.66.2076.

[105] Daniel H. E. Dubin. Cyclotron waves in a non-neutral plasma column. *Physics of Plasmas*, 20(4):042120, 04 2013. ISSN 1070-664X. doi: 10.1063/1.4802101. URL https://doi.org/10.1063/1.4802101.

[106] M. D. Tinkle and S. E. Barlow. Image charge forces inside conducting boundaries. *Journal of Applied Physics*, 90(3):1612–1624, 08 2001. ISSN 0021-8979. doi: 10.1063/1.1383016. URL https://doi.org/10.1063/1.1383016.

[107] R. S. Van Dyck, F. L. Moore, D. L. Farnham, and P. B. Schwinberg. Number dependency in the compensated penning trap. *Phys. Rev. A*, 40:6308–6313, Dec 1989. doi: 10.1103/PhysRevA.40.6308. URL https://link.aps.org/doi/10.1103/PhysRevA.40.6308.

[108] Eric W. Weisstein. Modified bessel function of the first kind. From MathWorld—A Wolfram Web Resource. URL https://mathworld.wolfram.com/ModifiedBesselFunctionoftheFirstKind.html.

[109] D. H. E. Dubin. Parallel velocity diffusion and slowing-down rate from long-range collisions in a magnetized plasma. *Physics of Plasmas*, 21(5):052108, 05 2014. ISSN 1070-664X. doi: 10.1063/1.4876749. URL https://doi.org/10.1063/1.4876749.

[110] P. H. Yoon. Collisional relaxation of bi-Maxwellian plasma temperatures in magnetized plasmas. *Physics of Plasmas*, 23(7):072114, 07 2016. ISSN 1070-664X. doi: 10.1063/1.4958813. URL https://doi.org/10.1063/1.4958813.

[111] A. W. Hyatt, C. F. Driscoll, and J. H. Malmberg. Measurement of the anisotropic temperature relaxation rate in a pure electron plasma. *Phys. Rev. Lett.*, 59:2975–2978, Dec 1987. doi: 10.1103/PhysRevLett.59.2975. URL https://link.aps.org/doi/10.1103/PhysRevLett.59.2975.

[112] Daniel H. E. Dubin. Collisional transport in non-neutral plasmas. *Physics of Plasmas*, 5(5):1688–1694, 05 1998. ISSN 1070-664X. doi: 10.1063/1.872837. URL https://doi.org/10.1063/1.872837.

[113] F. Anderegg, X.-P. Huang, C. F. Driscoll, E. M. Hollmann, T. M. O'Neil, and D. H. E. Dubin. Test particle transport due to long range interactions. *Phys. Rev. Lett.*, 78:2128–2131, Mar 1997. doi: 10.1103/PhysRevLett.78.2128. URL https://link.aps.org/doi/10.1103/PhysRevLett.78.2128.

[114] T. M. O'Neil. Collision operator for a strongly magnetized pure electron plasma. *The Physics of Fluids*, 26(8):2128–2135, 08 1983. ISSN 0031-9171. doi: 10.1063/1.864394. URL https://doi.org/10.1063/1.864394.

[115] D.R. Nicholson. *Introduction to Plasma Theory*. Wiley, 1983. ISBN 9780471090458. URL https://books.google.com/books?id=fyRRAAAAMAAJ.

[116] B. R. Beck, J. Fajans, and J. H. Malmberg. Measurement of collisional anisotropic temperature relaxation in a strongly magnetized pure electron plasma. *Phys. Rev. Lett.*, 68:317–320, Jan 1992. doi: 10.1103/PhysRevLett.68.317. URL https://link.aps.org/doi/10.1103/PhysRevLett.68.317.

[117] B. R. Beck, J. Fajans, and J. H. Malmberg. Temperature and anisotropic-temperature relaxation measurements in cold, pure-electron plasmas. *Physics of Plasmas*, 3(4):1250–1258, 04 1996. ISSN 1070-664X. doi: 10.1063/1.871749. URL https://doi.org/10.1063/1.871749.

[118] C. Amsler, H. Breuker, S. Chesnevskaya, G. Costantini, R. Ferragut, M. Giammarchi, A. Gligorova, G. Gosta, H. Higaki, E. D. Hunter, C. Killian, V. Kletzl, V. Kraxberger, N. Kuroda, A. Lanz, M. Leali, V. Mäckel, G. Maero, C. Malbrunot, V. Mascagna, Y. Matsuda, S. Migliorati, D. J. Murtagh, Y. Nagata, A. Nanda, L. Nowak, E. Pasino, M. Romé, M. C. Simon, M. Tajima, V. Toso, S. Ulmer, L. Venturelli, A. Weiser,

E. Widmann, T. Wolz, Y. Yamazaki, and J. Zmeskal. Reducing the background temperature for cyclotron cooling in a cryogenic Penning–Malmberg trap. *Physics of Plasmas*, 29(8):083303, 08 2022. ISSN 1070-664X. doi: 10.1063/5.0093360. URL https://doi.org/10.1063/5.0093360.

[119] T. B. Mitchell, J. J. Bollinger, X.-P. Huang, and W. M. Itano. Mode and transport studies of laser-cooled ion plasmas in a Penning trap. *AIP Conference Proceedings*, 457(1):309–318, 01 1999. ISSN 0094-243X. doi: 10.1063/1.57470. URL https://doi.org/10.1063/1.57470.

[120] A. Kabantsev and C. Driscoll. Experiments on neoclassical asymmetric superbanana ripple transport in electron plasma. *Problems of Atomic Science and Technology*, pages 26–30, 01 2010.

[121] G. W. Hart. The effect of a tilted magnetic field on the equilibrium of a pure electron plasma. *Physics of Fluids B: Plasma Physics*, 3(11):2987–2993, 11 1991. ISSN 0899-8221. doi: 10.1063/1.859777. URL https://doi.org/10.1063/1.859777.

[122] J. Aoki, Y. Kiwamoto, Y. Soga, and A. Sanpei. Novel application of electron vortex dynamics to the alignment of magnetic and cylinder axes. *Japanese Journal of Applied Physics*, 43(11R):7777, nov 2004. doi: 10.1143/JJAP.43.7777. URL https://dx.doi.org/10.1143/JJAP.43.7777.

[123] M. Singer, S. König, M. R. Stoneking, P. Steinbrunner, J. R. Danielson, L. Schweikhard, and T. Sunn Pedersen. Non-neutral plasma manipulation techniques in development of a high-capacity positron trap. *Review of Scientific Instruments*, 92(12):123504, 12 2021. ISSN 0034-6748. doi: 10.1063/5.0067666. URL https://doi.org/10.1063/5.0067666.

[124] S. Eliseev, K. Blaum, M. Block, C. Droese, M. Goncharov, E. Minaya Ramirez, D. A. Nesterenko, Yu. N. Novikov, and L. Schweikhard. Phase-imaging ion-cyclotron-resonance measurements for short-lived nuclides. *Phys. Rev. Lett.*, 110:082501, Feb 2013. doi: 10.1103/PhysRevLett.110.082501. URL https://link.aps.org/doi/10.1103/PhysRevLett.110.082501.

[125] D. A. Nesterenko, T. Eronen, A. Kankainen, L. Canete, A. Jokinen, I. D. Moore, H. Penttilä, S. Rinta-Antila, A. de Roubin, and M. Vilen. Phase-imaging ion-cyclotron-resonance technique at the jyfltrap double penning trap mass spectrometer. *The European Physical Journal A*, 54(9):154, Sep 2018. ISSN 1434-601X. doi: 10.1140/epja/i2018-12589-y. URL https://doi.org/10.1140/epja/i2018-12589-y.

[126] S. Chenmarev, Sz. Nagy, J. J. W. van de Laar, K. Blaum, M. Block, and Ch. E. Düllmann. First application of the phase-imaging ion-cyclotron resonance technique at triga-trap. *The European Physical Journal A*, 59(2):29, Feb 2023. ISSN 1434-601X. doi: 10.1140/epja/s10050-023-00935-7. URL https://doi.org/10.1140/epja/s10050-023-00935-7.

[127] A. Baños. The guiding centre approximation in lowest order. *Journal of Plasma Physics*, 1(3):305–316, 1967. doi: 10.1017/S0022377800003317.

[128] F. Heiße, S. Rau, F. Köhler-Langes, W. Quint, G. Werth, S. Sturm, and K. Blaum. High-precision mass spectrometer for light ions. *Phys. Rev. A*, 100:022518, Aug 2019. doi: 10.1103/PhysRevA.100.022518. URL https://link.aps.org/doi/10.1103/PhysRevA.100.022518.

[129] P. H. Richter. Estimating Errors in Least-Squares Fitting. *Telecommunications and Data Acquisition Progress Report*, 122:107–137, apr 1995.

[130] J. Tellinghuisen. Statistical error propagation. *The Journal of Physical Chemistry A*, 105(15):3917–3921, Apr 2001. ISSN 1089-5639. doi: 10.1021/jp003484u. URL https://doi.org/10.1021/jp003484u.

[131] D.A. Herrup, M.J. Syphers, D.E. Johnson, R.P. Johnson, A.V. Tollestrup, R.W. Hanft, B.C. Brown, M.J. Lamm, M. Kuchnir, and A.D. McInturff. Time variations of fields in superconducting magnets and their effects on accelerators. *IEEE Transactions on Magnetics*, 25(2):1643–1646, 1989. doi: 10.1109/20.92615.

[132] D.A. Herrup, M.J. Syphers, D.E. Johnson, R.P. Johnson, A.V. Tollestrup, R.W. Hanft, B.C. Brown, M.J. Lamm, M. Kuchnir, and A.D. McInturff. Time variations of fields in superconducting magnets and their effects on accelerators. *IEEE Transactions on Magnetics*, 25(2):1643–1646, 1989. doi: 10.1109/20.92615.

[133] B. J. Holzer. Impact of persistent currents on accelerator performance. In *ICTP School on Nonaccelerator Particle Astrophysics*, pages 123–141, 1995.

[134] C. Liu, D. Bruno, A. Marusic, M. Minty, P. Thieberger, and X. Wang. Mitigation of persistent current effects in the rhic superconducting magnets. *Phys. Rev. Accel. Beams*, 22:111003, Nov 2019. doi: 10.1103/PhysRevAccelBeams.22.111003. URL https://link.aps.org/doi/10.1103/PhysRevAccelBeams.22.111003.

[135] W. Fischer, A. Jain, and S. Tepikian. Beam-based measurements of persistent current decay in the relativistic heavy ion collider. *Phys. Rev. ST Accel. Beams*, 4:041002, Apr 2001. doi: 10.1103/PhysRevSTAB.4.041002. URL https://link.aps.org/doi/10.1103/PhysRevSTAB.4.041002.

[136] G. Velev, G. Chlachidze, J. Dimarco, and V. Kashikhin. Measurements of the persistent current decay and snapback effect in nb3sn fermilab-built accelerator prototype magnets. *IPAC 2012 - International Particle Accelerator Conference 2012*, 01 2012.

[137] X. Wang, G. Ambrosio, G. Chlachidze, E. W. Collings, D. R. Dietderich, J. DiMarco, H. Felice, A. K. Ghosh, Godeke A., Gourlay S. A., Marchevsky M., Prestemon S. O., Sabbi G. Sumption, G. V. Velev, Xu X., and A. V. Zlobin. Field errors induced by persistent currents in high-field superconducting accelerator magnets. URL https://lhc-div-mms.web.cern.ch/tests/MAG/docum/hilumi/HE-LHC/persistent/Wang_pc_2.pdf.

[138] S. Izquierdo Bermudez, L. Bottura, and E. Todesco. Persistent-current magnetization effects in high-field superconducting accelerator magnets. *IEEE Transactions on Applied Superconductivity*, 26(4):1–5, 2016. doi: 10.1109/TASC.2016.2519006.

[139] J.J Scholtz, D Dijkkamp, and R.W.A Schmitz. Secondary electron emission properties. *Philips Journal of Research*, 50(3):375–389, 1996. ISSN 0165-5817. doi: https://doi.org/10.1016/S0165-5817(97)84681-5. URL https://www.sciencedirect.com/science/article/pii/S0165581797846815. New Flat, Thin Display Technology.

[140] S. Schulte, G. Hartung, J. Kröger, M. Himmerlich, V. Petit, and M. Taborelli. Energy-resolved secondary-electron emission of candidate beam screen materials for electron cloud mitigation at the large hadron collider. *Phys. Rev. Accel. Beams*, 23:103101, Oct 2020. doi: 10.1103/PhysRevAccelBeams.23.103101. URL https://link.aps.org/doi/10.1103/PhysRevAccelBeams.23.103101.

[141] J. Fajans, E. Gilson, and L. Friedland. Autoresonant (nonstationary) excitation of the diocotron mode in non-neutral plasmas. *Phys. Rev. Lett.*, 82:4444–4447, May 1999. doi: 10.1103/PhysRevLett.82.4444. URL https://link.aps.org/doi/10.1103/PhysRevLett.82.4444.

[142] R. H. Parker, C. Yu, W. Zhong, B. Estey, and H. Müller. Measurement of the fine-structure constant as a test of the standard model. *Science*, 360(6385):191–195, 2018. doi: 10.1126/science.aap7706. URL https://www.science.org/doi/abs/10.1126/science.aap7706.

[143] J. D. Jackson. *Classical electrodynamics*. Wiley, New York, NY, 3rd ed. edition, 1999. ISBN 9780471309321. URL http://cdsweb.cern.ch/record/490457.

A1 Appendix: Electrostatics in a cylindrical conductor

A1.1 Constructing a finite-length solution from an infinite-length solution

Throughout this thesis I use a few analytic solutions to electrostatic problems in the presence of a conducting cylinder. This includes the potential due to a patch of voltage perturbation on the wall of the cylinder, the potential due to a cylindrical electrode, and the potential due to a charged cylinder inside of grounded conducting walls. Many would construct a Green's function for this geometry to solve these problems [143], but in this chapter I describe another method which is more intuitive and surprisingly versatile. It also yields an infinite sum rather than an integral. Of course, with some algebra, these two approaches can be shown to give equivalent results. For me, it is easier to evaluate infinite sums than it is to evaluate numerical integrals—I find that estimating the error due to truncating a sum is simpler than estimating the error from evaluating an integral numerically.

Usually I want to consider some voltage source or charge distribution in the presence of an otherwise grounded conducting cylinder of radius R_w. A general solution to the Laplace equation in cylindrical coordinates, with the boundary condition $V(R_w) = 0$, is:

$$V(r,\theta,z) = \sum_{n=0}^{\infty}\sum_{m=1}^{\infty} J_n\left(\frac{\alpha_m^n r}{R_w}\right)\left[a_m^n \exp\left(\frac{\alpha_m^n z}{R_w}\right)\cos(n\theta) + b_m^n \exp\left(\frac{\alpha_m^n z}{R_w}\right)\sin(n\theta)\right.$$
$$\left. + c_m^n \exp\left(-\frac{\alpha_m^n z}{R_w}\right)\cos(n\theta) + d_m^n \exp\left(-\frac{\alpha_m^n z}{R_w}\right)\sin(n\theta)\right], \quad \text{(A1.1)}$$

where $J_n(x)$ is the n'th Bessel function of the first kind, and α_m^n is its m'th zero (not including the one at $x = 0$ for $m \neq 0$). Please excuse my notational abuse putting n as a superscript; it has nothing to do with contraviariance versus covariance, it just helps keep track of which index is which.

Consider that we want to find the potential everywhere due to some charge distribution or voltage perturbation on the trap wall between $z = -l/2$ and $z = +l/2$. The charge distribution is only a function of r and θ: $\rho(r,\theta)$, and the voltage perturbation is along the trap wall, and it is only a function of θ. For example, consider a cylindrical electrode set to a voltage V_0 with a length l in the presence of an otherwise grounded conducting cylinder, as in Fig. A1.1.

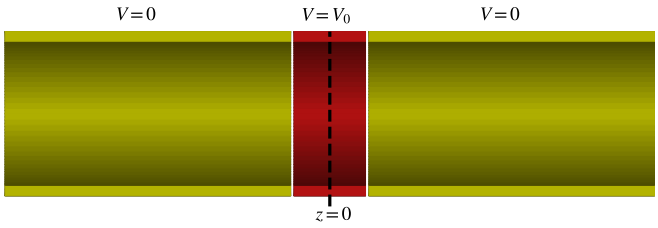

Figure A1.1: The situation we want to find an electrostatic solution for.

The first step is to solve the Poisson equation (or the Laplace equation in the case of a perturbation to the potential along the trap wall) in the situation where our perturbation extends from $z = -\infty$ to $z = +\infty$. This solution will be referred to as $V_{\text{inf}}(r, \theta)$. For the electrode, this is trivial; the voltage is simply $V_{\text{inf}}(r, \theta) = V_0$, as shown in Fig A1.2. Usually this step is trivial, or at least easily completed using image charges, Gauss' law, or the general solution to the Laplace equation in 2–D.

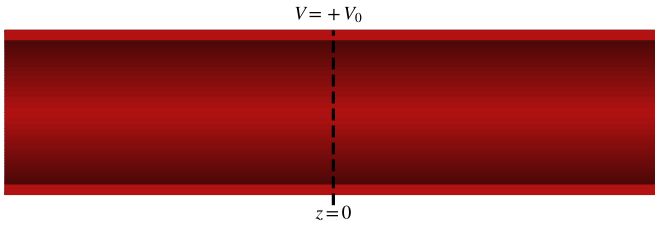

Figure A1.2: The first step to solving the situation in Fig. A1.1. We compose an infinite length version of the problem where the potential is trivially V_0 everywhere.

Next we find a solution to the Laplace equation with two semi-infinite voltage perturbations of opposite sign, as in Fig. A1.3. By symmetry, we know that the potential at $z = 0$ is zero, and the potential at $z = -z_0$ is -1 times the potential at $z = z_0$.

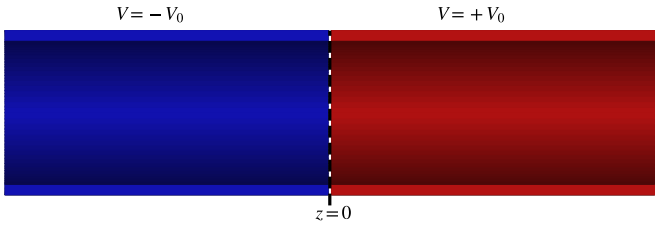

Figure A1.3: Two semi-infinite electrodes with opposite voltage. The second step toward solving the situation in Fig. A1.1.

Therefore we only need to solve for the potential at $z > 0$. Of course we can eliminate exponentially growing terms (and for this specific electrode problem, we can eliminate any term where $n \neq 0$). Because the terms in Eq. A1.1 are all zero at $r = R_w$ and they all solve the Laplace equation, we must add V_{inf}. We have the general solution:

$$V(r, \theta, z > 0) = V_{\text{inf}}(r, \theta) - \sum_{n=0}^{\infty} \sum_{m=1}^{\infty} J_n\left(\frac{\alpha_m^n r}{R_w}\right) \exp\left(-\frac{\alpha_m^n z}{R_w}\right) \left[a_m^n \cos(n\theta) + b_m^n \sin(n\theta)\right]. \quad \text{(A1.2)}$$

The coefficients a_m^n and b_m^n need to be chosen so that when $z = 0$, the boundary condition at $z = 0$ is satisfied. We can do this by finding a "Fourier-Bessel" series. Just like $\sin(n\theta)$ and $\cos(n\theta)$ form an orthogonal set of basis functions with respect to the inner product $\int_0^{2\pi} d\theta$, the Bessel functions $J_n(\alpha_m^n r/R_w)$ form an orthogonal set of basis functions with respect to the inner product $\int_0^{R_w} r dr$. Thus the coefficients can be found using:

$$a_m^n = \frac{2}{\pi R_w^2 J_{n+1}^2(\alpha_m^n)(1 + \delta_{n0})} \int_0^{R_w} r dr \int_0^{2\pi} J_n\left(\frac{\alpha_m^n r}{R_w}\right) \cos(n\theta) V_{\text{inf}}(r, \theta). \quad \text{(A1.3)}$$

$$b_m^{n\neq 0} = \frac{2}{\pi R_w^2 J_{n+1}^2(\alpha_m^n)} \int_0^{R_w} r dr \int_0^{2\pi} J_n\left(\frac{\alpha_m^n r}{R_w}\right) \sin(n\theta) V_{\text{inf}}(r,\theta). \tag{A1.4}$$

In my time using this method, I have found the following indefinite integrals to be useful:

$$\int J_0(cr) r dr = \frac{r J_1(rc)}{c} \tag{A1.5}$$

$$\int J_0(cr) r^3 dr = \frac{2r^2 J_2(rc) - r^3 c J_3(rc)}{c^2} \tag{A1.6}$$

$$\int J_0(cr) \log(r/r_0) r dr = \frac{rc J_1(rc) \log(r/r_0) + J_0(rc)}{c^2} \tag{A1.7}$$

$$\int J_m(cr) r^{m+1} dr = \frac{r^{m+1} J_{m+1}(rc)}{c} \tag{A1.8}$$

$$\int J_m(cr) r^{-m+1} dr = \frac{-r^{-m+1} J_{m-1}(rc)}{c} \tag{A1.9}$$

For our electrode example, of course a_m^n and b_m^n for $n \neq 0$ are 0. a_m^0 (which I will just call a_m) can be found using Eq. A1.5, giving $a_m = 2V_0/\alpha_m^0 J_1(\alpha_m^0)$. Finally, we can compose our desired electrode by adding together two of these solutions shifted left and right by a distance $l/2$, as shown in Fig. A1.4. Thus our general solution is:

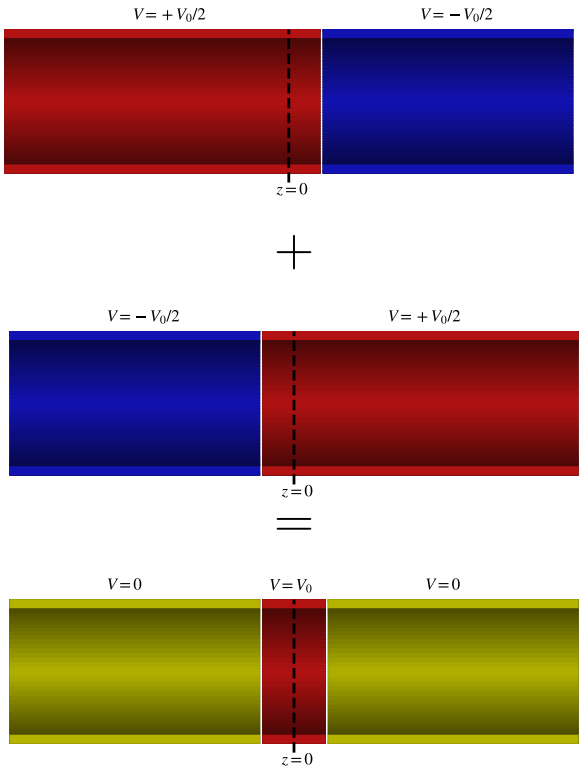

Figure A1.4: The method of solving the electrostatic situation in Fig. A1.1 by adding together two solutions of the situation in Fig. A1.3

$$V(r,\theta,z)=\begin{cases}\frac{1}{2}\sum_{n=0}^{\infty}\sum_{m=1}^{\infty}\left[a_m^n\cos(n\theta)+b_m^n\cos(n\theta)\right]\left[\exp\left(\alpha_m^n\frac{l/2+z}{R_w}\right)-\exp\left(-\alpha_m^n\frac{l/2-z}{R_w}\right)\right]J_n\left(\frac{\alpha_m^n r}{R_w}\right) & z<-\frac{l}{2}\\ \frac{1}{2}\sum_{n=0}^{\infty}\sum_{m=1}^{\infty}\left[a_m^n\cos(n\theta)+b_m^n\cos(n\theta)\right]\left[-\exp\left(-\alpha_m^n\frac{l/2+z}{R_w}\right)+\exp\left(\alpha_m^n\frac{l/2-z}{R_w}\right)\right]J_n\left(\frac{\alpha_m^n r}{R_w}\right) & z>\frac{l}{2}\\ V_{\inf}(r,\theta)-\frac{1}{2}\sum_{n=0}^{\infty}\sum_{m=1}^{\infty}\left[a_m^n\cos(n\theta)+b_m^n\cos(n\theta)\right]\left[\exp\left(-\alpha_m^n\frac{l/2+z}{R_w}\right)+\exp\left(-\alpha_m^n\frac{l/2-z}{R_w}\right)\right]J_n\left(\frac{\alpha_m^n r}{R_w}\right) & -\frac{l}{2}<z<\frac{l}{2}\end{cases} \tag{A1.10}$$

Or the version with azimuthal symmetry:

$$V(r,z)=\begin{cases}\frac{1}{2}\sum_{m=1}^{\infty}a_m\left[\exp\left(\alpha_m^0\frac{l/2+z}{R_w}\right)-\exp\left(-\alpha_m^0\frac{l/2-z}{R_w}\right)\right]J_0\left(\frac{\alpha_m^0 r}{R_w}\right) & z<-\frac{l}{2}\\ \frac{1}{2}\sum_{m=1}^{\infty}a_m\left[-\exp\left(-\alpha_m^0\frac{l/2+z}{R_w}\right)+\exp\left(\alpha_m^0\frac{l/2-z}{R_w}\right)\right]J_0\left(\frac{\alpha_m^0 r}{R_w}\right) & z>\frac{l}{2}\\ V_{\inf}(r)-\frac{1}{2}\sum_{m=1}^{\infty}a_m\left[\exp\left(-\alpha_m^0\frac{l/2+z}{R_w}\right)+\exp\left(-\alpha_m^0\frac{l/2-z}{R_w}\right)\right]J_0\left(\frac{\alpha_m^0 r}{R_w}\right) & -\frac{l}{2}<z<\frac{l}{2}\end{cases} \tag{A1.11}$$

For $z\neq\pm l/2$, these equations converge because for large m, α_m^n increases by π for each step of m, and the arguments of the exponentials are all increasingly negative with increasing m. Thus, it is easy to create an order of magnitude estimate for how many terms need to be summed to achieve a certain precision. However when z approaches $\pm l/2$, these sums typically form an alternating sum with the summand decreasing like $m^{-1/2}$—not very impressive convergence. The electric field typically diverges when z is exactly $\pm l/2$. When evaluating charged particle trajectories, for example, the electric field is actually what I am more interested in calculating. When evaluating these equations in code, I typically prepare the coefficients a_m^n and the zeros α_m^n ahead of time up to some maximum $n=N$ and $m=M$. I come to an estimate of how close I can get to the boundaries while achieving an approximate maximum error of $\epsilon\ll 1$ by setting $\ln\epsilon=M\pi(l/2-z)/R_w\rightarrow z-l/2=-R_w\ln\epsilon/M$. If I want to evaluate the electric field or the potential at smaller separations from the boundaries, I will simply evaluate these quantities at a few points farther from the boundary and extrapolate to the desired point.

A1.2 A charged cylinder in a grounded conducting cylinder

In most of my plasma equilibrium solvers, I represent the plasma as a grid of "charged rings" of length δz, outer radius r_o, and inner radius $r_i=r_o-\delta_r$. A grid is set up to record the charge density ρ in each charged ring. Once a guess is formed for the charge density, we need to find the potential in the center of each ring—the potential at $r=(r_i+r_0)/2$, or at $r=0$ for the innermost ring. To do this, we need to find the potential everywhere for a ring of charge density ρ with an inner and an outer radius and a length δz. The first step is to simply realize that we can form this situation by subtracting a cylinder of charge with radius $r_p=r_i$ from a cylinder with radius $r_p=r_o$, as shown in Fig. A1.5. Thus we really only need to find the potential everywhere due to a charged cylinder with radius r_p.

I use the subscript p standing for "plasma" because the same calculation comes up when we want to find the space charge potential of a cold nonneutral plasma (Debye length much smaller than radius) which is much longer than the trap wall radius, as discussed in the introduction. Using Gauss' law, we can find that the potential in this infinite length situation

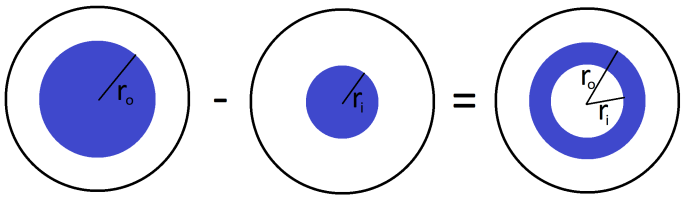

Figure A1.5: We subtract two charged cylinders to find an electrostatic solution for a cylindrical ring with an inner and an outer radius.

is:

$$V_{\inf}(r) = \begin{cases} \dfrac{\lambda}{2\pi\epsilon_0}\left[\ln\left(\dfrac{r_p}{R_w}\right) + \dfrac{r^2 - r_p^2}{2r_p^2}\right] & r < r_p \\ \dfrac{\lambda}{2\pi\epsilon_0}\ln\left(\dfrac{r}{R_w}\right) & r > r_p \end{cases} \tag{A1.12}$$

where $\lambda = \pi r_p^2 nq$ is the line charge density. Integrating Eq. 5.16 using Eqs. A1.5, A1.6, and A1.7, we get:

$$a_m = \frac{\lambda}{\pi\epsilon_0(\alpha_m^0)^2 J_1^2(\alpha_m^0)}\left[-J_0\left(\frac{r_p}{R_w}\alpha_m^0\right) - \frac{r_p a_m^0}{2R_w}J_1\left(\frac{r_p}{R_w}\alpha_m^0\right) + J_2\left(\frac{r_p}{R_w}\alpha_m^0\right) - \frac{r_p\alpha_m^0}{2R_w}J_3\left(\frac{r_p}{R_w}\alpha_m^0\right)\right]. \tag{A1.13}$$

These coefficients can be substituted into Eq. A1.11; then Eq. A1.11 gives the potential everywhere due to a finite-length charged cylinder of radius r_p.

A1.3 Patch electrode using contour integration

In this section I derive the potential due to a patch of length l and angular extent θ_0, as in Fig. A1.6. However, I will not use the technique presented earlier in this appendix. Rather, I will use a more general solution to the Laplace equation in cylindrical coordinates to show how the two methods are equivalent. In particular I hope to show that this method is less efficient. We start with the general solution to the Laplace equation in cylindrical coordinates

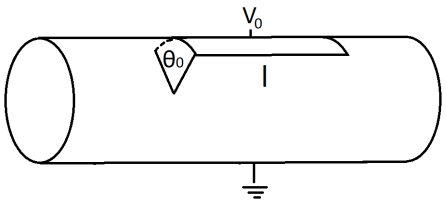

Figure A1.6: The patch of voltage perturbation.

(having already eliminated the sin terms by symmetry):

$$V(r,\theta,z) = \sum_{n=0}^{\infty}\cos(n\theta)\int_{-\infty}^{\infty}\frac{c_n(k)}{I_n(k)}\cos\left(\frac{kz}{R_w}\right)I_n\left(\frac{kr}{R_w}\right)dk, \tag{A1.14}$$

where I_n is the n'th modified Bessel function of the first kind. Setting $r = R_w$ we get our boundary condition, which looks like a Fourier series in θ and a Fourier transform in z:

$$V(R_w, \theta, z) = \sum_{n=0}^{\infty} \cos(n\theta) \int_{-\infty}^{\infty} c_n(k) \cos\left(\frac{kz}{R_w}\right) dk. \tag{A1.15}$$

The Fourier series of a function which is a constant value of 1 between $\theta = -\theta_0/2$ and $\theta = \theta_0/2$ is given by coefficients:

$$d_0 = \frac{\theta_0}{2\pi}; \quad d_{n\neq 0} = \frac{2}{n\pi} \sin(n\theta_0/2). \tag{A1.16}$$

And the Fourier transform of a function which is V_0 from $-l/2$ to $l/2$ and 0 everywhere else is:

$$\frac{1}{2\pi R_w} \int_{-L/2}^{L/2} cos\left(\frac{kz}{R_w}\right) dz = \frac{1}{\pi k} \sin\left(\frac{kL}{2r_w}\right). \tag{A1.17}$$

Thus our voltage everywhere can be written:

$$V = \sum_{n=0}^{\infty} d_n \cos(n\theta) \int_{-\infty}^{\infty} \frac{\sin(kL/2R_w)}{\pi k I_n(k)} \cos\left(\frac{kz}{R_w}\right) I_n\left(\frac{kr}{R_w}\right) dk. \tag{A1.18}$$

Often this is where one leaves things. However, I want to show that we can reach the same answer that we would with the methods presented in the previous section, and I would rather have a sum version of this potential. So to prepare for contour integration, I will rewrite this as:

$$V = \sum_{n=0}^{\infty} d_n \cos(n\theta) \mathrm{Im}\left[\int_{-\infty}^{\infty} \frac{\exp(ik(l/2+z)/R_w) + \exp(ik(l/2-z)/R_w)}{2\pi k I_n(k)} I_n\left(\frac{kr}{R_w}\right) dk\right]. \tag{A1.19}$$

We have to solve integrals of the form

$$\int_{-\infty}^{\infty} \frac{\exp(ikz)}{2\pi k I_m(k)} I_m(kr/r_w) dk. \tag{A1.20}$$

Noting the following relationship between I_m and J_m

$$I_n(r) = i^{-n} J_n(ir);\ I_n(ir) = i^{-n} J_n(-r) = i^n J_n(r), \tag{A1.21}$$

we realize that the integrand has poles at ix wherever $J_n(x)$ has zeros at x. We use the contours shown in Fig. A1.7 to solve this integral. I won't bore the reader with the justifications of why the function falls off sufficiently quickly in every direction to justify these contours. The pole at the origin has residue $(1/2\pi)(r/R_w)^n$. Note that this residue is included in the value of the contour integral if the origin is encircled, but either way half his value should be subtracted from the contour integral to correctly get the value of the line integral. After some algebra, we arrive at an expression that is clearly in a similar form to what we would

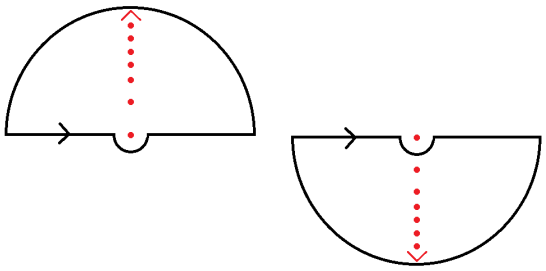

Figure A1.7: We use these two contours when the $z > 0$ and $z < 0$ respectively to solve the integral shown in Eq. A1.20. The red dots show the sequence of poles we encircle, corresponding to zeros of J_n.

have obtained if we solved this the easier way:

$$V(r,\theta,z) = \begin{cases} V_0 \sum_{n=0}^{\infty} d_n \cos(n\theta) \sum_{m=1}^{\infty} \frac{\exp\left(\alpha_m^n \frac{L/2+z}{R_w}\right) - \exp\left(-\alpha_m^n \frac{L/2-z}{R_w}\right)}{\alpha_m^n J_{n+1}(\alpha_m^n)} J_n\left(\alpha_m^n \frac{r}{R_w}\right) & z > l/2 \\ V_0 \sum_{n=0}^{\infty} d_n \cos(n\theta) \sum_{m=1}^{\infty} \frac{-\exp\left(-\alpha_m^n \frac{L/2+z}{R_w}\right) + \exp\left(\alpha_m^n \frac{L/2-z}{R_w}\right)}{\alpha_m^n J_{n+1}(\alpha_m^n)} J_n\left(\alpha_m^n \frac{r}{R_w}\right) & z < -l/2 \\ V_0 \sum_{n=0}^{\infty} d_n \cos(n\theta) \left[\left(\frac{r}{R_w}\right)^n - \sum_{m=1}^{\infty} \frac{\exp\left(-\alpha_m^n \frac{L/2+z}{R_w}\right) + \exp\left(-\alpha_m^n \frac{L/2-z}{R_w}\right)}{\alpha_m^n J_{n+1}(\alpha_m^n)} J_n\left(\alpha_m^n \frac{r}{R_w}\right)\right] & -l/2 < z < l/2 \end{cases} \tag{A1.22}$$